CHEMICAL REVIEWS

pubs.acs.org/CR

Review

Covalent Organic Frameworks: Design, Synthesis, and Functions

Keyu Geng, Ting He, Ruoyang Liu, Sasanka Dalapati, Ke Tian Tan, Zhongping Li, Shanshan Tao, Yifan Gong, Qiuhong Jiang, and Donglin Jiang*

Cite This: *Chem. Rev.* 2020, 120, 8814–8933

Read Online

ACCESS | Metrics & More | Article Recommendations

ABSTRACT: Covalent organic frameworks (COFs) are a class of crystalline porous organic polymers with permanent porosity and highly ordered structures. Unlike other polymers, a significant feature of COFs is that they are structurally predesignable, synthetically controllable, and functionally manageable. In principle, the topological design diagram offers geometric guidance for the structural tiling of extended porous polygons, and the polycondensation reactions provide synthetic ways to construct the predesigned primary and high-order structures. Progress over the past decade in the chemistry of these two aspects undoubtedly established the base of the COF field. By virtue of the availability of organic units and the diversity of topologies and linkages, COFs have emerged as a new field of organic materials that offer a powerful molecular platform for complex structural design and tailor-made functional development. Here we target a comprehensive review of the COF field, provide a historic overview of the chemistry of the COF field, survey the advances in the topology design and synthetic reactions, illustrate the structural features and diversities, scrutinize the development and potential of various functions through elucidating structure–function correlations based on interactions with photons, electrons, holes, spins, ions, and molecules, discuss the key fundamental and challenging issues that need to be addressed, and predict the future directions from chemistry, physics, and materials perspectives.

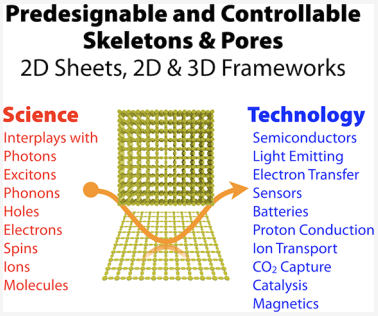

CONTENTS

Special Issue: Porous Framework Chemistry

Received: September 3, 2019
Published: January 22, 2020

https://dx.doi.org/10.1021/acs.chemrev.9b00550
Chem. Rev. 2020, 120, 8814–8933

1. INTRODUCTION

Chemistry is the central science that enables the design and synthesis of new molecules and elucidates molecular origins of various physicochemical properties and functions at different structural levels and time scales. In this context, crystalline molecules are unique because they hold long-range molecular orderings and provide a discrete molecular space or interface in triggering and controlling a diversity of interactions and interplays that constitute the mechanisms of various molecular systems. In particular,, the integration of individual small molecules into ordered structures is an authentic chemical diagram that could not only create new polymers and organic materials but also manifest new properties and functions. However, covalently linking organic molecules to form synthetic macromolecules with well-defined and precise primary and high-order structures, as found in biological polymers such as protein, enzyme, DNA, and RNA systems, is challenging.[1−4] Despite the great advances in polymer chemistry over the past 100 years, synthetic organic polymers are still hardly designed or synthesized, with orderings at both the primary and high-order structural levels.[5]

Biological polymer systems, such as DNA, RNA, and proteins combine covalent bonds and noncovalent interactions to grow

https://dx.doi.org/10.1021/acs.chemrev.9b00550
Chem. Rev. 2020, 120, 8814−8933

well-defined structures in which the covalent bonds determine the sequence of the primary-order chain structure and the noncovalent forces precisely shape up the high-order morphology.[6−8] These coded reaction systems enable the sequential connection of building blocks into covalently linked yet ordered chains in which specific sites or segments are *in situ* programmed and readily organized into high-order structure via noncovalent interactions. By contrast, although it is possible for sequenced chain formation of up to four or five different monomers in synthetic polymerization systems, currently it is almost impossible to create specific sites or segments that can direct hierarchical structural organization through noncovalent interactions to form a well-defined high-order structure; predesignable or programmable high-order structure formation is too far to reach in real synthetic systems. This situation does not become better or is even worse when the polymerization system involves the formation of more complex networks. Inspired by the biological polymer systems, the merge of covalent bonds and noncovalent interactions in one polymerization system to generate a primary-order structure with specific sites or segments that are ready to guide the high-order structure formation seems to hold the key to achieving polymers with predesigned primary and high-order structures. Such a tailor-made polymer system is the ultimate target of chemical science. Ground-breaking synthetic covalent organic frameworks (COFs) enforcing this goal have emerged in the past decade by elaborating the covalent bonds and noncovalent interactions in the polymerization systems.[9]

Using covalent bonds to control the chain conformation is largely dependent on the dimensionality of polymer structures. The basic concept is an exact confinement of the chain growth over a 2D plane in which the polymer skeleton is aligned and ordered.[10] To fulfill such a growth pattern, the geometry-directed topology diagram is the key to guiding each monomer into specific sites on the 2D plane, and the monomers with desired geometries and multiple reactive sites are essential to securing the 2D polymer growth.[11] Consequently, the resulting 2D polymers generate extended polygons with specific units at the knots and edges.[12] The regular 2D polymers are capable of using polygon topology to direct the noncovalent interactions between planes to form layered and extended 2D polymer frameworks with a well-defined high-order structure, named COFs.[13−19] In the same way, if the growth of polymer backbone is precisely guided in a well-defined 3D manner, then 3D COFs with extended structures will become possible.

COFs are a class of fully predesignable polymer that is achieved by topology-diagram-directed polymer growth in conjunction with geometry matching between monomers. This molecular design principle is totally different from those of linear polymers, hyperbranched polymers, cross-linked polymers, and biopolymers, increasing our ability to predesign primary and high-order structures to an unprecedented level. COFs are polymers with unique conformations and morphologies that generate a confined molecular space and interface to interplay with photons, excitons, electrons, holes, spins, ions, and molecules, creating new molecular platforms for structural design and functional development. Progress over the past decade in the field of COFs has continuously increased the freedom of molecular design and steadily shifted it from the structural design to the functional design arena. Most COFs are synthesized as insoluble solids. This limited processability greatly restricts the application scope of COFs. Recently, the development of new synthetic methods including microfluidic systems and gelation-mediated 3D printings has opened a way to explore processable COFs and devices.[20,21] Herein we survey the advances in the basic concepts, design principles, and synthetic reactions; demonstrate the structural features and diversities; deliberate the development and potential of various functions through elucidating structure−function correlations; discuss the bottleneck and challenging issues; and predict the future directions from chemistry, physics, and materials perspectives.

2. DESIGN PRINCIPLE

The essence of the topology design diagram is to elaborate on the direction of covalent bond formation and to guide the polymer backbone growth. To ensure a clear direction of each covalent bond, the monomers are required to have relatively rigid backbones in which the reactive sites are distributed in a distinct geometry. This design concept can be simplified and illustrated with the block model, as shown in Figure 1. Each monomer is present with a specific geometry that reflects the relative positions of reactive sites. The covalent bonds guide the spatial orientation and determine the relative positions of the next monomer units; repeating this rule in each connection confines the chain growth directions in a manner that strictly follows the predesigned topology diagram. This topology diagram and the geometry matching of monomers create the chemical base for the growth and control of the primary-order structure.

As shown in Figure 1A, the combination of planar monomers restricts the growth of the polymer backbones in a 2D manner, leading to the generation of 2D atomic layers with specific topologies.[12−19,21−23] At the same time, the growth of the polymer chain leaves periodically ordered open polygon spaces on the 2D $x-y$ planes. These 2D covalent polymers constitute not only the extended polygon-based primary-order structure but also inherent discrete nanopores.[10,13] Moreover, the rigid skeleton of the 2D covalent polymer endows the system with spatial lattice orientation and crystallinity. Indeed, organic monomers with rigid backbones that meet these requirements are widely available, and they usually hold π-systems.[24] This elementary feature enables another freedom in exploring noncovalent interactions to guide the formation of well-defined high-order structures. Because the π-units in the 2D covalent polymers are located at specific positions with desired orientations, the rigid 2D polymers favor the formation of layered structures in which the relative positions of neighboring layers are directed and mostly controlled by the interlayer interactions. To maximize the attractive energy in the layered structures, 2D covalent polymers stack in a way in which each monomer unit is overlapped. This alignment of 2D covalent polymers along the z direction constitutes the high-order structure of 2D COFs. Therefore, a unique feature of 2D COFs is that they create not only fully ordered π-arrays but also 1D open channels. Clearly, both primary and high-order structures of 2D COFs are predesignable by the monomer structure.

2.1. Two-Dimensional COFs

2D COFs can be designed by using a variety of different topologies; both regular (isotropic topologies) and irregular (anisotropic topologies) polygon skeletons have been developed for the design of COFs. In each case, the lattice structure is highly ordered, and the pore is discrete. The topological diversity provides the basis of the structural diversity of 2D

https://dx.doi.org/10.1021/acs.chemrev.9b00550
Chem. Rev. 2020, 120, 8814−8933

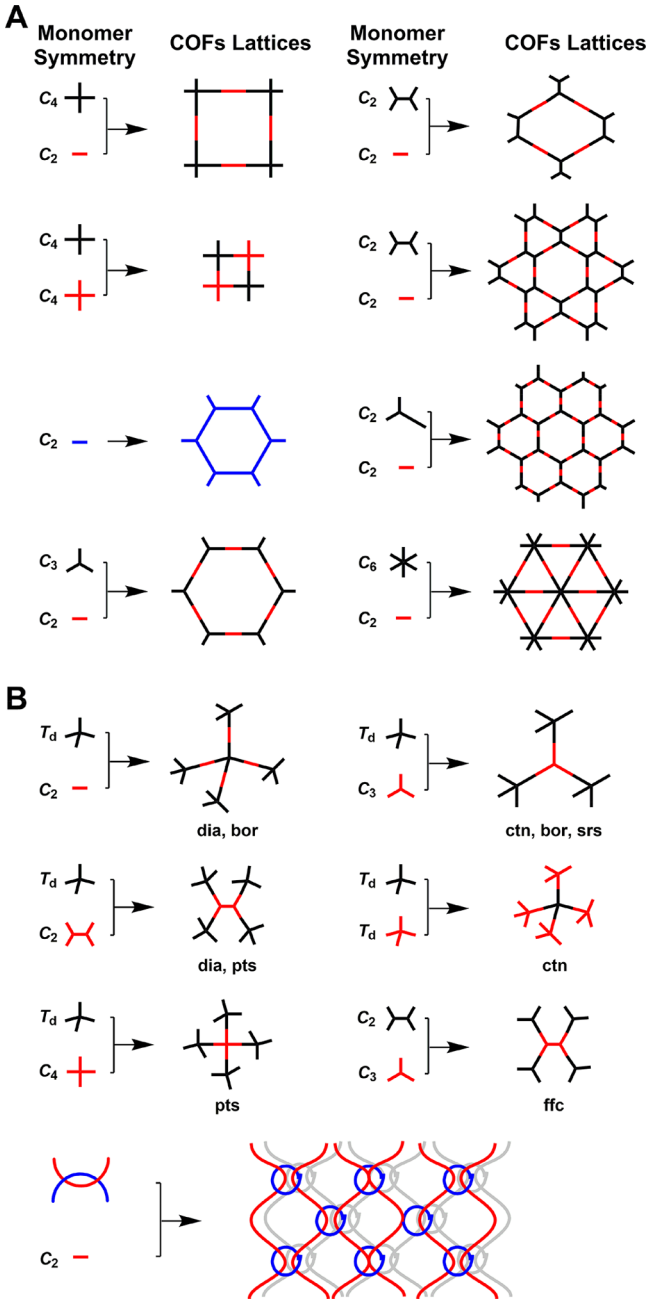

Figure 1. Basic topological diagrams for the design of 2D and 3D COFs.

COFs. Behind each topology, there are huge members of COFs with different building blocks and linkers.

2.1.1. Symmetric Topologies. The topology diagram allows for different combinations of a diversity of monomer geometries to design COFs with different skeletons and pores, leading to the different structural orderings of the frameworks (Figure 1A).[12−14,16,19,25] For example, the combination of $[C_3 + C_2]$ generates hexagonal 2D COFs,[9,26,27] whereas those of $[C_2 + C_2 + C_2]$ and $[C_3 + C_3]$ also form hexagonal COFs but with different pore sizes and π-orderings.[9,26,28] Tetragonal COFs have been synthesized by using the $[C_4 + C_2]$ and $[C_4 + C_4]$ combinations.[29−34] The topology diagram determines the pore size. For example, in the case of $[C_2 + C_2 + C_2]$ and $[C_4 + C_4]$ combinations, the resulting COFs have a possibility of possessing micropores, whereas the $[C_3 + C_2]$, $[C_3 + C_3]$, and $[C_4 + C_2]$ combinations usually yield mesoporous COFs. Moreover, the topology diagram also controls the π-density of the skeletons. The development of the $[C_6 + C_2]$ topology diagram opens a way to design the microporous COFs with the highest π-density and the smallest pore.[12,35] As shown in Figure 2, the resulting COFs have triangular pores with a pore size of only $L/\sqrt{3}$, which is $1/\sqrt{3}$ and 1/3 times those of tetragonal and hexagonal COFs, respectively, and the distance between two vertices is fixed at L. Moreover, the π-unit density is $2/\sqrt{3}\ L^{-2}$, which is $2/\sqrt{3}$ and 2/3 times those of tetragonal and hexagonal COFs, respectively. The small micropore and high π-unit density render the trigonal COFs able to develop molecular separation and semiconducting functionalities. Furthermore, hexa-substituted C_3-symmetric vertices enable the construction of triangular lattices with dual-pore structures.[35]

By developing a C_3-symmetric macrocyclic as a knot, a kagome COF with one central dodecagonal and six periphery triangular pores has been demonstrated (Figure 1A). Another interesting topology diagram is the $[C_2 + C_2]$ combination that yields two different skeletons and pore structures (Figure 1A). One type is the rhombic skeleton with one kind of pore, and the other type is the kagome skeleton that has one central hexagonal mesopore and six periphery trigonal micropores. The knot and linker structures determine the resulting topology; the bulkiness of the knot unit and the strength of interlayer interactions likely dominate the type of topology.[36,37] A general tendency is that the C_2-symmetric knots with large π-systems that favor strong $\pi-\pi$ interactions lead to the formation of the rhombic polygons, whereas other C_2-symmetric knots results in kagome-type architectures. The weak interlayer $\pi-\pi$ interactions in the kagome polygon can be compensated by the docking effect of the linker parts that originates from their twisted structures.[38]

2.1.2. Asymmetric Topologies. The above topology diagrams are based on the [1 + 1] two-component systems consisting of one knot and one linker that are alternately linked to form regular polygons and isotropic tiling structures. However, the conventional [1 + 1] two-component combination prerequisite for COFs greatly limits the diversity of COFs. For example, in the case of 1 knot and 10 linkers, only 10 different COFs can be designed and generated. The introduction of a multiple-component (MC) concept to the design of COFs breaks this [1 + 1] combination-based diversity limitation. The essence of the multiple-component strategy is to use two or three different linkers for the design of COF skeletons (Figure 3A,B).[11,39] For example, a combination of one C_3-symmetric knot and 10 C_2-symmetric linkers could generate 210 different hexagonal COFs. The [1 + 2] three-component strategies lead to the generation of two different hexagonal COFs depending on the molar ratio of two linkers at 1/2 or 2/1. The [1 + 3] four-component strategy generates hexagonal COFs that consist of three different pairs of edges. Because of the existence of the MCs in the skeletons, the structural complexity is greatly enhanced.

In relation to this point, one significant feature of the multiple-component strategy is that the lattice changes from isotopic tiling in [1 + 1] two-component systems to anisotropic tiling, and the pore changes from a regular hexagonal pore to an unusually shaped hexagonal pore. Indeed, 10 different C_2-symmetric linkers with different lengths, π-systems, and redox activities have been synthesized. For example, 48 three-component COFs have been prepared from 24 different combinations of the [1 + 2] scheme, and eight four-component COFs have been prepared based on the [1 + 3] scheme.[11] All of these COFs have a discrete lattice structure and single type of

https://dx.doi.org/10.1021/acs.chemrev.9b00550
Chem. Rev. 2020, 120, 8814−8933

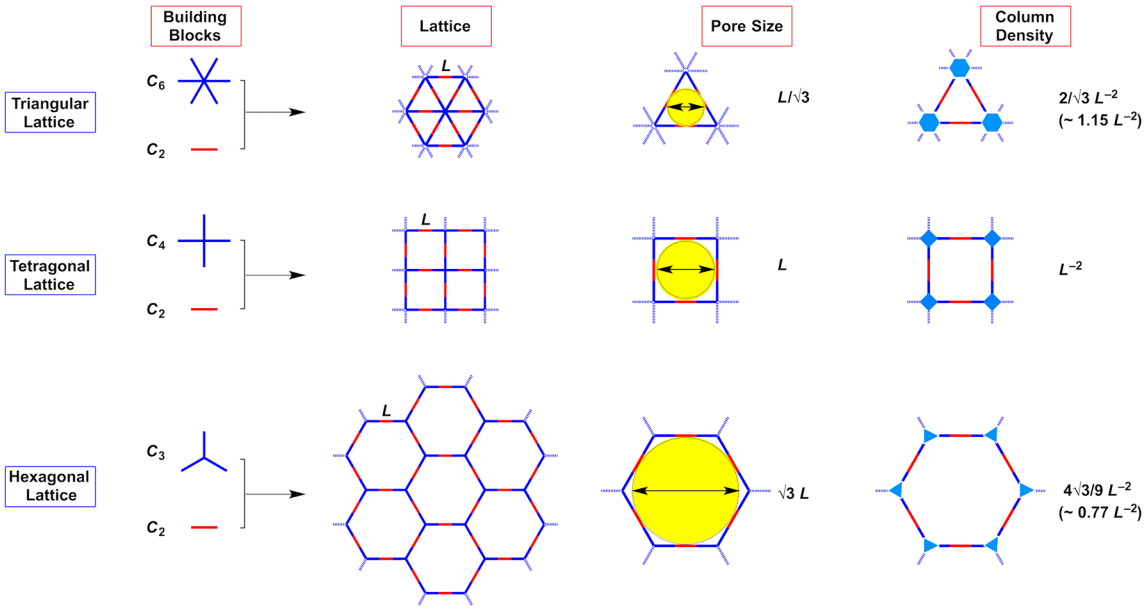

Figure 2. Dependency of pore size and column π-density of 2D COFs on topologies.

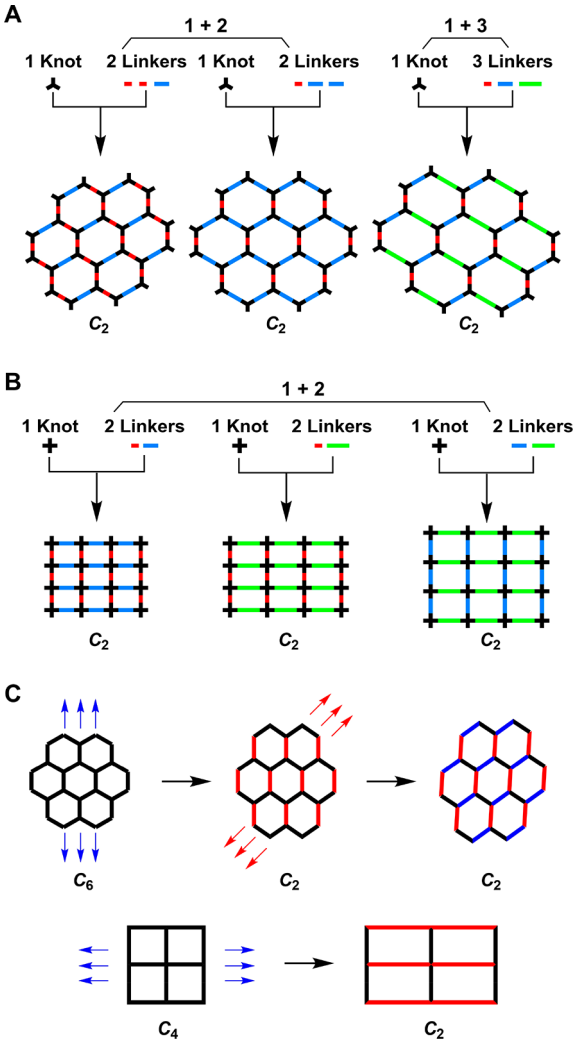

Figure 3. Multicomponent (MC) design strategy for (A) hexagonal COFs, (B) tetragonal COFs, and (C) stretching of regular polygons by MC strategy.

pores, suggesting the phase integrity of multicomponent COFs. This strategy is tolerant for integrating multiple-component donor and acceptor units into one framework. In these COFs, the specific arrays of donor and acceptor π-columns could trigger intercolumnar interactions, thus leading to the generation of exceptional conductivity that is not a simple summation of the [1 + 1] COF counterparts. Notably, this multiple-component strategy is not limited to hexagonal COFs but is applicable to tetragonal skeletons as well (Figure 3B). In this case, the combination of one knot and two linkers based on the [1 + 2] three-component strategy can increase the number of tetragonal COFs and the yields anisotropic tiling and specially shaped pores (Figure 3B). Using phthalocyanine units as one knot and combining with 10 different linkers can generate 45 tetragonal COFs in which the two sets of edges are different from each other and are tiled in an asymmetric manner.[11] Similarly, the [2 + 1] three-component system using two C_3-symmetric units with different sizes as knots and one C_2-symmetric linker also enable the design of an asymmetric hexagonal COF.[40]

An effective route to multiple-pore COF construction has been achieved by using a desymmetrized knot.[41] The desymmetry units including 5-(4-formylphenyl) isophthalaldehyde and 5-((4-formylphenyl) ethylene)isophthalaldehyde) bear arms of different lengths; upon condensation with C_2-symmetric edges, these desymmetrized vertices form HP-COF-1 and HP-COF-2, which possess two types of hexagonal pores with different shapes and sizes (Figure 1A).[42] As a powerful tool for constructing heterogonous porous structures in one COF skeleton, the multiple-component strategy has also been applied to a special kagome topology that endows the TPE-based COFs with an intrinsic dual-pore structure (Figure 1A). For example, the condensation of TPE knots (4,4′,4″,4‴-(ethene-1,1,2,2-tetrayl)tetraaniline (ETTA)) with two dialdehydes of different lengths at a 1/1 molar ratio leads to the synthesis of two triple-pore COFs, that is, SIOC-COF-1 and SIOC-COF-2.[39]

2.2. Three-Dimensional COFs

In contrast with 2D COFs that usually require planar building units, the design of 3D COFs needs at least one building unit

https://dx.doi.org/10.1021/acs.chemrev.9b00550
Chem. Rev. 2020, 120, 8814−8933

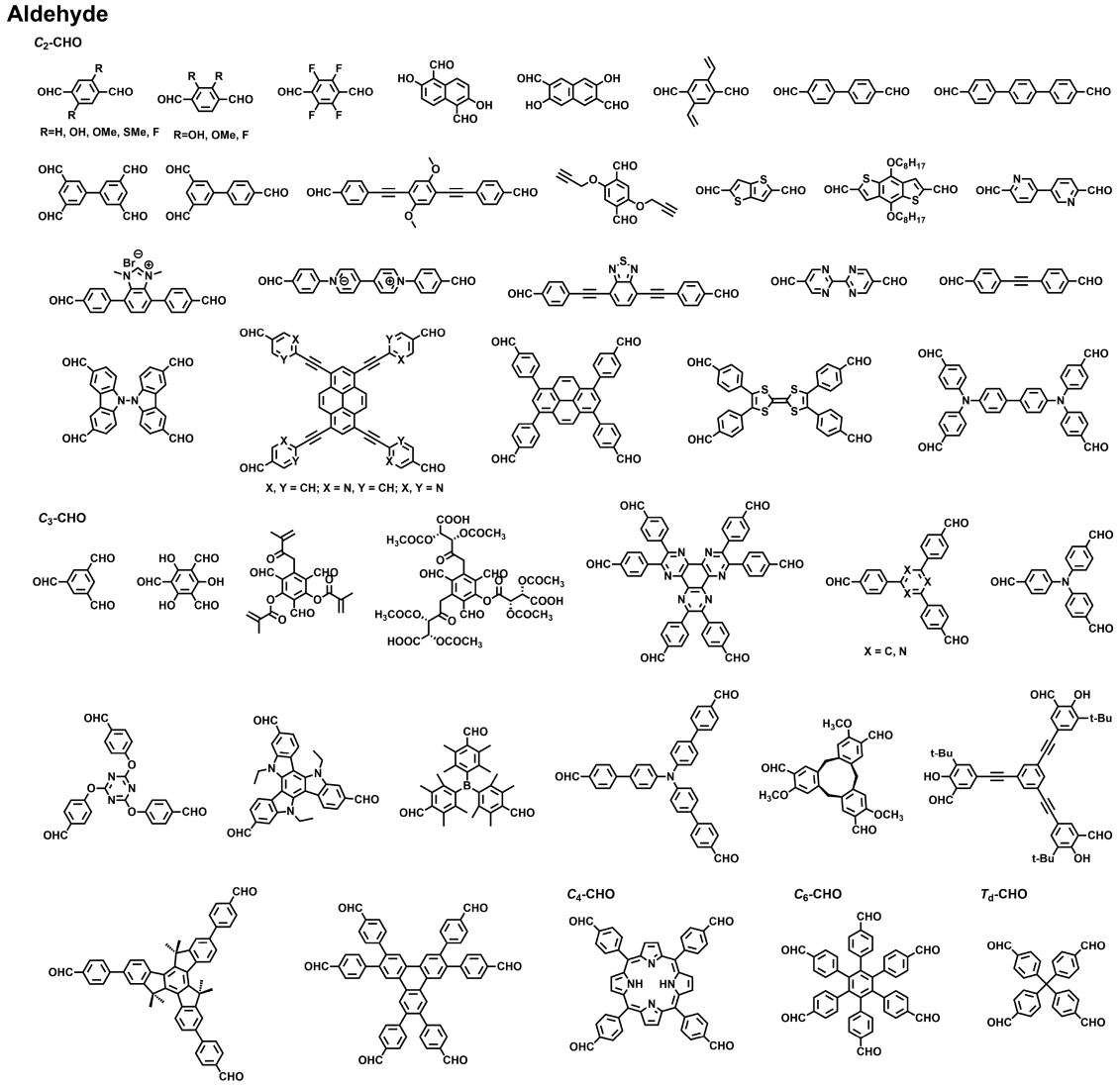

Figure 4. Typical examples of C_2, C_3, C_4, C_6, and T_d symmetric monomers with aldehyde functional groups for the synthesis of COFs.

having T_d or orthogonal geometry that guides the extension of the polymer backbone into a covalently linked 3D network (Figure 1B). For this purpose, there are different combinations for merging T_d or an orthogonal knot with C_1, C_2, C_3, C_4, and T_d to form 3D COFs, and the polymer chains are interpenetrated and folded in different multifolds to form skeletons and pores (Figure 1B).[13,19,43−46]

On the basis of the topology diagrams, 3D COFs can be categorized into different networks, including **ctn**, **bor**, **dia**, **srs**, **rra**, and **pts** (Figure 1B). The **ctn** or **bor** network can be achieved by the $[T_d + C_3]$ diagram, which offers a skeleton free of interpenetration, leading to large surface areas.[47−49] The ctn network can also be produced by the $[T_d + T_d]$ diagram.[47] The **dia** network is designed by the $[T_d + C_2]$ diagram that constitutes the largest family of 3D COFs as a result of the broad diversity of linker units.[50−55] In these cases, the polymer backbones are interpenetrated in a multifold manner to form 1D channels. These 1D polygon channels are usually microporous with pore sizes between 0.7 and 1.5 nm. The **srs** net can be formed from a $[T_d + C_3]$ diagram, and SiCOF-5 is the only example that contains a two-fold interpenetrated network.[56] The **pts** network is designed by the $[T_d + C_2]$ and $[T_d + C_4]$ diagrams in which the C_2- or C_4-symmetric unit needs to possess four reactive sites, which form two-fold interpenetrated 3D COFs.[45,57,58] Condensing an orthogonal Cu(II) complex of phenanthroline as a knot with a C_2-symmetric linker forms an interwoven 3D helix COF-505 (Figure 1A).[59] Recently, a rare example of the $[C_2 + C_3]$ diagram has also been developed lately for producing 3D COFs with genetic structural units (GSUs).[46]

Owing to the interpenetrated structures, the topology diagram of 3D COFs hardly predicts how many folds a specific COF would have. This is because the chemical parameter that controls the folding phenomena is still unclear. In this context, distinct from 2D COFs, 3D COFs are hardly predesignable and synthetically controllable. Most 3D COFs are microporous materials; however, they usually have much lower porosity than expected owing to the fact that multifold interpenetration occupies the space. Indeed, how to manage interpenetration and folding remains an issue to be addressed.

3. BUILDING BLOCKS AND STRUCTURAL DIVERSITY

The topology diagram enables the design of COFs with different skeletons and pores and is the origin of COFs diversity. In the topology diagram, the geometry matching of monomers is necessary for the design of COFs (Figure 4−6). The building blocks usually have π-backbones and a rigid conformation to

https://dx.doi.org/10.1021/acs.chemrev.9b00550
Chem. Rev. 2020, 120, 8814−8933

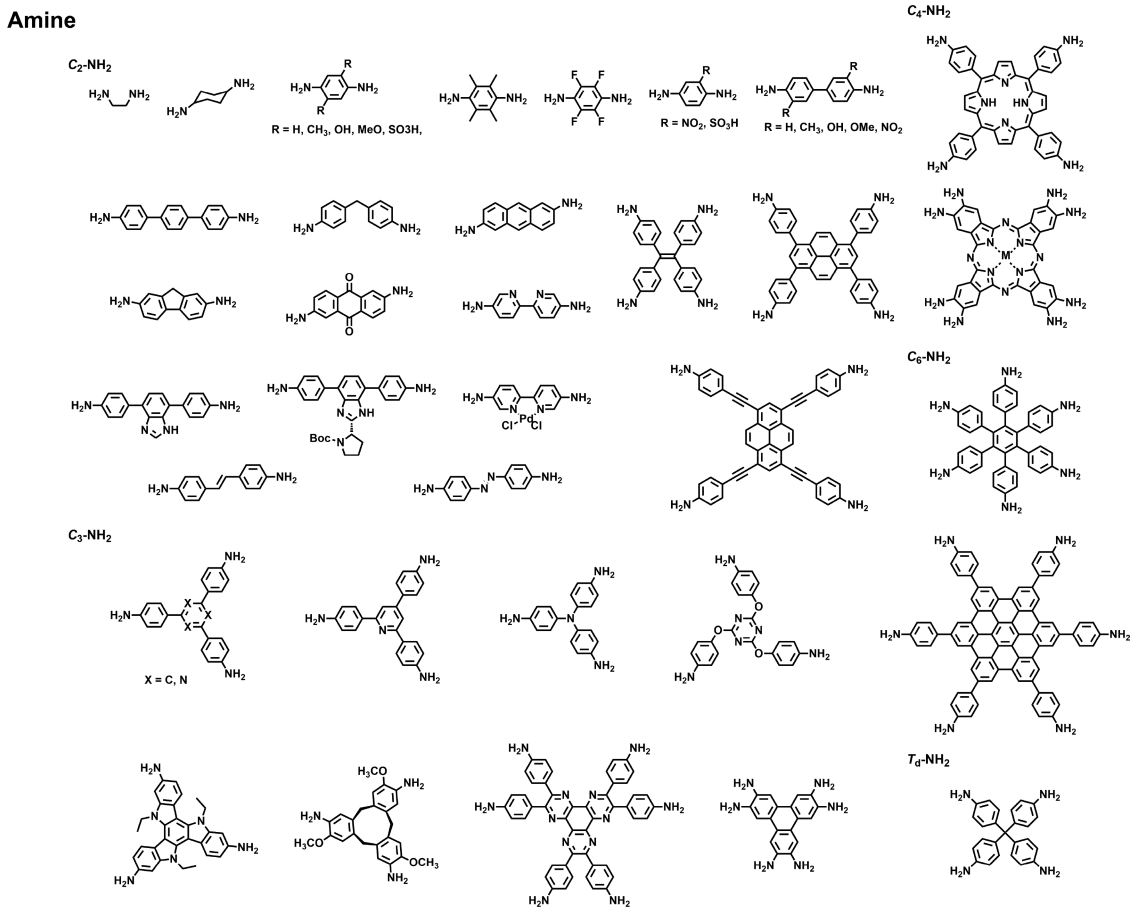

Figure 5. Typical examples of C_2, C_3, C_4, C_6 and T_d symmetric monomers with amine functional groups for the synthesis of COFs.

assume topology-directed bond formation and maintain the 2D planarity of the extended polygons. Indeed, besides geometry, monomers have been explored to show a broad diversity of structures, including different sizes, docking sites, reactive groups, chiral centers, and redox-active, catalytic, and photoactive groups. These variances lead to the generation of various COFs with different structures and functions. Because the structural diversity is highly dependent on the availability of monomers, 3D COFs have less structural diversity that is limited by the availability of T_d-symmetric or orthogonal nodes. The newly developed [C_4 + C_3] strategy expands the structural diversity of 3D COFs. Nevertheless, 3D COFs possess a great potential for expanding their library by developing various π-units as linkers for the condensation with the T_d-symmetric or orthogonal monomers or exploring the possibility of GSUs for constructing 3D structures.

Figures 4−6 illustrate the monomer structures with typical backbone and reactive sites. The backbone ranges from benzene to simple arenes, heterocycles, and macrocycles and can be designed to have different C_2, C_3, C_4, C_6, and T_d geometries. Therefore, more than hundreds of monomers have been explored.

3.1. Two-Dimensional COFs

Two-dimensional COFs are the major family of COFs, owing to the broad diversity of building units. Combining the topology diagram, size, and structure of building units and linkages, 2D COFs can be designed and synthesized into different topologies, skeletons, and pores. This structural diversity reflects the rich chemistry of organic molecules and opens a new route to the multifunctional materials platform.

3.1.1. Hexagonal COFs. On the basis of the different geometries of monomers, hexagonal, tetragonal, kagome, and trigonal COFs have been designed and synthesized (Figures 1A and 4−6). These COFs have different yet discrete π-skeletons as well as pore sizes and shapes. On the basis of the knot structure, the building units of hexagonal COFs can be categorized into different classes, including benzene, triazine, triphenyl benzene, and triphenylene derivatives (Figures 4−6). The smallest benzene knot enables the construction of various COFs, including the boroxine-linked COF-1, the boronate-ester-linked COF-6, COF-11, COF-14, COF-16, COF-18, and Ph-An-COF (pore size = 0.64−2.9 nm),[26,60,61] the imine-linked NUS-9(R), NUS-10(R), COF-LZU1, TpPa-COFs, TpBD-COFs, TpPa-SO_3H-COF, TpPa-(SO_3H-Py)-COF, TpPa-Py-COF, TpBpy-COF, EB-COF:X (X = F, Cl, Br, I), DAAQ-TFP, PI-2-COF, and Tp-Azo, Tp-Stb COFs (pore size = 0.84−2.5 nm),[62−70] the hydrazone-linked COF-42 and COF-JLU4 (pore size = 2.2−2.3 nm),[71,72] the azine-linked ACOF-1 and COF-JLU2 (pore size = 0.94−0.96 nm),[73,74] and the triazine-linked CTF-1 (pore size = 1.2 nm)[75] as well as the C═C-linked COF-701, g-$C_{40}N_3$-COF, g-$C_{31}N_3$-COF, and g-$C_{37}N_3$-COF (pore size = 1.1−3.2 nm).[76] Triphenylbenzene, because of its large size, generates only mesoporous COFs, including the boronate-ester-linked COF-8 and BTP-COF (pore size = 1.64−4.0 nm),[26,77] the imine-linked COF-DhaTab, 2,3-DhaTta, 2,3-DhaTab, TPB-DMTP-COF, TAPB-PDA COF, LZU-20, TPB-TP-COFs, and PI-3-COF (pore size = 3.26−3.9 nm),[70,78−82] the hydrazone-linked LZU-

https://dx.doi.org/10.1021/acs.chemrev.9b00550
Chem. Rev. 2020, 120, 8814−8933

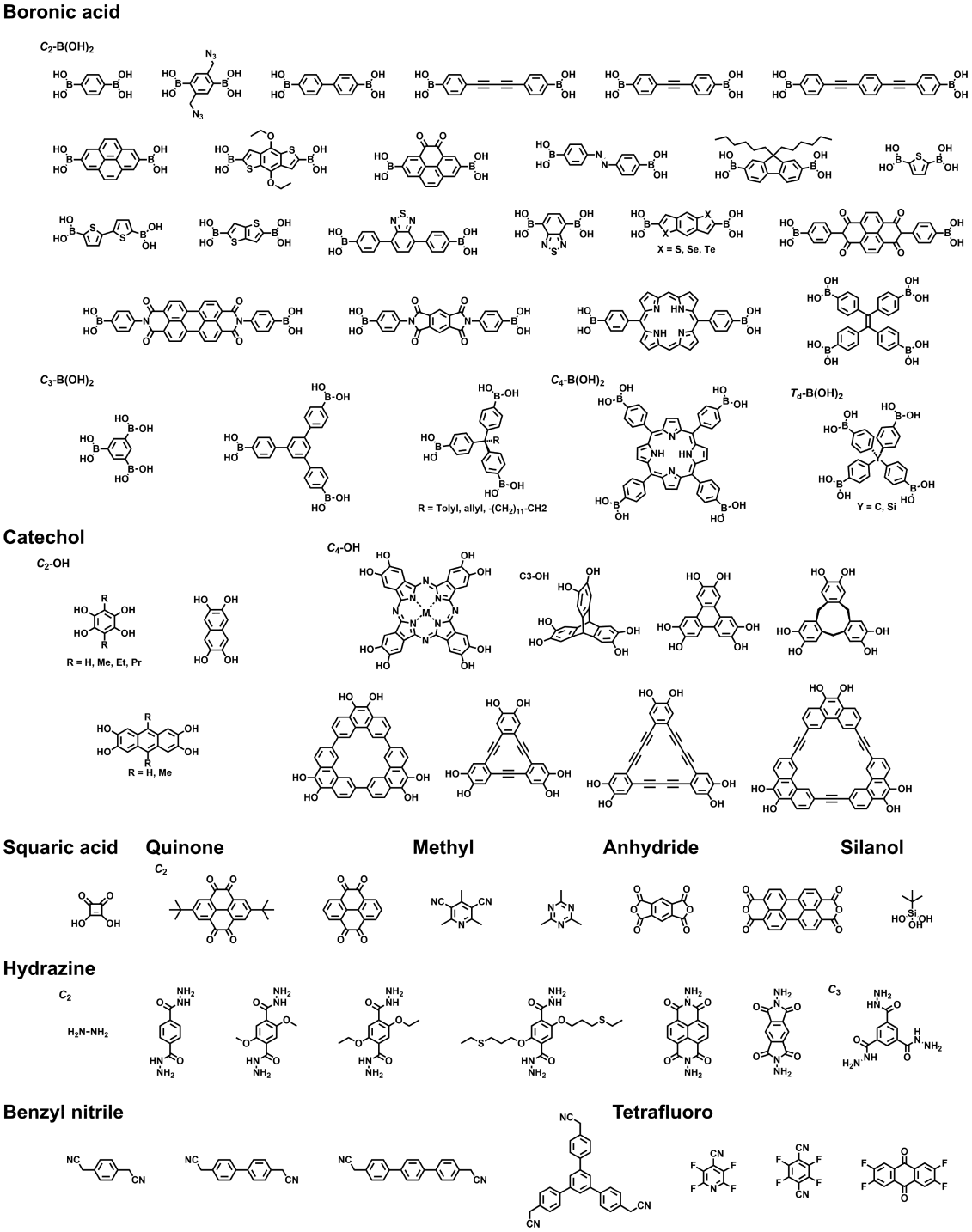

Figure 6. Typical examples of C_2, C_3, C_4, C_6 and T_d symmetric monomers with other functional groups for the synthesis of COFs.

21, COF-43, and TFPT-COF (pore size = 3.5−3.8 nm),[71,78,83] the azine-linked COF-JLU3, LZU-22, and N_x-COF (x = 0, 1, 2, 3) (pore size = 2.4−2.6 nm),[78,84,85] the imide-linked PI-COF-1, PI-COF-2, and PI-COF-3 (pore size = 2.9−5.1 nm),[49] and the C═C-bond-linked 2D-CV-PPVs (pore size = 1.45−3.24 nm)[86] as well as the double-stage-linked NTU-COF-1, NTU-COF-2, TATTA-FPBA-COF, TATTA-FFPBA-COF, TATTA-DFFPBA-COF, HHTP-FPBA-TATTA-COF, HHTP-FFPBA-TATTA-COF, and HHTP-DFFPBA-TATTA-COF (pore size = 2.3−3.1 nm).[87,88] The triphenylene knot leads to the generation of various hexagonal boronate-ester-linked COFs, such as COF-5, COF-6, COF-8, COF-10, TP-COF, HHTP-DBB COF, D−A COF, D_{TP}-A_{NDI}-COF, D_{TP}-A_{PyrDI}-COF, MC-COF-TP, TP-Por COF, COF-316 (JUC-505), COF-318, and JUC-506 (pore size = 1.2−5.3 nm).[9,11,26,27,89−95] Therefore, the [C_3 + C_2] combination is powerful in designing mesoporous hexagonal COFs. Figure 7 illustrates the one-pore structure of typical hexagonal COFs.

3.1.2. Tetragonal COFs. The tetragonal topology diagram enables the use of C_2- and C_4-symmetric monomers as linkers and knots for the structural construction. The C_2-symmetric monomers cover a large number of backbones, including phenyl,

https://dx.doi.org/10.1021/acs.chemrev.9b00550
Chem. Rev. 2020, 120, 8814−8933

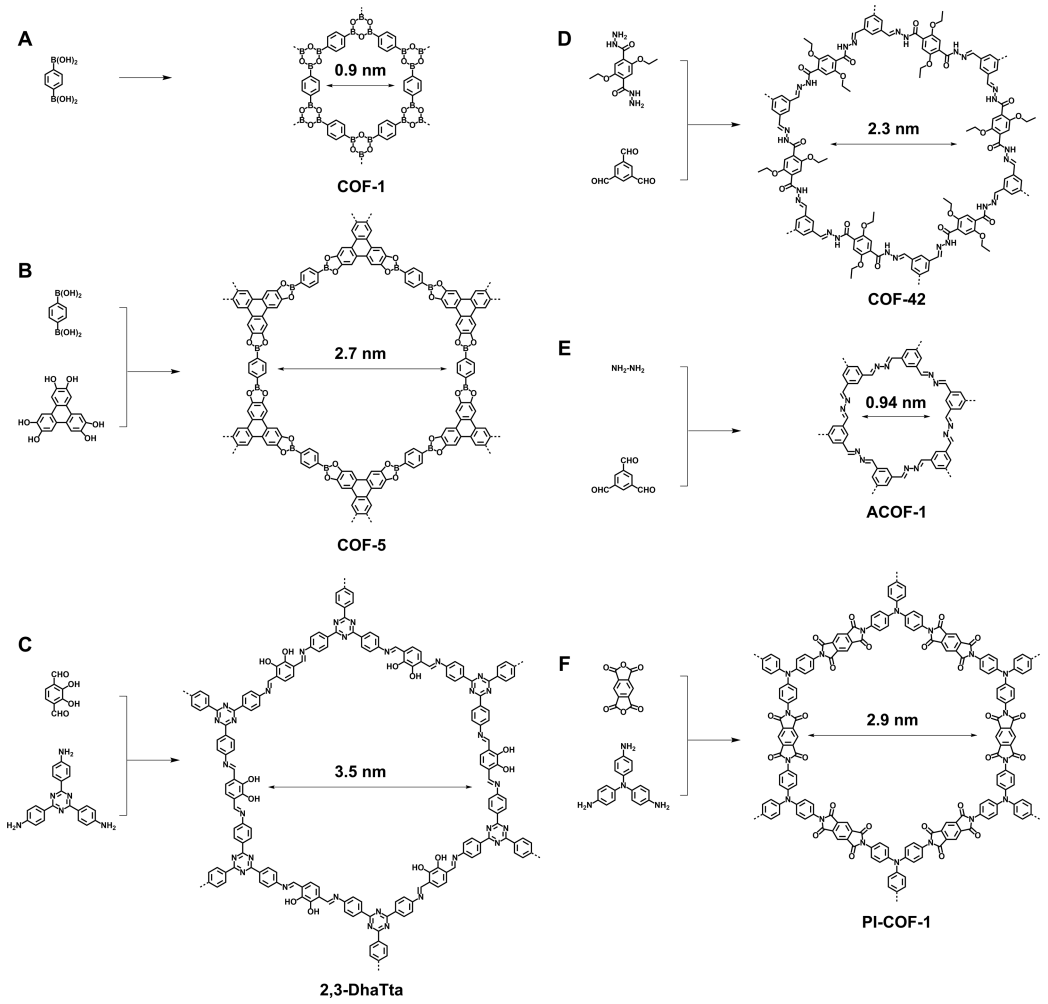

Figure 7. Skeleton design of hexagonal COFs from the $[C_3 + C_2]$ combination of building blocks for (A) the boroxine-linked COF-1, (B) the boronate-ester-linked COF-5, (C) the imine-linked 2,3-DhaTta COF, (D) the hydrazone-linked COF-42, (E) the azine-linked ACOF-1, and (F) the imide-linked PI-COF-1. The COFs with the phenyl linkers are selected as examples.

biphenyl, triphenyl, thiophene, pyridine, bipyridine, biphenylazo, stilbene, thiadiazole, tetraphenylethene (TPE), tetraphenyl pyrene, and porphyrin. On the contrary, the C_4-symmetric monomers are representative of porphyrin and phthalocyanine knots. By tuning the knots and linkers, the combination of C_4-symmetric vertices with C_2-symmetric edges assumes the generation of a vast number of tetragonal architectures with pores ranging from micropores to mesopores (pore size = 1.8−4.4 nm).[13,19,30,32,33,96−105] As for the linkages, tetragonal structures can be generated by using the boronate ester, imine, C═C bond, and double-stage linkages. On the basis of the knot structure, the tetragonal COFs can be categorized as porphyrin and phthalocyanine frameworks. For porphyrin-based COFs, the boronate-ester-linked frameworks have a broad diversity of different skeletons and pore sizes, including COF-66 and MP-COFs (M = H_2, Co, Cu, Zn) (pore size = 2.3−2.5 nm).[31,99,106] Similarly, the imine-linked COFs have been synthesized with different linkers that lead to different pore sizes, such as DmaTph-COF, DhaTph-COF, Mp-Ph-COF, Mp-DMPh-COF, Mp-DHPh-COFs (M = H_2, Cu, Ni), Mp-DHPh$_x$-COFs (x = 25, 50, 75%), COF-366-M (M = H, Co), COF-367-M (M = Co, Co/Cu), Mp-PyTTPh-COF, Mp-2,3-DHPh-COF (M = Cu, Ni, Zn), Cup-DHNAPh-COF, CuP-BPy-Ph-COF, CuP-Ph-COF, CuP-TFPh$_{50}$-COF, and CuP-TFPh-COF (pore size = 1.8−2.9 nm).[33,98,100,106−108] The boronate-ester-linked phthalocyanine COFs constitute planar layer structures and yield different structures, including Pc-PBBA COF, NiPc-COF, NiPc-BTDA COF, MC-COFs-NiPc, MPc-COFs (M = Co, Cu, Zn), ZnPc-Py-COF, ZnPc-NDI-COF, ZnPc-DPB-COF, ZnPc-PPE-COF, Pc-PorDBA COF, M_1DPP-M_2Pc COFs (M_1 = H_2, Zn, Cu; M_2 = Ni, Cu), D_{CuPc}-A_{PyrDI}-COF, D_{NiPc}-A_{PyrDI}-COF, D_{CuPc}-A_{NDI}-COF, D_{NiPc}-A_{NDI}-COF, D_{CuPc}-A_{PDI}-COF, and D_{ZnPc}-A_{PDI}-COF (pore size = 2.0−4.4 nm).[11,29,30,32,101−104,109]

The double-stage strategy offers a combination of boroxine, boronate ester, imine, and hydrazone linkages together with a variety of knots, including porphyrin and phthalocyanine derivatives.[87] In these cases, the skeletons are very heterogeneous because of the presence of anisotropic lattice points. These COFs include microporous CuPc-FPBA-ETTA (pore size = 1.8 nm) and mesoporous CuPc-FPBA-PyTTA, CuPc-FPBA-TABPy, CuPc-FPBA-ZnP, CuPc-FPBA-TMBDA, and CuPc-FPBA-DETHz COFs (pore size = 2.1−3.7 nm).[87] Notably, the $[C_4 + C_4]$ topology can combine porphyrin and phthalocyanine knots into extended π-grids. Moreover, the porphyrin and phthalocyanine units can tune their central metals to generate microporous porphyrin-*co*-phthalocyanine M_1TPP-M_2Pc-COFs (M_1 = H_2, Zn, Cu; M_2 = Ni, Cu) while retaining the

https://dx.doi.org/10.1021/acs.chemrev.9b00550
Chem. Rev. 2020, 120, 8814−8933

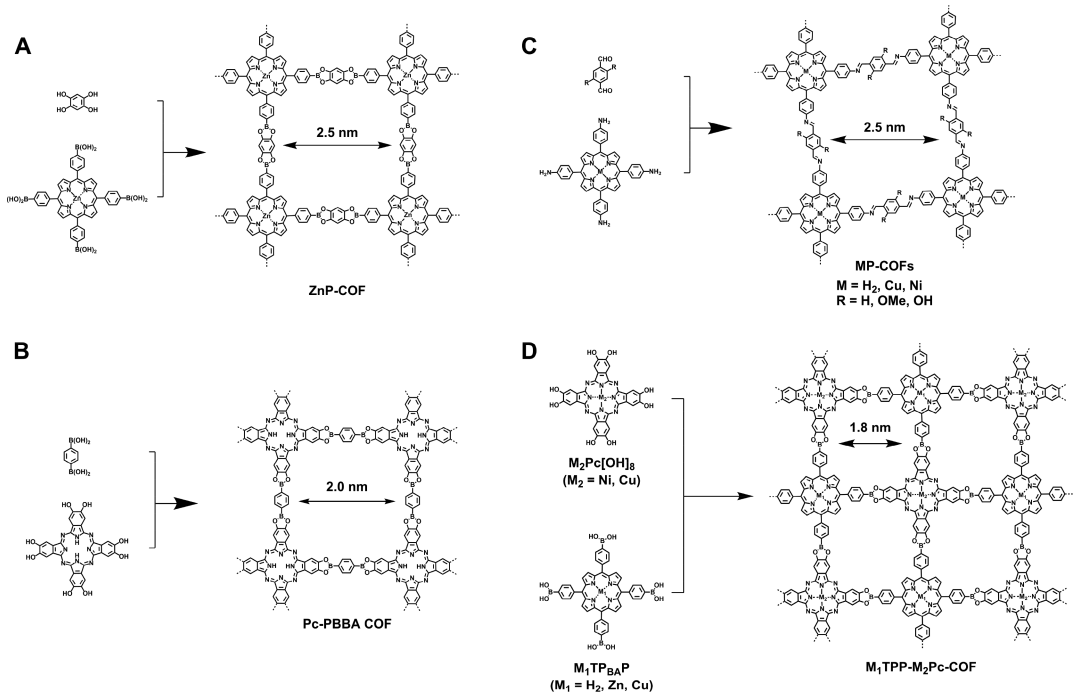

Figure 8. Skeleton design of tetragonal COFs from the $[C_4 + C_2]$ diagram for (A) the boronate-ester-linked ZnP-COF, (B) the boronate-ester-linked Pc-PBBA COF, and (C) the imine-linked MP-COFs (M = H_2, Cu, Ni). (D) Skeleton design of tetragonal M_1TPP-M_2Pc-COFs (M_1 = H_2, Zn, Cu and M_2 = Ni, Cu) from the $[C_4 + C_4]$ diagram.

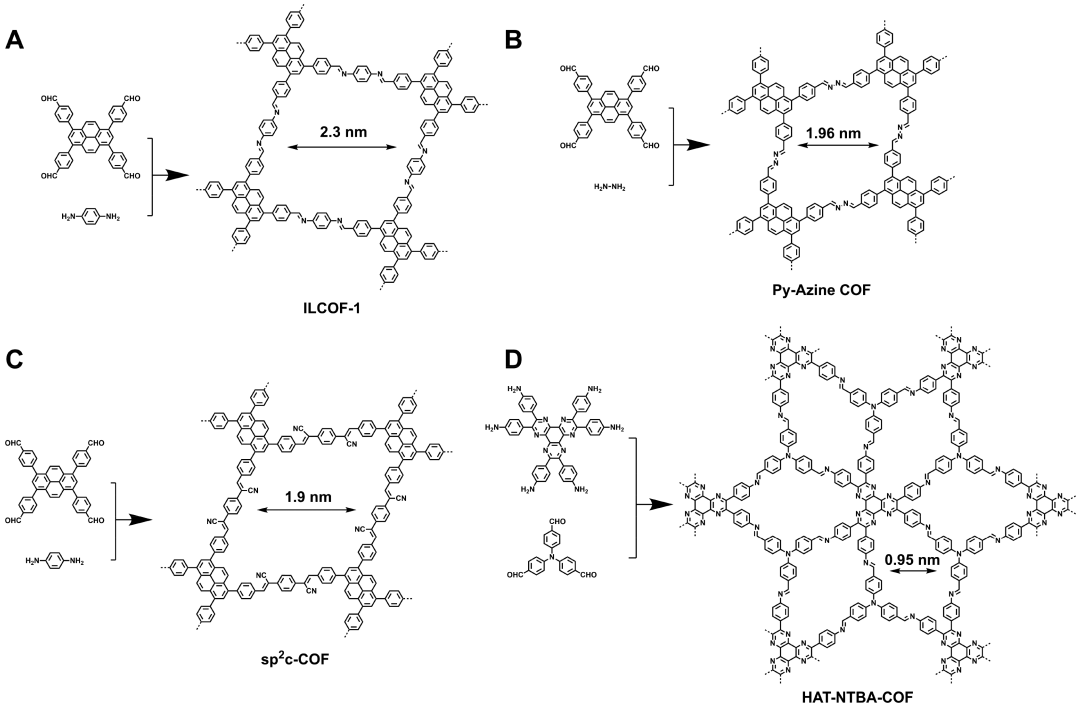

Figure 9. Design of single-pore rhombic skeleton from the $[C_2 + C_2]$ diagram for (A) imine-linked ILCOF-1, (B) azine-linked Py-Azine COF, and (C) C═C bond-linked sp^2c-COF and the $[C_3 + C_3]$ diagram for (D) HAT-NTBA-COF.

same pore size of 1.8 nm.[109] Figure 8 illustrates the typical one-pore structure of tetragonal COFs.

3.1.3. Rhombic COFs. Rhombic shaped COFs have been prepared by using the $[C_2 + C_2]$ topology diagram with tetraphenyl pyrene knots that lead to the generation of imine-linked, azine-linked, and C═C-linked COFs, including ILCOF-1, Py-Azine COF, Py-DHPh COF, Py-2,3-DHPh COF, Py-2,21-BPyPh COF, Py-3,31-BPyPh COF, BPy-COFs, Py-1P COF, Py-1PF COF, Py-2P COF, Py-2PE COF, Py-3PE COF, Py-$3PE_{BTD}$ COF, sp^2c-COF, sp^2c-COF-2, sp^2c-COF-3, and por-sp^2c-COF (pore size = 1.7−2.79 nm).[34,37,110−115] The rhombic geometry of HAT-NTBA-COF can also be achieved through the $[C_3 + C_3]$ diagram (Figure 9D).[116] Figure 9 illustrates the typical examples of rhombic lattices.

https://dx.doi.org/10.1021/acs.chemrev.9b00550
Chem. Rev. 2020, 120, 8814−8933

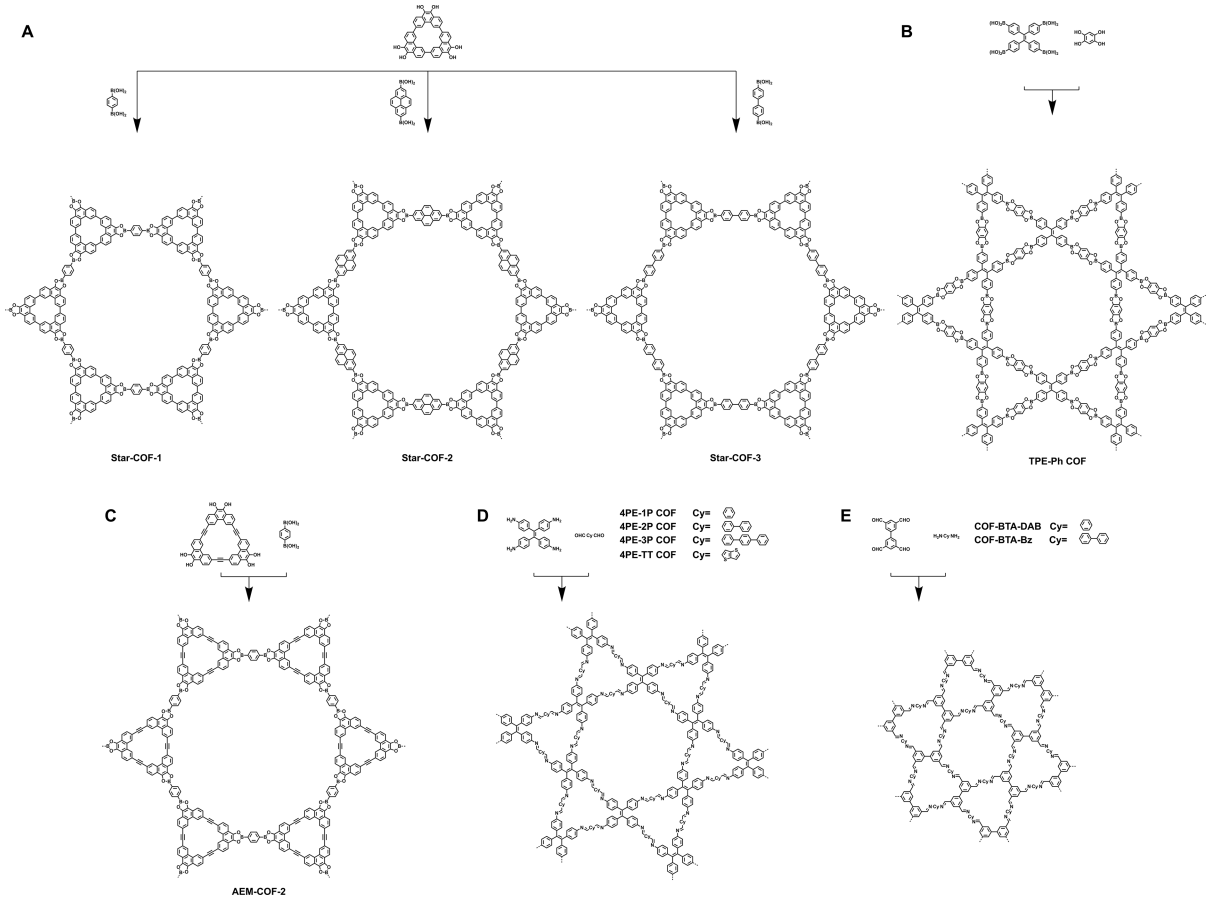

Figure 10. Design of dual-pore kagome skeletons from the $[C_2 + C_2]$ combination of building blocks for (A) star-COFs, (B) TPE-Ph COF, (C) AEM-COF-2, (D) 4PE-1P COF, 4PE-2P COF, 4PE-3P COF, and 4PE-TT COF, and (E) COF-BTA-DAB and COF-BTA-Bz.

3.1.4. Kagome COFs. Kagome-type COFs have been designed by using the $[C_3 + C_2]$ or $[C_2 + C_2]$ diagram. The $[C_2 + C_2]$ diagram typically uses the C_2-symmetric TPE knot and the C_2-symmetric linker. The $[C_2 + C_2]$ diagram yields the boronate-ester-linked TPE-Ph COF and the imine-linked COF-TPA (4PE-1P COF), COF-BPDA (4PE-2P COF), COF-TPDA (4PE-3P COF), SIOC-COF-1, and SIOC-COF-2.[36,38,39,117] COF-BTA-DAB and COF-BTA-BA using [1,1′-biphenyl]-3,3′,5,5′-tetracarbaldehyde (BTA) knots also achieve kagome topology.[118] The $[C_3 + C_2]$ topology diagram using C_3-symmetric macrocycles can also yield kagome-type COFs, including the boronic-ester-linked Star-COF-1, Star-COF-2, Star-COF-3, CTC-COF, CTC-COF-2, CTC-COF-3, DBA-COF 1 (= AEM-COF-1), DBA-COF 2, AEM-COF-2, Py-DBA-COF 1, Py-DBA-COF 2, and Py-MV-DBA-COF.[25,40,119−122]

The kagome lattice constitutes both the triangular micropore (pore size = 0.71−1.8 nm) and the hexagonal or dodecagonal mesopore (pore size = 2.6−4.5 nm). In the case of the $[C_2 + C_2]$ diagram, through introducing substituents into the C_2-symmetry linker, this diagram can yield either a dual-pore kagome COF or a single-pore rhombic COF, which is highly dependent on the bulkiness of the substituents. After polymerizing with TPE, terephthalaldehyde (BDA) with hydroxy side groups generates a kagome topology, whereas 2,5-diethoxyterephthalaldehyde (DETA) and 2,5-dibutoxyterephthalaldehyde (DBTA) with longer alkyl side chains yield rhombic topology.[123] Figure 10 illustrates the typical examples of kagome lattices.

3.1.5. Triangular COFs. The triangular topology allows the construction of microporous (pore size = 1.1−1.8 nm) HPB-COF, HBC-COF, and HEX-COF 1 by using the C_6-symmetric knots (hexaphenylbenzene or hexabenzocoronene derivatives) (Figure 11A,B).[12,124] The dual-pore triangular COFs can be prepared by the condensation of the C_3-symmetric hexaaza-triphenylene derivative (HAT-6NH_2) or triphenyleneand derivative (HFPTP), the C_2-symmetric BDA, or 1,1′-biphenyl-4,4′-diamine (BPDA).[35,125] The pore sizes of HAT-COF are 1.13 and 1.52 nm (Figure 11C), and the pore sizes of HFPTP-BPDA are 1.27 and 1.55 nm (Figure 11D). The sp^2c-carbon-linked 2D CCP-HATN with pore sizes of 0.68 and 1.28 nm has also been explored recently.[126] Figure 11 illustrates the typical examples of triangular COFs.

3.1.6. Heteropore COFs. COFs with three different kinds of pores can be designed through the combination of vertex truncation based on a multiple-linking-site strategy. Dual-pore PT_2B- and PY_2B-COFs (pore size = 1.83 and 2.37 nm) can be achieved by using pyrene tetraaniline as the tetratopic linker and triazine tribenzaldehyde or benzene tripicolinaldehyde as the tritopic linkers.[127] Triple-pore TP-COF-DAB and TP-COF-BZ can be achieved by using [1,1′:3′,1″-terphenyl]-3,3″,5,5″-tetracarbaldehyde (TPTCA) as the knot.[128] TP-COF-DAB exhibits pore sizes of 1.61 and 3.18 nm, whereas TP-COF-BA has pore sizes of 2.56 and 3.91 nm; the size of their rectangle-like pores could not be identified because they are too small to be detected.

The combination of the C_2-symmetrical building blocks and linear linkers can produce heteropore structures. For example, the polycondensation of 4′-(bis(4-formylphenyl)amino)-[1,1′-biphenyl]-3,5-dicarbaldehyde (BABD) and 1,4-diaminoben-

https://dx.doi.org/10.1021/acs.chemrev.9b00550
Chem. Rev. 2020, 120, 8814−8933

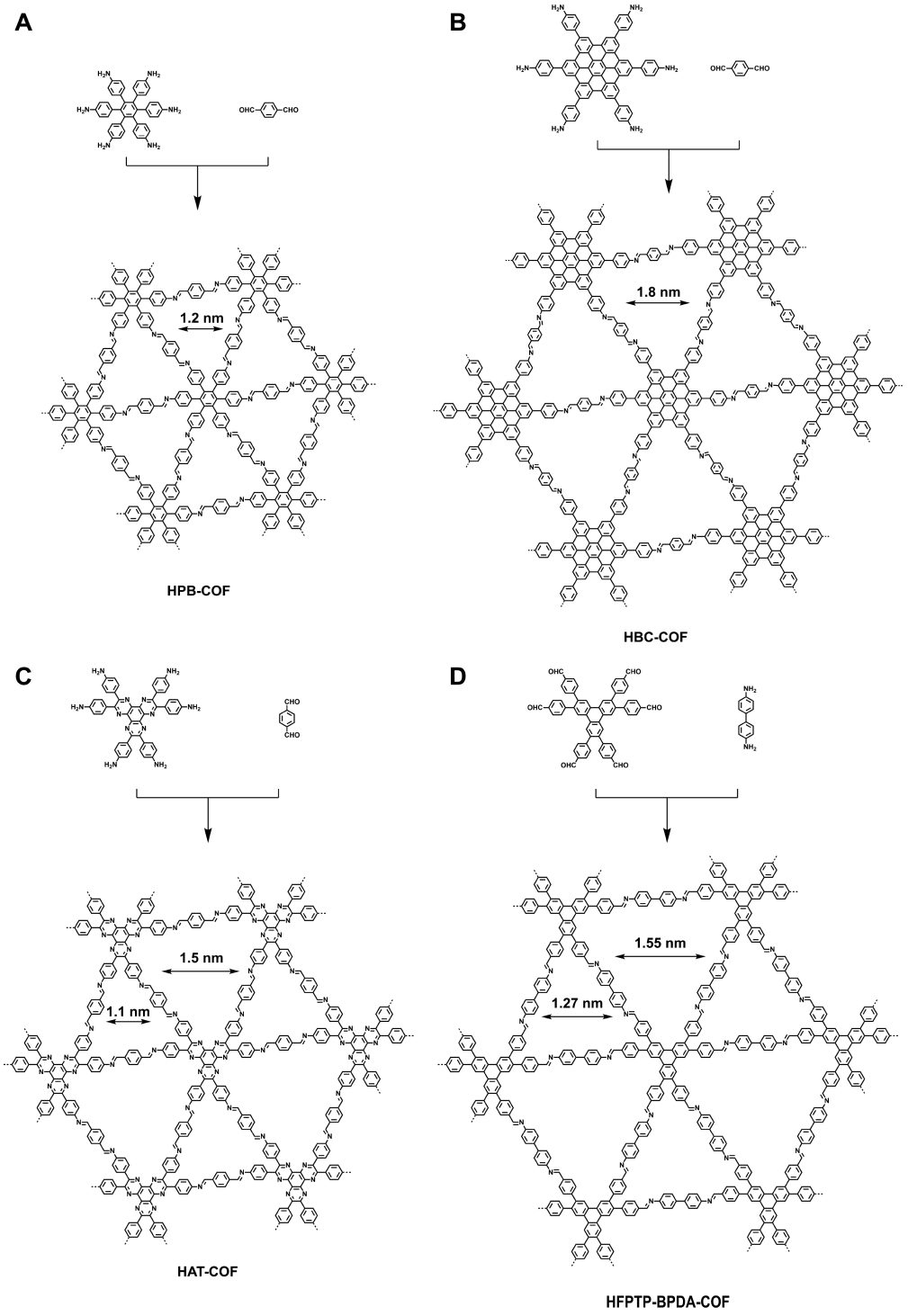

Figure 11. Skeleton design of single-pore triangular COFs from the $[C_6 + C_2]$ diagram for (A) HPB-COF and (B) HBC-COF. (C) Skeleton design of dual-pore triangular HAT-COF using the $[C_3 + C_2]$ diagram. (D) Skeleton design of dual-pore trigonal HFPTP-BPDA-COF using the $[C_3 + C_2]$ diagram.

zene (DAB) or benzidine in *o*-dichlorobenzene/*n*-butyl alcohol/aqueous acetic acid (AcOH, 6 M) (v/v/v 5:5:1) yields COF-BABD-DB (pore size = 0.98 and 1.72 nm) and COF-BABD-BZ (pore size = 1.8 and 2.5 nm), respectively.[129] Similarly, through orthogonal reactions, COF-DA-DB and COF-DA-DB-TB with a diformylphenylboronic acid (DFPBA) knot assume a heteropore topology.[130] The main pore size of COF-DA-DB is 1.84 nm, whereas COF-DA-TB has two different pore sizes of 1.28 and 1.52 nm. Figure 12 shows the typical examples of COFs with heteropores.

3.1.7. Pore-Surface Engineering. Not only the skeleton and pore size but also the pore wall can be designed to have different surface structures. To date, there are three approaches to systematically design pore walls via control over substituents on the edges, ionic exchange, and pore-surface engineering.[13,19,68,131,132] The approach based on edge unit substitutions utilizes the alkyl-substituted phenyl units as edges that can

https://dx.doi.org/10.1021/acs.chemrev.9b00550
Chem. Rev. 2020, 120, 8814−8933

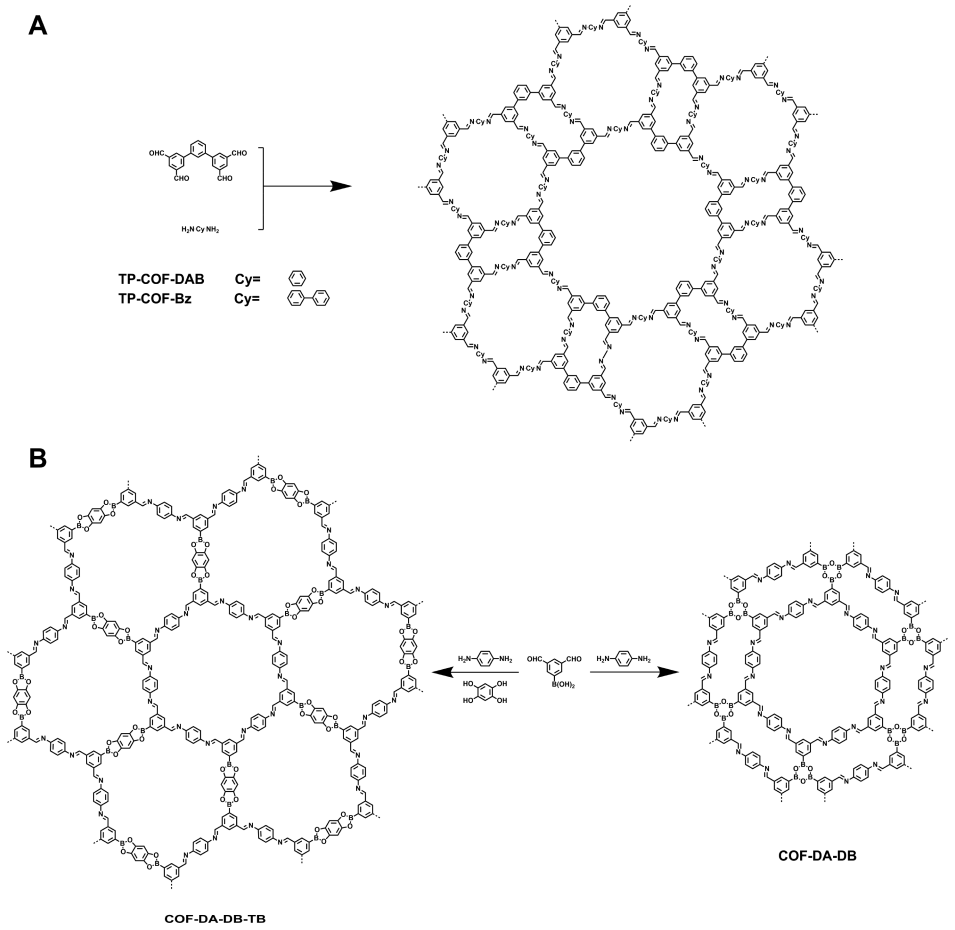

Figure 12. Skeleton design of heteropore COFs of (A) TP-COF-DAB and TP-COF-Bz as well as (B) COF-DA-DB and COF-DA-DB-TB.

introduce alkyl chains to the pores so that the pore sizes are tunable from 1.8 to 1.1 nm, depending on the length of the alkyl chains. For example, a series of COFs, including COF-18 Å, COF-16 Å, COF-14 Å, and COF-11 Å, have been prepared with various substituents on the pore walls, such as hydrogen, methyl, ethyl, and propyl units (Figure 13).[131,132] By using ion exchange as a tool, cationic EB-COF:X (X = Br) can replace its counteranion located in the pores from F^- to Cl^-, Br^-, and I^-. As a result, the pore size can be tuned from 1.84 to 1.56 nm, depending on the counteranions.[68]

A more general and effective strategy, that is, pore-surface engineering, has been developed for the design of pore walls of COFs.[133] In this strategy, a linker functionalized with hydroxyl, azide, or alkyne reactive groups is used to construct 2D COFs (Figure 14). The resulting COFs with an anchored hydroxyl, azide, or alkyne unit on the pore walls undergo quantitative addition or a click reaction to create specific pore surfaces. The pore-surface engineering strategy has been widely employed for engineering hexagonal and tetragonal COFs, and the pore size can be finely tuned within 1.2 to 3.0 nm (Figure 14A) for the hexagonal COF-5 family, from 0.75 to 2.2 nm for tetragonal NiPc-COFs (Figure 14B), and from 1.5 to 2.2 nm for the tetragonal porphyrin COFs (Figure 14C). Remarkably, the pore-surface engineering strategy is general to integrate a variety of functional groups, such as alkyl chains, alcohols, acids, bases, redox-active units, photofunctional groups, and catalytic sites onto the pore walls. More importantly, these functional groups can be introduced at a predesigned density, thus enabling the creation of tailor-made interfaces on the pore walls, which control the interaction with elemental particles, charges, ions, and molecules, thus creating new physiochemical properties and functions.

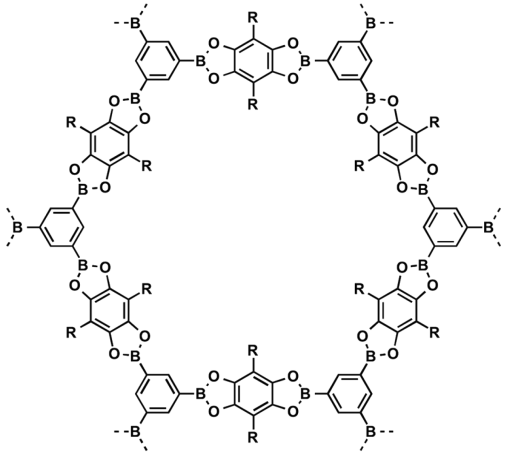

Figure 13. Pore-size modulation of COFs by introducing alkyl chains onto the pore walls.

https://dx.doi.org/10.1021/acs.chemrev.9b00550
Chem. Rev. 2020, 120, 8814−8933

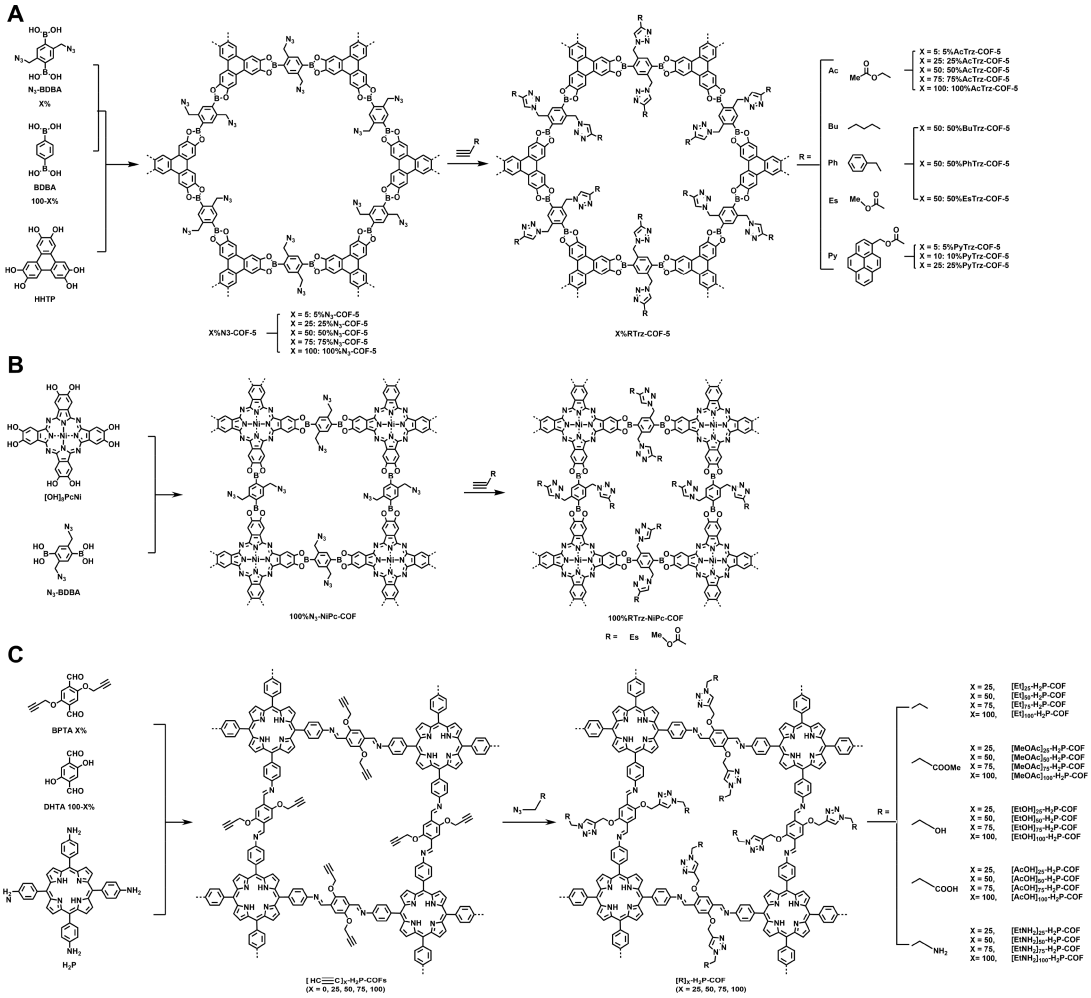

Figure 14. Pore-surface engineering strategies for (A) the hexagonal COF-5 family, (B) tetragonal NiPc-COFs, and (C) tetragonal porphyrin COFs.

3.2. Three-Dimensional COFs

3D COFs can be designed using different topology diagrams, including the $[T_d + T_d]$, $[T_d + C_2]$, $[T_d + C_3]$, $[T_d + C_4]$, and $[C_2 + C_3]$ diagrams (Figures 1B and 4−6),[13,19,46,134] which yield **dia** or **pts**, **bor** or **ctn**, **pts**, **ctn**, and **ffc** nets, respectively.[43] Different types of the T_d-symmetric nodes have been developed for the synthesis of 3D COFs, including tetra(4-dihydroxyborylphenyl)methane (TBPM), tetra(4-dihydroxyborylphenyl)silane (TBPS), *tert*-butylsilane triol (^{t}BuSi(OH)$_3$), tetra-(4-aminophenyl)methane (TAPM), 1,3,5,7-tetraaminoadamantane (TAA), complex salt Cu(I)-bis[4,4′-(1,10-phenanthroline-2,9-diyl)dibenzaldehyde]-tetrafluoroborate (Cu(PDB)$_2$(BF$_4$)), and Cu-(PDB)$_2$PO$_2$Ph$_2$.[13,19,47,50,54,57,59,134−152] Recently, a C_4-symmetric knot, that is, ETTA, has been developed for constructing 3D COFs upon the combination with C_3-symmetric linkers.[46] 3D COFs can be synthesized using the boroxine, boronate ester, borosilicate, imine, imide, and spiroborate linkages.[13,19,46,47,50,54,57,59,134−150,153]

The boroxine-linked 3D COF-102 and COF-103 were prepared with the **ctn** topology (pore size = 1.15 and 1.25 nm).[47] The boronate-ester-linked 3D COFs have been prepared with different topologies, including COF-105 (**ctn**, pore size = 1.83 nm), COF-108 (**bor**, pore size = 2.6 nm), and DBA-3D-COF 1 (**bor**, pore size = 2.96 nm), whereas the borosilicate-linked COF-202 has the **ctn** topology (pore size = 1.1 nm).[47,48,148] The imine-linked 3D COFs have been prepared with the **dia** topology, including COF-300 (pore size = 0.72 nm), COF-320 (pore size 1.35 × 0.62 nm^2), COF-505, LZU-301 (pore size from 0.58 × 1.04 nm^2 of contracted form to 0.96 × 1.04 nm^2 of expanded form), 3D-ionic-COF-1 (pore size = 0.86 nm), 3D-ionic-COF-2 (pore size = 0.82 nm), 3D-CCOF-5 (pore size = 0.62 and 0.74 nm), SP-3D-COF-1 (pore size = 1.2 nm), SP-3D-COF-2 (pore size = 1.5 nm), and 3D-Salphen-COFs (JUC-508, pore size = 1.3 nm; JUC-509, pore size = 1.2 nm); the **ctn** topology, including BF-COF-1 (pore size = 0.83 nm) and BF-COF-2 (pore size = 0.81 nm); and the **pts** topology, such as 3D-Py-COF (pore size = 0.59 nm), 3D-Por-COF (pore size = 0.60 and 1.07 nm), 3D-CuPor-COF (pore size = 0.63 and 1.18 nm), 3D-TPE-COF (pore size = 0.57 nm) and COF-500 (pore size = 1.23 nm).[45,50−53,55,57−59,135,142,152] The imide-linked 3D PI-COF-4 (pore size = 1.3 nm) and PI-COF-5 (pore size = 1.0 nm) have been prepared with the **dia** topology.[54] The spiroborate-linked 3D CD-COFs adopt an **rra** topology.[153] The **ffc** topology of 3D-ETTA-TFPB and 3D-ETTA-TFPA has been designed by a gene partition method of GSUs with reactive sites and quasi-reactive assembly algorithms (QReaxAA), with pore size of 1.73 and 1.49 nm, respectively.[46] The **srs** net of SiCOF-5 has been designed via a hypercoordinate silicon linkage.[56] Figure 15 presents the typical examples of 3D COFs.

https://dx.doi.org/10.1021/acs.chemrev.9b00550
Chem. Rev. 2020, 120, 8814−8933

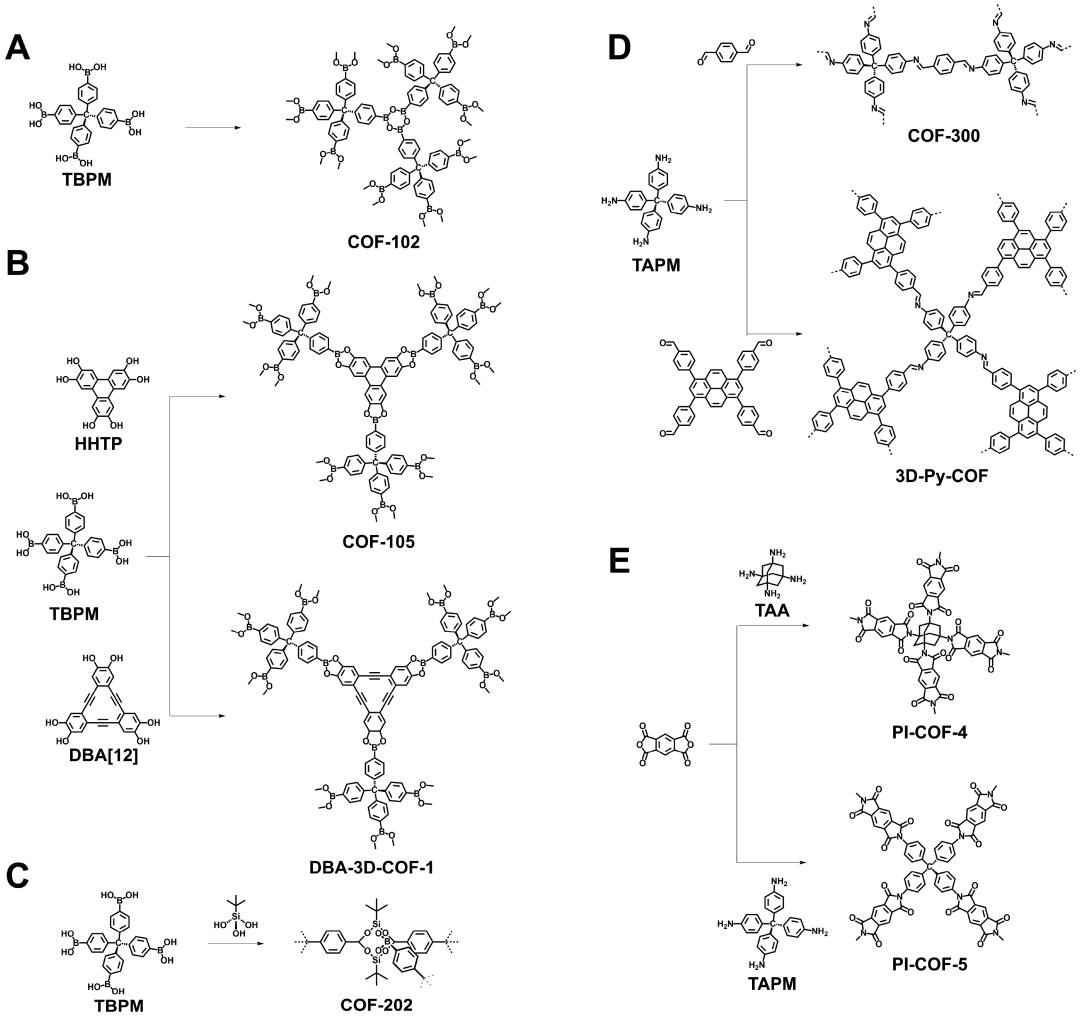

Figure 15. Skeleton design of 3D COFs from T_d-symmetric building blocks for (A) boroxine-linked COF-102, (B) boronate-ester-linked COF-105 and DBA-3D-COF-1, (C) borosilicate-linked COF-202, (D) imine-linked COF-300 and 3D-Py-COF, and (E) imide-linked PI-COF-4 and PI-COF-5.

4. STRUCTURE ANALYSIS

4.1. Crystallography

Three-dimensional imine-based COFs (COF-300, hydrated form of COF-300, COF-303, LZU-79, and LZU-111) have been prepared as single crystals, and their structures have been resolved using single-crystal X-ray diffraction (SXRD) at a resolution of 0.85 Å.[154] Through the SXRD measurements, the detailed crystal parameters including the unit-cell parameters of the specific space group, atomic positions, and geometric parameters (bond lengths and angles) have be precisely resolved. This offers a great potential to explore the structure-related properties as well as the uptake of the guest molecules, thus offering a way to an in-depth mechanism study of COFs.

4.2. Powder X-ray Diffraction and Theoretical Simulation

The primary requirement to evaluate the structure of the COFs is to observe the crystallinity by powder X-ray diffraction (PXRD) experiment.[13,155] COFs should have clear PXRD patterns with strong diffraction signals, which reflect the high homogeneity of the 2D or 3D structural periodicity. Structural simulations (*vide infra*) together with the PXRD pattern matching are utilized to determine the COF structure. To date, multiscale computations have been explored in predicting the structures of COFs.[156,157] For example, the *ab initio* quantum calculation methods including the density functional theory (DFT) and the density functional tight binding (DFTB) with Lennard-Jones (LJ) dispersion potential are useful in predicting the structures of COFs.[13,87,92,100,158] Moreover, classical simulations like the grand canonical Monte Carlo (GCMC) method offer a powerful tool to evaluate the ideal sorption behavior of COFs, which is useful for validating the porous structure of COFs in comparison with the experimentally observed sorption patterns.[12,111,156]

Different from the PXRD method, *in situ* small-angle and wide-angle X-ray scattering (SAXS/WAWS) measurements provide direct monitoring of the polymerization and the crystallization of COFs,[159,160] and the *in solvo* XRD technique can detect the crystallinity of COF colloidal suspensions in a real-time mode.[160,161] The *in situ* XRD method has also been utilized to provide in-depth insight into the structural changes of COFs at high temperatures as well as under high pressures. During the process, COF powders loaded in a thick-walled Kapton capillary are constantly heated under helium flow or pressurized under a helium atmosphere while PXRD patterns of those microcrystalline powders are continuously recorded on a 2D Pilatus detector and are radially integrated to produce 1D patterns.[162] The plots of heat or pressure versus diffraction intensity are able to reveal the thermal and pressure stabilities of crystalline COFs under operando conditions; a high temper-

https://dx.doi.org/10.1021/acs.chemrev.9b00550
Chem. Rev. 2020, 120, 8814−8933

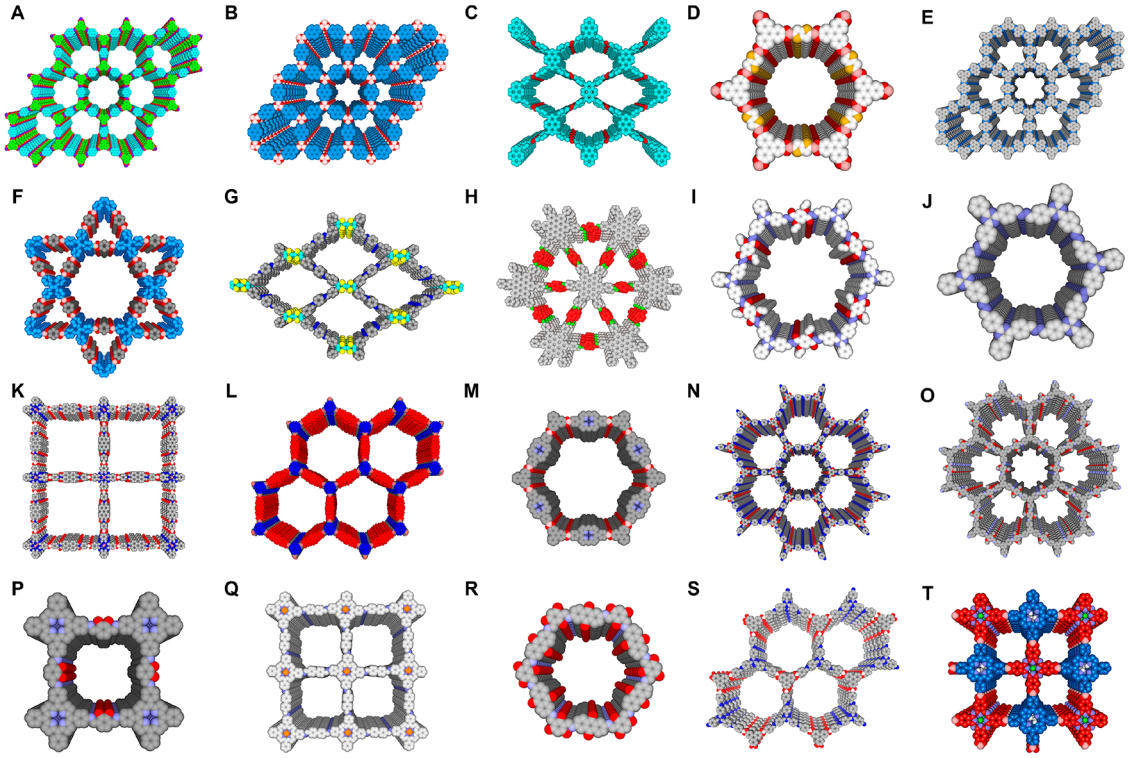

Figure 16. Examples of 2D COFs with layered stacking structures for (A) TP-COF, (B) PPy-COF, (C) Py-Azine COF, (D) T COF 4, (E) CS-COF, (F) TPE-Ph COF, (G) TTF-Ph, (H) HBC-COF, (I) TFPT-CPF, (J) N_3-COF, (K) D_{TP}-A_{NDI}-COF, (L) RA-COF, (M) TP-POR COF, (N) TATA-TPBA COF, (O) TPB-DMTP-COF, (P) CuP-2,3-DHTP COF, (Q) COF-367-Co, (R) DAAQ-TFP COF, (S) HHTP-FPBA-TATTA COF, and (T) H_2TPP-NiPc-COF.

ature leads to the destruction of crystallites, whereas a high pressure such as 100 bar does not change the crystallinity.

To authenticate the experimentally observed PXRD patterns, especially to evaluate the stacking layer patterns of 2D COFs, DFTB calculations are useful methods. In the DFTB method, a monolayer structure of COFs is first built up and optimized in its conformation. Then, stacked structures are constructed by varying the stacked distances and horizontal offsets between layers. For example, the hexagonal 2D honeycomb structure is an **hca** network with two major forms (**bnn** and **gra**), depending on the stacking modes.[13,163,164] In the **bnn** topology, lattice points of successive layers are exactly top of each other, leading to the generation of eclipsed AA stacking frameworks (Figure 16). In contrast, in the **gra** topology, consecutive layers are translated to each other by half of a unit cell, giving rise to staggered AB stacking structures.[43] Between these eclipsed and staggered stacking modes, there are intermediate structures with slipped AA-stacking modes that are generally slightly more stable than eclipsed and staggered stacking modes in energy. The slip distance is dependent on the topology, bulkiness, and planarity of vertices, edges, and linkages.[165] Notably, the AA-stacking modes with different slip distances exhibit similar PXRD patterns because their peaks are usually too broad to identify small differences. However, the stacking energies change greatly as the slipped distance is changed. This difference offers a standard to determine the most stable slipped structure by using self-consistent charge−density-functional-based tight-binding (SCC-DFTB) calculations. Interestingly, the successive layer shift (zigzag and armchair) with an offset distance of 1.4 Å maximizes the attractive Coulomb interactions, as observed for COF-1, COF-5, COF-6, and COF-8, other than the London-dispersion interactions in the eclipsed AA-stacking mode. For the HHTP-DPB COF, a lateral offset distance of 1.7 Å between successive layers is preferable, as predicted from the potential energy surface (PES) calculations.[157] On the contrary, the DFTB calculations including the LJ dispersion corrections result in a 0.8 to 1.0 Å offset between layers for a variety of COFs, including H_2P-COF, CuPc-COF, ZnPc-COF, CoPc-COF, CuP-TFPh-COF, HBC-COF, D−A COF, and CS-COF.[11,12,87,92,100,108,158,166,167] Usually, the AB-staggered structures have a low stabilization energy due to the loss of interlayer $\pi-\pi$ interactions, and the simulated XRD patterns mismatch the experimentally observed PXRD profiles. On the basis of the optimal stacking structures with specific space groups, it is useful to compare the simulated PXRD patterns with the experimentally observed profiles and assign the crystal facet of each peak. By the combination of simulated crystal structures and the experimentally observed profiles, Pawley refinement offers a measure to justify the correctness of space groups of COFs, as indicated by the values of convergent parameters R_{wp} and R_p.

4.3. Other General Methods for Characterization

Besides the PXRD technique to evaluate the structure of COFs, 3D rotation electron diffraction (3D-RED) or 3D electron diffraction tomography (3D-EDT) data collection methods by using transmission electron microscopy (TEM) or high-resolution (HR) TEM have been developed for the single-crystal structural evaluation of micrometer- or sub-micrometer-sized COF crystals (Figure 17).[59,115,142,168,169] Unlike the traditional HR-TEM whereby the electron beam easily causes damage to the COF structure and results in limited resolution, the low-dose TEM technique using the direct-detection electron-counting camera is able to capture images containing useful structural information at a resolution of 4 Å. The

https://dx.doi.org/10.1021/acs.chemrev.9b00550
Chem. Rev. 2020, 120, 8814−8933

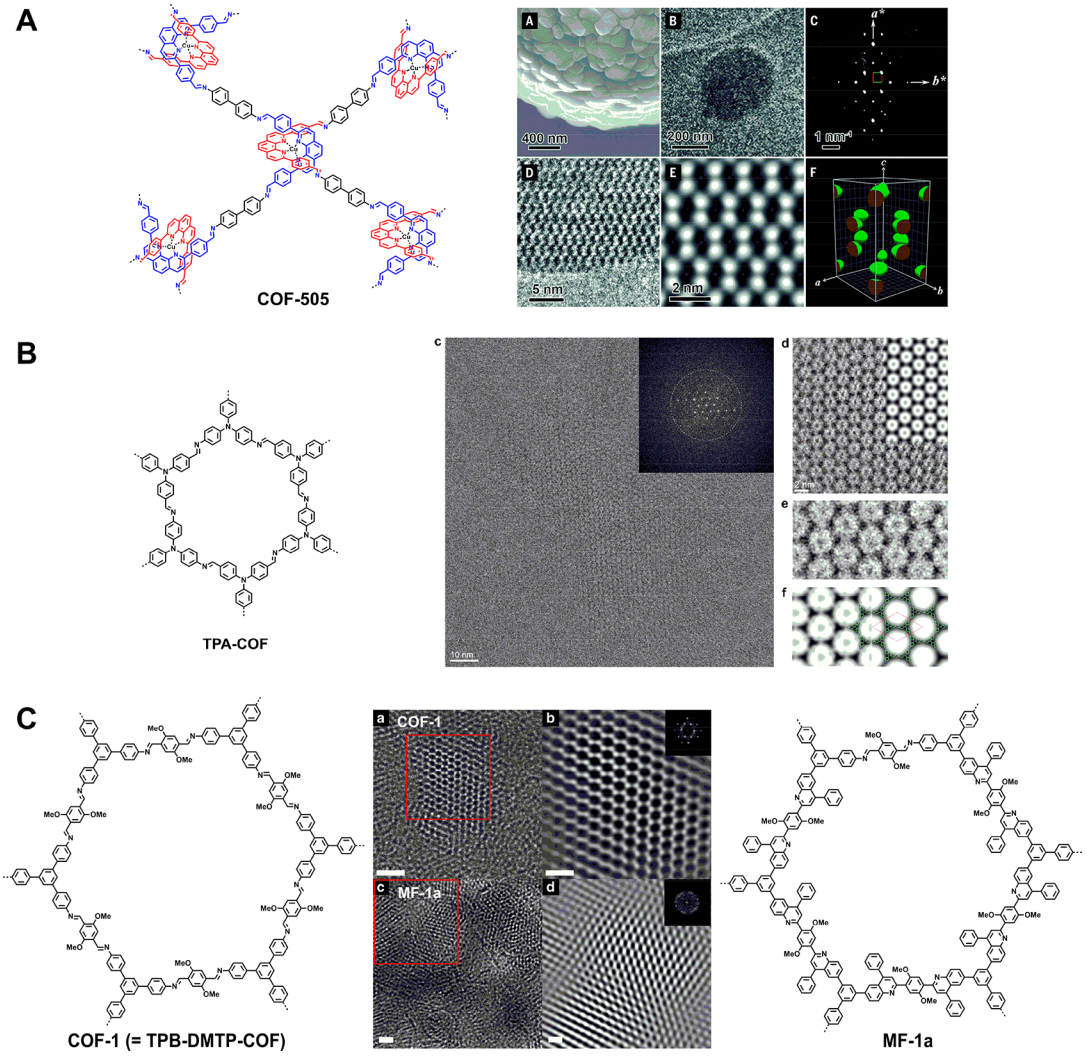

Figure 17. Examples of TEM characteristic of (A) COF-505, adapted with permission from ref 59, Copyright 2016 American Association for the Advancement of Science; (B) TPA-COF, adapted from ref 168, Copyright 2017 American Chemical Society; and (C) TPB-DMTP-COF and MF-1a, adapted with permission from ref 169, Copyright 2018 Springer Nature.

honeycomb structure of COFs can be clearly observed on low-dose TEM images (Figure 17B,C).[168,169] In addition, the fast Fourier transform (FFT) of the TEM images enables the identification of the lattice structure.

Moreover, the grazing-incidence X-ray diffraction (GID) analysis provides useful information about the crystallinity and the preferred orientation of the COF films.[103,170−174] Great progress has been made for the characterization of monolayer COFs on different substrates by using scanning tunneling microscopy (STM).[175−185] Other tools, such as Fourier transform infrared spectroscopy (FT-IR), solid-state nuclear magnetic resonance (ssNMR), elemental analysis, X-ray photoelectron spectroscopy (XPS), field-emission scanning electron microscopy (FE-SEM), atomic force microscopy (AFM), thermogravimetric analysis (TGA), optical transient absorption (TA) spectroscopy, and Brunauer−Emmett−Teller (BET) surface area (S_{BET}) and pore size evaluation by gas sorption isotherm measurements are general and useful for characterizing and confirming the structure and composition of various COFs. In addition to the static detection methods, dynamic light scattering (DLS) measurements tell the number-average size of COF particles in the polymerization system,[160,161] and the turbidity of the reaction system is useful for determining the rate of COF formation as well as its sensitivity to the polymerization conditions of initially homogeneous systems.[186]

5. SYNTHESIS

The synthesis of organic compounds usually employs kinetically controlled reactions for the formation of irreversible chemical bonds.[187] In contrast, if the reaction is reversible, that is, mismatched covalent linkages are allowed to break up for correction during the reaction, then the products are formed under thermodynamic control.[188] These reversible covalent bond formation reactions render the products able to form self-healing structures. The self-healing process involves the error-checking and proofreading of structures, which are important for the reactions consisting of multiple reactive sites to reach a final structure without defects. In particular, for the polycondensation reaction systems, reversible reactions can lead to the generation of thermodynamically stable polymers.[189] In the case of COFs, the topology diagram requires the covalent connection of organic units in an ordered and predesigned manner. Moreover, to fulfill the growth of extended polygon structures, the reaction occurs at multiple reactive sites. These reaction features require

https://dx.doi.org/10.1021/acs.chemrev.9b00550
Chem. Rev. 2020, 120, 8814−8933

the use of reversible covalent bond formation reactions for the synthesis of COFs.[190,191] Surprisingly, irreversible reactions, including phanazine linkage, dioxin linkage, as well as C=C linkage, have been synthesized through irreversible nucleophilic aromatic substitution reactions,[76,94,95,114,192,193] which would further expand the development of COFs.

5.1. Synthetic Methods

5.1.1. Solvothermal Synthesis. Most COFs have been synthesized under solvothermal methods in which reaction conditions are highly dependent on the solubility and reactivity of building blocks and the reversibility of the reactions. Moreover, the reaction time, temperature, solvent conditions, and catalyst concentration are the most important factors to be considered in preparing crystalline porous COFs by the solvothermal method. As a general synthetic protocol, a mixture of suitable monomers for vertices and edges, the catalyst, and solvents or a mixture of solvents are placed in a Pyrex tube of suitable volume. The mixture is sonicated for a short period, degassed via freeze−pump−thaw cycles, sealed with a gas burner, and kept at a suitable temperature for a certain period. The tube is cooled at room temperature, and the precipitate is collected by centrifugation or filtration and washed with an appropriate solvent at room temperature or by Soxhlet extraction to exchange high-boiling-point solvents or remove oligomers. The residue is dried under vacuum at 80−120 °C and kept under nitrogen or argon in the dark. Notably, by using this method, some COFs can be prepared on a large scale. For example, TPT-COF-1 from 2,4,6-tris(4-aminophenoxy)-1,3,5-triazine (TPT-NH_2) and 2,4,6-tris(4-formylphenoxy)-1,3,5-triazine (TPT-CHO) could be easily prepared on a gram scale, and the resulting TPT-COF-1 possesses a BET surface area of 1589 m^2 g^{-1} and a high crystallinity.[23]

5.1.2. Microwave Synthesis. Considering the fact that the solvothermal methods require a long reaction time, the microwave method has been explored for the rapid preparation of crystalline porous COFs. Until now, boronate-ester-linked COF-5 (Figure 5B), COF-102 (Figure 12A),[194,195] and imine-linked TpPa-COF[196] have been successfully synthesized by using the microwave method. A general microwave method is described as follows. A mixture of monomers in a suitable solvent is sealed in a microwave tube under nitrogen or vacuum and heated with stirring for 60 min at a designated temperature, such as 100 °C. To synthesize the boron-based COF-5 and COF-102, the crude product is collected, mixed with acetone, and reacted at 65 °C with stirring for another 20 min as a process of solvent extraction. The resulting precipitate is collected by filtration and dried under vacuum. A feature of the microwave solvent extraction method is that it could remove oligomers in the COFs more efficiently and the resulting COFs possess better porosity. Different from the boron-based COFs, after the microwave reaction, the resulting imine-linked COFs are collected by filtration, washed with mesitylene and acetone, extracted with tetrahydrofuran (THF) by using a Soxhlet extractor to remove any oligomers adsorbed in the pores, and dried at 100 °C under vacuum. In addition, three crystalline covalent triazine frameworks (CTFs), that is, P1M, P2M, and P4M, have been synthesized by using microwave methods.[197] The synthetic protocol is described as follows. First, a mixture of trifluoromethanesulfonic acid and monomers in a reaction vessel is sealed and stirred at 110 °C for 30 min. Second, the precipitate is collected, carefully ground into a powder, and washed with ammonia solution. Finally, the powder is washed with water, ethanol, acetone, and THF and dried under vacuum to yield CTFs.

5.1.3. Ionothermal Synthesis. Although they have broad diversity of monomers, most CTFs are amorphous materials and lack long-range molecular orderings. Nevertheless, two CTFs, that is, CTF-1 and CTF-2, synthesized under ionothermal conditions are crystalline porous materials.[75,198] In a typical method, the monomer and $ZnCl_2$ in a Pyrex ampule are evacuated, sealed, and heated to 400 °C for 40 h. The mixture is cooled to room temperature, ground, and thoroughly washed with water to remove $ZnCl_2$. The powder is further stirred in a diluted HCl solution for 15 h to remove $ZnCl_2$, collected by filtration, washed with water and THF, and dried under vacuum to yield CTF-1 and CTF-2. During the synthetic process, the molten salt acts as the solvent and catalyzes the trimerization reaction, which is likely reversible at this temperature. Recently, CTF-1 has been successfully synthesized by using a *p*-toluene sulfonic acid catalyst under microwave conditions (vide infra).[197] As a complemental energy-consumable and relatively complex solvothermal strategy, using ionic liquid as a solvent offers a simple, mild, and green synthetic route for the preparation of 3D COFs as well. A series of 3D ionic-liquid-containing COFs (3D-IL-COFs) have been successfully synthesized by using 1-butyl-3-methylimidazolium bis-((trifluoromethyl)sulfonyl)imide ([BMIm][NTf2]) as a green solvent.[199] The polycondensation proceeds under facile ambient temperature and pressure and can be completed at a high reaction rate (3 min for 3D-IL-COF-1).

5.1.4. Mechanochemical Synthesis. Because both solvothermal and microwave reactions are conducted under complicated conditions (e.g., reaction in a sealed Pyrex tube, inert atmosphere, suitable solvents and temperature for crystallization, etc.), the exploration of a simple synthetic method is highly desired. In particular, a mechanochemical synthesis that constructs bonds through a simple, economical, and environmentally benign route could overcome the limitations of solvothermal methods. In the mechanochemical synthesis, the monomers are placed in a mortar and ground by using a pestle at room temperature to yield the COFs, including TpPa-1, TpPa-2, TpPa-NO_2, TpPa-F_4, TpBD, TpBD-$(NO_2)_2$, TpBD-Me_2, and TpBD-$(OMe)_2$.[63,200] To explore the full potential of this method with the appropriately optimized mechanochemical conditions, the liquid-assisted grinding method has been developed. While grinding the monomers, a small amount of catalyst solution is added to the mortar; this enhances the reaction rate by facilitating the homogeneity of reactants, which leads to an improved crystallinity.[66,67,201]

5.1.5. Interfacial Synthesis. Compared with the aforementioned synthetic approaches that mainly result in insoluble and unprocessable powders, the interfacial synthetic strategy is a novel and efficient method for fabricating COF thin films with simultaneous control of their thickness.[202−204] Tp-Bpy, Tp-Azo, Tp-Ttba, and Tp-Tta have been synthesized in the interface of two solvents, in which 1,3,5-triformylphloroglucinol (TFP) is dissolved in dichloromethane and an aqueous solution of diamine and *p*-toluenesulfonic acid (PTSA) or a water/acetonitrile (7/3 v/v) solution of triamine and PTSA is paved on the dichloromethane layer.[202] On the contrary, the COF-TTA-DHTA film has been prepared by dissolving 4,4′,4′′-(1,3,5-triazine-2,4,6-triyl)trianiline (TTA) monomer, $Sc(OTf)_3$ catalyst, and acetic acid in water,[203] and the water was superspread on the hydrogel immersed under the oil phase of 2,5-dihydroxyterethaldehyde (DHTA).[204] This method enables

https://dx.doi.org/10.1021/acs.chemrev.9b00550
Chem. Rev. 2020, 120, 8814−8933

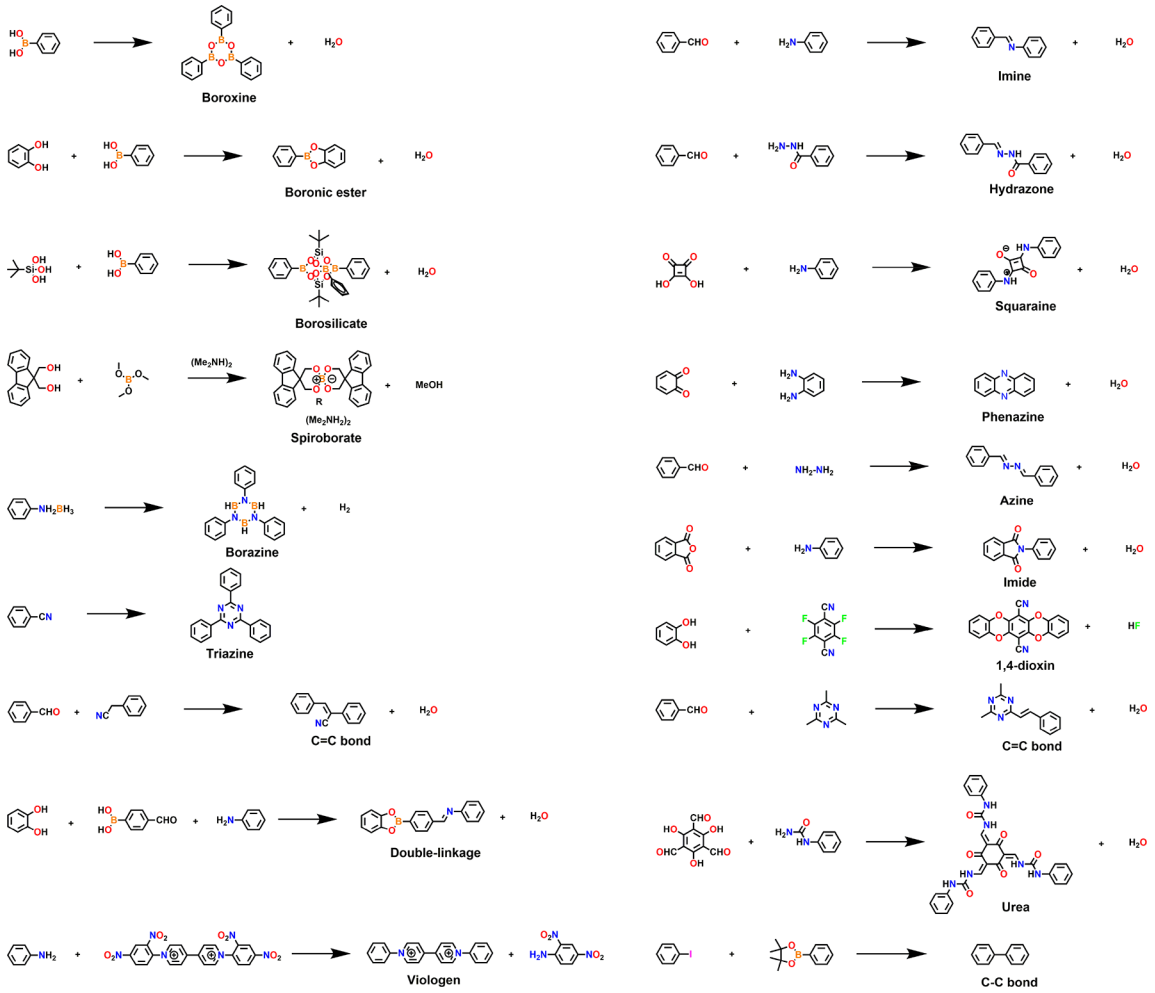

Figure 18. Various linkages explored for the synthesis of COFs.

the production of films with a tunable thickness from 4 to 150 nm. Recently, 2DCCOF1 and 2DCCOF2 with C−C linkages have been synthesized through the Suzuki coupling reaction. A dilute toluene solution of monomers and the catalyst $Pd(PPh_3)_4$ is laid on the top of an aqueous solution of K_2CO_3, and reactions occur at the toluene−water interface under an argon atmosphere at 2 °C. Stable and large area sheets of AB-staggered COFs have been obtained after 1 month.[205]

5.1.6. Synthesis under Ambient Conditions. Although most COFs are produced under solvothermal conditions, the synthesis of COFs at room temperature is attractive, especially for cases of fragile building blocks or sensitive substrates. Indeed, room-temperature vapor-assisted synthesis is efficient in producing boroxine-based COF films. A mixture of acetone and ethanol solution (150−200 μL) of COF precursors is drop-cast on a clean glass substrate, which is further placed into a desiccator along with a small vessel containing mesitylene and dioxane (1/1 v/v) for 72 h at room temperature to prepare BDT-COF and COF-5 thin films.[206] Water-tolerant Lewis acids such as metal triflates are efficient in accelerating the formation of imine-linked 2D COFs at room temperature. In contrast with the conventional solvothermal synthesis of the TAPB-PDA COF that requires a high temperature (>70 °C) and long reaction time (>24 h), the TAPB-PDA COF can be produced with $Sc(OTf)_3$ catalyst in a mixture of 1,4-dioxane (DOX) and mesitylene (4:1 v/v) within 10 min at ambient temperature.[207] On the contrary, at room temperature, imine-linked COF-LZU1 can be prepared by the polycondensation of 1,3,5-triformylbenzene (TFB) and *p*-phenylenediamine (PPDA) in CO_2/water solvent at 4.5 MPa in 24 h,[208] whereas JUC-520, JUC-521, JUC-522, and JUC-523 with β-ketoenamine linkages and a 1,3,5-tris(3-dimethylamino-1-oxoprop-2-en-yl)benzene (TDOEB) knot can be prepared in aqueous systems at room temperature and under ambient pressure.[209]

Mixing 1,3,5-tris(4-aminophenyl)benzene (TAPB) and benzene tricarbaldehyde (BTCA) monomers with acetic acid in either *m*-cresol or dimethyl sulfoxide (DMSO) forms yellow gels, which yield crystalline RT-COF-1 after they are washed with methanol and THF and dried under an open atmosphere for 2 days.[210] This room-temperature synthetic strategy with the gel as the intermediate offers a way to make COFs processable, for example, by lithographically controlled wetting (LCW).

Interestingly, a polydimethylsiloxane (PDMS) microfluidic device that comprises four input channels connecting to a main microfluidic channel has been explored to prepare COF fibers under ambient pressure and temperature. In a typical experiment, acetic acid solutions of TAPB and BTCA monomers are injected into two channels while pure acetic acid is injected into the other edge channels through a syringe pump system; the resulting MF-COF-1 is sponge-like and can be directly printed on surfaces while retaining high crystallinity and porosity.[211] Adding supramolecular 3D-printing template Pluronic F127 to amorphous imine or β-ketoenamine with a limited polymerization degree forms 3D-printable hydrogels, which, upon

https://dx.doi.org/10.1021/acs.chemrev.9b00550
Chem. Rev. 2020, 120, 8814−8933

heating, can extensively promote polymerization and yield a 3D-printed monolith network. The amorphous network can transform into crystalline imine or β-ketoenamine-linked COFs by removing F127 and upon solvent annealing.[212]

5.2. Linkage Diversities and Reaction Conditions

The building blocks of COFs usually have rigid π-backbones and possess multiple reactive sites. Their solubility in solvent is highly dependent on the size of the π systems and the type of reactive units. In general, the synthesis of COFs employs the mixture of polar solvent and nonpolar solvent as a reaction medium for the reversible covalent bond formation reaction. The combinations of solvents, catalyst, reaction temperature, and reaction time are major factors to be considered for the thermodynamic control of the reaction. These factors determine the crystallinity and porosity of the resulting COFs. Depending on the nature of chemical reactions, COFs have been synthesized with boroxine,[9] boronate-ester,[9,27,121,213] borosilicate,[148] triazine,[75] imine,[50,108,214] hydrazone,[71] borazine,[215] squaraine,[216] azine,[111] phenazine,[158] imide,[49] double-stage,[87,88] spiroborate,[217] C=C,[76,114,192,218] amide,[219] viologen,[220] hypercoordinate silicon,[56] urea,[221] and 1,4-dioxin linkages[94,95] (Figure 18).

5.2.1. Boroxine Linkage. The self-condensation of boronic acids yields cyclic six-membered boroxine with a planar structure and water byproduct.[9,47,222] The boroxine-linked 2D COF-1 and PPy-COF have been synthesized from the self-condensation of 1,4-benzenediboronic acid (BDBA) and pyrene-2,7-diboronic acid (PDBA), respectively, in a sealed Pyrex tube at 120 °C (Figure 19).[9,27] The reaction medium is a

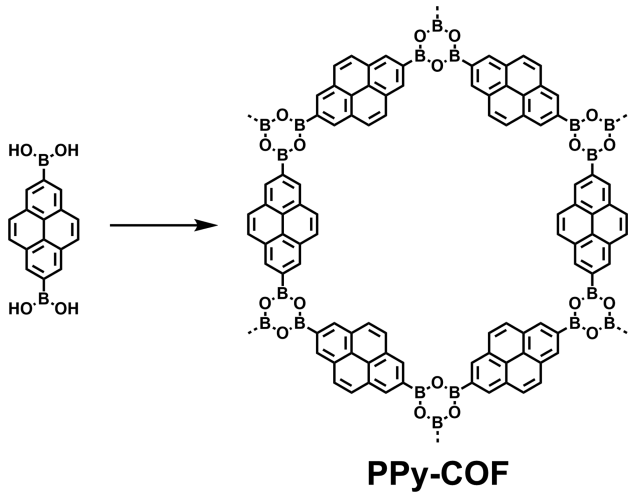

Figure 19. Schematic for the synthesis of PPy-COF.

mixture of DOX/mesitylene (1/1 v/v) for both COFs, and the reaction time is 3 days for COF-1 and 2 days for PPy-COF. Interestingly, a T_d-symmetric monomer TBPM upon self-condensation yields a 3D COF-102 in a mixture of DOX/mesitylene (1/1 v/v) at 85 °C for 4 days.[47] Similarly, 3D COF-103 has been synthesized from the self-condensation of TBPS in a mixture of DOX/mesitylene (1/3 v/v) at 85 °C for 4 days.

5.2.2. Boronate-Ester Linkage. The cyclic five-membered boronate ester is a planar linkage and can be formed by the condensation of boronic acids and catechol derivatives. The condensation of the 2,3,6,7,10,11-hexahydroxy triphenylene (HHTP) knot and BDBA edge units in a mixture of DOX/mesitylene at 100 °C for 3 days yielded boronate-ester-linked COF-5 (Table 1, Figure 7B).[9] The reaction can be promoted to complete in a short time by using a microwave reaction.[77,194,195] The boronate-ester linkage has been widely explored for the synthesis of 2D COFs in various π-systems including benzene, biphenyl, thiophene, anthracene, biphenyl acetylene, triphenyl benzene, triphenylene, TPE, porphyrin, and phthalocyanine derivatives. These combinations lead to the generation of a variety of COFs, including COF-6, COF-8, COF-10, TP-COF, D−A COF, TT-COF, T-COFs, HHTP-DPB COF, TPE-Ph COF, H_2P-COF, CuP-COF, ZnP-COF, and COF-66. Similarly, 3D COFs such as COF-105, COF-108, MCOF-1, and DBA-3D-COF 1 have been synthesized by using TBPM, TBPS, and TAA as the T_d-symmetric nodes in conjunction with the C_2- or C_3-symmetric linker. These boronate-ester-linked 2D and 3D COFs have been prepared under solvothermal conditions; the ratio of DOX to mesitylene, the reaction temperature, and the reaction time are dependent on the monomer structures and need to be optimized for different monomer combinations (Table 1).[26,27,90,91,117,149,223,224] Figure 20 illuminates the typical synthetic procedures of boronate-ester-linked TP-COF.

Boronate ester linkage, owing to its planarity and high reversibility yields highly crystalline COFs. Remarkably, boronate ester linkage has been explored for the integration of electron donor and acceptor units into donor−acceptor COFs in which the donor and acceptor moieties are segregated into bicontinuous donor-on-donor and acceptor-on-acceptor arrays. As shown in Table 1, a series of boronate-ester-linked donor−acceptors D_{TP}-A_{NDI}-COF, D_{TP}-A_{PyrDI}-COF, NiPc-BTDA COF, D_{MPc}-A_{PyrDI}-COFs (M = Cu, Ni), D_{MPc}-A_{NDI}-COFs (M = Cu, Ni), and D_{MPc}-A_{PDI}-COF (M = Cu, Zn) have been synthesized from triphenylene or phthalocyanine donors and naphthalene dianhydride, benzothiadiazole (BTDA), and pyromellitic dianhydride (PMDA) acceptor units in highly polar solvent mixtures, such as *N*,*N*-dimethylformamide (DMF)/mesitylene and *N*,*N*-dimethylacetamide (DMAc)/*o*-dichlorobenzene (*o*-DCB), respectively.[92] Phthalocyanine-knotted COFs require polar solvents due to the poor solubility of phthalocyanine monomers (Table 1).[30,32,101−104] The boronate ester linkage can also be formed through the reaction of boronic acids and acetonide monomers (protected catechols) in the presence of a Lewis acid (BF_3·OEt_2) catalyst.[29,225]

5.2.3. Imine Linkage. An imine linkage can be formed by the reaction of aromatic amine and aldehyde in the presence of organic acid or Lewis acid catalyst (Figure 21). According to the topology diagrams, the imine-linked 2D COFs can be classified into five types, including hexagonal, tetragonal, rhombic, kagome, and trigonal architectures. A variety of π-units such as benzene,[65,70,135,175,201,226−228] triphenylbenzene,[38,78−81,175,207,210,219,229−234] triphenyltriazine,[82,235−237] tetraphenylpyrene,[37,57,107,113,238−244] TPE,[36,38,39,219,243] tetrathiafulvalene,[172,238,245] porphyrin,[33,96−98,100,106−108,167,246−248] hexaazatriphenylene (HAT),[35,116] hexaphenylbenzene (HPB),[12] and hexabenzocoronene (HBC)[12] have been developed as knots, whereas benzene,[12,33,35,36,38,39,50,65,79,80,96,100,106,108,113,128,175,201,207,214,219,226,238,249,250] ortho-substituted benzene,[37,80−82,98,100,108,123,167,230−232,234,237,246−248,251] biphenyl,[38,59,70,128,207,214] triphenyl,[38,39,128,241] bipyridine,[37,51,78,107,240,252] and thiophene[38] derivatives have been employed as edges. A broad diversity of solvents such as DOX, DOX/mesitylene, *o*-DCB/*n*-butanol (*n*-BuOH), ethanol (EtOH), DOX/*o*-DCB, THF/mesitylene, and DMAc/*o*-DCB have been employed for the solvothermal reactions at different temperatures (Table 2). In contrast with the broad diversity of

https://dx.doi.org/10.1021/acs.chemrev.9b00550
Chem. Rev. 2020, 120, 8814−8933

Table 1. Typical Reaction Conditions for Boronate-Ester-Linked COFs

COFs	solvents (v/v)	temperature (°C)	reaction time (day)	ref
COF-5, AEM-COF-1	DOX/mesitylene (1/1)	100	3 or 7	9, 121
COF-6	DOX/mesitylene (1/1)	85	5	26
COF-8, COF-10, TP-COF	DOX/mesitylene (1/1)	85	3	26, 27
COF-105	DOX/mesitylene (1/1)	85	9	47
COF-108	DOX/mesitylene (2/1)	85	4	47
MCOF-1	DOX/mesitylene (2/1)	90	3	149
DBA-3D-COF 1	DOX/mesitylene (10/1)	95	3	48
D−A COF, COF-66, T-COFs, MC-COFs-TP, MC-COFs-NiPc	DOX/mesitylene (1/1)	120	3	11, 90, 106, 224
TT-COF	DOX/mesitylene (1/1)	150	3	223
HHTP-DPB COF, TPE-Ph COF	DOX/mesitylene (1/1)	90	3	91, 117
H_2P-COF	DOX/mesitylene (1/9)	120	4	99
ZnP-COF	DOX/mesitylene (1/9)	120	15	99
CuP-COF	DOX/mesitylene (1/9)	120	2	99
D_{TP}-A_{NDI}-COF	DMF/mesitylene (1/1)	120	7	92
D_{TP}-A_{PyrDI}-COF	DMAc/*o*-DCB (1/1)	120	7	92
Pc-PBBA COF	mesitylene/1,2-dichloroethane (1/1)	85	6	29
MPc-COFs (M = Ni, Co, Cu), NiPc-BTDA COF, D_{ZnPc}-A_{PDI}-COF, M_1DPP-M_2*Pc*-COFs (M_1 = H_2, Zn, Cu; M_2 = Ni, Cu)	DMAc/*o*-DCB (2/1)	120	7	30, 32, 42, 102, 104
ZnPc-COF, M_1TPP-M_2*Pc*-COFs (M_1 = H_2, Zn, Cu; M_2 = Ni, Cu), AEM-COF-2	DMAc/*o*-DCB (1/1)	120	7	32, 109, 121
ZnPc-Py-COF, ZnPc-NDI-COF	DOX/MeOH (2/1)	120	3	103
ZnPc-DPB-COF	DOX/MeOH (3/1)	120	3	103
ZnPc-PPE-COF	DOX/MeOH (5/1)	120	3	103
D_{ZnPc}-A_{NDI}-COF	DMAc/*o*-DCB (2/1)	120	14	166
D_{MPc}-A_{PyrDI}-COFs (M = Cu, Ni), D_{MPc}-A_{NDI}-COFs (M = Cu, Ni), CoPc-PorDBA COF	DMAc/*o*-DCB (2/1)	120	3	101, 102
D_{CuPc}-A_{PDI}-COF	DMAc/*o*-DCB (4/1)	120	7	102

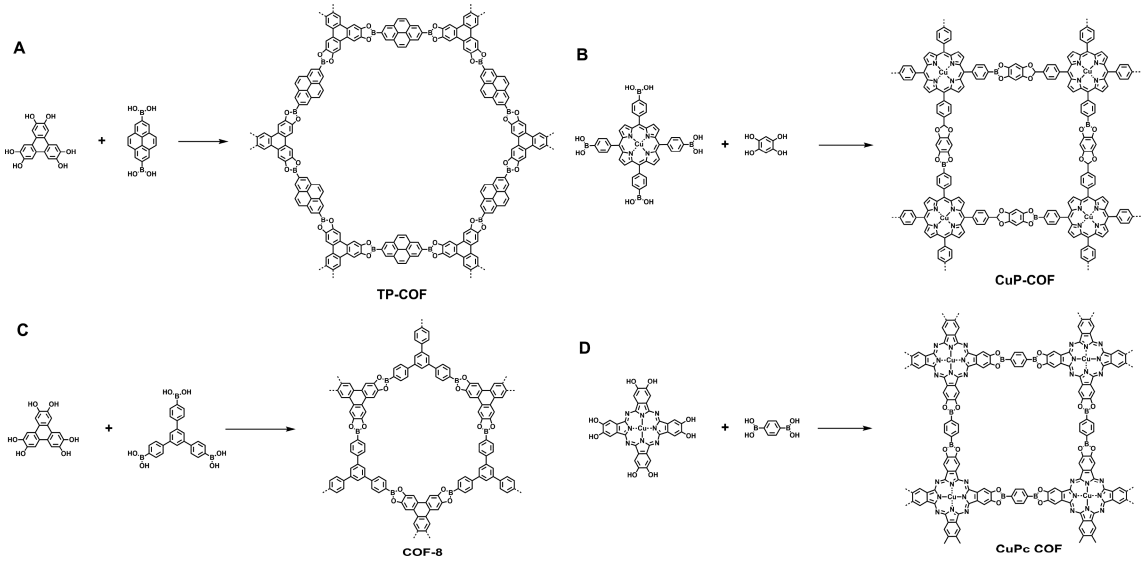

Figure 20. Schematics for the synthesis of (A) TP-COF, (B) CuP-COF, (C) COF-8, and (D) CuPc-COF.

knots for 2D COFs, the suitable monomers as a node for 3D COFs have been mostly limited to TAPM and TAA, which lead to the generation of 3D COF-300, COF-320, BF-COF-1, BF-COF-2, LZU-301, and 3D-Por-COF.[36,45,50,51,65,110,142,253] A series of 3D-Salphen-COFs, JUC-508, JUC-509, and JUC-509-Y (Y = Mn, Cu, or Eu), have been synthesized through the polycondensation of tetrakis(3-formyl-4-hydroxylphenyl)-methane (TFHPM) with 4,5-difluorophenylene-1,2-diamine (DFPDA) or 4,5-dichlorophenylene-1,2-diamine (DCPDA) in the presence of dioxane and mesitylene with acetic acid at 120 °C for 3 days (Table 2).[53] In addition to the solvothermal conditions, the use of the mechanochemical method via reactions at room temperature offers convenient access to COFs, including TpPa-1, TpPa-2, TpBD, LZU-1 (LAG), and DhaTph (LAG).[200,201] Nevertheless, the reactivity of monomers, the crystallinity, and the porosity of COFs synthesized by these mechanochemical methods are key factors to be considered and addressed.

5.2.4. Hydrazone Linkage. A hydrazone linkage is formed via the reaction of aldehyde with hydrazide in the presence of

https://dx.doi.org/10.1021/acs.chemrev.9b00550
Chem. Rev. 2020, 120, 8814−8933

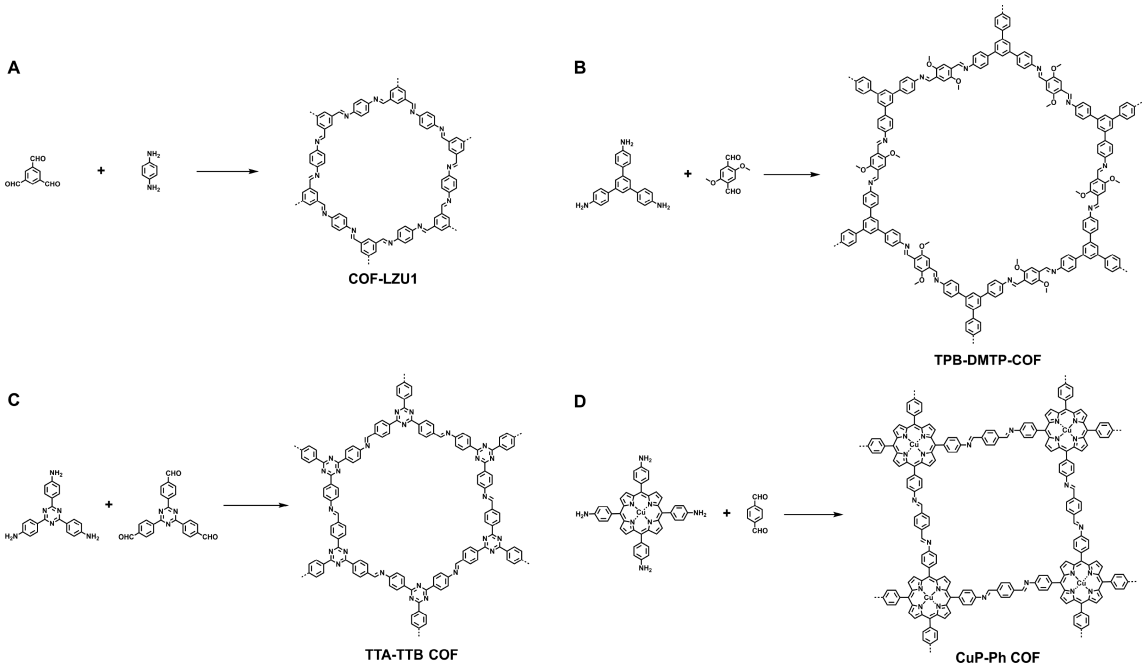

Figure 21. Schematics for the synthesis of (A) COF-LZU1, (B) TPB-DMTP-COF, (C) TTA-TTB-COF, and (D) CuP-Ph COF.

AcOH catalyst. Developing a hydrazone linkage to synthesize COFs requires the integration of an ethoxy group to the ortho position of edge units (e.g., 2,5-diethoxy-terephthalohydrazide (DETH)), which helps to secure the 2D conformation and promotes the formation of crystalline products. By using this strategy, five typical examples have been successfully synthesized. Under solvothermal conditions at 120 °C, COF-42, COF-43 (Figure 22), TFPT-COF, and COF-JLU4 have been synthesized in mixtures of DOX and mesitylene, whereas LZU-21 has been synthesized in mixtures of THF and mesitylene.[72,78]

5.2.5. Azine Linkage. The azine linkage takes advantage of the shortest hydrazine monomer to connect two aldehydes into polygon skeletons that form the smallest pores among various linkages. A variety of knots have been explored, including substituted benzene, triphenyl benzene, triphenyl triazine, and pyrene monomers, which lead to the synthesis of hexagonal, rhombic, and trigonal COFs (Figure 23).[42,73,74,78,84,85,111,124,267−271] As shown in Table 3, they have been designed and synthesized in different reaction media at various reaction temperatures depending on the solubility and reactivity of the π-knots.

5.2.6. Imide Linkage. The imide linkage can be synthesized via the reaction between amine derivatives and acetic anhydride; this reaction is less reversible and requires a high reaction temperature as high as 250 °C. Mesoporous 2D PI-COF-1, PI-COF-2, and PI-COF-3 have been synthesized under solvothermal conditions in a mixture of *N*-methyl-2-pyrrolidone (NMP)/mesitylene/isoquinoline (10/10/1 v/v/v) (Figure 24).[49] The PI-COF-1 and PI-COF-2 have been prepared upon reaction at 200 °C for 5 days, whereas PI-COF-3 is obtained under 250 °C for 7 days. Microporous 3D PI-COF-4 and PI-COF-5 have been synthesized upon reaction in a mixture of NMP/mesitylene/isoquinoline (10/50/1 v/v/v) at 160 °C for 5 days.[54]

5.2.7. C═C Linkages. The C═C-linked fully π-conjugated COFs have been achieved via the Knoevenagel condensation of aldehydes and benzyl cyanides in the presence of a base catalyst. The first example of C═C-linked COF is prepared by the condensation of tetrakis(4-formylphenyl)pyrene (TFPPy) and 1,4-phenylenediacetonitrile in the mixture of mesitylene/dioxane (1/5 v/v) at 110 °C for 3 days, catalyzed by aqueous NaOH solution (4 M) to yield sp^2c-COF in 89% yield (Figure 9C).[114] Similarly, a series of sp^2c-COFs with different linkers has been synthesized (Figure 25A).[115] In the presence of Cs_2CO_3 catalyst, the C═C-linked 2DPPV has been prepared in *o*-DCB at 150 °C for 3 days (Figure 25B).[192] The porphyrin-based sp^2c-COF has been synthesized under the catalysis of 1,8-diazabicyclo[5.4.0]undec-7-ene (dbu, 3 M) in *o*-DCB,[34] whereas hexaazatrinaphthalene 2D CCP-HATN has been prepared in a mixture of DMAc and *o*-DCB.[126] TP-COF (Figure 25B) has been prepared from the (2,4,6-tris(4-formylphenyl)-1,3,5-triazine) knot in a mixture of dioxane/chloroform (0.05% chloroform).[272] The unsubstituted olefin-linked COF-701 (Figure 25C) has been synthesized through the aldol condensation of 2,4,6-trimethyl-1,3,5-triazine and 4,4′-biphenyldicarbaldehyde in mesitylene/DOX/acetonitrile (18/18/1 v/v/v) in the presence of trifluoroacetic acid at 150 °C for 3 days.[218] A series of olefin-linked hexagonal COFs *g*-$C_{40}N_3$-COF, *g*-$C_{31}N_3$-COF, and *g*-$C_{37}N_3$-COF have been synthesized by the condensation of 3,5-dicyano-2,4,6-trimethylpyridine and 4,4′′-diformyl-*p*-terphenyl, 4,4′-diformyl-1,1′-biphenyl, and 1,3,5-tris(4-formylphenyl)benzene, respectively, catalyzed by piperidine in an anhydrous deoxygenated DMF at 150 °C for 3 days (Figure 25D).[76]

5.2.8. 1,4-Dioxin Linkage. COFs with a 1,4-dioxin linkage have be synthesized by the condensation of *ortho*-difluoro benzene or pyridine and catechol building units in the present of a base catalyst; the resulting COFs exhibit high chemical stability owing to the irreversible dioxin linkage. Three typical 1,4-dioxin-linked COFs have been successfully synthesized through this strategy (Figure 26). COF-316 (= JUC-505) has been prepared by the reaction of 2,3,6,7,10,11-hexahydroxytriphenylene (HHTP) and tetrafluorophthalonitrile (TFPN) in DOX (COF-316) or *N*-methylpyrrolidone/mesitylene (2/1 v/v JUC-505) with triethylamine (COF-316) or K_2CO_3 (JUC-505) at 120 °C for 3 days.[94,95] Meanwhile, HHTP and 2,3,5,6-

https://dx.doi.org/10.1021/acs.chemrev.9b00550
Chem. Rev. 2020, 120, 8814−8933

Table 2. Typical Reaction Conditions for the Imine-Linked COFs

COFs	solvents (v/v)	temperature (°C)	reaction time (day)	catalyst	ref
COF-LZU1, ILCOF-1, COF-300, COF-320	DOX	120	3	3 M AcOH	50, 65, 110, 142
2,3-DhaTta COF, 2,3-DhaTab COF	DOX/mesitylene (0.3/1.7)	120	3	3 M AcOH	82
Py-1P COF, Py-1PF COF, Py-2P COF	DOX/mesitylene (1/2)	120	3	6 M AcOH	113
Py-2PE COF	mesitylene/DOX/BuOH (6.67/4/4)	120	5	6 M AcOH	
Py-3PE COF, Py-3PE$_{BTD}$ COF	mesitylene/BuOH (2/1)	120	5	6 M AcOH	
3D-Py-COF	*o*-DCB/BuOH (0.7/0.3)	120	3	6 M AcOH	57
COF-DhaTab	DOX/mesitylene (0.3/1.7)	120	3	8 M AcOH	81
PI-2-COF, Py-DHPh COF, Py-2,3-DHPh COF, Py-2,20-BPyPh COF, Py-3,30-BPyPh COF, EB-COF:X (X = F, Cl, Br, I)	DOX/mesitylene (1/1)	120	3	6 M AcOH	37, 68, 70
PI-3-COF	DOX/mesitylene (10/1)	120	3	6 M AcOH	
BF-COF-1, BF-COF-2	mesitylene	120	5	3 M AcOH	135
COF-LZU8	DOX/mesitylene (1/3)	120	3	6 M AcOH	254
TPT-COF-1	EtOH	120	3	3 M AcOH	23, 64, 240
TPT-COF-2, Bpy-COFs, TpPa-1, TpPa-2	DOX/mesitylene (1/1)	120	3	3 M AcOH	
COF-BPDA, COF-TPDA, COF-TPA	DOX	120	3 or 4	6 M AcOH	36, 39
SIOC-COF-1, SIOC-COF-2	DOX/toluene (1/2)	120	3	9 M AcOH	39
3PA-2P COF	anisole/DOX (19/1)	120	3	6 M AcOH	38
3PA-TT COF	mesitylene/benzyl alcohol (9/1)	120	4	6 M AcOH	
3PB-TT COF	anisole/EtOH (9/1)	100	5	6 M AcOH	
Tp-Azo, Tp-Stb	DMAc/*o*-DCB (1/1)	120	3	NIL	62
DAAQ-TFP-COF	DMAc	90 or 120	2	6 M AcOH	69
TH-COF-1	DOX/*o*-DCB	120	3	NIL	255
LZU-20	THF/mesitylene (2/3)	120	7	3 M AcOH	78
HAT-COF	DMAc/mesitylene (1/1)	120	3	6 M AcOH	35
H_2P-Bph-COF, COF-366	EtOH/mesitylene (1/1)	120	3	6 M AcOH	106, 256
TpBDH COF, TfpBDH COF	DOX/DMAc (1/2)	120	3	6 M AcOH	257
TTF-Ph-COF, TTF-COF, H_2P-COFs	DOX/mesitylene (1/1)	120	3	3 M AcOH	172, 238, 247
TTF-Py-COF	*o*-DCB/BuOH (1/1)	120	3	3 M AcOH	
TPB-DMTP-COF, Py-An COF	*o*-DCB/BuOH (1/1)	120	3 or 5	6 M AcOH	80, 239
TFPT-COF	DOX/mesitylene (1/2)	120	3	6 M AcOH	83
CTV-COF-1, CTV-COF-2	EtOH	90	5 or 6	3 M AcOH	214
TFP-DABA COF	DOX/mesitylene (4/1)	100	3	3 M AcOH	258
TAPB-TFPB, TAPB-TFP, *i*PrTAPB-TFPB, *i*PrTAPB-TFP	DOX	110	5	6 M AcOH	259
HPB-COF	toluene	120	9	3 M AcOH	12
HBC-COF	DOX/BuOH (19/1)	120	12	6 M AcOH	
CCOF-1, CCOF-2	DOX	100	3	9 M AcOH	260
LZU-72	DOX/mesitylene (1/4)	90	3	3 M AcOH	227
LZU-76	DMAc	100	2	6 M AcOH	
COF-505	THF	120	3	6 M AcOH	59
FL-COF-1	*o*-DCB/DMAC (1/1)	120	3	3 M AcOH	261
TAPB-PDA COF	DOX/mesitylene (4/1)	20	3	7.5 μM Sc(OTf)$_3$	207
LZU-301	DOX	120	3	6 M AcOH	51
Salen-COFs	DOX/EtOH (4/1)	120	3	3 M AcOH	262
PPN-30, PPN-31	DMF	120	3	6 M AcOH	228
3D-Por-COF, 3D-CuPor-COF	*o*-DCB/BuOH (1/1)	120	7	6 M AcOH	45
CCOF-5	DOX	120	3	6 M AcOH	52
SP-3D-COF-1	*o*-DCB/BuOH (7/3)	130	3	AcOH	55
SP-3D-COF-2	*o*-DCB/BuOH (1/1)	130	3	AcOH	
3D-TPE-COF	*o*-DCB/mesitylene (1/1)	120	7	6 M AcOH	58
JUC-508	DOX/mesitylene (4/1)	120	3	6 M AcOH	53
JUC-509	DOX/mesitylene (7/3)	120	3	6 M AcOH	
H-ImCOF	EtOH/mesitylene (4/1)	120	3	6 M AcOH	263
CCOF-7	EtOH/mesitylene (3/1)	120	3	9 M AcOH	264
CCOF-8	EtOH/mesitylene (5/1)	120	3	9 M AcOH	
3D-TPB-COF-H	$CHCl_3$/BuOH (20/1)	100	7	6 M AcOH	265
3D-TPB-COF-Me	$CHCl_3$/BuOH (2/1)	110	7	6 M AcOH	
3D-TPB-COF-H	DOX/*o*-DCB (21/9)	120	7	6 M AcOH	

https://dx.doi.org/10.1021/acs.chemrev.9b00550
Chem. Rev. 2020, 120, 8814−8933

Table 2. continued

COFs	solvents (v/v)	temperature (°C)	reaction time (day)	catalyst	ref
COF-1-Zn	DOX/BuOH (2/1)	120	3	3 M AcOH	266
COF-2-Zn	DOX/BuOH (2/1)	120	3	3 M AcOH	

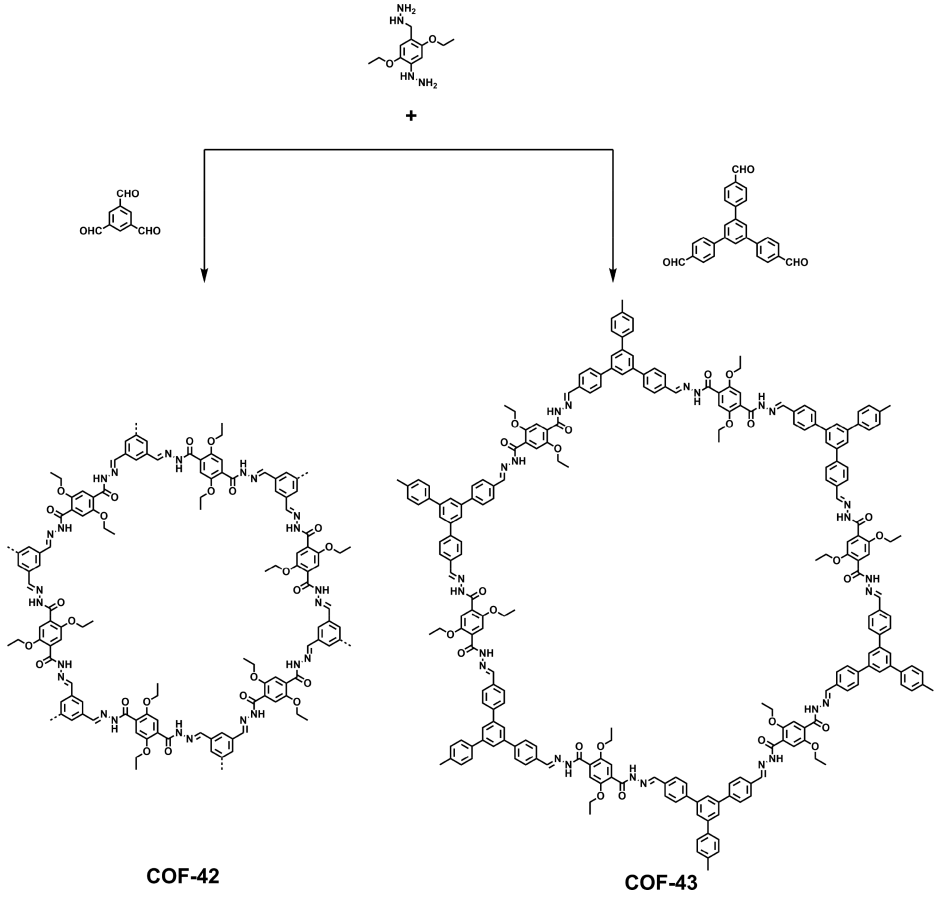

Figure 22. Schematics for the synthesis of COF-42 and COF-43.

tetrafluoro-4-pyridinecarbonitrile are condensed to form COF-318 in a mixture of DOX and mesitylene (1/1 v/v).[94] JUC-506 has been synthesized by the condensation of HHTP and 2,3,6,7-tetrafluoroanthraquinone catalyzed by K_2CO_3 in a mixture of NMP/mesitylene (2/1 v/v) at 160 °C for 3 days.[95]

5.2.9. Other Linkages. CTFs have been synthesized by the cyclotrimerization of 1,4-benzonitrile in molten $ZnCl_2$ at 450 °C (Figure 27A).[75] Because of the limited reversibility of the reaction and the insufficient availability of the suitable monomers, CTFs have limited members and relatively low crystallinity. Replacing molten $ZnCl_2$ with trifluoromethanesulfonic acid as the catalyst enables the synthesis of CTFs at room temperature or under microwave conditions.[197] The latter approach leads to the generation of CTFs with high purity owing to the absence of $ZnCl_2$.

The phenazine linkage owing to its fused planar structure and high stability affords π-conjugated and stable CS-COF (CS stands for conjugated and stable, Figures 16E and 27B) upon the condensation of triphenylene hexamine (TPHA) and *tert*-butylpyrene tetraone (PT) monomers under solvothermal condition in a mixture of ethylene glycol/3 M AcOH (1/1 v/v) at 120 °C for 3 days.[158] More recently, phthalocyanine-based COF-DC-8 (Figure 27C) has been synthesized through the aromatic annulation of 2,3,9,10,16,17,23,24-octaaminophthalocyanine nickel(II) and pyrene-4,5,9,10-tetraone.[273]

The squaraine-linked CuP-SQ COF (Figure 27D) has been synthesized by the condensation of copper(II) 5,10,15,20-tetrakis(4-aminophenyl)porphyrin (TAP-CuP) and squaric acid (SQ) under solvothermal conditions (*o*-DCB/*n*-BuOH 1/1 v/v) at 85 °C for 7 days.[216] This linkage enables the construction of a zwitterionic structure on the pore walls.

The borazine-linked BLP-2(H) COF (Figure 27E) has been synthesized by the thermal decomposition of 1,3,5-(*p*-aminophenyl)-benzene-borane in a mixture of mesitylene/toluene (1/4 v/v) at 120 °C for 3 days.[215]

Spiroborate-linked ionic COFs (ICOF-1 and ICOF-2) (Figure 27F) have been synthesized under solvothermal conditions in DMF at 120 °C for 7 days.[217] This linkage is relatively stable in water and base (1 M LiOH for 2 days), which is different from other boron-based linkages.

A π-conjugated viologen-based COGF (Figure 27G) has been synthesized via the Zincke reaction between 1,1′-bis(2,4-dinitrophenyl)-[4,4′-bipyridine]-1,1′-diium dichloride (BDB) and TAPB under both solvothermal and microwave conditions.[220]

https://dx.doi.org/10.1021/acs.chemrev.9b00550
Chem. Rev. 2020, 120, 8814−8933

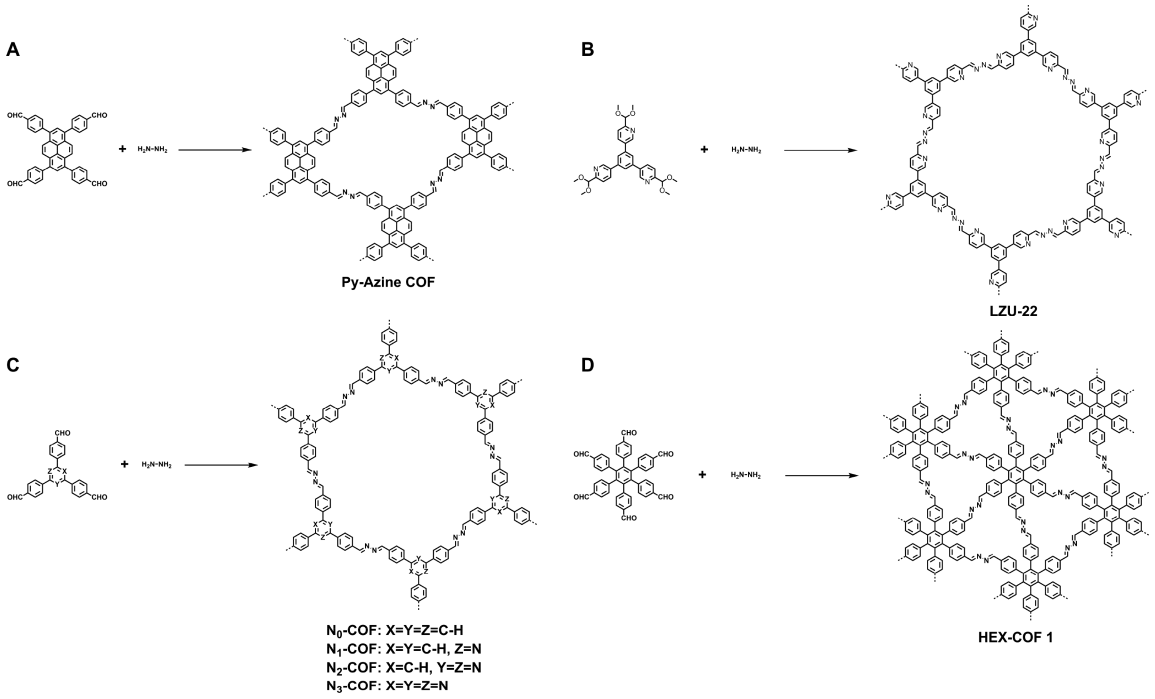

Figure 23. Schematics for the synthesis of (A) Py-Azine COF, (B) LZU-22, (C) N_x-COF (x = 0, 1, 2, and 3), and (D) HEX-COF 1.

Table 3. Typical Reaction Conditions for the Azine-Linked COFs

COFs	solvents (v/v)	temperature (°C)	reaction time (day)	catalyst	ref
Py-Azine-COF, NF-COF, TF-COF 1, TF-COF 2, AB COF	*o*-DCB/BuOH (19/1)	120	3 or 7	6 M AcOH	111, 267, 268
ACOF-1	DOX/mesitylene (1/1)	120	3	6 M AcOH	73
HEX-COF 1, N_x-COFs (x = 0, 1, 2, 3)	DOX/mesitylene (1/2)	120	3	6 M AcOH	85, 124
ATFG COF	DOX/mesitylene (12/1)	120	3	6 M AcOH	267
COF-JLU2	THF/MeOH (1/1)	120	5	6 M AcOH	74
COF-JLU3	DMF	120	3	3 M AcOH	84
LZU-22	THF/mesitylene (2/3)	120	7	3 M AcOH	60
HP-COF-1, 2	DOX/*o*-DCB (2/1)	150	4	6 M AcOH	42
CTF-HUST-1	DMSO	120	3	Cs_2CO_3	269
*p*CTF-1	NA	400		P_2O_5	270
CTF-HUST-C1, CTF-HUST-C5, CTF-HUST-C5	DMSO	100	1	Cs_2CO_3	271
		180	1.5		

The 2D π-conjugated PD (Figure 27H), BD, and TPA COFs have been prepared via the Michael addition−elimination reaction of various β-ketoenols with amines under acidic conditions.[274] The 2D conjugated aromatic polymer linked by the C−C bond has been prepared via the surface-assisted debromination and aryl−aryl coupling reaction between tetrabromopolyaromatic monomers,[275] whereas the C−C-bonded 2DCCOF (Figure 27I) films have been achieved through Suzuki coupling reaction at a liquid−liquid interface.[205] The π-conjugated covalent organic radical frameworks linked by the C−C bond have been prepared at a liquid/liquid (dichloromethane/H_2O) interfacial acetylenic homocoupling of triethynyl-polychlorotriphenylmethane monomers.[276]

Recently, hypercoordinate silicon linkages have been developed for the synthesis of 3D SiCOF-5 with a composition of $Na_2[Si(C_{18}H_6O_6)]$ through the combination of dianionic hexacoordinate $[SiO_6]^{2-}$ nodes and triangular triphenylene building blocks.[56]

COF-117 (Figure 27J) and COF-118 bearing flexible urea linkages have been synthesized by the condensation of TFP with 1,4-phenylenediurea (BDU) or 1,1′-(3,3′-dimethyl-[1,1′-biphenyl]-4,4′-diyl)diurea (DMBDU).[221]

5.2.10. Double-Stage Linkages. In addition of the above strategies using one linkage for COFs, the use of two different linkages for the construction of one COF, that is, the double-stage linkage strategy, has been explored (Figures 28 and 29). In this strategy, one monomer is required to have bifunctional reactive sites; 4-formylphenyl boronic acid (Figure 28A, FPBA) is a typical example that allows the formation of boroxine with imine linkages, boronate ester with imine linkages, and boronate ester with hydrazone linkages.[87,88,277] This double-stage strategy has been successfully explored for the synthesis of hexagonal (Figure 28), rhombic-shaped (Figure 29A), and tetragonal (Figure 29B) COFs and a greatly enhanced structural complexity and diversity of COFs. For example, HHTP-, triphenyl-benzene-, triphenyl-triazine-, and TATTA-based COFs have been synthesized in DOX/mesitylene mixed solvents, whereas the phthalocyanine-based COFs have been prepared in a mixture of DMAc/*o*-DCB (Table 4).

https://dx.doi.org/10.1021/acs.chemrev.9b00550
Chem. Rev. 2020, 120, 8814−8933

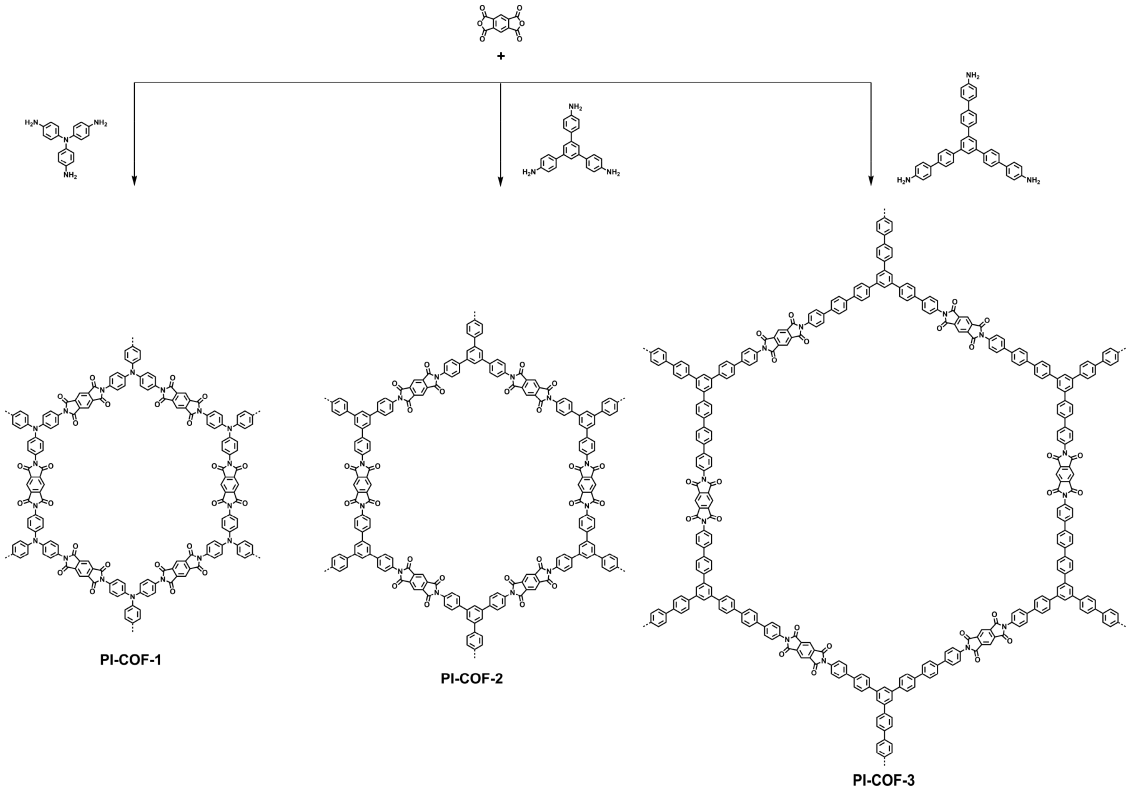

Figure 24. Schematics for the synthesis of 2D PI-COF-1, PI-COF-2, and PI-COF-3.

5.2.11. Linkage Transformation. The linkage transformation is a facile way to synthesize COFs with linkages that are difficult to be synthesized directly. The oxidation of the imine linkage enables the conversion of the imine-linked TPB-TP-COF to an amide-linked COF (Figure 30A),[219] whereas the reduction of the imine-linked 3D-COF-300 and 2D-COF-366-M (Figure 30B) with $NaBH_4$ yields their corresponding amine-linked COFs.[278] The imine linkage in ILCOF-1 has been converted to oxazole and thiazole linkages through consecutive linker substitution and oxidative cyclization, respectively (Figure 30C, R = S, thiazole; R = O, oxazole).[279]

Oxazole-linked LZU-192 has been synthesized from ILCOF-1 upon the reaction with 2,5-diaminobenzene-1,4-dithiol dihydrochloride in DMF/water (3/1 vol) at 85 °C for 1 day, whereas thiazole-linked COF-921 has been prepared by the reaction with 2,5-diaminobenzene-1,4-dithiol dihydrochloride in ILCOF-1 in DMF/water (85/15 vol). At a high temperature such as 350 °C, sulfur reacts with aromatic imines of TTI-COF to first oxidize the imine to a thioamide and subsequently oxidatively cyclizes the thioamide group to form TTT-COF with thiazole linkages.[280] The imine linkages of TPB-DMTP-COF have been kinetically fixed via an aza-Diels−Alder cycloaddition reaction to form quinoline-linked COFs (Figure 30D).[169] Cyclic carbamate and thiocarbamate-linked COFs have been synthesized from COF-170 through a multistep solid-state organic synthetic process (Figure 30E).[193]

5.3. Reaction Mechanisms

Mechanistic studies on the formation of crystalline porous COFs are of special importance to reveal the nature of polycondensation and crystallization because these two different processes occur in one pot. The polycondensation reaction involves the generation of oligomers of different sizes that can further react with each other to yield a polymer mixture of various structures and sizes. This reaction diagram makes the polycondensation system complex and the formation of crystalline frameworks difficult. Despite the difficulty, mechanistic studies have shown insights into polymerization as well as crystallization, opening a way to uncover a full picture of the formation of crystalline porous COFs.

5.3.1. Mechanistic Studies and Understandings. The formation mechanism of boronate-ester-linked COFs synthesized from the condensation of polyfunctional boronic acid with acetonide-protected catechol reactants catalyzed by $BF_3{\cdot}OEt_2$ has been explored.[225] Studies on the soluble acetonide compound using $BF_3{\cdot}OEt_2$ to catalyze its hydrolysis followed by the condensation with boronic acid show the formation of a boronate ester compound (Figure 31). Simultaneously, the side reaction involves the trimerization of the boronic acid reactant to form a boroxine compound and water. The acetonide hydrolysis is the rate-limiting step before the free boronic acid reactant is used up; thereafter, the rate-limiting step changes to the boroxine hydrolysis. As the boroxine hydrolysis dominates the boronate ester formation, the COF formation rate is highly dependent on the water content. Combining the above mechanistic studies on model compounds with the crossover experiments between simple boronate esters, it is concluded that the hydrolysis of the acetonide-protected catechol monomer is the dominant process in the $BF_3{\cdot}OEt_2$-catalyzed COF formation.

To gain insight into the nucleation, a kinetic study on the boronate-ester COF formation has been conducted by using homogeneous reaction systems. The homogeneous reaction condition can be made by adding a small amount of MeOH to the mixture of mesitylene/DOX that is used in the conventional COF-5 synthesis, in which the turbidity change of the solution offers an unprecedented measure to determine the rate of COF

https://dx.doi.org/10.1021/acs.chemrev.9b00550
Chem. Rev. 2020, 120, 8814−8933

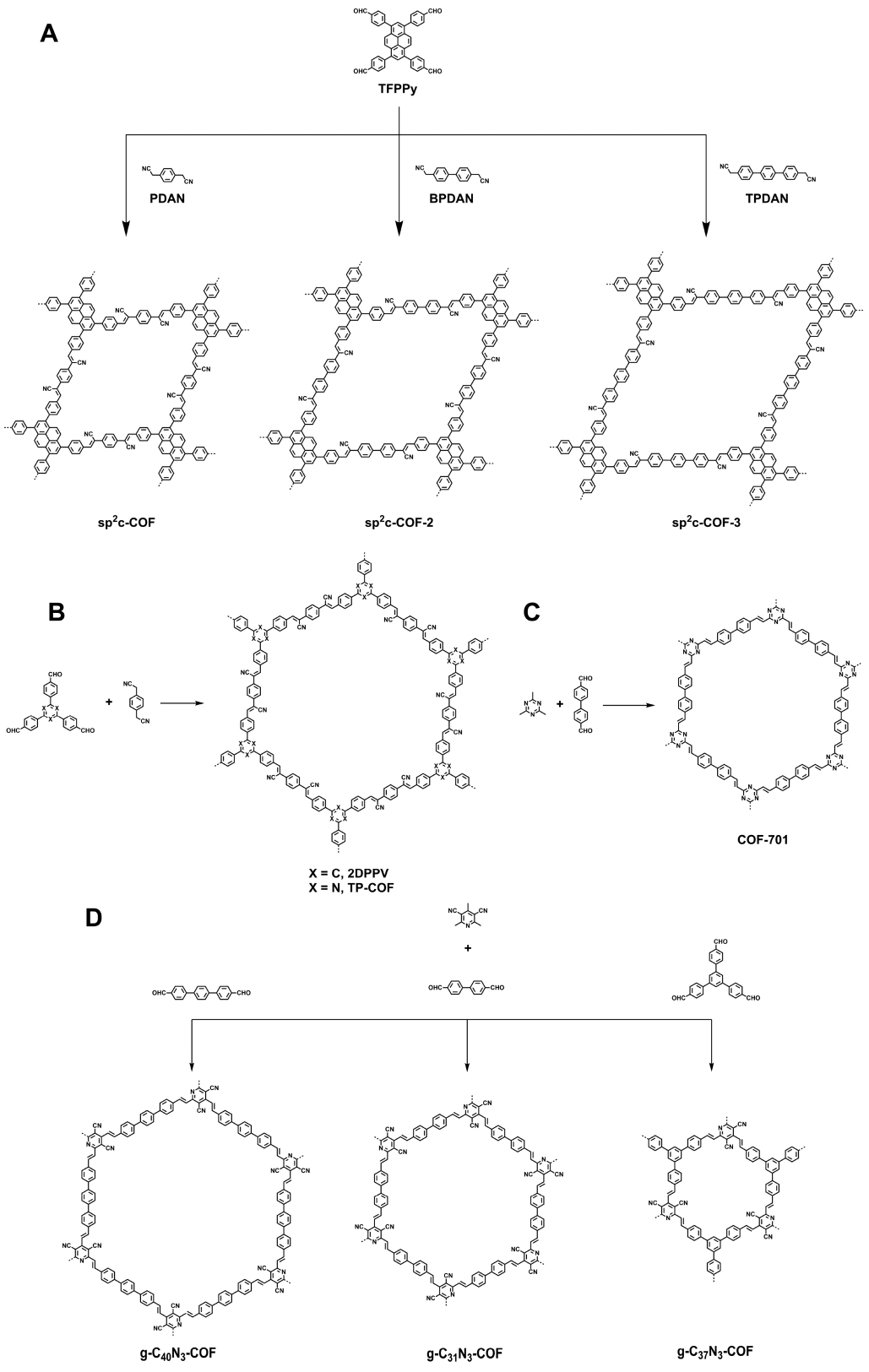

Figure 25. Schematics for the synthesis of (A) sp²c-COF, sp²c-COF-2, and sp²c-COF-3; (B) 2DPPV and TP-COF; (C) COF-701; and (D) *g*-$C_{40}N_3$-COF, *g*-$C_{31}N_3$-COF, and *g*-$C_{37}N_3$-COF.

formation.[186] The COF formation rate is proportional to the *in situ* optical turbidity of the reaction mixture at 1310 nm, where the solvent and monomers have minimized absorption. For example, at 90 °C, the formation of COF-5 starts after an induction period of 2 min and proceeds at a constant growth rate for several minutes, thereafter followed by continuous growth but at a decreased rate. In general, the condensation of monomers proceeds to form oligomers during the induction

https://dx.doi.org/10.1021/acs.chemrev.9b00550
Chem. Rev. 2020, 120, 8814−8933

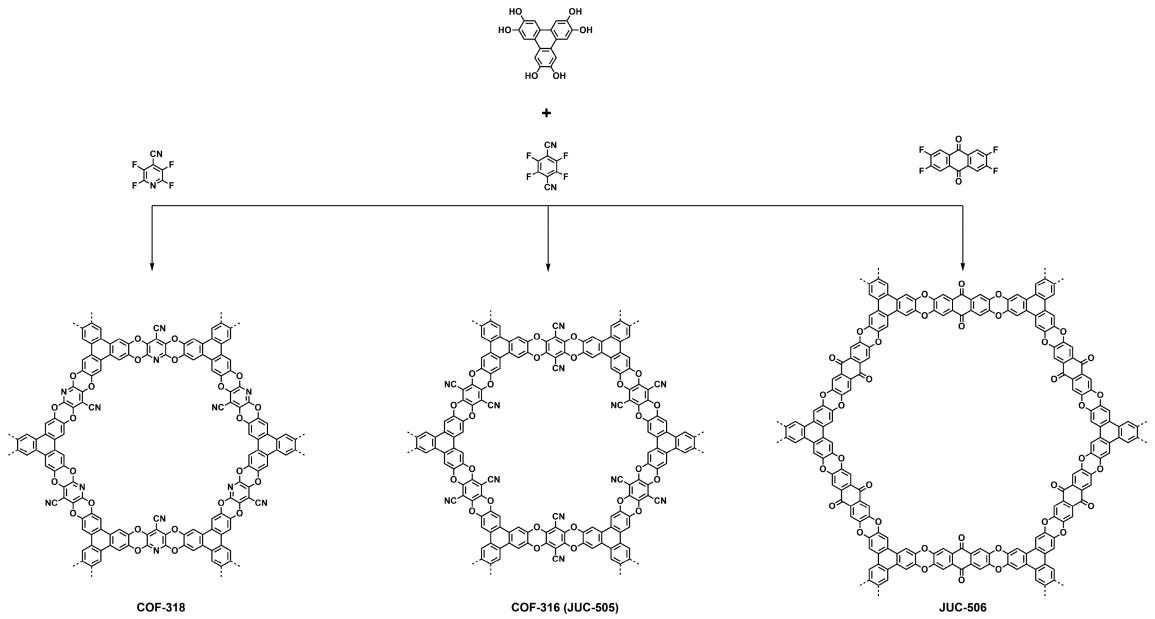

Figure 26. Schematics for the synthesis of COF-318, COF-316 (JUC-505), and JUC-506.

period, and the subsequent nucleation process involves reversible bond formation for defect self-healing and an irreversible crystallization step, leading to the formation of final polycrystals (Figure 32). The irreversibility of the crystalline step is demonstrated by adding a monofunctional 4-*tert*-butylcatechol (TCAT) to the reaction system at different reaction times. The addition of TCAT reduces the polymerization rate but does not change either the yield or the composition of COF-5; the monofunctionalized TCAT unit is hardly found in COF-5, indicating that once the COF-5 crystallite forms, there is a very limited chance to further react with monofunctional TCAT. The resulting COF-5 (Figure 7B) synthesized under homogeneous reaction conditions exhibits high crystallinity and porosity (S_{BET} = 2000 m^2 g^{-1}), which is greatly superior to conventional COF-5 (1590 m^2 g^{-1}). Further mechanistic studies reveal that the crystallization rate of COFs also depends on the pore size and the interlayer interactions. The interlayer π-stacking is likely the rate-determining process; a large π-unit will greatly enhance the interlayer attraction, leading to a high rate of growth. Taking COFs with similar bonding and topologies, for example, the growing rate is dramatically increased from HHTP-DPB COF to COF-10, COF-5, and TP-COF as the π-units become larger.[89,186]

Recently, a kinetic Monte Carlo (KMC) model has been developed to simulate the formation of a prototypical boronate-ester-linked COF-5 in solution.[281] Through combining the experimental and theoretical results, the nucleation and growth of COF-5 have been revealed. The formation of oligomers is the first stage and influences the length of the induction period; two nucleation pathways of lateral growth of small stacked structures and stacking between large oligomers have been identified. During the growth of COF-5, both the diameter and the height increase linearly with time. The lateral growth is determined by the monomers, whereas the vertical growth is primarily due to oligomer stacking. Adding water shifts the equilibrium away from large oligomers, favoring lateral growth other than vertical growth and resulting in COF-5 crystals with larger diameters. Because oligomers are crucial in the nucleation process and dominate vertical growth, the crystallization of COF-5 is reminiscent of crystallization by particle attachment (CPA).

Distinct from the formation of boronate-ester linked COFs, the formation of imine-linked COFs is dependent on the dynamic imine-bond exchange.[79] As exemplified by the TAPB-PDA COF, in the initial stage, the solid rapidly precipitates upon the addition of aqueous acetic acid as the catalyst to the homogeneous solution of monomers at room temperature, and the resulting powders are obtained in 95% yield as amorphous polymers with a low surface area. Subsequently, the amorphous networks transform into crystalline COFs. Even in the absence of free monomers, those amorphous powders will transform into crystalline COFs to display intense diffraction peaks, but the transformation will be inhibited in the absence of acetic acid. In this case, the BET surface area increases as the reaction time is extended, indicating that the amorphous polymer-to-crystalline COF transformation is a must for the imine-linked COFs. Indeed, the poor-quality COFs can be transformed into high-quality COFs as a result of crystalline structural reconstruction by controlling the pH value of the reaction media (pH 6 to 7) and the reaction time (>12 h) at room temperature.[253] Clearly, this capability of structural reconstruction can extend the lifetime of COFs.

Inspired by the growth process of the imine-linked 2D COF, further efforts have been made to obtain a deep understanding of the mechanism. With the decreased concentration of monomers, the WAXS diffraction reveals the smaller crystalline domains of the resulting colloids, indicating that both the COF particle size and the average crystalline domain size decrease with the initial monomer concentration. Notably, time-dependent studies using *in situ* SAXS/WAXS reveal that the formation of COF particles is faster than the crystallization, indicating that the polymerization and crystallization processes are not synchronized in the formation of the imine-linked COF. These results show a clear picture of the mechanism for the imine-linked COF formation driven by the amorphous polymer-to-crystalline framework transformation.[160]

Similarly, the crystal formation of imine-linked 3D COFs, as exemplified by COF-300 and COF-320, involves a two-step

https://dx.doi.org/10.1021/acs.chemrev.9b00550
Chem. Rev. 2020, 120, 8814−8933

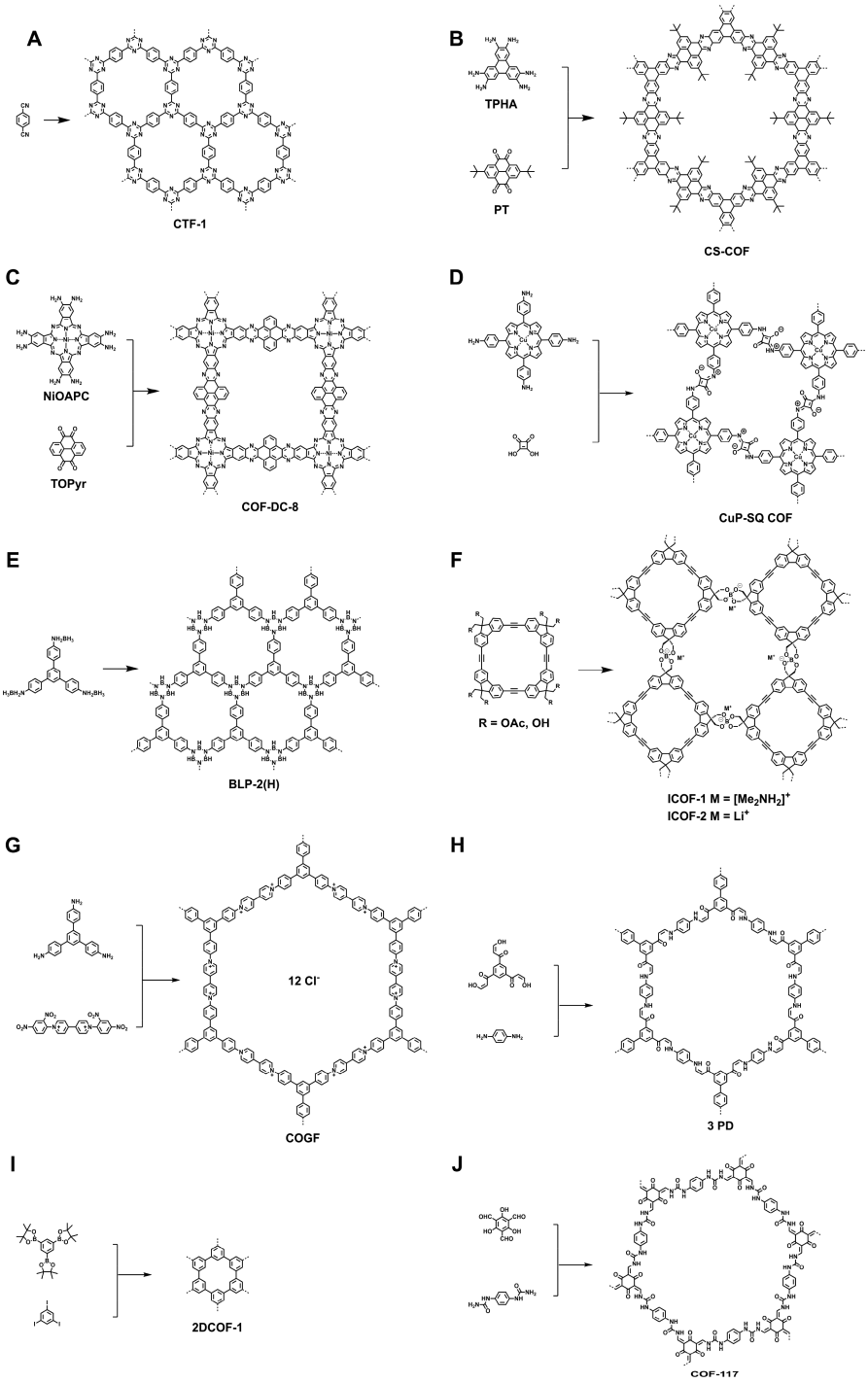

Figure 27. Schematics for the synthesis of (A) the triazine-linked CTF-1, (B) the phenazine-linked CS-COF, (C) the phthalocyanine-based COF-DC-8, (D) the squaraine-linked CuP-SQ COF, (E) the borazine-linked BLP-2(H), (F) the spiroborate-linked ionic ICOF-1 and ICOF-2, (G) the π-conjugated viologen-based COGF, (H) the 2D π-conjugated 3 PD, (I) the C−C linked 2DCOF-1, and (J) COF-117 with a urea linkage.

transformation mechanism.[282] The 3D COFs first form an initial amorphous nonporous solid, which can be isolated and re-exposed to growth conditions to transform into 3D COF crystallites with high porosity.

5.3.2. Single-Crystal COFs. Crystallinity is the key feature that distinguishes COFs from other polymers, including conjugated microporous polymers, cross-linked polymers, and amorphous porous organic polymers. The single crystal is related to one of the most important and challenging issues of the COF field in revealing structural insights into functions and properties. Synthetic efforts have been devoted to controlling the crystallinity and nucleation of COFs.[283] Using nitrile-containing acetonitrile as a solvent that prevents the aggregation and precipitation yields stable colloidal suspension COF nanoparticles, and slowly adding monomers achieves the seeded growth of single crystals of boronate-ester-linked 2D COF-5, COF-10, and TP-COF.[161] The seeded colloid size can be monitored by DLS, and the multilayer nanocrystal structure of COFs can be characterized by HR-TEM and optical TA spectroscopy.

https://dx.doi.org/10.1021/acs.chemrev.9b00550
Chem. Rev. 2020, 120, 8814−8933

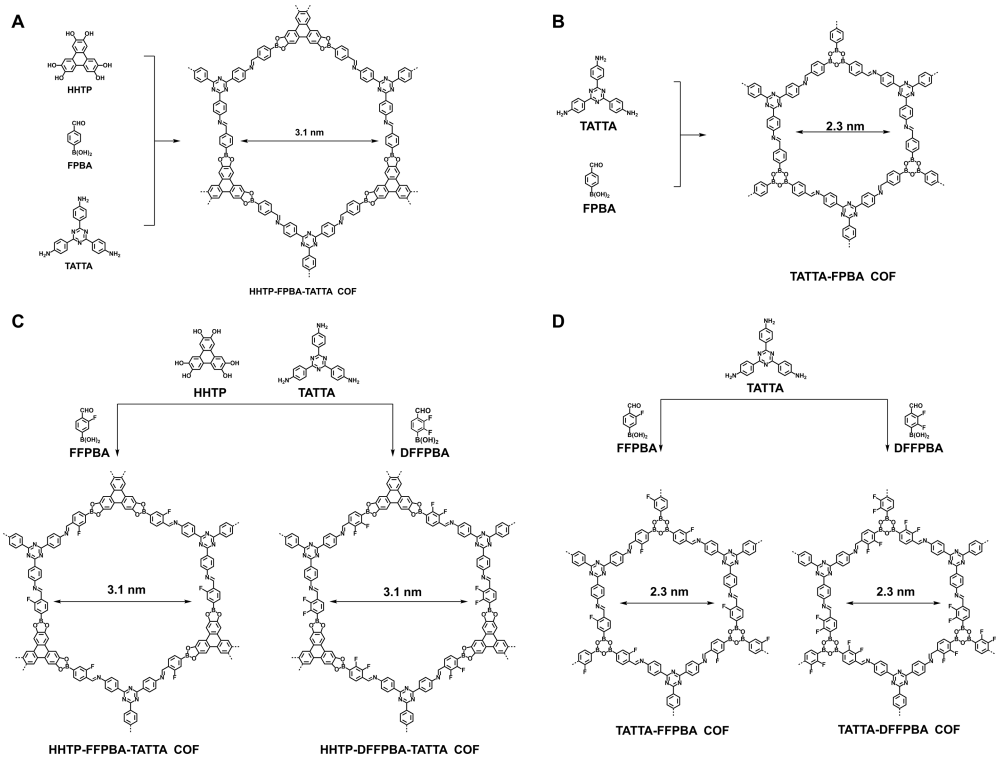

Figure 28. Schematics of the double-stage COFs for (A) HHTP-FPBA-TATTA COF, (B) TATTA-FPBA COF, (C) HHTP-FFPBA-TATTA COF and HHTP-DFFPBA-TATTA COF, and (D) TATTA-FFPBA COF and TATTA-DFFPBA COF.

Remarkably, single crystals of 3D COFs have been reported for imine-linked COF-300, COF-303, LZU-79, and LZU-111 (Figure 33).[154] In these cases, the addition of a large excess amount of monofunctional monomer, that is, aniline, as a modulator that forms terminal phenyleneimine moieties on the crystal surface offers a long enough time for error correction, leading to the formation of single crystals of 3D COFs. Nevertheless, exploring a more efficient method to prepare single crystals of both 2D and 3D COFs is still a challenge.

5.3.3. Controlled Synthesis. An efficient strategy for optimizing the crystallinity, domain size, and porosity of COF-5 is to use monoboronic acid as a modulator under solvothermal conditions.[284] The monofunctional modulator serves as a capping agent that terminates the 2D sheets during lateral growth. By repetitive attachment and detachment, the modulator slows down the COF formation, thus facilitating the self-healing and bringing the system closer to the thermodynamic equilibrium. Furthermore, the modulator can fill point or line defects, thus reducing strains in crystals and increasing the stability of overall crystals. Recent theoretical research has explored the inherent mechanism of the formation of COF-5 crystals. During the assembly of COF-5, strong stacking interactions are at least partially responsible for the small crystallite sizes of other 2D COFs.[285] In this case, the most direct way to increase the crystallite size relies on identifying solvents that can effectively diminish stacking interactions.

According to theoretical calculations, a lateral offset between adjacent layers of certain COFs is energetically favorable and results in slipped structures rather than fully eclipsed structures. This conformational mode would decrease the crystallinity of the COF. To compensate such a slipped structure, a strategy based on a lock-and-key molecular mechanism has been employed in which the conformation of building blocks unambiguously defines the position of each building unit within adjacent COF layers. The multidentate central units with a lock-and-key-like molecular conformation guides the attachment of the successive layers, which enhance the crystallinity and stability of COFs.[38] Four TPE-based COFs, that is, 4PE-1P, 4PE-2P, 4PE-3P, and 4PE-TT, have been successfully synthesized under solvothermal conditions by using the above strategy (Figure 10). The four phenyl groups in the knot assume a screw-like arrangement and thus allow the TPE knots of a successive COF layer to lock into a single and well-defined lateral position. Notably, these COFs possess high physicochemical stabilities, surface areas, and crystallinities. This strategy is potentially applicable in designing and synthesizing various COFs to achieve high structural ordering and exceptional stability.

Tailoring the structure of COFs by modulating the supramolecular interactions is another efficient way to enhance the crystallinity and porosity. Introducing as-synthesized acid-diamine salts that possess different reactivities toward the aldehyde (Tp) depending upon their N−H···O hydrogen-bonding strength, a series of TpPa-based COFs have been synthesized from PTSA-diamine salts with sharp diffraction peak that corresponds to the (100) planes.[286] Considering the fact that the strong hydrogen-bonded acid-diamine salts hinder the imine bond formation because of their low reactivity with aldehyde, the intermolecular N_{amine}−H···O_{acid} hydrogen-bonding interaction plays a pivotal role in controlling the reactivity of these acid-diamine salts. Experimentally, when synthesized from PSA-Pa-2, COF-TpPa-2 exhibits a BET surface area as high as 969 $m^2 g^{-1}$, whereas a similar COF has a BET surface area of 407 and 430 $m^2 g^{-1}$ when synthesized from BSA-Pa-2 and PTSA-Pa-2 salts, respectively. Compared with the hydrogen-bonding distance (d_{av}) of PTSA-Pa-2 (1.875 Å) and BSA-Pa-2 (1.869 Å), the d_{av} value (2.119 Å) of PSA-Pa-2 is more suitable; a strong hydrogen-bonding interaction (a short d_{av} distance) prohibits

https://dx.doi.org/10.1021/acs.chemrev.9b00550
Chem. Rev. 2020, 120, 8814−8933

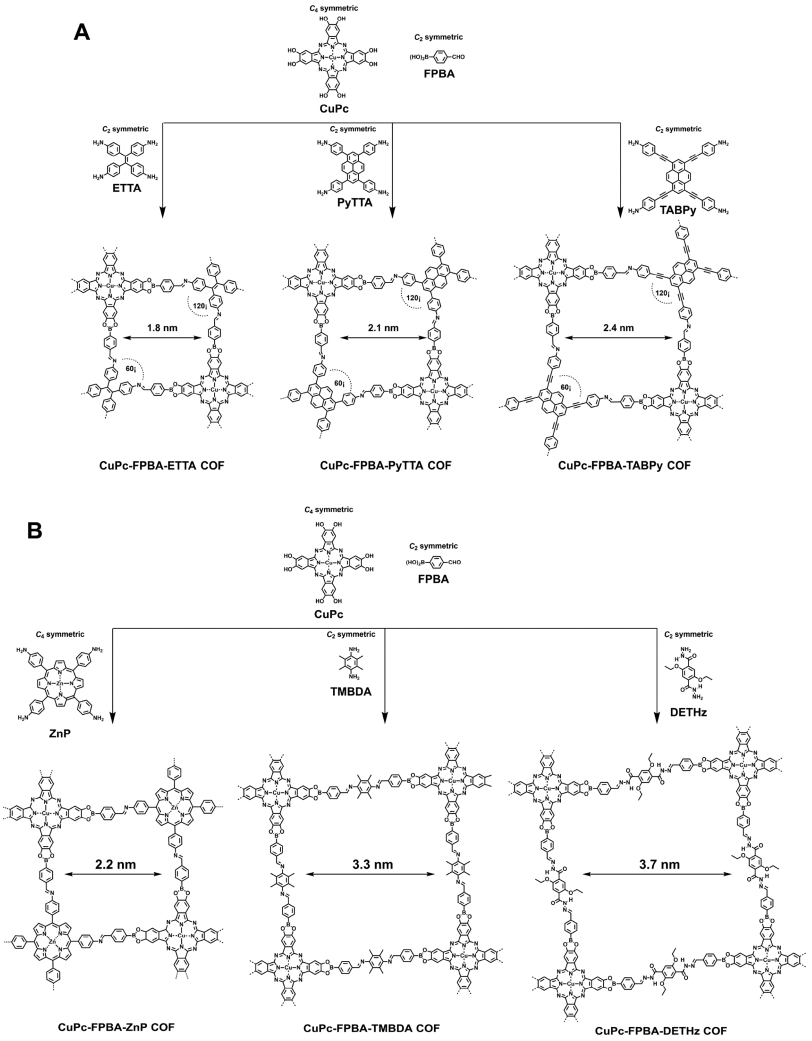

Figure 29. (A) Phthalocyanine-based double-stage COFs for CuPc-FPBA-ETTA COF, CuPc-FPBA-PyTTA COF, and CuPc-FPBA-TABPy COF. (B) Porphyrin- and phthalocyanine-based double-stage COFs for CuPc-FPBA-ZnP COF, CuPc-FPBA-TMBDA COF, and CuPc-FPBA-DETHz COF.

Table 4. Typical Reaction Conditions for the Double-Stage Linking COFs

COFs	solvents (v/v)	temperature (°C)	reaction time (day)	ref
NTU-COF-1, DL-COF-1, DL-COF-2	DOX/mesitylene (1/1)	120	3	88, 277
NTU-COF-2	DOX/mesitylene (1/3)	120	3	88, 277
TATTA-FPBA-COF, TATTA-FFPBA-COF, TATTA-DFFPBA-COF	DOX/mesitylene (1/9)	120	7	87
HHTP-FPBA-TATTA-COF	DOX/mesitylene (1/1)	120	7	87
HHTP-FFPBA-TATTA-COF, HHTP-DFFPBA-TATTA-COF	DOX/mesitylene (1/3)	120	7	87
CuPc-FPBA-ETTA COF, CuPc-FPBA-ZnP COF, CuPc-FPBA-TMBDA COF	DMAc/*o*-DCB (2/1)	120	7	87
CuPc-FPBA-TABPy COF, CuPc-FPBA-PyTTA COF	DMAc/*o*-DCB (3/1)	120	7	87
CuPc-FPBA-DETHz COF	DMAc/*o*-DCB (1/3)	120	7	87

the formation of long-range ordering and results in the poor crystallinity and porosity of resulting COFs.

Moreover, compared with the direct condensation of amine and aldehyde, changing aldehyde monomers into benzophenone-imine-protected monomers yields the BND-TFB COF with an enhanced BET surface area.[287] The BET surface area of directly synthesized BND-TFB-COF is 1496 $m^2\ g^{-1}$, which is increased to 2618 $m^2\ g^{-1}$ upon imine protection. However, because of the irreversible tautomerization from imine to β-ketoenamine, the defect correction process is unfavorable, which results in a low crystallinity and BET surface area of β-ketoenamine-linked COFs.

Recently, the systematic study of the mechanism of thin-film growth of a typical imine-linked COF on modified silicon substrates has revealed the kinetics and thermodynamics associated with the orientation or control over the solution-based growth process.[288] 2D GIWAXS studies indicate that the oriented growth of 2D COF thin films adopts an anisotropic "face-on" arrangement, whereas both *ex situ* concentration- and time-dependent studies have uncovered an unusual re-entrant transition in the orientation during the thin-film growth. The

https://dx.doi.org/10.1021/acs.chemrev.9b00550
Chem. Rev. 2020, 120, 8814−8933

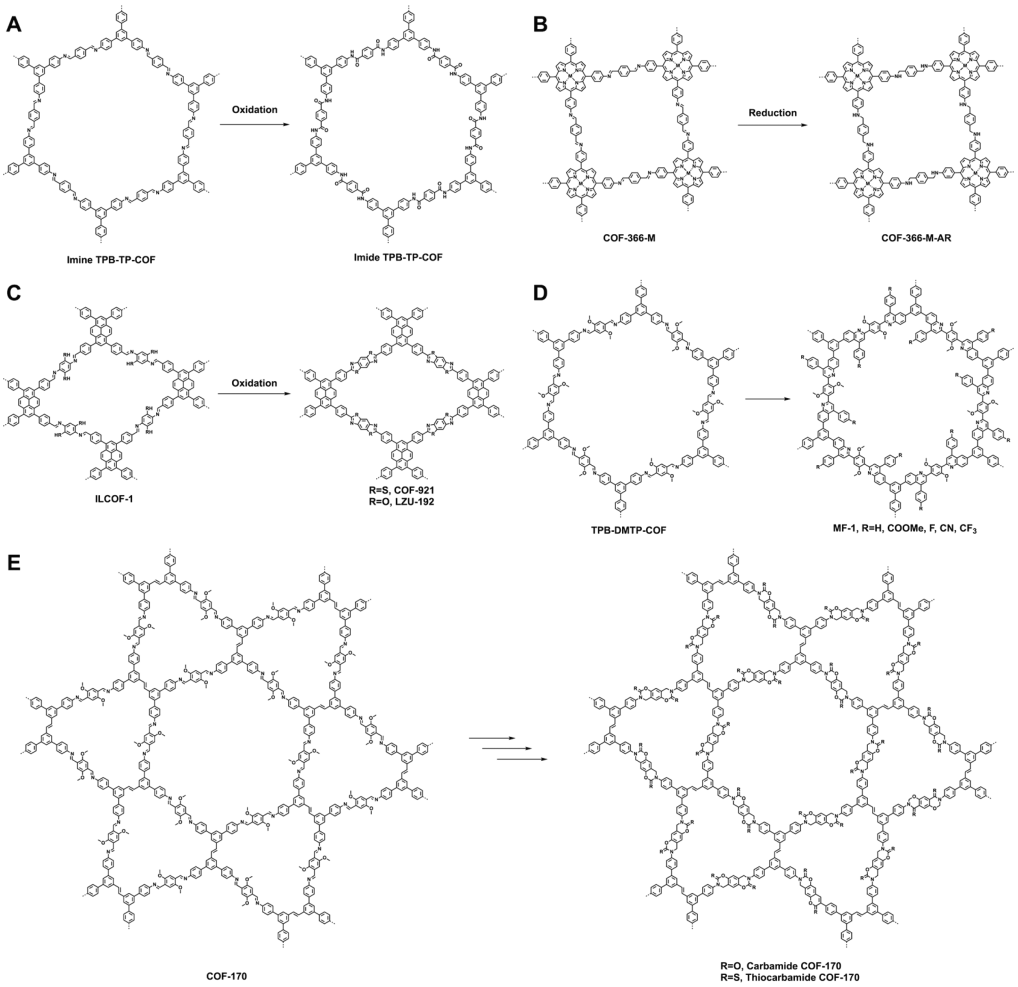

Figure 30. Schematics of the COFs synthesized via linkage transformation for (A) imide TPB-TP-COF, (B) COF-366-M-AR, (C) COF-921 and LZU-192, (D) MF-1, and (E) carbamide COF-170 and thiocarbamide COF-170.

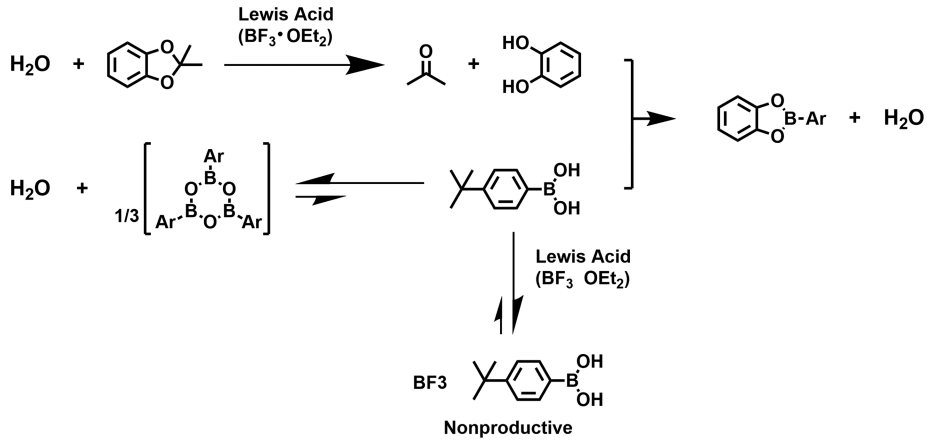

Figure 31. Proposed mechanism of the $BF_3{\cdot}OEt_2$-catalyzed boronate ester formation reaction for the synthesis of the COF.

solution-based COFs grow with the appearance of a disoriented phase. The first appearance of the oriented phase at the beginning of the COF growth and the disappearance of the disoriented phase at the later stage suggest an interface-initiated templating effect owing to the reversibility of the cross-linking chemistry.

The main driving force for the structural formation of COFs is the covalent bond that connects organic units into 3D polygons and further interlocks the interpenetrated framework. The covalent growth of 3D COFs proceeds along all three dimensions, in which the control of interpenetration is a difficult task. Recently, the interpenetration isomerism of 3D COF-300 has been identified. Before heating to 120 °C for 72 h, the reaction mixture is kept at room temperature for 72 h and then warmed to 50 °C for 72 h. COF-300 synthesized without an aging process assumes a **dia-c$_5$** topology. In contrast, COF-300

https://dx.doi.org/10.1021/acs.chemrev.9b00550
Chem. Rev. 2020, 120, 8814−8933

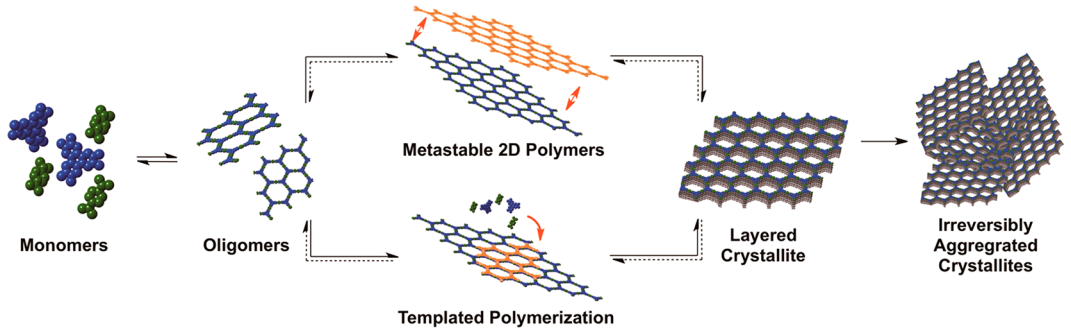

Figure 32. Proposed growth mechanism of boronate-ester COFs. Reprinted from ref 186. Copyright 2014 American Chemical Society.

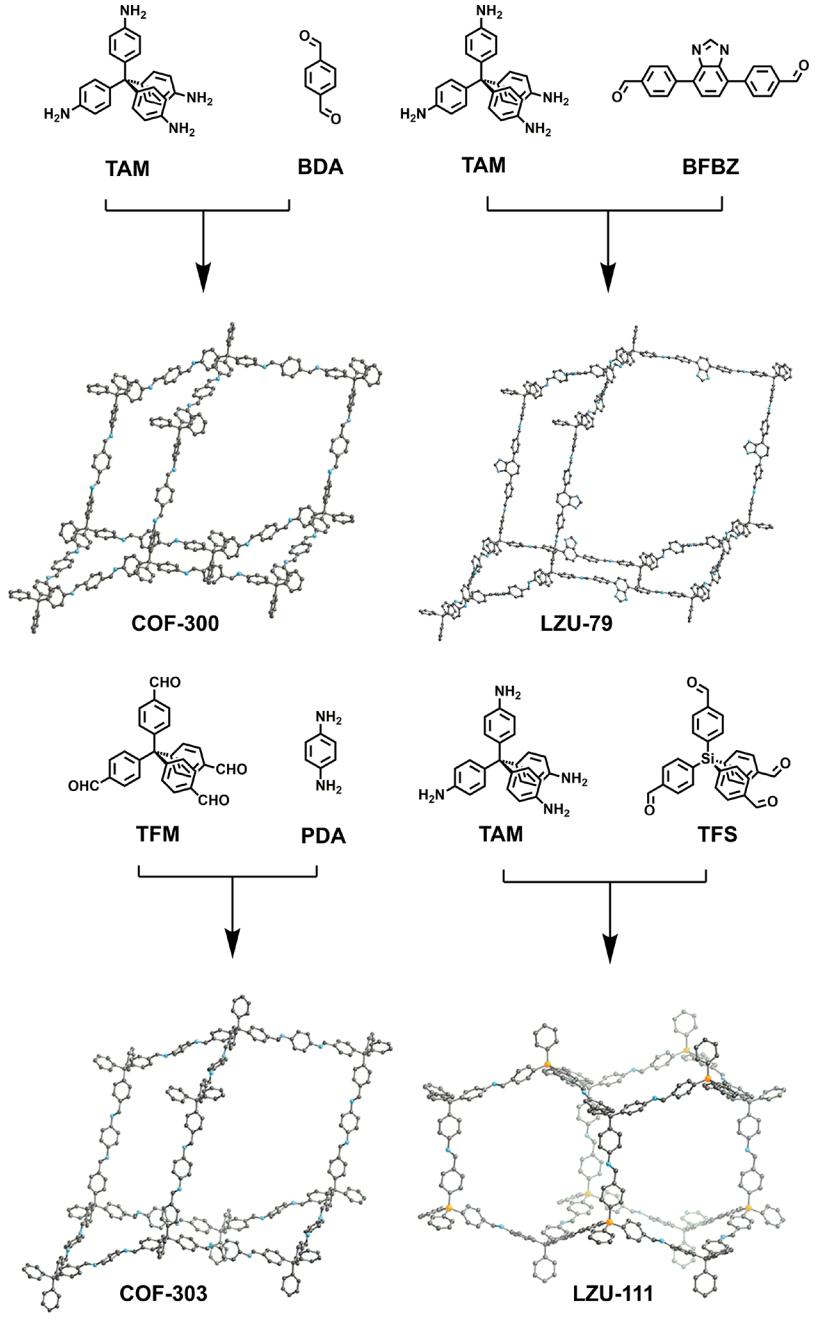

Figure 33. Schematics of the single crystal of imine-linked 3D COFs, including COF-300, COF-303, LZU-79, and LZU-111. Adapted with permission from ref 154. Copyright 2018 American Association for the Advancement of Science.

https://dx.doi.org/10.1021/acs.chemrev.9b00550
Chem. Rev. 2020, 120, 8814−8933

produced upon aging exhibits a seven-fold interpenetrated **dia-c$_7$** diamond topology.[289]

The key factors that guide the formation of 2D COFs are the intralayer covalent bonds and the interlayer noncovalent interactions. In addition to these molecular interactions within skeletons, the growth of crystallites is affected by nuclei, reaction media, temperature, and duration. In general, the morphology of crystallites is irregular, and their shape control is almost impossible. Nevertheless, a careful design of knots and edges, controlled synthetic conditions, and template-assisted replication enable the growth of well-shaped COF crystallites.[27,31,81,82,85,210,222,290,291] Indeed, the macroscopic shape control of 2D COFs has been successfully achieved for some typical examples.

5.3.4. Morphology Control. Well-defined cubes have been developed for boronate-ester-linked ZnP-COF (Figure 34A).[31]

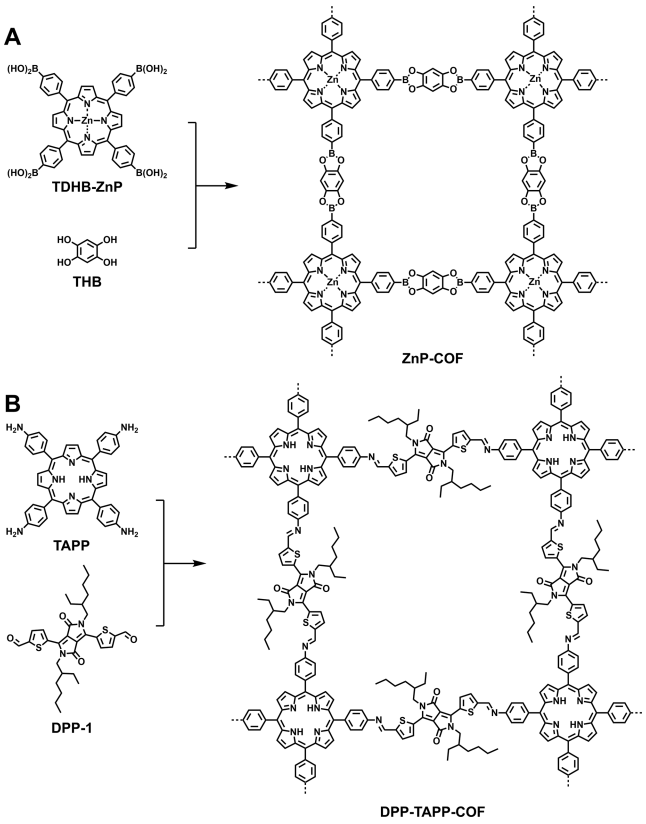

Figure 34. Synthesis of (A) boronate-ester-linked ZnP-COF and (B) imine-linked DPP-TAPP-COF.

In this case, the reaction medium and time are important. As the volume ratio of mesitylene to DOX in the solvent is changed from 4/1 to 9/1, the morphology of the resulting crystallites changes from irregular particles to regular cubes. As the volume ratio is changed to 19/1, a deformation of morphology from a cube to a disk-like shape is observed while retaining the crystallinity. Time-dependent experiments reveal that the growth of 2D COFs is along the x and y directions. For example, upon extending the reaction time from 1 day to 2, 4 and 6 days, the average length and width of cubes change from 360 ± 30 to 427 ± 35, 508 ± 35, and 588 ± 35 nm, respectively. The length and width of the cubes are leveled off and reach 666 ± 35 nm after 15 days. The AFM images of the cubes at different reaction times reveal that the cubes retain their thickness between 10 and 30 nm. Interestingly, the surface area and pore volume of the resulting ZnP-COF are gradually increased from 85 to 1742 $m^2 g^{-1}$ and from 0.069 to 1.11 $cm^3 g^{-1}$, respectively, as the reaction time is extended from 1 to 15 days. Different from the tetragonal ZnP-COF, a kagome-type dual-pore TPE-Ph COF has been prepared as well-defined belts.[117] As the reaction time is tuned from 3 days to 10, 20, and 30 days, the length of the belt-shaped crystallite changes from 4 to 6, 16, and 53 μm, respectively, while it keeps its clear edges and smooth surfaces.

On the basis of the surface energy minimization, hollow-sphere COFs have been prepared for the imine-linked DhaTab COF with a nonplanar TAPB (= Tab or TPB) knot and the 2,5-dihydroxyterephthalaldehyde (2,5-DhTa or 2,5-Dha) edge via self-assemblies driven by the Ostwald ripening mechanism.[81] In this case, the reaction time is critical. For example, rod-like crystallites are formed after the initial 12 h reaction and are transformed into hollow spheres after the 24 h reaction. As the reaction time is increased to 36, 48, and 72 h, hollow spheres with smooth surfaces are formed. The inner core width of the hollow sphere is in the macroporous range (0.5−2 μm), whereas the outer surface is constructed from rod-like COFs with a width of 20−40 nm. Similarly, the 2,3-DhaTab COF constructed from the condensation of the Tab knot and a 2,3-dihydroxyterephthalaldehyde (2,3-DhTa or 2,3-Dha) edge forms hollow spheres with a size of ∼400 nm. Interestingly, by changing the knot from Tab to a planar 1,3,5-tris(4-aminophenyl)triazine (Tta), the morphology of the resulting COFs changes from a hollow sphere to a ribbon.[82,85] The 2,3-DhaTta COF (Figure 7C) is a ribbon-shaped crystallite with a length of ∼200 nm, as evidenced by the TEM analysis. Notably, PXRD analysis together with the DFTB calculations reveal that the $\pi-\pi$ stacking interaction energy for the 2,3-DhaTta COF (−1634.2 kJ mol^{-1}) is lower than that of the 2,3-DhaTab COF (−1578.7 kJ mol^{-1}). The interlayer $\pi-\pi$ interactions for the 2,3-DhaTta COF are strong due to its planar knot, and thus the crystallite prefers growth in the z direction other than along the $x-y$ plane to form ribbons. In contrast, the low stacking energy in the 2,3-DhaTab COF originates from the nonplanar knots that weaken the growth of the COF along the z direction and result in small rods that further self-assemble to form more stable hollow spheres.

Recently, the microtubular self-assembly based on COFs has been developed. The imine-linked DPP-TAPP-COF (Figure 34B) consisting of 5,10,15,20-tetrakis(4-aminophenyl)-21*H*,23*H*-porphine (TAPP) and tetraphenylporphyrin (TPP) moieties yields hollow microtubular assemblies with outer and inner tube diameters of approximately 300 and 90 nm, respectively.[292] Time-dependent morphology studies reveal the transformation process from initial sheet-like agglomerates into tubular microstructures.

A dynamic covalent chemistry (DCC)-based postsynthetic approach has been developed for the assembly of hierarchical architectures. Through adjusting the loading amount of 1,4-diaminonaphthalene (Naph) in the solid−liquid reaction of Naph and COF-Ph, a part of the 1,4-diaminobenzene (Ph = DAB) of COF-Ph is replaced by Naph via postsynthetic exchange.[293] The homogeneously mixed COF-Ph-Naph exhibits a spherical hollow structure with a shell thickness of 70−100 nm. In contrast, the condensation of COF-Naph with DAB yields hollow spheres with a thickness of ∼180 nm.

Furthermore, through the amorphous-to-crystalline transformation by virtue of dynamic imine exchange, fibrous imine-linked TpBD-COF and TfBD-COF have been prepared.[294] This is achieved by a two-step process; the first step is the

https://dx.doi.org/10.1021/acs.chemrev.9b00550
Chem. Rev. 2020, 120, 8814−8933

polymerization to form amorphous polyazomethine (PAM) fibers that control the formation of morphologies, and the second step promotes the solvothermal crystallization while retaining the fiber morphology and size.

The shape and surface of the crystallites can be tuned by the nature and amount of catalysts.[291] For example, the imine-linked COF-366 (Figure 8C) has been synthesized by the condensation of TAPP and terephthaldehyde (TA) in a mixture of mesitylene/EtOH (5/5 vol) at 120 °C. The COF is controlled by using different amounts of various organic acid catalysts, including AcOH, benzoic acid (BA), salicylic acid (SA), oxalic acid (OA), and *p*-(dodecyloxy)benzoic acid (*p*-DBA). For example, when an aqueous AcOH solution (6 M) is used, an irregular morphology is generated, as evidenced by the FE-SEM measurement.[291] In contrast, the use of pure AcOH (0.35 mL) significantly improves the morphology and yields regular octahedrons of 2 μm. As the acid amount is reduced to 0.05 mL and the reaction time is extended from 1 to 36 and 72 h, complex microsized octahedrons decorated with perpendicularly aligned nanoplates are formed. On the contrary, when BA or *p*-DBA is used, nanoplates with different sizes are observed. The use of OA yields a mixture of micro-octahedrons and microplates, whereas SA (100 mg) guides the formation of mostly micro-octahedrons with the coexistence of a very small portion of nanoparticles. By reducing the amount of SA from 100 to 50 mg, only pure and uniform micro-octahedrons are observed. The reaction temperature affects the morphology due to the dynamic nature of the imine linkages. The reaction is carried out at room temperature at different time intervals. For example, a 3 min reaction produces only irregular nanoplates, which are converted to regular octahedrons upon a 6 day reaction. However, the surface of the octahedrons upon the room-temperature reaction is not smooth. In contrast, octahedron crystallites with clear and smooth surfaces are obtained at 120 °C after a 72 h reaction. This is attributed to the dynamic nature of the imine linkages, in which the nanoplates are kinetically formed after a short reaction time or at a low reaction temperature followed by the aggregation of nanoplates through noncovalent interactions to form octahedrons with rough surfaces. As the reaction was conducted over a long time or at high temperature, the surface of the octahedron became smooth with clear faces through the thermodynamic control of "error-checking" and "proofreading" processes.

From the above typical examples, the principle for the synthetic control over the growth of COFs to achieve macroscopically well-defined and desired shapes remains to be established. The exploration of a general way to systematically tune COF structures and reaction conditions plays a key role in meeting the goal of rational control over the morphology.

5.4. Synthesis on Substrates

In contrast with the bulk syntheses of microsized crystallites, the preparation of free-standing thin films remains a substantial synthetic challenge. Nevertheless, the preparation of thin films on various substrates has been investigated, including single-layer graphene (SLG),[170,174] highly oriented pyrolytic graphite (HOPG),[183,295−299] metal substrates Ag(111),[300,301] Au(111),[177,229,302−305] and copper foil (SLG-copper),[226] the glass substrate,[306,307] three-dimensional graphene (3DG),[308] porous ceramic α-Al_2O_3 substrate,[140] amine-modified reduced graphene oxide (NH_2−*r*GO),[309] hexagonal boron nitride (hBN),[310] polydopamine-coated capillary,[311] 3-aminopropyltrimethoxysilane (AMS)-functionalized silicon wafer (Si-AMS),[312] amino-functionalized carbon nanotubes (CNTs),[237] and diboronic-acid-attached graphene oxide (GO).[313] Among these substrates, SLG, HOPG, the glass substrate, hBN, metal substrates (Ag(111), Au(111)), and copper foil (SLG-copper)) have been used to prepare single-layer COFs (sCOFs) (Table 5).

Table 5. Typical Examples of COFs Prepared on Different Substrates

COFs	substrates	ref
COF-5, ZnPc-PBBA COF	single-layer graphene (SLG)	170, 174
COF-320	porous ceramic α-Al_2O_3 substrate	140
ZnPc-PBBA COF	SLG	174
2D covalent monolayer	air/water interface	314
boroxine-linked COFs	highly oriented pyrolytic graphite (HOPG)	178
BDT-COF/COF-5	glass substrate	306
COF_{ABBA}	gas/HOPG interface	297
SCOF-IC1/SCOF-LZU1	HOPG	175
$COF_{DAAQ\text{-}BTA}$	three-dimensional graphene (3DG)	308
COF-5	polydopamine-coated capillary	311
COF-LZU1	amine-modified reduced graphene oxide (NH_2−*r*GO)	309
Schiff-base COFs	HOPG	183
COF-LZU1	silicon wafer (Si-AMS)	312
COF-LZU1	copper foil (SLG-copper)	226
COF-366	hexagonal boron nitride (hBN)	310
COF-1/COF-5	Ag(111)	300
HHTP-DPB COF	SLG/SiO_2	91
TFPB-DATP-COF	Au(111)	304
TFPB-TAPB-COF		
carbon-based COF	Ag(111)	301
metalloporphyrin-based COFs	HOPG	299
2D $COF_{TTA-DHTA}$	amino-functionalized carbon nanotubes	237
COF-1	diboronic-acid-attached graphene oxide	313
COF-366-Co	HOPG	315

5.4.1. COFs on Porous Ceramic α-Al_2O_3 Substrate.

COFs have been prepared on the surface of porous metal oxides. For example, an approach to grow 3D COF-320 (Figure 35A) on porous ceramic α-Al_2O_3 has been developed.[140] In this method, the surface of porous α-Al_2O_3 is functionalized with 3-

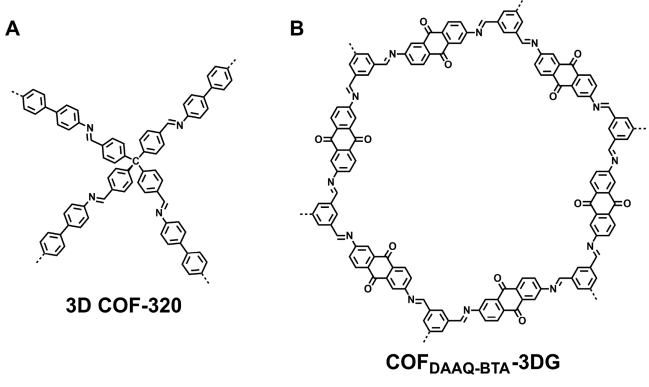

Figure 35. Schematics of (A) 3D COF-320 and (B) $COF_{DAAQ\text{-}BTA}$-3DG.

https://dx.doi.org/10.1021/acs.chemrev.9b00550
Chem. Rev. 2020, 120, 8814−8933

aminopropyltriethoxysilane (APTES), which works as a linker between the COF and α-Al_2O_3. Second, the surface-modified α-Al_2O_3 substrate is added into a DOX mixture of TAPM and BPDA monomers and AcOH catalyst, and the mixture is degassed by three freeze−pump−thaw cycles and sealed to remain at 120 °C for 72 h. The substrate is washed with anhydrous THF and dried under vacuum at 100 °C to yield a yellow COF-320 membrane on the α-Al_2O_3 substrate. The thickness of the COF layer is ∼4 μm. The 3D COF-320 membrane is hydrogen-selective with a high hydrogen permeance of 5.67×10^{-7} mol $(m^2\ s\ Pa)^{-1}$, and its permselectivity for H_2/CH_4 and H_2/N_2 is about 2.5 and 3.5, respectively, which is close to the ideal separation factors (2.83 for H_2/CH_4 and 3.74 for H_2/N_2) that are theoretically calculated by the Knudsen diffusion mechanism.

5.4.2. COFs on Three-Dimensional Graphene Substrate. $COF_{DAAQ\text{-}BTA}$-3DG (Figure 35B) has been synthesized by using an interfacial polymerization method. In this method, a DMAc solution of 2,6-diaminoanthraquinone (DAAQ) and benzene-1,3,5-tricarbaldehyde (BTA) is added to deionized water at a 6% volume ratio. The resulting suspension is directly soaked by 3DG. The composite is heated to 140 °C for 5 h and annealed at 205 °C for 1 h under argon to yield $COF_{DAAQ\text{-}BTA}$-3DG.[308]

5.4.3. COFs on Graphene Oxide Substrate. GO is a 2D carbon material with various functional groups on surface and edges. In a typical protocol, the amino-functionalized NH_2−*r*GO is dispersed in DOX and stirred for 0.5 h. TFB, PPDA, and acetic acid are added to the dispersed GO solution under mild stirring. The amine groups of GO enable the formation of imine bonds and anchor COFs on GO. The mixture is transferred to a Teflon-lined autoclave and heated to 120 °C for 2 days. The obtained solid is washed with DMF and THF and dried to yield a COF/NH_2−*r*GO composite.[309] Under the solvothermal condition in methanol, benzene-1,4-diboronic acid (DBA) molecules react with the −OH groups of GO to covalently anchor on the surface of GO. The unreacted −OH groups of DBA serve as reaction sites for the polycondensation to form COF-1 in a mixture of mesitylene/dioxane. By using this method, single-layer COF-1 can be covalently attached and oriented perpendicular to the GO surface.[313]

5.4.4. COFs on Silicon Wafer Substrate. In this method, the surface of silicon wafer is functionalized with amino groups using AMS to obtain Si-AMS.[312] The Si-AMS wafer is allowed to react with TFB in the presence of AcOH catalyst at 120 °C for 24 h to form Si-AMS-CHO-1. After cooling to room temperature, the Si-AMS-CHO-1 wafer is washed with EtOH and reacted with PPDA in the presence of AcOH catalyst at 120 °C for 24 h to form Si-AMS-NH_2-1. The amino-functionalized COF films (Si-AMS-NH_2-4) on Si-AMS are obtained by repeating the above processes three times. The thickness of the films is estimated to be 4−28 nm.

5.4.5. COFs on Capillary. The capillary substrate is modified by polydopamine to obtain polydopamine-coated capillary (polydopamine@capillary) (Figure 36). A mesitylene/DOX solution of BDBA and HHTP monomers is slowly added at a rate of 0.05 mL h^{-1} in 10 min to the polydopamine@capillary. The capillary is sealed and heated to 100 °C for 20 h, washed with methanol, and dried with nitrogen flow to yield a COF-5 polydopamine capillary. Repeating the above processes enables the preparation of multilayered COF-5 (Figure 7B) on the capillary.[311]

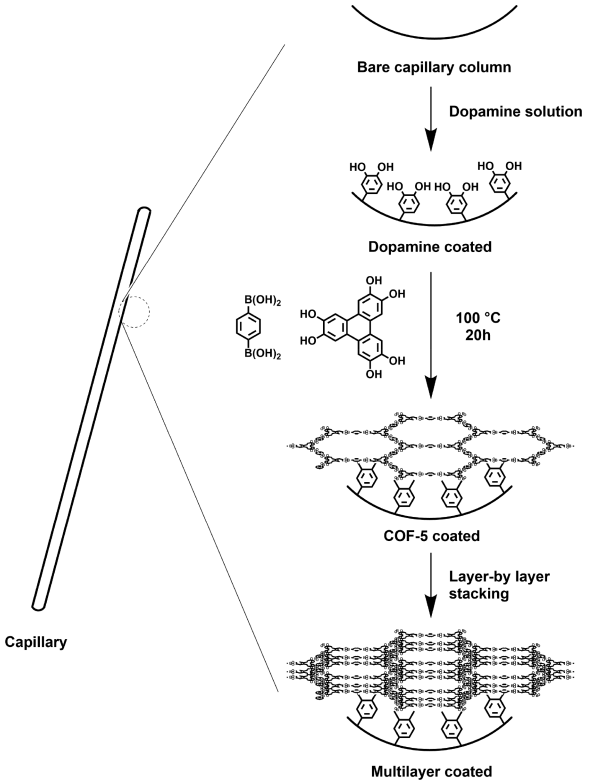

Figure 36. Schematic of synthesizing the COF film on a capillary.

5.4.6. Single-Layer COFs on Substrates. A variety of sCOFs have been synthesized by depositing on various substrates (Table 5), and their domain structures have been studied by using STM. For example, the formation of single layer COF-1 (Figure 7A) on the Ag(111) surface is based on the dehydration of BDBA under an ultrahigh vacuum (UHV) at 10^{-10} mbar, and the deposition rate is ∼0.5 monolayers per minute.[300] In relation to this method, two different synthetic methods have been tested for the preparation of 2D COF-1 monolayers on graphite.[184] One method is the prepolymerization of BDBA into nanocrystalline COF-1 precursors, which are then drop-cast onto the graphite. This method enables the understanding of reaction parameters that determine the formation of COF-1. Another approach is to directly deposit the monomer solution onto the graphite for polymerization. This process is efficient for the preparation of 2D COF monolayers. Notably, controlling the water concentration to regulate the reaction equilibrium enables the growth of large-scale high-quality sCOFs. For example, the control of water concentration is achieved by placing the $CuSO_4{\cdot}5H_2O$ solid in a closed system.[295] Interestingly, during the heating process, the water molecules are released from $CuSO_4{\cdot}5H_2O$ and promote the defect remedy. During the cooling process, water molecules are adsorbed by $CuSO_4$ so that the decomposition of the sCOFs is avoided.

For the preparation of 2D COFs on HOPG, HOPG is deposited into a freshly sonicated solution of TAPP and 5,10,15,20-tetrakis(4-aminophenyl) zinc porphyrin (Zn-TAPP) in toluene or 1,2,4-trichlorobenzene and added to TA solid or solution. With $CuSO_4{\cdot}5H_2O$ at the bottom of the tube, the reaction is carried out at 120−150 °C in an oven for 2−24 h. Similarly, BTA and PDA are dissolved in octanoic acid at a concentration of 0.1 mg g^{-1}, and the mixture is drop-cast for

https://dx.doi.org/10.1021/acs.chemrev.9b00550
Chem. Rev. 2020, 120, 8814−8933

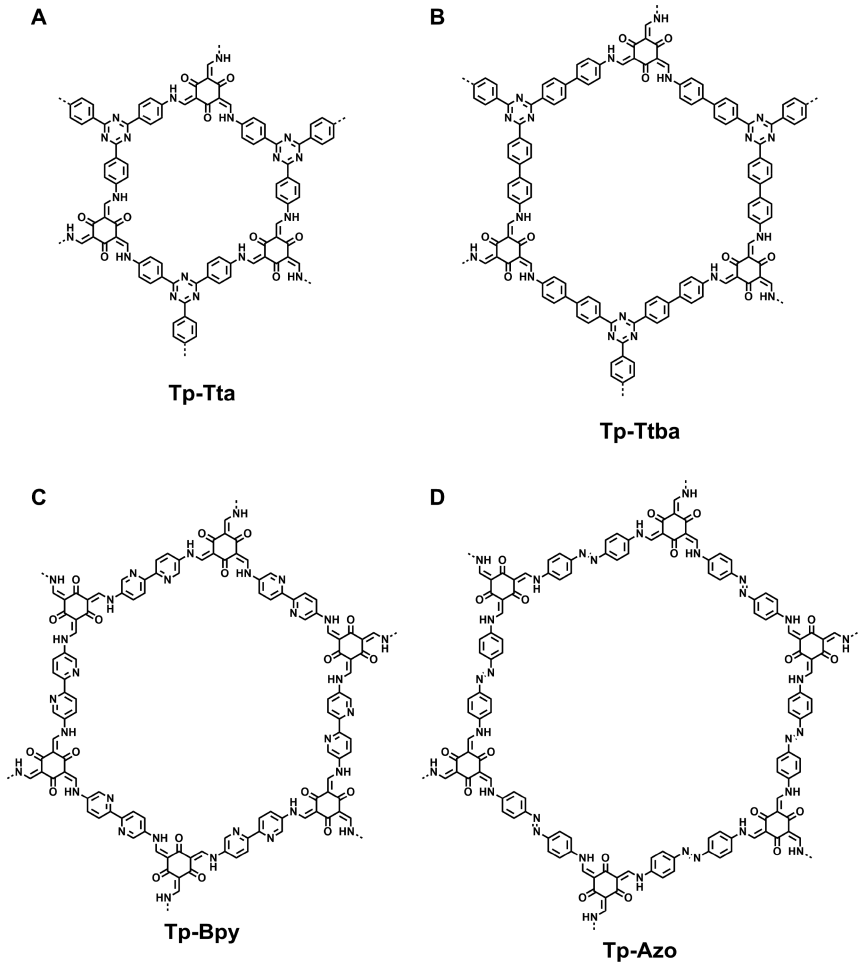

Figure 37. Schematics of (A) Tp-Tta, (B) Tp-Ttba, (C) Tp-Bpy, and (D) Tp-Azo.

dehydration on the SLG on copper foil (SLG-copper) to produce an sCOF on SLG-copper.[226]

The imine-linked sCOFs have been synthesized on the HOPG substrate. The condensation of tetrathiafulvalene-based monomers with four benzaldehyde groups (4ATTF) and diamines such as PPDA and 1-1′-biphenyl-4,4′-diamine dihydrochloride in the presence of HOPG forms sCOFs on HOPG.[296] Changing the terminal functional groups of the monomers offers a way to get insight into the general kinetics of the structural development.[316] Another example is to produce sCOFs on HOPG by using $CuSO_4{\cdot}5H_2O$ to adjust the water content. A freshly cleaved HOPG is drop-cast with a THF solution of TAPB (10^{-5} M) or TFB (10^{-4} M) monomer and is allowed to dry.[175] HOPG and $CuSO_4{\cdot}5H_2O$ are transferred to an autoclave under different reaction temperatures for 3 h to yield sCOFs. This approach based on the self-limiting solid−vapor interface generates high-quality and ordered 2D TAPB-TFB sCOFs. This method is also applicable to another imine-linked TPA-TAPB sCOF. A typical protocol is shown as follows. First, the TAPB monomer is drop-cast onto HOPG. Second, the terephthaldicarboxaldehyde (TPA) monomer is introduced, and the reaction container with $CuSO_4{\cdot}5H_2O$ is sealed. The reactor is kept at a designated temperature, and the TPA monomer vaporizes to land on the surface of HOPG that is covered with TAPB. The reaction temperature and the concentration of TAPB and $CuSO_4{\cdot}5H_2O$ have a significant influence on the quality of sCOF. Notably, if the order of the monomer loading is reversed, then no sCOF forms on HOPG; a full vaporization of TPA before TAPB on the surface does not form a sCOF. The monolayer COF can be further developed for the construction of the host−guest architecture. For example, HOPG-supported COF-1 serves as a host to stabilize hydrophobic fullerene guests at the solution/solid interface and forms functional host−guest materials.[317]

5.4.7. Thin Films. Because of the high porosity and periodically ordered structures, COFs have shown a variety of potential applications; some of these applications require oriented thin films. To date, several approaches have been explored based on different strategies.[318] Encoding electrostatic repulsion into the COF skeleton can withstand the interlayer $\pi-\pi$ stacking and produces PyVg-COF with both crystallinity and high solubility in various organic solvents.[319] It can be self-exfoliated into large-area monolayer or multilayer nanosheets when dissolved.

Vapor-phase deposition is one of the most established methods used in fabricating organic semiconductor thin films. The COF-1 (Figure 7A) and COF-5 (Figure 7B) thin films on the Ag(111) surface have been fabricated by the sublimation of BDBA and HHTP monomers from two heated molybdenum crucible evaporators under UHV conditions. The monolayer COF thin films are confirmed by STM analysis. However, without the solvothermal conditions like bulk polymerization, these thin films consist of polygons defects, such as five-, seven-, and eight-membered cycles. From the STM images, the

https://dx.doi.org/10.1021/acs.chemrev.9b00550
Chem. Rev. 2020, 120, 8814−8933

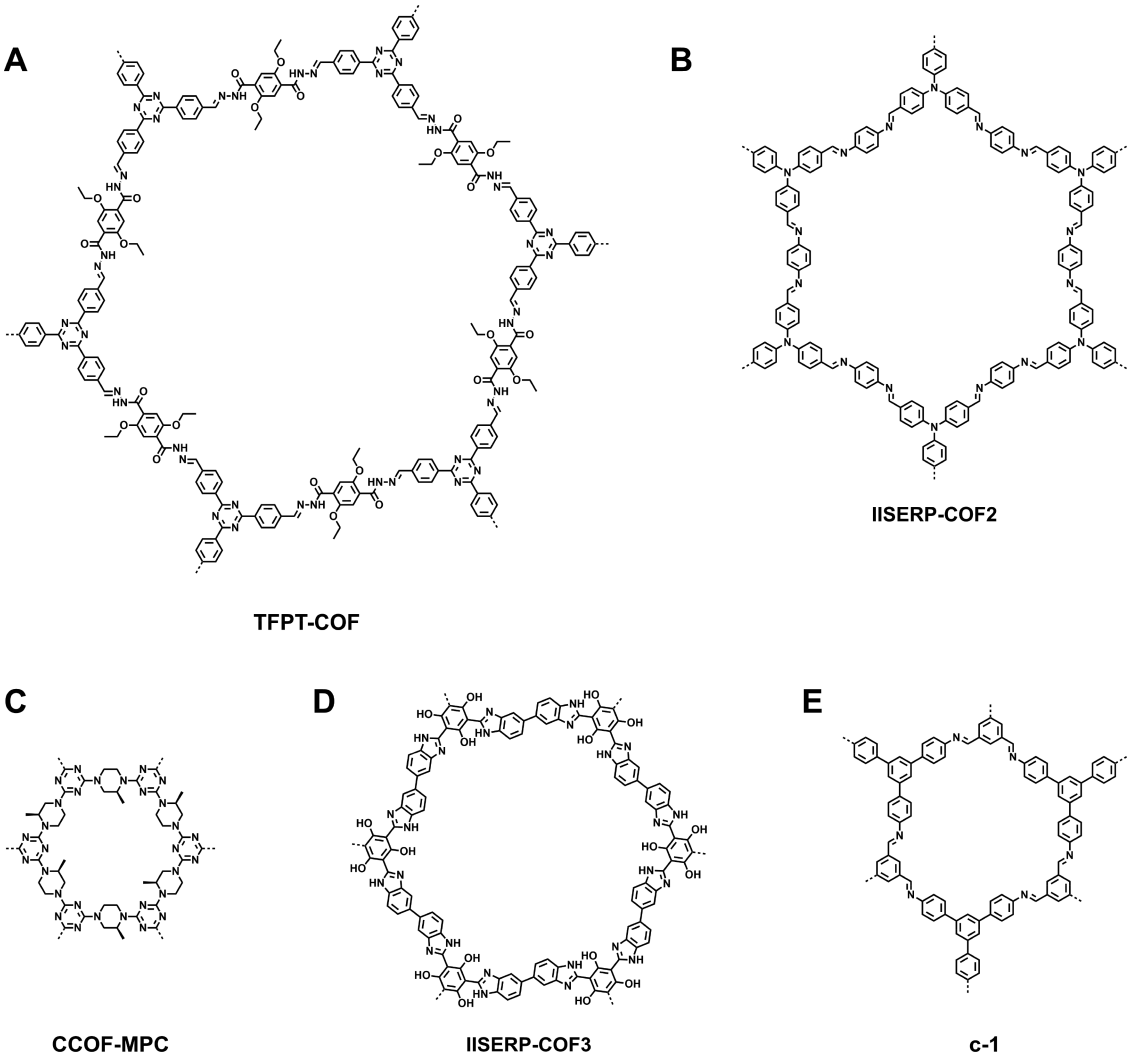

Figure 38. Schematics of (A) TFPT-COF, (B) IISERP-COF2, (C) CCOF-MPC, (D) IISERP-COF3, and (E) c-1.

coverage and domain structure of the thin films can be easily identified. Lacking the self-healing process is one of the main reasons for the formation of structural defects in the thin films.[300,320]

Considering the necessity of the solvothermal-controlled crystallization and self-repairing process of COFs on the substrates, *in situ* deposition by growing COFs in solution on graphene or other substrates is an elegant method. Using this method, orientated boronate-ester-linked films have been prepared, as evidenced by the GID signals that match with the PXRD signals of the bulk COF powders. By controlling the reaction conditions, thin films with different thicknesses of hexagonal and tetragonal boronate-ester-linked COFs have been synthesized on various substrates.[170] Organic solar cells based on COF active layers have been achieved through the *in situ* deposition method.[223] However, the film morphology is not qualified enough for application in optoelectronic devices. Tuning the monomer concentration and reaction system has the potential to improve the film morphology.[91,103,171,310] These tries would open an alternate platform to conventional polymers or organic molecule-based film devices.[93]

Among the solution-based film-fabricating processes, spin coating of organic materials, as established for soluble conjugated polymers, is the main method to prepare a high-quality thin film on various substrates. However, spin coating is hardly applicable to COFs owing to their poor solubility. Nevertheless, adding long alkyl or alkoxy chains to the COF skeletons could increase the dispersibility of COFs in solutions. For example, introducing *tert*-butyl groups to the pyrene tetraone monomer results in CS-COF/C_{60} (CS-COF, Figure 27B), which can be well dispersed in NMP. Spin coating of the dispersed solution onto the ITO substrate yields COF-based thin films.[158]

The COF thin films on substrates have been synthesized at the solution/air interface extended in a covered Petri dish.[321] This method produces films with good morphologies and smooth surfaces with controlled thicknesses. Similarly, using the liquid−liquid interface for the bottom-up interfacial crystallization yields large-scale thin COF films under ambient conditions. Introducing a salt-mediated technique (amine-PTSA salt) instead of free amine in the aqueous phase, in which hydrogen-bonding interactions slow down the diffusion rate, β-ketoenamine Tp-Tta (Figure 37A), Tp-Ttba (Figure 37B), Tp-Bpy (Figure 37C), and Tp-Azo (Figure 37D) COF thin films with the thickness from ∼50 to 200 nm can be achieved.[202]

Owing to the layered structures, dispersion of COFs upon exfoliation through sonication is possible, and the successive

https://dx.doi.org/10.1021/acs.chemrev.9b00550
Chem. Rev. 2020, 120, 8814−8933

spin coating of the supernatant onto substrates can produce thin films. Notably, the thin films fabricated by this method are crystalline and have smooth surfaces.[322] Recently, the temperature-swing gas exfoliation approach has been developed for the fabrication of ultrathin 2D COF nanosheets.[323] By heating to 300 °C for 10 min in air and immediately immersing into liquid N_2 until the liquid N_2 gasifies completely, 2D nanosheets of NUS-30−32 can be successfully prepared via the expansion of the interlayer distance.

A convenient method for preparing high-quality 2D COFs thin films has been established by employing continuous-flow synthesis in a quartz crystal microbalance (QCM) flow cell.[324] The polymerization of HHTP and bis(boronic acid), including 1,4-phenylenebis(boronic acid), 4,4′-diphenyl-butadiynebis-(boronic acid), 2,7-pyrenebis(boronic acid), and 4,4′-biphenylbis(boronic acid), to provide the boronate-ester-linked frameworks, is conducted in a flow cell in a mixture of mesitylene/dioxane with a small amount of MeOH added to dissolve both monomers. Those homogeneous solutions are pumped through the tube at 90 °C for a given residence time and pass over a substrate. 2D COF powders then form downstream on the substrate if the residence time and conditions are chosen judiciously. By using this method, the thickness of films and their growth rate can be controlled, thus offering a route to high-quality films with the low surface roughness that is necessary for some applications.[172,310,325]

5.5. Synthesis of COF Composites

The well-defined channels of COFs are open and accessible to dock other nanosized materials, whereas the skeletons offer an interface for constructing composites or hybrids on the surface. COF composites have been developed to showcase the potential of pores and skeletons for creating new materials that might combine the advantages of two materials into one composite, opening a new dimension to the designed synthesis of hybridized molecular systems.

5.5.1. COF−Nanoparticle Composites. Platinum (Pt) nanoparticles can be loaded onto COFs via an *in situ* photodeposition approach. COFs are dispersed in an aqueous solution containing a triethanolamine (TEOA) sacrificial electron donor and hexachloroplatinic acid (H_2PtCl_6), and irradiation with a Xe lamp generates Pt nanoparticles to yield Pt/COF composites. The Pt-loaded TFPT-COF[83] (Figure 38A) and Nx-COFs[85] (Figure 23C) are produced using this method.

Metal nanoparticles can grow within the COF support via a solution approach. For example, adding a methanol solution of $NiCl_2{\cdot}6H_2O$ or $CoCl_2{\cdot}6H_2O$ to an *n*-hexane suspension of IISERP-COF2 (Figure 38B) yields a solid, which is isolated, dispersed in water, and reduced with an aqueous solution of $NaBH_4$ to form IISERP-COF2 composites with uniform Ni or Co nanoparticles (<2 nm in diameter) on the COF surface.[249] Similarly, through a solution infiltration method using $NaBH_4$ as a reductant to reduce Na_2PdCl_4, Pd nanoparticles (7 ± 3 nm) can be immobilized into the TpPa-1 COF, whereas Pd@CCOF-MPC (CCOF-MPC, Figure 38C) with Pd nanoparticles of 2−5 nm size can be produced from palladium nitrate.[326]

On the contrary, nickel nitride (NiN_3) nanoparticles can be loaded onto the COF via solid-state synthesis. A mixture of IISERP-COF3 (Figure 38D) and nickel acetate is grounded with urea and heated to 350 °C for 6 h in air, and the resulting solid is washed with water and methanol to remove any unreacted starting materials, forming an IISERP-COF3-NiN_3 composite. Using hexamethylene tetraamine (HMTA) to replace urea as the ammonia source yields an IISERP-COF3-NiN_3 composite with larger NiN_3 particles.[327]

Interestingly, a two-step strategy has been developed to enable the encapsulation of nanoparticles into imine-linked COF spheres. The direct polymerization of monomers in the presence of a variety of metallic/metal-oxide nanoparticles forms amorphous and nonporous imine-linked polymers, which upon reaction in acetic acid forms an NP@COF hybrid with nanoparticles in spheres.[328] NP@c-1 (c-1, Figure 38E) constructed with TAPB and BTCA is the typical example of this strategy.

5.5.2. COF-on-COF Composites. COFs are formed by π-stacking of 2D layers, which offer an approach to prepare COF-on-COF composites. For example, using a temperature-swing solvothermal approach to regulate the growth of imine-linked COF-LZU1 (Figure 21A) and azine-linked ACOF-1 (Figure 7E) enables the formation of a 2D bilayer membrane with a stacked COF-on-COF composite on the Al_2O_3 substrate, which is pretreated with APTES, TFB, and the PDA/hydrazine hydrate mixture.[329]

5.5.3. COF−MOF Composites. COF−MOF composites can be synthesized by growing MOFs on COFs. A polyaniline (PANI)-modified porous SiO_2 disk is used to synthesize a COF-300 (Figure 15D) membrane on the surface, which is added to a Teflon-lined autoclave containing a $Zn_2(bdc)_2(dabco)$ mother solution or ZIF-8 mother solution; the $Zn_2(bdc)_2(dabco)$ or ZIF-8 MOF membrane forms on the COF-300 membrane to yield COF−MOF composite membranes.[330] On the contrary, MOF crystals can be encapsulated within COF spheres. Spray-drying is used to encapsulate UiO-66-NH_2 or Zr-fumarate MOF crystals into amorphous TAPB-BTCA polymer beads, which are then transformed into COF-TAPB-BTCA (= c-1, Figure 38E) under solvothermal conditions to yield composites with UiO-66-NH_2 or Zr-fumarate MOF encapsulated within COF-TAPB-BTCA.[331]

6. STABILITY CONTROL

Different from conventional polymers, COFs exhibit high thermal stability owing to the covalent bonds, high content of robust aromatic systems, and crystalline nature.[214] In general, COFs are thermally stable between 250 and 450 °C under an inert atmosphere. The residual percentage upon pyrolysis under nitrogen is dependent on the structures of knots, edges, and linkages. The thermal stability and residual weight are important for the carbonization of COFs.

The strength of chemical bonds determines the overall chemical stability of COFs; in particular, the linkages are key to the chemical stability. However, a stable linkage reduces the reversibility of the COF formation reaction and is expected to result in a limited crystallinity. For example, the boroxine or boronate-ester linkage formation is highly reversible compared with the imine linkage, as the C═N bond is more robust than the B−O bond. Therefore, in general, the boroxine- or boronate-ester-linked COFs possess higher crystallinity than those of imine-linked COFs, whereas the chemical stability is in the reverse order.

6.1. Boron-Based Linkages

Indeed, the boroxine- or boronate-ester-linked COFs are not stable under humid or protic conditions.[332] The hydrolysis of the boronate ester linkage includes the reaction of one water molecule with one B−O bond and the breaking of the five-membered ring and the reaction of another water molecule with

https://dx.doi.org/10.1021/acs.chemrev.9b00550
Chem. Rev. 2020, 120, 8814−8933

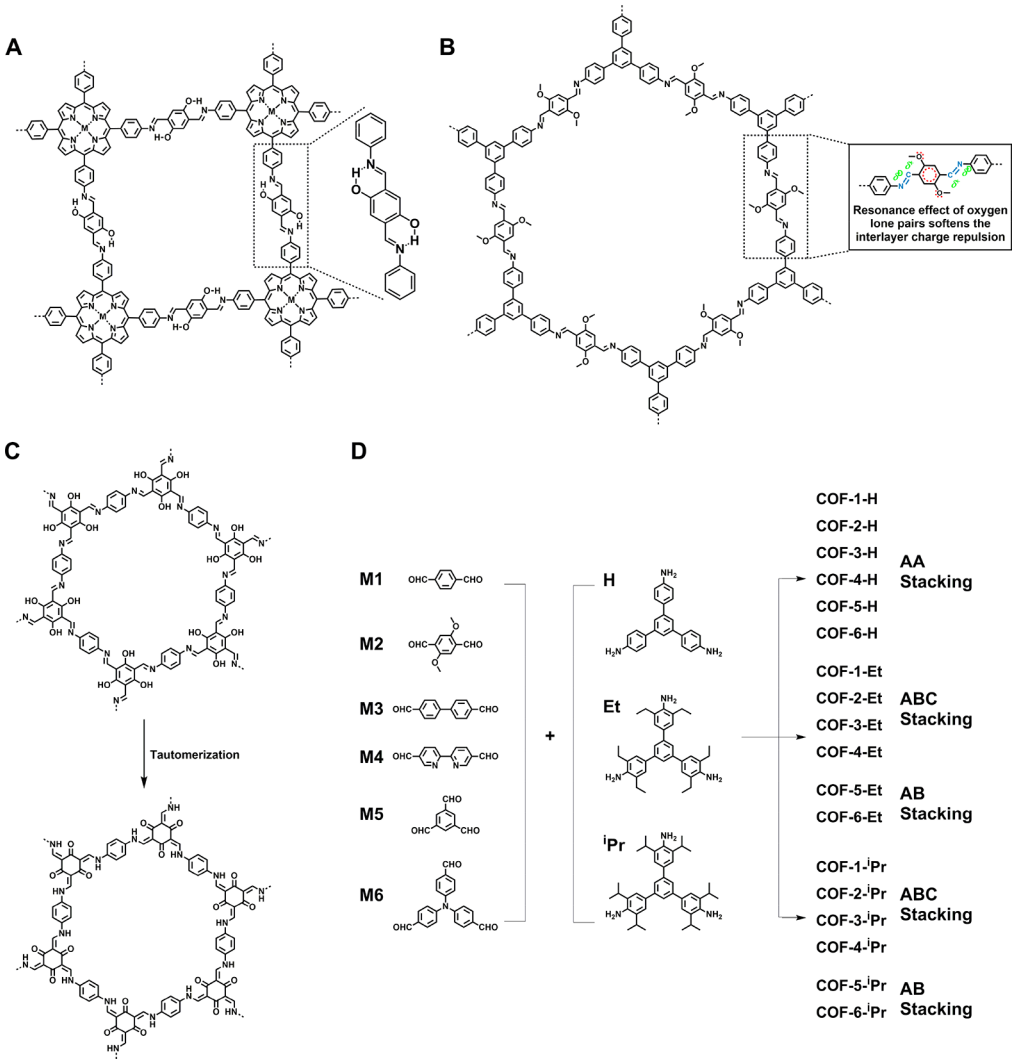

Figure 39. Strategies for the stability control of COFs by using (A) hydrogen bonding, (B) interlayer interactions, (C) tautomerization, and (D) the interlayer complementary method.

the remaining B−O bond to generate monomers, and the additional water molecule is found to greatly assist the hydrolysis by lowering the reaction barriers of these two steps. This is attributed to the increased interactions of monomers with the water molecules as well as the weakening of the B−O bonds.[333]

In general, the boroxine- and boronate-ester-linked COFs need to be washed with anhydrous solvents, which are essential to reduce the degradation of COFs. Several strategies have been developed to stabilize the boroxine- or boronate-ester-linked COFs.[131,334,335] For example, the direct synthesis of the boronate-ester-linked COFs from alkylated edge units (COF-14 Å, Figure 13) or pyridine-assisted post-synthetic modification (COF-10) endows the COFs with enhanced hydrolytic stability.[131,334] An ionic spiroborate-linked COF (ICOF) with an sp^3-hybridized anionic boron center exhibits excellent hydrolytic stability (Figure 27F).[217] The enhanced hydrolytic stability originates from the effective protection of the electrophilic boron centers from the nucleophile attack.

6.2. Nitrogen-Based Linkages

Unlike the boronate ester and boroxine-linked COFs, most nitrogen-based COFs, including imine, azine, hydrazone, squaraine, phenazine, imide, and triazine-linked COFs, exhibit remarkable hydrolytic stability.

The strength of interlayer interactions plays an important role in enhancing the chemical stability of COFs. In particular, the introduction of additional noncovalent interactions to the skeletons can greatly enhance the chemical stability. Two different strategies, that is, intralayer hydrogen-bonding interactions and interlayer complementary π-interactions, have been developed.[80,98,100] The condensation of TAPP with DHTP (= 2,5-Dha) and BDA or 2,5-dimethoxyterephthalaldehyde (2,5-Dma or DMTP) yields the MP-DHTP COFs (or DhaTph COF) and MP-Ph (or DmaTph COF), respectively (Figure 39A).[98] The MP-DHTP COFs exhibit enhanced crystallinity and chemical stability in comparison with the MP-Ph or DmaTph COF, due to the presence of hydroxyl-functionalized edge units that form an intramolecular hydrogen-bonding interaction with the imine bond. Moreover, the presence of the hydrogen-bonding interaction enhances the structural rigidity and crystallinity, thus protecting the imine linkages from chemical attack.[100] By introducing complementary π-interactions between layers to reinforce the interlayer interactions, the resulting COFs exhibit greatly enhanced crystallinity, porosity, and stability.[336]

Remarkably, the imine-linked COFs have been designed to possess ultrahigh stability in boiling water, strong acid, and base

https://dx.doi.org/10.1021/acs.chemrev.9b00550
Chem. Rev. 2020, 120, 8814−8933

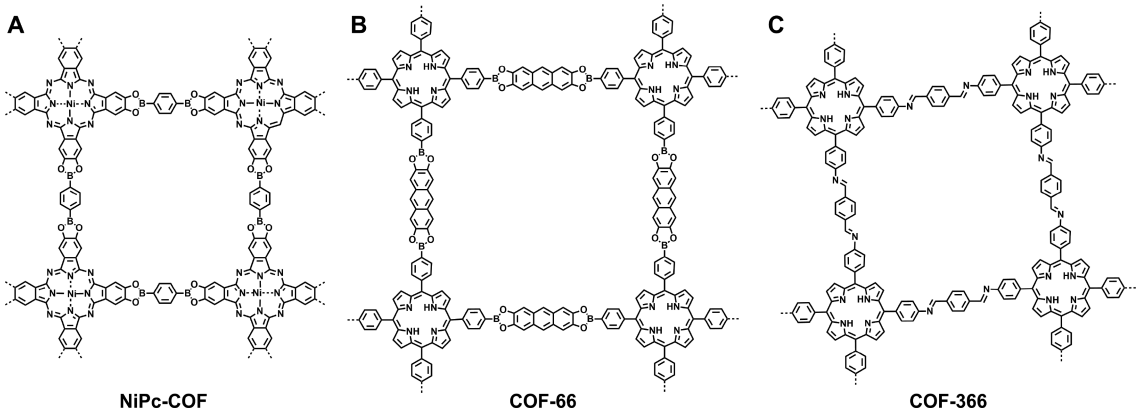

Figure 40. p-Type conducting COF of (A) NiPc-COF, (B) COF-66, and (C) COF-366.

media. This is achieved by introducing resonance effects to the phenyl edge units that soften electrostatic repulsions between layers caused by the polarization of the C═N bonds. The condensation of TAPB with DMTP yields TPB-DMTP-COF (Figures 16O and 39B).[80,81] TPB-DMTP-COF exhibited ultrahigh stability against boiling water, strong acids (12 M HCl), and strong bases (14 M NaOH) for 7 days while retaining high crystallinity and porosity.

Similarly, integrating electron-donating groups into the knots will also enhance the stability of imine-based COFs through providing significant steric hindrance and the hydrophobic environment around the imine bonds. TpOMe-Pa1, TpOMe-$BD(NO_2)_2$, TpOMe-Azo, and TpOMe-BPy with a 2,4,6-trimethoxy-1,3,5-benzenetricarbaldehyde (TpOMe) knot exhibit high chemical stability in H_2SO_4 (18 M), HCl (12 M), NaOH (9 M), boiling water, and common organic solvents for several days.[337] Using TFP (= Tp or Tfp) as a knot that enables the transformation of the imine linkages to a more stable enamine bond via enol-keto tautomerization yields TpPa-1 and TpPa-2, which are stable in aqueous HCl solution (9 M), boiling water, and aqueous NaOH solution (9 M) (Figure 39C).[64]

Apart from incorporating methoxy groups adjacent to the aldehydes or introducing enol−keto tautomerization into the skeleton, adjusting ethyl or isopropyl groups adjacent to each amine and di- or trialdehyde offers a synthetic strategy to control the interlayer stacking (AA, AB, and ABC) (Figure 39D), thus modulating the chemical stability of the resulting COFs.[336] The chemical stability of COFs is relevant to the density of incorporated alkyl groups that can protect the imine linkage and hydrolytically susceptible backbones. The COFs decorated with isopropyl groups can maintain crystallinity in aqueous NaOH solution (20 M) at 100 °C for 1 week.

6.3. Stable Skeletons

Compared with other nitrogen-based linkages, such as imine, azine, and hydrazine linkages, CS-COF and CTFs exhibit exceptional chemical stability owing to the formation of ring-fused phenazine and triazine units, respectively.[75,158] The crystalline structure of phenazine-linked CS-COF (Figures 16E and 27B) remains intact after it is immersed in organic solvents, including methanol, benzene, $CHCl_3$, and hexane, irrespective of their polarity, as well as aqueous HCl and NaOH solutions (1 M) for 24 h.[153] Apart from nitrogen-based stable linkages, the C═C-linked sp^2c-COFs (Figure 25A) offer extremely stable frameworks that keep their crystallinity and porosity under 1 week of immersion in water, strong acid, or base or upon 1 year of exposure to air.[115] The irreversible dioxine linkage offers excellent stability to the resulting COFs. The FT-IR spectra and PXRD patterns of COF-316 and COF-318 (Figure 26) are retained after treatment in 12 M HCl (aq) for 3 days,[94] whereas JUC-505 and JUC-506 (Figure 26) retain their crystalline structure after treatment under various conditions, including NMP, DMF, THF, dichloromethane, EtOH, acetone, *n*-hexane, *m*-cresol, boiling water, concentrated HCl (12 M), concentrated H_2SO4 (18 M), HF (40%), saturated NaOH (14 M), MeONa (5 M in MeOH), chromic acid solution (0.1 M $K_2Cr_2O_7$ in concentrated H_2SO_4), and $LiAlH_4$ (2.4 M in THF) for 1 week.[95]

Because the skeletons and pores of COFs can be systematically designed by the topology diagram and can be synthetically controlled, the functions of COFs could be designed and managed. This designability of both structures and functions is the unique feature of COFs that casts a sharp contrast with other porous materials. The design of COFs to create porous structures includes the design and control of the pore shape, size, and environment, which are key parameters that determine the sorption, separation, catalysis, and energy-storage properties. On the contrary, the design of the COF skeleton integrates knot, edge and linkage units into periodically ordered columnar π-arrays, which endow the frameworks with outstanding physicochemical properties, including optoelectronic properties, charge separation and charge-carrier conduction, and energy storage and energy conversion. Indeed, to achieve a specific function, the complementary design of the pores and skeletons offers a general way to trigger synergistic effects on COFs.[16,21,338] In this section, the functional design of COFs based on the pores and skeletons and their complementary utilization are demonstrated.

7. SEMICONDUCTORS

Most COFs contain rigid π-units in their skeletons as they employ π-units for designing and constructing skeletons to form topologically ordered columnar π-arrays. These periodically ordered π-structures are unique and inaccessible to conventional organic crystals and any other organic polymers. These columnar π-arrays trigger intracolumn electronic coupling and provide preorganized pathways for promoting charge-carrier transport. Depending on the structures of knots and linkers, COFs can be predesigned to control their conducting nature and achieve hole, electron, and ambipolar conductions. Remarkably, by integrating electron-donating π-units at the knots and electron-accepting segments on the linkers, donor−acceptor COFs with segregated and bicontinuous donor and acceptor π-

https://dx.doi.org/10.1021/acs.chemrev.9b00550
Chem. Rev. 2020, 120, 8814−8933

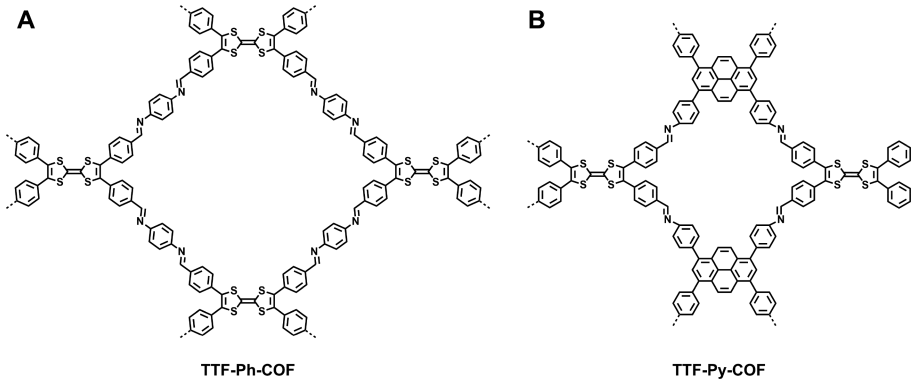

Figure 41. p-Type conducting COFs of (A) TTF-Ph-COF and (B) TTF-Py-COF.

arrays have been developed, and they offer a new molecular mechanism for photoenergy conversion based on a superb heterojunction interface that is ideal for charge separation and π-columns for ambipolar charge transport.[93,102,158,166,223]

7.1. p-Type Semiconductors

TP-COF with triphenylene vertices and pyrene edges is the first example of a semiconducting COF (Figure 20A). Electrical conductivity measurements using a two-probe method reveal the electric conducting with a current of 4.3 nA at a bias voltage of 2 V.[27] In sharp contrast, the monomer mixture shows only a negligible current (79 pA) under otherwise identical conditions. Upon doping with iodine, the current is greatly enhanced. The electrical current can be on−off switched many times without deterioration. Notably, PPy-COF with only pyrene units in the skeleton exhibits excellent electrical current on−off switching (Figure 19B). Upon visible-light irradiation, these p-type semiconductors TP-COF and PPy-COF become photoconductive and exhibit prominent photocurrents with (2 and 8) $\times 10^4$ on−off ratios, respectively.[222] The difference in photocurrents of the two COFs is attributed to the self-assembled pyrene structure in PPy-COF that promotes exciton migration across the framework.

To promote the charge-carrier transport, NiPc-COF (Figure 40A) with phthalocyanine units at the knots of the tetragonal lattice, has been prepared by condensing [NiPc(OH)$_8$] with BDBA.[30] The experimentally observed PXRD pattern together with the DFTB simulation results suggest that the phthalocyanine units stack in an eclipsed fashion to form a 2D layered structure, which forms phthalocyanine π-arrays to facilitate charge-carrier transport. Flash photolysis time-resolved microwave conductivity (FP-TRMC) measurements have been employed for the investigation of carrier mobility. An extrapolation at 0 V bias voltage yields a charge-carrier number of 3.8×10^8 with a carrier generation efficiency of 3.0×10^{-5} at a photon density of 6.5×10^{14} photon cm^{-2}. The charge-carrier numbers are invariant with the variable measurement atmospheres, indicating that the carriers are mainly from the holes with a minimum carrier mobility of 1.3 cm^2 V^{-1} s^{-1}. Interestingly, the carrier mobility is greatly dependent on the central metal ions at the phthalocyanine cores.[32] Upon excitation with a 355 nm pulsed laser at a photon density of 9.1×10^{15} photon cm^{-2} under air, CuPc-COF yields a $\phi\Sigma\mu$ (ϕ is the photocarrier generation quantum yield and $\Sigma\mu$ is the sum of charge-carrier mobilities) value of 1.4×10^{-4} cm^2 V^{-1} s^{-1}. On the contrary, ZnPc-COF and CoPc-COF exhibit an enhanced $\phi\Sigma\mu$ value of (2.2 and 2.6) $\times 10^{-4}$ cm^2 V^{-1} s^{-1}, respectively. Therefore, the central metal ions in the phthalocyanine macrocycles play a vital role in determining the conducting properties.

The boronate-ester-linked COF-66 (Figure 40B) and the imine-linked COF-366 (Figure 40C) with free-base porphyrin vertices are also p-type semiconductors.[106] On the basis of FP-TRMC measurements, COF-66 and COF-366 have a $\phi\Sigma\mu$ value of (1.7 and 4.1) $\times 10^{-5}$ cm^2 V^{-1} s^{-1}, respectively, at a photon density of 9.1×10^{15} photons cm^{-2}. Time-of-flight (TOF) measurements of 1.5 μm thick COF-66/poly(methyl methacrylate) (60/40 wt %) and COF-366/poly(methyl methacrylate) (60/40 wt %) composites reveal that the hole mobility ($\Sigma\mu$) can reach 3.0 and 8.1 cm^2 V^{-1} s^{-1}, respectively.

The columnar packing affects the carrier mobilities of COFs. The introduction of tetrathiafulvalene (TTF) units into the skeleton enables the synthesis of TTF-Ph-COF (= TTF-COF, Figures 16G and 41A)[245] and TTF-Py-COF (Figure 41B).[238,339] FP-TRMC measurements of the bare TTF-Ph-COF and TTF-Py-COF upon 355 nm pulsed laser excitation at a photon density of 9.1×10^{15} photon cm^{-2} reveal that the carrier mobility for TTF-Ph-COF and TTF-Py-COF was 0.2 and 0.08 cm^2 V^{-1} s^{-1}, respectively. The tight packing and low distortion of the phenyl linkers in TTF-Ph-COF account for the high carrier mobility. A very distinct difference is observed for the imine-linked triangular HPB-COF and HBC-COF (Figure 11A, B) that possess propeller-shaped HPB vertices and the nearly planar nanographene-like HBC vertices, respectively.[12] FP-TRMC measurements reveal that HBC-COF has a $\phi\Sigma\mu$ value of 1.0 $\times 10^{-5}$ cm^2 V^{-1} s^{-1}, which is twice that of HPB-COF (0.5×10^{-5} cm^2 V^{-1} s^{-1}) and even one to two orders of magnitude higher than those of TTF-based COFs. The intrinsic hole mobility of HBC-COF is as high as 0.7 cm^2 V^{-1} s^{-1}, which is 40−70 times higher than those of the triphenylene-based COF (0.01 cm^2 V^{-1} s^{-1}) and porphyrin-knotted ZnP-COF (0.016 cm^2 V^{-1} s^{-1}). These findings together with the DFTB calculations indicate that the disc-like larger π-core of the tightly bound HBC columns is superior to the loosely packed TTF or HPB columns for carrier transport.

The phenazine-linked CS-COF (Figures 16E and 27B) with conjugated chains in all three dimensions is a p-type semiconductor as well.[158] On the basis of the FP-TRMC measurement, CS-COF exhibits a $\phi\Sigma\mu$ value of 0.50 cm^2 V^{-1} s^{-1} at a proton density of 2.6×10^{16} photons cm^{-2}. The number of charge carriers estimated by extrapolation of the bias at 0 V is 3.2×10^{15} with a yield of φ = 12% (φ is the number of charge carriers/number of photons). Therefore, CS-COF is a high-rate hole-conducting framework with an exceptional mobility of 4.2 cm^2 V^{-1} s^{-1}, which is superior to that of the state-of-the-art

https://dx.doi.org/10.1021/acs.chemrev.9b00550
Chem. Rev. 2020, 120, 8814−8933

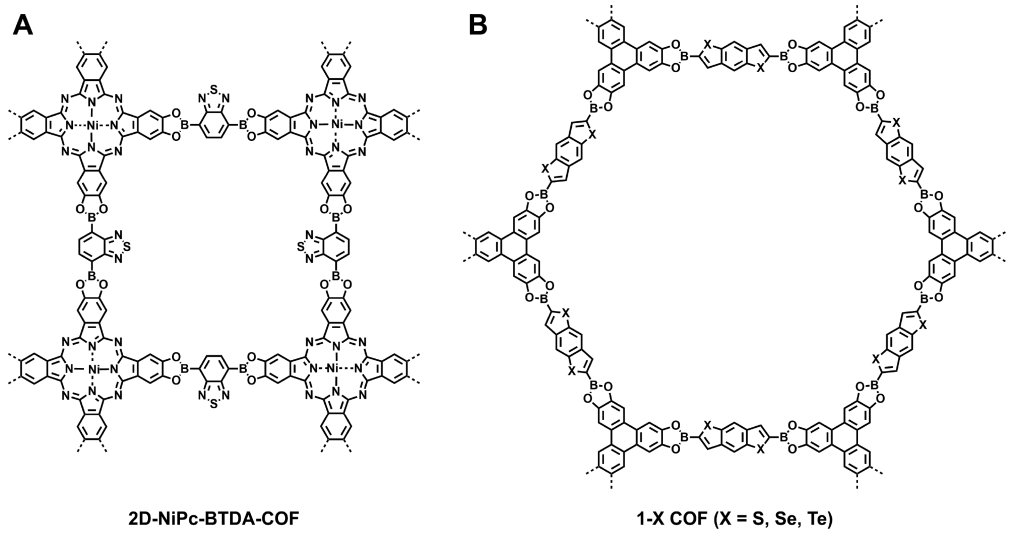

Figure 42. n-Type conducting COFs of (A) 2D-NiPc-BTDA-COF and (B) 1-*X* COF (*X* = S, Se, Te).

semiconducting polymer, RR-P3HT (μ = 0.014 cm^2 V^{-1} s^{-1}).[340−343]

7.2. n-Type Semiconductors

The charge-carrier transport not only depends on the nature of knots but also is highly sensitive to the edge units as well. By changing the edge units from electron-rich to electron-deficient units, the conducting nature of COFs can be reversed. In contrast with NiPc-COF, which is hole-conducting, 2D NiPc-BTDA-COF (Figure 42A) with the electron-deficient BTDA edges is an electron conductor.[104] Indeed, 2D NiPc-BTDA-COF achieves an electron mobility as high as 0.6 cm^2 V^{-1} s^{-1}. Both NiPc-COF and NiPc-BTDA-COF exhibit a broad absorbance from the ultraviolet to the near-infrared region.[30,104] Upon irradiation with a xenon light source (>400 nm), NiPc-COF exhibits a significant increase in current from 20 nA (dark current) to 3 mA (photocurrent). On the contrary, NiPc-BTDA-COF exhibits an enhancement of photocurrent from 250 nA (dark current) to 15 μA (photocurrent). Both NiPc-COF and NiPc-BTDA-COF can switch the photocurrent on and off many times without deterioration. Because of their broad absorption bands, both COFs panchromatically respond to the photons over a wide range of wavelengths and are extremely sensitive to infrared light. The high sensitivity and photoconductivity originate from the combination of increased light-harvesting capability and enhanced carrier mobility.

By varying the chalcogen atoms in the edge units, the electrical conductivity can be tuned systematically. For example, the condensation of the HHTP knot with benzodichalgenophene diboronic acid edges (chalcogens: S, Se, and Te) yields a series of boronate-ester-linked COFs (1-S, 1-Se, 1-Te; Figure 42B).[344] The conductivity is estimated to be 3.7 ($\pm$0.4) × 10^{-10} S cm^{-1} for 1-S, 8.4 ($\pm$3.8) × 10^{-9} S cm^{-1} for 1-Se, and 1.3 ($\pm$0.1) × 10^{-7} S cm^{-1} for 1-Te, respectively. The high conductivity of 1-Te compared with 1-S and 1-Se originates from the presence of heavier chalcogen Te atoms, which improve the interlayer orbital overlap that facilitates the conduction across the π-arrays.

7.3. Ambipolar-Type Semiconductors

Porphyrins are a class of macrocycles (Figure 8C) with extended π-conjugation and show diverse functionalities, where the charge-carrier transport is highly dependent on the central metal ions.[99] Free-base porphyrin H_2P-COF is a hole-conducting framework with a mobility of 3.5 cm^2 V^{-1} s^{-1}, whereas CuP-COF consists of copper(II) porphyrin, an electron-transporting framework with a mobility of 0.19 cm^2 V^{-1} s^{-1}. By contrast, ZnP-COF with zinc(II) porphyrin knot is an ambipolar conducting material with hole and electron mobilities of 0.032 and 0.016 cm^2 V^{-1} s^{-1}, respectively. Upon irradiation with a xenon light (>400 nm), ZnP-COF generates a photocurrent of 26.8 nA, whereas the photocurrents of CuP-COF and H_2P-COF are only 0.6 and 0.01 nA, respectively. Remarkably, ZnP-COF exhibits an on−off ratio of 5 × 10^4, which is far superior to the those of CuP-COF (300) and H_2P-COF (4).

7.4. Donor−Acceptor COFs

Ambipolar conducting COFs have been rationally designed and synthesized by creating a segregated bicontinuous donor (D)−acceptor (A) heterojunction, where donor-on-donor and acceptor-on-acceptor π-columns offer pathways for hole and electron transport, respectively.[90] Vertically oriented and self-sorted donor−acceptor bicontinuous heterojunctions have been constructed into 2D D−A COFs (Figure 43A) by employing HHTP as a donor at the vertices and BTDA as an acceptor at the edges. The total $\phi\Sigma\mu$ value is 1.51 × 10^{-4} cm^2 V^{-1} s^{-1}, whereas the hole and electron mobilities are 0.01 and 0.04 cm^2 V^{-1} s^{-1}, respectively. Upon irradiation, the 2D D−A COF exhibits an increased current from 0.8 pA (dark) to 10.1 nA. Note that this segregated column in D−A COF is hardly accessible to the conventional supramolecular assembly of donor and acceptor components, which usually results in donor-on-acceptor alignment owing to the electrostatic interaction between the donor and the acceptor.[345,346]

The photocurrent can be switched on and off many times without deterioration. In contrast, a simple mixture of monomers remains silent under otherwise identical irradiation conditions. Such an ordered heterojunction is important for photovoltaic devices.[93,223] Through incorporating donor−acceptor-type isoindigo- and thienoisoindigo-based building blocks, Py-pII (Figure 43C), Py-pTII (Figure 43D), and Py-tTII COFs (Figure 43E) exhibit low band gaps of 1.78, 1.48, and 1.36 eV, respectively, demonstrating them as UV- to NIR-responsive photodetectors.[347]

By developing metallophthalocyanines and diimides as electron-donating and -accepting building blocks, D_{MPc}-A_{DI}-

https://dx.doi.org/10.1021/acs.chemrev.9b00550
Chem. Rev. 2020, 120, 8814−8933

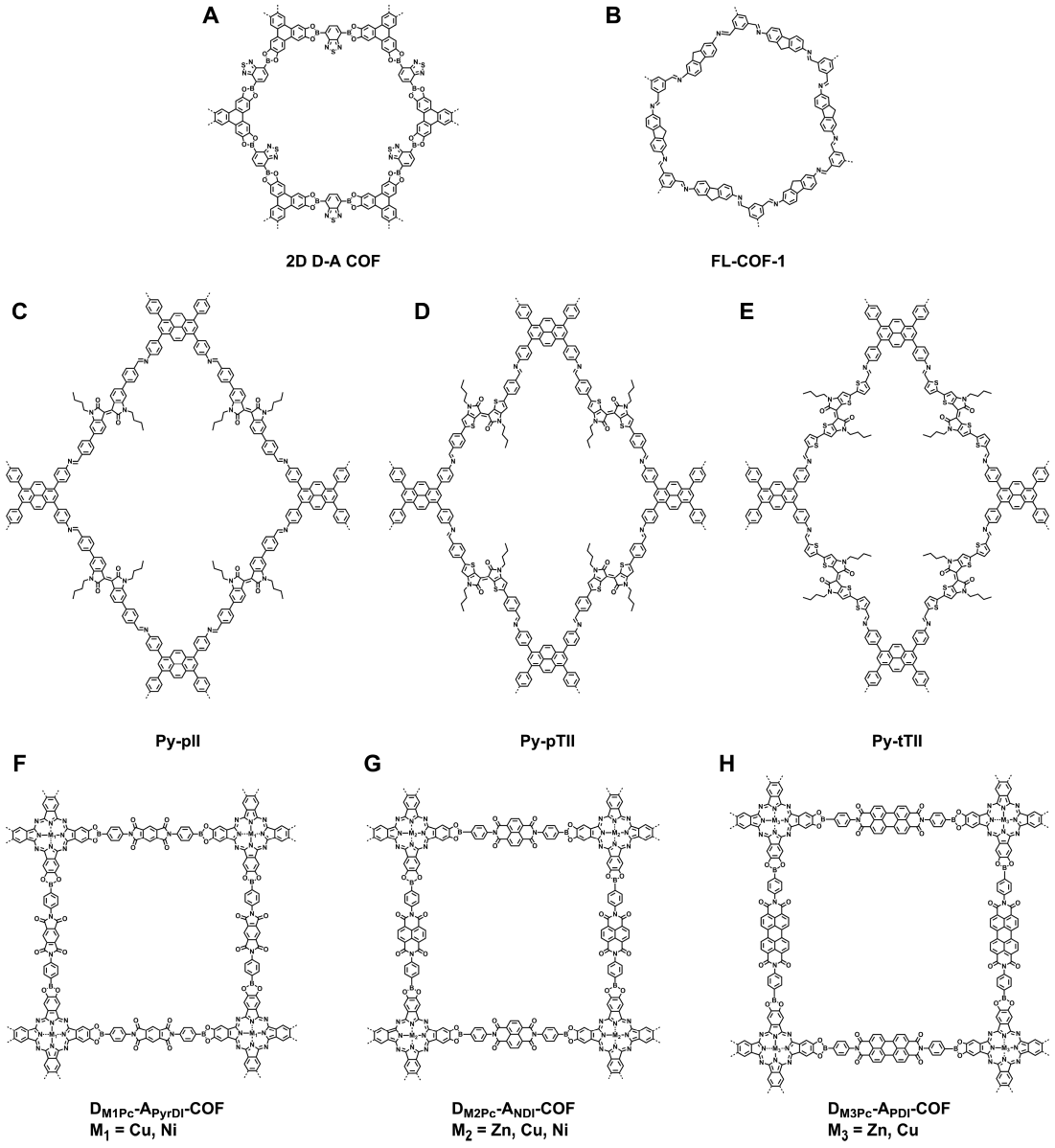

Figure 43. Donor–acceptor COFs of (A) 2D D–A COF, (B) FL-COF-1, (C) Py-pII, (D) Py-pTII, (E) Py-tTII COFs, (F) D_{M1Pc}-A_{PyrDI}-COFs (M_1 = Cu, Ni), (G) D_{M2Pc}-A_{NDI}-COFs (M_2 = Zn, Cu, Ni), and (H) D_{M3Pc}-A_{PDI}-COFs (M_3 = Zn, Cu).

COFs (M = Cu, Ni, Zn) (Figure 43F–H) with periodically ordered electron-donor and -acceptor π-columnar arrays have been synthesized via direct polycondensation reactions.[102,166] Upon the excitation of CuPc and NiPc at 355 nm in benzonitrile, the TA spectra of those COFs exhibit negative absorption bands, which are the mirror images of the steady-state absorption spectra of corresponding COFs with a 10–15 nm red shift. These mirror images indicate that the charge delocalization along the extensive π-columns takes place after the fast photoinduced charge separation between the adjacent donor–acceptor units.[166] Among D_{MPc}-A_{DI}-COFs with different metal centers, D_{CuPc}-A_{DI}-COFs exhibit the longest lifetime (τ) of 33 μs for the charge-separated state, demonstrating that CuPc is superior as an electron donor to form the long-lived charge-separated state with the PyrDI acceptor.[102] In these systems, the elemental photochemical processes from light absorption to photoinduced electron transfer and charge separation are completed within 1.4 ps, indicating that COFs enable an ultrafast photochemical event.

In the donor–acceptor COFs, the electron-donor and -acceptor components are assembled into bicontinuous segregated π-columnar arrays (Figure 44). This alignment

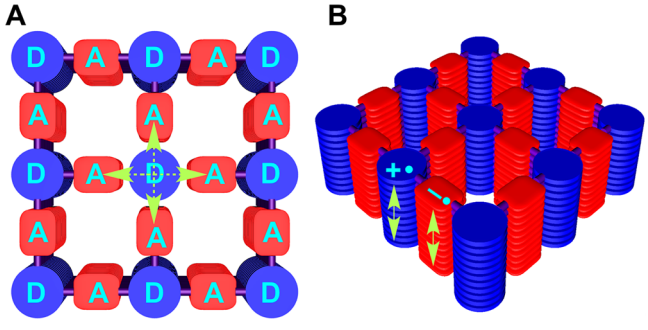

Figure 44. Donor–acceptor COFs with bicontinuous segregated donor–acceptor columns for (A) photoinduced electron transfer and (B) charge-carrier migration and collection.

https://dx.doi.org/10.1021/acs.chemrev.9b00550
Chem. Rev. 2020, 120, 8814–8933

features a specific π-structure for photoinduced electron transfer. First, in the 2D layer, each electron donor and acceptor are covalently linked to form a heterojunction; this topology-guided heterojunction yields exceptionally dense heterojunction across the framework, constituting a superheterojunction structure (Figure 44A) that is inaccessible to other polymers and organic semiconductors. This structure is ideal for photoinduced electron transfer. Second, in the layered framework, the π-columns allow for the migration of radical species, which is ideal for preventing backward electron transfer and for realizing a long-lived charge separation state (Figure 44B). Moreover, the π-columns offer pathways for charge collection; that is, donor columns transport holes, and acceptor columns move electrons. These interplays work together in one material to offer a new and ideal molecular mechanism for photoenergy conversion.[102]

Organic semiconductors are also ideal flexible thermoelectric materials due to their low thermal conductivity and material abundancy. After doping with iodine, the fluorene-based I_2@FL-COF-1 (Figure 43B) exhibits an electrical conductivity of 1.0×10^{-4} S cm^{-1}, a Seebeck coefficient of 2450 μV K^{-1}, and a power factor of 0.063 μW m^{-1} K^{-2} at room temperature, and this Seebeck coefficient is the highest reported for conducting polymers.[261,348]

7.5. Thin Films

Beside the investigations of the conductivity of bulk COF samples or processed COF−polymer composite films, the preparation of high-quality free-standing COF films or highly oriented films on substrates remains a challenge and is a prerequisite for optoelectronic devices.

Highly stable conjugated CS-COFs (Figure 16E, Figure 27B) that enables the delocalization of electrons into all three dimensions have been synthesized.[158] The FP-TRMC measurements with 355 nm pulsed laser excitation at a photon density of 2.6×10^{16} photons cm^{-2} under Ar yielded a $\phi\Sigma\mu$ of 0.6 cm^2 V^{-1} s^{-1}. An invariant $\phi\Sigma\mu$ value under SF_6 (electron quencher) suggests that holes are the major charge carriers for conduction. The yield of charge carriers is estimated to be as high as 12% by TOF transient conductivity measurements. Therefore, CS-COF is a hole-conducting material with an exceptional carrier mobility of 4.2 cm^2 V^{-1} s^{-1}, which is much higher than those of porphyrin-based H_2P-COF (1.8×10^{-4} cm^2 V^{-1} s^{-1})[99] and COF-66 (3.0 cm^2 V^{-1} s^{-1}).[106]

The TTF-COF (= TTF-Ph-COF, Figure 42A) thin films (thickness ~150 nm) have been prepared via the solution-based *in situ* growth of COFs on Si/SiO_2 substrate or transparent ITO-coated glass.[172] Grazing-incidence wide-angle X-ray scattering (GIWAXS) of the thin films suggests the polycrystalline nature with a preferred column orientation normal to the substrate. In contrast, the powder COF samples exhibit a random orientation of the crystallites. These results suggest that the GIWAXS characterization technique is powerful to examine the structural ordering of COF crystallites.[171,307] The COF films (grown on a 300 nm Si/SiO_2 substrate with a prefabricated Au/Cr electrode of 3 nm × 50 nm × 150 μm dimensions) exhibit a linear $I-V$ curve with a conductivity of 1.2×10^{-4} S m^{-1}. The conductivity is increased to 0.28 S m^{-1} upon iodine doping and is saturated after 24 h. Electron absorption and electron paramagnetic resonance (EPR) spectral analyses suggest the formation of a radical cation ($TTF^{\bullet+}$) upon iodine/TCNQ (tetracyanoquinodimethane) doping, which accounts for the high conductivity of films in the doped state. Moreover, the open pores of TTF-COF allow the efficient diffusion of iodine to form a charge-transfer state, and the aligned columnar stacking of the TTF units enables the delocalization of radical cations to form more conductive mixed-valence species.

Highly oriented COFs films enable an enhanced photoresponse, as demonstrated by TT-COF (Figure 45).[349] The

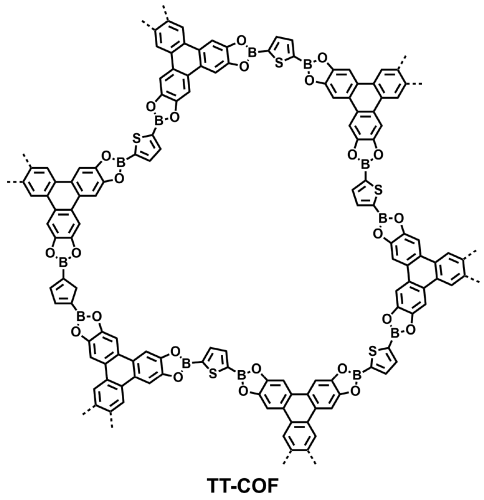

Figure 45. Schematic of TT-COF.

GID profile of the COF films on Si/SiO_2 or transparent glass substrates together with the PXRD analysis of the COF powder suggest that the preferred orientation of the COF films is parallel to the substrates. Upon white-light irradiation with a xenon lamp, the TT-COF films exhibit an enhanced photocurrent at an applied voltage of 1.0 V with an on/off ratio of 1.7. The photoresponse time and decay time for TT-COF is 1.9 s. In contrast, disordered COF films prepared from the drop-casting of the COF powder exhibit an extremely long response and decay time of 10.2 and 9.6 s, respectively. The high speed of photoresponse can be attributed to the highly oriented COF films, which facilitate exciton migration and allow rapid carrier transport. The photoconducting properties of the TT-COF films are highly dependent on the film thickness and their morphology. For example, the TT-COF films prepared upon a 4 h reaction exhibit a rough surface, a low dark current of 0.02 pA, and a photocurrent of 0.1 pA. By increasing the reaction time to 6 h, the COF films exhibit an increased dark current and photocurrent to 0.1 and 0.7 pA, respectively, owing to an improved surface smoothness. As the reaction time is increased to 17 h, the dark current and photocurrent are improved to 0.4 and 0.8 pA, respectively. By fabricating the vertical field-effect transistor (VFET) device based on the SLG/$COF_{TFPy\text{-}PPDA}$ (= ILCOF-1, Figure 9A) film heterostructure, a high $J_{on/off}$ ratio of 10^6 in the p-type regime and 10^5 in n-type zone can be obtained at a low bias voltage, and the highest on-current density reaches 6.8 A cm^{-2} for hole transport and 4.1 A cm^{-2} for electron conduction.[242] In fact, it is higher than those of reported VFET devices such as graphene−P3HT (3.4 A cm^{-2})[350] and graphene−DNTT (1.2 A cm^{-2}).[351] The high semiconducting performance demonstrates that oriented COFs films on SLG exhibit great potential in advanced driving cells of OLEDs and flexible organic electronic devices.

The well-defined π-stacking structures render COFs able to construct various predesignable pathways for promoting hole

https://dx.doi.org/10.1021/acs.chemrev.9b00550
Chem. Rev. 2020, 120, 8814−8933

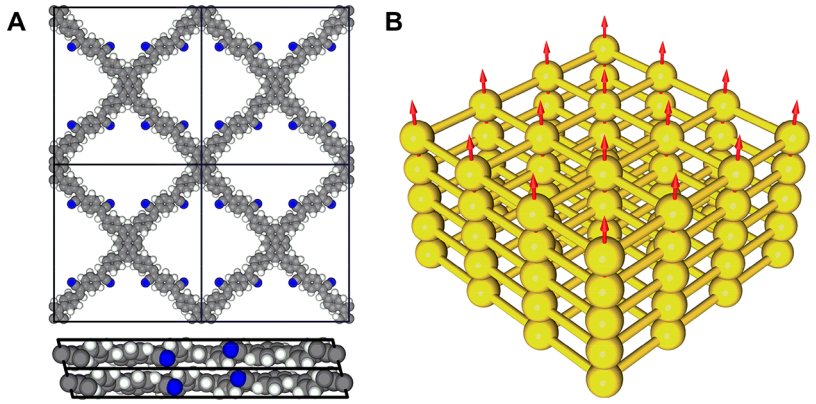

Figure 46. (A) Reconstructed crystal structure at top and side views. (B) Schematic of spin alignment in sp^2c-COF (three-by-three lattice). Red arrows represent spins.

and electron transport, in which the vertices, the edges, and the linkers are key to carrier mobility and conduction nature.

7.6. Spin Alignment and Magnetic Properties

Spintronics is an emerging field in electronics that brings about advantages such as increased processing speed, decreased power consumption, and increased integration density. However, the lifetime and alignment of spins are key challenges that need to be addressed before producing high-performance spintronics. Recently, the first crystalline sp^2-carbon-conjugated COF constructed from pyrene and phenylenevinylene with a band gap of 1.9 eV has been reported. The oxidation of the sp^2c-COF (Figures 9C and 46A) with iodine yields a 12 order of magnitude increase in conductivity, and the generated radicals are densely localized at pyrene knots, which can be aligned unidirectionally below 10 K to yield a ferromagnetic structure (Figure 46B).[114] Such spin structures cannot be accessed by 1D conjugated polymers[352,353] or conventional 2D COFs,[16] which eventually yield bipolarons. Following this pioneer work, a 2D covalent organic radical framework (CORF) PTM-CORF (Figure 47) has been reported via the postsynthetic deprotonation and oxidation of the polychlorotriphenylmethyl (PTM) COF precursor. PTM-CORF is stable under ambient air and light conditions with a low optical band gap of 0.87 eV. The adjacent radicals between neighboring PTM units show antiferromagnetic coupling behavior. Nevertheless, the low-lying lowest unoccupied molecular orbital (LUMO) of PTM-CORF was exploited for use as an electrocatalyst for the oxygen reduction reaction (ORR).[276]

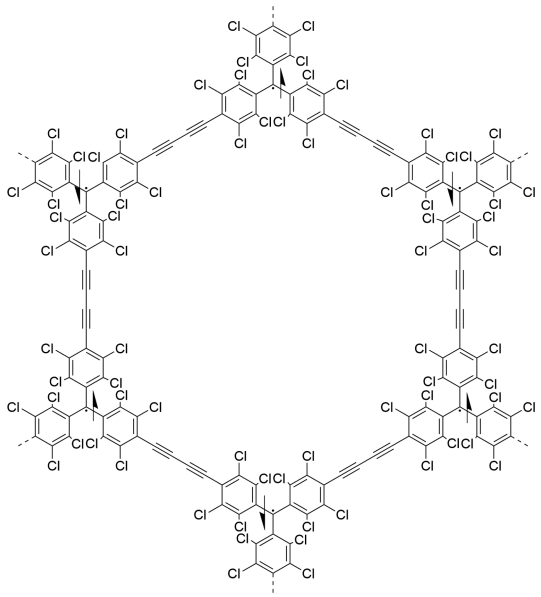

Figure 47. Chemical structure of 2D covalent radical frameworks (PTM-CORF).

8. LUMINESCENCE AND SENSORS

8.1. Design Principle

Over the past several decades, intensive research efforts have been made to develop luminescent materials due to their broad applications, such as sensors, bioprobes, optoelectronics, and photovoltaics.[354,355] Luminescent small molecules are easily accessible and cost-effective.[356−361] However, they have disadvantages, such as low sensitivity, stability, and reusability. Luminescent polymeric systems have a high probability of resolving the shortcomings of small molecules. Compared with conventional 1D or 3D polymeric systems, COFs are unique in that they can be rationally designed to create ordered π-structures in which the luminescent segments can be spatially preorganized.[111]

2D COFs consist of layered structures formed by $\pi-\pi$ stacking, which usually results in weak luminescence due to the aggregation-caused quenching effect (ACQ).[117] How to endow COFs with luminescent activity is challenging. At the same time, this issue is critical in exploring sensing applications. Nevertheless, one significant feature is that COFs enable the complementary utilization of ordered π- for exciton migration and nanopores for guest accommodation. These features endow COFs systems with selectivity and sensitivity and allow for the detection of a broad range of analytes from explosives to hazardous molecules and toxic metal ions.[259,355]

The luminescent behavior of COFs has been demonstrated first for the boronate-ester-linked TP-COF (Figures 16A and 48A) and boroxine-linked PPy-COF (Figures 16B and 19B). Upon the excitation of the pyrene units, these COFs emit brilliant blue luminescence at 474 and 484 nm, respectively, as a result of pyrene excimer luminescence from the $\pi-\pi$-stacked pyrene arrays.[27,222] By changing the nature of vertices, the boronate-ester-linked DBA-COF 1 and DBA-COF 2 with planar π-conjugated dehydrobenzoannulene (DBA[12] and DBA[18]) macrocycles at the vertices and BDBA on the edges exhibit

https://dx.doi.org/10.1021/acs.chemrev.9b00550
Chem. Rev. 2020, 120, 8814−8933

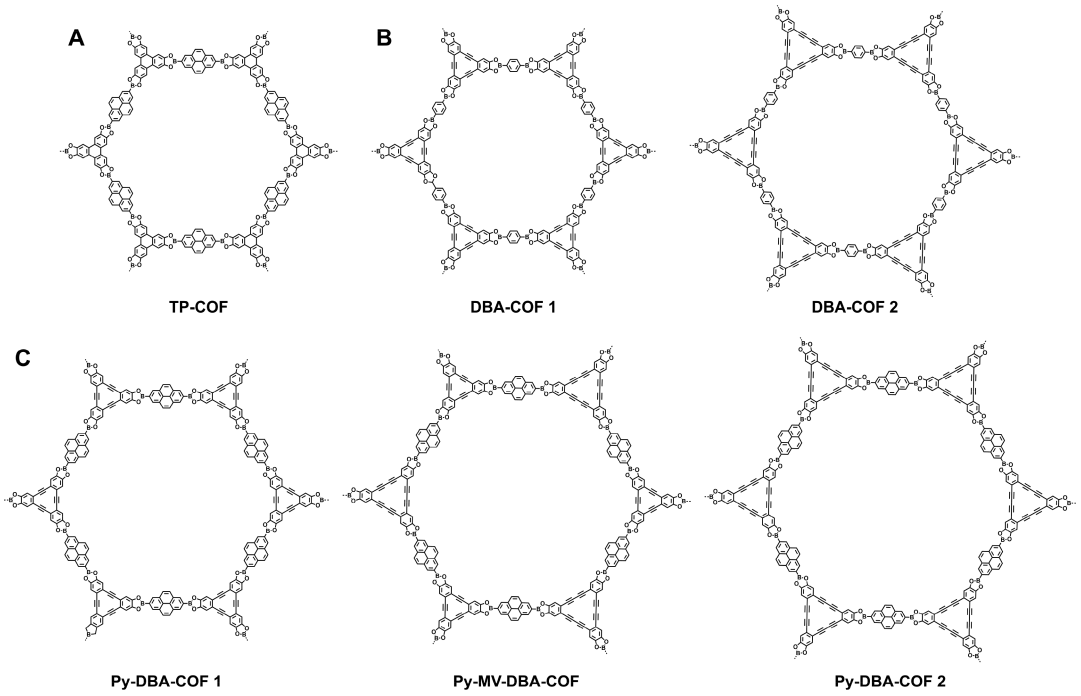

Figure 48. Schematics of (A) TP-COF, (B) DBA-COF 1 and DBA-COF 2, and (C) Py-DBA-COF 1, Py-MV-DBA-COF, and Py-DBA-COF 2.

different luminescence behaviors (Figure 48B).[120] For example, DBA-COF 1 strongly emits at 530 nm upon excitation at 365 nm. In contrast, DBA-COF 2 is nonluminescent under otherwise identical conditions. Partially replacing the BDBA edge units with PDBA generates a series of COFs with a heterogeneous distribution of DBA vertices, including Py-DBA-COF 1, Py-MV-DBA-COF, and Py-DBA-COF 2 (Figure 48C); this mixed-vertex strategy can tune the luminescence of COFs.[40] Indeed, Py-DBA-COF 2 exhibits blue-greenish luminescence, whereas Py-DBA-COF 1 and Py-MV-DBA-COF emit yellow light. The design strategy is based on the excimer luminescence of stacked pyrene arrays that dominate the light-emitting properties of COFs.

To design highly efficient light-emitting COFs, a new design strategy has been developed in which the aggregation-induced emission (AIE) mechanism is integrated to the skeletons.[362] By using AIE-active TPE units as vertices, the boronate-ester-linked 2D TPE-Ph COF (Figures 16F and 49) has been established as the luminescent benchmark for COFs, with the highest absolute fluorescence quantum yield of 32% reported to date.[117] The TPE-Ph COF exhibits belt-like morphology, as revealed by FE-SEM images, and is highly luminescent irrespective of the belt length. By contrast, a model compound (TPE-pinacol ester) exhibits a fluorescence quantum yield of only 15%. The significant gap in quantum yield is attributed to their structural differences. The free rotation of the four phenyl groups in the TPE units is restricted by the boronate ester linkages in the TPE-Ph COF monolayer. Importantly, the interlayer stacking in the TPE-Ph COF further restricts the rotation of the four phenyl groups. Therefore, intralayer covalent bonds and interlayer noncovalent $\pi-\pi$ stacks work synergistically in decreasing the rotation-related thermal dissipation of the photoexcited state, thus significantly enhancing the fluorescence quantum yield of the TPE-Ph COF. The exceptional fluorescence quantum yield of the AIE-based TPE-Ph COF opens a new route to light-emitting COFs.

Using the same core units, the imine-based Py-TPE-COF has been designed and synthesized by condensing 1,3,6,8-tetrakis(4-aminophenyl)pyrene (Py-NH2) with 1,1,2,2-tetrakis(4-formylphenyl)ethane (TPE-4CHO) (Figure 50A).[363] The resulting Py-TPE-COF consists of spheres of submicron size. This COF exhibits a photoluminescent quantum yield in organic solvents up to 21.1%, which is attributed to the nonplanar TPE units that reduce interlayer $\pi-\pi$ interactions. Using the same strategy, AIE-based 3D-TPE-COF has been synthesized via the polycondensation of TAPM with 1,1,2,2-tetrakis(4-formyl-(1,1′-biphenyl))ethane (Figure 50B).[58] Upon excitation, 3D-TPE-COF emits yellow and achieves a luminescence quantum yield of 20%.

Besides luminescent COFs, phosphorescent COFs have been explored via crystallization-induced phosphorescence (CIP). The integration of an organic phosphor benzil into a triphenylene knotted skeleton forms BZL-COF, which emits phosphorescence at 545 nm for as-prepared BZL-COF and at 540 nm for as-activated BZL-COF (Figure 50C).[364] By removing the trapped solvent molecules, the interlayer distance of BZL-COF changes from 0.37 to 0.34 nm, which decreases the phosphorescence lifetime from 1.27 to 1.02 ms.

8.2. Band-Gap Engineering and Color Tuning

Introducing the bulky *tert*-butyl groups to the skeleton can adjust the interlayer $\pi-\pi$ interaction to offer high luminescence efficiency of the material. COF-JLU3 solid (Figure 51) exhibits a strong orange-red luminescence at 601 nm upon excitation at 424 nm.[84] The absolute fluorescence quantum yield is as high as 9.91%.

Compared with the planar linkage, the contorted linkages can weaken $\pi-\pi$ interaction and ACQ effects and are suitable for creating light-emitting materials. The hydrazone linkage assumes a nonpolar structure and yields luminescent COFs. The hydrazone-based COF-LZU8 (Figure 52A) powder exhibits blue emission at 460 nm with an absolute quantum yield of 3.5% upon excitation at 390 nm.[254] To control the light-

https://dx.doi.org/10.1021/acs.chemrev.9b00550
Chem. Rev. 2020, 120, 8814−8933

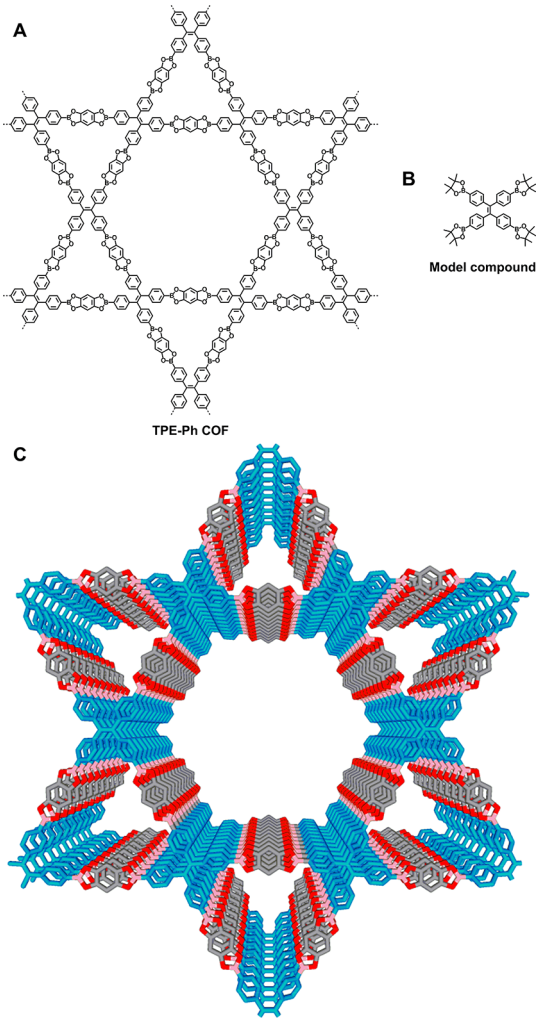

Figure 49. Schematics of (A) TPE-based highly emissive TPE-Ph COF, (B) model compound, and (C) the AA-stacking model of TPE-Ph COF.

emitting activity, the hydrazone-based Tf-DHzDR COF (Figure 52B) and the TFPB-DHzDR COF (Figure 52C) have been synthesized to bear different alkyl chains to control the equilibrium of different states whereby interlayer and intralayer hydrogen-bonding interactions endow COFs with different colors from blue to yellow and nearly white.[365]

IMDEA-COF-1 and IMDEA-COF-2 have been designed by using 1,6-diaminopyrene (DAP) as the linker and 1,3,5-benzenetricarbaldehyde (BTCA) or 2,4,6-triformylphloroglucinol (TP) as the knot (Figure 53).[366] These COFs adopt staggered conformations that greatly weaken interlayer $\pi-\pi$ interactions and become luminescent. Indeed, the solid sample of IMDEA-COF-1 exhibits green emission at 501 nm with an absolute luminescence quantum yield of 3.5%.

In contrast with the nonconjugated frameworks, recently, fully π-conjugated sp^2-carbon COFs have been synthesized and explored as luminescent materials (Figure 25A).[115] In sp^2c-COFs, the C═C linkages topologically connect pyrene knots and arylene vinylene linkers into 2D all-sp^2-carbon lattices that are π-conjugated along both the x and y directions. The resulting sp^2c-COFs are capable of tuning the band gap and emission by the linkers and are highly luminescent under various conditions. In layered frameworks, the linker units in sp^2c-COFs are key to the π-conjugation and luminescence, whereas in the exfoliated

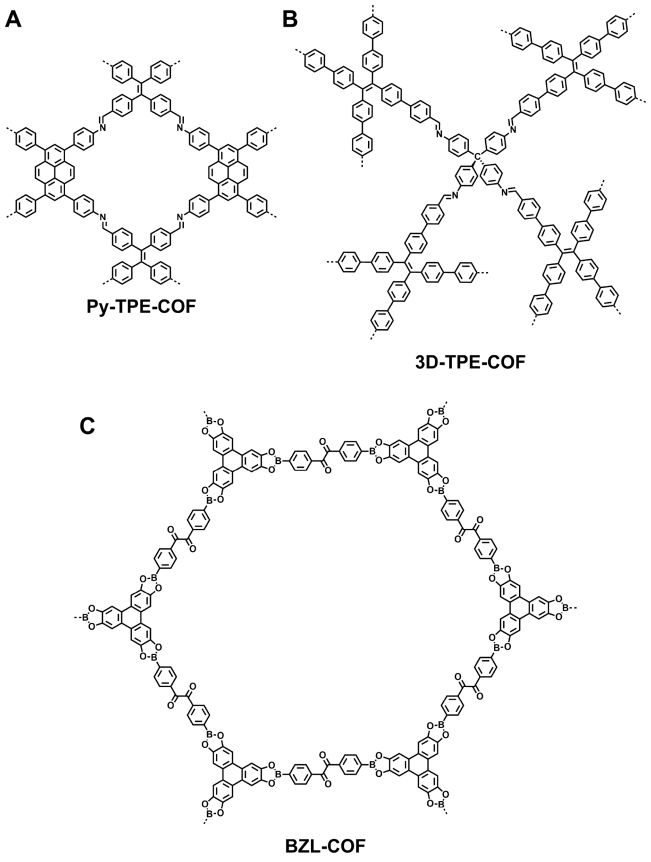

Figure 50. Schematics of (A) Py-TPE-COF, (B) 3D-TPE-COF, and (C) BZL-COF.

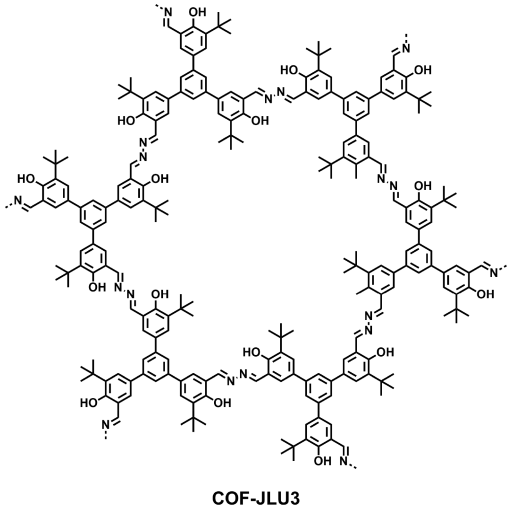

Figure 51. Schematic of COF-JLU3.

nanosheets, the pyrene knots play a key role in controlling the luminescence. Through adjusting the length of arylene vinylene linkers, the differences in the twisted angles cause different degrees of π-cloud overlap along the sp^2 carbon backbone. The propagation of twisted structures along the backbone decreases the degree of π-cloud overlap between neighboring segments and weakens the extension of π-conjugation over the 2D skeletons. Indeed, changing the linker from phenyl to biphenyl and triphenyl, the absorption band of the COFs shifts from 498 nm to 475 and 462 nm, respectively, whereas the luminescence

https://dx.doi.org/10.1021/acs.chemrev.9b00550
Chem. Rev. 2020, 120, 8814−8933

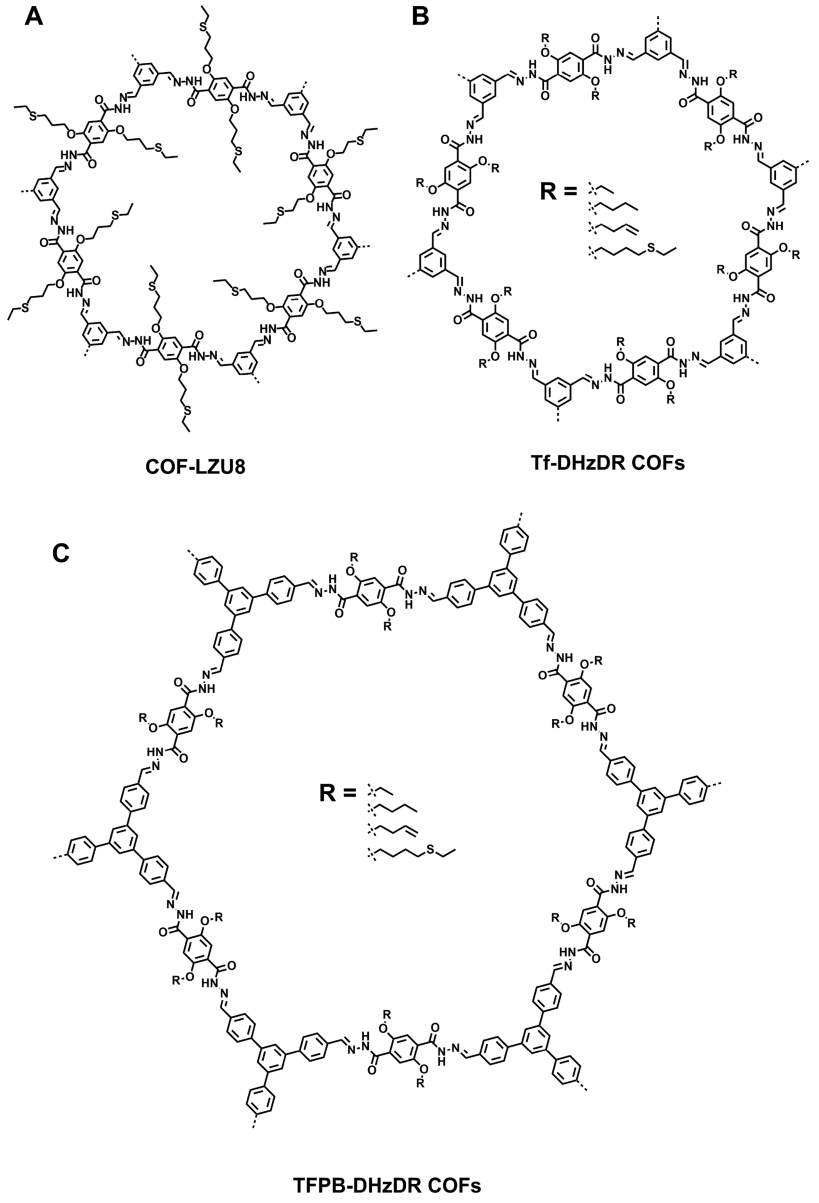

Figure 52. Schematics of (A) COF-LZU8, (B) Tf-DHzDR COFs, and (C) TFPB-DHzDR COFs.

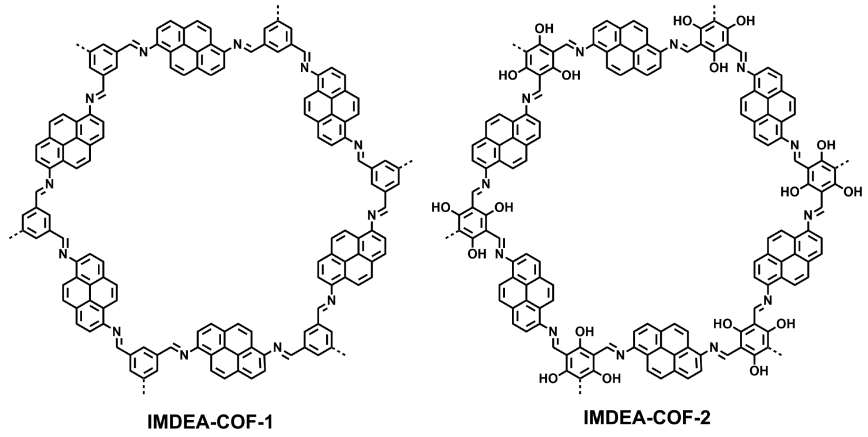

Figure 53. Schematics of IMDEA-COF-1 and IMDEA-COF-2

quantum yield decreases from 14 to 10 and 6%, respectively. Notably, the absorption and emission bands of sp^2c-CONs (covalent organic nanosheets) are blue-shifted, compared with those of sp^2c-COFs. These results suggest that the photo-

https://dx.doi.org/10.1021/acs.chemrev.9b00550
Chem. Rev. 2020, 120, 8814−8933

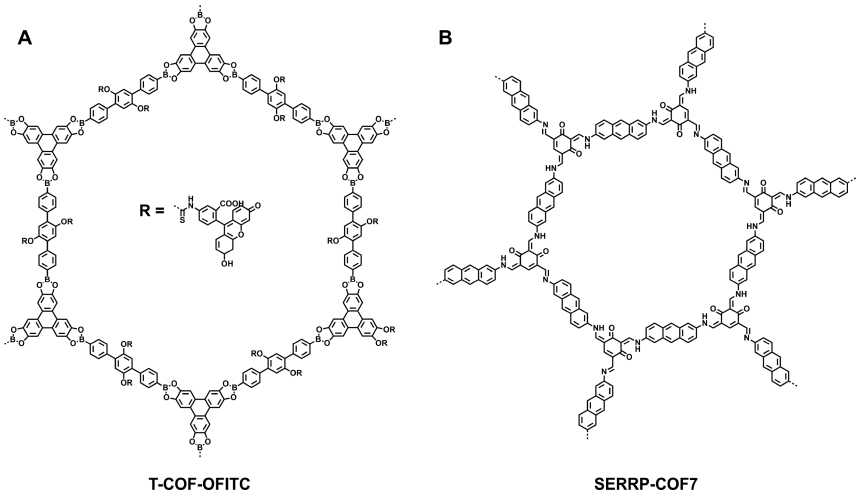

Figure 54. Schematics of (A) T-COF-OFITC and (B) SERRP-COF7.

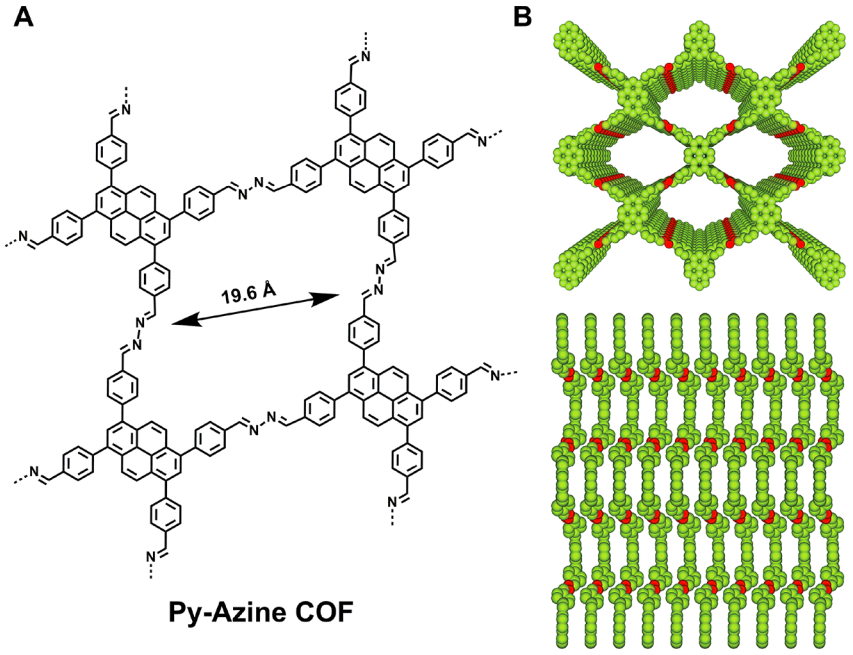

Figure 55. (A) Schematic of the Py-Azine COF for explosive sensing. (B) Top and side views of the AA-stacked Py-Azine COF, exhibiting azine sites (red for nitrogen atoms) for hydrogen-bonding interactions.

chemical events are controlled by the layered and exfoliated sheet status, which are strongly associated with their primary (nanosheets) and high-order (layer framework) structures.

Apart from the direct skeleton design to achieve luminescent COFs, pore-surface engineering has been used to fabricate luminescent COFs. Through a postsynthetic modification approach, fluorescein-isothiocyanate (FITC) is carried out into the pore wall of T-COF-OH (Figure 54A).[367] The resulting T-COF-OFITC emits strong fluorescence.

The anthracene-resorcinol-based SERRP-COF7 has been prepared via the condensation of 2,4-dihydroxybenzene-1,3,5-tricarbaldehyde and anthracene-2,6-diamine (Figure 54B).[368] The keto-enol−enamine tautomerization on the pore corners can cause a drastic change in the framework luminescence from blue to green and red by using O-donor (THF) and N-donor (pyridine) solvents. Steady-state and time-resolved spectroscopic studies indicate that the blue emission originates from the π-column of the column, whereas the red and green double emissions are derived from the keto−enol tautomerization resorcinol unit. The flexible COF@PMMA film with 0.32 wt % of IISERP-COF7 emits white light with a CIE coordinate of (0.35, 0.36).

8.3. Sensors for Detecting Explosives

An azine-linked pyrene COF (Py-Azine COF, Figure 55) has been explored in developing hydrogen-bonding interactions for sensing explosives.[111] The Py-Azine COF exhibits high crystallinity, large porosity (S_{BET} = 1210 m^2 g^{-1}), and excellent chemical stability (1 M HCl and 1 M NaOH). The Py-Azine COF consists of azine units with two nitrogen atoms that act as hydrogen-bonding acceptors to form hydrogen bonds with hydrogen-bonding donors of phenol −OH groups. This structural feature enables the construction of a detection system based on the strength of hydrogen-bonding interactions between targeted molecules and the COF skeleton. A dispersion of Py-Azine COF powder in acetonitrile exhibits an excimer

https://dx.doi.org/10.1021/acs.chemrev.9b00550
Chem. Rev. 2020, 120, 8814−8933

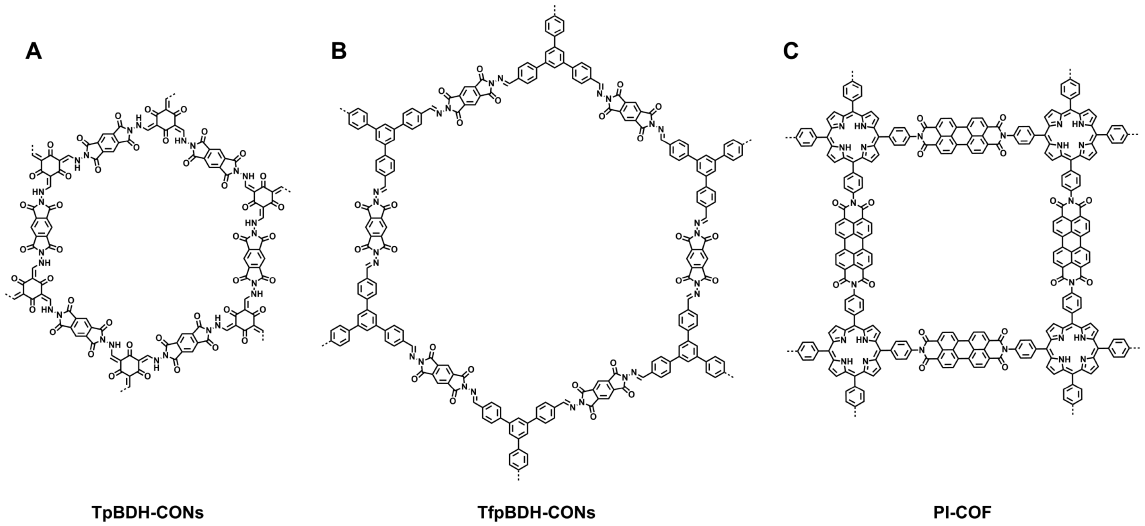

Figure 56. Schematics of (A) TpBDH-CONs, (B) TfpBDH-CONs, and (C) amide-linked PI-COF for sensing explosives.

emission at 522 nm due to the presence of periodically ordered pyrene π-arrays. This luminescence can be quenched by different nitrophenols in which the quenching degree is highly dependent on the structures of nitrophenols. For example, 2,4,6-trinitrophenol (TNP) exhibits a quenching degree of 69% at 70 ppm, whereas only very low quenching degrees of 13, 5, 3, and 3% are observed for 2,4-dinitrophenol (DNP), 2,4-dinitrotoluene (DNT), 2-nitrophenol (NP), and 2-nitrotoluene (NT), respectively. The Stern−Volmer (SV) quenching constant (k_{SV}) for TNP is as high as 7.8×10^4 M^{-1}, which is 40 and 80 times those of DNP (2.1×10^3 M^{-1}) and DNT (9.1×10^2 M^{-1}), respectively. This result suggests that a nitrophenol with more electron-withdrawing nitro units can form stronger hydrogen-bonding interactions with the azine units, leading to more fluorescence quenching. The selectivity and sensitivity for TNP originate from the most effective hydrogen-bonding interactions. The lifetime of the Py-Azine COF is independent of the TNP concentration, suggesting that the luminescence quenching is dominated by the ground-state hydrogen-bonding interactions. Moreover, the exceptional fluorescence quenching rate of 9.8×10^{13} M^{-1} s^{-1} indicates a static quenching mechanism. In the ordered 2D Py-Azine COF, the pyrene units serve as a luminescence emitter, and the azine linkers on the 1D pore walls function as open docking sites for hydrogen-bonding interactions. These synergistic effects of the vertices and edges enable the Py-azine COF to detect TNP-type explosives in a selective and sensitive manner.

Changing the dimensionality of COFs from 2D to 3D greatly affects the luminescence behavior; in particular, the excimer luminescence of pyrene units for 2D COFs will disappear in 3D COFs. Indeed, 3D COFs emit a luminescence similar to that of an isolated pyrene molecule.[57] A DMF-dispersed imine-linked ultramicroporous 3D-Py-COF (pore size = 0.59 nm) emits a blue emission at 484 nm upon excitation at 408 nm (Figure 15D). The 3D-Py-COF powder dispersed in DMF is capable of fluorescence sensing of TNP-type explosives, as demonstrated by the fluorescence quenching upon the addition of TNP. The degree of fluorescence quenching is as high as 75%, whereas the TNP concentration is only 20 ppm. The k_{SV} value is 3.1×10^4 M^{-1}, indicating the high sensitivity of the 3D COF skeleton.

Upon the liquid-phase exfoliation of 2D COFs, the resulting CONs such as TpBDH-CONs and TfpBDH-CONs have been investigated for sensing explosives (Figure 56A,B).[257] The TfpBDH-CONs suspended in isopropyl alcohol (IPA) exhibit 63% fluorescence quenching at a TNP concentration of 5.4×10^{-5} M. In contrast, the fluorescence quenching degree is only 31% for 2,4,6-trinitrotoluene (TNT), 3% for 2,6-DNT, 23% for 2,6-DNP, and 4% for NP. The k_{SV} value for TNP is as high as 2.6×10^4 M^{-1} and follows a decreasing tendency of TNP ≫ TNT > 2,6-DNP > NP > 2,6-DNT. The high quenching efficiency of TNP originates from the efficient charge transfer from the picrate anion (TNP^{-1}) to the protonated TfpBDH-CONs, as revealed by the shortened fluorescence lifetime of TfpBDH-CONs from the original 0.75 to 0.35 ns in the presence of 5.4×10^{-5} M TNP.

The amide-linked PI-COF (Figure 56C) has been constructed via the condensation of TAPP with perylenetetracarboxylic dianhydride.[369] PI-COF emits a strong fluorescence due to the presence of a p−n heterojunction between TAPP and PTCA units. The light-emitting activity of the powder sample is further enhanced by exfoliation into nanosheets (PI-CONs). The quantum yield of PI-CONs is as high as 8%, which is higher than that of PI-COF (4%). PI-CONs dispersed in ethanol serve as an efficient fluorescent probe for the highly sensitive and selective detection of TNP, which is attributed to the combination of electron transfer and the inner filter effect owing to the overlap of the excitation band of PI-CONs with the absorption band of TNP. The detection limit is down to 0.25 μM.

β-Ketoenamine COFs have been constructed by a new dynamic polymerization via the Michael addition−elimination reaction of various β-ketoenols with amines.[274] Interestingly, the solid samples of COFs 3BD and 3′PD (Figure 27H) emit orange luminescence at 547 and 560 nm, respectively, with a short fluorescence lifetime (<0.5 ns). Those two COF dispersions in dichloromethane can detect triacetone triperoxide (TATP) explosives via fluorescence quenching and possess a detection onset of ~1 μM of TATP. In contrast, conventional conjugated polymers without any specific interactions with TATP and commercialized Fido Paxpoint for the detection of hydroperoxides will present as impurities or generate *in situ* through the chemical or photochemical treatment of TATP.[370]

Exfoliated nanosheets show great potential for directly detecting pollutants in water. Upon the sonication of pyrene-

https://dx.doi.org/10.1021/acs.chemrev.9b00550
Chem. Rev. 2020, 120, 8814−8933

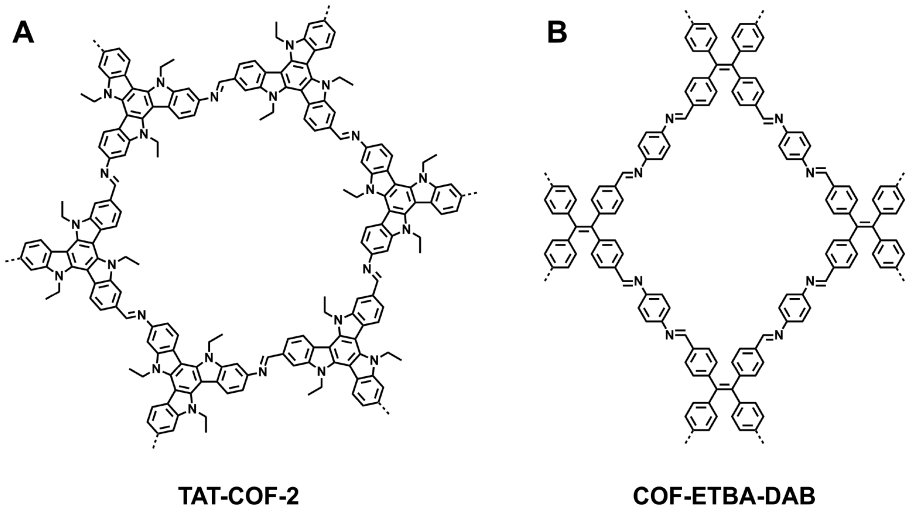

Figure 57. Schematics of COFs as volatile chemical sensors of (A) TAT-COF-2 and (B) COF-ETBA-DAB.

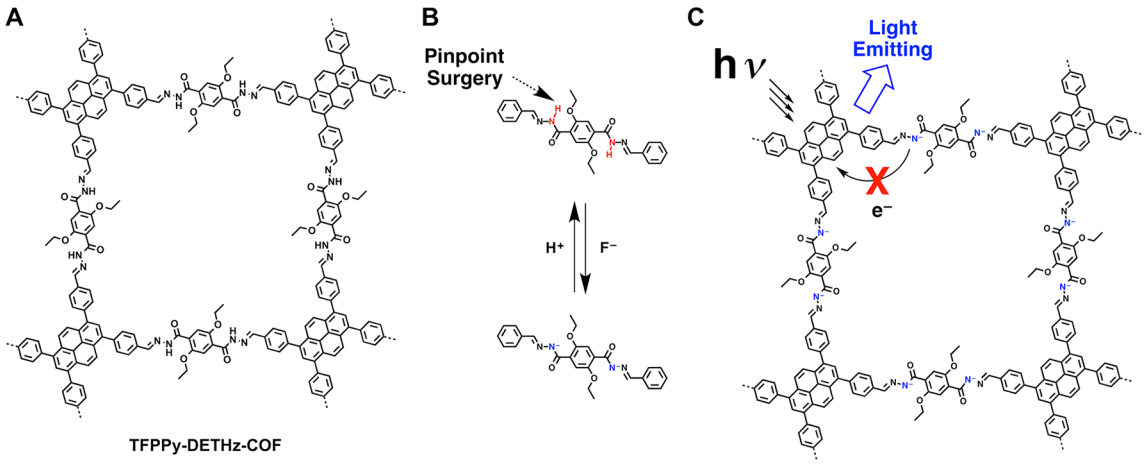

Figure 58. Schematic of TFPPy-DETHz-COF.

IMDEA-COF-1 (1 mg, Figure 53A) in water (25 mL), the resulting CON suspensions are stable to emit emissions at 450 and 510 nm.[371] The IMDEA-COF-1 colloids in water are capable of detecting organic dyes and nitrobenzene derivatives. For example, the IMDEA-COF-1 colloids are notably sensitive and exhibit a fluorescence quenching efficiency of 22% and a quenching constant of 2.32×10^3 M^{-1} to detect nitrobenzene at a concentration as low as 5.66×10^{-5} M.

8.4. Sensing Volatile Chemicals

Certain toxic vapors or gases are colorless or even odorless but cause a profound effect on environmental contaminations released from natural, laboratory, and industrial plants. Therefore, the effective detection of toxic vapors or gases is critical to evaluate the toxicity level and prevents environmental pollution. An imine-linked hexagonal triazatruxene TAT-COF-2 (Figure 57A) is luminescent in ethanol and can be quenched upon the addition of electron-deficient arenes such as nitrobenzene, NT, and phenol owing to the photoinduced electron transfer (PET) from the COF skeleton to the electron-deficient guests.[28] Notably, TAT-COF-2 exhibits a turn-on fluorescence response, and the fluorescence intensity is enhanced upon the addition of electron-rich arenes such as toluene, chlorobenzene, and *o*-DCB. The thin-layer TAT-COF-2 samples exhibit similar fluorescence-on or -off sensing behavior upon exposure to the arene vapors. For example, the fluorescence intensity of the thin-layer samples increases by 60% upon the exposure to the saturated chlorobenzene for 60 s, whereas the fluorescence intensity decreases by 50% upon the exposure to nitrobenzene. By removing the arenes from the pores, the COF can recover its fluorescence to a level similar to its original intensity.

The sensing application of the highly luminescent TPE-Ph COF has been investigated by the host−guest interaction between the TPE-Ph COF and ammonia gas. The boronate-ester linkage has a strong affinity to ammonia to form Lewis acid−base adducts.[372] The fluorescence intensity of the TPE-Ph COF dispersed in toluene is significantly quenched by the addition of ammonia at the ppm level.[117] The apparent quenching rate constant reaches 6.3×10^{14} M^{-1} s^{-1}, reflecting a high sensitivity of the TPE-Ph COF toward ammonia gas. The imine-linked TPE COF, that is, COF-ETBA-DAB, (Figure 57B) has been synthesized as yellow crystallites via the condensation of 4,4′,4′′,4′′′-(ethane-1,1,2,2-tetrayl)tetrabenzaldehyde (ETBA) with DAB.[373] COF-ETBA-DAB exhibits a fast response and high sensitivity toward HCl gas with clear changes in both color and fluorescence emission, which can be recovered upon exposure to ammonia vapor.

https://dx.doi.org/10.1021/acs.chemrev.9b00550
Chem. Rev. 2020, 120, 8814−8933

8.5. Sensing Anions

Recently, a strategy based on pinpoint surgery on the N−H unit of the hydrazone-linked COFs has been developed for sensing anions.[244] Hydrazone-linked TFPPy-DETHz-COF (Figure 58A) with a pyrene knot is less luminescent due to the photoinduced electron transfer from the hydrazone N−H site to the pyrene unit. Notably, the N−H bond can be cleaved by F^- through acid−base reaction because the N−H sites in TFPPy-DETHz-COF located on the pore walls are accessible to F^- (Figure 58B). Consequently, the addition of F^- eliminates the photoinduced electron-transfer path and directly improves the luminescence activity (Figure 58C). The luminescence intensity is enhanced in a linear proportion to the amount of added F^-, whereas the absolute luminescence quantum yield can increase to 17%, which is 3.8 times as high as that (4.5%) of as-synthesized TFPPy-DETHz-COF. In contrast, other halogen anions including Cl^-, Br^-, I^-, and NO_3^- are intact, leading to a high selectivity of F^-. This switch-on sensing achieves a detection limit down to 50.5 ppb of F^- anion, which is the best among F^- sensors.[374] This strategy offers a new approach to F^- detection in a quantitative manner with high accuracy and selectivity. From these results, luminescent COFs for chemo- and biosensing are driven by photoinduced electron transfer; promoting electron transfer by target molecules will cause a fluorescence quench that leads to a switch-off sensing, and preventing electron transfer can improve luminescence to yield a switch-on sensing.

8.6. Sensing Toxic Metals

A trace amount of certain metal ions is required for the biological process, but some are toxic upon accumulation.[356−359,375] Therefore, the detection of toxic transition metals in water and soil is an important issue in relation to environmental pollution. The aforementioned azine-linked COF-JLU3 has been developed to detect Cu(II) in a selective and sensitive way (Figure 51).[84] The THF-dispersed COF-JLU3 samples exhibit unusual selectivity and sensitivity toward the Cu(II) ion, even in the coexistence of other metal ions (Li(I), K(I), Mg(II), Ca(II), Ba(II), Zn(II), Cd(II), Ni(II), Pb(II), Co(II), Ag(I), Fe(III), and Al(III)). The detection limit for Cu(II) can decrease to 0.31 μM. This sensitivity is retained even in the aqueous solutions over a wide pH range (5−11). The high sensitivity is attributed to the effective photoinduced electron transfer (PET) from the COF to Cu(II), as evidenced by fluorescence lifetime measurements. Indeed, the lifetime of COF-JLU3 decreases from 1.5 to 0.7 ns as the Cu(II) concentration is increased from 0 to 2×10^{-4} M. The regeneration of COF-JLU3 is easy by removing Cu(II) from the system with ethylenediamine-tetraacetic acid disodium salt (EDTA). The high sensitivity, selectivity, and reusability open a new avenue for utilizing crystalline porous COFs toward metal-ion sensing.

A hydrazone-linked COF-LZU8 (Figure 52A) anchored with a thioether group on the pore walls has been designed and synthesized for the selective and sensitive detection of Hg(II).[254] COF-LZU8 exhibited high crystallinity, medium porosity (S_{BET} = 454 $m^2 g^{-1}$), and robust thermal stability (310 °C). A solid-state sample of COF-LZU8 emits at 460 nm with an absolute fluorescence quantum yield of 3.5% upon excitation at 390 nm. The luminescence activity in the solid state most likely originates from the inhibition of the ACQ effect due to the twisted structure of the COF skeleton as well as the presence of the thioether group. The COF-LZU8 in acetonitrile exhibits a fluorescence quenching degree of 83% in the presence of 33.3 μM Hg(II). In contrast, a control sample based on ethoxy-substituted COF-42 without thioether units on the pore walls exhibits a low quenching degree. This big difference in the fluorescence activity of two COFs originates from the strong binding of Hg(II) to the thioether groups of COF-LZU8, whereas this binding is not possible in COF-42. The detection limit of COF-LZU8 is estimated to be 25 ppb, which is superior to other thioether-based chemosensors. Importantly, COF-LZU8 is highly selective and sensitive toward the Hg(II) ion, irrespective of the presence of other metal ions (Li(I), Na(I), K(I), Mg(II), Ca(II), Ba(II), Sr(II), Zn(II), Cd(II), Ni(II), Pb(II), Co(II), Cu(II), Ag(I), Fe(II), and Fe(III)), even at high concentrations. Interestingly, COF-LZU8 (5 mg) can remove 98% Hg(II) from a solution of 10 ppm of Hg(II) (10 mL water). COF-LZU8 can be reused three times without a significant loss of its sensitivity. COF-LZU8 can be easily regenerated by treating COF-LZU8@Hg with an aqueous Na_2S solution. The unique structural arrangement of 2D COF-LZU8 enables sensitive fluorescence detection, and the 1.3 nm sized channels promote the access to and binding of the Hg(II).

Another hydrazone-linked Bth-Dma COF with O,N,O′-chelating sites on the pore walls (Figure 59) has been prepared

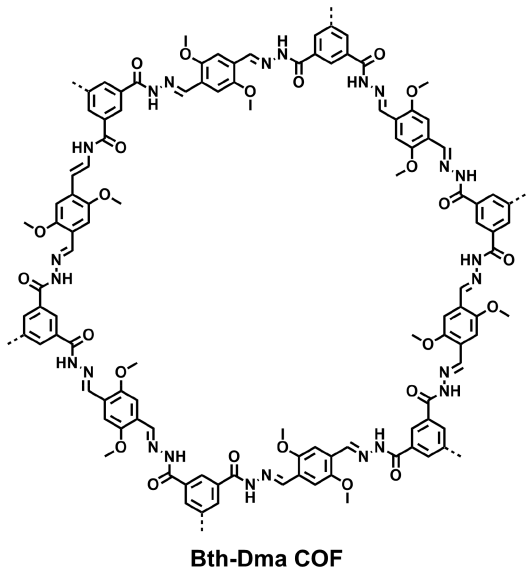

Figure 59. Schematic of Bth-Dma COF.

by condensing 2,5-Dha with benzene-1,3,5-tricarbohydrazide (Bth).[376] The resulting Bth-Dma COF exhibits strong fluorescence in the solid state and in an aqueous dispersion. Interestingly, the as-synthesized Bth-Dma COF serves as an Fe(III) sensor to achieve high selectivity and sensitivity with a detection limit of 0.17 μM, which is attributed to the coordination between Fe(III) and the O,N,O′-chelating sites on the pore walls.

8.7. Biosensors

Beside the chemosensing with crystallites and thin layers (vide supra), the COF films grown on the amino-functionalized silica substrate (Si-AMS) serve as a biosensor for bovine serum albumin (BSA) adsorption and DNA immobilization.[312] The electrochemical impedance spectroscopy (EIS) measurements of the amino-functionalized Si-AMS-NH_2-4 reveal a strong electrochemical response in the presence of BSA or DNA. The interactions between the COF film and BSA and DNA are

https://dx.doi.org/10.1021/acs.chemrev.9b00550
Chem. Rev. 2020, 120, 8814−8933

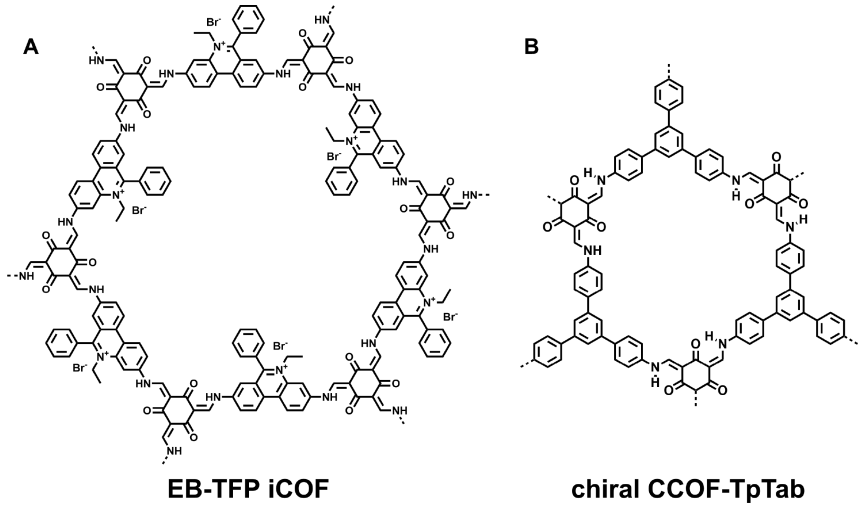

Figure 60. Schematics of COFs as biosensors for (A) EB-TFP iCOF and (B) chiral CCOF-TpTab.

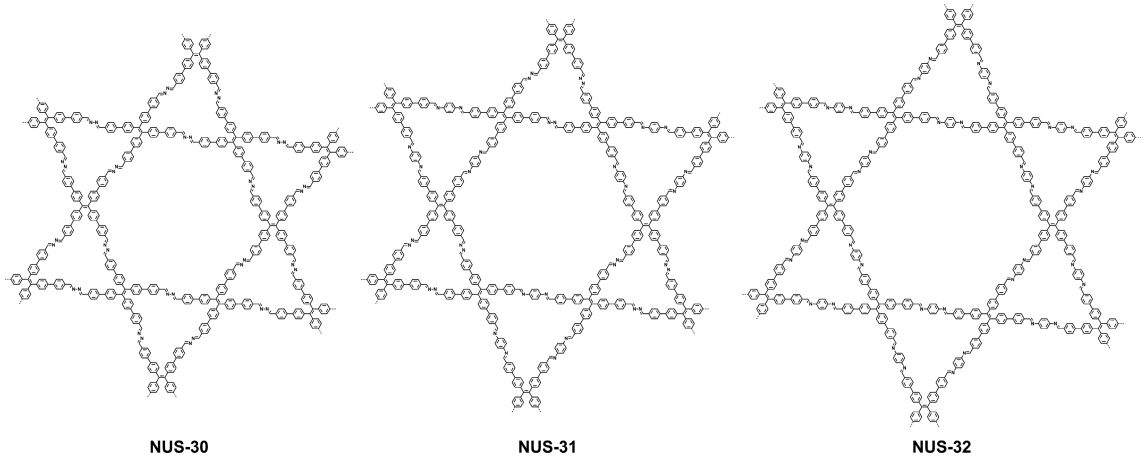

Figure 61. Schematics of NUS-30−32.

attributed to the presence of free amino groups in the COF films, the rough surface, and the cross-linked pores. EB-TFP-iCONs (Figure 60A) exhibit a selective detection of double-stranded DNA (dsDNA).[377] The addition of negatively charged calf thymus DNA (ctDNA) to the aqueous dispersion of EB-TFP-iCONs leads to the reduction of emission intensity at 510 nm (λ_{ex} = 350 nm) and triggers a new band at 600 nm, which contributes to the reassembly of EB-TFP-iCONs in the presence of ctDNA.

The imine-linked 2D TPA-COF (Figure 17B) has been designed and synthesized by using C_3-symmetric flexible tris(4-aminophenyl)amine and tris(4-formylphenyl)amine.[168] The flexible vertices decrease interlayer stacking and cause an easy exfoliation of TPA-COF into CONs. The SEM and TEM images clearly indicate nanosheet structures. Moreover, the AFM image confirms a thickness of 3.5 ± 0.3 nm. The targeted two hairpin DNAs are labeled with a fluorescent dye. The fluorescence intensity of the labeled DNA is quenched upon adsorption on the surface of TPA-COF nanosheets owing to $\pi-\pi$ stacking interactions. The detection limit is as low as 20 ppm, which is superior to most 2D nanomaterial-based fluorescence DNA sensors, including GO-loaded carboxyfluorescein (FAM),[378−380] 6-carboxy-X-rhodamine (ROX),[379,380] cyanine 5 (Cy5),[379] silver nanoclusters,[381] graphene quantum dots,[382] g-C_3N_4-loaded FAM and ROX,[383] MoS_2-loaded FAM,[384,385] WS_2-loaded tetramethylrhodamine (TAMRA),[386] TaS_2-loaded FAM and Texas Red,[387] Cu-TCPP MOF NS-loaded Texas Red, and tetrafluorescein (TET).[388] The fluorescence quenching degree of the single-base mismatched DNA and random DNA is lower than that of the target DNA. Therefore, the CONs show the high selectivity and sensitivity of the labeled fluorescence hairpin DNAs.

A series of chiral COFs (CCOFs) have been crystallized from achiral COF precursors upon mixture with chiral small molecules such as chiral 1-phenylethylamine.[389] The chiral CCOF-TpTab (Figure 60B) emits green luminescence at 540 nm in water and serves as a fluorescence sensor for chiral carbohydrates. This COF exhibits high enantioselectivity toward a wide range of saccharides, including D-glucose, D-mannitol, D-sucrose, D-lactose, D-maltose, D-sorbitol, D-fructose, D-gentiobiose, D-lactobionic acid, D-glucuronic acid, and D-gluconic acid. For example, the quantum yield of chiral CCOF-TpTab decreases from 2 to 1% upon the addition of D-cellobiose. This fluorescence quenching is driven by the supramolecular interactions between CCOF-TpTab and saccharides that form diastereomeric complexes.

The three azine-linked and imine-linked NUS-30−32 (Figure 61) have been prepared by condensing TPE moieties or hydrazine hydrate or PPDA, in which NUS-30 and NUS-32 are dual pore and NUS-31 is triple pore.[323] The ultrathin

https://dx.doi.org/10.1021/acs.chemrev.9b00550
Chem. Rev. 2020, 120, 8814−8933

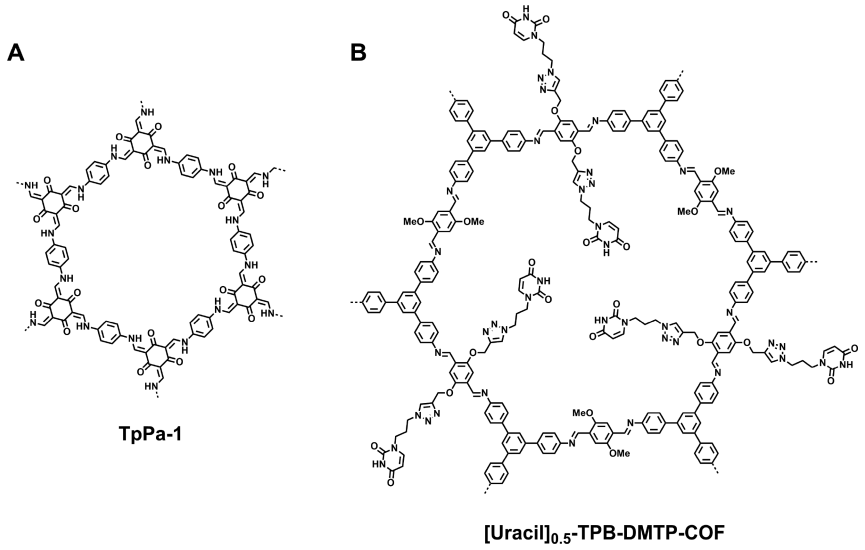

Figure 62. Schematics of (A) TpPa-1 and (B) $[uracil]_{0.5}$-TPB-DMTP-COF.

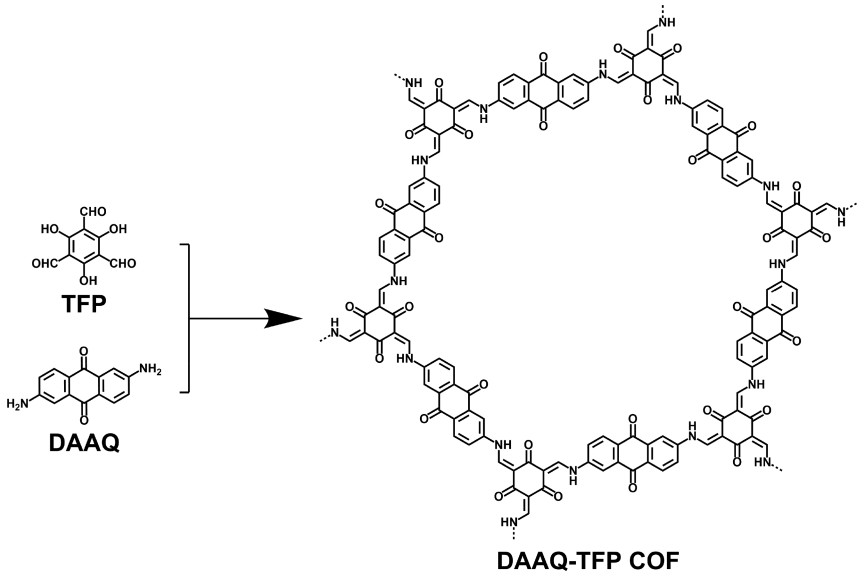

Figure 63. Synthesis of the redox-active DAAQ-TFP COF for capacitive energy storage.

nanosheets (thickness = 2−4 nm) are prepared by using a temperature-swing gas exfoliation approach. These CONs can detect amino acids, including L-phenylalanine, L-alanine, L-threonine, L-tryptophan, and L-DOPA through hydrogen bonds between guest molecules and COF nanosheets. The fluorescence intensity of NUS-30 nanosheets is greatly quenched to 61% of the original value upon the addition of L-phenylalanine (1.0 mM). The quenching degree is higher than those of NUS-31 and NUS-32 nanosheets. NUS-30 nanosheets are active toward L-DOPA with a K_{SV} value of 1.5×10^4 M^{-1}, which is higher than those of NUS-31 nanosheets (1.2×10^4 M^{-1}) and NUS-32 nanosheets (3.7×10^3 M^{-1}). Increasing the number of azine moieties in the COF skeleton triggers a stronger binding affinity toward amino acids, resulting in fluorescence quenching.

Magnetic $Fe_3O4_{@}$TpPa-1 (Figure 62A) exhibits an ultralow detection limit (28 fmol), satisfactory selectivity, and high recovery in the detection of IgG, indicating the great potential of COFs in glycoproteomic studies.[390] Integrating uracil groups into the pore walls via pore-surface engineering yields $[uracil]_{0.5}$-TPB-DMTP-COF (Figure 62B), which exhibits a remarkable selective recognition toward adenine in aqueous media.[391]

9. ENERGY STORAGE

Our planet is full of various energy resources, such as sunlight, fossil fuel, wind, hydro, geothermal, and nuclear powers, which are transformed via suitable devices into electricity, a direct power in driving civilization, modernization, and daily life. In this context, storing electricity is an important subject that is particularly relevant to sustainable future development. Over the past decades, great advances have been achieved in exploring electrode materials and devices for storing electricity, which is widespread in daily lives. Among various types of energy-storage devices, the potential of COFs as electrodes for supercapacitors, lithium ion batteries, and lithium sulfur batteries has been investigated.[392−394] COFs can be designed to possess redox-active skeletons, a discrete pore size, and special pore walls; these structural features are important for the electrochemical processes involved in energy storage, as the redox-active

https://dx.doi.org/10.1021/acs.chemrev.9b00550
Chem. Rev. 2020, 120, 8814−8933

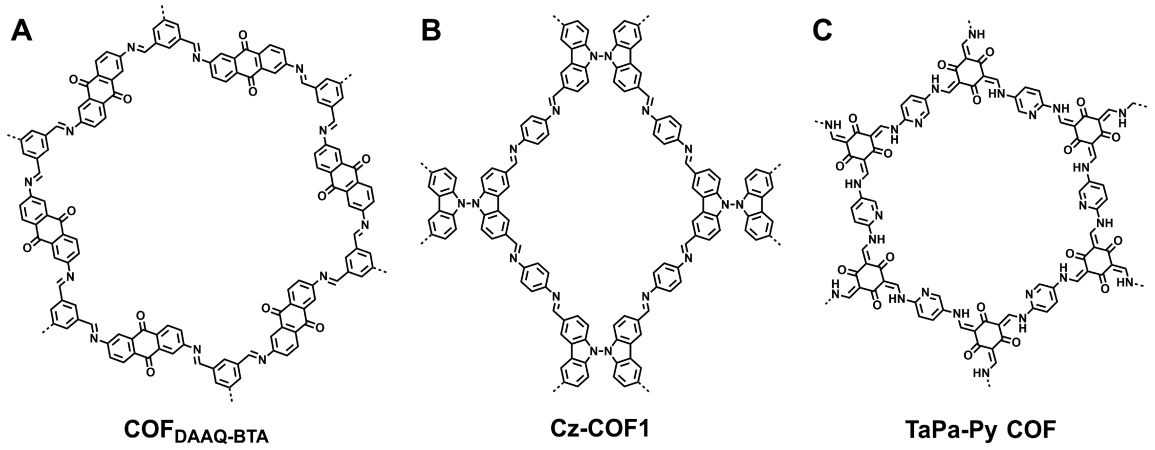

Figure 64. Schematics of COFs utilizing redox-active species for the energy storage of (A) COF$_{DAAQ-BTA}$, (B) bicarbazole Cz-COF1, and (C) TaPa-Py COF.

skeletons promote energy storage and the pores offer room for ion storage and transport. How to facilitate the redox reaction, ion diffusion, and electron conduction is the subject to be considered in the exploration of COFs for energy storage.

9.1. Capacitive Energy Storage

9.1.1. Skeleton Design. Capacitors utilize redox-active species to trigger electrochemical reactions in the electrodes in the charge and discharge processes for storing electricity. Redox-active DAAQ units are successfully introduced to the edges of the imine-linked DAAQ-TFP COF (Figures 16R and 63) via the condensation with TFP as the knot units.[395] The reversible redox reaction between anthraquinone and 9,10-dihydroxyanthracenes involves a two-electron and two-proton process that endows the COF with pseudocapacity. The redox peak separation of the DAAQ-TFP COF is only 4 mV, which is much lower than that of the DAAQ monomer (160 mV), indicating the facilitated electron transport between the electrode and the redox sites in the COF skeleton. In the galvanostatic charge−discharge experiments, the DAAQ-TFP COF exhibits a capacitance of 48 ± 10 F g^{-1} and is stable after 5000 charge−discharge cycles. By contrast, the DAB-TFP COF analogue without redox-active DAAQ units in the COF skeleton exhibits a specific capacitance of 15 ± 6 F g^{-1} under the otherwise identical conditions. Owing to the randomly oriented DAAQ-TFP COF crystallites in the electrode, only 2.5% of the redox-active units contribute to the capacitive energy storage. This situation can be greatly improved by growing oriented COF thin films on gold. In this case, 80−99% of the redox-active sites are involved in the energy storage.[171] For example, the capacitance of a 200 nm thick film is drastically increased to 3.0 mF cm^{-2} compared with that of (0.40 mF cm^{-2}) COF powder. The film is stable for cycle use, with only a 7% loss of capacity after 5000 cycles, indicating that the β-ketoenamine-linked framework is robust in charge−discharge cycles.

A similar approach based on the COF$_{DAAQ-BTA}$ (Figure 64A) thin films grown on a 3D graphene substrate shows that the capacitance of the COF−graphene composite can reach 31.7 mF cm^{-2}, indicating that a good conductivity contributed from graphene improves the use of the redox-active anthraquinones sites in energy storage.[308] Bicarbazole is another typical redox-active π-unit that can be integrated into COFs for ultra-high-performance energy storage. The microporous bicarbazole Cz-COF1 (Figure 64B) shows a capacity as high as 628 mA h g^{-1} at a current density of 100 mA g^{-1}, which is much higher than those of the state-of-the-art porous organic polymers, and its Coulombic efficiency is >99%.[396] A TaPa-Py COF (Figure 64C) with a redox-active pyridine unit is also able to deliver a high capacitance of 209 F g^{-1} at a current density of 0.5 F g^{-1}.[397] At a high current density of 5 A g^{-1}, it still exhibits a capacitance of 164 F g^{-1} due to the presence of the redox-active unit and its high surface area. Other conventional materials such as activated carbon, despite being highly conductive and porous, can only deliver electrochemical double-layer capacitance, which greatly limits it capacity to a value that is much lower than those of COFs with the contribution of both redox and double-layer capacity.[398] For instance, activated carbon possessing a very high surface area of 2315 m^2 g^{-1} can only deliver up to 125 F g^{-1}, whereas TaPa-Py delivers a similar capacitance at a much lower surface area 687 m^2 g^{-1}, demonstrating that the integration of redox-active units to the backbone is necessary for energy storage.[399] These works manifest that redox-active units are essential to explore the energy-storage functions of COFs.

Integrating a conducting polymer, such as polyethylenedioxythiophene (PEDOT), into the 1D channels of redox-active COF films can increase the conductivity, as demonstrated by the DAAQ-TFP COF (Figures 16R and 63), which endows the electrode with a high rate of energy-storage capability with high volumetric energy density.[400] The COF composite films exhibit Faradaic charge storage capacity up to 9.3 mC, corresponding to 97% accessible anthraquinone redox-active sites.[401] Notably, they enhance the capacitance by 40-fold compared with the unmodified COF film. Moreover, the COF composite film enables a high rate of charge−discharge performance at 100 °C, which requires only 36 s for a full charge or discharge. It retains 50% of its maximum capacitance (350 F cm^{-3}) at a rate of even 1600 C, corresponding to a time of only 2.25 s for a complete charging. Importantly, the COF composite film exhibits a stable performance over 10 000 charge−discharge cycles. The enhanced high rate response and exceptional volumetric capacitance of the COF composite film most likely originate from the wire effect of the specially confined conducting PEDOT within the 1D channels that facilitates the accessibility of the redox-active sites as well as the promotion of ion conduction.

The PEDOT@AQ-COF (Figure 65) nanocomposite also displays excellent electrical conductivity of 1.1 S cm^{-1}, high capacitance of 1663 F g^{-1} (at 1 A g^{-1}), ultrafast high-rate performance (998 F g^{-1} at 500 A g^{-1}), and excellent stability for

https://dx.doi.org/10.1021/acs.chemrev.9b00550
Chem. Rev. 2020, 120, 8814−8933

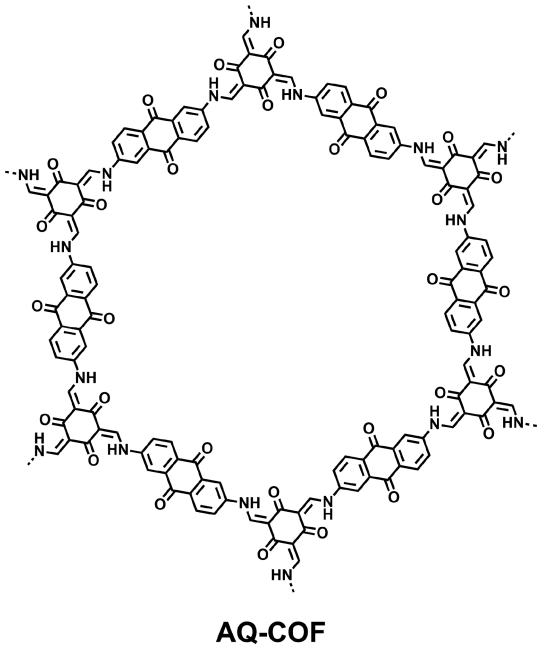

Figure 65. Schematic of AQ-COF that is composited with conducting polymers for energy storage.

10 000 cycles.[402] Similarly, using PANI as a conducting polymer, the composite of TpPa-COF@PANI (Figure 62A) exhibits a specific capacitance of 95 F g^{-1} at a current density of 0.2 A g^{-1} while the capacity retention rate of the battery is retained at as high as 83% after 30 000 cycles, which reveals the long-term cycling performance of the TpPa-COF@PANI electrode.[403]

Introducing an intramolecular hydrogen-bonding interaction can enhance the stability of the imine-linked COF as a pseudocapacitor. A hydroquinone species is protected by the hydroxyl groups integrated within the framework of the TpPa-$(OH)_2$ COF (Figure 66A).[404] This hydroxyl group prohibits the degradation of benzoquinone formed in the charging process, thereby enabling the reversible charge−discharge process. As a result, a high capacitance of 416 F g^{-1} at 0.5 A g^{-1} is achieved with 43% accessibility of hydroquinone moieties. A TpOMe-DAQ COF (Figure 66B) with intramolecular hydrogen bonds possesses high stability under extreme acidic (12 M HCl, 18 M H_2SO_4) and basic conditions (9 M NaOH).[405] This allows the coupling of this imine COF to a highly acidic electrolyte (3 M H_2SO_4) and achieves a promising capacitance of 169 F g^{-1} at 3.3 mA cm^{-2}.

Fabricating a free-standing COF electrode is crucial to the preparation of supercapacitors. Integrating π-electron-rich moieties such as 2,6-diaminoanthracene as well as redox-active anthraquinone in the Dq_1Da_1Tp COF (Figure 67A) can improve the mechanical strength of the material and achieves a capacitance of 111 F g^{-1} at a scan rate of 1.56 mA cm^{-2}.[406]

A microporous PIBN-G COF (Figure 67B) with abundant carbonyl groups has been prepared by condensing tetramino-benzoquinone (TABQ) with PMDA.[407] At a current density of 0.1 C, a high discharge capacity of 271.0 mA h g^{-1} is delivered by the PIBN-G anode, which corresponds to the utilization of 96.8% of the carbonyl species. The abundant carbonyl groups in this PIBN-G COF enable the binding of 10 Li^+ ions per unit, which enhances the capacity.

9.1.2. Pore-Surface Engineering. Although COFs with redox-active skeletons are attractive for energy storage, their further development is restricted to the limited availability of redox-active monomers. A general strategy that enables the conversion of conventional COFs into redox-active electrode materials has been explored via pore-surface engineering. The open lattice of the NiP-COF is converted to segregated redox-active phases via a click reaction with 4-azido-2,2,6,6-tetramethyl-1-piperidinyloxy (TEMPO) and yields $[TEMPO]_X$-NiP-COFs (X = 0, 50, and 100%, Figure 68) that bear electrochemically active radicals (TEMPO) on the pore walls.[248]

The $[TEMPO]_X$-NiP-COFs exhibited a pair of reversible peaks in the CV diagram, which are assigned to the one-electron redox reaction of the TEMPO radical switching between the neutral radical and the oxoammonium cation. The specific capacitance of $[TEMPO]_{100\%}$-NiP-COF is higher than that of $[TEMPO]_{50\%}$-NiP-COF owing to the higher radical content. On the contrary, $[TEMPO]_{50\%}$-NiP-COF enables a faster reversible charge−discharge reaction, as evidenced by a narrower separation between the oxidative and reductive peaks. The

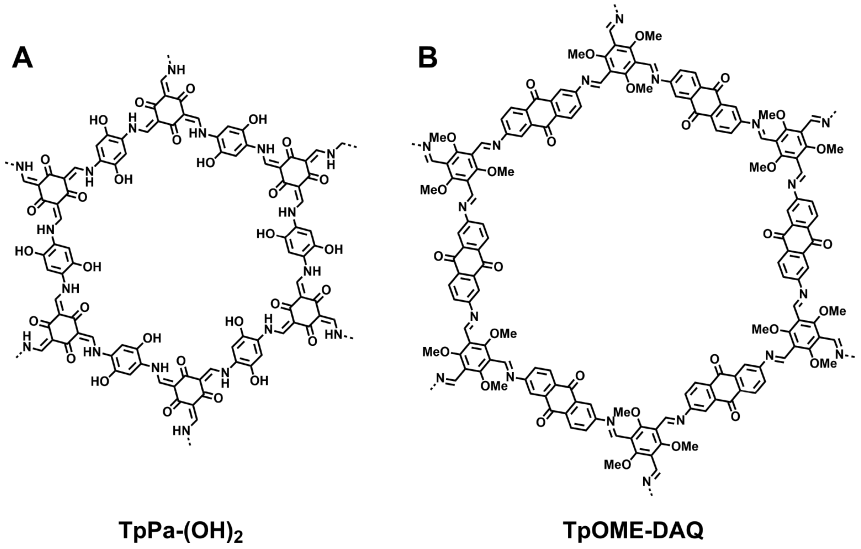

Figure 66. Schematics of (A) TpPa-$(OH)_2$ COF and (B) TpOMe-DAQ COF with intramolecular hydrogen bonds for energy storage.

https://dx.doi.org/10.1021/acs.chemrev.9b00550
Chem. Rev. 2020, 120, 8814−8933

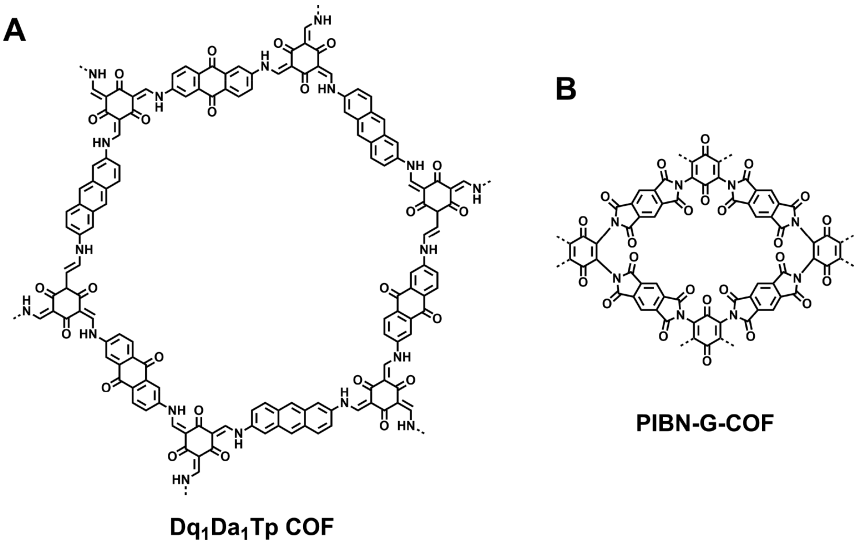

Figure 67. Schematics of (A) Dq_1Da_1Tp COF as a free-standing COF electrode and (B) PIBN-G COF with abundant carbonyl groups.

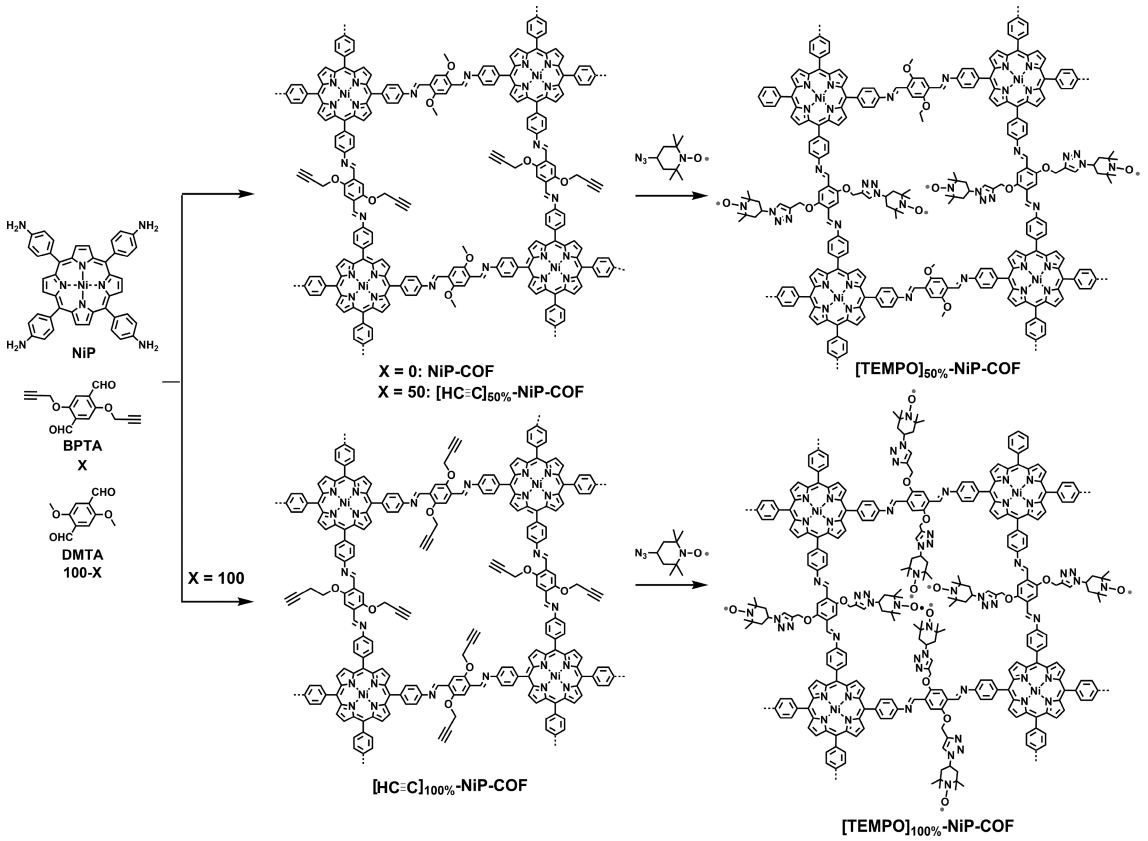

Figure 68. Pore-surface engineering strategy for the synthesis of radical COFs for energy storage.

capacitances of $[TEMPO]_{50\%}$-NiP-COF and $[TEMPO]_{100\%}$-NiP-COF are 167 and 124 F g^{-1}, respectively, which are comparable to or even higher than those of metal-ion-based redox-active MOFs[408−411] and are much higher than that of the redox-active DAAQ-TFP COF (40 ± 9 F g^{-1}).[395] The robust covalent bonds between COF skeletons and redox-active sites on the walls lead to structural stability that accounts for the improved cycle performance in the galvanostatic charge−discharge process. At a current density of 500 mA g^{-1}, $[TEMPO]_{50\%}$-NiP-COF retains its high capacitance over 100 cycles.

9.1.3. COF-Derived Hybrid and Carbon Materials. The covalent hybridization of COFs with graphene has been realized through a one-step reaction between TFB, PPDA, and amine-functionalized graphene oxide (NH_2−*r*GO (COF = COF-LZU1, Figure 21A)).[309] The COF/NH_2−*r*GO hybrid structure is evidenced by TEM, PXRD, FT-IR, ^{13}C CP/MAS, and XPS measurements. Electrochemical studies are carried out by a three-electrode system with a platinum electrode as the counter electrode and a saturated calomel electrode (SCE) as the reference electrode in an aqueous Na_2SO_4 solution (1 M) as the electrolyte. Under a potential in the range from 0 to 0.5 V, the

https://dx.doi.org/10.1021/acs.chemrev.9b00550
Chem. Rev. 2020, 120, 8814−8933

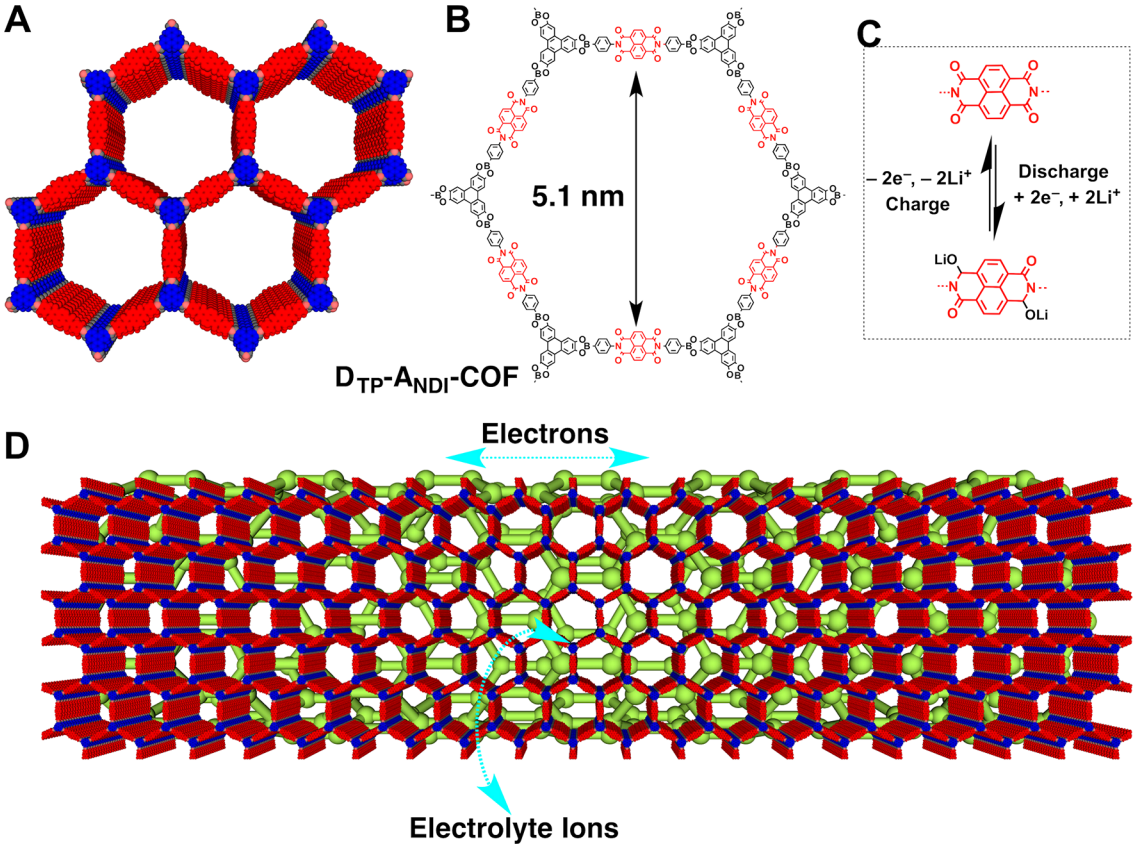

Figure 69. Schematics of (A) the stacked model and (B) the chemical structure of donor–acceptor D_{TP}-A_{NDI}-COF. (C) Redox reaction of NDI edge units and (D) D_{TP}-A_{NDI}-COF@CNT composite as an electrode in a lithium-ion battery.

CV curve of the COF/NH_2–*r*GO hybrid shows an obvious deviation from a rectangular shape at a scan rate from 10 to 100 mV s^{-1}. In the galvanostatic charge–discharge measurements at a current density of 0.2 A g^{-1}, the COF/NH_2–*r*GO hybrid achieves a specific capacitance of 533 F g^{-1} that is much higher than those of the COF itself (226 F g^{-1}) and NH_2–*r*GO (190 F g^{-1}). Notably, after 1000 charge–discharge cycles, the specific capacitance of COF/NH_2–*r*GO hybrid retains 79% of its initial value. The great enhancement of specific capacitance likely originates from the enhanced conductivity of the hybrid owing to the presence of graphene.

Carbon materials are electric conductors and can improve the high rate of performance in the supercapacitors. Moreover, introducing pores that are compatible in size with the electrolyte ions would facilitate ion transport, and integrating heteroatoms to carbon materials would enhance the number of capacitive sites, which would improve the capacity. The predesignable structures endow the COFs with a precise atom location, a tunable chemical composition, and a specific pore structure; all of these features can be optimized with appropriate monomers. In this context, COFs are ideal precursors for preparing porous carbon electrodes. For example, increasing the reaction temperature from 400 to 700 °C, CTF-1 (Figure 27A) can be converted into nitrogen-doped porous carbon PTF-700 with plenty of microporosity and an increased surface area from 1212 to 2482 m^2 g^{-1}.[412] In a conventional two-electrode symmetric supercapacitor system with a room-temperature ionic liquid ($EMIMBF_4$) electrolyte, PTF-700 works in the potential range of 0–3.5 V and achieves the energy and power densities of 62.7 W h kg^{-1} and 8750 W kg^{-1}, respectively, which are the best among a series of carbons prepared at different temperatures. The PTF-700-based supercapacitor, after charged at 3.5 V, can drive commercially available white-light-emitting diodes (LEDs) or red LEDs at 2.2 V. Temperature-dependent studies reveal that the polymerization temperature exerts two distinct effects on the capacitive properties. First, a high temperature leads to a better conductivity that accounts for a better high-rate capacity. Indeed, PTF-700 keeps all quasi-rectangular *C*–*V* curves at a scan speed of 100 mV s^{-1}, shows isosceles-triangular galvanostatic charge–discharge curves at a current density up to 7 A g^{-1}, and retains 85% specific capacitance after 10 000 cycles. Second, the nitrogen content as well as the electroactive surface area decrease at a high reaction temperature. As a result, the specific capacitance of carbons prepared at different temperatures is almost unchanged between 147.1 and 151.3 F g^{-1} at a current density of 0.1 A g^{-1}.

Similarly, B-doped porous carbon electrodes have been produced by the pyrolysis of COF-5 (Figure 7B) at 700 °C.[413] The electrochemical properties are evaluated in a two-electrode cell supercapacitor in an aqueous sulfuric acid solution (1.0 M) with a potential window from −0.5 to 0.5 V. The COF-5-derived BC-MS-700-14 achieves a specific capacitance of 160 F g^{-1} at a scan rate of 10 mV s^{-1} and retains 77% of its initial capacitance.

Nanocoating of TpPa-COF (= TpPa-1, Figure 62A) on nickel nanowires (NiNWs) yields a metal–COF composite material, NiNWs@TpPa-COF.[414] This composite material endows the redox-active COF material with a high conductivity as well as high capacitance. Remarkably, the resulting composite has a high specific capacitance of 426 F g^{-1} at a current density of 2 A

https://dx.doi.org/10.1021/acs.chemrev.9b00550
Chem. Rev. 2020, 120, 8814–8933

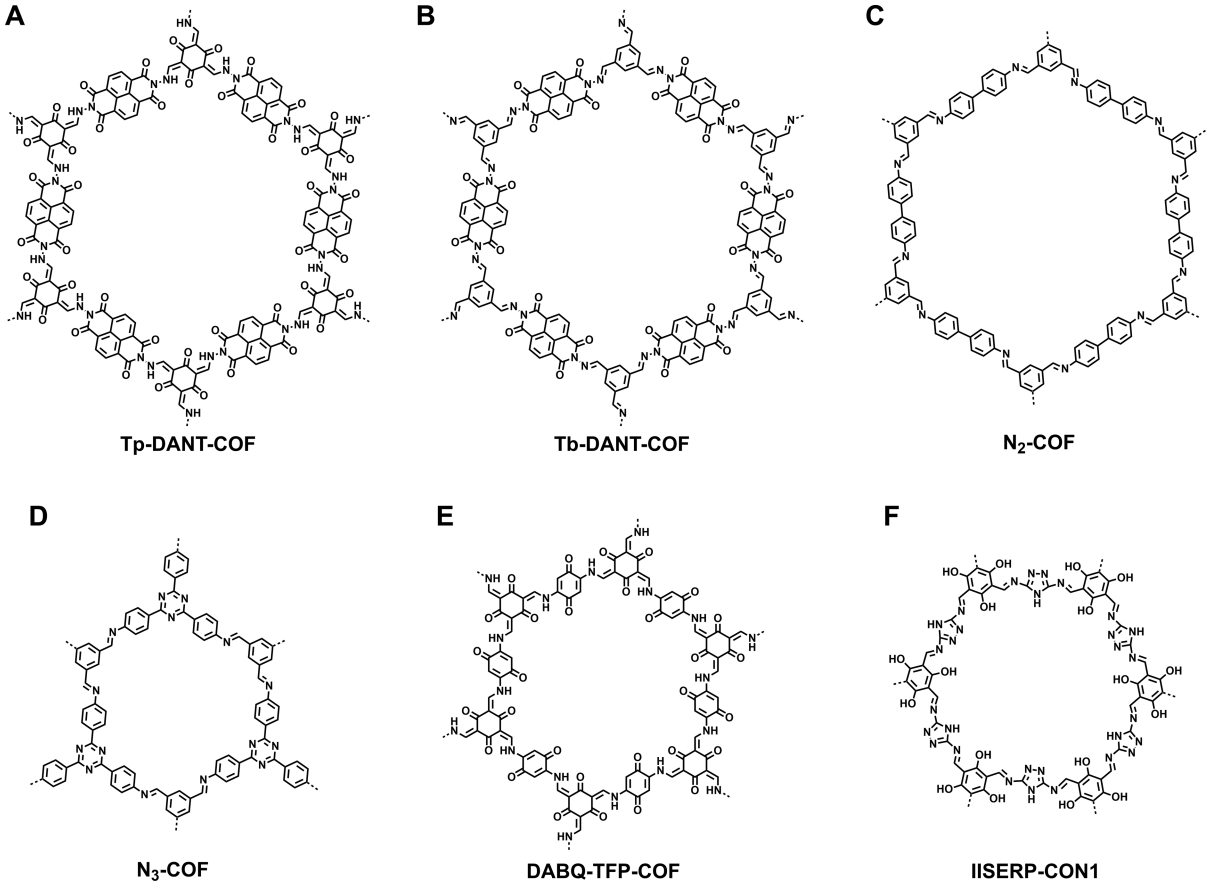

Figure 70. Schematics of COFs with conjugated backbones for the lithium-ion battery: (A) Tp-DANT-COF, (B) Tb-DANT-COF, (C) N_2-COF, (D) N_3-COF, (E) DABQ-TFP-COF, and (F) IISERP-CON1.

g^{-1} and retains a high capacitance of 314 F g^{-1} at a high current density of 50 A g^{-1}.

9.2. Lithium-Ion Battery

Organic electrodes for the lithium-ion batteries usually have poor rate performance and cycle stability, the main hurdles to be addressed. A small dilithium rhodizonate compound with abundant carbonyl groups delivers a capacity of 580 mAh g^{-1} but shows a drastic decrease in the capacity upon cycling due to the loss of active dilithium rhodizonate via dissolving in the electrolyte.[415] Anchoring redox-active units on COF skeletons via covalent bonds is expected to enhance the cycle performance by avoiding the leak of active materials during lithiation and delithiation processes. Moreover, the open channels can facilitate ion transport that is necessary for a high rate of performance. Nevertheless, the limited electric conductivity of COFs is an issue that needs to be addressed before achieving a quick electrochemical process in the lithium-ion battery. Hybrids of a redox-active COF with CNTs or conducting polymers open a way to boost electric conductivity and achieve a high rate of performance in lithium ion batteries.

As a proof of concept, the COF−CNT composites, that is, D_{TP}-A_{NDI}-COF@CNTs (Figure 69A), have been developed as the cathode for lithium-ion batteries by *in situ* growing the mesoporous D_{TP}-A_{NDI}-COF containing redox-active naphthalene diimide (NDI) units onto CNTs; the NDI units undergo a reversible two-electron redox reaction during lithiation and delithiation processes (Figure 69B).[416]

Indeed, the discharge−charge curve for lithium-ion batteries with the D_{TP}-A_{NDI}-COF@CNT cathode is symmetric, indicating the reversibility of oxidation and reduction processes. The Coulombic efficiency retains 100% after 100 cycles. The capacity of D_{TP}-A_{NDI}-COF@CNTs is as high as 67 mA h g^{-1} at a current density of 2.4 C, corresponding to an efficiency of 82% in utilizing the redox-active sites. In the long-term stability tests at a current density of 2.4 C, D_{TP}-A_{NDI}-COF@CNT stabilizes the capacity at 74 mA h g^{-1} after 700 cycles and achieves the redox-active site utilization efficiency of 90%. The charge-transfer resistance is decreased from 129 ohm for D_{TP}-A_{NDI}-COF to 8.3 ohm for D_{TP}-A_{NDI}-COF@CNTs, which accounts for the outstanding performance.

Usually, the C═C bond in the phenyl unit and imine bond hardly serve as redox-active units for energy storage. Recently, a study on COF-LZU1 breaks this limitation. Through growing a few layers of COF-LZU1 on CNTs, the resulting COF@CNT (Figure 21A) composite can deliver a reversible capacity as high as 1536 mA h g^{-1} upon stepwise activation at a current density of 100 mA g^{-1}, and the lithium-storage mechanism involves a 14-electron redox process with one lithium ion per C═N group and six lithium ions per benzene ring.[417]

Conjugated backbones in the COF are beneficial for lithium-ion storage. The COF backbone with an extended π-conjugated system is important for conquering the low intrinsic electrical conductivity of the COF. Tp-DANT-COF (Figure 70A) and Tb-DANT-COF (Figure 70B) with a conjugated NDI unit have been prepared as cathodes for the lithium-ion battery.[418] The initial charge and discharge capacities of Tp-DANT-COF are 78.9 and 93.4 mA h g^{-1} at a current density of 1.5 C respectively, which are slightly lower than those of the monomer control, 2,7-

https://dx.doi.org/10.1021/acs.chemrev.9b00550
Chem. Rev. 2020, 120, 8814−8933

bis((*E*)-benzylideneamino)benzo[*lmn*][3,8]phenanthroline-1,3,6,8(2*H*,7*H*)-tetraone (DANTB), with an initial capacity of 125 mA h g^{-1}. Notably, both the Tp-DANT COF and the Tb-DANT COF have better cycling performances than the control. For instance, at a high current density of 7.5 C, the Tp-DANT COF cathode can deliver the reversible charge and discharge capacities of 72.8 and 71.7 mA h g^{-1} after 600 cycles. The Tb-DANT COF can retain a reversible capacity of 80.1 mA h g^{-1} after 300 cycles at 3.4 C. The cycling stability of the Tp-DANT COF and the Tb-DANT COF illustrates that the integration of the DANT unit in the bulk material prevents the degradation of the redox-active unit. In comparison, an amorphous conjugated microporous polymer HATN-CMP achieves a high initial capacity of 147 mAh g^{-1} at a current density of 100 mA g^{-1}, but the capacity drops to 65 mAh g^{-1} at a high current density of 500 mA h^{-1}.[419] N_2-COF (Figure 70C) and N_3-COF (Figures 16J and 70D) with conjugated backbones exhibit high initial charge capacities of 737 (discharge) and 731 mA h g^{-1} (charge) for N_2-COF and 689 (discharge) and 707 mA h g^{-1} (charge) for N_3-COF at a current density of 1 A g^{-1}.[420] Both of them exhibit good cycle stability to retain 82% (N_2-COF) and 81% (N_3-COF) of the initial capacities after 500 cycles.

Compared with the pristine COFs, the exfoliated CONs with shorter Li^+ diffusion pathways exhibit a higher utilization efficiency of redox sites and faster kinetics for lithium storage. The ion-diffusion-controlled electrochemical process in pristine COF-based cathodes will turn to a charge-transfer-dominated process in CONs. Specifically, DAAQ-ECOF (exfoliation of DAAQ-TFP-COF, Figures 16R and 63) shows an excellent rechargeability with a 98% capacity retention after 1800 cycles at a current density of 20 mA g^{-1} and a fast charge−discharge ability with a 74% retention at a current density of 500 mA g^{-1}; both of them are much higher than those of bulk DABQ-TFP-COF (Figure 70E).[232] A self-exfoliated IISERP-CON1 (Figure 70F) anode has been prepared by condensing the triazole with trialdehyde.[421] This CON exhibits 720 mA h g^{-1} at a current density of 100 mA g^{-1} in lieu of an abundance of organic functional groups such as hydroxyl and N atoms that enable the reversible binding of Li^+ ions.

9.3. Lithium Sulfur Battery

Sulfur is attractive as the electrode because of its high capacity and low cost. However, sulfur cannot be used directly as an electrode owing to its insulating character. Moreover, the shuttling loss of intermediate lithium polysulfides eventually causes the deterioration of cycle performance. Specific separators such as polymeric membranes decorated with alumina or silica are capable of retaining the cycle performance;[422,423] However, the design and preparation of these membranes are complex and costly. To address these drawbacks, trapping sulfur into porous materials offers a promising route, and the pore size and volume are key factors to be considered.

The impregnation of sulfur into CTF-1 (Figure 27A) has been investigated by heating the mixture of CTF-1 and sulfur (3:2, in wt %) at 155 °C for 15 h.[424] The sulfur content in CTF-1 can reach 34 wt %, as confirmed by TGA. According to the galvanostatic discharge curves at a current density of 0.1 C, the capacity of CTF-1/s@155 °C decreases from 1197 to 762 mA h g^{-1} after 50 charge−discharge cycles, corresponding to a retention of 64% capacity and a Coulombic efficiency of 97%. By contrast, the physical mixture of CTF-1 and the sulfur (CTF-1/S@RT) cathode exhibits a much faster capacity decay from 1015 to 480 mA h g^{-1} after only 20 cycles. The distinct features for CTF-1/s@155 °C and CTF-1/S@RT suggest that loading sulfur into the CTF-1 pores greatly improves the cycle performance.

On the contrary, covalently anchoring sulfur to S-CTF-1 (Figure 71), which consists of a sulfur content of 62 wt %, has

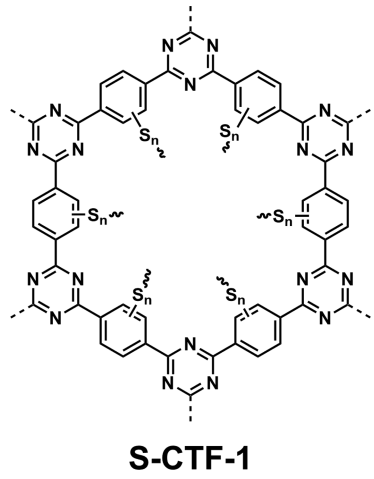

Figure 71. Schematic of S-CTF-1 for Li−S batteries.

been synthesized by heating sulfur and 1,4-dicyanobenzene to 400 °C.[425] This synthetic process combines the initiation of sulfur polymerization, the trimerization of nitrile groups, and the C−H insertion reaction between sulfur and CTF-1. The resulting S-CTF-1 exhibits good stability in the charge−discharge cycle test. At current densities of 1 and 2 C, S-CTF-1 retains 85.8 and 81.0% of the initial capacities (482.2 and 406.3 mA h g^{-1}) and 100% Coulombic efficiency, even after 300 cycles. This grafting strategy exceeds the performance of hydroxylated graphene nanosheets that enables only physisorption interactions with sulfur and decreases the capacity to 85% only after 100 cycles.[426] The covalent C−S bonds are stable during the cycle process, as confirmed by XPS after 100 cycles. Similarly, loading sulfur to microporous porphyrin-based Por-COF (Figure 72A), mesoporous Azo-COF (Figure 72B) and COF-V (Figure 72C), pyrene-based Py-COF (= ILCOF-1, Figure 9A), imine-linked TAPB-PDA-COF (Figure 72D), and boronic-ester-linked COF-1 (Figure 7A) has been explored for Li−S batteries.[96,427−431]

The confinement of polysulfides in fluorinated CTFs, that is, FCTF-S (Figure 72E), achieves good performance in the Li−S battery.[432] The polar C−F bond interacts more strongly with the sulfur species, in contrast with the nonfluorinated CTF, thus offering a more effective way to mitigate the dissolution of polysulfide intermediates. For example, FCTF-S exhibits an initial capacity of 1296 mA h g^{-1} at a current density of 0.1 C, which is comparable to that of CTF-S (1243 mA h g^{-1}). However, the cycling study reveals that FCTF-S can retain the capacity more effectively than CTF-S, as evidenced by a lower capacity fading rate of FCTF-S (0.17% per cycle) compared with that of CTF-S (0.30% per cycle). Fluorinated COF-F (Figure 72F) has been prepared for the lithium sulfur battery[433] because this COF undergoes an S_NAr substitution reaction for the covalent binding of sulfur. This enables 61 wt % sulfur loading in the material that exhibits an initial discharge capacity of 1120 mA h g^{-1} at a current density of 0.1 C. A slow capacity decay rate of 0.04% drop per cycle is observed over 100 cycles, indicating that the covalent bonding of sulfur with the COF-F prevents the

https://dx.doi.org/10.1021/acs.chemrev.9b00550
Chem. Rev. 2020, 120, 8814−8933

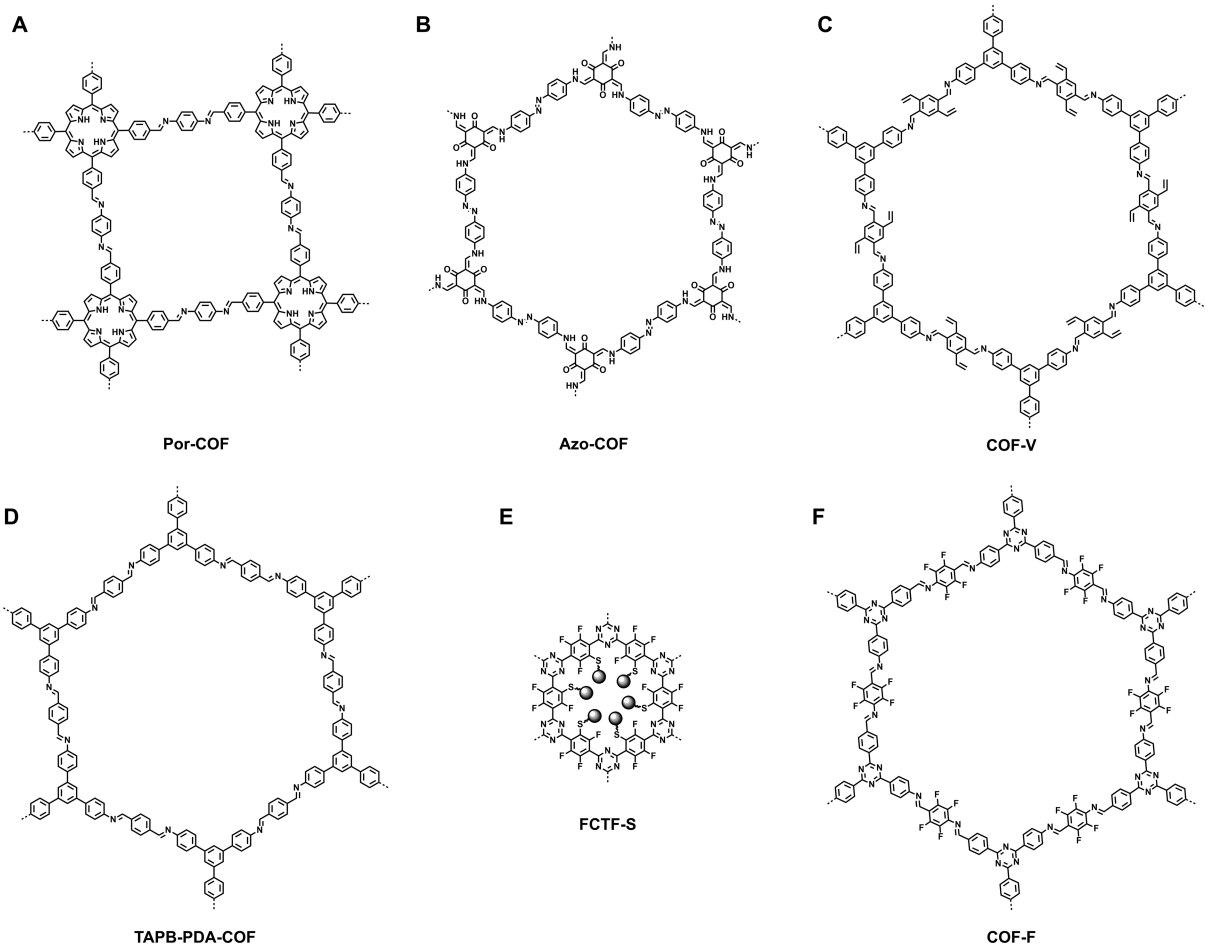

Figure 72. Schematics of COFs explored for the performance screening of Li−S batteries: (A) Por-COF, (B) Azo-COF, (C) COF-V, (D) TAPB-PDA-COF, (E) FCTF-S, and (F) COF-F.

dissolution of the polysulfide species. It is compatible with that of the *r*GO/MoS_2-coated separator that has a low-capacity fading rate of 0.116% after 500 cycles at 1 C.[434]

Immobilizing polysulfide chains into the imine-linked framework, TFPPy-ETTA-COF (= Py-TPE-COF, Figure 50A) can prevent the shuttling of polysulfides.[243] By heating sulfur with TFPPy-ETTA-COF at 300 °C, the C═N imine units in the COF trigger the polymerization of sulfur to form polysulfide chains and anchor them onto the pore walls via C−S bonds. This covalent immobilization transforms a redox-inactive TFPPy-ETTA-COF to a redox-active polysulfide@TFPPy-ETTA-COF with 64 wt % polysulfide loading. This polysulfide@TFPPy-ETTA-COF exhibits a stable capacity after 60 cycles and retains up to 54% of the initial capacity (1069 mA h g^{-1}) after 130 cycles. The slow decay of the capacity reveals that covalently bonded polysulfide is critical for improving the Li−S battery performance.

The long-term charge−discharge stability of Li−S batteries is highly affected by the accumulation of electron-inert Li_2S_2/Li_2S intermediates that are generated in the redox process. To solve this problem, iCOF−CNT hybrid electrodes are constructed by *in situ* growing COF-1 (Figure 7A) on CNT sheets and are used as an interlayer between the sulfur cathode and the separator membrane.[435] As a result, the cell maintains 84% of its original capacity after 300 cycles at a current density of 2 C. The interlayer can trap Li_2S by the micropores of COF-1, and the S−B bonding between Li_2S and COF-1 mitigates the electrostatic repulsion between Li_2S and S_6^{2-} $(S_3^*)^-$. These effects facilitate the reversion from insoluble Li_2S to soluble Li_2S_x, thus preventing the aggregation of insulating Li_2S on the CNTs and enhancing the cycle stability.

9.4. Sodium- and Potassium-Ion Batteries

Sodium- and potassium-ion batteries have been developed as next-generation batteries owing to the high cost and shortage of lithium metal. A drawback for sodium- and potassium-ion batteries is the sluggish kinetics in the electrode owing to the high mass of Na^+ and K^+ ions, giving rise to a low capacity compared with those of lithium-ion batteries. Designing anodes that allow a high rate of ion diffusion is a main concern. COFs are promising to achieve a high reversible capacity because their high porosity enables fast ion diffusion and their covalent skeletons prevent the dissolution of redox-active units.

2D COFs with redox-active units have been explored as rechargeable anode materials in sodium- and potassium-ion batteries.[209] Ball-milling of the DAAQ-TFP COF (Figures 16R and 63) generates CONs with a thickness of 100−250 nm in 30 min, which can be further treated with methane sulfonic acid, followed by reprecipitation with methanol to yield CONs with a thickness of 4−12 nm. The resulting CONs exhibit excellent performance with capacities as high as 500 and 450 mA h g^{-1} at current densities of 50 and 75 mA g^{-1}, respectively. Remarkably, the capacity retentivity can reach 99% after 10 000 cycles, demonstrating a promising cyclic stability.

https://dx.doi.org/10.1021/acs.chemrev.9b00550
Chem. Rev. 2020, 120, 8814−8933

COF-10 (Figure 73) has been grown onto a CNT to have a thickness of 6 nm, and the resulting COF-10@CNT hybrid

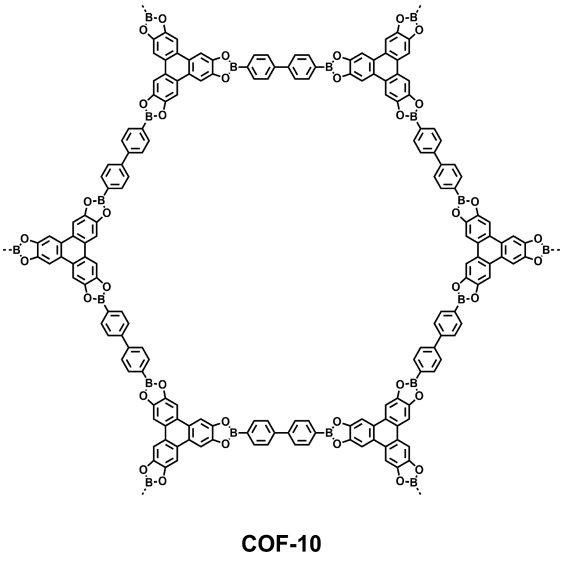

Figure 73. Schematic of COF-10 explored for potassium-ion batteries.

serves as an anode for potassium-ion batteries.[436] It exhibits an initial charge capacity of 348 mA h g^{-1}, which is far superior to that (130 mA h g^{-1}) of COF-10. COF-10@CNT shows a reversible capacity to reach 288 mA h g^{-1} after 500 cycles at a current density of 0.1 A g^{-1}. After the repetitive charge−discharge cycle, the interlayer spacing of COF-10 increases from 0.35 to 0.41 nm as a result of the intercalation of K^+ between COF-10 layers. Therefore, the K^+ storage is driven by π-cation interactions between K^+ and the π-clouds of aromatic backbones of COF-10. This result is encouraging because the π-system in COFs is ubiquitous and the π-skeletons can be explored for the intercalation of ions for developing energy-storage systems.

10. MASS TRANSPORT

How to design materials with the capability of transporting holes, electrons, ions, and molecules is a central subject in the fields of semiconductors, optoelectronics, and energy devices.[93,158,173,223,224,437] The key to facilitating the charge-carrier transport is to create ordered structures. In this context, 2D COFs provide a powerful platform in designing ordered π-arrays and aligned 1D open channels. The ordered π-arrays in 2D COFs formed by the $\pi-\pi$ stacking of knots and edges offer preorganized and built-in pathways for hole and electron conductions.

2D COFs offer 1D open nanochannels that are accessible to external guest molecules and ions. In particular, 2D COFs provide a versatile platform for the complementary design of skeletons and 1D open pores that can accommodate specific guest molecules or ions, so that the resulting COFs are capable of high-rate ion conductions.[217,438]

10.1. Proton Conduction

Proton transport is ubiquitous in biological systems and plays a key role in important technology such as fuel cells for chemical-to-electricity energy conversion.[439−441] Pentafluorinated sulfonic-acid-functionalized polymer membrane, that is, Nafion, is the benchmark material for proton conduction. Owing to its unique morphological and structural characteristics, Nafion exhibits a high proton conductivity (e.g., 10^{-1} S cm^{-1}) at moderate temperature (60−80 °C) under high relative humid conditions (98% RH).[62] Because of its high cost and low efficiency at high operating temperature (120−200 °C), long-term efforts over the past five decades have been made with the aim to explore new materials that surpass Nafion.

Materials with inherent pores are promising to provide a pathway for ion conduction across the nanopores. The combination of well-defined structural ordering, tunable porosity and functionality, and robust thermal and chemical stability in COFs is hardly achieved by other porous materials; recent advances have demonstrated that COFs offer a new platform for the molecular design of proton-conducting materials.[62,67,230,442] In particular, the ordered 1D channels of 2D COFs are accessible to proton carriers that form a hydrogen-bonding network that improves the proton conductivity beyond the level of Nafion.[70,192,216,222,223]

10.1.1. Organic Proton Carriers. By developing a stable skeleton, TPB-DMTP-COF (Figures 16O, 21B, and 74) has

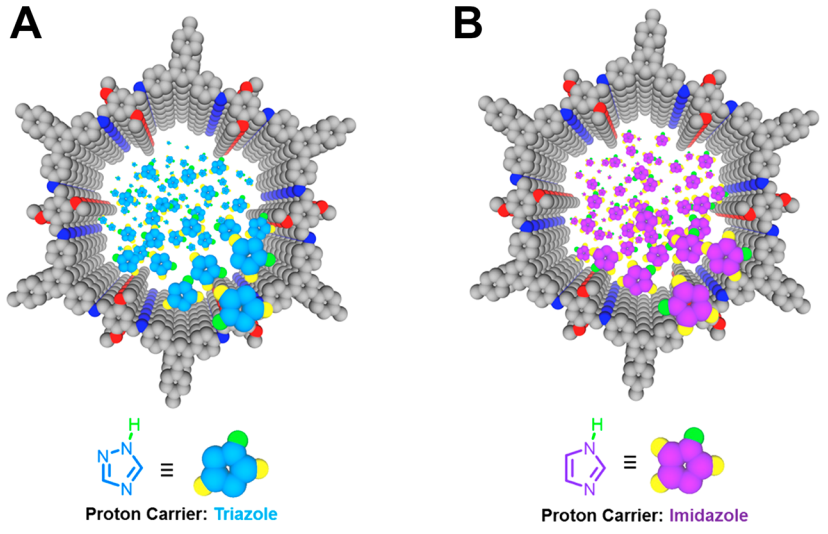

Figure 74. Mesoporous 2D TPB-DMTP-COF. Schematic of stacked 2D TPB-DMTP-COF with (A) triazole and (B) imidazole proton carriers loaded in the 1D channels.

https://dx.doi.org/10.1021/acs.chemrev.9b00550
Chem. Rev. 2020, 120, 8814−8933

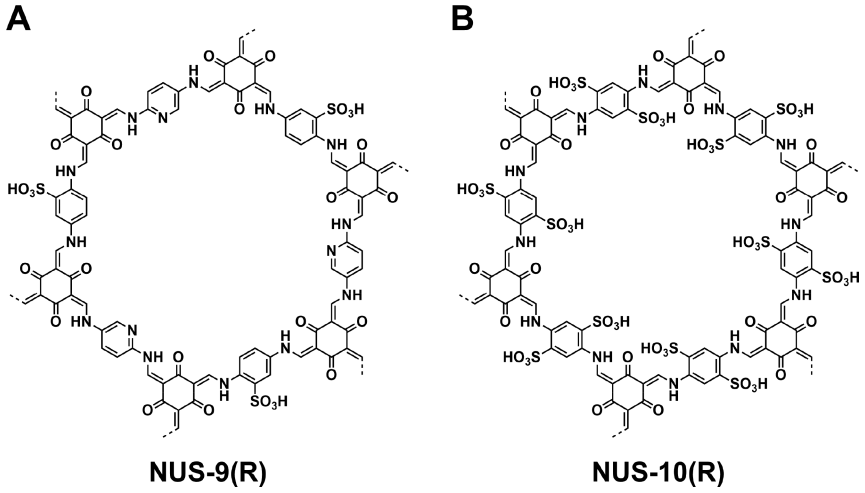

Figure 75. Schematics of (A) NUS-9(R) and (B) NUS-10(R) for proton conduction.

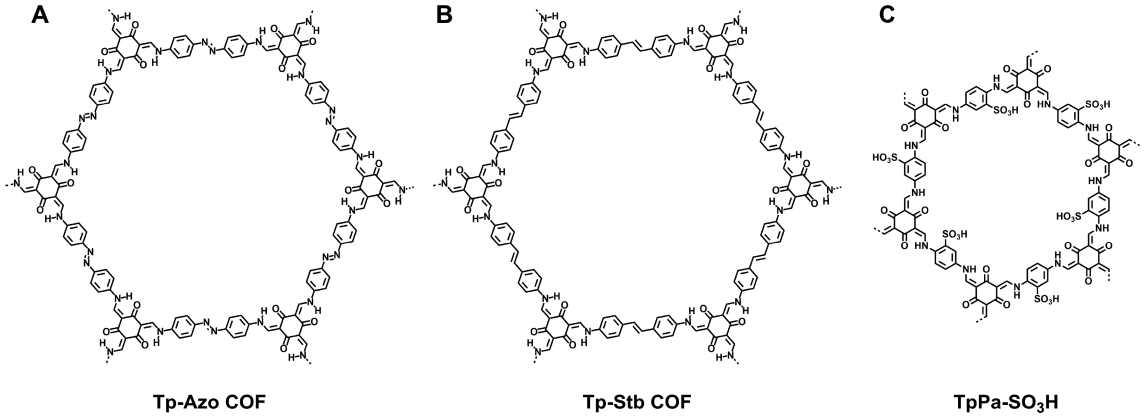

Figure 76. Schematics of (A) the Tp-Azo COF, (B) the TP-Stb COF, and (C) TpPa-SO_3H for proton conduction.

shown its high capability of loading organic proton carriers in the 3.2 nm mesoporous channels. TPB-DMTP-COF can accommodate 180 wt % triazole (trz) and 155 wt % imidazole (im) within its mesopores, which are close to the theoretical loading contents of 186 and 164 wt %, respectively.[230] The anhydrous proton conductivity of trz@TPB-DMTP and im@TPB-DMTP COFs is as high as $(1.1 \text{ and } 4.37) \times 10^{-3}$ S cm^{-1}, respectively, at 130 °C. In contrast, MOF $[Al(\mu_2\text{-OH})(1,4\text{-d.c.})]_n$ with imidazole in the pores exhibits a much lower proton conductivity of 2.2×10^{-5} S cm^{-1} at 120 °C.[443] The difference between im@TPB-DMTP-COF and trz@TPB-DMTP-COF indicates a great effect of proton carriers on the conductivity. By decreasing the loading content of im or trz, the resulting materials greatly decrease the proton conductivity. For example, im@TPB-DMTP-COF with a loading content of 82 wt % exhibits a conductivity of 2.03×10^{-4} S cm^{-1} at 130 °C. Notably, the conductivity of TPB-DMTP-COF is four orders of magnitude higher than that of amorphous analogue im@TPB-TP-COF under otherwise identical conditions, indicating the importance of aligned 1D channels for the proton conduction. Clearly, the activation energy (E_a) for amorphous im@TPB-TP-COF is 0.91 eV, which is much higher than that (0.38 eV) of im@TPB-DMTP-COF, indicating that the ordered 1D mesopores facilitate proton conduction. The low activation energy indicates that the proton conduction is dominated by a hopping mechanism, and the im and trz molecules in the mesopores form hydrogen-bonding networks through which the protons move forward across the channels.

The proton conductivity of NUS-9(R) (Figure 75A) containing monosulfonyl group-functionalized edge units is 1.24×10^{-2} S cm^{-1} under 97% RH at 25 °C.[67] The conductivity increases to 3.96×10^{-2} S cm^{-1} for NUS-10(R) (Figure 75B) containing bifunctionalized ($(-SO_3H)_2$) edge units under otherwise identical conditions. The proton conductivities of sulfonated COFs NUS-9(R) and NUS-10(R) are the highest among other sulfonated porous frameworks, such as Nafion with a proton conductivity of 1.0×10^{-2} S cm^{-1} under 98% RH at 80 °C,[444] UiO-66-$(SO_3H)_2$ with a proton conductivity of 1.42×10^{-2} S cm^{-1} under 90% RH at 25 °C,[445] and phytic@TpPa-(SO_3H-Py) with a proton conductivity of 0.50×10^{-4} S cm^{-1} under anhydrous conditions at 120 °C.[446] Notably, NUS-10(R) exhibits excellent stability at 25 °C and 97% RH without a significant loss of conductivity, even after continuous operation after 15 days. Clearly, the drastic increment is attributed to the presence of water guests in the confined nanochannel and their enhanced interactions with hydrophilic sulfonic acid groups in establishing pathways for efficient proton motion. The NUS-9(R) and NUS-10(R) COFs can form composite membranes by mixing COFs with nonconductive PVDF (polyvinylidene fluoride) via a solution-casting process. Among various membranes with different loading contents of COFs, NUS-9(R)@PVDF-50 and NUS-10(R)@PVDF-50 have shown the best proton conductivity upon the direct soak of the COF

https://dx.doi.org/10.1021/acs.chemrev.9b00550
Chem. Rev. 2020, 120, 8814−8933

membrane with ultrapure water. For example, NUS-9(R)@PVDF-50 exhibits high conductivities of (2.06 and 5.06) × 10^{-3} S cm^{-1} at 25 and 80 °C, respectively. More significantly, NUS-10(R)@PVDF-50 exhibits further increased conductivities of 5.16 × 10^{-3} and 1.58 × 10^{-2} S cm^{-1} at 25 and 80 °C, respectively. The E_a value of NUS-9(R)@PVDF-50 and NUS-10(R)@PVDF-50 membranes is 0.2 and 0.21 eV, respectively, indicating that these membranes are dominated by a hopping mechanism for proton conduction via the hydrogen-bonding networks formed between sulfonic groups and water molecules in the pores.

10.1.2. Inorganic Acid Proton Carriers. Similarly, the phosphoric-acid (H_3PO_4, PA)-loaded Tp-Azo COF (Figure 76A) has been investigated for proton conduction under humid and anhydrous condition by changing the temperature from 22 to 142 °C.[62] The PA@Tp-Azo COF with a PA content of 5.4 wt % exhibits a proton conductivity of 6.7 × 10^{-5} S cm^{-1} at 67 °C under anhydrous conditions. The conductivity increases upon humidification and reaches 9.9 × 10^{-4} S cm^{-1} at 59 °C under 98% RH. The proton conductivity of the PA@Tp-Azo COF is lower than that of MOF counterparts, such as ferrous oxalate dehydrate (1.3 × 10^{-3} S cm^{-1} at 25 °C, 98% RH)[447] and 1,2,4-triazole-loaded β-PCMOF2 (5 × 10^{-4} S cm^{-1} at 150 °C under anhydrous hydrogen).[448] In contrast, the PA@Tp-Stb COF (2.8 wt % PA, Figure 76B) without azo units exhibits almost no proton conductivity under otherwise identical conditions. The conductivity of both COFs increases by increasing the humidity. For example, PA@Tp-Azo and PA@Tp-Stb COFs exhibit a proton conductivity of 9.9 × 10^{-4} and 2.3 × 10^{-5} S cm^{-1}, respectively, at 59 °C under 98% RH. The different behaviors between azo-functionalized (—N═N—) and nonazo (—C═C—) COFs clearly demonstrate that the presence of azo units makes a remarkable contribution to the proton conduction. The protonated azo units on the 1D channel walls of the Tp-Azo COF under humid conditions form a hydrogen-bonding network that promotes proton conduction. The TpBpy-ST COF and TpBpy-MC COF (= Tp-Bpy, Figure 31E; ST and MC stand for solvothermal and mechanochemical synthesis, respectively) show a proton conductivity of (1.98 and 2.5) × 10^{-3} S cm^{-1}, respectively, at 120 °C under 0% RH.[66] The high proton conductivity of the PA@TpBpy COF is attributed to the presence of bipyridine sites, a hydrogen-bonded phosphoric acid channel, and low activation energy (0.11 to 0.12 eV).

Similarly, the cationic EB-COF:PW_{12} (PW_{12} stands for polyoxomethalates (POM); $PW_{12}O_{40}^{3-}$) under 97% RH at room temperature exhibits a proton conductivity of 3.32 × 10^{-3} S cm^{-1}, which is much higher than that (2.82 × 10^{-6} S cm^{-1}) of the analogous cationic EB-COF:Br (= EB-TFP iCOF, Figure 60A).[68] This result indicates that POM in the ordered 1D open channels facilitates the proton hopping in EB-COF:PW_{12}. The proton conductivity is compatible with those of MOF materials, such as Fe-CAT-5 (5 × 10^{-2} S cm^{-1}), Ti-CAT-5 (8.2 × 10^{-4} S cm^{-1}),[449] and $Fe(ox)_2H_2O$ (1.3 × 10^{-3} S cm^{-1}).[447] Upon treatment of two aza-fused COFs, that is, aza-COF-1_H and aza-COF-2_H with H_3PO_4,[450] the proton conductivity increases from 1.51 × 10^{-5} (aza-COF-1) and 8.78 × 10^{-6} (aza-COF-2) to 1.23 × 10^{-3} (aza-COF-1_H) and 4.80 × 10^{-3} S cm^{-1} (aza-COF-2_H), respectively, under 97% RH at 50 °C. Clearly, the E_a value decreases from 0.78 eV for aza-COF-1 to 0.29 eV for aza-COF-1_H and from 0.96 eV for aza-COF-2 to 0.45 eV for aza-COF-2_H. These results indicate that the proton conduction in these H_3PO_4-loaded aza-COFs is driven by a hopping mechanism.

Intrinsic and extrinsic proton conductivities of COFs have been investigated for TpPa-SO_3H (Figure 76C), TpPa-(SO_3H-Py) (= NUS-9(R), Figure 75A), and TpPa-Py COFs (Figure 64C) under anhydrous condition by using alternating-current impedance spectroscopic measurements.[442] In the sulfonic-acid-functionalized TpPa-SO_3H COF, sulfonic acid groups on the 1D porous channel act as intrinsic proton-conducting units. The intrinsic proton conductivity of the TpPa-SO_3H COF is 1.2 × 10^{-5} S cm^{-1} at 25 °C and 1.7 × 10^{-5} S cm^{-1} at 120 °C. The conductivity is improved for the phytic acid@TpPa-SO_3H COF and reaches 7.5 × 10^{-5} S cm^{-1} at 120 °C owing to the presence of extrinsic conductivity. On the contrary, the phytic acid@TpPa-Py COF has a conductivity of 3.0 × 10^{-4} S cm^{-1} at 120 °C, which is higher than that of the phytic acid@TpPa-SO_3H COF due to the immobilization of phytic acid on the pyridine centers. Notably, phytic acid@TpPa-(SO_3H-Py) exhibits a proton conductivity as high as 5.0 × 10^{-4} S cm^{-1} at 120 °C owing to the coexistence of intrinsic and extrinsic proton-conducting pathways.

The entrapment of *p*-toluene sulfonic acid in COF membranes is another efficient strategy to achieve high proton conductivity. Although TpAzo COF membranes exhibit a low proton conductivity of 3.4 × 10^{-5} S cm^{-1} at 80 °C under 95% RH, PTSA@TpAzo achieves a proton conductivity of 6.3 × 10^{-2} S cm^{-1} at 30 °C under 95% RH, whereas the conductivity increases as temperature is increased and reaches a maximum of 7.8 × 10^{-2} S cm^{-1} at 80 °C.[451] The thickness of TpAzo COF membranes can vary between 100 to 300 μm by changing the thickness of the molds, and the proton conductivity further increases upon decreasing the thickness of the *in situ* PTSA·H_2O-loaded COF membranes.

10.2. Ion Conduction

Spiroborates are ionic derivatives of boronic acids and possess high resistance toward hydrolysis. In this context, COFs that are linked by spiroborate can be used as ion conductors. ICOF-2 (Figure 27F) consisting of Li^+ ions acts as solid-state electrolytes in lithium ion batteries.[217] Because of its light weight and high thermal and chemical stability, the Li^+-ion-containing ICOF-2 exhibits an ion conductivity of 3.05 × 10^{-5} S cm^{-1} at room temperature, and the conductivity shows a linear enhancement with the temperature. The Li^+-ion transference number for traditional solid-state polymer electrolytes with lithium salt is usually 0.2 to 0.5.[452] By contrast, the Li^+-ion transference number for ICOF-2 is as high as 0.8, as determined by using the Bruce—Vincent—Evans (BVE) method, indicating that ICOF-2 has the potential to serve as a high-voltage cathode material. LiCl@RT-COF-1 (Figure 77) that is produced by the postsynthetic treatment of RT-COF-1 with LiCl exhibits a conductivity of 6.45 × 10^{-3} S cm^{-1} (at 40 °C and 100% RH).[453] It is among the highest reported so far for both COFs and MOFs under similar operating conditions, as represented by MFM-500(Ni) (4.5 × 10^{-4} S cm^{-1} at 25 °C and 98% RH),[454] MOF (Cu—TCPP) (3.9 × 10^{-3} S cm^{-1} at 25 °C and 98% RH),[455] and In(III)-isophthalate-based MOF In-IA-2D-1 (3.4 × 10^{-3} S cm^{-1} at 27 °C and 98% RH).[456]

The preferred orientation of 2D COF layers has been developed by pressing the COF powders, which facilitate mass transport within the aligned cylindrical pores in the COF pellets.[438] For example, the powder samples of COF-5 (Figure 7B) and TpPa-1 (Figure 62A) COFs upon treatment with 1 M $LiClO_4$/THF for 48 h can load 3.77 mol % Li^+ ions. The resulting pellets exhibit ionic conductivities of (2.6 and 1.5) ×

https://dx.doi.org/10.1021/acs.chemrev.9b00550
Chem. Rev. 2020, 120, 8814−8933

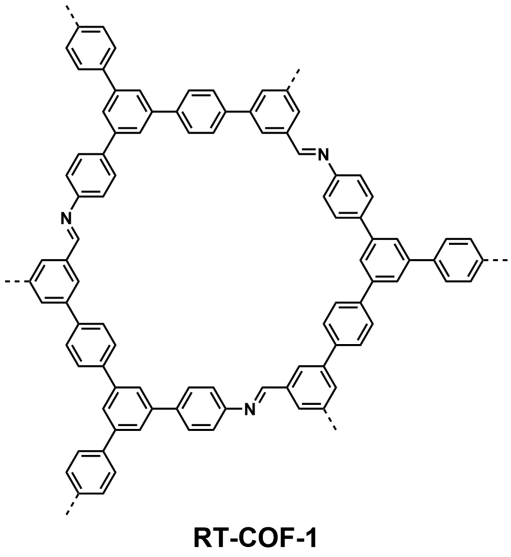

Figure 77. Schematic of RT-COF-1 for ion conduction.

10^{-4} S cm^{-1}, respectively, at room temperature, which is compatible with other materials such as a spiroborate-based COF (3×10^{-5} S cm^{-1}),[217] borate amorphous organic porous polymers (2.7×10^{-4} S cm^{-1}),[457] and other inorganic materials LiGePS (1.2×10^{-3} S cm^{-1}).[458] The pallets without Li^+ salts are insulators for ion conduction. Moreover, by using a linear Arrhenius plot, the E_a value is as low as 0.037 ± 0.004 eV for COF-5. The reason for this extremely low activation energy is still unclear.

Integrating flexible oligo(ethylene oxide) (OEO) chains onto the pore walls of COFs forms a polyelectrolyte interface in the nanochannels and offers a pathway for lithium ion transport (Figure 78).[459] After loading with $LiClO_4$ through the solution diffusion method, the resulting Li^+@TPB-BMTP-COF (Figure 78B) achieves ion conductivities of 6.04×10^{-6}, 2.85×10^{-5}, and 1.66×10^{-4} S cm^{-1} at 40, 60, and 80 °C, respectively, which are 44, 42, and 30 times higher than those of Li^+@TPB-DMTP-COF (Figure 78A). Notably, the ion conductivity of poly(ethylene oxide)−Li^+ complex is only 8.0×10^{-8} S cm^{-1} at 40 °C. This indicates that the polyelectrolyte chains aligned on the pore walls of the COFs greatly promote the ion motion. The greatly enhanced ion conductivity observed for Li^+@TPB-BMTP-COF originates from the presence of dense poly(ethylene oxide) (PEO) chains that form a polyelectrolyte interface in the channels, which promotes the dissociation of Li salts and the Li^+ motion. The activation energy is 0.96 eV for the Li^+@TPB-DMTP-COF and 0.87 eV for the Li^+@TPB-BMTP-COF, indicating a vehicle mechanism.

Similarly, anchoring PEO in the COF yields COF-PEO-3, COF-PEO-6, and COF-PEO-9 (Figure 78C−E).[460] The conductivity increases with the increase in chain length under otherwise identical conditions. COF-PEO-9-Li at 200 °C in argon shows a conductivity of 1.33×10^{-3} S cm^{-1}. These results show that COFs offer a promising platform for designing solid-state ion conduction and transportation. Interestingly, through adjusting the electronegativity of the COF skeleton, the Li^+ conduction of COF-PEO can be controlled.[461] Mixing COFs with Li salt and PEG (= PEO) forms PEG-Li^+@CD-COF-Li, PEG-Li^+@COF-300, PEG-Li^+@COF-5, and PEG-Li^+@EB-COF-ClO_4, whose conductivities are 2.60×10^{-5}, 1.40×10^{-6}, 3.60×10^{-8}, and 1.93×10^{-5} S cm^{-1} at 30 °C and $1.30 \times$

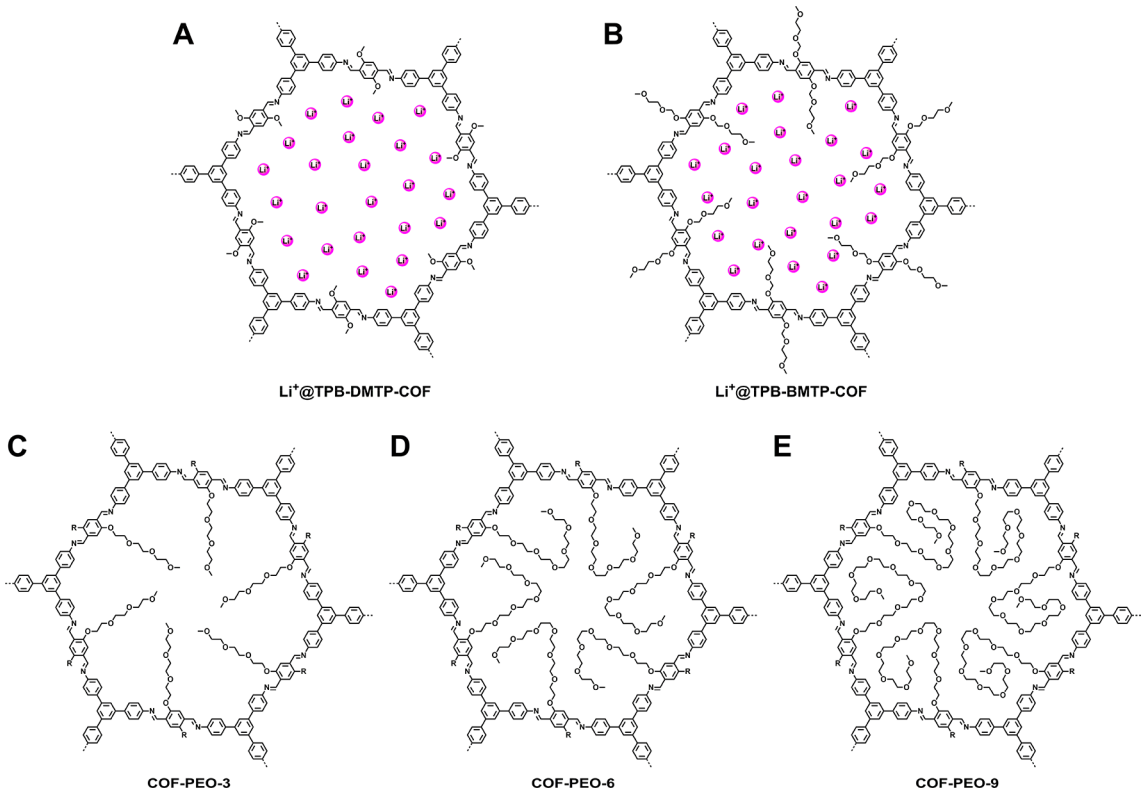

Figure 78. Schematics of COFs with integrated flexible PEO chains for lithium ion transport: (A) Li^+@TPB-DMTP-COF, (B) Li^+@TPB-BMTP-COF, (C) COF-PEO-3, (D) COF-PEO-6, and (E) COF-PEO-9.

https://dx.doi.org/10.1021/acs.chemrev.9b00550
Chem. Rev. 2020, 120, 8814−8933

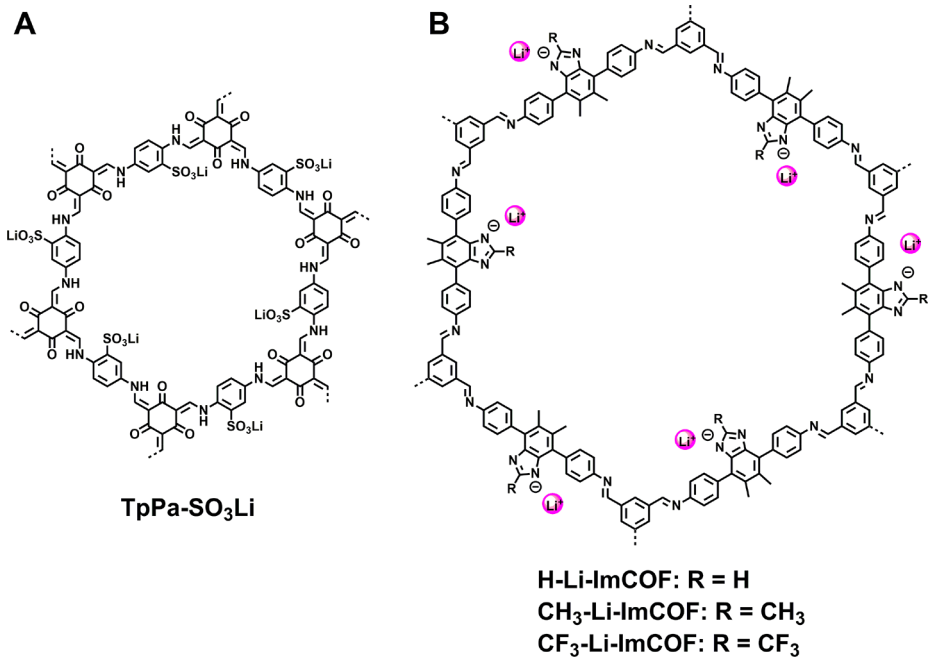

Figure 79. Schematics of (A) TpPa-SO_3Li and (B) Li-ImCOFs for ion conduction.

10^{-4}, 9.11×10^{-5}, 3.49×10^{-5}, and 1.78×10^{-3} S cm^{-1} at 120 °C, respectively. The activation energy is 0.17, 0.20, 0.35, and 0.21 eV, respectively. The ionic COFs display higher ion conductivity than those with a neutral framework owing to the large polarizability of the ionic COFs that increases the dissociation of Li salt. When the same amount of Li salt is loaded into the COFs without PEG, there is no ion conduction in the three COFs except for the low conductivity of 7.81×10^{-7} S cm^{-1} at 120 °C in Li^+@CD-COF-Li. The PEG plays a key role in the mass transport of Li^+.

To solve the problem of dendritic Li growth caused by the freely mobile anion and organic solvents in the electrolytes, a single Li^+ ion conductor TpPa-SO_3Li (Figure 79A) without freely mobile anions and solvents has been prepared.[462] At room temperature, the conductivity is 2.7×10^{-5} S cm^{-1} without any addition of Li salts or organic solvents, and the E_a value is 0.18 eV. Notably, this conductivity is compatible with those of propylene carbonate (PC) solvent-containing ion conductors based on the anionic COF composite (3.05×10^{-5} S cm^{-1})[217] and MOF composite (5.7×10^{-5} S cm^{-1}).[463] Another similar method to immobilize ions in the Li-ImCOFs (Figure 79B) is to diffuse Li^+ ion through the channels owing to the interaction between Li^+ and imidazole.[263] Interestingly, the electron-withdrawing substituent weakens the ion-pair interaction and improves the conductivity. At room temperature, the conductivity is 5.3×10^{-3}, 7.2×10^{-3}, and 8.0×10^{-5} S cm^{-1} for H-Li-ImCOF, CF_3-Li-ImCOF, and CH_3-Li-ImCOF, respectively. Their E_a values are 0.12, 0.10, and 0.27 eV, respectively.

Anion conductivity in COFs has been investigated using COFs with anion charges. The as-synthesized TpBD-MeQA$^+Br^-$, via ion exchange by washing with aqueous KOH solution, is transformed into TpBD-MeQA$^+OH^-$,[464] which further forms TpBD-MeQA$^+HCO_3^-$ via the reaction of OH^- anions with CO_2 upon exposure to air. The conductivity increases from 4.6×10^{-3} S cm^{-1} for TpBD-MeQA$^+Br^-$ at 20 °C to 8.4×10^{-3} S cm^{-1} at 20 °C and 2.7×10^{-2} S cm^{-1} at 80 °C.

11. PORE DESIGN OF FUNCTIONS

11.1. Features of Pores and Porosity Design

COFs offer a platform for designing pores to achieve a discrete pore shape, size, and environment. In particular, in 2D COFs, their pores display distinct features that are inaccessible to other porous materials, namely, (1) the 1D pores are open and accessible only from the top and bottom sides of the 2D layers; (2) they are independent space and are free of interpenetration; (3) they are uniform in shape with a predesignable polygon; (4) they have a discrete pore size that is predesignable and tunable from micropore to mesopore with atomic level accuracy; and (5) they can be designed to produce various tailor-made interfaces on the pore walls to control the interactions with guests. The pore shape and size can be designed by using a different topology diagram, whereas the tailor-made pore interface can be achieved by pore-surface engineering. Therefore, the pore chemistry of 2D COFs offers straightforward strategies for designing the parameters of 1D channels. This structural designability is the most distinctive feature of the porous structure of COFs. It enables the exploration of various interfaces and functions based on the same COF skeleton, greatly expanding the structural availability and diversity.

2D COFs consist of stacked layer structures in which the dense π-units in the skeletons limit the development of ultrahigh porosity. 3D COFs evolve extended skeletons that usually contain folded structures, which also decreases their porosity. How to develop strategies that enable the full exploration of the porosity of 2D and 3D COFs is a subject of high interest but remains a challenge. In particular, exceptional surface area and large pore volume are two key parameters to be achieved in developing porosity. Indeed, the porosity of COFs is highly dependent on the building blocks, especially their bulkiness and molecular weight, and is also affected by the crystallinity of the COF samples. On the basis of theoretical predictions, some COFs can reach high porosity. For example, the theoretical surface area of 2D ILCOF-1 (Figure 9A) is as high as 5070 m^2 g^{-1}, whereas the calculated surface area of 3D COF-340 can

https://dx.doi.org/10.1021/acs.chemrev.9b00550
Chem. Rev. 2020, 120, 8814−8933

Table 6. Typical Examples of COFs with the BET Surface Area, Pore Volume, and Pore Width

COFs	linkage	S_{BET} (m^2 g^{-1})	pore volume (cm^3 g^{-1})	pore width (nm)	ref
COF-1	boroxine	711	0.32	0.9	9
COF-5	boronate ester	1590	0.998	2.7	9
COF-6	boronate ester	980	0.32	0.64	26
COF-8	boronate ester	1400	0.69	1.87	26
COF-10	boronate ester	2080	1.44	3.41	26
COF-102	boroxine	3472	1.35	1.15	47
COF-103	boroxine	4210	1.66	1.25	47
DBA-3D-COF 1	boronate ester	5083	1.59	2.6	467
TP-COF	boronate ester	868	0.79	3.26	27
COF-18 Å	boronate ester	1263	0.69	1.8	132
COF-16 Å	boronate ester	753	0.39	1.6	132
COF-14 Å	boronate ester	805	0.41	1.4	132
COF-11 Å	boronate ester	105	0.052	1.1	132
COF-202	borosilicate	2690	1.09	1.1	148
PPy-COF	boroxine	923	0.53	1.88	222
COF-5 (microwave)	boronate-ester	2019		2.7	194
COF-102 (microwave)	boroxine	2926		1.2	194
ATPES-COF-1	boroxine	490			335
COF-102-allyl	boroxine	1445			141
COF-102-SPr	boroxine	1424			141
T-COF 1	boronate ester	927		2.04	224
T-COF 2	boronate ester	562		1.36	224
T-COF 3	boronate ester	544		3.15	224
T-COF 4	boronate ester	904		2.75−2.94	224
CTC-COF	boronate ester	1710		2.26	119
1-S	boronate ester	1125			344
1-Se	boronate ester	1056			344
1-Te	boronate ester	302−352			344
HHTP-DPB COF	boronate ester	930		4.7	91
DBA-COF 1	boronate ester	1952	1.27	3.4	120
DBA-COF 2	boronate ester	984	0.741	3.8	120
AEM-COF-1	boronate ester	1445	1.15	3.2	121
AEM-COF-1	boronate ester	1487	1.38	3.8	121
COF-66	boronate ester	360	0.20	2.49	106
TP-Por-COF	boronate ester	890	1.1	4.6	93
COF-5−10%	boronate ester	2100	1.14		284
COF-5−25%	boronate ester	1500			284
COF-5−50%	boronate ester	1450			284
COF-5−60%	boronate ester	1110			284
ICOF-1	spiroborate	1022		1.1	217
ICOF-2	spiroborate	1259		2.2	217
BDT-OEt COF	boronate ester	1844	1.07	2.9	213
ZnPc-Py COF	boronate ester	420		3.1	103
ZnPc-DPB COF	boronate ester	485		3.1	103
ZnPc-NDI COF	boronate ester	490		3.1	103
ZnPc-PPE COF	boronate ester	440		3.4	103
NiPc COF	boronate ester	624	0.4854	1.9	30
2D-NiPc-BTDA COF	boronate ester	877	0.36	2.2	104
CuPc-COF	boronate ester	1360	0.52−0.55	2.2	32
ZnPc-COF	boronate ester	985	0.52−0.55	2.2	32
CoPc-COF	boronate ester	517	0.52−0.55	2.2	32
D_{ZnPc}-A_{NDI}-COF	boronate ester	1410	1.25	3.6	166
D_{CuPc}-A_{PyrDI}-COF	boronate ester	1357	1.13	3.6	102
D_{NiPc}-A_{PyrDI}-COF	boronate ester	1172	0.95	3.6	102
D_{CuPc}-A_{NDI}-COF	boronate ester	1726	1.46	3.6	102
D_{NiPc}-A_{NDI}-COF	boronate ester	1432	1.15	3.6	102
D_{CuPc}-A_{PDI}-COF	boronate ester	414	0.48	4.0	102
D_{NiPc}-A_{PDI}-COF	boronate ester	519	0.55	4.0	102
D_{TP}-A_{NDI}-COF	boronate ester	1910	2.37	5.3	92
D_{TP}-A_{PyrDI}-COF	boronate ester	1604	1.98	5.3	92
H_2P-COF	boronate ester	1894		2.5	99

https://dx.doi.org/10.1021/acs.chemrev.9b00550
Chem. Rev. 2020, 120, 8814−8933

Table 6. continued

COFs	linkage	S_{BET} (m^2 g^{-1})	pore volume (cm^3 g^{-1})	pore width (nm)	ref
ZnP-COF	boronate ester	1713		2.5	99
CuP-COF	boronate ester	1724	1.1153	2.5	99
2D D−A COF	boronate ester	2021	1.5	2.8	90
Star-COF-1	boronate ester	2120		2.8	25
Star-COF-2	boronate ester	1767		4.4	25
Star-COF-3	boronate ester	2129		4.7	25
5%N_3-COF-5	boronate ester	2160	1.184	2.949	133
25%N_3-COF-5	boronate ester	1865	1.071	2.757	133
50%N_3-COF-5	boronate ester	1722	1.016	2.587	133
75%N_3-COF-5	boronate ester	1641	0.946	2.585	133
100%N_3-COF-5	boronate ester	1421	0.835	2.274	133
5%AcTrz-COF-5	boronate ester	2000	1.481	2.978	133
25%AcTrz-COF-5	boronate ester	1561	0.946	2.426	133
50%AcTrz-COF-5	boronate ester	914	0.638	1.560	133
75%AcTrz-COF-5	boronate ester	142	0.152	1.532	133
100%AcTrz-COF-5	boronate ester	36	0.0297	1.248	133
50%BuTrz-COF-5	boronate ester	1080	0.684	2.426	133
50%PhTrz-COF-5	boronate ester	1001	0.810	2.134	133
50%EsTrz-COF-5	boronate ester	996	0.898	2.274	133
5%PyTrz-COF-5	boronate ester	1906	1.212	2.892	133
10%PyTrz-COF-5	boronate ester	1674	1.065	2.424	133
25%PyTrz-COF-5	boronate ester	674	0.610	2.212	133
ZnPc-COF	boronate ester	1300	0.79	2.3	133
10%N_3-ZnPc-COF	boronate ester	1051	0.70	2.3	133
25%N_3-ZnPc-COF	boronate ester	1000	0.66	2.2	133
50%N_3-ZnPc-COF	boronate ester	886	0.63	2.1	133
$[C_{60}]_{0.3}$-ZnPc-COF	boronate ester	393	0.43	1.52	437
$[C_{60}]_{0.4}$-ZnPc-COF	boronate ester	129	0.21	1.40	437
$[C_{60}]_{0.5}$-ZnPc-COF	boronate ester	51	0.14		437
Ph-An-COF	boronate ester	1864	1.24	2.9	61
TPE-Ph-COF	boronate ester	962	0.5	1.3/1.6	117
BLP-2(H)	borazine	1178	0.59	0.64	215
MC-COF-TP-$E_1^1E_7^2$	boronate ester	1892		3.2	11
MC-COF-TP-$E_1^2E_7^1$	boronate ester	1534		2.9	11
MC-COF-TP-$E_1E_3E_7$	boronate ester	1887		2.9	11
MC-COF-NiPc-E_1E_7	boronate ester	672		2.6	11
Py-DBA-COF 1	boronate ester	1392	1.21	3.6	40
Py-MV-DBA-COF	boronate ester	1134	1.06	4.1	40
Py-DBA-COF 2	boronate ester	1354	1.21	4.3	40
FLT-COF-1	boronate ester	1180		3.7	468
FLT-COF-2	boronate ester	555		1.0	468
FLT-COF-3	boronate ester	515		2.0	468
TpBD-Me_2 COF	imine	3109		1.4	469
COF-366	imine	735	0.32	1.76	106
COF-366-Co	imine	1470		2.4	33
COF-300	imine	1360	0.72	0.72	50
IISERP-COF2	imine	557		1.9/2.1	249
DmaTph	imine	431		1.8	98
DhaTph	imine	1305	0.809	2	98
TpPa-1	imine	535		1.3	63
TpPa (microwave)	imine	725		1.3	196
TpPa-2	imine	339		1.4	63
TpBD	imine	537		1.7	63
TpPa-NO_2	imine	129		1.4	63
TpPa-F_4	imine	438		1.4	63
TpBD-$(NO_2)_2$	imine	295		1.7	63
TpBDMe$_2$	imine	468		1.4	63
TpBD-$(OMe_2)_2$	imine	330		1.4	63
COF-DhaTab	imine	1480		3.7	81
Tp-Azo	imine	1328		1.6−2.5	62
Tp-Stb	imine	422		1.6−2.5	62

https://dx.doi.org/10.1021/acs.chemrev.9b00550
Chem. Rev. 2020, 120, 8814−8933

Table 6. continued

COFs	linkage	S_{BET} (m^2 g^{-1})	pore volume (cm^3 g^{-1})	pore width (nm)	ref
TpPa-SO_3H	imine	215	0.431	1.45	442
TpPa-(SO_3H-Py)	imine	235	0.273	1.45	442
TpPa-Py	imine	370	0.281	1.48	442
TpBpy	imine	1667		2.1	442
Co-TpBpy	imine	450		2.1	470
COF-LZU1	imine	410		1.8	65
N-COF	imine	1700	0.84	1.1	235
ILCOF-1	imine	2723	1.21	2.3	110
TAPB-TFP	imine	567		2.6	471
*i*PrTAPB-TFP	imine	756		3.4	471
TAPB-TFPB	imine	229		4.0	471
*i*PrTAPB-TFPB	imine	391		5.0	471
TRITER-1	imine	716	0.32	1.7	472
RT-COF-1	imine	329	0.22	1.2	210
3D-Py-COF	imine	1290	0.72	0.59/0.89/1.05	57
HAT-COF	imine	486	0.708	1.13/1.52	35
dual-pore COF	imine	1771	3.189	0.73/2.52	36
DAB-TFP COF	imine	365			69
DAAQ-TFP COF	imine	435		2.0	69
EB-COF:Br	imine	774		1.66	68
EB-COF:F	imine	1002		1.84	68
EB-COF:Cl	imine	954		1.73	68
EB-COF:I	imine	616		1.56	68
4PE-2P COF	imine	2070	1.53	3.8	38
4PE-3P COF	imine	1000	0.844	4.5	38
4PE-TT COF	imine	1990	1.24	3.2	38
COF-BPDA	imine	477.76	0.47	1.27/3.18	39
SIOC-COF-1	imine	478.41	0.10	0.73/1.18/3.06	39
SIOC-COF-2	imine	46.13		1.13/1.38/3.27	39
NUS-10(G)	imine	69		0.84	67
Py-DHPh COF	imine	1895	1.45	1.99	37
Py-2,3-DHPh COF	imine	1932	1.51	1.95	37
Py-2,2′-BPyPh COF	imine	2349	1.85	2.45	37
Py-3,3′-BPyPh COF	imine	2200	1.49	2.52	37
CuP-PyTTPh COF	imine	1127	0.82	1.8	107
NiP-PyTTPh COF	imine	1070	0.76	1.8	107
ZnP-PyTTPh COF	imine	1026	0.75	1.8	107
CuP-2,3-DHPh COF	imine	1099	0.78	2.5	107
NiP-2,3-DHPh COF	imine	854	0.60	2.5	107
ZnP-2,3-DHPh COF	imine	1064	0.77	2.5	107
CuP-DHNAPh COF	imine	1656	1.38	2.8	107
CuP-BPyPh COF	imine	883	0.64	2.9	107
TPB-DMTP-COF	imine	2105	1.28	3.26	80
$[(S)\text{-Py}]_{0.17}$TPB-DMTP-COF	imine	1970	1.13	3.07	80
$[(S)\text{-Py}]_{0.34}$TPB-DMTP-COF	imine	1802	1.04	2.95	80
$[(S)\text{-Py}]_{0.50}$TPB-DMTP-COF	imine	1612	0.83	2.86	80
TTF-Ph-COF	imine	1014	1.22	2.2	238
TTF-Py-COF	imine	817	0.76	1.3	238
Py-An-COF	imine	1479	0.7	2.4	239
HPB-COF	imine	965	0.79	1.2	12
HBC-COF	imine	469	0.29	1.8	12
CuP-Ph COF	imine	926		2.5	108
CuP-TFPh COF	imine	979		2.5	108
CuP-Ph_{25} COF	imine	1389		2.5	108
CuP-Ph_{50} COF	imine	1287	1.11	2.5	108
CuP-Ph_{75} COF	imine	1185		2.5	108
H_2P-$DHPh_{25}$ COF	imine	186	0.1618	2.5	108
H_2P-$DHPh_{50}$ COF	imine	361	0.2617	2.5	108
H_2P-$DHPh_{75}$ COF	imine	843	0.5457	2.5	108
H_2P-$DHPh_{100}$ COF	imine	916	0.6317	2.5	108
CuP-$DHPh_{25}$ COF	imine	365	0.2733	2.5	108

https://dx.doi.org/10.1021/acs.chemrev.9b00550
Chem. Rev. 2020, 120, 8814−8933

Table 6. continued

COFs	linkage	S_{BET} (m^2 g^{-1})	pore volume (cm^3 g^{-1})	pore width (nm)	ref
CuP-$DHPh_{50}$ COF	imine	485	0.3037	2.5	108
CuP-$DHPh_{75}$ COF	imine	762	0.5696	2.5	108
CuP-$DHPh_{100}$ COF	imine	1094	0.7824	2.5	108
NiP-$DHPh_{25}$ COF	imine	337	0.2523	2.5	108
NiP-$DHPh_{50}$ COF	imine	681	0.4750	2.5	108
NiP-$DHPh_{75}$ COF	imine	861	0.6261	2.5	108
NiP-$DHPh_{100}$ COF	imine	951	0.6927	2.5	108
$[HO]_{25\%}$-H_2P-COF	imine	1054	0.89	2.5	246
$[HO]_{50\%}$-H_2P-COF	imine	1089	0.91	2.5	246
$[HO]_{75\%}$-H_2P-COF	imine	1153	0.96	2.5	246
$[HO]_{100\%}$-H_2P-COF	imine	1284	1.02	2.5	246
$[HO_2C]_{25\%}$-H_2P-COF	imine	786	0.78	2.2	246
$[HO_2C]_{50\%}$-H_2P-COF	imine	673	0.66	1.9	246
$[HO_2C]_{75\%}$-H_2P-COF	imine	482	0.54	1.7	246
$[HO_2C]_{100\%}$-H_2P-COF	imine	364	0.43	1.4	246
$[HC{\equiv}C]_{0}$-H_2P-COF	imine	1474		2.5	247
$[HC{\equiv}C]_{25}$-H_2P-COF	imine	1431		2.3	247
$[HC{\equiv}C]_{50}$-H_2P-COF	imine	962		2.1	247
$[HC{\equiv}C]_{75}$-H_2P-COF	imine	683		1.9	247
$[HC{\equiv}C]_{100}$-H_2P-COF	imine	426		1.6	247
$[Et]_{25}$-H_2P-COF	imine	1326		2.2	247
$[Et]_{50}$-H_2P-COF	imine	821		1.9	247
$[Et]_{75}$-H_2P-COF	imine	485		1.6	247
$[Et]_{100}$-H_2P-COF	imine	187		1.5	247
$[MeOAc]_{25}$-H_2P-COF	imine	1238		2.1	247
$[MeOAc]_{50}$-H_2P-COF	imine	754		1.8	247
$[MeOAc]_{75}$-H_2P-COF	imine	472		1.5	247
$[MeOAc]_{100}$-H_2P-COF	imine	156		1.1	247
$[AcOH]_{25}$-H_2P-COF	imine	1252		2.2	247
$[AcOH]_{50}$-H_2P-COF	imine	866		1.8	247
$[AcOH]_{75}$-H_2P-COF	imine	402		1.5	247
$[AcOH]_{100}$-H_2P-COF	imine	186		1.3	247
$[EtOH]_{25}$-H_2P-COF	imine	1248		2.2	247
$[EtOH]_{50}$-H_2P-COF	imine	784		1.9	247
$[EtOH]_{75}$-H_2P-COF	imine	486		1.6	247
$[EtOH]_{100}$-H_2P-COF	imine	214		1.4	247
$[EtNH_2]_{25}$-H_2P-COF	imine	1402		2.2	247
$[EtNH_2]_{50}$-H_2P-COF	imine	1044		1.9	247
$[EtNH_2]_{75}$-H_2P-COF	imine	568		1.6	247
$[EtNH_2]_{100}$-H_2P-COF	imine	382		1.3	247
$[Pyr]_{25}$-H_2P-COF	imine	960		1.9	167
$[Pyr]_{50}$-H_2P-COF	imine	675		1.6	167
$[Pyr]_{75}$-H_2P-COF	imine	86		1.4	167
$[Pyr]_{100}$-H_2P-COF	imine	63		1.4	167
NiP-COF	imine	1447		2.06	248
$[HC{\equiv}C]_{50\%}$-NiP-COF	imine	1219		1.88	248
$[HC{\equiv}C]_{100\%}$-NiP-COF	imine	975		1.63	248
$[TEMPO]_{50\%}$-NiP-COF	imine	264		1.6	248
$[TEMPO]_{100\%}$-NiP-COF	imine	5.2		1.4	248
$[N{=}N]_{25\%}$-TAPH-COF	imine	702	0.72	1.7	473
$[N{=}N]_{50\%}$-TAPH-COF	imine	560	0.64	1.4	473
$[N{=}N]_{75\%}$-TAPH-COF	imine	320	0.59	1.3	473
$[N{=}N]_{100\%}$-TAPH-COFs	imine	250	0.54	1.2	473
$[C{=}C]_{25\%}$-TAPH-COF	imine	680	0.70	1.7	473
$[C{=}C]_{50\%}$-TAPH-COF	imine	460	0.66	1.6	473
$[C{=}C]_{75\%}$-TAPH-COF	imine	390	0.55	1.3	473
$[C{=}C]_{100\%}$-TAPH-COF	imine	310	0.51	1.2	473
$[HO]_{0\%}$-Py-COF	imine	1697	1.51	2.2	112
$[HO]_{25\%}$-Py-COF	imine	1977	2.16	2.2	112
$[HO]_{50\%}$-Py-COF	imine	2153	2.29	2.2	112
$[HO]_{75\%}$-Py-COF	imine	2250	2.35	2.2	112

https://dx.doi.org/10.1021/acs.chemrev.9b00550
Chem. Rev. 2020, 120, 8814−8933

Table 6. continued

COFs	linkage	S_{BET} (m^2 g^{-1})	pore volume (cm^3 g^{-1})	pore width (nm)	ref
$[HO]_{100\%}$-Py-COF	imine	2362	2.72	2.2	112
$[Et_4NBr]_{25\%}$-Py-COF	imine	919	1.05	2.0	112
$[Et_4NBr]_{50\%}$-Py-COF	imine	700	0.99	1.6	112
PyTTA-BFBIm-iCOF	imine	1532	0.7	2.3	241
TPB-DMTP-COF	imine	1927	1.28	3.3	234
TTA-TTB-COF	imine	1733	1.01	2.2	234
TAPT-DHTA-COF	imine	2170	1.08	3.1	474
Py-a4T_{Me}-COF	imine	1000		3.1	475
BND-TFB COF	imine	2618		2.4	287
FS-COF	imine	1288		2.76	58
S-COF	imine	985		2.28	58
TP-COF	imine	919		2.90	58
CuP-SQ COF	squaraine	539	0.6410	2.1	216
CS-COF	phenazine	776	0.34	1.6	158
COF-42	hydrazone	710	0.31	2.3	71
COF-43	hydrazone	620	0.36	3.8	71
NUS-3	hydrazone	757		1.8	476
COF-LZU8	hydrazone	454	0.36	1.3	254
TFPT-COF	hydrazone	1603	1.03	3.4	83
TFPPy-DETHz-COF	hydrazone	1090	0.54	2.1	244
ACOF-1	azine	1176	0.91	0.94	73
HEX-COF1	azine	1214	0.62	1.1	124
COF-JLU2	azine	415	0.56	0.96	74
HP-COF-1	azine	1197	0.8	1.06/1.96	42
HP-COF-2	azine	804	1.07	1.26/1.89	42
Py-azine COF	azine	1210	0.72	1.76	111
N_0-COF	azine	702		2.4	85
N_1-COF	azine	326		2.4	85
N_2-COF	azine	1046		2.4	85
N_3-COF	azine	1537		2.4	85
PI-COF-1	imide	1027	0.53	2.9	49
PI-COF-2	imide	1297	0.67	3.3	49
PI-COF-3	imide	2346	1.34	5.1	49
PI-COF-4	imide	2403		1.3	54
PI-COF-5	imide	1876		1.0	54
3PD		505	0.36	1.27	274
3BD		478		1.33	274
3′PD		258		3.19, 4.52	274
2TPA		252		9.70	274
COF-316	dioxin	557		1.2	94
COF-318	dioxin	576		1.5	94
sp^2c-COF	C═C	692	0.30	1.88	114, 115
sp^2c-COF-2	C═C	322	0.14	2.38	115
sp^2c-COF-3	C═C	737	0.32	2.69	115
2D-CAP	C−C	539	0.35	0.6	275
PTM-H-COF	C−C	80		1.6	276
PTM-CORF	C−C	43		5.1	276
NTU-COF-2	imine/boronate ester	1619	0.86	2.5	88
HHTP-FPBA-TATTA	imine/boronate ester	1975	1.17	3.24	87
TATTA-FPBA	imine/boroxine	1015	0.54	2.34	87
CuPc-FPBA-ETTA	imine/boronate ester	557	0.28	1.53	87
CuPc-FPBA-PyTTA	imine/boronate ester	1541	0.85	2.03	87
CuPc-FPBA-TABPy	imine/boronate ester	667	0.67	2.21	87
CuPc-FPBA-ZnP	imine/boronate ester	642	0.41	2.01	87
CuPc-FPBA-TMBDA	imine/boronate ester	1141	0.70	3.11	87
CuPc-FPBA-DETHz	hydrazone/boronate ester	738	0.72	3.55	87
HHTP-FFPBA-TATTA	imine/boronate ester	1748	1.03	3.17	87
HHTP-DFFPBA-TATTA	imine/boronate ester	1697	1.02	3.17	87
TATTA-FFPBA	imine/boroxine	1582	0.78	2.32	87
TATTA-DFFPBA	imine/boroxine	1489	0.81	2.23	87

https://dx.doi.org/10.1021/acs.chemrev.9b00550
Chem. Rev. 2020, 120, 8814−8933

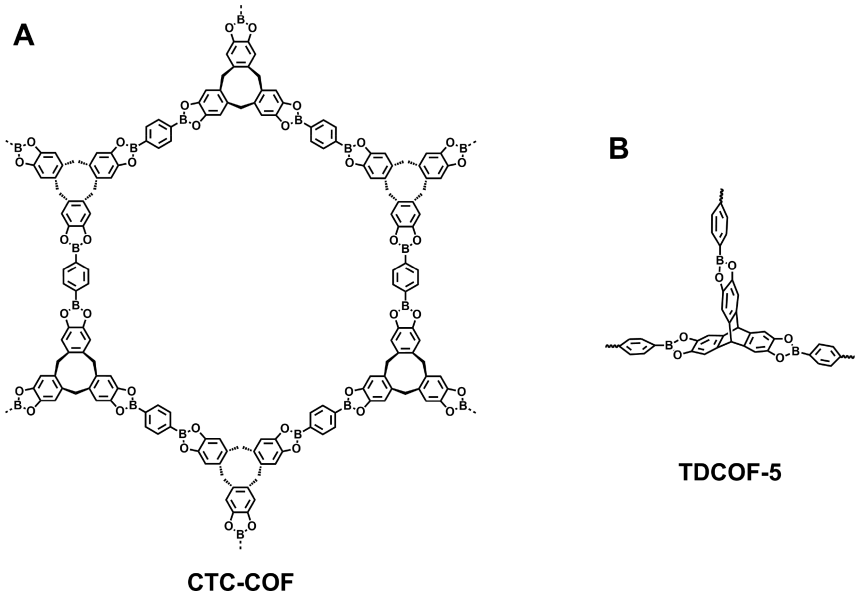

Figure 80. Schematics of (A) CTC-COF and (B) TDCOF-5.

reach 9200 m^2 g^{-1}.[110,465] These results indicate that COFs are highly porous materials whose surface area and pore volume are comparable to those other porous solids.[466] Table 6 summarizes the porosity of the main COFs reported. However, from these data, it is still difficult to elucidate a general trend to show a direct correlation between the structure and the porosity, even for COFs with the same linkage.

11.2. Pore-Surface Engineering

Besides the pore shape and size, the pore environment, that is, the pore surface on the pore walls, is crucial for triggering interactions between pores and guest ions and molecules, as the surfaces constitutes the interface that communicates with guests. How to create a special surface on the pore walls is of fundamental importance in developing pore chemistry for structural design and functional exploration. A general strategy has been established for designing tailor-made pore surfaces based on pore-surface engineering.[133,247] This strategy has four distinctive features: (1) It is widely applicable to various linkages, different topologies, and pore sizes; (2) it enables the integration of various functional units, including alkyl chains, polyelectrolyte chains, alcohols, esters, ethers, acid, base, photofunctional units, redox-active groups, catalytic sites, and so on; (3) it controls the composition and density of the functional groups; and (4) it develops the interface and simultaneously changes the porosity. By using a pore-surface engineering strategy, various pore interfaces can be designed and constructed; this greatly enhances our capability of designing pores to meet the specific requirements of interactions and functions. Owing to the availability of functional groups, this strategy offers a powerful tool to broaden the diversity and increase the complexity of porous structures of COFs. For example, pore-surface engineering allows for a systematic tuning of the pore surface by integrating various functional groups at desired contents on the pore walls, thus enabling the screening of impact of different groups on a specific function and property.[133] The hexagonal COF-5 and the tetragonal NiPc-COF with quantitative contents (5, 10, 25, 50, 75, and 100%) of the azide units appended at the 2,5-positions of BDBA edges have been designed and synthesized (Figure 14A,B). The azide groups can react with ethynyl groups via a click reaction to introduce various functional groups onto the pore walls. By using this method, a series of COFs with discrete contents of functional groups on the pore walls have been prepared, including a variety of alkyl chains and various aromatic units. The surface area of the hexagonal COF-5 family can be varied from 2160 to 36 m^2 g^{-1}, whereas the surface areas of the tetragonal NiPc-COF series are between 624 and 675 m^2 g^{-1}.

12. ADSORPTION AND SEPARATION

COFs enable the designed synthesis of porous structures through the topology diagram and pore-surface engineering, offering a unique porous platform for exploring molecular adsorption and separation. The adsorption and separation are highly dependent on the porous structures of COFs, that is, the pore size, pore shape, and pore environment. Over the past decade, great progress has been made along this aspect and has demonstrated the great potential of COFs in designing specific materials that can target specific molecules in terms of adsorption and separation.

Owing to their structural designability and diversity, COFs have been developed for various target molecules, from hydrogen to carbon dioxide, iodine, organic compounds, metal ions, and so on, offering a chemical tool to tackle environmental and energy issues.

12.1. Gas and Vapor Adsorption

12.1.1. Hydrogen Adsorption. Hydrogen adsorption using porous materials is an important subject related to green energy resources and fuel supply. COFs, with their low density and high surface area, show a potential for hydrogen capture with capacities of 0.3 7.2 wt % at 77 K, which are compatible to those of MOFs (the best one around 7.6 wt %),[477] porous polymers such as porous polymer networks (PPNs) (the best around 8.4 wt %),[478] polymers of intrinsic microporosity (PIMs) (the best around 4 wt %),[479] and hyper-cross-linked polymers (HCPs) (the best around 3 wt %).[480]

Owing to a larger surface area and pore volume, the H_2 uptake capacities of 3D COFs at 77 K are predicted to be 2.5 to 3 times higher than those of 2D COFs.[481] For example, 3D COF-102 (Figure 15A) with the BET surface area of 3620 m^2 g^{-1} and pore

https://dx.doi.org/10.1021/acs.chemrev.9b00550
Chem. Rev. 2020, 120, 8814−8933

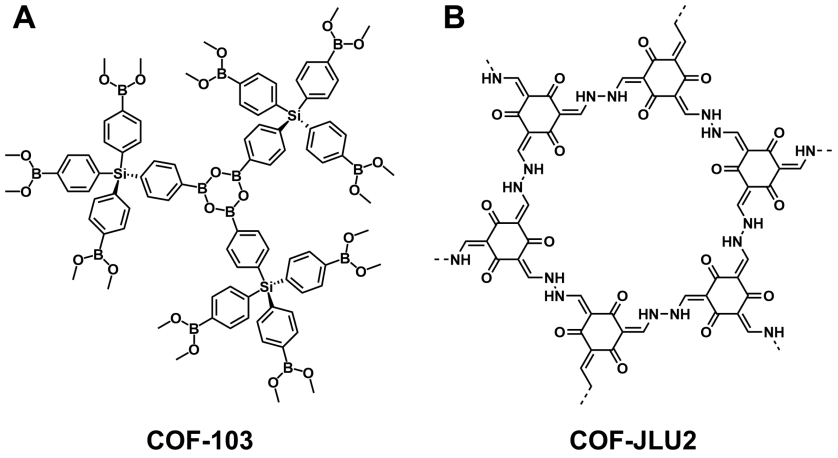

Figure 81. Schematics of (A) COF-103 and (B) COF-JLU2.

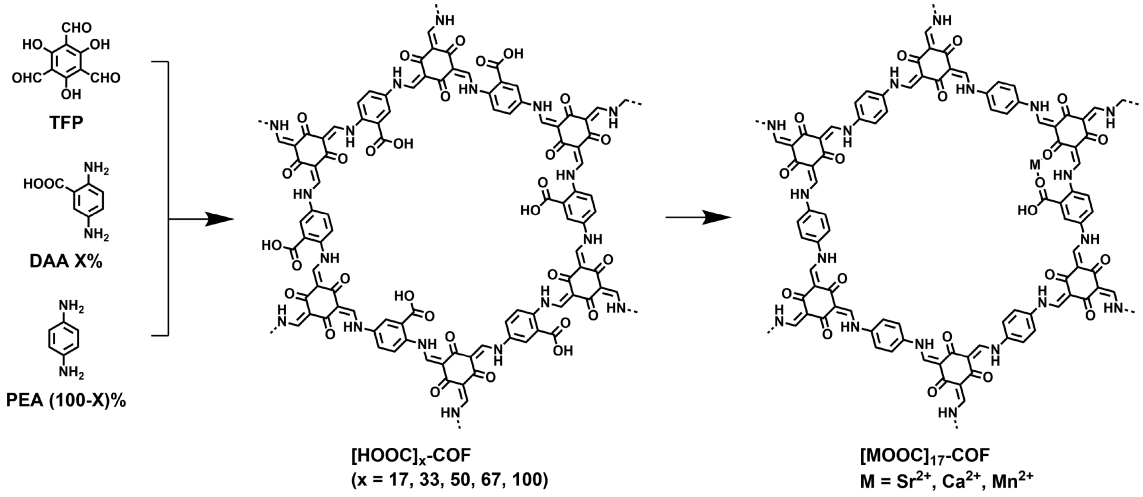

Figure 82. Schematics of $[MOOC]_{17}$-COF.

size of 1.2 nm exhibits the highest H_2 uptake capacity of 72.4 mg g^{-1} (7.24 wt %) at 77 K and 25 bar (saturation adsorption). In contrast, 2D COF-10 (Figure 73, S_{BET} = 1760 m^2 g^{-1}, pore size = 3.2 nm) exhibits a H_2 adsorption capacity of 39.2 mg g^{-1} (3.92 wt %) under otherwise identical conditions. Theoretical studies reveal that tetra-pyridine-bridged porphyrin-COF can reach a high gravimetric and volumetric uptake of 5 wt % and 20 gH_2/L due to its increased interlayer spacing and accessible volume for loading H_2.[482]

Interestingly, the bowl-shaped cyclotricatechylene (CTC) has been developed as knots to prepare 2D CTC-COF (Figure 80A) for low-pressure H_2 uptake.[119] The CTC-COF has a BET surface area of 1710 m^2 g^{-1} and a pore size of 2.26 nm. The H_2 uptake at 800 mmHg and 77 K is 1.12 wt %, which is higher than that of COF-10 and comparable to those of COF-102 and COF-103. The enhanced H_2 uptake capacity of CTC-COF is attributed to the additional adsorption in the bowl-shaped CTC cavity. Remarkably, a triptycene-knotted 2D TDCOF-5 (Figure 80B) with a BET surface area of 2497 m^2 g^{-1} and a pore size of 2.6 nm achieves a capacity of 1.6 wt % at 1 bar and 77 K, which is similar to that of COF-JLU2 and is the highest capacity among 2D and 3D COFs under this condition.[74,483] Clearly, how to increase the porosity and pore volume for exceptional H_2 uptake at 77 K is still a difficult task for the field of COFs. In particular, how to develop chemistry that enables the confinement of H_2 in the nanospace of COFs at a relatively high temperature deserves our further attention.

12.1.2. Methane Adsorption. Similar to the case of H_2 adsorption, methane adsorption requires a large pore volume and surface area. It is still a challenging subject for COFs to be designed with these features. At 298 K, the best uptake performance of amorphous porous polymer is 45 wt %,[484] as observed for PCN-68, whereas the best performance of MOFs is realized by MOF-210, which achieves a methane uptake of 48 wt %.[485]

3D COFs are superior to 2D COFs with respect to the CH_4 adsorption. The 3D COF-102 (Figure 15A) with a pore volume of 1.55 cm^3 g^{-1} and COF-103 (Figure 81A) with a pore volume of 1.54 cm^3 g^{-1} exhibit remarkable high-pressure CH_4 uptake capacities of 187 (18.7 wt %) and 175 mg g^{-1} (17.5 wt %), respectively, at 35 bar and 298 K, which are the highest among COFs.[256] On the contrary, 2D COF-5 with a pore volume of 1.07 cm^3 g^{-1} shows a CH_4 uptake capacity of 89 mg g^{-1} (8.9 wt %) under otherwise identical conditions, which is the highest among 2D COFs. At a low pressure, such as 1 bar, 2D COFs with small pores including ILCOF-1 (Figure 9A), ACOF-1 (Figure 7E), and COF-JLU2 (Figure 81B) achieve a considerable uptake capacity of 0.9, 1.15, and 3.8 wt %, respectively, at 273 K.[73,74,110] On the basis of grand-canonical Monte Carlo simulations, a COF with carbon−carbon-bonded triazine linkers in the **tbd**

https://dx.doi.org/10.1021/acs.chemrev.9b00550
Chem. Rev. 2020, 120, 8814−8933

Table 7. Typical Examples of COFs for CO_2 Capture[a]

COFs	linkage	S_{BET} (m^2 g^{-1})	pore width (nm)	pore volume (cm^3 g^{-1})	CO_2 uptake (mg g^{-1}) 273 K	CO_2 uptake (mg g^{-1}) 298 K	selectivity CO_2/N_2	Q_{st} (kJ mol^{-1})	ref
COF-1	boroxine	750	0.9	0.3	102	230[b]			481
COF-5	boronate ester	1670	2.7	1.07	62	870[b]			481
COF-6	boronate ester	750	0.9	0.32	170	310[b]			481
COF-8	boronate ester	1350	1.6	0.69	66	630[b]			481
COF-10	boronate ester	1760	3.2	1.44	54	1010[b]			481
COF-102	boroxine	3620	1.2	1.55	68	1200[b]			481
COF-103	boroxine	3530	1.2	1.54	76	1190[b]			481
APTES-COF-1	boroxine	490			46				335
ILCOF-1	imine	2723	2.3	1.21	62	35			110
TpPa-1	imine	535	1.3		160				64
TpPa-2	imine	339	1.4		126				64
TpPa-NO_2	imine	129	1.4		146				63
TpPa-F_4	imine	438	1.4		70				63
TpBD	imine	537	1.7		80				63
TpBD-Me_2	imine	468	1.4		74				63
TpBD-$(OMe)_2$	imine	330	1.4		54				63
TpBD-$(NO_2)_2$	imine	195	1.7		104				63
TpPa-COF (Microwave)	imine	725	1.3	1.1	218	87	32	34.1	196
TAPB-TFPB	imine	229	4.4		40				259
*i*PrTAPB-TFPB	imine	390.6	5.0		31				259
TAPB-TFP	imine	567	2.6		180				259
*i*PrTAPB-TFP	imine	756	3.4		105				259
N-COF	imine	1700	1.1	0.84	122.4	64.8			253
TH-COF-1	imine	684	1.1	0.74	128	97	19	31	255
TRITER-1	imine	716	1.7	0.32	589b	137[c]			472
3D-Py-COF	imine	1290	0.59	0.72	156		22.2	17.4	57
$[HO]_{25\%}$-H_2P-COF	imine	1054	2.5	0.89	54	31		32.2	246
$[HO]_{50\%}$-H_2P-COF	imine	1089	2.5	0.91	46	34		29.4	246
$[HO]_{75\%}$-H_2P-COF	imine	1153	2.5	0.96	52	32		31.5	246
$[HO]_{100\%}$-H_2P-COF	imine	1284	2.5	1.02	63	35	8	36.4	246
$[HO_2C]_{25\%}$-H_2P-COF	imine	786	2.2	0.78	96	58		38.2	246
$[HO_2C]_{50\%}$-H_2P-COF	imine	673	1.9	0.66	134	67		39.6	246
$[HO_2C]_{75\%}$-H_2P-COF	imine	482	1.7	0.54	157	72		41.2	246
$[HO_2C]_{100\%}$-H_2P-COF	imine	364	1.4	0.43	174	76	77	43.5	246
$[HC\equiv C]_0$-H_2P-COF	imine	1474	2.5		72	38		17.2	247
$[HC\equiv C]_{25}$-H_2P-COF	imine	1431	2.3		54	29		16.8	247
$[HC\equiv C]_{50}$-H_2P-COF	imine	962	2.1		48	26		16.5	247
$[HC\equiv C]_{75}$-H_2P-COF	imine	683	1.9		43	24		15.7	247
$[HC\equiv C]_{100}$-H_2P-COF	imine	426	1.6		39	20		15.3	247
$[Et]_{25}$-H_2P-COF	imine	1326	2.2		55	29		15.5	247
$[Et]_{50}$-H_2P-COF	imine	821	1.9		46	25		15.3	247
$[Et]_{75}$-H_2P-COF	imine	485	1.6		41	23		15.6	247
$[Et]_{100}$-H_2P-COF	imine	187	1.5		38	21		15.3	247
$[MeOAc]_{25}$-H_2P-COF	imine	1238	2.1		84	42		16.4	247
$[MeOAc]_{50}$-H_2P-COF	imine	754	1.8		88	47		17.1	247
$[MeOAc]_{75}$-H_2P-COF	imine	472	1.5		82	42		16.7	247
$[MeOAc]_{100}$-H_2P-COF	imine	156	1.1		65	34		17.8	247
$[AcOH]_{25}$-H_2P-COF	imine	1252	2.2		94	50		17.7	247
$[AcOH]_{50}$-H_2P-COF	imine	866	1.8		117	64		17.8	247
$[AcOH]_{75}$-H_2P-COF	imine	402	1.5		109	58		18.3	247
$[AcOH]_{100}$-H_2P-COF	imine	186	1.3		96	50		18.8	247
$[EtOH]_{25}$-H_2P-COF	imine	1248	2.2		92	50		18.2	247
$[EtOH]_{50}$-H_2P-COF	imine	784	1.9		124	71		19.7	247
$[EtOH]_{75}$-H_2P-COF	imine	486	1.6		117	63		19.2	247
$[EtOH]_{100}$-H_2P-COF	imine	214	1.4		84	44		19.3	247
$[EtNH_2]_{25}$-H_2P-COF	imine	1402	2.2		116	60		20.4	247
$[EtNH_2]_{50}$-H_2P-COF	imine	1044	1.9		157	82		20.9	247
$[EtNH_2]_{75}$-H_2P-COF	imine	568	1.6		133	67		20.8	247

https://dx.doi.org/10.1021/acs.chemrev.9b00550
Chem. Rev. 2020, 120, 8814−8933

Table 7. continued

COFs	linkage	S_{BET} (m^2 g^{-1})	pore width (nm)	pore volume (cm^3 g^{-1})	CO_2 uptake (mg g^{-1}) 273 K	CO_2 uptake (mg g^{-1}) 298 K	selectivity CO_2/N_2	Q_{st} (kJ mol^{-1})	ref
$[EtNH_2]_{100}$-H_2P-COF	imine	382	1.3		97	52		20.9	247
$[HO]_{25\%}$-TAPH-COF	imine	927	2.0	0.75	58	32	15	30.9	473
$[HO]_{50\%}$-TAPH-COF	imine	930	2.0	0.89	56	37	13	28.2	473
$[HO]_{75\%}$-TAPH-COF	imine	944	2.0	0.99	61	38	14	28.3	473
$[HO]_{100\%}$-TAPH-COF	imine	1056	2.0	1.02	62	38	16	31.1	473
$[N{=}N]_{25\%}$-TAPH-COF	imine	702	1.7	0.72	207	115	78	43.4	473
$[N{=}N]_{50\%}$-TAPH-COF	imine	560	1.4	0.64	112	67	49	36	473
$[N{=}N]_{75\%}$-TAPH-COF	imine	320	1.3	0.59	77	44	48	31	473
$[N{=}N]_{100\%}$-TAPH-COFs	imine	250	1.2	0.54	60	39	57	30.7	473
$[C{=}C]_{25\%}$-TAPH-COF	imine	680	1.7	0.70	61	40	18	30.3	473
$[C{=}C]_{50\%}$-TAPH-COF	imine	460	1.6	0.66	63	41	16	29	473
$[C{=}C]_{75\%}$-TAPH-COF	imine	390	1.3	0.55	55	34	22	28.7	473
$[C{=}C]_{100\%}$-TAPH-COF	imine	310	1.2	0.51	51	34	27	28.5	473
$[HO]_{25\%}$-Py-COF	imine	1977	2.2	2.16	91.7	72.4		16.9	112
$[HO]_{50\%}$-Py-COF	imine	2153	2.2	2.72	114.2	68.6		17.3	112
$[Et_4NBr]_{25\%}$-Py-COF	imine	1014	2.0	1.05	119.6	80.9		22.9	112
$[Et_4NBr]_{25\%}$-Py-COF	imine	879	1.6	0.99	164.6	87.3		28.7	112
TFPA−TAPB-COF	imine	540	1.72	0.25	61	33	13	21.1	233
BTMA−TAPA-COF	imine	630	1.59	0.32	84	45	16.8	24.6	233
TFPA−TAPA-COF	imine	660	1.59	0.32	105	52	21	28.4	233
TPE-COF-I	imine	1535	1.18	1.65	68.6	37.8			233
TPE-COF-II	imine	2168	1.19	2.14	118.8	60.5			233
ACOF-1	azine	1176	0.94	0.91	177	90	40	27.6	73
COF-JLU2	azine	410	0.96	0.56	217	165	77	31	74
HEX-COF1	azine	1214	1.1	0.62	200	120		42	124
Acac-CTF-5-400	azine	1131	2.5	0.90	126	83	38	23.0	499
Acac-CTF-10-400	azine	1150	2.5	0.95	135	86	20	25.5	499
Acac-CTF-5−500	azine	1556	2.5	1.20	145	87	45	28.6	499
Acac-CTF-10-500	azine	1626	2.5	1.60	139	84	21	23.6	499
NTU-COF-2	imine/boronate ester	1619	2.5	0.86	104			27.0	88

[a]CO_2 uptake at 1 bar unless marked otherwise. [b]CO_2 uptake at 55 bar. [c]CO_2 uptake at 5 bar.

topology is predicted to have the highest 65-bar deliverable capacity of 216 v STP/v, which can direct the structural design of COFs for CH_4 adsorption.[486]

12.1.3. Ammonia Adsorption. The boronate-ester-linked COFs are highly active for the storage of ammonia due to the strong Lewis acid−base interactions between the boron p_z open orbital and the nitrogen lone pair of ammonia.[487] For example, the boronate-ester-linked COF-10 (Figure 73) has the highest capacity of 15 mol kg^{-1} for ammonia capture at 298 K and 1 bar.[372] Notably, ammonia can be released by pumping and heating, and COF-10 can be reused three times in a reversible manner without a significant drop in capacity. The structural integrity of COF-10 is maintained after each cycle. These results suggest that the integration of specific interaction sites onto the pore walls of COFs is important in ammonia gas adsorption. Moreover, combining active groups, such as −N−H, —C═O, and carboxyl groups, and a metal site (e.g., Sr^{2+}), $[MOOC]_{17}$-COF (Figure 82) reaches an ammonia adsorption capacity of 14.3 and 19.8 mmol g^{-1} at 298 and 283 K, respectively, and the heat of adsorption (Q_{st}) is 91.2 kJ mol^{-1}.[488] The adsorption capacity is higher than those of many other sorbent materials such as 13X zeolite (9.0 mmol g^{-1}),[489] but it is still lower than the highest capacity of 19.79 mmol g^{-1}, as observed for Cu_2Cl_2BBTA.[490]

12.1.4. Carbon Dioxide Adsorption. Carbon dioxide (CO_2) is the main gas of the greenhouse effect, and its content in the atmosphere has continued to increase to reach 415 ppm at the present. How to reduce the carbon emission and mitigate the greenhouse effect is a subject of public concern. Different from other gases, CO_2 has no dipole moment but exhibits a high quadrupole moment. Using this basic feature of CO_2 in designing a porous structure to enhance interactions with CO_2 is necessary to increase the uptake capacity and selectivity. Owing to the combined features of the precise structural design and chemical stability, COFs offer a new platform for designing porous structures to store and separate CO_2; Table 7 summarizes the typical COFs developed for CO_2 capture and separation (Table 7).[491−494] In particular, total control over the surface area, pore size, and pore volume is critical in enhancing the capacity and selectivity. More importantly, incorporating functional groups that enhance interactions with CO_2 to the pore walls of COFs is an efficient way to facilitate CO_2 capture.[235,246,255,360,472,495,496] COFs are superior to most porous polymers (<60 mg g^{-1})[497] in CO_2 capture and are compatible with the best performing MOFs, such as Mg_2(dodbc) (360 mg g^{-1} at 298 K and 1 bar).[498]

12.1.4.1. Skeleton Design. To illustrate how the skeleton affects the CO_2 capture, a series of COFs with different skeletons but similar pore sizes and pore volumes have been designed. For this purpose, triphenylamine, triphenyl benzene, and triphenyl triazine units that are capable of interaction with CO_2 at different strengths have been developed as knots for the synthesis of

https://dx.doi.org/10.1021/acs.chemrev.9b00550
Chem. Rev. 2020, 120, 8814−8933

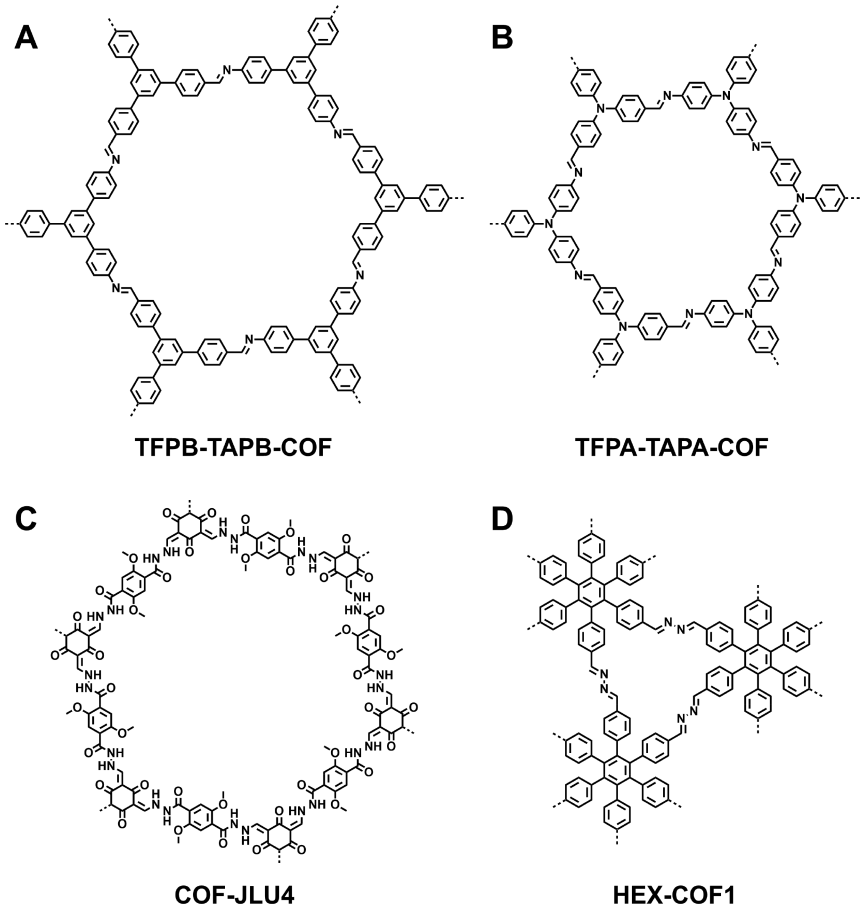

Figure 83. Schematics of (A) TFPB-TAPB-COF, (B) TFPA-TAPA-COF, (C) COF-JLU4, and (D) HEX-COF1 designed for CO_2 capture.

hexagonal microporous COFs. The CO_2 uptake capacity increases monotonically with the triarylamine content in COFs. Compared with the TFPB−TAPB−COF (Figure 83A) without any triarylamine units in the backbone, TFPA-TAPA-COF (Figure 83B) bearing six triarylamine units in the hexagon exhibits CO_2 uptakes of 52 and 105 mg g^{-1} at 298 and 273 K, respectively, which are more than four and five times higher than those of TFPB-TAPB-COF.[233] These comparative studies reveal that although a single triphenylamine unit has a limited interaction with CO_2, upon integration into the skeleton of COFs, the effect is amplified to an unexpected level that leads to a greatly enhanced uptake capacity. These results also indicate the importance of selecting suitable building blocks for designing COFs to store CO_2.

Besides building blocks, the design of the linkage is also key to the CO_2 adsorption. Azine-linked hexagonal microporous ACOF-1 (Figure 7E, pore size = 0.94−0.96 nm), COF-JLU2 (Figure 81B), COF-JLU3 (Figure 51), and COF-JLU4 (Figure 83C) have been designed and synthesized for CO_2 capture with excellent selectivity.[73,74] The BET surface areas of ACOF-1 and COF-JLU2 are 1176 and 415 m^2 g^{-1}, respectively. ACOF-1 and COF-JLU2 exhibit a CO_2 uptake capacity of 177 and 217 mg g^{-1}, respectively, at 273 K and 1 bar. The CO_2/N_2 selectivity is as high as 40 for ACOF-1 and 77 for COF-JLU2, respectively. Interestingly, the CO_2 capture capacity can be further enhanced by using the trigonal COF. A triangular HEX-COF1 (Figure 83D) with a surface area of 1200 m^2 g^{-1} and pore size of 1 nm exhibits a CO_2 uptake capacity of 200 mg g^{-1} at 273 K and 1 bar. The high uptake capacity for the azine-linked COFs originates from its small pore size and the presence of CO_2-philic nitrogen atoms as well as the quadrupole interactions with CO_2 triggered by nitrogen lone pairs in the azine linkages of COFs.[124]

12.1.4.2. Pore-Surface Engineering. Because CO_2 adsorption occurs on the pore walls, the chemical environment of pore walls is key to the capacity and selectivity. In this context, pore-surface engineering offers a versatile approach to integrate desirable functional groups onto the pore walls at designated contents for designing tailor-made interface for CO_2 capture. For example, the click reaction between the ethynyl groups on the pore walls and the functionalized azide compounds anchors various functional groups on the pore walls of the imine-linked porphyrin COFs (Figure 14C, $[HC{\equiv}C]_x$-H_2P, x = 25, 50, 75, and 100%).[247] Consequently, a series of $[R]_x$-H_2P COFs (R = Et, MeOAc, EtOH, AcOH, and $EtNH_2$) with different functional groups ranging from hydrophobic to hydrophilic and from basic to acidic, have been prepared in a predesigned manner. Among various functional groups, the amino unit is the best one in improving the CO_2 adsorption capacity. For example, $[EtNH_2]_{50\%}$-H_2P-COF with ethylamine groups on the pore walls exhibits an adsorption capacity of 157 mg g^{-1} at 273 K and 1 bar, which is three times greater than those of $[Et]_{50\%}$-H_2P-COF and $[HC{\equiv}C]_{50\%}$-H_2P-COF under otherwise identical conditions. These results suggest that pore-surface engineering provides a useful tool to design specific pore interfaces and to facilitate the CO_2 adsorption of COFs.

COFs with positively charged pore walls can improve the CO_2 adsorption. For example, an ionic-liquid-immobilized $[Et_4NBr]_{50\%}$-Py-COF (Figure 84A) exhibits an impressive

https://dx.doi.org/10.1021/acs.chemrev.9b00550
Chem. Rev. 2020, 120, 8814−8933

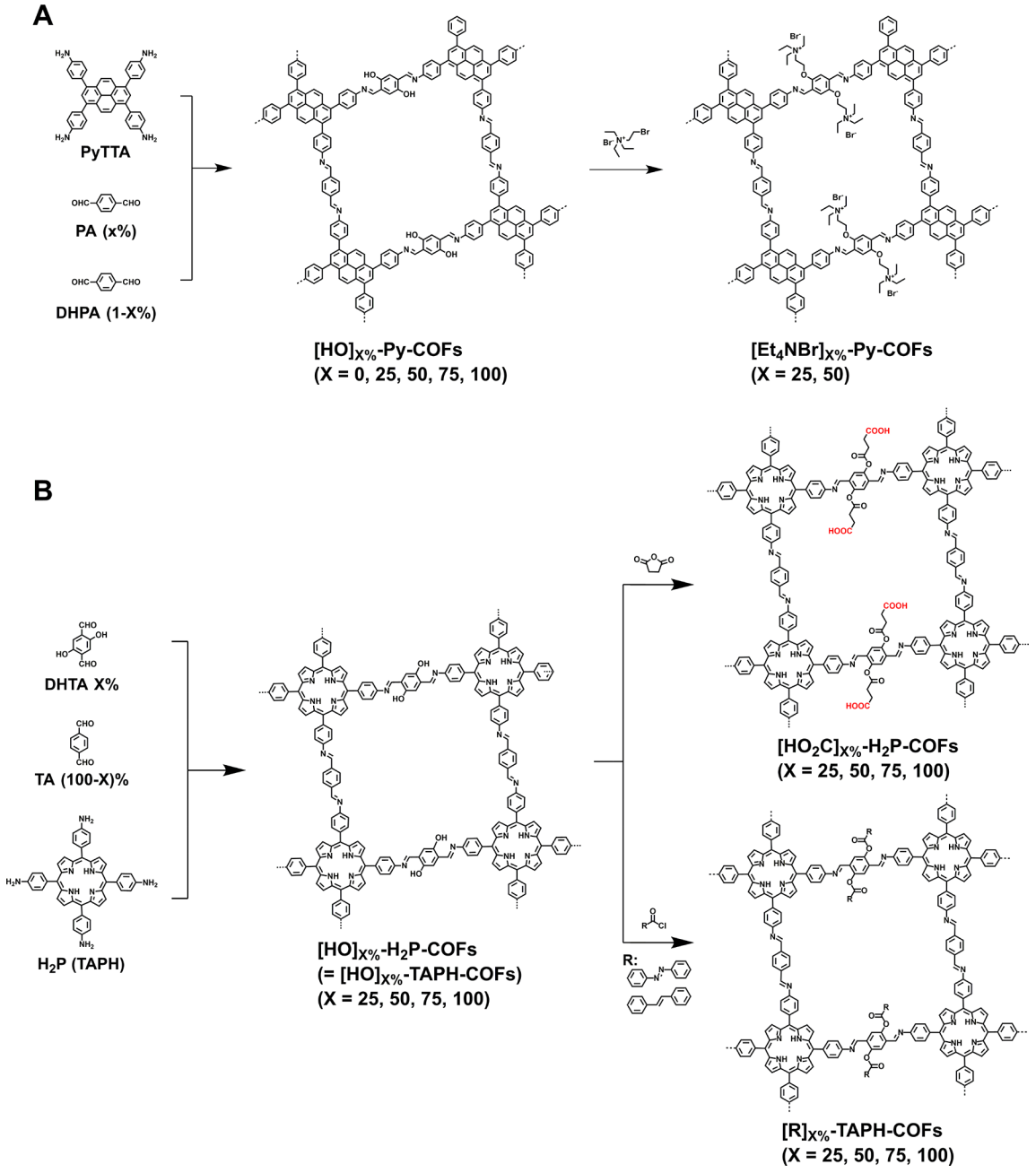

Figure 84. Schematics of pore-wall functionalization of (A) Py-COFs and (B) porphyrin-based COFs for efficient CO_2 capture.

CO_2 uptake capacity of 164.6 mg g^{-1} at 273 K and 1 bar.[112] On the contrary, functionalization with carboxylic acid groups is also effective to improve the CO_2 adsorption.[246] For example, the imine-linked porphyrin COFs (Figure 84B, $[HO_2C]_x$-H_2P-COFs, x = 25, 50, 75, and 100%) with carboxylic acid units on the pore walls exhibit a high CO_2 uptake capacity. These COFs are synthesized via channel-wall functionalization through a quantitative ring-opening reaction between the phenolic −OH units of $[OH]_x$-H_2P-COFs and succinic anhydride. A general tendency is that the CO_2 capture capacity of $[HO_2C]_x$-H_2P-COFs and the Q_{st} values increase with the increment of the carboxylic acid content. The $[HO_2C]_{100\%}$-H_2P-COF reaches a capacity of 174 mg g^{-1} at 273 K and 1 bar. Moreover, these COFs exhibit excellent cycle stability. Ideal adsorbed solution theory (IAST) calculations for $[HO_2C]_{100\%}$-H_2P-COF suggest that the breakthrough time is much longer than that of its precursor. A longer breakthrough time is desirable and important for efficient CO_2 capture and separation.

Azo units owing to the presence of nitrogen atoms can improve the CO_2 adsorption. For example, the azo-functionalized $[R]_x$-TAPH-COFs (Figure 76B, R = PhAzo or "N=N", x = 25, 50, 75, and 100%) improve the CO_2 uptake capacity owing to the CO_2-philicity and N_2-phobicity of the 4-phenylazobenzoyl (PhAzo) groups on the pore walls.[473] Among the series, $[N{=}N]_{25\%}$-TAPH-COF exhibits a remarkable CO_2 uptake capacity as high as 207 mg g^{-1} at 273 K. A further increment of the azo content causes a decrease in the capacity owing to a decreased surface area, indicating the importance of a balance between enough porosity and functionalization.

In short, these typical examples demonstrate that the introduction of amine, azo, ionic liquid, and carboxylic acid units onto the pore walls of COFs promotes the electrostatic

https://dx.doi.org/10.1021/acs.chemrev.9b00550
Chem. Rev. 2020, 120, 8814−8933

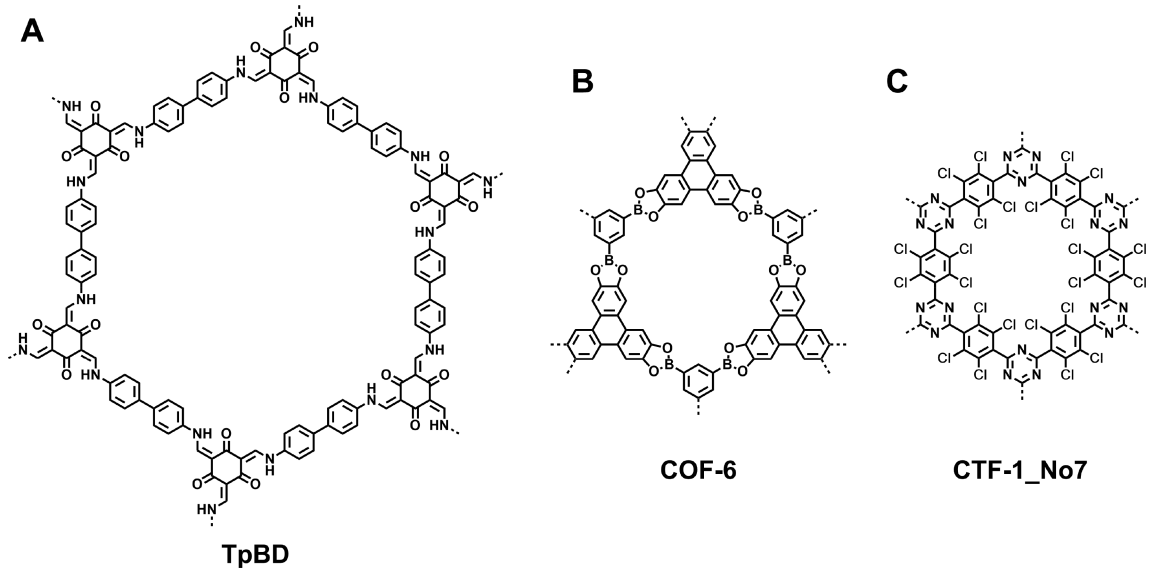

Figure 85. Schematics of (A) TpBD, (B) COF-6, and (C) CTF-1_No7.

hydrogen-bonding and quadrupole interactions with CO_2, which serve as a key driving force in facilitating CO_2 uptake.

12.2. Gas Separation

Gas separation technology by using porous membranes is a kinetics-based process that relies on differences in the diffusion rates of gas molecules across the membrane materials, which offers an energy-saving process for replacing the traditional distillation method. COFs are usually obtained as insoluble and unprocessable microcrystalline powders and are difficult process into well-defined membranes. A simple route to introduce COFs materials into membrane-based applications is to incorporate COFs into a processable polymer matrix to make hybrid membranes. The feature of this strategy is that it combines film processability with separation selectivity. Distinct from other porous solids, COFs have two advantages. One is that COFs can be rationally designed using different structures and compositions to achieve stability. Another is that the broad diversity of building blocks and linkages provides an attractive platform for pore-wall surface engineering, which could create tailor-made interfaces to manage the interactions with the gas molecules for separation.

12.2.1. COF-Based Membranes. The azine-linked NUS-2 (= COF-JLU-2; Figure 81B) and hydrazone-linked NUS-3 (= COF-JLU-4; Figure 83C) have different pore sizes of 0.9 (S_{BET} = 415 $m^2\ g^{-1}$) and 2.1 nm (S_{BET} = 757 $m^2\ g^{-1}$), respectively.[476] Both COFs can be exfoliated into nanosheets and form membranes upon mixture with commercially available poly(ether imide) (Ultem) or polybenzimidazole (PBI), forming homogeneous textures due to the compatibility between COFs and polymer matrices. The CO_2 uptake capacity of both COFs is much higher than those of other gases such as CH_4 and H_2 under otherwise identical conditions. On the basis of single gas sorption isotherms, IAST calculations suggest that NUS-2 for a mixture of equimolar binary gases exhibits a CO_2/CH_4 selectivity of 58.8 and a CO_2/H_2 selectivity of 116.8, respectively, at 273 K and 1 bar, whereas those of NUS-3 are only 29.3 and 22.0, respectively. Notably, the gas permeability (P) can be described as $P = S \times D$, where S is the solubility of specific gas molecules in the polymer matrix and D is the diffusivity of the gas. Adding COFs into the polymer matrix greatly enhances the D value because the free volume of membranes is dramatically increased. Membranes with different thicknesses of 50−100 μm, such as NUS-2@Ultem, NUS-3@Ultem, NUS-2@PBI, and NUS-3@PBI, have been demonstrated for CO_2/CH_4 and CO_2/H_2 separations. At low loading levels of COFs in Ultem, such as 10 and 20 wt %, the solubility and diffusivity of CO_2 increase as the loading content is increased. The further increment to a COF content of 30 wt % in NUS-2@Ultem enhances the CO_2 permeability to 7.98 ± 0.01 but reduces the CO_2/CH_4 selectivity to 16.7 under 5 bar, whereas both the permeability and selectivity are decreased to 8.38 ± 0.04 and 8.64 for NUS-3@Ultem under 5 bar. The decreased selectivity can be attributed to the fact that a high-content loading prohibits the formation of homogeneous membranes and leaves more defects in the membranes. NUS-2/NUS-3@PBI at a 20 wt % loading content achieves a high H_2 permeability of 4.08 ± 0.03 and a H_2/CO_2 selectivity of 31.4 under 5 bar, which surpasses the 2008 Robeson upper bound.

A series of TpPa-1@PBI-BuI (TpPa-1, Figure 62A) and TpBD@PBI-BuI hybrid COF (TpBD, Figure 85A) flexible membranes have been prepared by using substituted PBI (PBI-BuI) as a matrix.[467] The gas permeance (H_2, N_2, CH_4, and CO_2) of COFs(n)@PBI-BuI (n = 20, 40, and 50%, thickness = 47−80 μm) has been tested at 308 K and 20 atm upstream pressure. Interestingly, the H_2 and CO_2 permeabilities of these hybrid membranes increase almost linearly with the increased COF loading content. The H_2 permeability increased from 6.2 (for pristine PBI-BUI) to 18.8 barrer for the TpPa-1(40)@PBI-BuI hybrid membrane. These results correspond to an enhanced H_2/CH_4 selectivity from 155 to 165.5 and an improved H_2/N_2 selectivity from 69 to 79.

Theoretically, after the computational screening of 298 COFs membranes, including 41 3D COFs with **ctn**, **bor**, **dia**, or **pts** topology, as well as 268 2D COFs with triangular, square, hexagonal, octagonal, heteromorphic, or hybrid pores, three types of structural features of COFs are analyzed and summarized for high-performance CO_2/CH_4 separation.[500] COFs with extremely small pores (3.3 Å < pore-limiting diameter (PLD) < 3.8 Å), staggered stacking 2D-COFs, and interpenetrated 3D-COFs as well as skeletons of COFs with CO_2-favorable interaction sites are predicted to achieve $CO_2/$

https://dx.doi.org/10.1021/acs.chemrev.9b00550
Chem. Rev. 2020, 120, 8814−8933

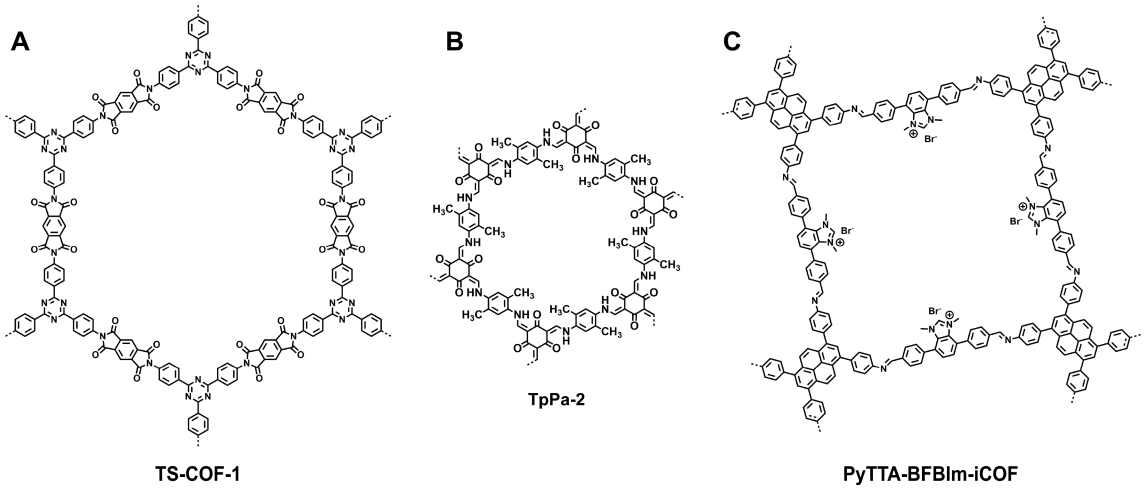

Figure 86. Schematics of (A) TS-COF-1, (B) TpPa-2, and (C) PyTTA-BFBIm-iCOF.

CH_4 separation over Robeson's upper bound. Specifically, COF-6 (Figure 85B) displays the lowest CO_2/CH_4 membrane selectivity of 3.88, whereas the −Cl-functionalized CTF-1_No7 membrane (Figure 85C) exhibits the highest CO_2/CH_4 selectivity of 187.87 with the largest Q_{st} value of 18.9 kJ/mol among all of the investigated COF samples.

12.2.2. COF−COF Composite Membranes. The COF-LZU1-ACOF-1 (COF-LZU1, Figure 21A; ACOF-1, Figure 7E) bilayer membrane displays desirable hydrogen selectivity. Owing to the formation of interlaced pore networks, the mixed gas selectivities of the COF-LZU1-ACOF-1 for equimolar H_2/CO_2, H_2/N_2, and H_2/CH_4 gas pairs are 24.2, 83.9, and 100.2, respectively, which are much higher than those of two pure COF membranes (6.1, 8.6, and 9.7 for COF-LZU1 membrane as well as 14.1, 21.6, and 24.7 for ACOF-1 membrane).[329]

12.2.3. COF−MOF Composite Membranes. COF−MOF composite membranes have been fabricated by mixing COF-300 (Figure 15D) with $Zn_2(bdc)_2(dabco)$ and ZIF-8, respectively.[330] The [COF-300]-[$Zn_2(bdc)_2(dabco)$] composite membrane for the separation of a binary gas mixture of H_2/CO_2 (1/1 vol) at room temperature and 1 bar exhibits a H_2/CO_2 selectivity of 12.6, which is higher than those of COF-300 (6.0) and $Zn_2(bdc)_2(dabco)$ (7.0) membranes. Similarly, the [COF-300]-[ZIF-8] composite membrane exhibits an enhanced H_2/CO_2 selectivity of 13.5, which is higher than that of the COF-300 membrane (6.0) and the ZIF-8 membrane (9.1). The superior gas separation performance of the [COF-300]-[ZIF-8] composite membrane is attributed to the formation of chemical bonds between different components (support, COF, MOF) in the membranes. The interlayer in the composite membrane between COF-300 and ZIF-8 is built up from COF-300 nanocrystallite and amorphous MOF material in which MOF fills up the space between the COF-300 nanocrystallites.

12.3. Iodine Adsorption

To show the potential of 1D channels of 2D COFs for molecular adsorption, 2D COFs with various building blocks, topologies, and pore sizes have been designed and synthesized for the adsorption of iodine. Surprisingly, with the 1D open channels that are free of pore jams and path blockings, COFs exhibit an exceptional high capacity and speedy capture of iodine, whose isotopes ^{127}I and ^{129}I are radioactive pollutants as a byproduct of nuclear plants.[234,501−503] "Soft" 3D COF-DL229 (= COF-300, Figure 15D) can trigger structural fitting to iodine while keeping the covalent connectivity and degree of interpenetration, achieving an uptake capacity of 8.24 g g^{-1},[503] which outperforms other porous materials such as PAF-24 (7.3 g g^{-1})[504] and ZIF-8 (5.56 g g^{-1}).[505]

2D COFs with mesoporous 1D channels are fully accessible to iodine, leading to exceptional uptake capacity.[234] After being exposed to iodine vapor at 350 K under ambient pressure, TPB-DMTP-COF (Figures 16O and 21B) with a size of 3.3 nm and a pore volume of 1.28 cm^3 g^{-1} can reach its adsorption saturation in 48 h, achieving an exceptional capacity of 6.26 g g^{-1}, which is >99% of its theoretical maximum (6.3 g g^{-1}) and is the highest value reported for porous materials. Notably, TPB-DMTP-COF can retain its >97% pore accessibility after five cycles upon recycling through a methanol rinse of the iodine-captured COF samples. Detailed studies using hexagonal mesoporous TTA-TTB-COF (Figure 21C) with a pore size of 2.2. nm and a pore volume of 1.01 cm^3 g^{-1} reveal that the 1D channels can be fully occupied by iodine to reach a capacity of 5.0 g g^{-1}. To investigate if the microporous 1D channels show the same features, a hexagonal TTA-TFB COF (= N_3-COF, Figure 70D) with a pore size of 1.6 nm and a pore volume of 0.55 cm^3 g^{-1} and a tetragonal TFBCz-PDA COF (= Cz-COF1, Figure 64B) with a pore size of 1.5 nm and a pore volume of 0.74 cm^3 g^{-1} have been synthesized. Notably, the TTA-TFB COF and TFBCz-PDA COF achieve capacities of 2.78 and 3.7 g g^{-1}, respectively. Moreover, a dual-pore kagome-type ETTA-TPA COF (= 4PE-1P COF, Figure 10C) with pore sizes of 1.4 and 2.7 nm and a pore volume of 0.95 cm^3 g^{-1} exhibits an iodine capture capacity of 4.7 g g^{-1}. All of these values are close to the theoretical uptake maxima based on their pore volumes of corresponding COFs, indicating that 1D channels are fully accessible to guest molecules. These results suggest a general strategy for designing COFs for molecular uptake, that is, to enhance the pore volume, as it determines the maximum uptake capacity.

12.4. Organic Compound Adsorption and Separation

Contributing to the high density of heteroatoms in the pore walls, imide-linked mesoporous TS-COF-1 (Figure 86A) with a pore volume of 0.90 cm^3 g^{-1} exhibits a high capacity of 1691 mg g^{-1} for the adsorption of cationic methylene blue dye.[506] The TpPa-2-COF/polysulfone mixed membrane (Figure 86B, TpPa-2-COF) shows a retention of organic foulants of >90%.[507] The self-standing ketoenamine COF-TpBD mem-

https://dx.doi.org/10.1021/acs.chemrev.9b00550
Chem. Rev. 2020, 120, 8814−8933

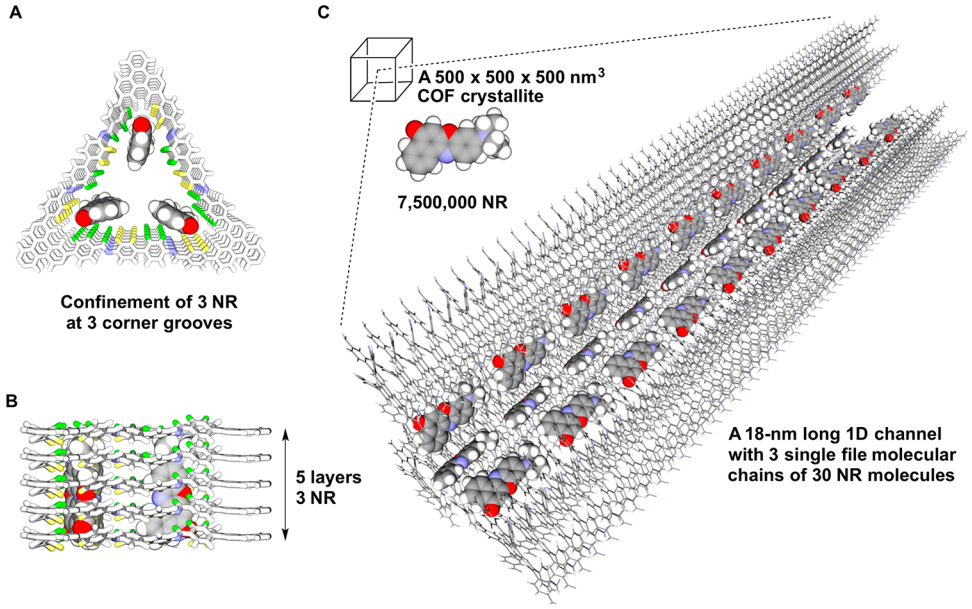

Figure 87. Schematics of the size recognition and nanoconfinement process by HFPTP-BPDA-COF: reconstructed structure of (A) top and (B) side views of three NR molecules in a 15.5 Å triangular channel over five layers and with 1.8 nm length. (C) Cubic HFPTP-BPDA-COF crystallite with dimensions of 500 × 500 × 500 nm^3 confines over 7 500 000 NR molecules. Inset: a reconstructed triangular channel structure in 50 layers over 18 nm length for the confinement of 30 NR molecules into three single-file molecular chains at its nanogrooves.

brane (Figure 85A) can remove organic dyes from water. It rejects anionic Rose Bengal (RB) to the extent of 99%, whereas for anionic Congo Red (CR) and methylene blue (MB), the rejection values are 96 and 94% respectively.[508]

COFs with positively charged walls, that is, PyTTA-BFBIm-iCOF (Figure 86C), have been designed. Owing to the charged walls, PyTTA-BFBIm-iCOF powder can remove anionic methyl orange with a capacity as high as 553 mg g^{-1} at room temperature to reach >99.9% removal efficiency.[241] In contrast, PyTTA-BFBIm-iCOF does not uptake neutral or cationic organic dyes, showing a great selectivity based on electrostatic interactions. Moreover, PyTTA-BFBIm-iCOF exhibits a high adsorption efficiency (pseudo-second-order $k = 5.32 \times 10^{-2}$ g mg^{-1} min^{-1}). This value is two orders of magnitude greater those of other porous materials such as MOF-235 ($k = 7.67 \times 10^{-4}$ g mg^{-1} min^{-1}).[509]

Because of the weak dipole interaction between aprotic solvents and the charged interface aligned on the channel walls, the cationic EB-COF:Br (= EB-TFP iCOF, Figure 60A) membrane exhibits excellent permeance toward protic solvents and organic aprotic solvents, including deionized water (546 L m^{-2} h^{-1} bar^{-1}), ethanol (564 L m^{-2} h^{-1} bar^{-1}), acetone (2640 L m^{-2} h^{-1} bar^{-1}), THF (1532 L m^{-2} h^{-1} bar^{-1}), and DMAc (565 L m^{-2} h^{-1} bar^{-1}).[510] The EB-COF:Br membrane has an excellent selective sieving performance for different dye molecules/ions, which is mainly attributed to their positively charged sites on the walls as well as small pores. To be specific, it can reject anionic dyes MO, fluorescein sodium salt (FSS), and potassium permanganate (PP) up to 99.6, 99.2, and 98.1%, respectively. The rejection values of cationic dyes RB, MB, and *N*,*N*-dimethyl-*p*-phenylenediamine dihydrochloride (DMPD) are 91.2, 87.2, and 84.9%, respectively, whereas for the neutral dyes of calcein (CA), Nile Red (NR), and *p*-nitroaniline (NA), the rejection values are 74.4, 22.3, and 15.7%, respectively. Compared with other reported membranes for nanofiltration, the EB-COF:Br membrane exhibits a high rejection of 99.6% toward small molecules such as MO (0.52 × 1.46 nm^2), whereas other porous materials are used for large molecules. For example, ZIF-8/PES rejects Rose Bengal (1.2 × 1.54 nm^2) at 98.95%,[511] and ZIF-8/PA 99.98% rejects Congo Red (0.7 × 1.9 nm^2);[512] these molecules are larger than MO.

The above separation of organic dyes/compounds is dominated by electrostatic interactions between guests and charged pore walls. How to develop the porous space of COFs for precise molecular separation, especially size-exclusive separation, remains a challenge. Recently, the 1D channels of COFs have been developed for size-exclusive molecular separation.[125] A trigonal COF, that is, HFPTP-BPDA-COF (Figure 11D), has been engineered to possess a superlattice of 1D channels with a persistent triangular shape and a discrete pore size that enable accurate size recognition. HFPTP-BPDA-COF is synthesized by the topology-directed polycondensation of the C_3-symmetric HFPTP and the C_2-symmetric BPDA under solvothermal conditions. HFPTP-BPDA-COF exhibits a BET surface area of 1024 m^2 g^{-1} and possesses trigonal 1D channels. HFPTP-BPDA-COF enables the size recognition of nanosized organic compounds, including NR, coumarin 6 (C6), and 7-(diethylamino)-3-phenylcoumarin (DAPC); these compounds are similar in the π-backbone, are bulky enough to contain more than 40 atoms, and have a difference of only one atom between NR and C6.

Notably, HFPTP-BPDA-COF allows the uptake of NR molecules while excluding C6 and DAPC completely; this size sieving is based on the slight difference in their molecular sizes. The uptake of NR by HFPTP-BPDA-COF is a very rapid process that completes within 2 min. Remarkably, HFPTP-BPDA-COF uptakes NR, even in the mixtures with C6 or DAPC, leading to the selective separation of these nanosized organic compounds. Interestingly, open columns of HFPTP-BPDA-COF allow an instant separation of mixtures to flush out C6 or DAPC in 2 min and yield 100% purity of each fraction and infinite selectivity. Porosity measurements confirm that the 1.5 nm sized 1D channels are occupied by NR molecules. Control experiments using the hexagonal and tetragonal COFs reveal

https://dx.doi.org/10.1021/acs.chemrev.9b00550
Chem. Rev. 2020, 120, 8814−8933

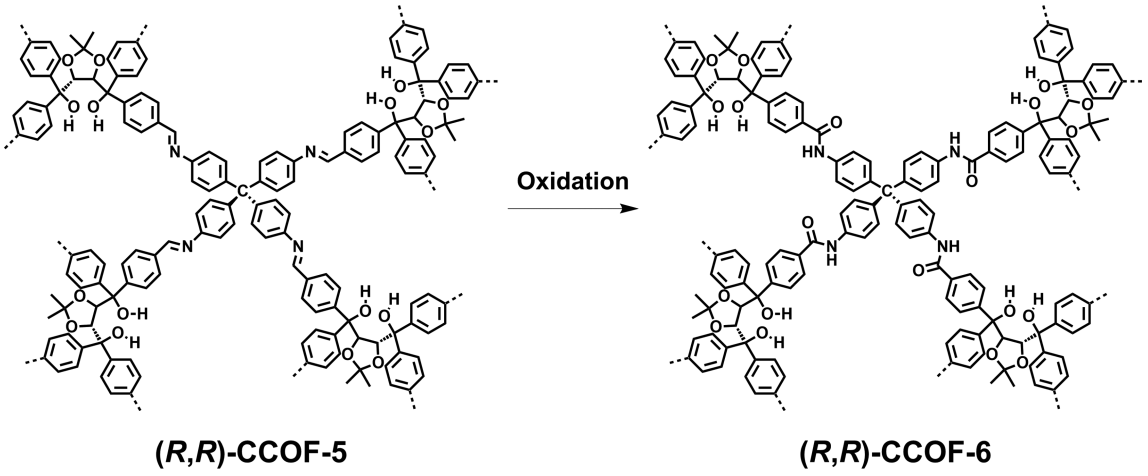

Figure 88. Schematics of (*R*,*R*)-CCOF-5 and (*R*,*R*)-CCOF-6.

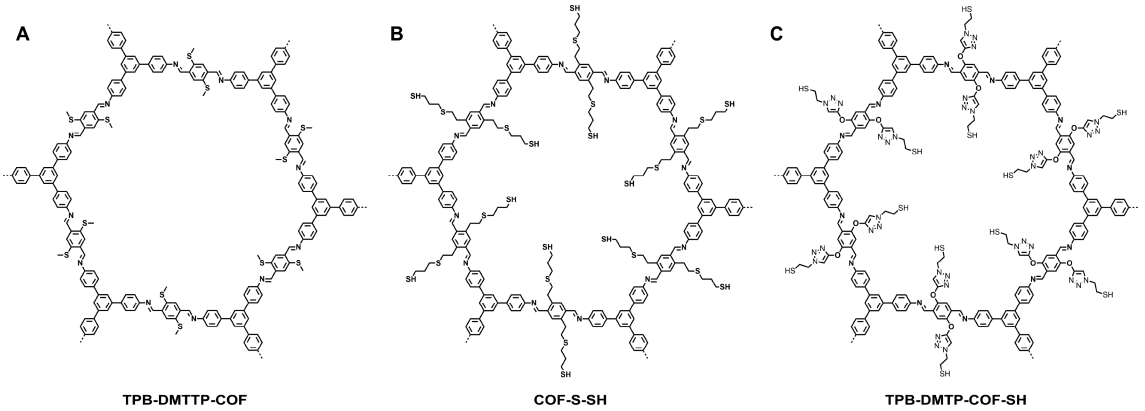

Figure 89. 2D COFs with different sites for mercury removal: (A) TPB-DMTTP-COF, (B) COF-S-SH, and (C) TPB-DMTP-COF-SH.

that the COF topology is key to this molecular separation; hexagonal and tetragonal COFs cannot separate these molecules.

A possible scenario of the molecular recognition is elucidated by molecular dynamics simulations at femtosecond precision based on a global minimum energy protocol. When approaching HFPTP-BPDA-COF, the guest molecules likely adopt an orientation with their π-backbones parallel to the π-surface of the COF to minimize the potential energy. If the size of guest molecules such as DARP and C6 is larger than the pore window, then the triangular aperture rejects their entry and leaves them in solution. After NR passes the window, it rotates in the 1D channels to assume a diving posture so that its π-backbone is parallel to the long axis of the 1D channels (Figure 87A,B). The NR molecules are then confined at the corner nanogrooves to form single-file molecular chains in the channel. These four successive processes are very quick and complete in 10 ps. Because each 15.5 Å sized 1D channel possesses three nanogrooves and can dock three single-file molecular chains, an 18 nm long 1D channel confines 30 NR molecules at three nanogrooves (Figure 87C). Indeed, a cubic HFPTP-BPDA-COF crystallite with dimensions of only 500 × 500 × 500 nm^3 can accommodate 7 500 000 NR molecules (Figure 87C, inset). This extraordinary uptake originates from the full accessibility of all channel corners. In this case, one NR molecule is locked by 9 C−H···π interactions with the C−H units and London dispersion forces from two neighboring walls. These multipoint interactions harvest a binding energy of 41.1 kcal mol^{-1}. On the contrary, virtually inserting C6 into the 1D channel results in a binding energy of 40.6 kcal mol^{-1}, which is the same level as that of NR. This result excludes the possibility of C6 entering the 1D channels.

12.5. Chiral Compound Separation

Recently, chiral 3D COFs have been developed as a stationary phase for liquid chromatography to enable enantioselective separation. (*R*,*R*)-CCOF-5 (Figure 88) has been synthesized via condensation of the tetrahedral TAPM with a tetraaldehyde derived from the chiral tetraaryl-1,3-dioxolane-4,5-dimethanols (TADDOLs).[52] It is further oxidized into amide-linked (*R*,*R*)-CCOF-6 (Figure 88). Racemic 1-phenyl-2-propanol can be successfully separated on a 3D-CCOF-5/silicon column with a good selectivity α of 1.19 and a chromatographic resolution R_s of 1.52 in 40 min. CCOF-6 exhibits an improved resolution compared with CCOF-5. It can baseline-resolve all racemates of 1-phenyl-2-propanol, 1-phenyl-1-pentanol, 1-phenyl-1-propanol, and 1-(4-bromophenyl)ethanol, affording α/R_s = 1.29/1.78, 1.21/1.58, 1.33/2.47, and 1.24/1.54, respectively. CCOF-5 and CCOF-6 are similar to other chiral stationary phases (CSPs) for high-performance liquid chromatography (HPLC). For example, *g*-CD MOF achieves α = 2.43 and R_s = 1.55.[513] Both CCOF-5 and CCOF-6 are more chemically stable than MOF-based CSPs in application.

Covalently immobilizing a series of biomolecules into achiral COFs is another efficient way to induce chirality into COFs. Through the coupling reaction between the amino units of

https://dx.doi.org/10.1021/acs.chemrev.9b00550
Chem. Rev. 2020, 120, 8814−8933

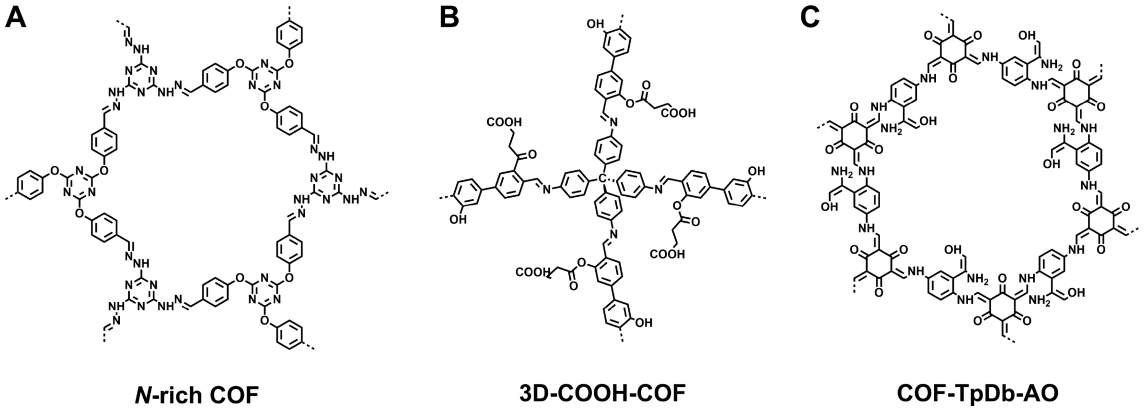

Figure 90. 2D COFs with different sites for binding metal ions in (A) *N*-rich COF, (B) 3D-COOH-COF, and (C) COF-TpDb-AO.

biomolecules and carboxylic acid groups of COFs, biomolecules, including lysozyme, tripeptide Lys-Val-Phe, and L-lysine, have been covalently linked to COFs to form biomolecules⊂COFs, and the leakages of peptide and L-lysine are only 6 and 7%.[514] The resulting biomolecules⊂COFs show a great potential for chiral separation. For example, lysozyme⊂COF 1 exhibits the highest separation efficiency for all tested racemates and separates benzoin to achieve excellent α and R_s values of 1.57 and 3.71, respectively.

12.6. Metal-Ion Adsorption

Developing novel materials that can remove heavy metal ions completely and efficiently is highly desirable nowadays. In relation to the aforementioned Hg(II) sensing, TPB-DMTTP-COF, COF-S-SH, and TPB-DMTP-COF-SH have been developed by integrating methyl sulfide and thiol units on the pore walls.[231,251,515] The TPB-DMTTP-COF (Figure 89A) exhibits an outstanding mercury removal capacity of 734 mg g^{-1}.[231] Owing to the resonance effect, it is extremely stable in aqueous solutions over a wide pH range, and it retains 92% capture efficiency after six cycles. This COF shows a highly selective removal of heavy metal ions, such as Hg(II) and Pb(II), whereas it is not active for other metals such as Zn(II), Fe(III), Mg(II), Ca(II), and K(I). In contrast, COF-S-SH (Figure 89B) exhibits a better Hg(II) removal capacity as high as 1350 mg g^{-1} and high Hg(0) uptake capacities of 863 mg g^{-1}.[411] COF-S-SH exhibits a high distribution coefficient K_d value of 2.3×10^9 mL g^{-1}, which allows it to rapidly reduce the Hg(II) concentration from 5 ppm to <0.1 ppb, even in the presence of a high concentration of background metal ions such as Ca(II), Zn(II), Mg(II), and Na(I). Integrating triazole and thiol groups via pore-wall surface engineering to the channel walls, TPB-DMTP-COF-SH (Figure 89C) exhibited the highest recorded saturation Hg(II) uptake capacity of 4395 mg g^{-1} with an exceptional distribution coefficient value K_d of 3.23×10^9, in which the triazole moiety contributes greatly to its outstanding sorbent efficiency.[515] Notably, TPB-DMTP-COF-SH exhibits high mercury removal capacity, even in the presence of other metal ions, including Na(I), Ca(II), Cu(III), Mg(II), or Zn(II). This COF functions well even in seawater to remove Hg(II). In a mixture of typical heavy metal ions, TPB-DMTP-COF-SH exhibits a high removal capacity for Hg(II) (98%) and Sn(II) (97%), a medium capacity for Pb(II) (49%), and a low capacity for Cd(II) (21%) and As(III) (19%). Moreover, TPB-DMTP-COF-SH has a higher uptake capacity than other sorbents functionalized with thio groups, such as PAF-1-SH (1014 mg g^{-1})[516] and MOS_2 nanosheets (2506 mg g^{-1}).[517] These COFs open a new avenue for the design of COFs for coping with environmental metal-ion pollutions. Similarly, *N*-rich THAT-TFPTA-COF (THAT = 2,4,6-tris(hydrazino)-1,3,5-triazine, TFPTA = tri-(4-formacylphenoxy)-1,3,5-triazine) (Figure 90A) exhibits excellent performance in Cd(II) removal with a high capacity of 396 mg g^{-1}.[518] Ketoenamine ACOF (= COF-JLU2, Figure 81B) exhibits high uptake capacities of 169 mg g^{-1} for U(VI) and of 175 mg g^{-1} for Hg(II).[519] ACOF with the C═O units enables strong coordination with metal ions. The selectivity of U(VI) increases as the pH is decreased and reaches 96.2% when the pH value is 1.5.

Other than Hg(II) removal, the selective extraction of lanthanide ions has been explored with carboxy-functionalized 3D-COOH-COF (Figure 90B).[520] Through a postsynthetic modification of a hydroxyl-functionalized 3D-OH-COF with carboxylic acid, the resulting 3D-COOH-COF exhibits an uptake capacity of 0.71 mmol g^{-1} for Nd(III), 0.72 mmol g^{-1} for Sr(II), and 4.86 mmol g^{-1} for Fe(III). The Nd(III) ion exhibits the highest affinity among these ions to yield Langmuir parameters of 15.87, 0.85, and 0.08 mm^{-1} for Nd(III), Sr(II), and Fe(III), respectively. After amidoximated by treatment with hydroxylamine in methanol, amidoxime-functionalized COF-TpDb-AO (Figure 90C) serves as a selective solid-phase sorbent for U(VI) capture.[521] At an initial concentration range of 23.1−265.2 ppm, COF-TpDb-AO reaches an adsorption capacity of 408 mg g^{-1}, which is 1.15 times as high as that of amorphous POP-TpDb-AO. Notably, COF-TpDb-AO exhibits a much steeper adsorption profile for U(VI) ions to achieve a high K_d value of 3.6×10^8 (0.14 ppb), which is more than an order of magnitude higher than that of the amorphous one.

12.7. Other Molecular Adsorption and Separation

The field of molecular adsorption and separation has recently attracted increasing attention. The predesignable pores of COFs makes them suitable for the adsorption of a broad diversity of molecules, including aromatic derivatives,[311,522,523] bisphenol chemicals,[524−527] peptides,[528,529] pharmaceutical pollutants,[526,530] arylene vinylene macrocycles,[531] as well as per- and polyfluorinated alkyl substances (PFASs).[532] COF-LZU-1 (Figure 21A) and COF-5 (Figure 7B) have been modified into fused silica and utilized as the stationary phase in electrochromatography.[311,522] Strong $\pi-\pi$ interactions between the COF stationary phase and guest molecules facilitate the separation of aromatic compounds, including alkyl benzenes, polyaromatic hydrocarbons, aniline derivatives, naphthalene, and 4-methylbiphenyl. Grafting COF-TpPa-1 (Figure 62A) onto the surface-modified Fe_3O_4 nanoparticles endows the

https://dx.doi.org/10.1021/acs.chemrev.9b00550
Chem. Rev. 2020, 120, 8814−8933

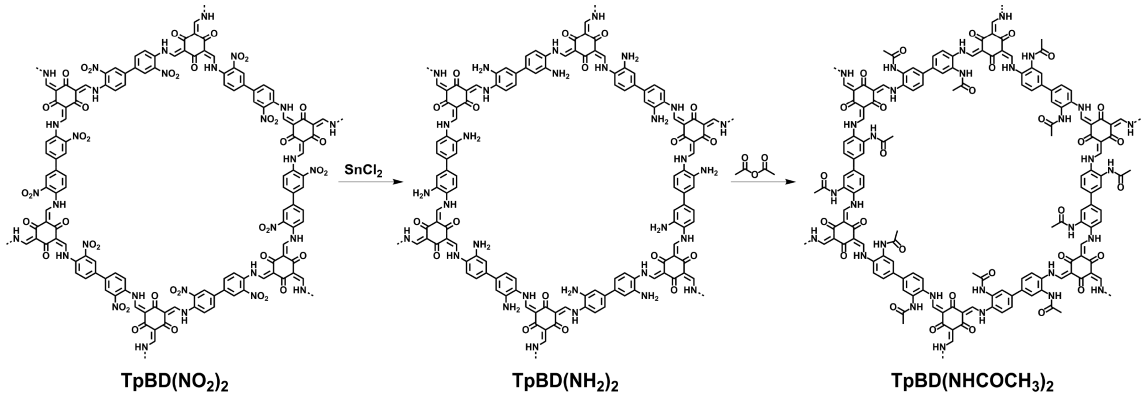

Figure 91. Schematics of sequential pore-wall modification of 2D COFs for lactic acid adsorption.

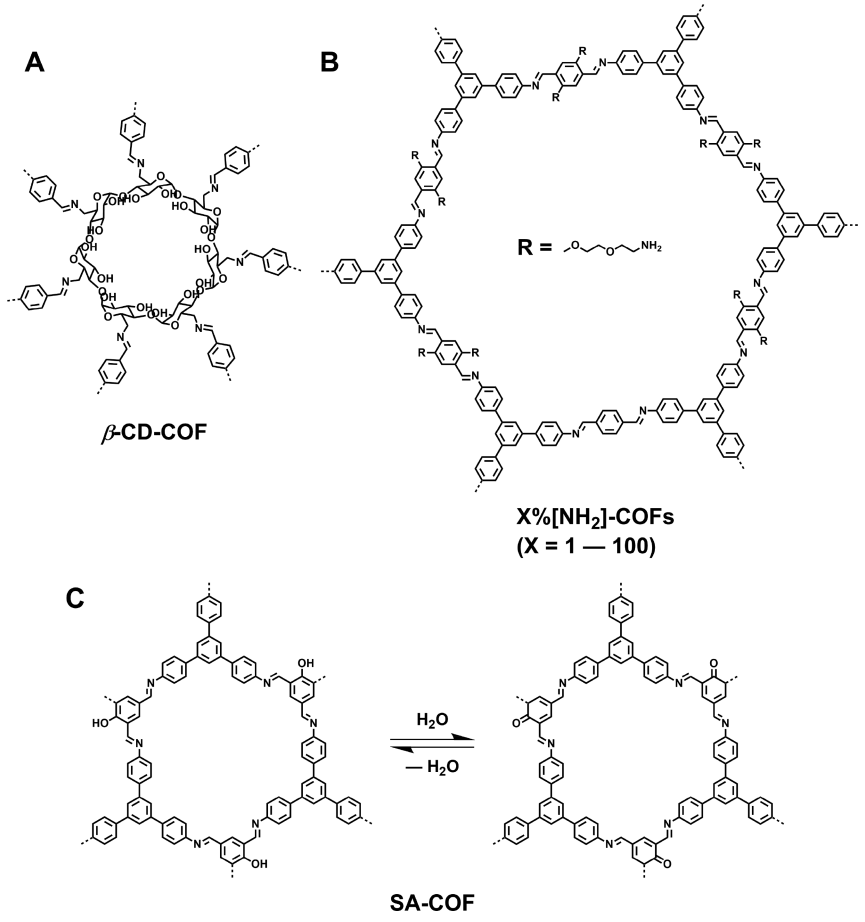

Figure 92. Schematics of (A) β-CD-COF, (B) X%[NH_2]-COFs, and (C) SA-COF.

hybrid with a large specific surface area, high porosity, and supermagnetism, making it an ideal sorbent to extract organic compounds with a benzene unit and amino or hydroxyl groups by using a magnetic field.[523] Through magnetic solid-phase extraction (MSPE), magnetic TpPa-1 can detect polycyclic aromatic hydrocarbons (PAHs) in the range from 0.24 to 1.01 ng L^{-1}.

The TpBD(NO_2)$_2$, TpBD(N_2H)$_2$, and TpBD($NHCOCH_3$)$_2$ COFs (Figure 91) have been applied for lactic acid (2-hydroxypropanoic acid) adsorption.[533] These COFs have been synthesized by sequential pore-wall modification (Figure 91). The lactic acid adsorption abilities of COFs can be monitored by high-performance liquid chromatography from aqueous solutions at their natural pH (pH 2.2 for an aqueous 0.1 M lactic acid solution). The amino-functionalized TpBD(N_2H)$_2$ exhibits the highest adsorption capacity of 6.6 wt % compared with TpBD($NHCOCH_3$)$_2$ (4.0 wt %) and TpBD(NO_2)$_2$ (2.5 wt %) as a result of the better affinity with lactic acid. Because lactic acid serves as both a hydrogen-bonding donor and acceptor, the amino $-NH_2$ groups in TpBD(N_2H)$_2$ or TpBD($NHCOCH_3$)$_2$ that act as both hydrogen-bonding donors and acceptors facilitate the adsorption of lactic acid, whereas TpBD(NO_2)$_2$ with only hydrogen-bonding accepting sites shows inferior adsorption ability. These results indicate that supramolecular interactions in the COF channels play a key role in the adsorption of lactic acid.

https://dx.doi.org/10.1021/acs.chemrev.9b00550
Chem. Rev. 2020, 120, 8814−8933

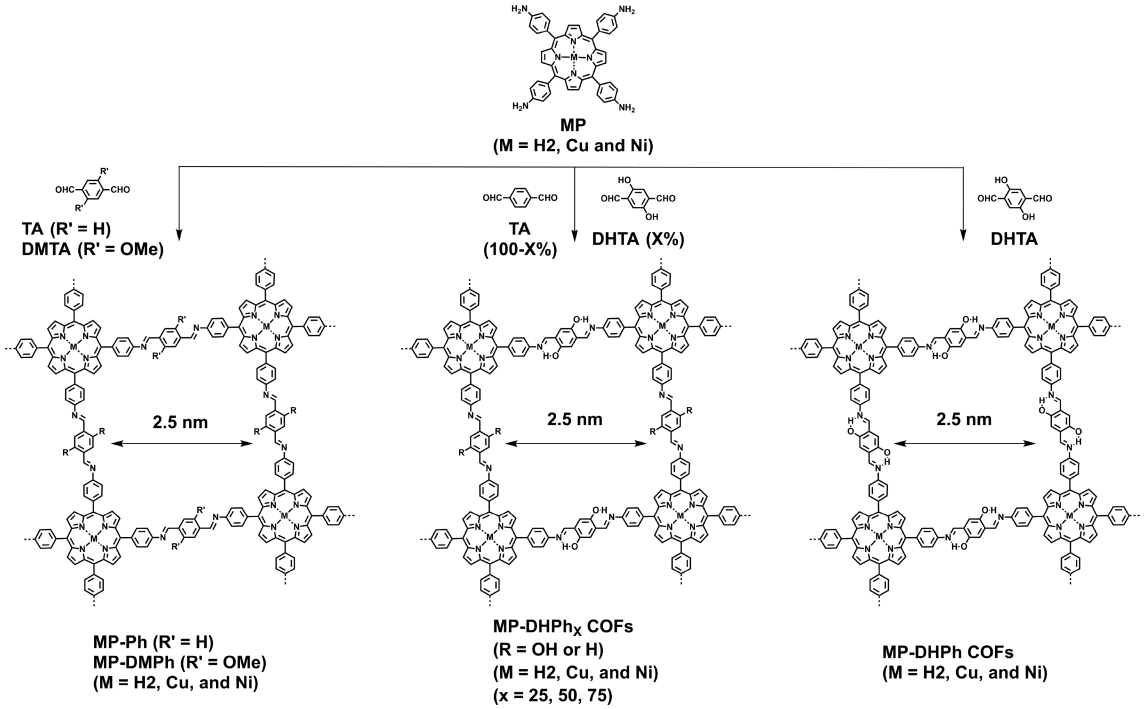

Figure 93. Schematics of the controlled synthesis of porphyrin COFs with hydrogen-bonding edges and their effects on photocatalytic singlet oxygen generation.

Magnetic core−shell Fe_3O_4@COF-TpBD (Figure 85A, COF-TpBD) nanospheres have been developed for the removal of bisphenol A (BPA) and bisphenol AF (BPAF) from aqueous solution. The adsorption isotherms of BPA and BPAF on Fe_3O_4@TpBD with typical Langmuir adsorption character achieve a maximum capacity of 160.6 and 236.7 mg g^{-1}, respectively.[524] β-CD-COF (Figure 92A), owing to the presence of β-cyclodextrin units, facilitates molecular recognition toward (*S*)-naproxen, 4-nonyl phenol, BPA, and rhodamine B. These molecules contain carboxylic or phenolic functionalities and phenyl or naphthyl moieties that can complex with the β-CD cavity.[526] In neutral water, β-CD-COF exhibits 78 and 98% removal efficiencies for ibuprofen and naproxen in 10 min with the k_{obs} values of 1.4 and 25 g mg^{-1} min^{-1}, respectively, whereas the removal of neutral compounds of BPA and 4-nonyl phenol reaches k_{obs} values of 1.7−6.8 g mg^{-1} min^{-1}. Moreover, TpBD-COF-coated solid-phase microextraction (SPME) fiber coupled to constant-flow desorption ionization mass spectrometry exhibits limits of detection and qualification of 0.92 and 3.1 ng L^{-1} for tetrabromobisphenol A (TBBPA) in aqueous media.[527]

TpPa-2-Ti^{4+} modified with Ti(IV) has been developed for phosphopeptide enrichment and achieves a maximum adsorption capacity of 100 μg mg^{-1}.[529] Because of the strong van der Waals and $\pi-\pi$ stacking interactions between the phenyl groups of the peptide and the COF shell, Fe_3O_4@TAPB-TPA-COF (Figure 72D, TAPB-TPA-COF = TAPB-PDA-COF) selectively removes 99% of peptide Phe-Gly-Phe-Gly-Phe (FGFGF, grand average of hydropathy (GRAVY) = 1.52) with little loss of Gly-Gly-Phe-Gly-Gly (GGFGG, GRAVY = 0.24, <5%).[528]

Imine-linked surface COF_{DB} serves as a host template to separate arylene vinylene macrocycles (AVM2) from their linear byproducts, as AVM2 can be immobilized in the cavity of COF_{DB} owing to strong binding interactions between the AVM2 molecules (2.4 nm) and COF_{DB}.[531] After reduction from azides to amines, *X*%[NH_2]-COFs (Figure 92B) exhibit a high affinity for anionic PFAS.[532] 20%[NH_2]-COF exhibits the highest removal efficiency of 97% for GenX with the highest capacity of 240 mg g^{-1}.

The salicylideneaniline-based COF (SA-COF) (Figure 92C) can undergo reversible solvatochromism triggered by the adsorption and desorption of water molecules, and the tautomerization of SA-COF causes dynamic changes in the ionic and chemical properties.[534] On the basis of the size-dependent separation, SA-COF can completely separate the MB and CA mixture by reducing the concentration of MB by 99.9%. Because the −OH and −NH moieties in SA-COF can be deprotonated or protonated under basic or acidic conditions, the AA (anthraflavic acid) and MB mixtures can be separated by their charges, yielding a sharp decrease in the MB concentration by 95.2%. Owing to the basic N−H moiety in the *trans*-ketoenamine form, SA-COF selectively binds −OH over $-NH_2$ groups under neutral conditions, yielding a high chemoselectivity. For example, treating a mixture of 1,4-dihydroxyanthraquinone (DHQ) and 1,4-diaminoanthraquinone (DAQ) (1/1 mol) with the SA-COF powder enriches the DAQ component to reach a 1:6 ratio of DHQ/DAQ in the filtrate within 10 min because SA-COF selectively uptakes DHQ.

13. CATALYSIS

COFs possess well-defined skeletons and discrete pores in which the skeletons, pores, and pore walls are the main domains that are useful in accommodating the catalytic sites[535] to design which domain for loading catalytic sites is dependent on the types of the targeted catalytic reactions. Because COFs are insoluble in solvents, they offer a platform for designing heterogeneous catalytic systems in which the open nanopores of COFs provide a confined space to serve as nanoreactors. Therefore, a significant feature is that the COF-based catalysts allow for an easy separation of the catalyst from the reaction mixture via filtration or centrifugation and can be reactivated for

https://dx.doi.org/10.1021/acs.chemrev.9b00550
Chem. Rev. 2020, 120, 8814−8933

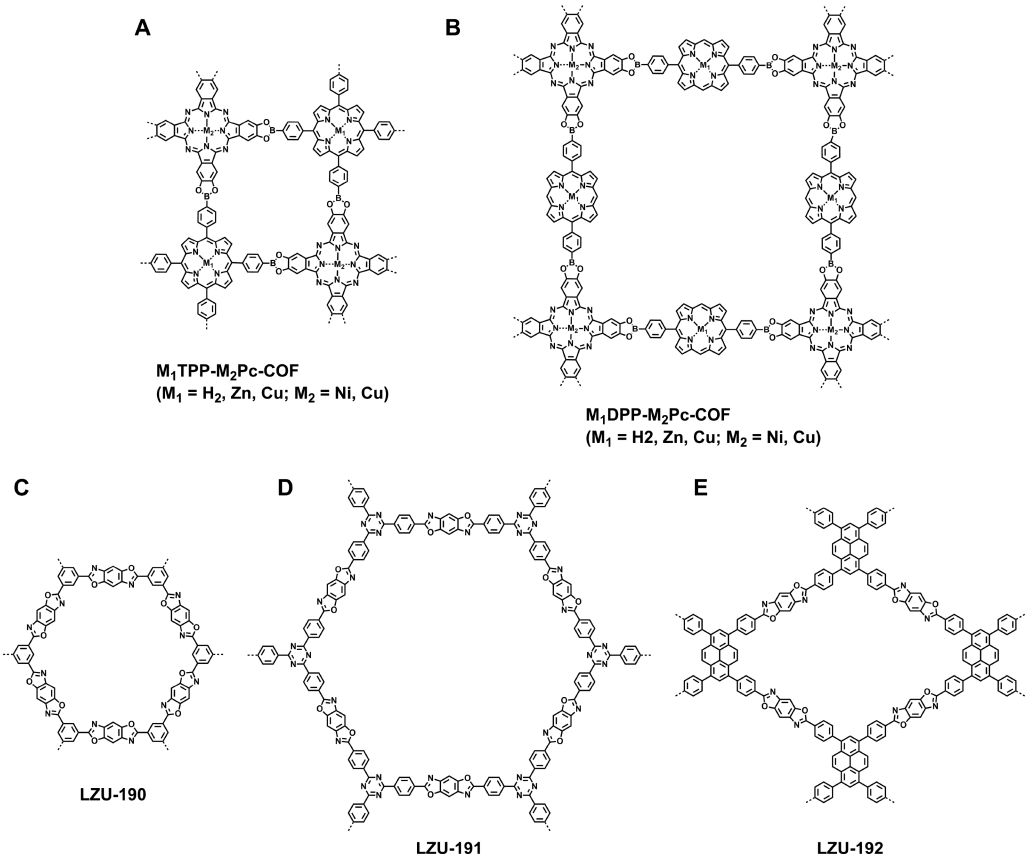

Figure 94. Schematics of COFs as a catalyst for singlet oxygen generation: (A) M_1TPP-M_2Pc-COF (M_1 = H_2, Zn, Cu; M_2 = Ni, Cu), (B) M_1DPP-M_2Pc-COF (M_1 = H_2, Zn, Cu; M_2 = Ni, Cu), (C) LZU-190, (D) LZU-191, and (E) LZU-192.

cycle use. By virtue of a broad structural diversity, COFs enable the integration of various catalytic systems or sites into the structures and are tolerant to different types of catalytic reactions.[262] Asymmetric catalysis, photocatalysis, electrocatalysis, metal-based catalysis, and other types of catalysis have been developed and have shown the great potential of COFs as a predesignable porous platform in exploring heterogeneous catalytic systems.[258]

13.1. Photocatalysis

The development of photocatalysts is important in relation to artificial photosynthesis and photoenergy conversion.[536] In nature photosynthetic systems, well-defined chlorophyll arrays organized in a manner of wheel-like assemblies are key to efficient light harvesting and energy transfer to the reaction center. This design principle has inspired synthetic chemists to design artificial light-harvesting antennae and photocatalytic systems by organizing chromophores into well-ordered extended structures. COFs are versatile in integrating various π-units into extended ordered structures and are promising as a superb platform for designing photocatalysts.

Porphyrin is a typical visible-light absorption pigment with a similar structure to that of chlorophyll. By virtue of its excellent light-harvesting performance in the visible region, porphyrin-based COFs serve as a photocatalyst for the singlet oxygen generation. In this case, a triplet state of the photocatalyst is demanded for the transformation of the triplet molecular oxygen into the singlet oxygen, which can barely be satisfied by the conventional porphyrin derivatives. Importantly, the ordered COF architecture plays a key role in controlling photogenerated excited states for the steady conversion of molecular oxygen into singlet oxygen.

13.1.1. Singlet Oxygen Generation Reactions. A squaraine-linked CuP-SQ COF (Figure 27C) has been synthesized by the condensation of SQ and TAP-CuP and serves as a photocatalyst for singlet oxygen generation.[216] The CuP-SQ COF consists of a zigzag conformation that protects the layered structure from sideslip, provides an extended π-conjugation over 2D networks, and has high chemical stability. Owing to the intralayer conjugation and well-defined interlayer π-stacking structure, the CuP-SQ COF exhibits a broadened and red-shifted Soret band as all well as an enhanced Q-band, which doubles the light-absorbing capability of the COF compared with the monomeric TAP-CuP unit. Indeed, the CuP-SQ COF exhibits an outstanding singlet oxygen generation, as demonstrated by the time-dependent electronic absorption spectral change of 1,3-diphenylisobenzofuran (DPBF, 50 μM) that serves as a tag to indicate the production of singlet oxygen in the presence of only 1 mg of COF (in 2.3 mL of oxygen-saturated DMF) upon 500 nm light excitation. By virtue of its controlled triplet state generation, high crystallinity, and broad absorption capability, the CuP-SQ COF is superior to the TAP-CuP monomer in single oxygen production.

Similarly, a series of imine-linked porphyrin COFs (CuP-DHPh, NiP-DHPh, and H_2P-DHPh, Figure 93) have been investigated for photocatalytic singlet oxygen generation.[100] The hydrogen-bonding interactions can suppress the torsion of the edge units and lock the tetragonal 2D sheets in a planar conformation, which enhances the interlayer interactions and allows extended π-conjugation over the 2D sheets. Compared

https://dx.doi.org/10.1021/acs.chemrev.9b00550
Chem. Rev. 2020, 120, 8814−8933

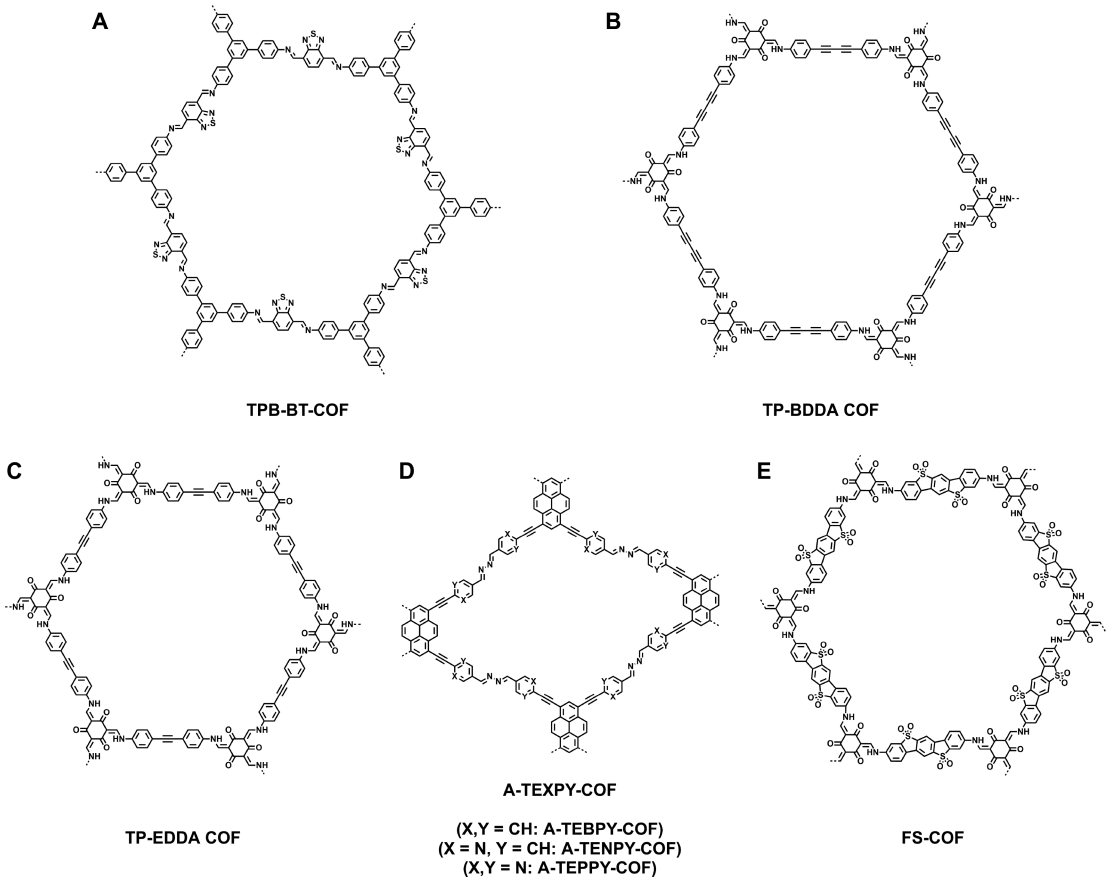

Figure 95. Schematics of (A) TPB-BT-COF, (B) TP-BDDA COF, (C) TP-EDDA COF, (D) A-TEXPY-COF, and (E) FS-COF for photocatalytic H_2 evolution.

with counterpart COFs without hydrogen bonds, the hydrogen-bonding COFs benefit from the planarization effects and achieve higher crystallinity and porosity, better light-harvesting capability, and a narrower band gap. As a result, the photocatalytic singlet oxygen generation is highly dependent on the content of intralayer hydrogen-bonding interaction sites. In fact, the CuP-DHPh COF with the 100% hydrogen-bonding sites on the edges achieves a 10−20-fold enhanced activity compared with those of other amorphous CuP derivatives. Interestingly, the free-base H_2P-DHPh COF exhibits better photocatalytic activity compared with the NiP-DHPh COF and the CuP-DHPh COF, indicating a facilitated electron-transfer process. The photocatalytic systems of singlet oxygen generation may find applications in photodynamic therapy.

Likewise, the incorporation of phthalocyanine units allows the preparation of M_1TPP-M_2Pc-COF (Figure 94A, M_1 = H_2, Zn, Cu; M_2 = Ni, Cu) and M_1DPP-M_2Pc-COF (Figure 94B, M_1 = H_2, Zn, Cu; M_2 = Ni, Cu) with heterobimetallic sites.[109] Owing to the near-infrared absorbance of phthalocyanine, the resulting COFs produce singlet oxygen even with low-energy photons. Other than porphyrin-based COFs, π-conjugated benzoxazole-based frameworks have also been explored as robust organo-photocatalysts. The benzoxazole-linked COFs LZU-190 (Figure 94C), LZU-191 (Figure 94D), and LZU-192 (Figure 94E) have been synthesized through the polycondensation of 2,5-diamino-1,4-benzenediol dihydrochloride with TFB, 2,4,6-tris(4-formyl-phenyl)-1,3,5-triazine, and TFPPy, respectively, in the mixture of NMP/mesitylene (1:1 vol) and an excess of benzimidazole (4.5 equiv).[537] Those COFs absorb light in the ultraviolet and visible regions with optical band gaps of 2.02, 2.38, and 2.10 eV, respectively. LZU-190 efficiently catalyzes the transformation of 4-carboxyphenylboronic acid to 4-hydroxybenzoic acid in 99% yield, whereas the amorphous analogue reaches only 78% yield and imine-linked COF-LZU1 (Figure 21A) is decomposed under the same conditions. LZU-190 even presents excellent and unchanged activity after 20 runs in the visible-light-driven oxidative hydroxylation of 4-carboxyphenylboronic acid. These works also demonstrate that metalloporphyrins without noble metals such as palladium and platinum could also exhibit remarkable activities for singlet oxygen generation.

13.1.2. Hydrogen Evolution Reactions. Photocatalytic water splitting to produce H_2 is an important chemical process for the generation of clean energy resources.[236,538,539] The designability of skeletons and the tunability of band structures are two key factors to be considered in developing photocatalysts for water splitting.[540] COFs serve as a photosensitizer to trigger photocatalytic H_2 evolution from water in conjunction with platinum (Pt) nanoparticles as electron relay stations. The hydrazone-linked TFPT-COF (Figure 38A) consisting of 1,3,5-tris(4-formyl-phenyl)triazine (TFPT) at the vertices and DETH at the edges functions as a photosensitizer for exciton generation and achieves continuous and constant H_2 production at a rate of 1970 mmol h^{-1} g^{-1}, corresponding to a quantum efficiency of 2.2%, in the presence of Pt nanoparticles as a proton reduction catalyst and aqueous TEOA as a sacrificial electron donor.[83]

Similarly, a series of azine-linked N_x-COFs (x = 0, 1, 2, and 3) have been designed for the photocatalytic hydrogen evaluation, and the number of nitrogen atoms at the central aryl rings of the

https://dx.doi.org/10.1021/acs.chemrev.9b00550
Chem. Rev. 2020, 120, 8814−8933

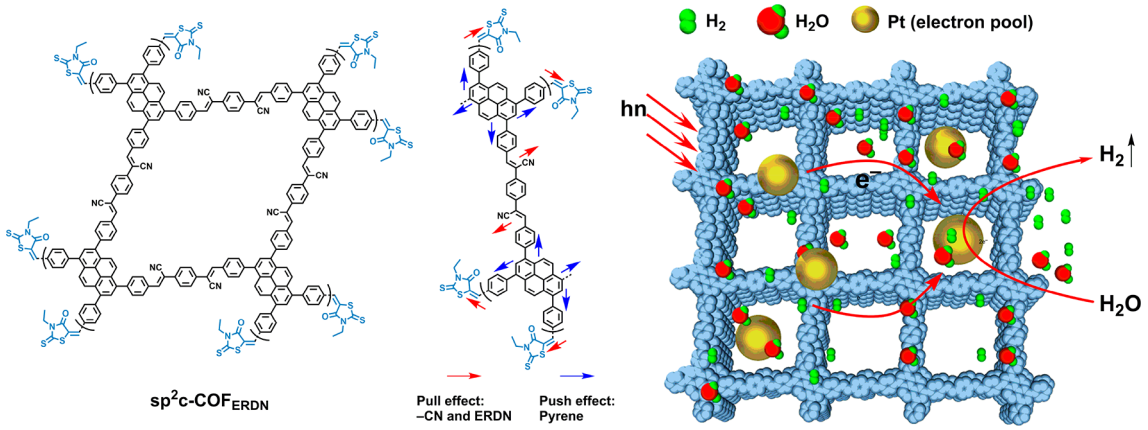

Figure 96. Schematics of stable 2D sp^2 carbon-conjugated COFs for H_2 production from water.

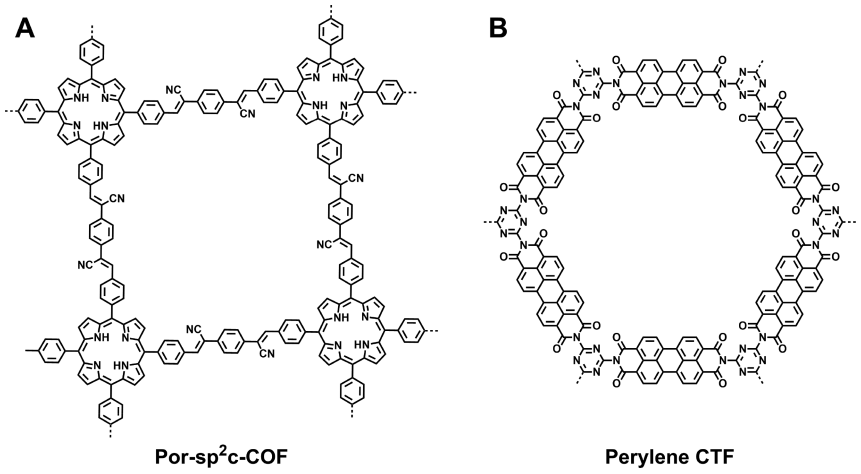

Figure 97. Schematics of (A) the sp^2 C═C-linked Por-sp^2-COF and (B) perylene CTF for photocatalytic organic reactions.

vertices is tunable between 0 and 3 (Figure 23C).[85] The N_x-COF/Pt (x = 0, 1, 2 and 3) systems achieve continuous H_2 production at a rate of 23, 90, 438, and 1703 mmol h^{-1} g^{-1} for N_0-COF, N_1-COF, N_2-COF, and N_3-COF, respectively. The superior activity of N_3-COF originates from the electron-deficient character of the central triazine knots, which stabilize the negative charges on the COF and facilitate the transfer of electrons to the proximate Pt sites. It is higher than those of Pt-modified amorphous melon (720 μmol h^{-1} g^{-1}),[541] g-C_3N_4 (840 μmol h^{-1} g^{-1}),[542] and crystalline poly(triazine imide) (864 μmol h^{-1} g^{-1})[541] under the same conditions.

Through introducing BTDA as acceptor sites into Nx-COFs, TPB-BT-COF (Figure 95A) achieves high activity for the photoreduction of Cr(VI) with >99% efficiency without any sacrificial agent or pH regulation.[543] Besides, azine-linked N_2-COF (Figure 23C) with chloro(pyridine)cobaloxime cocatalyst (Co-1) in the presence of TEOA as a sacrificial electron donor in a water/acetonitrile mixture can also achieve a H_2 evolution rate of 782 μmol h^{-1} g^{-1} and TON (turnover number) of 54.4 in the water/acetonitrile mixture.[544] This work demonstrates that the platinum cocatalyst is not a requirement for photocatalytic hydrogen generation.

The acetylene-functionalized β-ketoenamine COF TP-BDDA (Figure 95B) bearing diacetylene (−C≡C−C≡C−) moieties is an efficient and recyclable heterogeneous photocatalyst.[545] Compared with the COF TP-EDDA (Figure 95C) with an acetylene skeleton, the COF TP-BDDA with a band gap of 2.31 eV exhibits an enhanced catalyst performance, an average H_2 evolution rate of 324 ± 10 μmol h^{-1} g^{-1} over 10 h, and an apparent quantum efficiency (AQE) of 1.8% under 520 nm light. A-TEX-COF (Figure 95D) can further extend both the planarity and the π-conjugation by integrating alkyne moieties into the frameworks.[546] This is the first COF without any triazine or heptazine units that exhibits good photocatalytic activities. A-TEXPY-COF steadily produces H_2 for at least 24 h, whereas A-TEBPY-COF with the lowest nitrogen content produces H_2 at the highest rate of 98 μmol h^{-1} g^{-1}. Its current density (6 μA cm^{-2}) at the reversible hydrogen electrode (RHE) potential is approximately four times as high as that of A-TENPY-COF (1.5 μA cm^{-2}).

The nanopores of the TpPa-2 COF (Figure 86B) have been utilized to confine photoactive CdS nanoparticles by manipulating the energy level, stabilizing the nanoparticles, and suppressing the recombination of the photogenerated holes and electrons.[547] In the CdS-TpPa-2 hybrid, the H_2 production is significantly promoted from a rate of 124 to 3678 mmol h^{-1} g^{-1} by increasing the COF content from 0 to 10 wt %. This strategy is interesting because it opens a way to explore the local chemical environment for developing the potential of inorganic semiconducting catalysts.

FS-COF (Figure 95E) based on a benzo-bis(benzothiophene sulfone) moiety exhibits excellent activity for photochemical H_2 evolution, which is much higher than that of its amorphous or semicrystalline counterparts.[548] FS-COF constructed with 3,9-

https://dx.doi.org/10.1021/acs.chemrev.9b00550
Chem. Rev. 2020, 120, 8814−8933

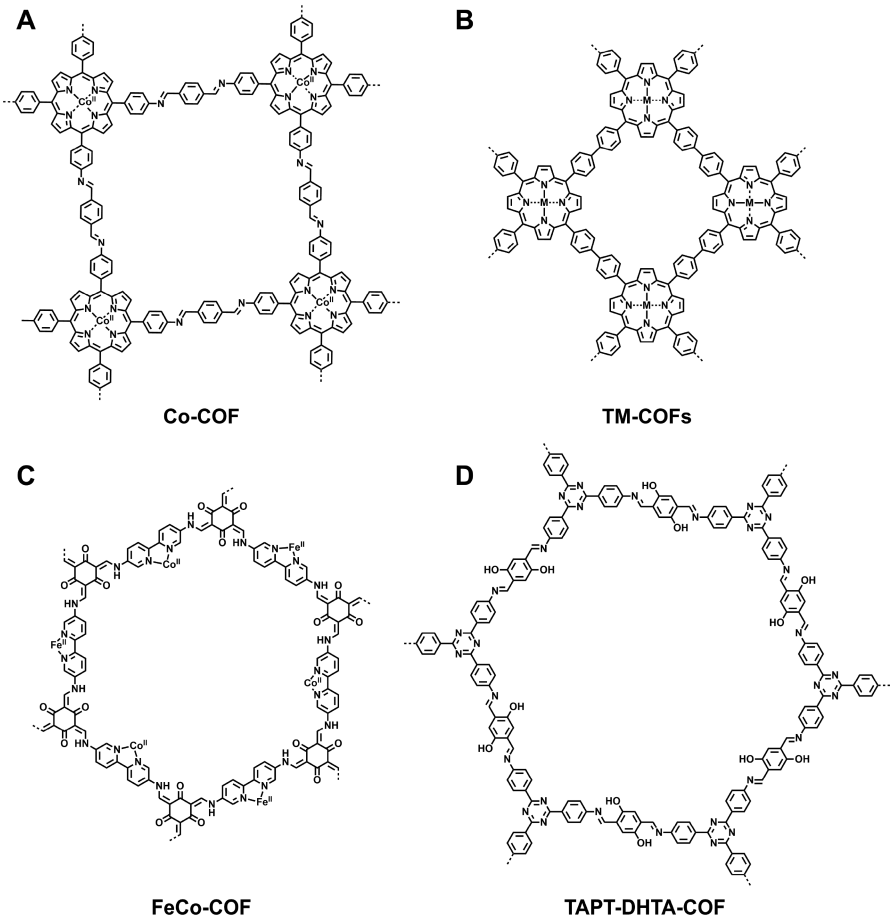

Figure 98. Schematics of (A) Co-COF, (B) TM-COFs, (C) FeCo-COF, and (D) TAPT-DHTA-COF for the electrocatalytic O_2 reduction reaction.

diamino-benzo[1,2-*b*:4,5-*b*′]bis[1]benzothiophene sulfone (FSA) exhibits H_2 evolution rates of 10.1 mmol g^{-1} h^{-1} with an external quantum efficiency of 3.2%. Upon dye sensitization with the near-infrared absorbing WS5F, FS-COF produces H_2 up to 16.3 mmol g^{-1} h^{-1}. Currently, this is the highest photocatalytic hydrogen efficiency of COFs.

Modified with a monofunctional electron-deficient terminal group of 3-ethylrhodanine (ERDN), the fully conjugated sp^2c-COF_{ERDN} (Figure 96) exhibits a hydrogen evolution rate of 2120 μmol h^{-1} g^{-1} in an aqueous solution in the presence of *in-situ*-generated Pt nanoparticles (3 wt %, 1−3 nm) and TEOA (10 vol %) under a 300 W xenon light source ($\lambda \geqslant 420$ nm).[549] The effect of ERDN terminals is prominent for its excellent photocatalytic efficiency. It can further enhance the π-conjugation through an electron donor−acceptor push−pull effect, decrease the band gap from 1.90 V of sp^2c-COF to 1.85 eV of sp^2c-COF_{ERDN}, and thus enable the near-infrared light harvesting to 800 nm and lower the reduction and oxidation potentials. This is the first time that the sp^2 carbon COFs have been explored for photocatalytic hydrogen evolution.

13.1.3. Organic Reactions. COFs exhibit prominent results in photocatalyzing organic transformations. An sp^2 C═C-linked COF, that is, Por-sp^2-COF (Figure 97A) exhibits strong absorbance in the visible region and catalyzes the aerobic oxidation of amine to imines.[34] Upon irradiation with a 3W white LED, the reaction proceeds almost quantitatively in 30 min and retains activity after five cycles. This outperforms many heterogeneous photocatalysts such as MOF 6 (83% yield in 1 h)[550] and PCN-222 (100% yield in 1 h).[551]

By drop-casting on a polyimide sheet, perylene-containing CTF films (Figure 97B) have been fabricated. The CTF film upon coupling to a rhodium complex and formate dehydrogenase facilitates the oxidation of NADH to NAD^+. Because of the large surface area for light harvesting and the photoactivity of CTF, the catalytic system allows the reduction of CO_2 to HCOOH at a rate of 881.3×10^6 nmol g^{-1} h^{-1}. This film-based catalytic system features a high stability and good reusability.[552]

13.2. Electrocatalysis

Electrocatalysis is a chemical process directly associated with energy conversions, including the conversion of electricity to chemical energy and the reverse conversion that transforms chemical energy into electricity. As an electrocatalyst, its electric conductivity is a key factor that determines the kinetics and efficiency of the systems. COFs are usually insulators without electric conductivity. To enhance the conductivity, pyrolysis is a useful way to covert COFs into carbons. However, in most cases, the resulting carbons lose the original features of the COFs. How to retain the structural features including the dimensionality and the porosity remains a challenge.

13.2.1. Oxygen Reduction Reactions. To replace the platinum catalyst for O_2 reduction reaction (ORR) in fuel cells, several porous carbons from a diversity of COFs precursors have been developed. For example, a cobalt porphyrin COF (Co-COF) (Figure 98A) has been utilized as a precursor for the pyrolysis preparation of a nanocomposite of well-distributed Co(0) nanoparticles and graphitized carbon structures.[553] In an aqueous solution of KOH (0.1 M), both the potential and

https://dx.doi.org/10.1021/acs.chemrev.9b00550
Chem. Rev. 2020, 120, 8814−8933

current responses obtained from pyrolyzed Co-COF-900 are comparable to those of the commercial 20% Pt/C catalyst. On the basis of the rotating ring disk electrode (RRDE) experiments, there are 3.85 electrons involved in the ORR, demonstrating that the O_2 reduction catalyzed by pyrolyzed Co-COF-900 involves a four-electron process. This work also demonstrates that cobalt-based materials have the potential to replace noble metals such as platinum in ORR.[554]

Among porphyrin-containing TM-COFs with 3d transition metals (Figure 98B), Fe-COFs with the minimum overpotentials of 0.482 V for ORR are predicted to be ideal in the four-electron transfer regime, whereas in the two-electron transfer regime, Ca-COF and Sr-COF are identified to be more efficient for the direct synthesis of H_2O_2 via an electrochemical approach.[555] Current research has also combined both Fe and Co alloy nanoparticles into Tp-Bpy-COF.[556] The obtained bimetallic FeCo-COF (Figure 98C) displays the overpotential of 1.59 eV in the catalysis of the oxygen evolution reaction (OER) at a current density of 10 mA cm^{-2}.

It is ideal to combine the skeleton design of 2D COFs and the template guidance of the pyrolysis for the generation of well-defined carbons. Converting conventional COFs into high-performance 2D carbons based on template carbonization can yield 2D graphitic carbon sheets with high conductivity, hierarchical micropores and mesopores, and abundant N- and P-doped heteroatom catalytic edges, which is ideal not only for energy storage but also for the carbon catalyst of the ORR.[474,557] Upon loading phytic acid (PA) into TAPT-DHTA-COF (Figure 98D), the resulting PA@TAPT-DHTA-COF is pyrolyzed at 1000 °C under N_2 to yield nitrogen and phosphorus codoped PA@TAPT-DHTA-COF_{1000}, which is further pyrolyzed in an ammonia atmosphere at 900 °C to produce PA@TAPT-DHTA-COF_{1000NH_3}. With an improved pore volume and maintained layer structure, PA@TAPT-DHTA-COF_{1000NH_3} exhibits a more positive reduction peak at −0.18 V, a more positive E_0 by 30 mV, a higher $E_{1/2}$ by 50 mV, a greatly enhanced j_{limit} by 1.2 mA cm^{-2}, and a much smaller Tafel slope of 110 mV $decade^{-1}$ compared with those of PA@TAPT-DHTA-COF_{1000} and Pt/C, which indicates a superior ORR activity. It also outperforms many carbon catalysts such as N-doped carbon nanotube frameworks (NCNTFs) (onset potential = 0.97 V, half-wave potential = 0.87 V, j_{limit} < 6 mA cm^{-2})[558] and N-doped graphene mesh (NGM) (onset potential = 0.89 V, half-wave potential = 0.77 V, j_{limit} = 6.41 mA cm^{-2}).[559]

13.2.2. Oxygen Evolution Reactions. The development of an efficient OER catalyst for oxidizing water molecules is a challenging issue due to the poor reaction kinetics under neutral pH conditions. The bipyridine-containing TpBpy COF has been developed as an OER catalyst by coordinating Co(II) ions to the bipyridine edges (Figure 99).[470] The electrochemical property of the Co-TpBpy COF (12% Co) is studied by CV and linear sweep voltammetry (LSV) with Co-TpBpy-COF-coated glassy carbon as a working electrode in an aqueous phosphate buffer (0.1 M) at pH 7. The CV profile shows the onset potential at 1.63 V and an overpotential of 400 mV at a current density of 1 mA cm^{-2}. The Co-TpBpy COF retains similar LSV patterns and roughness factors (1.46) even after 1000 scans and achieves 94% retention in the OER current. The inductively coupled plasma (ICP) analysis of the electrolyte reveals that no cobalt ion leaked from the Co-TpBpy COF electrode. The SEM and XPS analyses also confirm the intact structure of the Co-TpBpy COF after the

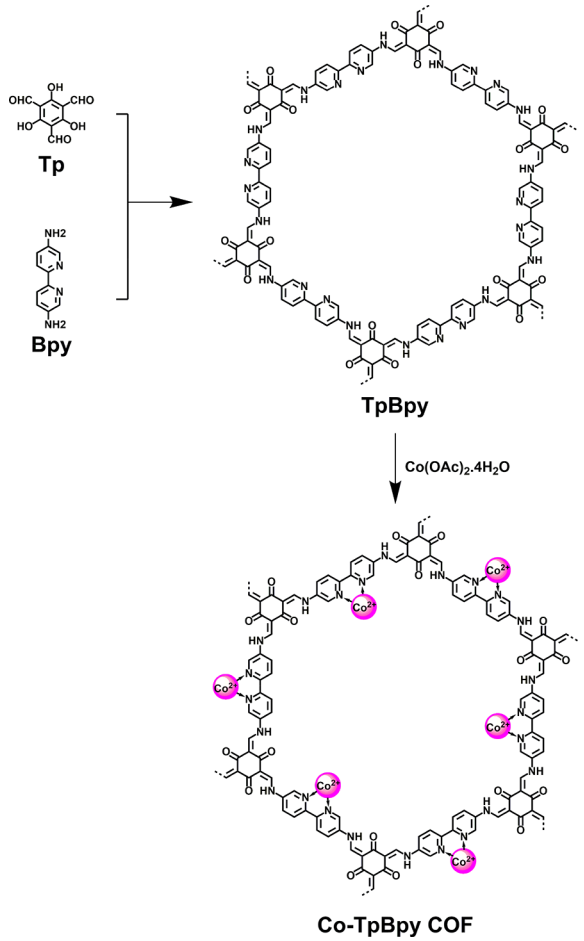

Figure 99. Schematics of the synthesis of the Co-TpBpy COF via the ligation of Co(II) to the bipyridine edge units as the O_2 evolution reaction catalyst.

OER process. These performances are compatible with other cobalt-containing OER catalysts.[560−562]

COFs can affect the electronic properties of the metal-based catalysts and thus have a chance to facilitate the OER process. For example, using an sp^3-nitrogen-rich COF (Figure 38B, IISERP-COF2) as a matrix to isolate the nickel metal nanoparticles can enhance the catalytic performance.[249] This method is further developed by a hybrid composite based on a benzimidazole COF (Figure 38D, IISERP-COF3); a hybrid system with the Ni_3N nanoparticles has been prepared by heating a mixture of IISERP-COF3, nickel acetate, and urea to 350 °C for 6 h.[327] The Ni_3N nanoparticles are distributed between the COF layers and confined inside the COF channels, as evidenced by the FE-SEM and HR-TEM measurements. For the electrochemical performance in an aqueous KOH solution (1 M) saturated with H_2, the hybrid catalyst achieves an onset potential at 1.43 V and an overpotential of 230 mV at a current density of 10 mA cm^{-2}. A Faradaic efficiency of 98% at a current density of 1 mA cm^{-2} is confirmed by the RRDE experiments. The O_2 evolution rate is as high as 230 mmol h^{-1} g^{-1} with a TOF value of 0.52 s^{-1} at an over potential of 300 mV, which is superior to those of other catalysts reported under similar conditions. The spatial confinement of the Ni_3N nanoparticles between the ordered nitrogen-rich COF layers accounts for the high performance. This proves to enhance the OER performance (lower overpotential) compared with other non-noble-metal-

https://dx.doi.org/10.1021/acs.chemrev.9b00550
Chem. Rev. 2020, 120, 8814−8933

based OER catalysts such as $LiCo_{0.8}Fe_{0.2}O_2$ (overpotential = 340 mV, Tafel slope = 50 mV dec^{-1})[563] and IrO_x (overpotential = 320 mV).[564]

13.2.3. Carbon Dioxide Reduction Reactions. The reduction of CO_2 into useful chemicals is an important subject that is relevant to carbon emission and energy resources. Various efforts have been made over the past decades to develop an efficient strategy for converting CO_2 to CO, MeOH, EtOH, CH_4, and so on. Exploring the electrochemical and photochemical properties of COFs to reduce CO_2 into CO and other chemicals has attracted great attention and has generated different catalytic systems.

A porphyrin-based COF has been developed for the electrochemical reduction of CO_2 to carbon monoxide. The imine-linked COF-366-Co and COF-367-Co (Figures 16Q and 100) consisting of cobalt porphyrin units at the vertices and

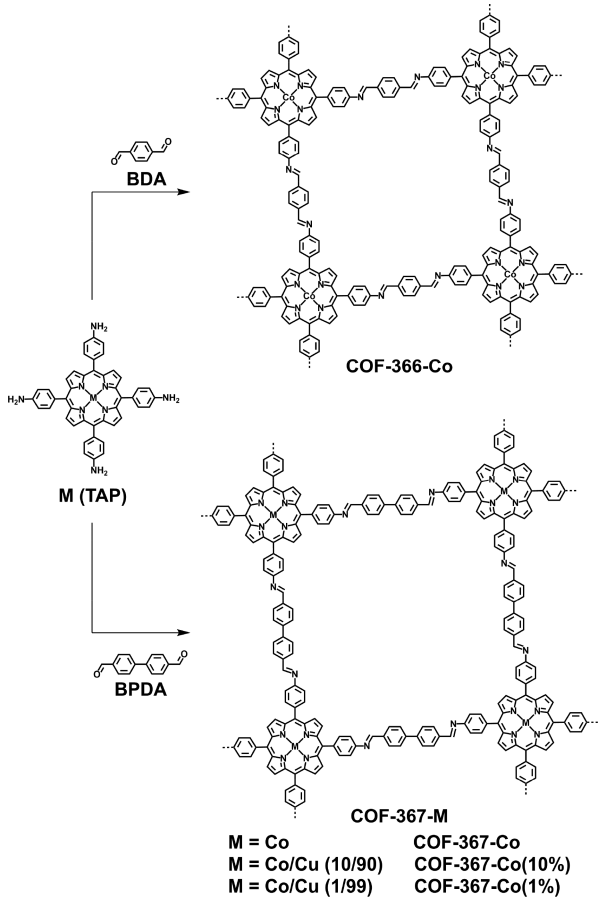

Figure 100. Schematics of synthesis of porphyrin COFs for the reduction of CO_2 to CO.

BDA and BPDA at the edges, respectively, serve as electrocatalysts for the reduction of CO_2 to CO.[33] COF-366-Co (Figure 100) exhibits 10% enhanced catalytic performance compared with the molecular cobalt porphyrin unit and achieves a TON of 1352 (TON per electroactive cobalt, TON_{EA} = 34 000) and an initial turnover frequency (TOF) of 98 h^{-1} (TOF per electroactive cobalt, TOF_{EA} = 2500). The Faradaic efficiency for CO (FE_{CO}) is as high as 90%. By contrast, the large-pore COF-367-Co promotes the CO evolution with a TON of 3901 (TON_{EA} = 48 000) during 24 h and affords a high selectivity of competing proton reduction (FE_{CO} = 91%).

A multivariate strategy to dilute the cobalt component by introducing copper porphyrin units has been developed, and the TOF_{EA} for these multivariate Co/Cu COF-367 catalysts shows substantial improvement with each 10-fold dilution of cobalt loading. The hybrid COF (COF-367-Co(1%)) with optimum active content achieves excellent performance with a very high TON_{EA} of 296 000 (TON > 24 000) and an initial TOF of 9400 h^{-1}.

Introducing different electron-donating or -withdrawing groups into the reticular structure, the electronic character of porphyrin active sites in COF-366-Co can be further improved. After growing COFs on HOPG to enhance the interaction with electrode surface, oriented COF-366-Co thin films exhibit significantly improved catalytic performance on a per-cobalt basis to achieve a current density of 45 mA mg^{-1} cobalt for the formation of CO and a Faradaic efficiency of 87%. Moreover, through covalently modifying the skeleton of COFs, the current density for CO formation will increase from 46 mA mg^{-1} for COF-366-$(OMe)_2$-Co to 65 mA mg^{-1} for COF-366-F-Co (Figure 101A).[315] Amine-linked COF-300-AR (Figure 101C), which is postsynthesized through imine-linked 3D COF-300 using $NaBH_4$, facilitates the electrochemical reduction of CO_2 to CO on the silver electrode via a carbamate intermediate. The reaction proceeds with a high selectivity and achieves a Faradaic efficiency of 80% at −0.85 V versus the RHE.[278] Benefiting from the superior light-harvesting and photocatalytic properties of rhenium complexes as well as the high electron conduction of the conjugated framework, as-synthesized Re-COF (Figure 101B) also displays a remarkable 98% selectivity in the reduction of CO_2 to CO.[565]

CTF derivatives show high selectivity in the electroreduction of CO_2. Perfluorinated FN-CTF-400 (Figure 101D) with a tetrafluoroterephthalonitrile building block can be obtained through the ionothermal synthesis in molten $ZnCl_2$ at 400 °C.[566] With the Faradaic efficiencies of 78.7% for CH_4 production and <15% for H_2 evolution at a potential range between −0.4 and −0.6 V, FN-CTF-400 serves as a highly selective catalyst for the electroreduction of CO_2 into CH_4, with a dominant competitive advantage over H_2 evolution reaction, and the Faradaic efficiency for CH_4 production can reach 99.3% in the potential range of −0.7 to −0.9 V. Moreover, FN-CTF-400 maintains a Faradaic efficiency for CH_4 production of 91.7% after a 5 h continuous conversion at −0.8 V, showing excellent stability in electrocatalysis. Recently, Co-CTF and Ni-CTF materials (Figure 101E) with metal ions coordinated to nitrogen sites have been developed to show an effective reduction of CO_2 to CO from −0.5 V versus the RHE, and the Faradaic efficiency of Ni-CTF for CO formation reaches 90% at −0.8 V (vs RHE).[567]

13.3. Chiral Catalysis

Asymmetric catalysis is of great importance among chemical transformations because it offers a straightforward way to synthesize many chiral intermediates, chemicals, and medicines.[568] To perform asymmetric transformation, a chiral catalytic system is essential that enables the selective formation of only one enantiomer. Heterogeneous asymmetric catalysts have the merits of easy separation from the reaction systems and cycle use, which are important from the viewpoint of the chemical process. The tunable skeletons and large pore sizes of COFs are rarely available for other porous materials. In this context, COFs offer a unique platform in designing heterogeneous asymmetric catalytic systems.

https://dx.doi.org/10.1021/acs.chemrev.9b00550
Chem. Rev. 2020, 120, 8814−8933

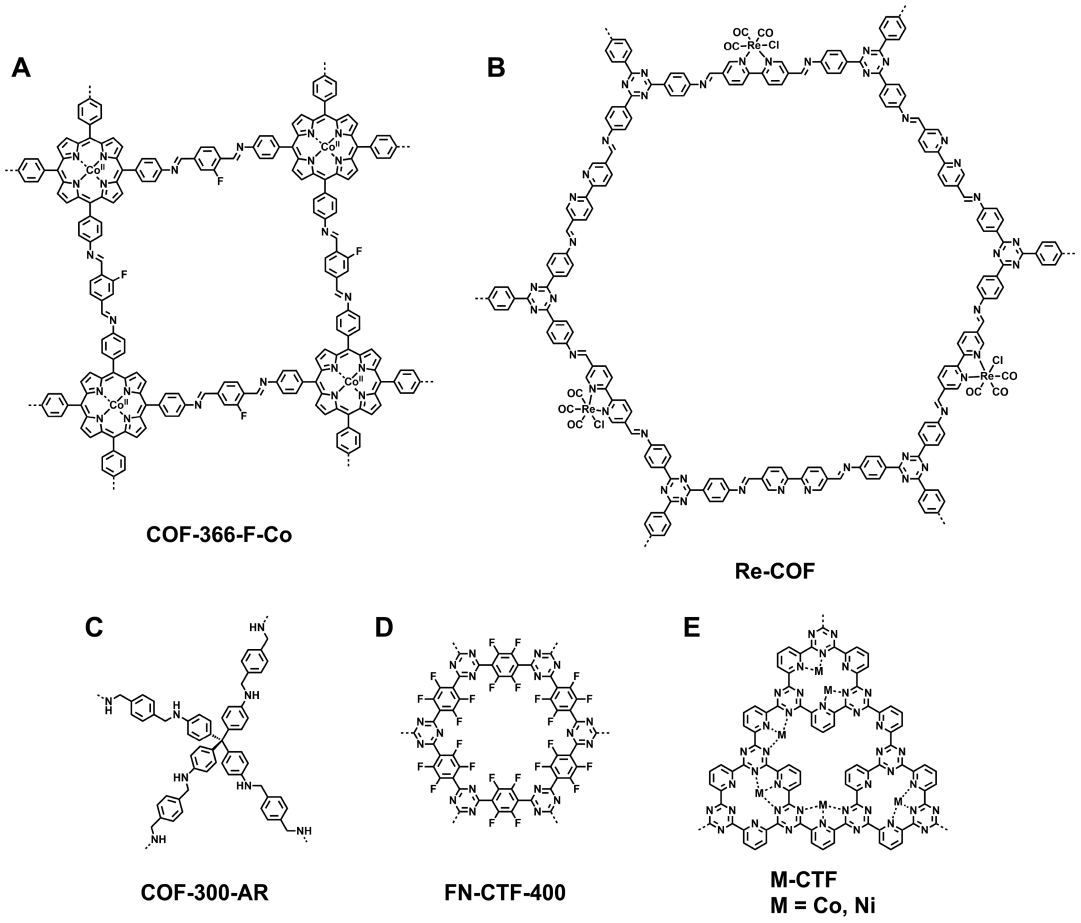

Figure 101. Schematics of (A) COF-366-F-Co, (B) Re-COF, (C) COF-300-AR, (D) FN-CTF-400, and (E) M-CTF for electrocatalytic CO_2 reduction.

CCOFs can be developed by anchoring chiral units onto the pore walls of achiral COFs through pore-surface engineering. This method enables the introduction of chiral sites to the predetermined positions on the pore walls at a desirable density. More importantly, pore-surface engineering allows for the introduction of chiral units at a relatively low temperature that is critical in retaining the chirality; the direct polymerization of chiral building units into the COF skeletons usually requires a long reaction period and a high temperature, which carry the risk of causing undesired thermal racemization and decreasing the enantioselectivity of the resulting catalysts. This lowered selectivity will directly deteriorate the catalytic performance in terms of the enantiomeric excess (ee) value.

13.3.1. Skeleton Design. Direct polymerization of enantiopure TADDOL with 4,4-diaminodiphenylmethane (4,4-DADPM) generates chiral CCOF-1 (Figure 102A) and CCOF-2 (Figure 102B), respectively.[260] These two COFs serve as the Lewis-acid catalyst in the asymmetric addition of diethylzinc (Et_2Zn) to the aromatic aldehydes and produce secondary alcohols (Figure 102, scheme a). Chelating the chiral dihydroxy-functionalized TADDOL units of CCOFs with $Ti(O^iPr)_4$ results in a composite catalyst that achieves 99% conversion with 95% ee value. Moreover, this catalyst tolerates a range of electron-donating and withdrawing groups such as methyl and chloro units. It can be reused up to four cycles without significant loss of catalytic activity and enantioselectivity. Notably, this is much superior to those of Cd-Binol-MOF and Cu-Binol-MOF (up to 99% conversion, 83% ee).[569,570] Similarly, direct condensation of a C_2-symmetric chiral edge unit (*S*)-4,4′-(2-(pyrrolidin-2-yl)-1*H*-benzo[*d*]imidazole-4,7-diyl)-dianiline and C_3-symmetric knots of TFB and TFP yields two CCOFs, that is, LZU-72 (Figure 102C) and LZU-76 (Figure 102D), respectively.[227] The *β*-ketoenamine linked LZU-76 is much more stable compared with the imine-linked LZU-72 and serves as a catalyst for the asymmetric aldol condensation reaction between aryl aldehyde and acetone (Figure 102, Scheme b), achieving a yield of 84%, with an ee value of 88%. It can be reused three times without the loss of enantioselectivity.

Polycondensation of a C_3-symmetric chiral knot unit TPBn with a C_2-symmetric edge DMTP produces several chiral DMTA-TPB1/n' COFs (n = 2−5) (Figure 102E).[571] The straight 1D channels within the 2D-CCOFs provide efficient access to uniformly distributed organocatalytic sites and facilitate the transport of reactants and products. This series of CCOFs catalyze a broad range of asymmetric reactions, such as the *α*-aminooxylation reactions between aldehydes and nitrosobenzene (Figure 102, Scheme c), Aldol reaction between aryl aldehyde sand cyclohexanone (Figure 102, scheme d) as well as the Diels−Alder reaction between substituted cinnamaldehydes and cyclopentadiene (Figure 102, Scheme e). Across the reactions screened, 70% yield and 92% ee have been achieved, which are better than those of MOF-based catalysts.[572−575] Upon ligating with various metal ions, salen-based CCOFs (Figure 102F) have been developed as recyclable heterogeneous chiral catalysts for asymmetric cyanation of aldehydes, Diels−Alder reaction, alkene epoxidation, epoxide ring-opening and

https://dx.doi.org/10.1021/acs.chemrev.9b00550
Chem. Rev. 2020, 120, 8814−8933

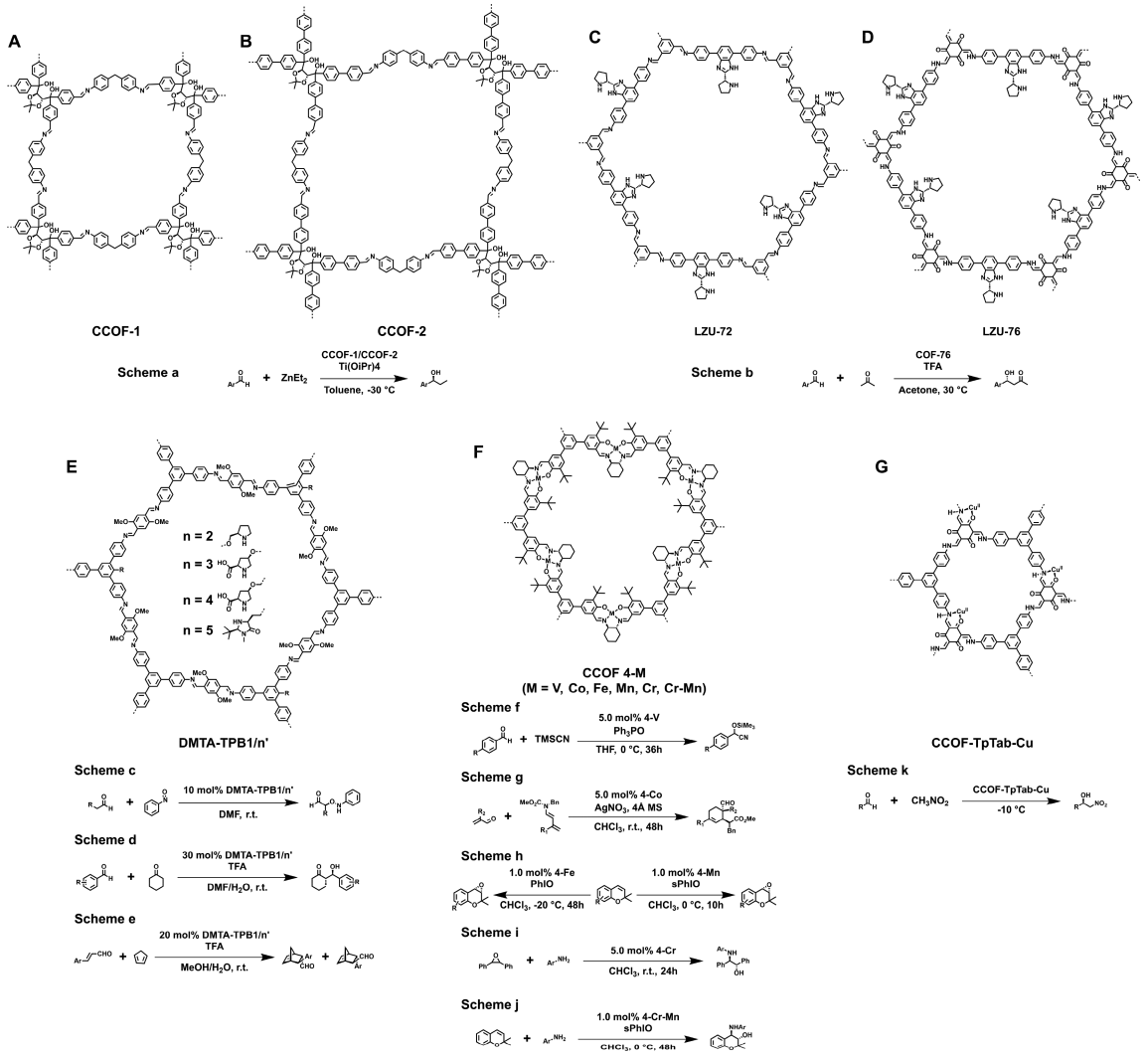

Figure 102. Schematics of the chiral catalysis of (A) CCOF-1, (B) CCOF-2, (C) LZU-72, (D) LZU-76, (E) DMTA-TPB, (F) CCOF-4-M, and (G) CCOF-TpTab-Cu and their corresponding reaction schemes.

related sequential reactions (Figure 102, Schemes f–j) with up to 88% yield and 97% ee value.[576] Salen-based CCOFs is more efficient than other salen-based heterogeneous catalysts such as MOFs.[577−579] A series of CCOFs, that is, TpPa-1, TpBD, TpBD-Me2 and TpTab upon postsynthetic modification of the enaminone groups with Cu(II) ions (Figure 102G) catalyze the asymmetric Henry reaction of nitroalkane with aldehydes (Figure 102, scheme k), albeit a 10% conversion and 35% ee value.[389]

13.3.2. Pore-Surface Engineering. By using the pore-surface engineering approach, an imine-linked achiral porphyrin COF with a pore size of 2.1 nm has been synthesized. The appended ethynyl groups can be predesigned in desired density onto the pore walls, which can be further functionalized via click reaction at room temperature to anchor chiral pyrrolidine units in a quantitative manner (Figure 103A).[167] Because the chiral pyrrolidine units serve as an asymmetric organocatalyst, the resulting $[Py]_x$-H_2P-COFs (x = 25, 50, 75, and 100%) promote Michael addition reactions with 100% conversion and 51% ee value (Figure 103, Scheme l).

To develop a robust catalytic system, the chemical stability of COFs is critical. As for the imine-linked COFs, the introduction of methoxy groups to the phenyl linker of the imine bonds triggers resonance effects that soften the polarization of the C═N bonds and reduce the charge repulsions between the layers. The resulting mesoporous TPB-DMTP-COF with a pore size of 3.26 nm has a high porosity (S_{BET} = 2105 m^2 g^{-1}) and is extremely stable in organic solvents and strong acids and bases. For example, the crystallinity and porosity are retained upon a 1 week treatment even in concentrated HCl, aqueous NaOH solution (14 M), and boiling water. On the basis of this stable skeleton structure, pore-surface engineering enables the integration of chiral pyrrolidine units onto the pore walls in a quantitative manner to generate a series of chiral $[(S)\text{-Py}]_x$-TPB-DMTP-COFs (Figure 103B, x = 0.17, 0.34, and 0.50).[80] After the chiral catalytic sites are introduced, the resulting $[(S)\text{-Pyr}]_x$-TPB-DMTP-COFs retain their crystallinity, porosity, and chemical stability, which endow the CCOFs with exceptional activity in the heterogeneous catalysis of asymmetric Michael addition reactions (Figure 103, Scheme m). The $[(S)\text{-Py}]_{0.17}$-TPB-DMTP-COF achieves 100% conversion in 12 h and an ee value of 92% in water at room temperature. Owing to the concentration effect of the nanopores, this $[(S)\text{-Py}]_{0.17}$-TPB-DMTP-COF is much more active compared with the molecular catalysts with the same catalytic structure. As the density of catalytic sites on the pore walls is increased, the catalytic activity

https://dx.doi.org/10.1021/acs.chemrev.9b00550
Chem. Rev. 2020, 120, 8814−8933

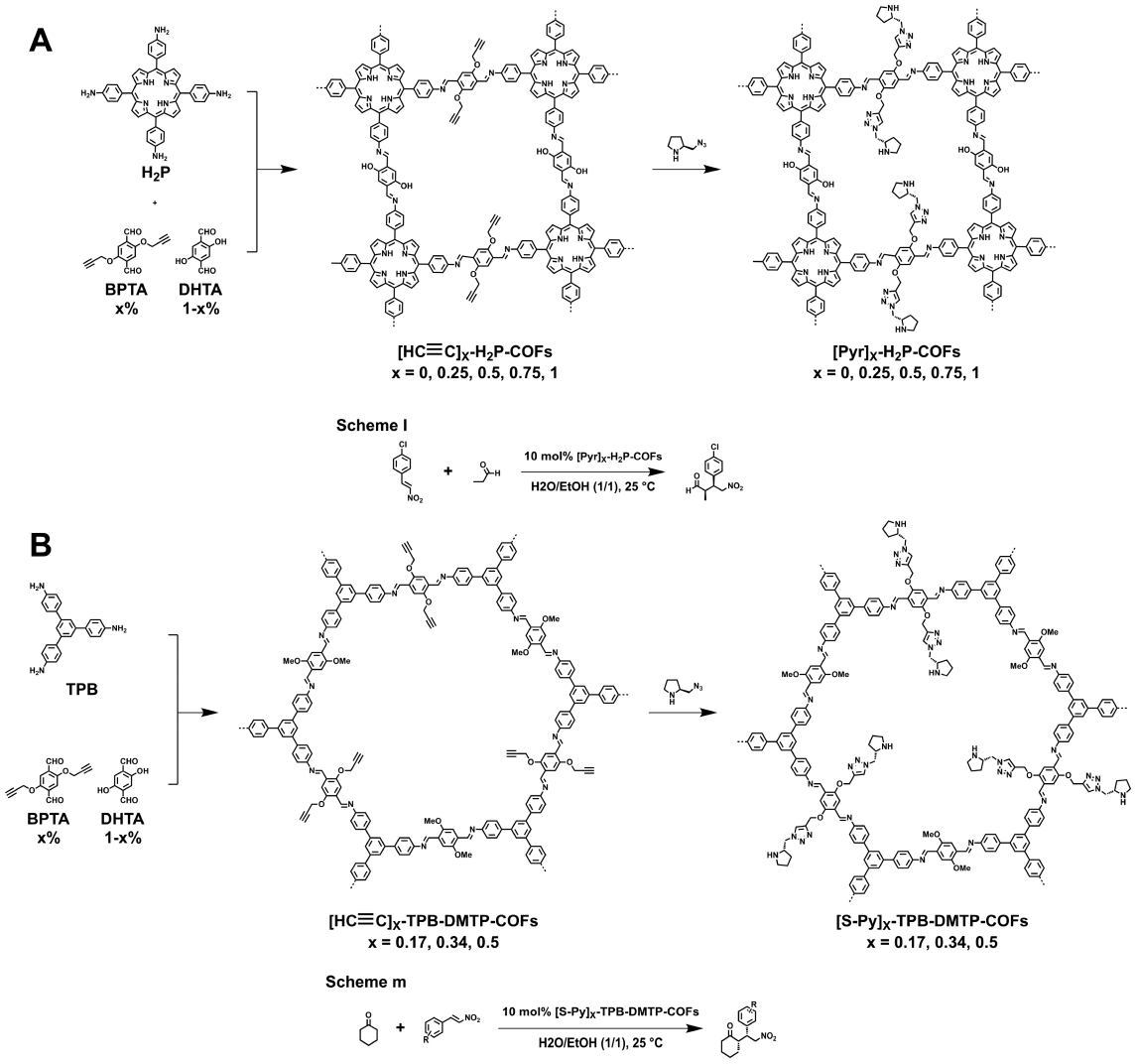

Figure 103. Schematics of the pore-surface engineering strategy to integrate chiral catalytic sites into (A) 2D H_2P-COFs and (B) TPB-DMTP-COFs as well as their catalytic reaction schemes.

shows a decreasing tendency owing to the limited space in the pores. Remarkably, the $[(S)\text{-Py}]_{0.17}$-TPB-DMTP-COF catalyst can be reused at least five cycles while retaining structural integrity and catalytic performance. The catalyst exhibits better recycling performance than other porous chiral polymers such as H-CPP (yield decreased from 96 to 39% after four cycles)[580] and chiral proline MOF MIL-101 (yield decreased from 66 to 48% after three cycles).[573]

The above systems demonstrate that COFs are promising in designing various catalysts for promoting asymmetric organic transformations; in particular, the use of large pore COFs offers a high freedom in developing various chiral catalysts with exceptional catalytic activity.

13.4. Metal-Based Catalysis

COFs offer a confined space to coordinate metal species that can be further developed as catalysts for organic transformation. For example, Pd(II) ions can coordinate to the imine bonds in the imine-linked COF-LZU1 (Figure 104A) to produce a catalyst for Suzuki−Miyaura coupling reaction (Figure 104, Scheme n).[65]

Remarkably, the bimetallically docked BPy-COFs with Pd(II) and Rh(I) catalytic sites (Figure 104B) enable a one-pot addition−oxidation cascade reaction (Figure 104, Scheme o).[240] The selective coordination of the two nitrogen ligands, that is, the imine linkages and bipyridine units with two different metal species, chloro(1,5-cyclooctadiene)rhodium(I) (Rh(COD)Cl) and $Pd(OAc)_2$, respectively, can be realized by using a successive docking method. The large and rigid Rh(COD)Cl predominantly coordinates with the bipyridine moieties, whereas the small and flexible $Pd(OAc)_2$ occupies the imine sites between the adjacent COF layers. The bimetallic Rh(I)/Pd(II)-based COF exhibits an excellent conversion of 90% in a one-pot addition−oxidation cascade reaction to yield an aromatic ketone (Figure 104, Scheme o). Notably, the individual single-metal-loaded COF composite did not show catalytic activity. Moreover, the Mn(II)/Pd(II) bimetallic-docked COFs can be fabricated via a similar programmed synthetic procedure and achieve a high catalytic activity in a Heck−epoxidation tandem reaction with a conversion up to 99%.[581]

Similarly, 2D porphyrin H_2P-Bph-COF (Figure 105A) and a 3D COF-300 (Figure 105B) are effective for the Suzuki, Heck, and Sonogashira cross-coupling reactions (Figure 105, Schemes p−t).[256,582] Their performances are superior to those of MOF-based[583] and SiO_2-based[584] heterogeneous catalysts. Interestingly, a series of 2,2′-bipyridine (BPy) COFs (Figures 105C)

https://dx.doi.org/10.1021/acs.chemrev.9b00550
Chem. Rev. 2020, 120, 8814−8933

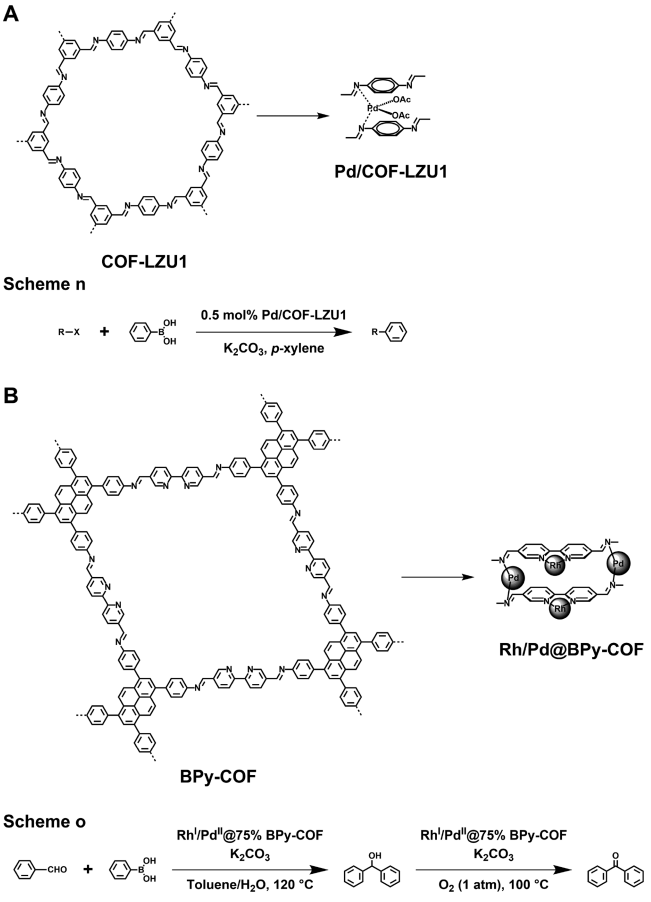

Figure 104. Schematics of catalytic binding sites of (A) Pd-loaded COF-LZU1 and (B) bimetallically docked BPy-COF and their catalytic reaction schemes.

with controlled contents of the Bpy edge units for Pd coordination have shown a high catalytic activity in the Heck coupling reaction (Figure 105, Scheme u).[252]

Vanadium-decorated TAPT-2,3-DHTA-COF (Figure 105D) and V@acac-CTF (Figure 105E) have been demonstrated to serve as efficient heterogeneous catalysts for a series of transformations, including the Prins reaction, sulfide oxidation and the Mannich reaction (Figure 105, Schemes v–x),[499,585] outperforming those of MIL-100 (Cr) (63% yield)[586] and MCM-41 (62% yield).[587] These results indicate the high capability of COF skeletons to discriminate different metal docking sites. This strategy opens a way to a novel type of catalytic cascade reaction. Moreover, immobilized with phosphomolybdic acid (PMA) and iron ions, Fe/PMA@CIN-1 (Figure 105F) acts as an efficient heterogeneous catalyst for the epoxidation of cyclooctene (Figure 105, Scheme y).[588] In addition to the docking of noble-metal complexes, a copper-infused imide-linked COF, that is, Cu@PI-COF (Figure 105G), promotes the Chan–Lam reaction between aryl boronic acids and amines (Figure 105, Scheme z), giving yields of up to 93% with good recyclability.[589]

13.5. Metal-Nanoparticle-Based Catalysis

The high porosity and large pore size of COFs in conjunction with the multiple chelating sites allow the accommodation of various metal nanoparticles to promote various organic transformations. For example, Pd nanoparticles can be anchored to the TpPa-1 COF to yield the Pd@TpPa-1 COF (Figure 106A). The Pd@TpPa-1 COF catalyzes Sonogashira coupling and Heck coupling reactions. Further studies show that it can catalyze a one-pot sequential Heck–Sonogashira reaction to achieve an 85% yield (Figure 106, Schemes aa–ac).[590] Similarly, loading Pd nanoparticles into the TpBpy COF (Figure 99) yields Pd@TpBpy, which serves as a reusable heterogeneous catalyst for the tandem Sonogashira coupling between 2-bromophenol and phenyl acetylene derivatives, producing benzo[*b*]furans at 70% yield.[591] In another study, Pd nanoparticles upon deposition on a CTF afford Pd@CTF (Figure 106B), which catalyzes the reduction of a wide range of nitroarenes to aryl amines with a yields of up to 99% and a high chemoselectivity of up to 99% in 2.5 h (Figure 106, Scheme ad).[592] This is better in terms of reaction time and temperature than Fe_2O_3/NGr@C (120 °C, 20–24 h)[593] and Fe-MMIO (70 °C, 0.67 to 1 h).[594]

Metal catalysts in conjunction with CCOFs has been developed for promoting asymmetric reactions by confining Pd nanoparticles into the channels of CCOFs. Starting from *S*-(+)-2-methylpiperazine and cyanuric chloride, Pd nanoparticles can be embedded into homochiral CCOF-MPC (Figure 106C). Pd@CCOF-MPC serves as a chiral catalyst for the asymmetric Henry reaction between aryl aldehydes and nitromethane (Figure 106, Scheme ae), providing an excellent yield of 99% and a 97% ee value. This catalyst is also active for the asymmetric Heck reaction between aryl bromides and 2-cyclohexen-1-one to achieve an excellent yield of 99% and a 97% ee value. For both reactions, the catalyst is tolerant for different functional groups and has excellent recyclability.[326] Remarkably, this catalyst is compatible with some recently reported catalysts for asymmetric Henry reactions, such as per-6-ABCD (98% yield, 90% ee)[595] and silica-supported (SBA-15) copper complex (97% yield, 97% ee).[596]

Confining metal nanoparticles into the 1D channels of COFs, that is, Thio-COF (Figure 106D), has also been explored by introducing thioether units to the pore walls that can coordinate with nanoparticles. Thio-COF shows strong binding with Pt nanoparticles to yield PtNPs@COF, which achieves a high catalytic activity in the reduction of 4-nitrophenol to 4-aminophenol (Figure 106, Scheme af) and reaches a full conversion in only 8 min. PdNPs@COF with 0.1 mol % loading of Pd nanoparticles catalyzes the Suzuki–Miyaura coupling between various aryl halides and phenylboronic acid (Figure 106, Scheme ag) up to a quantitative yield in only 3 h. Most importantly, in all cases, the catalyst achieves good recyclability for six cycles.[597]

13.6. Enzyme-Based Catalysis

The nanosized open channels of COFs offer a unique space to confine the enzyme in a spatially separated fashion. A mesoporous hollow spherical DhaTab COF has shown the possibility for the immobilization of a trypsin that is a serine protease to hydrolyze proteins.[81] The DhaTab COF (Figure 107A) has a BET surface area of 1480 $m^2\ g^{-1}$ and a pore size of 3.7 nm, and it is stable in water, an aqueous HCl solution (3 M), and the phosphate buffer (pH 7.4). By stirring the DhaTab COF in a trypsin buffer solution, trypsin can be successfully immobilized into the mesopores of the COF at a content of 15.5 μmol g^{-1}, as confirmed by PXRD, N_2 sorption, HR-TEM, and the confocal laser scanning microscopy (CLSM). Notably, this confinement enables the dispersion of the enzyme into the channels in a spatially separated way without causing any conformational change or blocking active sites, which, however,

https://dx.doi.org/10.1021/acs.chemrev.9b00550
Chem. Rev. 2020, 120, 8814–8933

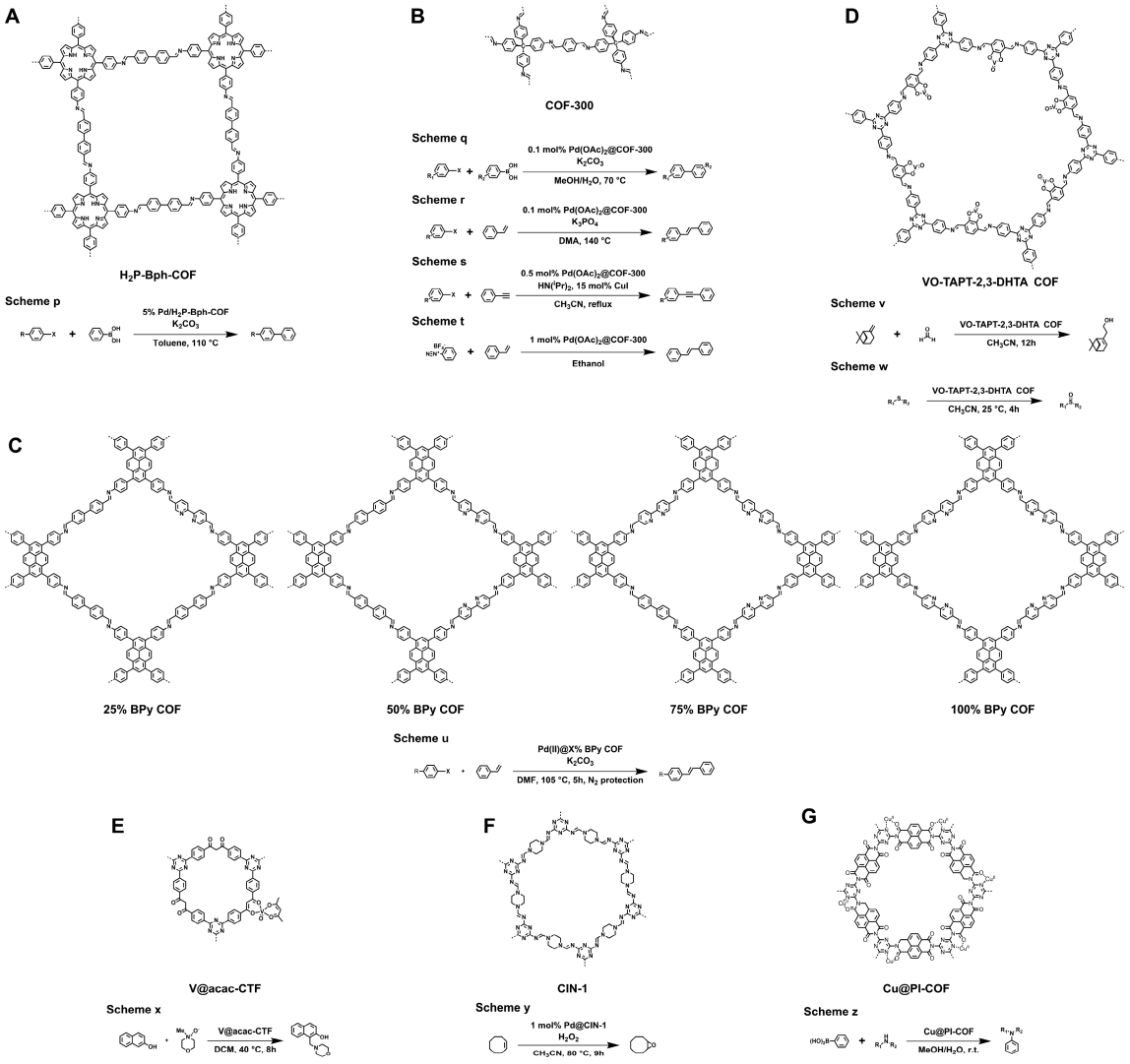

Figure 105. Schematics of catalytic binding sites of (A) H_2P-Bph-COF, (B) COF-300, (C) BPy-COFs (25% BPy COF, 50% BPy COF, 75% BPy COF, 100% BPy COF), (D) VO-TAPT-2,3-DHTA COF, (E) V@acac-CTF, (F) CIN-1, and (G) Cu@PI-COF as well as their catalytic reaction schemes.

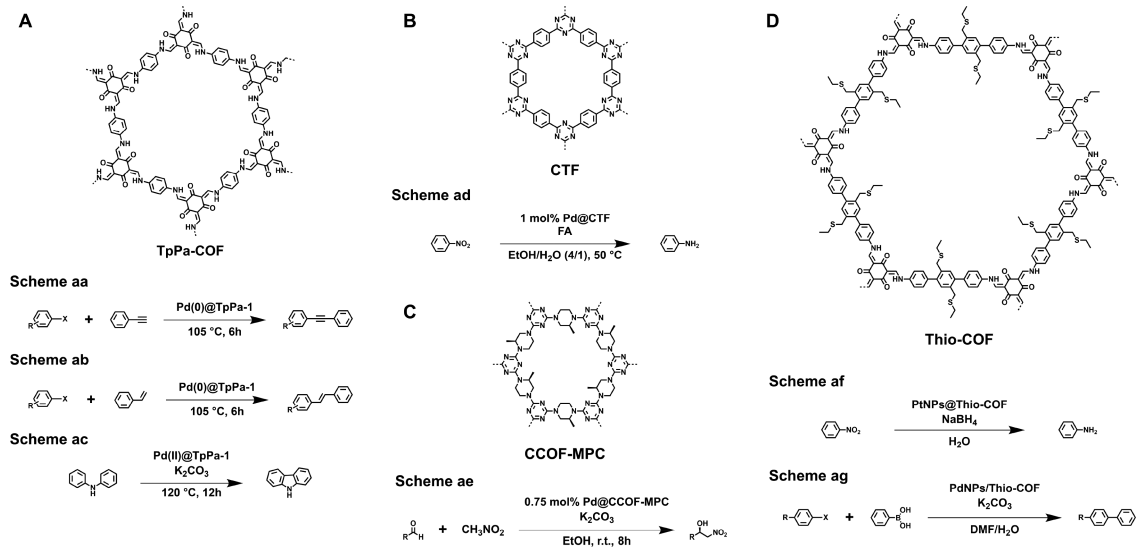

Figure 106. Schematics of (A) Pd@TpPa-COF, (B) Pd@CTF, (C) Pd@CCOF-MPC, and (D) M@Thio-COF for metal-nanoparticle-based catalysis.

https://dx.doi.org/10.1021/acs.chemrev.9b00550
Chem. Rev. 2020, 120, 8814−8933

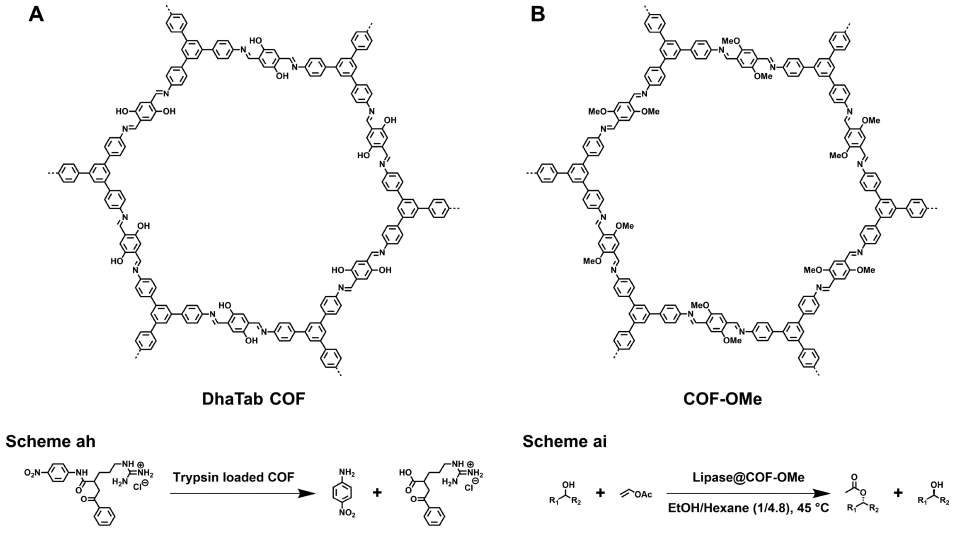

Figure 107. Schematics of (A) DhaTab COF and (B) COF-OMe for enzyme-based catalysis.

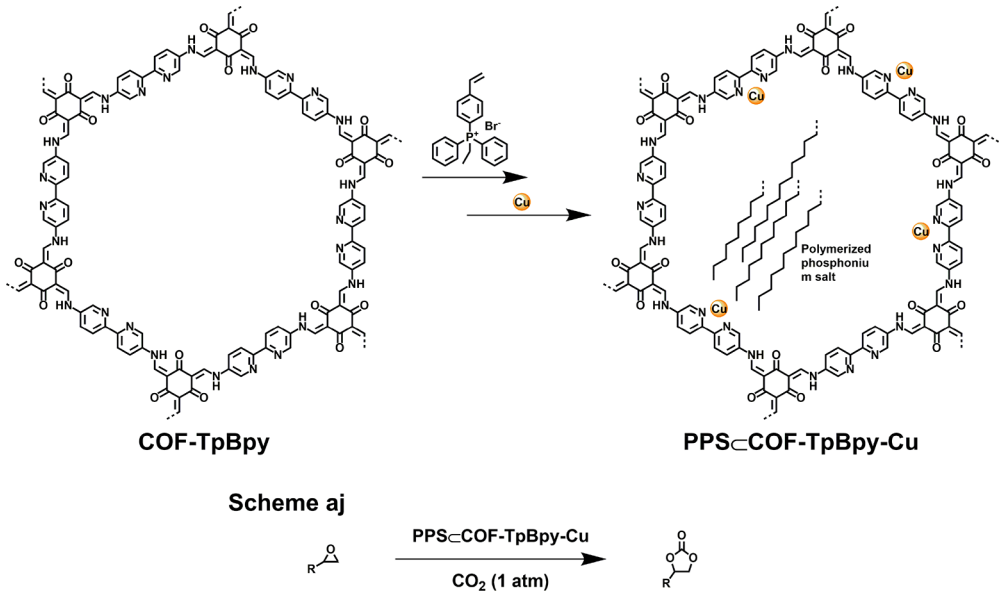

Figure 108. Schematic of the synthesis of PPS⊂COF-TpBpy and its catalytic reaction scheme.

usually happens in enzyme encapsulation and impairs the enzyme activity. The enzyme activity of the trypsin-loaded COF is evaluated by treating with *N*-benzoyl-L-arginine 4-nitroanilide (2 mM) in Tris buffer (pH 8) for 30 min (Figure 107, Scheme ah). A clear color change from colorless to yellow suggests the hydrolysis of *N*-benzoyl-L-arginine 4-nitroanilide, and the activity of the trypsin-loaded COF is 56.5 mmol g^{-1} min^{-1}, corresponding to 60% of the free enzyme activity. The DhaTab COF also exhibits higher trypsin loading and higher catalytic activity than SBA-15 (0.09 μmol g^{-1}, 44 μmol g^{-1} min^{-1})[598] and poly(epoxy-acrylamide) cryogel (2.8 μmol g^{-1}, 14.3 μmol g^{-1} min^{-1}) supported trypsin.[599]

Driven by favorable intermolecular interactions (hydrogen bonding, van der Waals forces, hydrophobic interactions) with the pore walls, the pores of COF-OMe (= TPB-DMTP-COF, Figure 107B) serve as a host for Amano lipase PS. The resulting host−guest system can be used for the kinetic resolution of racemic 1-phenylethanol with vinyl acetate (Figure 107, Scheme ai), which achieves a 49% conversion within 30 min, which is much higher than that of the free enzyme (3% conversion). It is suggested that binding enzymes to the COF initiates a conformational change that gives access to the catalytic site, thereby activating the enzyme to a more efficient status. Further studies reveal that the catalyst has a remarkable stability at high temperatures such as 120 °C, displays excellent recyclability, and is applicable to various alcohols.[600] Most importantly, this outperforms most enzyme-loaded mesoporous silica (50% conversion in 6 h)[601] and poly(vinyl alcohol) (42% conversion in 2 h).[602]

13.7. Polymerization

COFs are capable of *in situ* polymerization of the monomer to produce ionic linear polymers within the channels. This is interesting because it offers a secured approach to integrate ionic chains into the 1D channels. The condensation of 1,3,5-triformylphloroglucinaol (TP) and 5,5′-diamino-2,2′-bipyridine (Bpy) yields a chemically stable COF-TpBpy that possesses 2.1 nm sized pores and consists of open and accessible bipyridine sites that are ready for metal-ion coordination. In the presence of

https://dx.doi.org/10.1021/acs.chemrev.9b00550
Chem. Rev. 2020, 120, 8814−8933

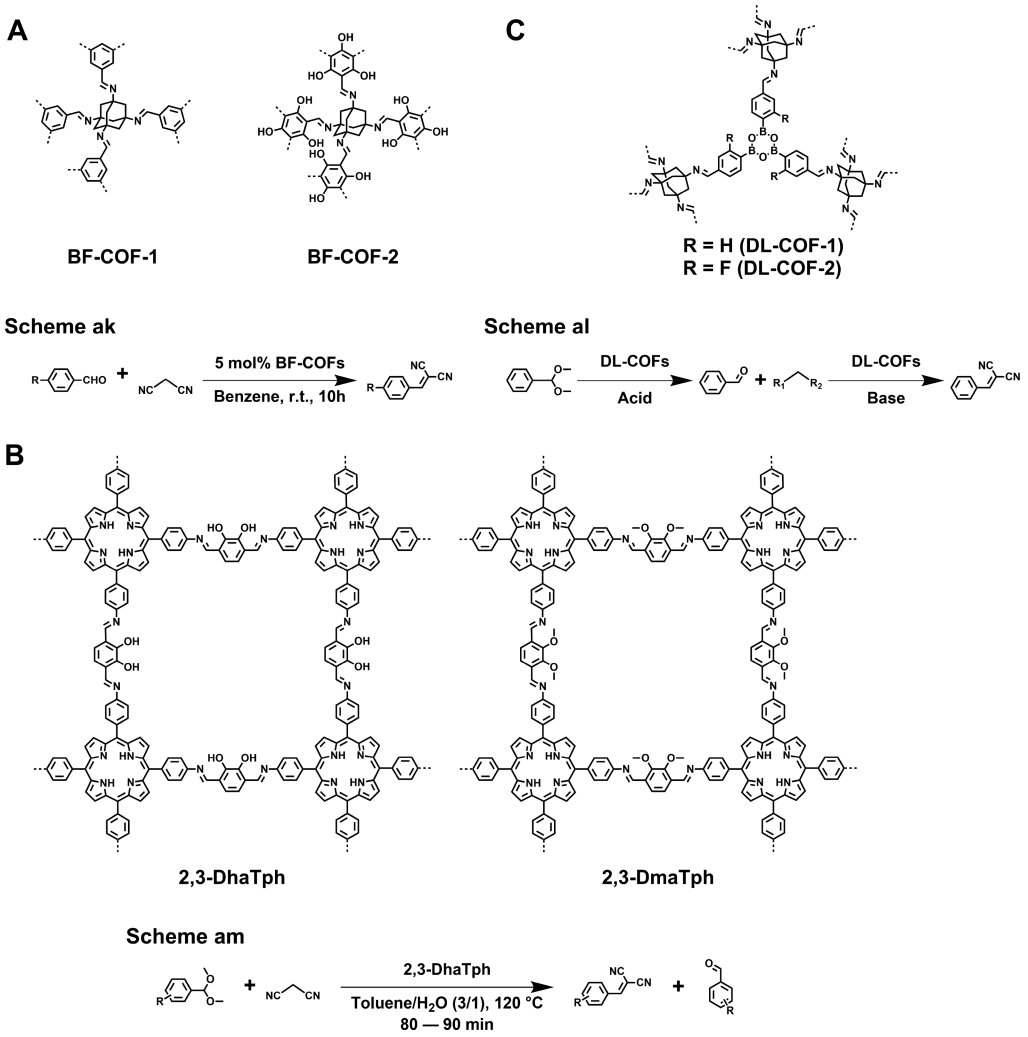

Figure 109. Schematics of other catalytic COFs of (A) BF-COF-1 and BF-COF-2, (B) 2,3-DhaTph and 2,3-DmaTph, and (C) DL-COFs.

COF-TpBpy, the polymerization of ethyldiphenyl(4-vinylphenyl)phosphonium bromide at 80 °C using azobis-(isobutyronitrile) (AIBN) as an initiator for 3 days yields PPS⊂COF-TpBpy (Figure 108), in which the polymeric phosphonium salts (PPSs) are confined within the nanopores of COF-TpBpy. Interestingly, the PPS chains in PPS⊂COF-TpBpy are flexible and movable, as evidenced by solid-state NMR measurements, indicating that COFs offer a quasi-homogeneous catalytic environment in the nanopores.

The bipyridine units on the pore walls of PPS⊂COF-TpBpy are active for coordination with Cu(II), yielding Cu(II)-ligated PPS⊂COF-TpBpy-Cu with a Cu loading content of 4.6 wt %. Notably, PPS⊂COF-TpBpy-Cu is still a porous material with a BET surface area of 496 $m^2 g^{-1}$, which enables the cooperation between the Lewis acids (Cu sites) on the pore walls of COFs and the bromide anions along the PPS chains for catalyzing the cycloaddition of epoxides with CO_2 to form cyclic carbonates (Figure 108, Scheme aj). Notably, the yield for carbonates reaches 95%, which is far superior to those of PPS (12%) and COF-TpBpy-Cu (5%). This PPS⊂COF-TpBpy-Cu catalyst is highly active for a variety of different epoxides and achieves impressive yields (93−98%) of corresponding carbonates. The confined nanospace in 2D COFs is fascinating because it can be designed to trigger cooperation between spatially uncorrelated Cu(II) sites and Br anions.[603]

13.8. Other Catalysis

The spatial confinement of reactants within the nanopores can induce specific interactions with the COF skeletons so that it promotes the catalytic reactions. For example, two 3D imine-linked microporous base-functionalized COFs, BF-COF-1 and BF-COF-2 (Figure 109A), have been synthesized via the condensation of tetrahedral TAA with TFB and TFP, respectively.[135] Because 1-adamatanamine is an alkyl amine and has a stronger basicity than aromatic amines, the resulting COFs have a stronger basicity than those of COFs made from aromatic amines. These two COFs serve as a base to catalyze the Knoevenagel condensation reaction (Figure 109, Scheme ak) and achieve excellent activity with a conversion >96%. Notably, BF-COF-1 with a pore size of 7.8 Å and a rectangular window of 7.8 × 11.3 $Å^2$ and BF-COF-2 with a cavity size of 7.7 Å and a rectangular window of 7.7 × 10.5 $Å^2$ are capable of size-selective catalysis.

The imine-linked porphyrin COFs, that is, 2,3-DhaTph and 2,3-DmaTph (Figure 109B), have been developed for one-pot acid−base-catalyzed cascade transformations of acetal into aldehyde and then malononitrile via Knoevenagel condensation (Figure 109, Scheme al).[97] The 2,3-DhaTph COF achieves a 96% conversion within 90 min, which makes a sharp contrast with the 2,3-DmaTph COF with only 52% conversion due to the absence of acidic −OH groups in the COF skeletons that are

https://dx.doi.org/10.1021/acs.chemrev.9b00550
Chem. Rev. 2020, 120, 8814−8933

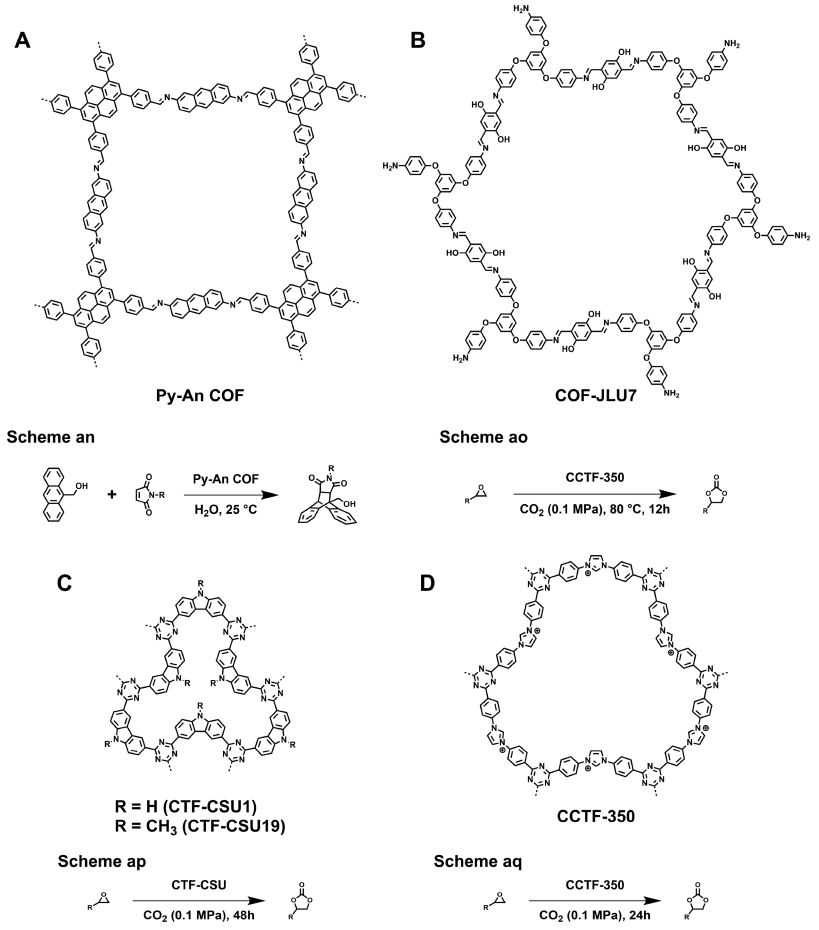

Figure 110. Schematics of (A) Py-An COF with anthracene edge units, (B) COF-JLU7, (C) CTF-CSU, and (D) CCTF-350.

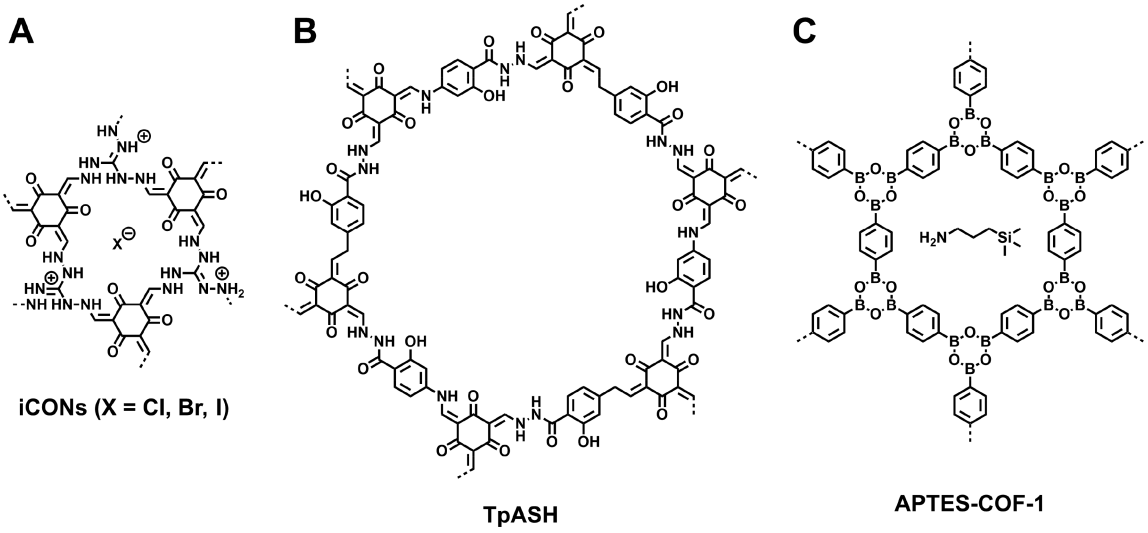

Figure 111. Schematics of (A) iCONs, (B) TpASH, and (C) APTES-COF-1.

required to catalyze in the first-step deacetalization reaction. The 2,3-DhaTph COF can be cycled five times. Similarly, double-linkage 3D COFs, including DL-COF-1 and DL-COF-2 (Figure 109C), have been developed for the acid−base-catalyzed one-pot cascade reaction with high yield up to 98% (Figure 109, Scheme am).[277]

Integrating anthracene units to the edges of an imine-linked 2D Py-An COF (Figure 110A) generates π-channels with anthracene C−H groups extruding from the pore walls. Remarkably, these extruded C−H units form C−H···π interactions with the reactants and promote Diels−Alder reactions in water to achieve 91% yield at room temperature in 48 h (Figure 110, Scheme an).[239] This environmentally benign condition for the Diels−Alder reaction is promising for the implementation of COF catalysts. Compared with MOF-1,

https://dx.doi.org/10.1021/acs.chemrev.9b00550
Chem. Rev. 2020, 120, 8814−8933

which requires heating,[604] The Py-An COF represents a more energy-efficient route for the Diels–Alder reaction.

Owing to the superior CO_2-philic properties of triazine moieties, triazine-based COF-JLU7 (Figure 110B), CTF-CSU (Figure 110C), and CCTF-350 (Figure 110D) are highly active in catalyzing the cycloaddition of CO_2 and epoxides to form cyclic carbamates, achieving almost quantitative yields under some conditions (Figure 110, Schemes ao–aq).[605−607]

14. BIO-RELATED FUNCTIONS AND APPLICATIONS

Combining outstanding thermal and chemical stabilities, structural designability, and inherent porosity in one material, COFs have shown their potential in biorelated applications. Currently, focus has been devoted to exploring COFs for antibacterial activity and drug delivery. The basic concept is that the skeletons have been developed for docking specific functional sites to trigger interplay with cells that cause antibacterial activity or target cancer cells, and the pores can be designed to load specific drugs for delivery into cells.

14.1. Antibacterial Activities

By appending charged species to the skeletons, a guanidinium-based ionic COF has shown antimicrobial function.[608] The guanidinium-based ionic covalent organic nanosheets (iCONs), that is, $TpTG_{Cl}$, $TpTG_{Br}$, and $TpTG_{I}$ (Figure 111A), have been synthesized via a condensation reaction between TFP and amines (TG_X) (X = Cl, Br, and I). The iCONs exhibit outstanding stability in water, common organic solvents, and an aqueous HCl solution (3 M). $TpTG_{Cl}$, $TpTG_{Br}$, and $TpTG_{I}$ exhibit antibacterial activity by showing a dramatic drop of colony forming units for both Gram-positive (*Staphylococcus aureus*) and Gram-negative (*Escherichia coli*) bacteria. FE-SEM studies reveal that both Gram-positive and Gram-negative bacteria lose their uniform morphology in the presence of iCONs and change into a ruptured, shrunken, and twisted morphology. These morphology changes are related to the collapse of the bacteria cell membrane, which is a negatively charged phospholipid bilayer; the interactions with iCONs eventually cause cellular content leaching and lead to the death of bacteria. The interplay is mainly an electrostatic interaction between the positively charged guanidinium units of iCONs and the negatively charged phospholipid bilayers of the cells. Inspired by the antibacterial property and strong stability of iCONs, a TpTGCl@PSF membrane of polysulfone (PSF) and TpTGCl on a porous nonwoven supported fabric has been prepared. The shrinking and rupture morphology of the bacteria on the TpTGCl@PSF membrane confirms the antibacterial nature of the membrane. Usually, guanidinium-based antibacterial agents are highly soluble and difficult to be cyclically used. The integration of guanidinium units to the COF skeletons offers a heterogeneous platform for constructing antibacterial materials with high stability and cycle capability.

14.2. Drug Delivery

The extensively explored nanoparticles, biocompatible polymeric materials, liposomes, and MOFs that are used as vectors for drug delivery usually lack functionality and chemical stability, and the tedious synthetic hurdles and unwanted toxic metal ions leached from the carriers might lead to unsatisfactory drug delivery performance.[609] In relation to the adsorption and encapsulation behaviors, the nanosized pores of COFs are useful for loading and delivering drugs. The imide-linked 3D PI-COF 4 and PI-COF 5 have shown the capability of drug delivery.[54] PI-COF 4 (Figure 15E) bearing a noninterpenetrated diamond net with a surface area of 2403 $m^2\ g^{-1}$ and a pore size of 13 Å is constructed by the condensation of PMDA and TAA. In contrast, PI-COF 5 (Figure 15E) with a four-fold-interpenetrated diamond network structure is synthesized by the condensation of PMDA and TAPM, which exhibits a BET surface of 1876 $m^2\ g^{-1}$ with a pore size of 10 Å. Ibuprofen (IBU) is a nonsteroidal anti-inflammatory drug with molecular size of 5 Å × 10 Å. PI-COF 4 and PI-COF 5 are loaded with IBU by stirring in a hexane solution of IBU for 2 h to achieve a loading content of 24 and 20 wt %, respectively. The drug release process is monitored by electronic absorption spectroscopy, and both COFs release 95% of IBU in simulated body fluid within 6 days. To show the generality of the drug release capability, another two drugs, that is, captopril and caffeine, have been investigated under similar conditions. The resulting COFs release these two drugs in a way that is similar to that of IBU-loaded COFs.

The biocompatibility and cell permeability are essential for drug delivery to the specific target. Imine-linked 2D PI-3-COF (= N_3-COF, Figure 70D) and PI-2-COF (= N_2-COF, Figure 70C) have been synthesized by the condensation of TFB and 2,4,6-tris(4-aminophenyl)-*s*-triazine and by the condensation of TFB and 4,4′-biphenyldiamine, respectively.[70] PI-3-COF has a BET surface area of 1000 $m^2\ g^{-1}$ and a pore size of 1.1 nm, whereas PI-2-COF has a BET surface area of 1700 $m^2\ g^{-1}$ and a pore size of 1.4 nm. PI-3-COF and PI-2-COF have a total pore volume of 0.662 and 1.138 $cm^3\ g^{-1}$, respectively. These two COFs form spherical nanoparticles upon dispersion in a phosphate-buffered saline (PBS, 0.02%). Drug-loaded COFs are prepared by immersing COFs into a hexane solution of 5-fluorouracil (5-FU) and stirring for 6 h; the loading amount was 20 and 30 wt % for PI-3-COF and PI-2-COF, respectively. By using MCF-7 cells (Michigan Cancer Foundation-7, a breast cancer cell line) as a typical example, the biocompatibility of these COFs has been investigated. Notably, the cell viability remains >80% upon a 24 h incubation in the presence of the bare COFs at a high concentration of 200 $\mu g\ mL^{-1}$, indicating the good biocompatibility of the COFs. The viability of the cells in the presence of 5-FU is only 20% after 24 h. As for the 5-FU-loaded COFs, the cell viability is 40% after 24 h and 10% after 48 h. Electronic absorption spectroscopy reveals that 5-FU has been released at a similar rate to reach 85% within 3 days. Confocal laser scanning microscopy images confirm that the COFs enter the cells via endocytosis. COFs loaded with captopril and IBU exhibit a similar release behavior as that of the 5-FU-loaded COFs.

Postsynthetic modification is an efficient method to endow COFs with drug delivery property. TpASH CON (Figure 111B) upon transformation of hydroxyl groups to amine units can anchor targeting ligands to trap specific cancers for the site-specific drug delivery.[610] The resulting TpASH-FA CON shows a 12% loading efficiency of 5-FU and release 74% of 5-FU in 72 h at pH = 5, which is the lysosomal pH value of cancer cells. This result suggests that COFs have the possibility of delivering drugs to cancers, which can minimize the side effects of nonspecific targeting.

The self-assembly of polyethylene-glycol-modified monofunctional curcumin derivatives (PEG-CCM) and amine-functionalized COF-1 can produce water-dispersible polymer–COF nanocomposites.[611] The entire structure of PEG-CCM@APTES-COF-1 can be regarded as a micelle with APTES-COF-1 (Figure 111C) as the oil phase and PEG-CCM as the surfactant. The surface modification of APTES-COF-1 with a pharmacokinetic modifier PEG-CCM enhances the

https://dx.doi.org/10.1021/acs.chemrev.9b00550
Chem. Rev. 2020, 120, 8814–8933

biocompatibility of the nanocomposites and prolongs their blood circulation time. For example, PEG_{2000}-CCM@APTES-COF-1 can load drug with a content of 9.71 ± 0.13 wt % and a high encapsulation efficiency of 90.5 ± 4.1%, which is much higher than those of bare APTES-COF-1. This loading efficiency is among the highest values for the existing drug-loaded COF systems and is comparable to the MOF carrier system as well. In the case of a drug DOX, PEG-CCM@APTES-COF-1@DOX displays higher penetration, longer retention, and better tumor inhibition compared with APTES-COF-1@DOX system. On the basis of the ex vivo fluorescence imaging of the drug distribution, PEG2000-CCM@APTES-COF-1@DOX exhibits the highest drug accumulation on the tumor as it shows the highest fluorescence intensity. This result demonstrates an efficient way to develop multifunctional platforms for in-vivo-targeted drug delivery to specific cancers.

15. SUMMARY, PERSPECTIVES, AND OPPORTUNITIES

Over the past decade, great efforts have been invested in developing the COF field. Unlike other porous materials including zeolites, mesoporous silicas, metal−organic frameworks, cage compounds, and amorphous porous organic polymers, COFs are a unique class of polymers and extended molecular frameworks. The uniqueness is that their structures can be predesigned via the topological design of building blocks, and the organization of extended structures is driven by either reversible or irreversible chemical reactions to assume crystallinity and structural integrity. Therefore, the chemistry involved in COFs is basically organic chemistry and polymer chemistry; this difference casts a sharp contrast with MOFs that are based on inorganic coordination chemistry, although both belong to the extended crystalline porous structures in addition to two other families of zeolites and mesoporous silicas.

During the past decade, the chemistry of COFs has been steadily developed, and this has lead to the rapid progress of the field. The advancement of this emerging polymer field is encouraging and is attracting increasing interest from different fields. Consequently, a careful nomenclature of novel COFs is necessary, and naming the same reported COFs differently should be avoided, which, however, is currently observable for certain COFs. Although a variety of different properties and functions have been developed, as analyzed in this Review, many key issues associated with the underlying chemical principles and the physical nature remain unclear and deserve to be disclosed. This means the potential of COFs is far from the levels that have been fully explored. There are still many aspects to be developed in relation to the chemistry, physics, materials science, and implementations. Herein we clarified the future directions of these aspects.

15.1. Chemistry

On the chemistry side of COFs, an important aspect is to make single crystals of COFs that would elucidate unidentified chemistry associated with the extended structures. The development of a general method that enables us to create single crystals of various COFs is highly desired. In relation to this, the recent studies on controlling the framework growth process are interesting and deserve a further extension to various frameworks. This would undoubtedly contribute to a better understanding of structure−function correlation and help to design unique structures for meeting the requirements from the materials side.

COFs are based on the topology design diagram using different combinations of monomers with different geometries. The development of new topology is of fundamental importance to the field. In addition to the regular polygon structures, COFs have an open chemistry that allows for the integration of ordered yet irregular polygon structures. Efforts in this direction are still limited but are promising to bring about a new chance for the field of COFs. Another issue of the same importance is to develop new reactions for the synthesis of COFs. New reactions not only greatly broaden the diversity of COFs structures but also enrich the chemistry, physics, and materials science of the field. One critical issue is that such a reaction must be able to create high crystallinity; some of the systems give rise to materials with very weak or even no XRD peaks. Indeed, materials with limited crystallinity may not be suitable to name as or categorize into the COF family. The expansion of the pores of COFs to a large size deserves further efforts, and developing the pore size down to several angstroms, close to the size of small molecules such as gases, is a subject of great interest for gas adsorption and separation. The exploration of new building blocks for COFs is a straightforward way to achieve new skeletons, pores, and functions. COFs have shown outstanding stabilities under acid and base conditions, and further advancement should be directed to the establishment of COFs that can meet the stability requirements for implementation.

15.2. Physics

COFs offer a predesignable platform for molecular architecture and materials construction. The extended organic structure based on the topological diagram renders COFs able to build up primary and high-order hierarchical structures. In the 3D COFs, the impact of multifold interpenetration and its control are interesting subjects to be further explored. This aspect is key to the development of efficient and specific space within the frameworks. The confined nanospaces produced by 3D COFs need to be further explored in terms of their diversity, tunability, and controllability. In particular, the interplay with photons, electrons, holes, charges, spins, ions, and molecules that is triggered in the confined nanospace needs to be extensively investigated and established. Considering the broad availability of the building blocks, 3D COFs can be further developed upon design and synthetic control to challenge more specific functions beyond the present scope. Studies along these directions would promote the structural and functional designs to a much accurate and pinpointed level.

In the case of 2D COFs, the unique dimensionality offers well-ordered intraframework domains to explore and develop various specific interplays over wide time and spatial spans. We envisage that the structural domains can be considered at three different zone aspects: (1) the skeletons associated with the π-arrays including knot, linker, and edge parts, (2) the pore walls including the orientation, distribution, density, and alignment of side units extruded from the walls to the pores, and (3) the 1D channels featured by the pore size, pore shape, and pore environment. These different zones separately and collectively work and enable us to trigger a variety of different interplays. At different structural levels of primary and high-order structures, these interplays are different in scale and strength and lead to different effects. To disclose these hierarchy structure-dependent differences and their origins is a must for the physics aspect of the COF field.

At the structural level of the 2D monolayer and a few layers, the interplay triggered by the skeletons is dependent on the local

https://dx.doi.org/10.1021/acs.chemrev.9b00550
Chem. Rev. 2020, 120, 8814−8933

knot, linker, and edge structures and is perturbed by the global extended 2D layer network, and the interactions between layers are weakened. Properties including mechanical strengths, electronic interactions, exciton diffusion, and the tunneling effect become much more prominent. The interplay mediated by the pore walls would decrease the collective effect and is more specific and restricted to point-to-point or side-to-side interactions. Thus to trigger effective interactions with pore walls, strong interactive sites are much preferred. Moreover, the interplay originating from the pores becomes more significantly dependent on the pore dimensionalities such as the pore size, pore shape, and pore depth. With the assistance of the specific units on the pore walls, the elucidation of interplay in the pores at this structural level might provide insights into the molecular separation and mass transport through single-layer or a few-layer COF membranes.

At the level of stacked structures of many layers and bulk materials, the interplay on the skeletons dominates a variety of phenomena such as exciton migration, charge-carrier transport, conduction, and redox reaction. These interactions are controlled by a collective effect of many layers and the extended 2D frameworks. In strong correlated cases, the frameworks can be treated and considered as single nanosized mega macromolecules, in which intramolecular interactions are greatly reinforced, so that some events even become coherent. The elucidation of how the skeletons interact with photons, excitons, phonons, spins, and charges is an interesting subject with a high possibility of new findings. The pore walls are the major factors that mediate the interplay with charges, ions, and molecules once they enter the pores. The different interactions such as hydrophobic interactions, the electrostatic effect,[241] the dipolar effect, C−H···π interactions, ligations, and electronic effects can be triggered and controlled by the pore walls. The understanding of how pore walls affect and control these interactions is important but remains to be well established. Moreover, the 1D nanopores of 2D COFs offer a discrete nanospace for each pore that is structurally independent from the neighboring channels. Such ordered channels are useful in molecular entrapment, separation, discrimination, stabilization, and transportation. The effects of pore size and pore shape are major factors to determine these processes, and the pore walls also interfere with the guest molecules, especially for the case of small pore size or the tight contact of guest molecules with the pore walls. To unravel these interactions would contribute to a deep understanding of the nature of these ordered 1D nanochannel arrays.

Clearly, these interplays, depending on their nature, cover a wide temporal span from femtosecond to picosecond, nanosecond, and further to minutes and even much longer times, and spatially, these interplays initiate on the angstrom scale of atoms and bonds, extended to nanometer scale of molecules and even much larger bulk materials. The understanding of these interplays is important and remains a challenge.

Therefore, in the aspect of physics, the clarification of the structure−function correlation at different temporal-spatial scales is essential for the field of COFs. In particular, the mechanisms underlying the functions and properties can provide feedback in regards to the structural design and can help to make unique COFs in targeting various functions. This helps in the innovative creation of COFs to a level of functional design. In this sense, understanding the structure−function relationships at the single-layer, few-layer, and bulk-materials levels of COFs is an important subject that remains to be well explored.

15.3. Materials

In relation to the materials science aspect, the potential of COFs remains a major subject to be extensively explored. The skeletons and pores are versatile for design and control; in this sense, COFs are powerful for systematic structural programming. The porous structures are key to a variety of functions, including gas sorption, storage and separation, catalysis, ion conduction, and energy storage. There are many issues related to the porosity that should be addressed in future. The synthesis of COFs with a high BET surface area, large pore volume, and suitable pore size should be taken into consideration on the molecular design stage. For example, designing COFs for CO_2 adsorption requires a total design of pore size, pore volume, and pore-wall functionalities. In particular, COFs with a high CO_2 uptake at low pressure (~0.15 bar) are requested for real applications. In this content, compared with 2D COFs, 3D COFs with substantially large free volume, porosity, and surface area are ideal for CO_2 capture.

In sharp contrast with inorganic porous materials like zeolites and clays that suffer from inherent low porosity, amorphous porous organic polymers with an intricate structure−property correlation, and most MOFs with low stability, stable COFs are attractive materials to remove pollutants because their open apertures and 1D channels free of chain entanglement and pore interpenetration enable full access to the porous space. Nevertheless, studies on the effective and rapid adsorption of pollutants, especially organic and antibiotic pollutants, are still limited and deserve further efforts.

COFs have shown their potentials for catalytic reactions; however, exploring COFs to have much higher catalytic activity and better recyclability is essential for heterogeneous catalysts. In clear contrast with MOFs, COFs are produced via the modular fashion synthetic strategy, which makes the straightforward incorporation of functional groups easy, thereby creating a promising playground for exploring COFs as heterogeneous catalysts, and the tunable pore environment of COFs is ideal for replicating the selectivity and precision of enzymes.

The ordered structures of COFs have an advantage over the small-molecule systems targeting for sensing in the terms of signal amplification and rapid signal transduction. Compared with MOFs, COFs have been proven to possess excellent luminescence activity combined with the unique features of low density and high chemical and thermal stability, which greatly expands their sensing scope. Further structural engineering toward the development of new fluorescent and phosphorescent materials is essential to expand the scope to biosensors or biomarkers, which is a promising future direction of the field. In relation to this, developing COF-based active layers to fabricate highly efficient LED diodes remains unexplored. An important direction for the application is to address environmental issues. Recent advancements have shown the great potential of COFs for the removal of toxic metals such as mercury from aqueous solutions. This direction should be further reinforced and broadened to cope with various types of environmental contamination in air, water, and soils.

A major advantage of COFs over MOFs is that COFs enable the design and synthesis of organic semiconductors and photoconductors that show inherent high mobility and achieve high conductivity upon oxidation or reduction. Further investigations of the fundamental electronic properties of COFs over a broad structural range are necessary for screening suitable candidates for such applications with the accompanying trial and error. Meanwhile, the development of high-quality

https://dx.doi.org/10.1021/acs.chemrev.9b00550
Chem. Rev. 2020, 120, 8814−8933

COFs thin films with controllable thickness and studies on their device performance in field-effect transistors and solar cells will shed light on this field.

Owing to their well-defined 1D channel structures, COFs have been explored for proton conduction, which is paramount for fuel cells. The innovative structural design of COFs would open a new avenue to a high-rate proton-conducting membrane, aiming to replace the high-cost Nafion with proton conductivity of 10^{-1} S cm^{-1}. Other proton-conducting polymers such as polyelectrolytes lack synthetic control over the complex structures. Block copolymers form a phase separation that makes it difficult to yield well-defined and stable channel structures. Most MOFs tend to decompose under energy-conversion conditions such as strong acidic and basic media, and certain metal species could be toxic and have environmental concerns. In contrast, COFs offer a predesignable platform that can solve these bottleneck issues, and the built-in highly ordered 1D channels offer an ideal proton-conducting pathway. In this regard, the further development of functionalized COFs with robust thermal and chemical stability under strong acidic conditions will achieve the targets.

The accessibility of redox-active sites, the electrolyte diffusion, and the electric conduction are important parameters required for energy storage, and they directly affect the energy density, power density, and cycle life of energy-storage devices. Atomic-precision structural designability, building block diversity, and high porosity endow the COFs with unique aspects such as an increased accessibility of the redox-active site, facilitated electrolyte diffusion, and enhanced cycle stability. However, COFs are usually insulators and have limited electric conductivity. A suitable method to enhance the conducting property is the carbonization of COFs. However, a strategy that can retain the COF structural features such as dimensionality and porosity is necessary. The development of a general strategy for the pyrolysis of COFs into carbons with retained structural features of COFs will further accelerate the applications of COFs in the field of energy storage and conversions.

As for the biorelated applications, rather than MOFs with toxic metal species, COFs could provide a unique platform for creating a predesigned nanospace with specifically sequenced docking sites. Efforts along this direction will pave the way to the selective encapsulation and separation of biomolecules in an efficient manner. In the case of drug delivery, the biocompatibility and toxicity of COFs need to be documented in detail, and the design of skeletons without toxicity is a minimum requirement.

Making COFs processable is crucial for exploring industrial and commercial applications, but most COFs are currently prepared as powders with limited processability. Microfluid and gelation systems have opened a way to endow COFs with remarkable processability while retaining crystallinity and porosity. Combining the COF structure designability and the processability is an attractive and important direction worth further efforts.

The practical implementation is mainly based on further achievements in the chemistry, physics, and materials science of COFs. We envisage that the COF field in the next decade will further grow in both deepness and broadness.

AUTHOR INFORMATION

Corresponding Author

Donglin Jiang − *Department of Chemistry, Faulty of Science, National University of Singapore, Singapore 117543 Singapore; Joint School of National University of Singapore and Tianjin University, International Campus of Tianjin University, Binhai New City, Fuzhou 350207, P. R. China;* orcid.org/0000-0002-3785-1330; Email: chmjd@nus.edu.sg

Authors

Keyu Geng − *Department of Chemistry, Faulty of Science, National University of Singapore, Singapore 117543 Singapore*

Ting He − *Department of Chemistry, Faulty of Science, National University of Singapore, Singapore 117543 Singapore*

Ruoyang Liu − *Department of Chemistry, Faulty of Science, National University of Singapore, Singapore 117543 Singapore*

Sasanka Dalapati − *Field of Environment and Energy, School of Materials Science, Japan Advanced Institute of Science and Technology, Nomi 923-1292, Japan*

Ke Tian Tan − *Department of Chemistry, Faulty of Science, National University of Singapore, Singapore 117543 Singapore*

Zhongping Li − *Department of Chemistry, Faulty of Science, National University of Singapore, Singapore 117543 Singapore*

Shanshan Tao − *Department of Chemistry, Faulty of Science, National University of Singapore, Singapore 117543 Singapore*

Yifan Gong − *Department of Chemistry, Faulty of Science, National University of Singapore, Singapore 117543 Singapore*

Qiuhong Jiang − *Department of Chemistry, Faulty of Science, National University of Singapore, Singapore 117543 Singapore*

Complete contact information is available at: https://pubs.acs.org/10.1021/acs.chemrev.9b00550

Notes

The authors declare no competing financial interest.

Biographies

Keyu Geng is currently a Ph.D. student at the National University of Singapore. He received his Bachelor's degree of Engineering in Macromolecular Materials and Engineering from Zhejiang University in 2017. He started his Ph.D. study at the Department of Chemistry, National University of Singapore under the supervision of Professor Donglin Jiang in 2018. His research interest focuses on exploring structural and functional diversities of sp^2-conjugated covalent organic frameworks.

Ting He received his Bachelor's degree from Sun Yat-sen University in 2010, his Master's degree from Lanzhou University in 2013, and his Ph.D. degree from Tianjin University in 2018. After that, he joined Professor Donglin Jiang's group at the National University of Singapore as a postdoctoral research fellow. His current interest focuses on designing COFs for photocatalysis.

Ruoyang Liu is currently a Ph.D. student in the Department of Chemistry at the National University of Singapore. He received his Bachelor's degree in Chemistry with honors from the National University of Singapore in 2018 and was awarded the President's Graduate Fellowship to pursue his Ph.D. studies in Professor Donglin Jiang's group. His current scientific interest focuses on the development of covalent organic frameworks (COFs) for photocatalytic applications.

Ke Tian Tan is currently a Ph.D. student at the National University of Singapore. She received her undergraduate degree at the National University of Singapore in 2018 and then joined Professor Donglin

https://dx.doi.org/10.1021/acs.chemrev.9b00550
Chem. Rev. 2020, 120, 8814−8933

Jiang for her Ph.D. study. Her research mainly focuses on the design synthesis of covalent organic frameworks.

Zhongping Li is a Ph.D. student at the School of Materials Science, Japan Advanced Institute of Science and Technology. He received his Master's degree in Chemistry from Jilin University in 2016. He received a JSPS scholarship as a Ph.D. student from 2018 to 2020 and joined Professor Donglin Jiang's group. His current scientific interest focuses on designing light-emitting COFs.

Shanshan Tao received her B.S. in 2011 at Xinyang Normal University and her Master's degree in 2014 from Beijing Normal University. In 2017, she got her Ph.D. degree in Physical of Sciences at SOKENDAI (The Graduate University for Advanced Studies). From October 2017 to March 2019, she was a JSPS PD fellowship at JAIST. From July 2018 to March 2019, she was a visiting researcher of JSPS at the National University of Singapore. She started her postdoctoral research at the National University of Singapore in April 2019. Her scientific interests focus on the design and preparation of covalent organic frameworks for ion conduction.

Yifan Gong is currently a Ph.D. student at the National University of Singapore. She obtained her Bachelor's degree in Polymer Materials and Engineering from Fudan University in 2019. She was selected for NUS's Graduate School for Integrative Science and Engineering (NGS) project under the supervision of Professor Donglin Jiang. Her current scientific interests are focused on the design and synthesis of semiconducting COFs.

Qiuhong Jiang studied at Biochemistry and Molecular Biology and received her doctoral degree under the supervision of Professor Hiroto Okayama at The University of Tokyo in 2005. She joined Professor Jiang's group since August 2016 as a research fellow. Her current research interests are on COFs for biomedical application.

Donglin Jiang received his B.Sc. degree (1989) from Zhejiang University and his Ph.D. degree (1998) from The University of Tokyo. In 1998. He took an assistant professorship (1998−2000) at The University of Tokyo, and in 2000 he was appointed as the group leader of AIDA Nanospace project, The Exploratory Research for Advanced Technology (ERATO), Japan Science and Technology (JST). In 2005, he moved to the Institute for Molecular Science (IMS), National Institutes of Nature Sciences (NINS) as an associate professor and took a concurrent associate professorship at SOKENDAI, Japan, where he started his independent laboratory and initiated the studies on covalent organic frameworks. During 2005−2009 and 2009−2013 he was appointed as a principal investigator by Precursory Research for Embryonic Science and Technology (PRESTO), Strategic Basic Research Programs, JST. In January 2016, he moved as a full professor to Japan Advanced Institute of Science and Technology. In 2018, he was appointed as the strategic hiring professor at the National University of Singapore.

ACKNOWLEDGMENTS

This work was supported by the start-up grant of the National University of Singapore (R-143-000-A28-133) and the Tier 1 grant of the Ministry of Education, Singapore (R-143-000-A71-114).

REFERENCES

(1) Fautrez, J.; Pisi, E.; Cavalli, G. Deoxyribonucleic Acid Content of the Nucleus and Nuclear Volume. *Nature* **1955**, *176*, 311−312.
(2) Powner, M. W.; Gerland, B.; Sutherland, J. D. Synthesis of Activated Pyrimidine Ribonucleotides in Prebiotically Plausible Conditions. *Nature* **2009**, *459*, 239−242.
(3) Kouwer, P. H. J.; Koepf, M.; Le Sage, V. A. A.; Jaspers, M.; van Buul, A. M.; Eksteen-Akeroyd, Z. H.; Woltinge, T.; Schwartz, E.; Kitto, H. J.; Hoogenboom, R.; Picken, S. J.; Nolte, R. J. M.; Mendes, E.; Rowan, A. E. Responsive Biomimetic Networks from Polyisocyanopeptide Hydrogels. *Nature* **2013**, *493*, 651−655.
(4) Gardel, M. L. Synthetic Polymers with Biological Rigidity. *Nature* **2013**, *493*, 619.
(5) Kricheldorf, H. R. Polypeptides and 100 Years of Chemistry of α-Amino Acid *N*-Carboxyanhydrides. *Angew. Chem., Int. Ed.* **2006**, *45*, 5752−5784.
(6) Philp, D.; Stoddart, J. F. Self-Assembly in Natural and Unnatural Systems. *Angew. Chem., Int. Ed. Engl.* **1996**, *35*, 1154−1196.
(7) Stoddart, J. F. Thither Supramolecular Chemistry? *Nat. Chem.* **2009**, *1*, 14−15.
(8) Fukui, T.; Kawai, S.; Fujinuma, S.; Matsushita, Y.; Yasuda, T.; Sakurai, T.; Seki, S.; Takeuchi, M.; Sugiyasu, K. Control over Differentiation of a Metastable Supramolecular Assembly in One and Two Dimensions. *Nat. Chem.* **2017**, *9*, 493−499.
(9) Côté, A. P.; Benin, A. I.; Ockwig, N. W.; O'Keeffe, M.; Matzger, A. J.; Yaghi, O. M. Porous, Crystalline, Covalent Organic Frameworks. *Science* **2005**, *310*, 1166−1170.
(10) Colson, J. W.; Dichtel, W. R. Rationally Synthesized Two-Dimensional Polymers. *Nat. Chem.* **2013**, *5*, 453−465.
(11) Huang, N.; Zhai, L.; Coupry, D. E.; Addicoat, M. A.; Okushita, K.; Nishimura, K.; Heine, T.; Jiang, D. Multiple-Component Covalent Organic Frameworks. *Nat. Commun.* **2016**, *7*, 12325.
(12) Dalapati, S.; Addicoat, M.; Jin, S.; Sakurai, T.; Gao, J.; Xu, H.; Irle, S.; Seki, S.; Jiang, D. Rational Design of Crystalline Supermicroporous Covalent Organic Frameworks with Triangular Topologies. *Nat. Commun.* **2015**, *6*, 7786.
(13) Feng, X.; Ding, X.; Jiang, D. Covalent Organic Frameworks. *Chem. Soc. Rev.* **2012**, *41*, 6010−22.
(14) Ding, S. Y.; Wang, W. Covalent Organic Frameworks (COFs): from Design to Applications. *Chem. Soc. Rev.* **2013**, *42*, 548−68.
(15) Segura, J. L.; Mancheno, M. J.; Zamora, F. Covalent Organic Frameworks Based on Schiff-Base Chemistry: Synthesis, Properties and Potential Applications. *Chem. Soc. Rev.* **2016**, *45*, 5635−5671.
(16) Huang, N.; Wang, P.; Jiang, D. Covalent Organic Frameworks: A Materials Platform for Structural and Functional Designs. *Nat. Rev. Mater.* **2016**, *1*, 16068.
(17) Lohse, M. S.; Bein, T. Covalent Organic Frameworks: Structures, Synthesis, and Applications. *Adv. Funct. Mater.* **2018**, *28*, 1705553.
(18) Bisbey, R. P.; Dichtel, W. R. Covalent Organic Frameworks as a Platform for Multidimensional Polymerization. *ACS Cent. Sci.* **2017**, *3*, 533−543.
(19) Chen, X.; Geng, K.; Liu, R.; Tan, K. T.; Gong, Y.; Li, Z.; Tao, S.; Jiang, Q.; Jiang, D. Covalent Organic Frameworks: Chemical Approaches to Designer Structures and Built-in Functions. *Angew. Chem., Int. Ed.* **2019**, DOI: 10.1002/anie.201904291.
(20) Rodríguez-San-Miguel, D.; Zamora, F. Processing of Covalent Organic Frameworks: An Ingredient for a Material to Succeed. *Chem. Soc. Rev.* **2019**, *48*, 4375−4386.
(21) Kandambeth, S.; Dey, K.; Banerjee, R. Covalent Organic Frameworks: Chemistry beyond the Structure. *J. Am. Chem. Soc.* **2019**, *141*, 1807−1822.
(22) Yang, L.; Wei, D.-C. Semiconducting Covalent Organic Frameworks: A Type of Two-Dimensional Conducting Polymers. *Chin. Chem. Lett.* **2016**, *27*, 1395−1404.
(23) Xu, L. Q.; Ding, S. Y.; Liu, J. M.; Sun, J. L.; Wang, W.; Zheng, Q. Y. Highly Crystalline Covalent Organic Frameworks from Flexible Building Blocks. *Chem. Commun.* **2016**, *52*, 4706−4709.
(24) Kouwer, P. H.; Koepf, M.; Le Sage, V. A.; Jaspers, M.; van Buul, A. M.; Eksteen-Akeroyd, Z. H.; Woltinge, T.; Schwartz, E.; Kitto, H. J.; Hoogenboom, R.; et al. Responsive Biomimetic Networks from Polyisocyanopeptide Hydrogels. *Nature* **2013**, *493*, 651.
(25) Feng, X.; Dong, Y.; Jiang, D. Star-Shaped Two-Dimensional Covalent Organic Frameworks. *CrystEngComm* **2013**, *15*, 1508−1511.

https://dx.doi.org/10.1021/acs.chemrev.9b00550
Chem. Rev. 2020, 120, 8814−8933

(26) Côté, A. P.; El-Kaderi, H. M.; Furukawa, H.; Hunt, J. R.; Yaghi, O. M. Reticular Synthesis of Microporous and Mesoporous 2D Covalent Organic Frameworks. *J. Am. Chem. Soc.* **2007**, *129*, 12914−12915.
(27) Wan, S.; Guo, J.; Kim, J.; Ihee, H.; Jiang, D. A Belt-Shaped, Blue Luminescent, and Semiconducting Covalent Organic Framework. *Angew. Chem., Int. Ed.* **2008**, *47*, 8826−8830.
(28) Xie, Y. F.; Ding, S. Y.; Liu, J. M.; Wang, W.; Zheng, Q. Y. Triazatruxene Based Covalent Organic Framework and Its Quick-Response Fluorescence-on Nature towards Electron Rich Arenes. *J. Mater. Chem. C* **2015**, *3*, 10066−10069.
(29) Spitler, E. L.; Dichtel, W. R. Lewis Acid-Catalysed Formation of Two-Dimensional Phthalocyanine Covalent Organic Frameworks. *Nat. Chem.* **2010**, *2*, 672.
(30) Ding, X.; Guo, J.; Feng, X.; Honsho, Y.; Guo, J.; Seki, S.; Maitarad, P.; Saeki, A.; Nagase, S.; Jiang, D. Synthesis of Metallophthalocyanine Covalent Organic Frameworks that Exhibit High Carrier Mobility and Photoconductivity. *Angew. Chem., Int. Ed.* **2011**, *50*, 1289−93.
(31) Feng, X.; Chen, L.; Dong, Y.; Jiang, D. Porphyrin-Based Two-Dimensional Covalent Organic Frameworks: Synchronized Synthetic Control of Macroscopic Structures and Pore Parameters. *Chem. Commun.* **2011**, *47*, 1979−81.
(32) Ding, X.; Feng, X.; Saeki, A.; Seki, S.; Nagai, A.; Jiang, D. Conducting Metallophthalocyanine 2D Covalent Organic Frameworks: the Role of Central Metals in Controlling π-Electronic Functions. *Chem. Commun.* **2012**, *48*, 8952−4.
(33) Lin, S.; Diercks, C. S.; Zhang, Y. B.; Kornienko, N.; Nichols, E. M.; Zhao, Y. B.; Paris, A. R.; Kim, D.; Yang, P.; Yaghi, O. M.; Chang, C. J. Covalent Organic Frameworks Comprising Cobalt Porphyrins for Catalytic CO_2 Reduction in Water. *Science* **2015**, *349*, 1208−1213.
(34) Chen, R.; Shi, J.-L.; Ma, Y.; Lin, G.; Lang, X.; Wang, C. Designed Synthesis of a 2D Porphyrin-Based sp^2 Carbon-Conjugated Covalent Organic Framework for Heterogeneous Photocatalysis. *Angew. Chem., Int. Ed.* **2019**, *58*, 6430−6434.
(35) Xu, S.-Q.; Zhan, T.-G.; Wen, Q.; Pang, Z.-F.; Zhao, X. Diversity of Covalent Organic Frameworks (COFs): A 2D COF Containing Two Kinds of Triangular Micropores of Different Sizes. *ACS Macro Lett.* **2016**, *5*, 99−102.
(36) Zhou, T.-Y.; Xu, S.-Q.; Wen, Q.; Pang, Z.-F.; Zhao, X. One-Step Construction of Two Different Kinds of Pores in a 2D Covalent Organic Framework. *J. Am. Chem. Soc.* **2014**, *136*, 15885−15888.
(37) Chen, X.; Huang, N.; Gao, J.; Xu, H.; Xu, F.; Jiang, D. Towards Covalent Organic Frameworks with Predesignable and Aligned Open Docking Sites. *Chem. Commun.* **2014**, *50*, 6161−3.
(38) Ascherl, L.; Sick, T.; Margraf, J. T.; Lapidus, S. H.; Calik, M.; Hettstedt, C.; Karaghiosoff, K.; Döblinger, M.; Clark, T.; Chapman, K. W.; Auras, F.; Bein, T. Molecular Docking Sites Designed for the Generation of Highly Crystalline Covalent Organic Frameworks. *Nat. Chem.* **2016**, *8*, 310−316.
(39) Pang, Z. F.; Xu, S. Q.; Zhou, T. Y.; Liang, R. R.; Zhan, T. G.; Zhao, X. Construction of Covalent Organic Frameworks Bearing Three Different Kinds of Pores through the Heterostructural Mixed Linker Strategy. *J. Am. Chem. Soc.* **2016**, *138*, 4710−3.
(40) Crowe, J. W.; Baldwin, L. A.; McGrier, P. L. Luminescent Covalent Organic Frameworks Containing a Homogeneous and Heterogeneous Distribution of Dehydrobenzoannulene Vertex Units. *J. Am. Chem. Soc.* **2016**, *138*, 10120−1013.
(41) Jin, Y.; Hu, Y.; Zhang, W. Tessellated Multiporous Two-Dimensional Covalent Organic Frameworks. *Nat. Rev. Chem.* **2017**, *1*, 0056.
(42) Zhu, Y.; Wan, S.; Jin, Y.; Zhang, W. Desymmetrized Vertex Design for the Synthesis of Covalent Organic Frameworks with Periodically Heterogeneous Pore Structures. *J. Am. Chem. Soc.* **2015**, *137*, 13772−5.
(43) Trewin, A.; Cooper, A. I. Predicting Microporous Crystalline Polyimides. *CrystEngComm* **2009**, *11*, 1819.
(44) Díaz, U.; Corma, A. Ordered Covalent Organic Frameworks, COFs and PAFs. From Preparation to Application. *Coord. Chem. Rev.* **2016**, *311*, 85−124.
(45) Lin, G.; Ding, H.; Chen, R.; Peng, Z.; Wang, B.; Wang, C. 3D Porphyrin-Based Covalent Organic Frameworks. *J. Am. Chem. Soc.* **2017**, *139*, 8705−8709.
(46) Lan, Y.; Han, X.; Tong, M.; Huang, H.; Yang, Q.; Liu, D.; Zhao, X.; Zhong, C. Materials Genomics Methods for High-throughput Construction of COFs and Targeted Synthesis. *Nat. Commun.* **2018**, *9*, 5274.
(47) El-Kaderi, H. M.; Hunt, J. R.; Mendoza-Cortés, J. L.; Côté, A. P.; Taylor, R. E.; O'Keeffe, M.; Yaghi, O. M. Designed Synthesis of 3D Covalent Organic Frameworks. *Science* **2007**, *316*, 268−272.
(48) Baldwin, L. A.; Crowe, J. W.; Pyles, D. A.; McGrier, P. L. Metalation of a Mesoporous Three-Dimensional Covalent Organic Framework. *J. Am. Chem. Soc.* **2016**, *138*, 15134−15137.
(49) Fang, Q.; Zhuang, Z.; Gu, S.; Kaspar, R. B.; Zheng, J.; Wang, J.; Qiu, S.; Yan, Y. Designed Synthesis of Large-Pore Crystalline Polyimide Covalent Organic Frameworks. *Nat. Commun.* **2014**, *5*, 4503.
(50) Uribe-Romo, F. J.; Hunt, J. R.; Furukawa, H.; Klöck, C.; O'Keeffe, M.; Yaghi, O. M. A Crystalline Imine-Linked 3-D Porous Covalent Organic Framework. *J. Am. Chem. Soc.* **2009**, *131*, 4570−4571.
(51) Ma, Y.-X.; Li, Z.-J.; Wei, L.; Ding, S.-Y.; Zhang, Y.-B.; Wang, W. A Dynamic Three-Dimensional Covalent Organic Framework. *J. Am. Chem. Soc.* **2017**, *139*, 4995−4998.
(52) Han, X.; Huang, J.; Yuan, C.; Liu, Y.; Cui, Y. Chiral 3D Covalent Organic Frameworks for High Performance Liquid Chromatographic Enantioseparation. *J. Am. Chem. Soc.* **2018**, *140*, 892−895.
(53) Yan, S.; Guan, X.; Li, H.; Li, D.; Xue, M.; Yan, Y.; Valtchev, V.; Qiu, S.; Fang, Q. Three-Dimensional Salphen-Based Covalent−Organic Frameworks as Catalytic Antioxidants. *J. Am. Chem. Soc.* **2019**, *141*, 2920−2924.
(54) Fang, Q.; Wang, J.; Gu, S.; Kaspar, R. B.; Zhuang, Z.; Zheng, J.; Guo, H.; Qiu, S.; Yan, Y. 3D Porous Crystalline Polyimide Covalent Organic Frameworks for Drug Delivery. *J. Am. Chem. Soc.* **2015**, *137*, 8352−8355.
(55) Wu, C.; Liu, Y.; Liu, H.; Duan, C.; Pan, Q.; Zhu, J.; Hu, F.; Ma, X.; Jiu, T.; Li, Z.; Zhao, Y. Highly Conjugated Three-Dimensional Covalent Organic Frameworks Based on Spirobifluorene for Perovskite Solar Cell Enhancement. *J. Am. Chem. Soc.* **2018**, *140*, 10016−10024.
(56) Yahiaoui, O.; Fitch, A. N.; Hoffmann, F.; Fröba, M.; Thomas, A.; Roeser, J. 3D Anionic Silicate Covalent Organic Framework with srs Topology. *J. Am. Chem. Soc.* **2018**, *140*, 5330−5333.
(57) Lin, G.; Ding, H.; Yuan, D.; Wang, B.; Wang, C. A Pyrene-Based, Fluorescent Three-Dimensional Covalent Organic Framework. *J. Am. Chem. Soc.* **2016**, *138*, 3302−3305.
(58) Ding, H.; Li, J.; Xie, G.; Lin, G.; Chen, R.; Peng, Z.; Yang, C.; Wang, B.; Sun, J.; Wang, C. An AIEgen-Based 3D Covalent Organic Framework for White Light-Emitting Diodes. *Nat. Commun.* **2018**, *9*, 5234.
(59) Liu, Y. Z.; Ma, Y. H.; Zhao, Y. B.; Sun, X. X.; Gandara, F.; Furukawa, H.; Liu, Z.; Zhu, H. Y.; Zhu, C. H.; Suenaga, K.; Oleynikov, P.; Alshammari, A. S.; Zhang, X.; Terasaki, O.; Yaghi, O. M. Weaving of Organic Threads into A Crystalline Covalent Organic Framework. *Science* **2016**, *351*, 365−369.
(60) Tilford, R. W.; Gemmill, W. R.; zur Loye, H.-C.; Lavigne, J. J. Facile Synthesis of a Highly Crystalline, Covalently Linked Porous Boronate Network. *Chem. Mater.* **2006**, *18*, 5296−5301.
(61) Huang, N.; Ding, X.; Kim, J.; Ihee, H.; Jiang, D. A Photoresponsive Smart Covalent Organic Framework. *Angew. Chem., Int. Ed.* **2015**, *54*, 8704−7.
(62) Chandra, S.; Kundu, T.; Kandambeth, S.; BabaRao, R.; Marathe, Y.; Kunjir, S. M.; Banerjee, R. Phosphoric Acid Loaded Azo (-N = N-) Based Covalent Organic Framework for Proton Conduction. *J. Am. Chem. Soc.* **2014**, *136*, 6570−6573.
(63) Chandra, S.; Kandambeth, S.; Biswal, B. P.; Lukose, B.; Kunjir, S. M.; Chaudhary, M.; Babarao, R.; Heine, T.; Banerjee, R. Chemically Stable Multilayered Covalent Organic Nanosheets from Covalent Organic Frameworks via Mechanical Delamination. *J. Am. Chem. Soc.* **2013**, *135*, 17853−17861.

https://dx.doi.org/10.1021/acs.chemrev.9b00550
Chem. Rev. 2020, 120, 8814−8933

(64) Kandambeth, S.; Mallick, A.; Lukose, B.; Mane, M. V.; Heine, T.; Banerjee, R. Construction of Crystalline 2D Covalent Organic Frameworks with Remarkable Chemical (Acid/Base) Stability via a Combined Reversible and Irreversible Route. *J. Am. Chem. Soc.* **2012**, *134*, 19524−19527.
(65) Ding, S. Y.; Gao, J.; Wang, Q.; Zhang, Y.; Song, W. G.; Su, C. Y.; Wang, W. Construction of Covalent Organic Framework for Catalysis: Pd/COF-LZU1 in Suzuki-Miyaura Coupling Reaction. *J. Am. Chem. Soc.* **2011**, *133*, 19816−19822.
(66) Shinde, D. B.; Aiyappa, H. B.; Bhadra, M.; Biswal, B. P.; Wadge, P.; Kandambeth, S.; Garai, B.; Kundu, T.; Kurungot, S.; Banerjee, R. A Mechanochemically Synthesized Covalent Organic Framework as a Proton-Conducting Solid Electrolyte. *J. Mater. Chem. A* **2016**, *4*, 2682−2690.
(67) Peng, Y.; Xu, G.; Hu, Z.; Cheng, Y.; Chi, C.; Yuan, D.; Cheng, H.; Zhao, D. Mechanoassisted Synthesis of Sulfonated Covalent Organic Frameworks with High Intrinsic Proton Conductivity. *ACS Appl. Mater. Interfaces* **2016**, *8*, 18505−12.
(68) Ma, H.; Liu, B.; Li, B.; Zhang, L.; Li, Y. G.; Tan, H. Q.; Zang, H. Y.; Zhu, G. Cationic Covalent Organic Frameworks: A Simple Platform of Anionic Exchange for Porosity Tuning and Proton Conduction. *J. Am. Chem. Soc.* **2016**, *138*, 5897−903.
(69) DeBlase, C. R.; Silberstein, K. E.; Truong, T. T.; Abruna, H. D.; Dichtel, W. R. beta-Ketoenamine-Linked Covalent Organic Frameworks Capable of Pseudocapacitive Energy Storage. *J. Am. Chem. Soc.* **2013**, *135*, 16821−16824.
(70) Bai, L. Y.; Phua, S. Z. F.; Lim, W. Q.; Jana, A.; Luo, Z.; Tham, H. P.; Zhao, L. Z.; Gao, Q.; Zhao, Y. L. Nanoscale Covalent Organic Frameworks as Smart Carriers for Drug Delivery. *Chem. Commun.* **2016**, *52*, 4128−4131.
(71) Uribe-Romo, F. J.; Doonan, C. J.; Furukawa, H.; Oisaki, K.; Yaghi, O. M. Crystalline Covalent Organic Frameworks with Hydrazone Linkages. *J. Am. Chem. Soc.* **2011**, *133*, 11478−11481.
(72) Zhang, Y.; Shen, X.; Feng, X.; Xia, H.; Mu, Y.; Liu, X. Covalent Organic Frameworks as pH Responsive Signaling Scaffolds. *Chem. Commun.* **2016**, *52*, 11088−11091.
(73) Li, Z. P.; Feng, X.; Zou, Y. C.; Zhang, Y. W.; Xia, H.; Liu, X. M.; Mu, Y. A 2D Azine-Linked Covalent Organic Framework for Gas Storage Applications. *Chem. Commun.* **2014**, *50*, 13825−13828.
(74) Li, Z.; Zhi, Y.; Feng, X.; Ding, X.; Zou, Y.; Liu, X.; Mu, Y. An Azine-Linked Covalent Organic Framework: Synthesis, Characterization and Efficient Gas Storage. *Chem. - Eur. J.* **2015**, *21*, 12079−84.
(75) Kuhn, P.; Antonietti, M.; Thomas, A. Porous, Covalent Triazine-Based Frameworks Prepared by Ionothermal Synthesis. *Angew. Chem., Int. Ed.* **2008**, *47*, 3450−3.
(76) Bi, S.; Yang, C.; Zhang, W.; Xu, J.; Liu, L.; Wu, D.; Wang, X.; Han, Y.; Liang, Q.; Zhang, F. Two-Dimensional Semiconducting Covalent Organic Frameworks via Condensation at Arylmethyl Carbon Atoms. *Nat. Commun.* **2019**, *10*, 2467.
(77) Dogru, M.; Sonnauer, A.; Gavryushin, A.; Knochel, P.; Bein, T. A Covalent Organic Framework with 4 nm Open Pores. *Chem. Commun.* **2011**, *47*, 1707−9.
(78) Li, Z. J.; Ding, S. Y.; Xue, H. D.; Cao, W.; Wang, W. Synthesis of -C = N- Linked Covalent Organic Frameworks via the Direct Condensation of Acetals and Amines. *Chem. Commun.* **2016**, *52*, 7217−7220.
(79) Smith, B. J.; Overholts, A. C.; Hwang, N.; Dichtel, W. R. Insight into the Crystallization of Amorphous Imine-Linked Polymer Networks to 2D Covalent Organic Frameworks. *Chem. Commun.* **2016**, *52*, 3690−3693.
(80) Xu, H.; Gao, J.; Jiang, D. Stable, Crystalline, Porous, Covalent Organic Frameworks as a Platform for Chiral Organocatalysts. *Nat. Chem.* **2015**, *7*, 905.
(81) Kandambeth, S.; Venkatesh, V.; Shinde, D. B.; Kumari, S.; Halder, A.; Verma, S.; Banerjee, R. Self-Templated Chemically Stable Hollow Spherical Covalent Organic Framework. *Nat. Commun.* **2015**, *6*, 6786.
(82) Halder, A.; Kandambeth, S.; Biswal, B. P.; Kaur, G.; Roy, N. C.; Addicoat, M.; Salunke, J. K.; Banerjee, S.; Vanka, K.; Heine, T.; Verma, S.; Banerjee, R. Decoding the Morphological Diversity in Two Dimensional Crystalline Porous Polymers by Core Planarity Modulation. *Angew. Chem., Int. Ed.* **2016**, *55*, 7806−10.
(83) Stegbauer, L.; Schwinghammer, K.; Lotsch, B. V. A hydrazone-Based Covalent Organic Framework for Photocatalytic Hydrogen Production. *Chem. Sci.* **2014**, *5*, 2789−2793.
(84) Li, Z. P.; Zhang, Y. W.; Xia, H.; Mu, Y.; Liu, X. M. A Robust and Luminescent Covalent Organic Framework as a Highly Sensitive and Selective Sensor for the Detection of Cu^{2+} Ions. *Chem. Commun.* **2016**, *52*, 6613−6616.
(85) Vyas, V. S.; Haase, F.; Stegbauer, L.; Savasci, G.; Podjaski, F.; Ochsenfeld, C.; Lotsch, B. V. A Tunable Azine Covalent Organic Framework Platform for Visible Light-Induced Hydrogen Generation. *Nat. Commun.* **2015**, *6*, 8508.
(86) Becker, D.; Biswal, B. P.; Kaleńczuk, P.; Chandrasekhar, N.; Giebeler, L.; Addicoat, M.; Paasch, S.; Brunner, E.; Leo, K.; Dianat, A.; Cuniberti, G.; Berger, R.; Feng, X. Fully sp^2-Carbon-Linked Crystalline Two-Dimensional Conjugated Polymers: Insight into 2D Poly(phenylenecyanovinylene) Formation and its Optoelectronic Properties. *Chem. - Eur. J.* **2019**, *25*, 6562−6568.
(87) Chen, X.; Addicoat, M.; Jin, E.; Xu, H.; Hayashi, T.; Xu, F.; Huang, N.; Irle, S.; Jiang, D. Designed Synthesis of Double-Stage Two-Dimensional Covalent Organic Frameworks. *Sci. Rep.* **2015**, *5*, 14650.
(88) Zeng, Y. F.; Zou, R. Y.; Luo, Z.; Zhang, H. C.; Yao, X.; Ma, X.; Zou, R. Q.; Zhao, Y. L. Covalent Organic Frameworks Formed with Two Types of Covalent Bonds Based on Orthogonal Reactions. *J. Am. Chem. Soc.* **2015**, *137*, 1020−1023.
(89) Smith, B. J.; Hwang, N.; Chavez, A. D.; Novotney, J. L.; Dichtel, W. R. Growth Rates and Water Stability of 2D Boronate Ester Covalent Organic Frameworks. *Chem. Commun.* **2015**, *51*, 7532−7535.
(90) Feng, X.; Chen, L.; Honsho, Y.; Saengsawang, O.; Liu, L.; Wang, L.; Saeki, A.; Irle, S.; Seki, S.; Dong, Y.; Jiang, D. An Ambipolar Conducting Covalent Organic Framework with Self-Sorted and Periodic Electron Donor-Acceptor Ordering. *Adv. Mater.* **2012**, *24*, 3026−31.
(91) Spitler, E. L.; Koo, B. T.; Novotney, J. L.; Colson, J. W.; Uribe-Romo, F. J.; Gutierrez, G. D.; Clancy, P.; Dichtel, W. R. A 2D Covalent Organic Framework with 4.7-nm Pores and Insight into Its Interlayer Stacking. *J. Am. Chem. Soc.* **2011**, *133*, 19416−19421.
(92) Jin, S.; Furukawa, K.; Addicoat, M.; Chen, L.; Takahashi, S.; Irle, S.; Nakamura, T.; Jiang, D. Large Pore Donor−Acceptor Covalent Organic Frameworks. *Chem. Sci.* **2013**, *4*, 4505−4511.
(93) Calik, M.; Auras, F.; Salonen, L. M.; Bader, K.; Grill, I.; Handloser, M.; Medina, D. D.; Dogru, M.; Lobermann, F.; Trauner, D.; Hartschuh, A.; Bein, T. Extraction of Photogenerated Electrons and Holes from a Covalent Organic Framework Integrated Heterojunction. *J. Am. Chem. Soc.* **2014**, *136*, 17802−17807.
(94) Zhang, B.; Wei, M.; Mao, H.; Pei, X.; Alshmimri, S. A.; Reimer, J. A.; Yaghi, O. M. Crystalline Dioxin-Linked Covalent Organic Frameworks from Irreversible Reactions. *J. Am. Chem. Soc.* **2018**, *140*, 12715−12719.
(95) Guan, X.; Li, H.; Ma, Y.; Xue, M.; Fang, Q.; Yan, Y.; Valtchev, V.; Qiu, S. Chemically Stable Polyarylether-Based Covalent Organic Frameworks. *Nat. Chem.* **2019**, *11*, 587−594.
(96) Liao, H.; Wang, H.; Ding, H.; Meng, X.; Xu, H.; Wang, B.; Ai, X.; Wang, C. A 2D Porous Porphyrin-Based Covalent Organic Framework for Sulfur Storage in Lithium-Sulfur Batteries. *J. Mater. Chem. A* **2016**, *4*, 7416−7421.
(97) Shinde, D. B.; Kandambeth, S.; Pachfule, P.; Kumar, R. R.; Banerjee, R. Bifunctional Covalent Organic Frameworks with Two Dimensional Organocatalytic Micropores. *Chem. Commun.* **2015**, *51*, 310−313.
(98) Kandambeth, S.; Shinde, D. B.; Panda, M. K.; Lukose, B.; Heine, T.; Banerjee, R. Enhancement of Chemical Stability and Crystallinity in Porphyrin-Containing Covalent Organic Frameworks by Intramolecular Hydrogen Bonds. *Angew. Chem., Int. Ed.* **2013**, *52*, 13052−6.
(99) Feng, X.; Liu, L.; Honsho, Y.; Saeki, A.; Seki, S.; Irle, S.; Dong, Y.; Nagai, A.; Jiang, D. High-Rate Charge-Carrier Transport in Porphyrin

https://dx.doi.org/10.1021/acs.chemrev.9b00550
Chem. Rev. 2020, 120, 8814−8933

Covalent Organic Frameworks: Switching from Hole to Electron to Ambipolar Conduction. *Angew. Chem., Int. Ed.* **2012**, *51*, 2618−2622.
(100) Chen, X.; Addicoat, M.; Jin, E. Q.; Zhai, L. P.; Xu, H.; Huang, N.; Guo, Z. Q.; Liu, L. L.; Irle, S.; Jiang, D. Locking Covalent Organic Frameworks with Hydrogen Bonds: General and Remarkable Effects on Crystalline Structure, Physical Properties, and Photochemical Activity. *J. Am. Chem. Soc.* **2015**, *137*, 3241−3247.
(101) Neti, V. S. P. K.; Wu, X.; Deng, S.; Echegoyen, L. Synthesis of a Phthalocyanine and Porphyrin 2D Covalent Organic Framework. *CrystEngComm* **2013**, *15*, 6892.
(102) Jin, S.; Supur, M.; Addicoat, M.; Furukawa, K.; Chen, L.; Nakamura, T.; Fukuzumi, S.; Irle, S.; Jiang, D. Creation of Superheterojunction Polymers via Direct Polycondensation: Segregated and Bicontinuous Donor-Acceptor π-Columnar Arrays in Covalent Organic Frameworks for Long-Lived Charge Separation. *J. Am. Chem. Soc.* **2015**, *137*, 7817−7827.
(103) Spitler, E. L.; Colson, J. W.; Uribe-Romo, F. J.; Woll, A. R.; Giovino, M. R.; Saldivar, A.; Dichtel, W. R. Lattice Expansion of Highly Oriented 2D Phthalocyanine Covalent Organic Framework Films. *Angew. Chem., Int. Ed.* **2012**, *51*, 2623−2627.
(104) Ding, X. S.; Chen, L.; Honsho, Y.; Feng, X.; Saengsawang, O.; Guo, J. D.; Saeki, A.; Seki, S.; Irle, S.; Nagase, S.; Parasuk, V.; Jiang, D. An *n*-Channel Two-Dimensional Covalent Organic Framework. *J. Am. Chem. Soc.* **2011**, *133*, 14510−14513.
(105) Dogru, M.; Bein, T. On the Road Towards Electroactive Covalent Organic Frameworks. *Chem. Commun.* **2014**, *50*, 5531−46.
(106) Wan, S.; Gándara, F.; Asano, A.; Furukawa, H.; Saeki, A.; Dey, S. K.; Liao, L.; Ambrogio, M. W.; Botros, Y. Y.; Duan, X.; Seki, S.; Stoddart, J. F.; Yaghi, O. M. Covalent Organic Frameworks with High Charge Carrier Mobility. *Chem. Mater.* **2011**, *23*, 4094−4097.
(107) Chen, X.; Gao, J.; Jiang, D. Designed Synthesis of Porphyrin-based Two-dimensional Covalent Organic Frameworks with Highly Ordered Structures. *Chem. Lett.* **2015**, *44*, 1257−1259.
(108) Chen, X.; Addicoat, M.; Irle, S.; Nagai, A.; Jiang, D. Control of Crystallinity and Porosity of Covalent Organic Frameworks by Managing Interlayer Interactions Based on Self-Complementary π-Electronic Force. *J. Am. Chem. Soc.* **2013**, *135*, 546−549.
(109) Feng, X.; Ding, X.; Chen, L.; Wu, Y.; Liu, L.; Addicoat, M.; Irle, S.; Dong, Y.; Jiang, D. Two-Dimensional Artificial Light-Harvesting Antennae with Predesigned High-Order Structure and Robust Photosensitising Activity. *Sci. Rep.* **2016**, *6*, 21944.
(110) Rabbani, M. G.; Sekizkardes, A. K.; Kahveci, Z.; Reich, T. E.; Ding, R.; El-Kaderi, H. M. A 2D Mesoporous Imine-Linked Covalent Organic Framework for High Pressure Gas Storage Applications. *Chem. - Eur. J.* **2013**, *19*, 3324−8.
(111) Dalapati, S.; Jin, S. B.; Gao, J.; Xu, Y. H.; Nagai, A.; Jiang, D. An Azine-Linked Covalent Organic Framework. *J. Am. Chem. Soc.* **2013**, *135*, 17310−17313.
(112) Dong, B.; Wang, L.; Zhao, S.; Ge, R.; Song, X.; Wang, Y.; Gao, Y. Immobilization of Ionic Liquids to Covalent Organic Frameworks for Catalyzing the Formylation of Amines with CO_2 and Phenylsilane. *Chem. Commun.* **2016**, *52*, 7082−7085.
(113) Auras, F.; Ascherl, L.; Hakimioun, A. H.; Margraf, J. T.; Hanusch, F. C.; Reuter, S.; Bessinger, D.; Doblinger, M.; Hettstedt, C.; Karaghiosoff, K.; Herbert, S.; Knochel, P.; Clark, T.; Bein, T. Synchronized Offset Stacking: A Concept for Growing Large-Domain and Highly Crystalline 2D Covalent Organic Frameworks. *J. Am. Chem. Soc.* **2016**, *138*, 16703−16710.
(114) Jin, E.; Asada, M.; Xu, Q.; Dalapati, S.; Addicoat, M. A.; Brady, M. A.; Xu, H.; Nakamura, T.; Heine, T.; Chen, Q.; et al. Two-Dimensional sp^2 Carbon−Conjugated Covalent Organic Frameworks. *Science* **2017**, *357*, 673−676.
(115) Jin, E.; Li, J.; Geng, K.; Jiang, Q.; Xu, H.; Xu, Q.; Jiang, D. Designed Synthesis of Stable Light-Emitting Two-Dimensional sp^2 Carbon-Conjugated Covalent Organic Frameworks. *Nat. Commun.* **2018**, *9*, 4143.
(116) Xu, S.-Q.; Liang, R.-R.; Zhan, T.-G.; Qi, Q.-Y.; Zhao, X. Construction of 2D Covalent Organic Frameworks by Taking Advantage of the Variable Orientation of Imine Bonds. *Chem. Commun.* **2017**, *53*, 2431−2434.
(117) Dalapati, S.; Jin, E.; Addicoat, M.; Heine, T.; Jiang, D. Highly Emissive Covalent Organic Frameworks. *J. Am. Chem. Soc.* **2016**, *138*, 5797−5800.
(118) Tian, Y.; Xu, S.-Q.; Liang, R.-R.; Qian, C.; Jiang, G.-F.; Zhao, X. Construction of Two Heteropore Covalent Organic Frameworks with Kagome Lattices. *CrystEngComm* **2017**, *19*, 4877−4881.
(119) Yu, J.-T.; Chen, Z.; Sun, J.; Huang, Z.-T.; Zheng, Q.-Y. Cyclotricatechylene Based Porous Crystalline Material: Synthesis and Applications in Gas Storage. *J. Mater. Chem.* **2012**, *22*, 5369.
(120) Baldwin, L. A.; Crowe, J. W.; Shannon, M. D.; Jaroniec, C. P.; McGrier, P. L. 2D Covalent Organic Frameworks with Alternating Triangular and Hexagonal Pores. *Chem. Mater.* **2015**, *27*, 6169−6172.
(121) Yang, H. S.; Du, Y.; Wan, S.; Trahan, G. D.; Jin, Y. H.; Zhang, W. Mesoporous 2D Covalent Organic Frameworks Based on Shape-Persistent Arylene-Ethynylene Macrocycles. *Chem. Sci.* **2015**, *6*, 4049−4053.
(122) Zhen, J.; Ding, S.; Wang, W.; Liu, J.; Sun, J.; Huang, Z.; Zheng, Q. Undulated 2D Covalent Organic Frameworks Based on Bowl-Shaped Cyclotricatechylene. *Chin. J. Chem.* **2016**, *34*, 783−787.
(123) Pang, Z.-F.; Zhou, T.-Y.; Liang, R.-R.; Qi, Q.-Y.; Zhao, X. Regulating the Topology of 2D Covalent Organic Frameworks by the Rational Introduction of Substituents. *Chem. Sci.* **2017**, *8*, 3866−3870.
(124) Alahakoon, S. B.; Thompson, C. M.; Nguyen, A. X.; Occhialini, G.; McCandless, G. T.; Smaldone, R. A. An Azine-Linked Hexaphenylbenzene Based Covalent Organic Framework. *Chem. Commun.* **2016**, *52*, 2843−2845.
(125) Jiang, D.; Wang, P.; Jiang, Q.; Chen, X.; Addicoat, M.; Huang, N.; Dalapati, S.; Heine, T.; Huo, F. High Precision Size Recognition and Separation in Synthetic 1D Nanochannels. *Angew. Chem., Int. Ed.* **2019**, *58*, 15922.
(126) Xu, S.; Wang, G.; Biswal, B. P.; Addicoat, M.; Paasch, S.; Sheng, W.; Zhuang, X.; Brunner, E.; Heine, T.; Berger, R.; Feng, X. A Nitrogen-Rich 2D sp^2-Carbon-Linked Conjugated Polymer Framework as a High-Performance Cathode for Lithium-Ion Batteries. *Angew. Chem., Int. Ed.* **2019**, *58*, 849−853.
(127) Banerjee, T.; Haase, F.; Trenker, S.; Biswal, B. P.; Savasci, G.; Duppel, V.; Moudrakovski, I.; Ochsenfeld, C.; Lotsch, B. V. Sub-Stoichiometric 2D Covalent Organic Frameworks from Tri- and Tetratopic Linkers. *Nat. Commun.* **2019**, *10*, 2689.
(128) Qian, C.; Qi, Q.-Y.; Jiang, G.-F.; Cui, F.-Z.; Tian, Y.; Zhao, X. Toward Covalent Organic Frameworks Bearing Three Different Kinds of Pores: The Strategy for Construction and COF-to-COF Transformation via Heterogeneous Linker Exchange. *J. Am. Chem. Soc.* **2017**, *139*, 6736−6743.
(129) Zhu, M.-W.; Xu, S.-Q.; Wang, X.-Z.; Chen, Y.; Dai, L.; Zhao, X. The Construction of Fluorescent Heteropore Covalent Organic Frameworks and Their Applications in Spectroscopic and Visual Detection of Trinitrophenol with High Selectivity and Sensitivity. *Chem. Commun.* **2018**, *54*, 2308−2311.
(130) Liang, R.-R.; Xu, S.-Q.; Pang, Z.-F.; Qi, Q.-Y.; Zhao, X. Self-Sorted Pore-Formation in the Construction of Heteropore Covalent organic Frameworks Based on Orthogonal Reactions. *Chem. Commun.* **2018**, *54*, 880−883.
(131) Lanni, L. M.; Tilford, R. W.; Bharathy, M.; Lavigne, J. J. Enhanced Hydrolytic Stability of Self-Assembling Alkylated Two-Dimensional Covalent Organic Frameworks. *J. Am. Chem. Soc.* **2011**, *133*, 13975−13983.
(132) Tilford, R. W.; Mugavero, S. J., 3rd; Pellechia, P. J.; Lavigne, J. J. Tailoring Microporosity in Covalent Organic Frameworks. *Adv. Mater.* **2008**, *20*, 2741−6.
(133) Nagai, A.; Guo, Z.; Feng, X.; Jin, S.; Chen, X.; Ding, X.; Jiang, D. Pore Surface Engineering in Covalent Organic Frameworks. *Nat. Commun.* **2011**, *2*, 536.
(134) Lukose, B.; Kuc, A.; Heine, T. Stability and Electronic Properties of 3D Covalent Organic Frameworks. *J. Mol. Model.* **2013**, *19*, 2143−8.

https://dx.doi.org/10.1021/acs.chemrev.9b00550
Chem. Rev. 2020, 120, 8814−8933

(135) Fang, Q.; Gu, S.; Zheng, J.; Zhuang, Z.; Qiu, S.; Yan, Y. 3D Microporous Base-Functionalized Covalent Organic Frameworks for Size-Selective Catalysis. *Angew. Chem., Int. Ed.* **2014**, *53*, 2878−82.
(136) Babarao, R.; Custelcean, R.; Hay, B. P.; Jiang, D.-e. Computer-Aided Design of Interpenetrated Tetrahydrofuran-Functionalized 3D Covalent Organic Frameworks for CO_2 Capture. *Cryst. Growth Des.* **2012**, *12*, 5349−5356.
(137) Li, X.-D.; Guo, J.-H.; Zhang, H.; Cheng, X.-L.; Liu, X.-Y. Design of 3D 1,3,5,7-Tetraphenyladamantane-Based Covalent Organic Frameworks as Hydrogen Storage Materials. *RSC Adv.* **2014**, *4*, 24526−24532.
(138) Brucks, S. D.; Bunck, D. N.; Dichtel, W. R. Functionalization of 3D Covalent Organic Frameworks Using Monofunctional Boronic Acids. *Polymer* **2014**, *55*, 330−334.
(139) Minar, N. K.; Hou, K.; Westermeier, C.; Doblinger, M.; Schuster, J.; Hanusch, F. C.; Nickel, B.; Ozin, G. A.; Bein, T. A Highly-Ordered 3D Covalent Fullerene Framework. *Angew. Chem., Int. Ed.* **2015**, *54*, 7577−81.
(140) Lu, H.; Wang, C.; Chen, J. J.; Ge, R. L.; Leng, W. G.; Dong, B.; Huang, J.; Gao, Y. N. A Novel 3D Covalent Organic Framework Membrane Grown on a Porous α-Al_2O_3 Substrate under Solvothermal Conditions. *Chem. Commun.* **2015**, *51*, 15562−15565.
(141) Bunck, D. N.; Dichtel, W. R. Postsynthetic Functionalization of 3D Covalent Organic Frameworks. *Chem. Commun.* **2013**, *49*, 2457−9.
(142) Zhang, Y. B.; Su, J.; Furukawa, H.; Yun, Y. F.; Gandara, F.; Duong, A.; Zou, X. D.; Yaghi, O. M. Single-Crystal Structure of a Covalent Organic Framework. *J. Am. Chem. Soc.* **2013**, *135*, 16336−16339.
(143) Yuan, Y.; Ren, H.; Sun, F. X.; Jing, X. F.; Cai, K.; Zhao, X. J.; Wang, Y.; Wei, Y.; Zhu, G. S. Targeted Synthesis of a 3D Crystalline Porous Aromatic Framework with Luminescence Quenching Ability for Hazardous and Explosive Molecules. *J. Phys. Chem. C* **2012**, *116*, 26431−26435.
(144) Han, S. S.; Furukawa, H.; Yaghi, O. M.; Goddard, W. A. Covalent Organic Frameworks as Exceptional Hydrogen Storage Materials. *J. Am. Chem. Soc.* **2008**, *130*, 11580−11581.
(145) Klontzas, E.; Tylianakis, E.; Froudakis, G. E. Designing 3D COFs with Enhanced Hydrogen Storage Capacity. *Nano Lett.* **2010**, *10*, 452−4.
(146) Klontzas, E.; Tylianakis, E.; Froudakis, G. E. Hydrogen Storage in 3D Covalent Organic Frameworks. A Multiscale Theoretical Investigation. *J. Phys. Chem. C* **2008**, *112*, 9095−9098.
(147) Cao, D.; Lan, J.; Wang, W.; Smit, B. Lithium-Doped 3D Covalent Organic Frameworks: High-Capacity Hydrogen Storage Materials. *Angew. Chem., Int. Ed.* **2009**, *48*, 4730−3.
(148) Hunt, J. R.; Doonan, C. J.; LeVangie, J. D.; Côté, A. P.; Yaghi, O. M. Reticular Synthesis of Covalent Organic Borosilicate Frameworks. *J. Am. Chem. Soc.* **2008**, *130*, 11872−11873.
(149) Ma, H.; Ren, H.; Meng, S.; Yan, Z.; Zhao, H.; Sun, F.; Zhu, G. A 3D Microporous Covalent Organic Framework with Exceedingly High C_3H_8/CH_4 and C_2 Hydrocarbon/CH_4 Selectivity. *Chem. Commun.* **2013**, *49*, 9773−5.
(150) Beaudoin, D.; Maris, T.; Wuest, J. D. Constructing Monocrystalline Covalent Organic Networks by Polymerization. *Nat. Chem.* **2013**, *5*, 830−834.
(151) Li, Z.; Li, H.; Guan, X.; Tang, J.; Yusran, Y.; Li, Z.; Xue, M.; Fang, Q.; Yan, Y.; Valtchev, V.; Qiu, S. Three-Dimensional Ionic Covalent Organic Frameworks for Rapid, Reversible, and Selective Ion Exchange. *J. Am. Chem. Soc.* **2017**, *139*, 17771−17774.
(152) Liu, Y.; Diercks, C. S.; Ma, Y.; Lyu, H.; Zhu, C.; Alshmimri, S. A.; Alshihri, S.; Yaghi, O. M. 3D Covalent Organic Frameworks of Interlocking 1D Square Ribbons. *J. Am. Chem. Soc.* **2019**, *141*, 677−683.
(153) Zhang, Y.; Duan, J.; Ma, D.; Li, P.; Li, S.; Li, H.; Zhou, J.; Ma, X.; Feng, X.; Wang, B. Three-Dimensional Anionic Cyclodextrin-Based Covalent Organic Frameworks. *Angew. Chem., Int. Ed.* **2017**, *56*, 16313−16317.
(154) Ma, T.; Kapustin, E. A.; Yin, S. X.; Liang, L.; Zhou, Z.; Niu, J.; Li, L.-H.; Wang, Y.; Su, J.; Li, J.; Wang, X.; Wang, W. D.; Wang, W.; Sun, J.; Yaghi, O. M. Single-Crystal X-ray Diffraction Structures of Covalent Organic Frameworks. *Science* **2018**, *361*, 48−52.
(155) Yu, S.-B.; Lyu, H.; Tian, J.; Wang, H.; Zhang, D.-W.; Liu, Y.; Li, Z.-T. A Polycationic Covalent Organic Framework: A Robust Adsorbent for Anionic Dye Pollutants. *Polym. Chem.* **2016**, *7*, 3392−3397.
(156) Tylianakis, E.; Klontzas, E.; Froudakis, G. E. Multi-Scale Theoretical Investigation of Hydrogen Storage in Covalent Organic Frameworks. *Nanoscale* **2011**, *3*, 856−69.
(157) Koo, B. T.; Dichtel, W. R.; Clancy, P. A Classification Scheme for the Stacking of Two-Dimensional Boronate Sster-Linked Covalent Organic Frameworks. *J. Mater. Chem.* **2012**, *22*, 17460.
(158) Guo, J.; Xu, Y.; Jin, S.; Chen, L.; Kaji, T.; Honsho, Y.; Addicoat, M. A.; Kim, J.; Saeki, A.; Ihee, H.; Seki, S.; Irle, S.; Hiramoto, M.; Gao, J.; Jiang, D. Conjugated Organic Framework with Three-Dimensionally Ordered Stable Structure and Delocalized π Clouds. *Nat. Commun.* **2013**, *4*, 2736.
(159) Smith, B. J.; Parent, L. R.; Overholts, A. C.; Beaucage, P. A.; Bisbey, R. P.; Chavez, A. D.; Hwang, N.; Park, C.; Evans, A. M.; Gianneschi, N. C.; Dichtel, W. R. Colloidal Covalent Organic Frameworks. *ACS Cent. Sci.* **2017**, *3*, 58−65.
(160) Li, R. L.; Flanders, N. C.; Evans, A. M.; Ji, W.; Castano, I.; Chen, L. X.; Gianneschi, N. C.; Dichtel, W. R. Controlled Growth of Imine-Linked Two-Dimensional Covalent Organic Framework Nanoparticles. *Chem. Sci.* **2019**, *10*, 3796−3801.
(161) Evans, A. M.; Parent, L. R.; Flanders, N. C.; Bisbey, R. P.; Vitaku, E.; Kirschner, M. S.; Schaller, R. D.; Chen, L. X.; Gianneschi, N. C.; Dichtel, W. R. Seeded Growth of Single-Crystal Two-Dimensional Covalent Organic Frameworks. *Science* **2018**, *361*, 52−57.
(162) Evans, A. M.; Ryder, M. R.; Flanders, N. C.; Vitaku, E.; Chen, L. X.; Dichtel, W. R. Buckling of Two-Dimensional Covalent Organic Frameworks under Thermal Stress. *Ind. Eng. Chem. Res.* **2019**, *58*, 9883−9887.
(163) Delgado-Friedrichs, O.; O'Keeffe, M.; Yaghi, O. M. Taxonomy of Periodic Nets and the Design of Materials. *Phys. Chem. Chem. Phys.* **2007**, *9*, 1035−43.
(164) Lukose, B.; Kuc, A.; Heine, T. The Structure of Layered Covalent-Organic Frameworks. *Chem. - Eur. J.* **2011**, *17*, 2388−92.
(165) Lukose, B.; Kuc, A.; Frenzel, J.; Heine, T. On the Reticular Construction Concept of Covalent Organic Frameworks. *Beilstein J. Nanotechnol.* **2010**, *1*, 60−70.
(166) Jin, S.; Ding, X.; Feng, X.; Supur, M.; Furukawa, K.; Takahashi, S.; Addicoat, M.; El-Khouly, M. E.; Nakamura, T.; Irle, S.; Fukuzumi, S.; Nagai, A.; Jiang, D. Charge Dynamics in a Donor-Acceptor Covalent Organic Framework with Periodically Ordered Bicontinuous Heterojunctions. *Angew. Chem., Int. Ed.* **2013**, *52*, 2017−21.
(167) Xu, H.; Chen, X.; Gao, J.; Lin, J.; Addicoat, M.; Irle, S.; Jiang, D. Catalytic Covalent Organic Frameworks via Pore Surface Engineering. *Chem. Commun.* **2014**, *50*, 1292−4.
(168) Peng, Y.; Huang, Y.; Zhu, Y.; Chen, B.; Wang, L.; Lai, Z.; Zhang, Z.; Zhao, M.; Tan, C.; Yang, N.; Shao, F.; Han, Y.; Zhang, H. Ultrathin Two-Dimensional Covalent Organic Framework Nanosheets: Preparation and Application in Highly Sensitive and Selective DNA Detection. *J. Am. Chem. Soc.* **2017**, *139*, 8698−8704.
(169) Li, X.; Zhang, C.; Cai, S.; Lei, X.; Altoe, V.; Hong, F.; Urban, J. J.; Ciston, J.; Chan, E. M.; Liu, Y. Facile Transformation of Imine Covalent Organic Frameworks into Ultrastable Crystalline Porous Aromatic Frameworks. *Nat. Commun.* **2018**, *9*, 2998.
(170) Colson, J. W.; Woll, A. R.; Mukherjee, A.; Levendorf, M. P.; Spitler, E. L.; Shields, V. B.; Spencer, M. G.; Park, J.; Dichtel, W. R. Oriented 2D Covalent Organic Framework Thin Films on Single-Layer Graphene. *Science* **2011**, *332*, 228−231.
(171) DeBlase, C. R.; Hernandez-Burgos, K.; Silberstein, K. E.; Rodriguez-Calero, G. G.; Bisbey, R. P.; Abruna, H. D.; Dichtel, W. R. Rapid and Efficient Redox Processes within 2D Covalent Organic Framework Thin Films. *ACS Nano* **2015**, *9*, 3178−3183.
(172) Cai, S. L.; Zhang, Y. B.; Pun, A. B.; He, B.; Yang, J. H.; Toma, F. M.; Sharp, I. D.; Yaghi, O. M.; Fan, J.; Zheng, S. R.; Zhang, W. G.; Liu, Y. Tunable Electrical Conductivity in Oriented Thin Films of

https://dx.doi.org/10.1021/acs.chemrev.9b00550
Chem. Rev. 2020, 120, 8814−8933

Tetrathiafulvalene-Based Covalent Organic Framework. *Chem. Sci.* **2014**, *5*, 4693−4700.
(173) Medina, D. D.; Werner, V.; Auras, F.; Tautz, R.; Dogru, M.; Schuster, J.; Linke, S.; Doblinger, M.; Feldmann, J.; Knochel, P.; Bein, T. Oriented Thin Films of a Benzodithiophene Covalent Organic Framework. *ACS Nano* **2014**, *8*, 4042−4052.
(174) Colson, J. W.; Mann, J. A.; DeBlase, C. R.; Dichtel, W. R. Patterned Growth of Oriented 2D Covalent Organic Framework Thin Films on Single-Layer Graphene. *J. Polym. Sci., Part A: Polym. Chem.* **2015**, *53*, 378−384.
(175) Liu, X. H.; Guan, C. Z.; Ding, S. Y.; Wang, W.; Yan, H. J.; Wang, D.; Wan, L. J. On-Surface Synthesis of Single-Layered Two-Dimensional Covalent Organic Frameworks via Solid-Vapor Interface Reactions. *J. Am. Chem. Soc.* **2013**, *135*, 10470−10474.
(176) Escalé, P.; Rubatat, L.; Billon, L.; Save, M. Recent Advances in Honeycomb-Structured Porous Polymer Films Prepared via Breath Figures. *Eur. Polym. J.* **2012**, *48*, 1001−1025.
(177) Marele, A. C.; Mas-Balleste, R.; Terracciano, L.; Rodriguez-Fernandez, J.; Berlanga, I.; Alexandre, S. S.; Otero, R.; Gallego, J. M.; Zamora, F.; Gomez-Rodriguez, J. M. Formation of a Surface Covalent Organic Framework Based on Polyester Condensation. *Chem. Commun.* **2012**, *48*, 6779−81.
(178) Dienstmaier, J. F.; Medina, D. D.; Dogru, M.; Knochel, P.; Bein, T.; Heckl, W. M.; Lackinger, M. Isoreticular Two-Dimensional Covalent Organic Frameworks Synthesized by On-Surface Condensation of Diboronic Acids. *ACS Nano* **2012**, *6*, 7234−7242.
(179) Plas, J.; Ivasenko, O.; Martsinovich, N.; Lackinger, M.; De Feyter, S. Nanopatterning of a Covalent Organic Framework Host-Guest System. *Chem. Commun.* **2016**, *52*, 68−71.
(180) Coratger, R.; Calmettes, B.; Abel, M.; Porte, L. STM Observations of the First Polymerization Steps between Hexahydroxy-Tri-Phenylene and Benzene-Di-Boronic Acid Molecules. *Surf. Sci.* **2011**, *605*, 831−837.
(181) Lackinger, M.; Heckl, W. M. A STM Perspective on Covalent Intermolecular Coupling Reactions on Surfaces. *J. Phys. D: Appl. Phys.* **2011**, *44*, 464011.
(182) Sun, X. L.; Fan, L. X.; Zhou, X.; Tian, W. Q.; Guo, Z. X.; Li, Z. B.; Li, X. K.; Lei, S. B. Surface Confined Synthesis of Porphyrin Containing Two-Dimensional Polymers: the Effect of Rigidity and Preferential Adsorption of Building Blocks. *Chem. Commun.* **2015**, *51*, 5864−5867.
(183) Xu, L. R.; Zhou, X.; Yu, Y. X.; Tian, W. Q.; Ma, J.; Lei, S. B. Surface-Confined Crystalline Two-Dimensional Covalent Organic Frameworks via on-Surface Schiff-Base Coupling. *ACS Nano* **2013**, *7*, 8066−8073.
(184) Dienstmaier, J. F.; Gigler, A. M.; Goetz, A. J.; Knochel, P.; Bein, T.; Lyapin, A.; Reichlmaier, S.; Heckl, W. M.; Lackinger, M. Synthesis of Well-Ordered COF Monolayers: Surface Growth of Nanocrystalline Precursors versus Direct On-Surface Polycondensation. *ACS Nano* **2011**, *5*, 9737−9745.
(185) Cui, D.; MacLeod, J. M.; Ebrahimi, M.; Rosei, F. Selective Binding in Different Adsorption Sites of a 2D Covalent Organic Framework. *CrystEngComm* **2017**, *19*, 4927−4932.
(186) Smith, B. J.; Dichtel, W. R. Mechanistic Studies of Two-Dimensional Covalent Organic Frameworks Rapidly Polymerized from Initially Homogenous Conditions. *J. Am. Chem. Soc.* **2014**, *136*, 8783−8789.
(187) Zhang, K. D.; Matile, S. Complex Functional Systems with Three Different Types of Dynamic Covalent Bonds. *Angew. Chem., Int. Ed.* **2015**, *54*, 8980−3.
(188) Wilson, A.; Gasparini, G.; Matile, S. Functional Systems with Orthogonal Dynamic Covalent Bonds. *Chem. Soc. Rev.* **2014**, *43*, 1948−1962.
(189) Rowan, S. J.; Cantrill, S. J.; Cousins, G. R. L.; Sanders, J. K. M.; Stoddart, J. F. Dynamic Covalent Chemistry. *Angew. Chem., Int. Ed.* **2002**, *41*, 898−952.
(190) Jin, Y.; Yu, C.; Denman, R. J.; Zhang, W. Recent Advances in Dynamic Covalent Chemistry. *Chem. Soc. Rev.* **2013**, *42*, 6634−6654.
(191) Jin, Y.; Wang, Q.; Taynton, P.; Zhang, W. Dynamic Covalent Chemistry Approaches Toward Macrocycles, Molecular Cages, and Polymers. *Acc. Chem. Res.* **2014**, *47*, 1575−1586.
(192) Zhuang, X.; Zhao, W.; Zhang, F.; Cao, Y.; Liu, F.; Bi, S.; Feng, X. A Two-Dimensional Conjugated Polymer Framework with Fully sp^2-Bonded Carbon Skeleton. *Polym. Chem.* **2016**, *7*, 4176−4181.
(193) Lyle, S. J.; Osborn Popp, T. M.; Waller, P. J.; Pei, X.; Reimer, J. A.; Yaghi, O. M. Multi-Step Solid-State Organic Synthesis of Carbamate-Linked Covalent Organic Frameworks. *J. Am. Chem. Soc.* **2019**, *141*, 11253−11258.
(194) Campbell, N. L.; Clowes, R.; Ritchie, L. K.; Cooper, A. I. Rapid Microwave Synthesis and Purification of Porous Covalent Organic Frameworks. *Chem. Mater.* **2009**, *21*, 204−206.
(195) Ritchie, L. K.; Trewin, A.; Reguera-Galan, A.; Hasell, T.; Cooper, A. I. Synthesis of COF-5 Using Microwave Irradiation and Conventional Solvothermal Routes. *Microporous Mesoporous Mater.* **2010**, *132*, 132−136.
(196) Wei, H.; Chai, S. Z.; Hu, N. T.; Yang, Z.; Wei, L. M.; Wang, L. The Microwave-Assisted Solvothermal Synthesis of a Crystalline Two-Dimensional Covalent Organic Framework with High CO_2 Capacity. *Chem. Commun.* **2015**, *51*, 12178−12181.
(197) Ren, S.; Bojdys, M. J.; Dawson, R.; Laybourn, A.; Khimyak, Y. Z.; Adams, D. J.; Cooper, A. I. Porous, Fluorescent, Covalent Triazine-Based Frameworks via Room-Temperature and Microwave-Assisted Synthesis. *Adv. Mater.* **2012**, *24*, 2357−61.
(198) Bojdys, M. J.; Jeromenok, J.; Thomas, A.; Antonietti, M. Rational Extension of the Family of Layered, Covalent, Triazine-Based Frameworks with Regular Porosity. *Adv. Mater.* **2010**, *22*, 2202−5.
(199) Guan, X.; Ma, Y.; Li, H.; Yusran, Y.; Xue, M.; Fang, Q.; Yan, Y.; Valtchev, V.; Qiu, S. Fast, Ambient Temperature and Pressure Ionothermal Synthesis of Three-Dimensional Covalent Organic Frameworks. *J. Am. Chem. Soc.* **2018**, *140*, 4494−4498.
(200) Biswal, B. P.; Chandra, S.; Kandambeth, S.; Lukose, B.; Heine, T.; Banerjee, R. Mechanochemical Synthesis of Chemically Stable Isoreticular Covalent Organic Frameworks. *J. Am. Chem. Soc.* **2013**, *135*, 5328−5331.
(201) Das, G.; Balaji Shinde, D.; Kandambeth, S.; Biswal, B. P.; Banerjee, R. Mechanosynthesis of Imine, β-Ketoenamine, and Hydrogen-Bonded Imine-Linked Covalent Organic Frameworks Using Liquid-Assisted Grinding. *Chem. Commun.* **2014**, *50*, 12615−12618.
(202) Dey, K.; Pal, M.; Rout, K. C.; Kunjattu H, S.; Das, A.; Mukherjee, R.; Kharul, U. K.; Banerjee, R. Selective Molecular Separation by Interfacially Crystallized Covalent Organic Framework Thin Films. *J. Am. Chem. Soc.* **2017**, *139*, 13083−13091.
(203) Matsumoto, M.; Valentino, L.; Stiehl, G. M.; Balch, H. B.; Corcos, A. R.; Wang, F.; Ralph, D. C.; Mariñas, B. J.; Dichtel, W. R. Lewis-Acid-Catalyzed Interfacial Polymerization of Covalent Organic Framework Films. *Chem.* **2018**, *4*, 308−317.
(204) Hao, Q.; Zhao, C.; Sun, B.; Lu, C.; Liu, J.; Liu, M.; Wan, L.-J.; Wang, D. Confined Synthesis of Two-Dimensional Covalent Organic Framework Thin Films within Superspreading Water Layer. *J. Am. Chem. Soc.* **2018**, *140*, 12152−12158.
(205) Zhou, D.; Tan, X.; Wu, H.; Tian, L.; Li, M. Synthesis of C−C Bonded Two-Dimensional Conjugated Covalent Organic Framework Films by Suzuki Polymerization on a Liquid−Liquid Interface. *Angew. Chem., Int. Ed.* **2019**, *58*, 1376−1381.
(206) Medina, D. D.; Rotter, J. M.; Hu, Y.; Dogru, M.; Werner, V.; Auras, F.; Markiewicz, J. T.; Knochel, P.; Bein, T. Room Temperature Synthesis of Covalent−Organic Framework Films through Vapor-Assisted Conversion. *J. Am. Chem. Soc.* **2015**, *137*, 1016−1019.
(207) Matsumoto, M.; Dasari, R. R.; Ji, W.; Feriante, C. H.; Parker, T. C.; Marder, S. R.; Dichtel, W. R. Rapid, Low Temperature Formation of Imine-Linked Covalent Organic Frameworks Catalyzed by Metal Triflates. *J. Am. Chem. Soc.* **2017**, *139*, 4999−5002.
(208) Zhang, F.; Zhang, J.; Zhang, B.; Tan, X.; Shao, D.; Shi, J.; Tan, D.; Liu, L.; Feng, J.; Han, B.; Yang, G.; Zheng, L.; Zhang, J. Room-Temperature Synthesis of Covalent Organic Framework (COF-LZU1) Nanobars in CO_2/Water Solvent. *ChemSusChem* **2018**, *11*, 3576−3580.

https://dx.doi.org/10.1021/acs.chemrev.9b00550
Chem. Rev. 2020, 120, 8814−8933

(209) Liu, Y.; Wang, Y.; Li, H.; Guan, X.; Zhu, L.; Xue, M.; Yan, Y.; Valtchev, V.; Qiu, S.; Fang, Q. Ambient Aqueous-Phase Synthesis of Covalent Organic Frameworks for Degradation of Organic Pollutants. *Chem. Sci.* **2019**, *10*, 10815−10820.
(210) de la Peña Ruigómez, A.; Rodríguez-San-Miguel, D.; Stylianou, K. C.; Cavallini, M.; Gentili, D.; Liscio, F.; Milita, S.; Roscioni , O. M.; Ruiz-González, M. L.; Carbonell, C.; Maspoch, D.; Mas-Ballesté, R.; Segura, J. L.; Zamora, F. Direct On-Surface Patterning of a Crystalline Laminar Covalent Organic Framework Synthesized at Room Temperature. *Chem. - Eur. J.* **2015**, *21*, 10666−10670.
(211) Rodríguez-San-Miguel, D.; Abrishamkar, A.; Navarro, J. A. R.; Rodriguez-Trujillo, R.; Amabilino, D. B.; Mas-Ballesté, R.; Zamora, F.; Puigmartí-Luis, J. Crystalline Fibres of a Covalent Organic Framework through Bottom-Up Microfluidic Synthesis. *Chem. Commun.* **2016**, *52*, 9212−9215.
(212) Zhang, M.; Li, L.; Lin, Q.; Tang, M.; Wu, Y.; Ke, C. Hierarchical-Coassembly-Enabled 3D-Printing of Homogeneous and Heterogeneous Covalent Organic Frameworks. *J. Am. Chem. Soc.* **2019**, *141*, 5154−5158.
(213) Lohse, M. S.; Rotter, J. M.; Margraf, J. T.; Werner, V.; Becker, M.; Herbert, S.; Knochel, P.; Clark, T.; Bein, T.; Medina, D. D. From Benzodithiophene to Diethoxy-Benzodithiophene Covalent Organic Frameworks - Structural Investigations. *CrystEngComm* **2016**, *18*, 4295−4302.
(214) Song, J. R.; Sun, J.; Liu, J.; Huang, Z. T.; Zheng, Q. Y. Thermally/Hydrolytically Stable Covalent Organic Frameworks from a Rigid Macrocyclic Host. *Chem. Commun.* **2014**, *50*, 788−91.
(215) Jackson, K. T.; Reich, T. E.; El-Kaderi, H. M. Targeted Synthesis of a Porous Borazine-Linked Covalent Organic Framework. *Chem. Commun.* **2012**, *48*, 8823−8825.
(216) Nagai, A.; Chen, X.; Feng, X.; Ding, X.; Guo, Z.; Jiang, D. A Squaraine-Linked Mesoporous Covalent Organic Framework. *Angew. Chem., Int. Ed.* **2013**, *52*, 3770−3774.
(217) Du, Y.; Yang, H.; Whiteley, J. M.; Wan, S.; Jin, Y.; Lee, S.-H.; Zhang, W. Ionic Covalent Organic Frameworks with Spiroborate Linkage. *Angew. Chem., Int. Ed.* **2016**, *55*, 1737−1741.
(218) Lyu, H.; Diercks, C. S.; Zhu, C.; Yaghi, O. M. Porous Crystalline Olefin-Linked Covalent Organic Frameworks. *J. Am. Chem. Soc.* **2019**, *141*, 6848−6852.
(219) Waller, P. J.; Lyle, S. J.; Osborn Popp, T. M.; Diercks, C. S.; Reimer, J. A.; Yaghi, O. M. Chemical Conversion of Linkages in Covalent Organic Frameworks. *J. Am. Chem. Soc.* **2016**, *138*, 15519−15522.
(220) Das, G.; Skorjanc, T.; Sharma, S. K.; Gándara, F.; Lusi, M.; Shankar Rao, D. S.; Vimala, S.; Krishna Prasad, S.; Raya, J.; Han, D. S.; Jagannathan, R.; Olsen, J.-C.; Trabolsi, A. Viologen-Based Conjugated Covalent Organic Networks via Zincke Reaction. *J. Am. Chem. Soc.* **2017**, *139*, 9558−9565.
(221) Zhao, C.; Diercks, C. S.; Zhu, C.; Hanikel, N.; Pei, X.; Yaghi, O. M. Urea-Linked Covalent Organic Frameworks. *J. Am. Chem. Soc.* **2018**, *140*, 16438−16441.
(222) Wan, S.; Guo, J.; Kim, J.; Ihee, H.; Jiang, D. A Photoconductive Covalent Organic Framework: Self-Condensed Arene Cubes Composed of Eclipsed 2D Polypyrene Sheets for Photocurrent Generation. *Angew. Chem., Int. Ed.* **2009**, *48*, 5439−42.
(223) Dogru, M.; Handloser, M.; Auras, F.; Kunz, T.; Medina, D.; Hartschuh, A.; Knochel, P.; Bein, T. A Photoconductive Thienothiophene-Based Covalent Organic Framework Showing Charge Transfer Towards Included Fullerene. *Angew. Chem., Int. Ed.* **2013**, *52*, 2920−4.
(224) Bertrand, G. H.; Michaelis, V. K.; Ong, T. C.; Griffin, R. G.; Dinca, M. Thiophene-Based Covalent Organic Frameworks. *Proc. Natl. Acad. Sci. U. S. A.* **2013**, *110*, 4923−8.
(225) Spitler, E. L.; Giovino, M. R.; White, S. L.; Dichtel, W. R. A Mechanistic Study of Lewis Acid-Catalyzed Covalent Organic Framework Formation. *Chem. Sci.* **2011**, *2*, 1588−1593.
(226) Xu, L.; Zhou, X.; Tian, W. Q.; Gao, T.; Zhang, Y. F.; Lei, S.; Liu, Z. F. Surface-Confined Single-Layer Covalent Organic Framework on Single-Layer Graphene Grown on Copper Foil. *Angew. Chem., Int. Ed.* **2014**, *53*, 9564−8.
(227) Xu, H. S.; Ding, S. Y.; An, W. K.; Wu, H.; Wang, W. Constructing Crystalline Covalent Organic Frameworks from Chiral Building Blocks. *J. Am. Chem. Soc.* **2016**, *138*, 11489−11492.
(228) Zou, L.; Yang, X.; Yuan, S.; Zhou, H.-C. Flexible Monomer-Based Covalent Organic Frameworks: Design, Structure and Functions. *CrystEngComm* **2017**, *19*, 4868−4871.
(229) Yue, J. Y.; Liu, X. H.; Sun, B.; Wang, D. The on-Surface Synthesis of Imine-Based Covalent Organic Frameworks with Non-Aromatic Linkage. *Chem. Commun.* **2015**, *51*, 14318−14321.
(230) Xu, H.; Tao, S.; Jiang, D. Proton Conduction in Crystalline and Porous Covalent Organic Frameworks. *Nat. Mater.* **2016**, *15*, 722−726.
(231) Huang, N.; Zhai, L.; Xu, H.; Jiang, D. Stable Covalent Organic Frameworks for Exceptional Mercury Removal from Aqueous Solutions. *J. Am. Chem. Soc.* **2017**, *139*, 2428−2434.
(232) Wang, S.; Wang, Q.; Shao, P.; Han, Y.; Gao, X.; Ma, L.; Yuan, S.; Ma, X.; Zhou, J.; Feng, X.; Wang, B. Exfoliation of Covalent Organic Frameworks into Few-Layer Redox-Active Nanosheets as Cathode Materials for Lithium-Ion Batteries. *J. Am. Chem. Soc.* **2017**, *139*, 4258−4261.
(233) Zhai, L.; Huang, N.; Xu, H.; Chen, Q.; Jiang, D. A Backbone Design Principle for Covalent Organic Frameworks: The Impact of Weakly Interacting Units on CO_2 Adsorption. *Chem. Commun.* **2017**, *53* (30), 4242−4245.
(234) Wang, P.; Xu, Q.; Li, Z.; Jiang, W.; Jiang, Q.; Jiang, D. Exceptional Iodine Capture in 2D Covalent Organic Frameworks. *Adv. Mater.* **2018**, *30*, 1801991.
(235) Gao, Q.; Bai, L.; Zhang, X.; Wang, P.; Li, P.; Zeng, Y.; Zou, R.; Zhao, Y. Synthesis of Microporous Nitrogen-Rich Covalent-Organic Framework and Its Application in CO_2 Capture. *Chin. J. Chem.* **2015**, *33*, 90−94.
(236) Vyas, V. S.; Lau, V. W.-h.; Lotsch, B. V. Soft Photocatalysis: Organic Polymers for Solar Fuel Production. *Chem. Mater.* **2016**, *28*, 5191−5204.
(237) Sun, B.; Liu, J.; Cao, A.; Song, W.; Wang, D. Interfacial Synthesis of Ordered and Stable Covalent Organic Frameworks on Amino-Functionalized Carbon Nanotubes with Enhanced Electrochemical Performance. *Chem. Commun.* **2017**, *53*, 6303−6306.
(238) Jin, S.; Sakurai, T.; Kowalczyk, T.; Dalapati, S.; Xu, F.; Wei, H.; Chen, X.; Gao, J.; Seki, S.; Irle, S.; Jiang, D. Two-Dimensional Tetrathiafulvalene Covalent Organic Frameworks: Towards Latticed Conductive Organic Salts. *Chem. - Eur. J.* **2014**, *20*, 14608−14613.
(239) Wu, Y.; Xu, H.; Chen, X.; Gao, J.; Jiang, D. A π-Electronic Covalent Organic Framework Catalyst: π-Walls as Catalytic Beds for Diels-Alder Reactions under Ambient Conditions. *Chem. Commun.* **2015**, *51*, 10096−10098.
(240) Leng, W.; Peng, Y.; Zhang, J.; Lu, H.; Feng, X.; Ge, R.; Dong, B.; Wang, B.; Hu, X.; Gao, Y. Sophisticated Design of Covalent Organic Frameworks with Controllable Bimetallic Docking for a Cascade Reaction. *Chem. - Eur. J.* **2016**, *22*, 9087−91.
(241) Huang, N.; Wang, P.; Addicoat, M. A.; Heine, T.; Jiang, D. Ionic Covalent Organic Frameworks: Design of a Charged Interface Aligned on 1D Channel Walls and Its Unusual Electrostatic Functions. *Angew. Chem.* **2017**, *129*, 5064.
(242) Sun, B.; Zhu, C.-H.; Liu, Y.; Wang, C.; Wan, L.-J.; Wang, D. Oriented Covalent Organic Framework Film on Graphene for Robust Ambipolar Vertical Organic Field-Effect Transistor. *Chem. Mater.* **2017**, *29*, 4367−4374.
(243) Xu, F.; Yang, S.; Chen, X.; Liu, Q.; Li, H.; Wang, H.; Wei, B.; Jiang, D. Energy-Storage Covalent Organic Frameworks: Improving Performance Via Engineering Polysulfide Chains on Walls. *Chem. Sci.* **2019**, *10*, 6001−6006.
(244) Li, Z.; Huang, N.; Lee, K. H.; Feng, Y.; Tao, S.; Jiang, Q.; Nagao, Y.; Irle, S.; Jiang, D. Light-Emitting Covalent Organic Frameworks: Fluorescence Improving Via Pinpoint Surgery and Selective Switch-on Sensing of Anions. *J. Am. Chem. Soc.* **2018**, *140*, 12374−12377.
(245) Ding, H.; Li, Y.; Hu, H.; Sun, Y.; Wang, J.; Wang, C.; Wang, C.; Zhang, G.; Wang, B.; Xu, W.; et al. A Tetrathiafulvalene-Based Electroactive Covalent Organic Framework. *Chem. - Eur. J.* **2014**, *20*, 14614−14618.

https://dx.doi.org/10.1021/acs.chemrev.9b00550
Chem. Rev. 2020, 120, 8814−8933

(246) Huang, N.; Chen, X.; Krishna, R.; Jiang, D. Two-Dimensional Covalent Organic Frameworks for Carbon Dioxide Capture through Channel-Wall Functionalization. *Angew. Chem., Int. Ed.* **2015**, *54*, 2986−90.
(247) Huang, N.; Krishna, R.; Jiang, D. Tailor-Made Pore Surface Engineering in Covalent Organic Frameworks: Systematic Functionalization for Performance Screening. *J. Am. Chem. Soc.* **2015**, *137*, 7079−7082.
(248) Xu, F.; Xu, H.; Chen, X.; Wu, D.; Wu, Y.; Liu, H.; Gu, C.; Fu, R.; Jiang, D. Radical Covalent Organic Frameworks: A General Strategy to Immobilize Open-Accessible Polyradicals for High-Performance Capacitive Energy Storage. *Angew. Chem., Int. Ed.* **2015**, *54*, 6814−8.
(249) Mullangi, D.; Dhavale, V.; Shalini, S.; Nandi, S.; Collins, S.; Woo, T.; Kurungot, S.; Vaidhyanathan, R. Low-Overpotential Electrocatalytic Water Splitting with Noble-Metal-Free Nanoparticles Supported in a sp^3 *N*-Rich Flexible Cof. *Adv. Energy Mater.* **2016**, *6*, 1600110.
(250) Peng, Y.; Wong, W. K.; Hu, Z.; Cheng, Y.; Yuan, D.; Khan, S. A.; Zhao, D. Room Temperature Batch and Continuous Flow Synthesis of Water-Stable Covalent Organic Frameworks (COFs). *Chem. Mater.* **2016**, *28*, 5095−5101.
(251) Sun, Q.; Aguila, B.; Perman, J.; Earl, L. D.; Abney, C. W.; Cheng, Y.; Wei, H.; Nguyen, N.; Wojtas, L.; Ma, S. Postsynthetically Modified Covalent Organic Frameworks for Efficient and Effective Mercury Removal. *J. Am. Chem. Soc.* **2017**, *139*, 2786−2793.
(252) Zhang, J.; Peng, Y.; Leng, W.; Gao, Y.; Xu, F.; Chai, J. Nitrogen Ligands in Two-Dimensional Covalent Organic Frameworks for Metal Catalysis. *Chin. J. Catal.* **2016**, *37*, 468−475.
(253) Gao, Q.; Bai, L.; Zeng, Y.; Wang, P.; Zhang, X.; Zou, R.; Zhao, Y. Reconstruction of Covalent Organic Frameworks by Dynamic Equilibrium. *Chem. - Eur. J.* **2015**, *21*, 16818−22.
(254) Ding, S. Y.; Dong, M.; Wang, Y. W.; Chen, Y. T.; Wang, H. Z.; Su, C. Y.; Wang, W. Thioether-Based Fluorescent Covalent Organic Framework for Selective Detection and Facile Removal of Mercury(II). *J. Am. Chem. Soc.* **2016**, *138*, 3031−7.
(255) Wang, L.; Dong, B.; Ge, R.; Jiang, F.; Xiong, J.; Gao, Y.; Xu, J. A Thiadiazole-Functionalized Covalent Organic Framework for Efficient CO_2 Capture and Separation. *Microporous Mesoporous Mater.* **2016**, *224*, 95−99.
(256) Hou, Y.; Zhang, X.; Sun, J.; Lin, S.; Qi, D.; Hong, R.; Li, D.; Xiao, X.; Jiang, J. Good Suzuki-Coupling Reaction Performance of Pd Immobilized at the Metal-Free Porphyrin-Based Covalent Organic Framework. *Microporous Mesoporous Mater.* **2015**, *214*, 108−114.
(257) Das, G.; Biswal, B. P.; Kandambeth, S.; Venkatesh, V.; Kaur, G.; Addicoat, M.; Heine, T.; Verma, S.; Banerjee, R. Chemical Sensing in Two Dimensional Porous Covalent Organic Nanosheets. *Chem. Sci.* **2015**, *6*, 3931−3939.
(258) Peng, Y.; Hu, Z.; Gao, Y.; Yuan, D.; Kang, Z.; Qian, Y.; Yan, N.; Zhao, D. Synthesis of a Sulfonated Two-Dimensional Covalent Organic Framework as an Efficient Solid Acid Catalyst for Biobased Chemical Conversion. *ChemSusChem* **2015**, *8*, 3208−12.
(259) Kaleeswaran, D.; Vishnoi, P.; Murugavel, R. [3 + 3] Imine and *β*-Ketoenamine Tethered Fluorescent Covalent-Organic Frameworks for CO_2 Uptake and Nitroaromatic Sensing. *J. Mater. Chem. C* **2015**, *3*, 7159−7171.
(260) Wang, X.; Han, X.; Zhang, J.; Wu, X.; Liu, Y.; Cui, Y. Homochiral 2D Porous Covalent Organic Frameworks for Heterogeneous Asymmetric Catalysis. *J. Am. Chem. Soc.* **2016**, *138*, 12332−12335.
(261) Wang, L.; Dong, B.; Ge, R.; Jiang, F.; Xu, J. Fluorene-Based Two-Dimensional Covalent Organic Framework with Thermoelectric Properties through Doping. *ACS Appl. Mater. Interfaces* **2017**, *9*, 7108−7114.
(262) Li, L.-H.; Feng, X.-L.; Cui, X.-H.; Ma, Y.-X.; Ding, S.-Y.; Wang, W. Salen-Based Covalent Organic Framework. *J. Am. Chem. Soc.* **2017**, *139*, 6042−6045.
(263) Hu, Y.; Dunlap, N.; Wan, S.; Lu, S.; Huang, S.; Sellinger, I.; Ortiz, M.; Jin, Y.; Lee, S.-h.; Zhang, W. Crystalline Lithium Imidazolate Covalent Organic Frameworks with High Li-Ion Conductivity. *J. Am. Chem. Soc.* **2019**, *141*, 7518−7525.
(264) Wu, X.; Han, X.; Xu, Q.; Liu, Y.; Yuan, C.; Yang, S.; Liu, Y.; Jiang, J.; Cui, Y. Chiral Binol-Based Covalent Organic Frameworks for Enantioselective Sensing. *J. Am. Chem. Soc.* **2019**, *141*, 7081−7089.
(265) Gao, C.; Li, J.; Yin, S.; Lin, G.; Ma, T.; Meng, Y.; Sun, J.; Wang, C. Isostructural Three-Dimensional Covalent Organic Frameworks. *Angew. Chem., Int. Ed.* **2019**, *58*, 9770−9775.
(266) Huang, J.; Han, X.; Yang, S.; Cao, Y.; Yuan, C.; Liu, Y.; Wang, J.; Cui, Y. Microporous 3D Covalent Organic Frameworks for Liquid Chromatographic Separation of Xylene Isomers and Ethylbenzene. *J. Am. Chem. Soc.* **2019**, *141*, 8996−9003.
(267) Stegbauer, L.; Hahn, M. W.; Jentys, A.; Savasci, G.; Ochsenfeld, C.; Lercher, J. A.; Lotsch, B. V. Tunable Water and CO_2 sorption Properties in Isostructural Azine-Based Covalent Organic Frameworks through Polarity Engineering. *Chem. Mater.* **2015**, *27*, 7874−7881.
(268) Alahakoon, S. B.; McCandless, G. T.; Karunathilake, A. A. K.; Thompson, C. M.; Smaldone, R. A. Enhanced Structural Organization in Covalent Organic Frameworks through Fluorination. *Chem. - Eur. J.* **2017**, *23*, 4255.
(269) Wang, K.; Yang, L.-M.; Wang, X.; Guo, L.; Cheng, G.; Zhang, C.; Jin, S.; Tan, B.; Cooper, A. Covalent Triazine Frameworks Via a Low-Temperature Polycondensation Approach. *Angew. Chem., Int. Ed.* **2017**, *56*, 14149−14153.
(270) Yu, S.-Y.; Mahmood, J.; Noh, H.-J.; Seo, J.-M.; Jung, S.-M.; Shin, S.-H.; Im, Y.-K.; Jeon, I.-Y.; Baek, J.-B. Direct Synthesis of a Covalent Triazine-Based Framework from Aromatic Amides. *Angew. Chem., Int. Ed.* **2018**, *57*, 8438−8442.
(271) Liu, M.; Huang, Q.; Wang, S.; Li, Z.; Li, B.; Jin, S.; Tan, B. Crystalline Covalent Triazine Frameworks by *in situ* Oxidation of Alcohols to Aldehyde Monomers. *Angew. Chem., Int. Ed.* **2018**, *57*, 11968−11972.
(272) Zhao, Y.; Liu, H.; Wu, C.; Zhang, Z.; Pan, Q.; Hu, F.; Wang, R.; Li, P.; Huang, X.; Li, Z. Fully Conjugated Two-Dimensional sp^2-Carbon Covalent Organic Frameworks as Artificial Photosystem I with High Efficiency. *Angew. Chem.* **2019**, *131*, 5430−5435.
(273) Meng, Z.; Stolz, R. M.; Mirica, K. A. Two-Dimensional Chemiresistive Covalent Organic Framework with High Intrinsic Conductivity. *J. Am. Chem. Soc.* **2019**, *141*, 11929−11937.
(274) Rao, M. R.; Fang, Y.; De Feyter, S.; Perepichka, D. F. Conjugated Covalent Organic Frameworks Via Michael Addition−Elimination. *J. Am. Chem. Soc.* **2017**, *139*, 2421−2427.
(275) Liu, W.; Luo, X.; Bao, Y.; Liu, Y. P.; Ning, G.-H.; Abdelwahab, I.; Li, L.; Nai, C. T.; Hu, Z. G.; Zhao, D.; Liu, B.; Quek, S. Y.; Loh, K. P. A Two-Dimensional Conjugated Aromatic Polymer Via C−C Coupling Reaction. *Nat. Chem.* **2017**, *9*, 563.
(276) Wu, S.; Li, M.; Phan, H.; Wang, D.; Herng, T. S.; Ding, J.; Lu, Z.; Wu, J. Toward Two-Dimensional *π*-Conjugated Covalent Organic Radical Frameworks. *Angew. Chem., Int. Ed.* **2018**, *57*, 8007−8011.
(277) Li, H.; Pan, Q.; Ma, Y.; Guan, X.; Xue, M.; Fang, Q.; Yan, Y.; Valtchev, V.; Qiu, S. Three-Dimensional Covalent Organic Frameworks with Dual Linkages for Bifunctional Cascade Catalysis. *J. Am. Chem. Soc.* **2016**, *138*, 14783−14788.
(278) Liu, H.; Chu, J.; Yin, Z.; Cai, X.; Zhuang, L.; Deng, H. Covalent Organic Frameworks Linked by Amine Bonding for Concerted Electrochemical Reduction of CO_2. *Chem.* **2018**, *4*, 1696−1709.
(279) Waller, P. J.; AlFaraj, Y. S.; Diercks, C. S.; Jarenwattananon, N. N.; Yaghi, O. M. Conversion of Imine to Oxazole and Thiazole Linkages in Covalent Organic Frameworks. *J. Am. Chem. Soc.* **2018**, *140*, 9099−9103.
(280) Haase, F.; Troschke, E.; Savasci, G.; Banerjee, T.; Duppel, V.; Dörfler, S.; Grundei, M. M. J.; Burow, A. M.; Ochsenfeld, C.; Kaskel, S.; Lotsch, B. V. Topochemical Conversion of an Imine- into a Thiazole-Linked Covalent Organic Framework Enabling Real Structure Analysis. *Nat. Commun.* **2018**, *9*, 2600.
(281) Li, H.; Chavez, A. D.; Li, H.; Li, H.; Dichtel, W. R.; Bredas, J.-L. Nucleation and Growth of Covalent Organic Frameworks from Solution: The Example of COF-5. *J. Am. Chem. Soc.* **2017**, *139*, 16310−16318.

https://dx.doi.org/10.1021/acs.chemrev.9b00550
Chem. Rev. 2020, 120, 8814−8933

(282) Fischbach, D. M.; Rhoades, G.; Espy, C.; Goldberg, F.; Smith, B. J. Controlling the Crystalline Structure of Imine-Linked 3D Covalent Organic Frameworks. *Chem. Commun.* **2019**, *55*, 3594−3597.
(283) Navarro, J. A. R. The Dynamic Art of Growing Cof Crystals. *Science* **2018**, *361*, 35−35.
(284) Calik, M.; Sick, T.; Dogru, M.; Doblinger, M.; Datz, S.; Budde, H.; Hartschuh, A.; Auras, F.; Bein, T. From Highly Crystalline to Outer Surface-Functionalized Covalent Organic Frameworks-a Modulation Approach. *J. Am. Chem. Soc.* **2016**, *138*, 1234−9.
(285) Nguyen, V.; Grünwald, M. Microscopic Origins of Poor Crystallinity in the Synthesis of Covalent Organic Framework COF-5. *J. Am. Chem. Soc.* **2018**, *140*, 3306−3311.
(286) Karak, S.; Kumar, S.; Pachfule, P.; Banerjee, R. Porosity Prediction through Hydrogen Bonding in Covalent Organic Frameworks. *J. Am. Chem. Soc.* **2018**, *140*, 5138−5145.
(287) Vitaku, E.; Dichtel, W. R. Synthesis of 2D Imine-Linked Covalent Organic Frameworks through Formal Transimination Reactions. *J. Am. Chem. Soc.* **2017**, *139*, 12911−12914.
(288) Wang, H.; He, B.; Liu, F.; Stevens, C.; Brady, M. A.; Cai, S.; Wang, C.; Russell, T. P.; Tan, T. W.; Liu, Y. Orientation Transitions During the Growth of Imine Covalent Organic Framework Thin Films. *J. Mater. Chem. C* **2017**, *5*, 5090−5095.
(289) Ma, T.; Li, J.; Niu, J.; Zhang, L.; Etman, A. S.; Lin, C.; Shi, D.; Chen, P.; Li, L.-H.; Du, X.; Sun, J.; Wang, W. Observation of Interpenetration Isomerism in Covalent Organic Frameworks. *J. Am. Chem. Soc.* **2018**, *140*, 6763−6766.
(290) Pachfule, P.; Kandmabeth, S.; Mallick, A.; Banerjee, R. Hollow Tubular Porous Covalent Organic Framework (COF) Nanostructures. *Chem. Commun.* **2015**, *51*, 11717−11720.
(291) Pan, L.; Chen, Z.; Deng, W.; Yan, G.; Liu, X. Morphology Controlled Synthesis of Octahedral Covalent Imine Frameworks through Acid Modulated Aldehyde-Amine Polycondensation. *Macromol. Res.* **2016**, *24*, 366−370.
(292) Gole, B.; Stepanenko, V.; Rager, S.; Grüne, M.; Medina, D. D.; Bein, T.; Würthner, F.; Beuerle, F. Microtubular Self-Assembly of Covalent Organic Frameworks. *Angew. Chem., Int. Ed.* **2018**, *57*, 846−850.
(293) Zhang, G.; Tsujimoto, M.; Packwood, D.; Duong, N. T.; Nishiyama, Y.; Kadota, K.; Kitagawa, S.; Horike, S. Construction of a Hierarchical Architecture of Covalent Organic Frameworks Via a Postsynthetic Approach. *J. Am. Chem. Soc.* **2018**, *140*, 2602−2609.
(294) Kong, W.; Jia, W.; Wang, R.; Gong, Y.; Wang, C.; Wu, P.; Guo, J. Amorphous-to-Crystalline Transformation toward Controllable Synthesis of Fibrous Covalent Organic Frameworks Enabling Promotion of Proton Transport. *Chem. Commun.* **2019**, *55*, 75−78.
(295) Guan, C. Z.; Wang, D.; Wan, L. J. Construction and Repair of Highly Ordered 2D Covalent Networks by Chemical Equilibrium Regulation. *Chem. Commun.* **2012**, *48*, 2943−5.
(296) Dong, W. L.; Wang, L.; Ding, H. M.; Zhao, L.; Wang, D.; Wang, C.; Wan, L. J. Substrate Orientation Effect in the on-Surface Synthesis of Tetrathiafulvalene-Integrated Single-Layer Covalent Organic Frameworks. *Langmuir* **2015**, *31*, 11755−9.
(297) Liu, C.; Zhang, W.; Zeng, Q.; Lei, S. A Photoresponsive Surface Covalent Organic Framework: Surface-Confined Synthesis, Isomerization, and Controlled Guest Capture and Release. *Chem. - Eur. J.* **2016**, *22*, 6768−6773.
(298) Sun, J.; Zhou, X.; Lei, S. Host-Guest Architectures with a Surface Confined Imine Covalent Organic Framework as Two-Dimensional Host Networks. *Chem. Commun.* **2016**, *52*, 8691−4.
(299) Seo, W.; White, D. L.; Star, A. Fabrication of Holey Graphene: Catalytic Oxidation by Metalloporphyrin-Based Covalent Organic Framework Immobilized on Highly Ordered Pyrolytic Graphite. *Chem. - Eur. J.* **2017**, *23*, 5652−5657.
(300) Zwaneveld, N. A. A.; Pawlak, R.; Abel, M.; Catalin, D.; Gigmes, D.; Bertin, D.; Porte, L. Organized Formation of 2D Extended Covalent Organic Frameworks at Surfaces. *J. Am. Chem. Soc.* **2008**, *130*, 6678−6679.
(301) Yang, B.; Bjork, J.; Lin, H.; Zhang, X.; Zhang, H.; Li, Y.; Fan, J.; Li, Q.; Chi, L. Synthesis of Surface Covalent Organic Frameworks Via Dimerization and Cyclotrimerization of Acetyls. *J. Am. Chem. Soc.* **2015**, *137*, 4904−4907.
(302) Blunt, M. O.; Russell, J. C.; Champness, N. R.; Beton, P. H. Templating Molecular Adsorption Using a Covalent Organic Framework. *Chem. Commun.* **2010**, *46*, 7157−9.
(303) Faury, T.; Clair, S.; Abel, M.; Dumur, F.; Gigmes, D.; Porte, L. Sequential Linking to Control Growth of a Surface Covalent Organic Framework. *J. Phys. Chem. C* **2012**, *116*, 4819−4823.
(304) Gong, Z.; Yang, B.; Lin, H.; Tang, Y.; Tang, Z.; Zhang, J.; Zhang, H.; Li, Y.; Xie, Y.; Li, Q.; Chi, L. Structural Variation in Surface-Supported Synthesis by Adjusting the Stoichiometric Ratio of the Reactants. *ACS Nano* **2016**, *10*, 4228−35.
(305) Peyrot, D.; Silly, F. On-Surface Synthesis of Two-Dimensional Covalent Organic Structures Versus Halogen-Bonded Self-Assembly: Competing Formation of Organic Nanoarchitectures. *ACS Nano* **2016**, *10*, 5490−8.
(306) Medina, D. D.; Rotter, J. M.; Hu, Y.; Dogru, M.; Werner, V.; Auras, F.; Markiewicz, J. T.; Knochel, P.; Bein, T. Room Temperature Synthesis of Covalent-Organic Framework Films through Vapor-Assisted Conversion. *J. Am. Chem. Soc.* **2015**, *137*, 1016−9.
(307) Gou, X.; Zhang, Q.; Wu, Y.; Zhao, Y.; Shi, X.; Fan, X.; Huang, L.; Lu, G. Preparation and Engineering of Oriented 2D Covalent Organic Framework Thin Films. *RSC Adv.* **2016**, *6*, 39198−39203.
(308) Zha, Z.; Xu, L.; Wang, Z.; Li, X.; Pan, Q.; Hu, P.; Lei, S. 3d Graphene Functionalized by Covalent Organic Framework Thin Film as Capacitive Electrode in Alkaline Media. *ACS Appl. Mater. Interfaces* **2015**, *7*, 17837−43.
(309) Wang, P.; Wu, Q.; Han, L.; Wang, S.; Fang, S.; Zhang, Z.; Sun, S. Synthesis of Conjugated Covalent Organic Frameworks/Graphene Composite for Supercapacitor Electrodes. *RSC Adv.* **2015**, *5*, 27290−27294.
(310) Sun, B.; Li, J.; Dong, W.-L.; Wu, M.-L.; Wang, D. Selective Growth of Covalent Organic Framework Ultrathin Films on Hexagonal Boron Nitride. *J. Phys. Chem. C* **2016**, *120*, 14706−14711.
(311) Bao, T.; Tang, P.; Kong, D.; Mao, Z.; Chen, Z. Polydopamine-Supported Immobilization of Covalent-Organic Framework-5 in Capillary as Stationary Phase for Electrochromatographic Separation. *J. Chromatogr. A* **2016**, *1445*, 140−8.
(312) Wang, P.; Kang, M.; Sun, S.; Liu, Q.; Zhang, Z.; Fang, S. Imine-Linked Covalent Organic Framework on Surface for Biosensor. *Chin. J. Chem.* **2014**, *32* (9), 838−843.
(313) Sun, J.; Klechikov, A.; Moise, C.; Prodana, M.; Enachescu, M.; Talyzin, A. V. A Molecular Pillar Approach to Grow Vertical Covalent Organic Framework Nanosheets on Graphene: Hybrid Materials for Energy Storage. *Angew. Chem., Int. Ed.* **2018**, *57*, 1034−1038.
(314) Dai, W.; Shao, F.; Szczerbinski, J.; McCaffrey, R.; Zenobi, R.; Jin, Y.; Schluter, A. D.; Zhang, W. Synthesis of a Two-Dimensional Covalent Organic Monolayer through Dynamic Imine Chemistry at the Air/Water Interface. *Angew. Chem., Int. Ed.* **2016**, *55*, 213−7.
(315) Diercks, C. S.; Lin, S.; Kornienko, N.; Kapustin, E. A.; Nichols, E. M.; Zhu, C.; Zhao, Y.; Chang, C. J.; Yaghi, O. M. Reticular Electronic Tuning of Porphyrin Active Sites in Covalent Organic Frameworks for Electrocatalytic Carbon Dioxide Reduction. *J. Am. Chem. Soc.* **2018**, *140*, 1116−1122.
(316) Liu, X. H.; Mo, Y. P.; Yue, J. Y.; Zheng, Q. N.; Yan, H. J.; Wang, D.; Wan, L. J. Isomeric Routes to Schiff-Base Single-Layered Covalent Organic Frameworks. *Small* **2014**, *10*, 4934−9.
(317) Cui, D.; MacLeod, J. M.; Ebrahimi, M.; Perepichka, D. F.; Rosei, F. Solution and Air Stable Host/Guest Architectures from a Single Layer Covalent Organic Framework. *Chem. Commun.* **2015**, *51*, 16510−16513.
(318) Wang, H.; Zeng, Z.; Xu, P.; Li, L.; Zeng, G.; Xiao, R.; Tang, Z.; Huang, D.; Tang, L.; Lai, C.; et al. Recent Progress in Covalent Organic Framework Thin Films: Fabrications, Applications and Perspectives. *Chem. Soc. Rev.* **2019**, *48*, 488−516.
(319) Wang, L.; Zeng, C.; Xu, H.; Yin, P.; Chen, D.; Deng, J.; Li, M.; Zheng, N.; Gu, C.; Ma, Y. A Highly Soluble, Crystalline Covalent Organic Framework Compatible with Device Implementation. *Chem. Sci.* **2019**, *10*, 1023−1028.

https://dx.doi.org/10.1021/acs.chemrev.9b00550
Chem. Rev. 2020, 120, 8814−8933

(320) Clair, S.; Abel, M.; Porte, L. Growth of Boronic Acid Based Two-Dimensional Covalent Networks on a Metal Surface under Ultrahigh Vacuum. *Chem. Commun.* **2014**, *50*, 9627−9635.
(321) Feldblyum, J. I.; McCreery, C. H.; Andrews, S. C.; Kurosawa, T.; Santos, E. J. G.; Duong, V.; Fang, L.; Ayzner, A. L.; Bao, Z. N. Few-Layer, Large-Area, 2D Covalent Organic Framework Semiconductor Thin Films. *Chem. Commun.* **2015**, *51*, 13894−13897.
(322) Berlanga, I.; Ruiz-Gonzalez, M. L.; Gonzalez-Calbet, J. M.; Fierro, J. L.; Mas-Balleste, R.; Zamora, F. Delamination of Layered Covalent Organic Frameworks. *Small* **2011**, *7*, 1207−11.
(323) Dong, J.; Li, X.; Peh, S. B.; Yuan, Y. D.; Wang, Y.; Ji, D.; Peng, S.; Liu, G.; Ying, S.; Yuan, D.; et al. Restriction of Molecular Rotors in Ultrathin Two-Dimensional Covalent Organic Framework Nanosheets for Sensing Signal Amplification. *Chem. Mater.* **2019**, *31*, 146−160.
(324) Bisbey, R. P.; DeBlase, C. R.; Smith, B. J.; Dichtel, W. R. Two-Dimensional Covalent Organic Framework Thin Films Grown in Flow. *J. Am. Chem. Soc.* **2016**, *138*, 11433−11436.
(325) Mahmood, J.; Lee, E. K.; Jung, M.; Shin, D.; Jeon, I. Y.; Jung, S. M.; Choi, H. J.; Seo, J. M.; Bae, S. Y.; Sohn, S. D.; Park, N.; Oh, J. H.; Shin, H. J.; Baek, J. B. Nitrogenated Holey Two-Dimensional Structures. *Nat. Commun.* **2015**, *6*, 6486.
(326) Ma, H.-C.; Kan, J.-L.; Chen, G.-J.; Chen, C.-X.; Dong, Y.-B. Pd Nps-Loaded Homochiral Covalent Organic Framework for Heterogeneous Asymmetric Catalysis. *Chem. Mater.* **2017**, *29*, 6518−6524.
(327) Nandi, S.; Singh, S. K.; Mullangi, D.; Illathvalappil, R.; George, L.; Vinod, C. P.; Kurungot, S.; Vaidhyanathan, R. Low Band Gap Benzimidazole Cof Supported Ni_3N as Highly Active OER Catalyst. *Adv. Energy Mater.* **2016**, *6*, 1601189.
(328) Rodríguez-San-Miguel, D.; Yazdi, A.; Guillerm, V.; Pérez-Carvajal, J.; Puntes, V.; Maspoch, D.; Zamora, F. Confining Functional Nanoparticles into Colloidal Imine-Based Cof Spheres by a Sequential Encapsulation−Crystallization Method. *Chem. - Eur. J.* **2017**, *23*, 8623−8627.
(329) Fan, H.; Mundstock, A.; Feldhoff, A.; Knebel, A.; Gu, J.; Meng, H.; Caro, J. Covalent Organic Framework−Covalent Organic Framework Bilayer Membranes for Highly Selective Gas Separation. *J. Am. Chem. Soc.* **2018**, *140*, 10094−10098.
(330) Fu, J.; Das, S.; Xing, G.; Ben, T.; Valtchev, V.; Qiu, S. Fabrication of COF-MOF Composite Membranes and Their Highly Selective Separation of H_2/CO_2. *J. Am. Chem. Soc.* **2016**, *138*, 7673−80.
(331) Garzón-Tovar, L.; Pérez-Carvajal, J.; Yazdi, A.; Hernández-Muñoz, J.; Tarazona, P.; Imaz, I.; Zamora, F.; Maspoch, D. A MOF@COF Composite with Enhanced Uptake through Interfacial Pore Generation. *Angew. Chem., Int. Ed.* **2019**, *58*, 9512−9516.
(332) Du, Y.; Mao, K.; Kamakoti, P.; Wooler, B.; Cundy, S.; Li, Q.; Ravikovitch, P.; Calabro, D. The Effects of Pyridine on the Structure of B-COFs and the Underlying Mechanism. *J. Mater. Chem. A* **2013**, *1*, 13171.
(333) Li, H.; Li, H.; Dai, Q.; Li, H.; Brédas, J.-L. Hydrolytic Stability of Boronate Ester-Linked Covalent Organic Frameworks. *Adv. Theory and Simul.* **2018**, *1*, 1700015.
(334) Du, Y.; Mao, K.; Kamakoti, P.; Ravikovitch, P.; Paur, C.; Cundy, S.; Li, Q.; Calabro, D. Experimental and Computational Studies of Pyridine-Assisted Post-Synthesis Modified Air Stable Covalent-Organic Frameworks. *Chem. Commun.* **2012**, *48*, 4606−8.
(335) Du, Y.; Calabro, D.; Wooler, B.; Kortunov, P.; Li, Q.; Cundy, S.; Mao, K. One Step Facile Synthesis of Amine-Functionalized Cof-1 with Enhanced Hydrostability. *Chem. Mater.* **2015**, *27*, 1445−1447.
(336) Wu, X.; Han, X.; Liu, Y.; Liu, Y.; Cui, Y. Control Interlayer Stacking and Chemical Stability of Two-Dimensional Covalent Organic Frameworks Via Steric Tuning. *J. Am. Chem. Soc.* **2018**, *140*, 16124−16133.
(337) Halder, A.; Karak, S.; Addicoat, M.; Bera, S.; Chakraborty, A.; Kunjattu, S. H.; Pachfule, P.; Heine, T.; Banerjee, R. Ultrastable Imine-Based Covalent Organic Frameworks for Sulfuric Acid Recovery: An Effect of Interlayer Hydrogen Bonding. *Angew. Chem., Int. Ed.* **2018**, *57*, 5797−5802.
(338) Song, Y.; Sun, Q.; Aguila, B.; Ma, S. Opportunities of Covalent Organic Frameworks for Advanced Applications. *Adv. Sci.* **2019**, *6*, 1801410.
(339) Nath, B.; Li, W.-H.; Huang, J.-H.; Wang, G.-E.; Fu, Z.-h.; Yao, M.-S.; Xu, G. A New Azodioxy-Linked Porphyrin-Based Semiconductive Covalent Organic Framework with I_2 Doping-Enhanced Photoconductivity. *CrystEngComm* **2016**, *18*, 4259−4263.
(340) Dicker, G.; de Haas, M. P.; Siebbeles, L. D. A.; Warman, J. M. Electrodeless Time-Resolved Microwave Conductivity Study of Charge-Carrier Photogeneration in Regioregular Poly(3-Hexylthiophene) Thin Films. *Phys. Rev. B: Condens. Matter Mater. Phys.* **2004**, *70*, 045203.
(341) Dicker, G.; de Haas, M. P.; Warman, J. M.; de Leeuw, D. M.; Siebbeles, L. D. A. The Disperse Charge-Carrier Kinetics in Regioregular Poly(3-Hexylthiophene). *J. Phys. Chem. B* **2004**, *108*, 17818−17824.
(342) Yamagami, R.; Kobayashi, K.; Saeki, A.; Seki, S.; Tagawa, S. Photogenerated Hole Mobility in DNA Measured by Time-Resolved Microwave Conductivity. *J. Am. Chem. Soc.* **2006**, *128*, 2212−2213.
(343) Saeki, A.; Ohsaki, S.-i.; Seki, S.; Tagawa, S. Electrodeless Determination of Charge Carrier Mobility in Poly(3-Hexylthiophene) Films Incorporating Perylenediimide as Photoconductivity Sensitizer and Spectroscopic Probe. *J. Phys. Chem. C* **2008**, *112*, 16643−16650.
(344) Duhović, S.; Dincă, M. Synthesis and Electrical Properties of Covalent Organic Frameworks with Heavy Chalcogens. *Chem. Mater.* **2015**, *27*, 5487−5490.
(345) Samorì, P.; Yin, X.; Tchebotareva, N.; Wang, Z.; Pakula, T.; Jäckel, F.; Watson, M. D.; Venturini, A.; Müllen, K.; Rabe, J. P. Self-Assembly of Electron Donor−Acceptor Dyads into Ordered Architectures in Two and Three Dimensions: Surface Patterning and Columnar "Double Cables. *J. Am. Chem. Soc.* **2004**, *126*, 3567−3575.
(346) Würthner, F.; Chen, Z.; Hoeben, F. J. M.; Osswald, P.; You, C.-C.; Jonkheijm, P.; Herrikhuyzen, J. v.; Schenning, A. P. H. J.; van der Schoot, P. P. A. M.; Meijer, E. W.; Beckers, E. H. A.; Meskers, S. C. J.; Janssen, R. A. J. Supramolecular p-n-Heterojunctions by Co-Self-Organization of Oligo(*p*-Phenylene Vinylene) and Perylene Bisimide Dyes. *J. Am. Chem. Soc.* **2004**, *126*, 10611−10618.
(347) Bessinger, D.; Ascherl, L.; Auras, F.; Bein, T. Spectrally Switchable Photodetection with near-Infrared-Absorbing Covalent Organic Frameworks. *J. Am. Chem. Soc.* **2017**, *139*, 12035−12042.
(348) Culebras, M.; Gómez, C.; Cantarero, A. Review on Polymers for Thermoelectric Applications. *Materials* **2014**, *7*, 6701.
(349) Chen, Y.; Cui, H. J.; Zhang, J. Q.; Zhao, K.; Ding, D. F.; Guo, J.; Li, L. S.; Tian, Z. Y.; Tang, Z. Y. Surface Growth of Highly Oriented Covalent Organic Framework Thin Film with Enhanced Photoresponse Speed. *RSC Adv.* **2015**, *5*, 92573−92576.
(350) Liu, Y.; Zhou, H.; Weiss, N. O.; Huang, Y.; Duan, X. High-Performance Organic Vertical Thin Film Transistor Using Graphene as a Tunable Contact. *ACS Nano* **2015**, *9*, 11102−11108.
(351) Lemaitre, M. G.; Donoghue, E. P.; McCarthy, M. A.; Liu, B.; Tongay, S.; Gila, B.; Kumar, P.; Singh, R. K.; Appleton, B. R.; Rinzler, A. G. Improved Transfer of Graphene for Gated Schottky-Junction, Vertical, Organic, Field-Effect Transistors. *ACS Nano* **2012**, *6*, 9095−9102.
(352) Bredas, J. L.; Street, G. B. Polarons, Bipolarons, and Solitons in Conducting Polymers. *Acc. Chem. Res.* **1985**, *18*, 309−315.
(353) Kuroda, S.; Marumoto, K.; Shimoi, Y.; Abe, S. Esr Spectroscopy of Polarons in Conjugated Electroluminescent Polymers. *Thin Solid Films* **2001**, *393*, 304−309.
(354) Mei, J.; Leung, N. L.; Kwok, R. T.; Lam, J. W.; Tang, B. Z. Aggregation-Induced Emission: Together We Shine, United We Soar! *Chem. Rev.* **2015**, *115*, 11718−940.
(355) Dalapati, S.; Gu, C.; Jiang, D. Luminescent Porous Polymers Based on Aggregation-Induced Mechanism: Design, Synthesis and Functions. *Small* **2016**, *12*, 6513−6527.
(356) Dalapati, S.; Jana, S.; Alam, M. A.; Guchhait, N. Multifunctional Fluorescent Probe Selective for Cu(II) and Fe(III) with Dual-Mode of Binding Approach. *Sens. Actuators, B* **2011**, *160*, 1106−1111.

https://dx.doi.org/10.1021/acs.chemrev.9b00550
Chem. Rev. 2020, 120, 8814−8933

(357) Dalapati, S.; Akhtarul Alam, M.; Saha, R.; Jana, S.; Guchhait, N. An Efficient Size-Selective Anion Binding Cleft-Shaped Receptor: A Novel $[F_2(H_2O)_3]_2$- Cluster with Pseudo-Encapsulated F- Ion. *CrystEngComm* **2012**, *14*, 1527−1530.
(358) Dalapati, S.; Alam, M. A.; Jana, S.; Guchhait, N. Reduced Schiff-Base Assisted Novel Dihydrogenphosphate-Water Polymer. *CrystEngComm* **2012**, *14*, 6029−6034.
(359) Dalapati, S.; Alam, M. A.; Jana, S.; Saha, R.; Biswas, S.; Guchhait, N. A Molecular Lock and Key: "Unlocked−Locked" Conformational Switching of a Receptor by Anions. *ChemPlusChem* **2012**, *77*, 93−97.
(360) Dalapati, S.; Jana, S.; Saha, R.; Alam, M. A.; Guchhait, N. Reusable Amine-Based Structural Motifs for Green House Gas (CO_2) Fixation. *Org. Lett.* **2012**, *14*, 3244−3247.
(361) Dalapati, S.; Saha, R.; Jana, S.; Patra, A. K.; Bhaumik, A.; Kumar, S.; Guchhait, N. A Multifunctional Porous Organic Schottky Barrier Diode. *Angew. Chem., Int. Ed.* **2012**, *51*, 12534−7.
(362) Ma, L.; Feng, X.; Wang, S.; Wang, B. Recent Advances in Aiegen-Based Luminescent Metal−Organic Frameworks and Covalent Organic Frameworks. *Mater. Chem. Front.* **2017**, *1*, 2474−2486.
(363) Gao, Q.; Li, X.; Ning, G.-H.; Leng, K.; Tian, B.; Liu, C.; Tang, W.; Xu, H.-S.; Loh, K. P. Highly Photoluminescent Two-Dimensional Imine-Based Covalent Organic Frameworks for Chemical Sensing. *Chem. Commun.* **2018**, *54*, 2349−2352.
(364) Wang, S.; Ma, L.; Wang, Q.; Shao, P.; Ma, D.; Yuan, S.; Lei, P.; Li, P.; Feng, X.; Wang, B. Covalent Organic Frameworks: A Platform for the Experimental Establishment of the Influence of Intermolecular Distance on Phosphorescence. *J. Mater. Chem. C* **2018**, *6*, 5369−5374.
(365) Li, X.; Gao, Q.; Wang, J.; Chen, Y.; Chen, Z.-H.; Xu, H.-S.; Tang, W.; Leng, K.; Ning, G.-H.; Wu, J.; et al. Tuneable near White-Emissive Two-Dimensional Covalent Organic Frameworks. *Nat. Commun.* **2018**, *9*, 2335.
(366) Albacete, P.; Martinez, J. I.; Li, X.; López-Moreno, A.; Mena-Hernando, S. a.; Platero-Prats, A. E.; Montoro, C.; Loh, K. P.; Perez, E. M.; Zamora, F. Layer-Stacking-Driven Fluorescence in a Two-Dimensional Imine-Linked Covalent Organic Framework. *J. Am. Chem. Soc.* **2018**, *140*, 12922−12929.
(367) Rager, S.; Dogru, M.; Werner, V.; Gavryushin, A.; Götz, M.; Engelke, H.; Medina, D. D.; Knochel, P.; Bein, T. Pore Wall Fluorescence Labeling of Covalent Organic Frameworks. *CrystEngComm* **2017**, *19*, 4886−4891.
(368) Haldar, S.; Chakraborty, D.; Roy, B.; Banappanavar, G.; Rinku, K.; Mullangi, D.; Hazra, P.; Kabra, D.; Vaidhyanathan, R. Anthracene-Resorcinol Derived Covalent Organic Framework as Flexible White Light Emitter. *J. Am. Chem. Soc.* **2018**, *140*, 13367−13374.
(369) Zhang, C.; Zhang, S.; Yan, Y.; Xia, F.; Huang, A.; Xian, Y. Highly Fluorescent Polyimide Covalent Organic Nanosheets as Sensing Probes for the Detection of 2, 4, 6-Trinitrophenol. *ACS Appl. Mater. Interfaces* **2017**, *9*, 13415−13421.
(370) Cotte-Rodríguez, I.; Hernández-Soto, H.; Chen, H.; Cooks, R. G. In Situ Trace Detection of Peroxide Explosives by Desorption Electrospray Ionization and Desorption Atmospheric Pressure Chemical Ionization. *Anal. Chem.* **2008**, *80*, 1512−1519.
(371) Albacete, P.; López-Moreno, A.; Mena-Hernando, S.; Platero-Prats, A. E.; Pérez, E. M.; Zamora, F. Chemical Sensing of Water Contaminants by a Colloid of a Fluorescent Imine-Linked Covalent Organic Framework. *Chem. Commun.* **2019**, *55* (10), 1382−1385.
(372) Doonan, C. J.; Tranchemontagne, D. J.; Glover, T. G.; Hunt, J. R.; Yaghi, O. M. Exceptional Ammonia Uptake by a Covalent Organic Framework. *Nat. Chem.* **2010**, *2*, 235−238.
(373) Cui, F.-Z.; Xie, J.-J.; Jiang, S.-Y.; Gan, S.-X.; Ma, D.-L.; Liang, R.-R.; Jiang, G.-F.; Zhao, X. A Gaseous Hydrogen Chloride Chemosensor Based on a 2D Covalent Organic Framework. *Chem. Commun.* **2019**, *55*, 4550−4553.
(374) Zhou, Y.; Zhang, J. F.; Yoon, J. Fluorescence and Colorimetric Chemosensors for Fluoride-Ion Detection. *Chem. Rev.* **2014**, *114*, 5511−5571.
(375) Dalapati, S.; Paul, B. K.; Jana, S.; Guchhait, N. Highly Selective and Sensitive Fluorescence Reporter for Toxic Hg(II) Ion by a Synthetic Symmetrical Azine Derivative. *Sens. Actuators, B* **2011**, *157*, 615−620.
(376) Chen, G.; Lan, H.-H.; Cai, S.-L.; Sun, B.; Li, X.-L.; He, Z.-H.; Zheng, S.-R.; Fan, J.; Liu, Y.; Zhang, W.-G. Stable Hydrazone-Linked Covalent Organic Frameworks Containing O, N, O'-Chelating Sites for Fe (III) Detection in Water. *ACS Appl. Mater. Interfaces* **2019**, *11*, 12830−12837.
(377) Mal, A.; Mishra, R. K.; Praveen, V. K.; Khayum, M. A.; Banerjee, R.; Ajayaghosh, A. Supramolecular Reassembly of Self-Exfoliated Ionic Covalent Organic Nanosheets for Label-Free Detection of Double-Stranded DNA. *Angew. Chem., Int. Ed.* **2018**, *57*, 8443−8447.
(378) Lu, C. H.; Yang, H. H.; Zhu, C. L.; Chen, X.; Chen, G. N. A Graphene Platform for Sensing Biomolecules. *Angew. Chem., Int. Ed.* **2009**, *48*, 4785−4787.
(379) He, S.; Song, B.; Li, D.; Zhu, C.; Qi, W.; Wen, Y.; Wang, L.; Song, S.; Fang, H.; Fan, C. A Graphene Nanoprobe for Rapid, Sensitive, and Multicolor Fluorescent DNA Analysis. *Adv. Funct. Mater.* **2010**, *20*, 453−459.
(380) Liu, X.; Aizen, R.; Freeman, R.; Yehezkeli, O.; Willner, I. Multiplexed Aptasensors and Amplified DNA Sensors Using Functionalized Graphene Oxide: Application for Logic Gate Operations. *ACS Nano* **2012**, *6*, 3553−3563.
(381) Liu, X.; Wang, F.; Aizen, R.; Yehezkeli, O.; Willner, I. Graphene Oxide/Nucleic-Acid-Stabilized Silver Nanoclusters: Functional Hybrid Materials for Optical Aptamer Sensing and Multiplexed Analysis of Pathogenic Dnas. *J. Am. Chem. Soc.* **2013**, *135*, 11832−11839.
(382) Qian, Z. S.; Shan, X. Y.; Chai, L. J.; Ma, J. J.; Chen, J. R.; Feng, H. A Universal Fluorescence Sensing Strategy Based on Biocompatible Graphene Quantum Dots and Graphene Oxide for the Detection of DNA. *Nanoscale* **2014**, *6*, 5671−5674.
(383) Wang, Q.; Wang, W.; Lei, J.; Xu, N.; Gao, F.; Ju, H. Fluorescence Quenching of Carbon Nitride Nanosheet through Its Interaction with DNA for Versatile Fluorescence Sensing. *Anal. Chem.* **2013**, *85*, 12182−12188.
(384) Zhu, C.; Zeng, Z.; Li, H.; Li, F.; Fan, C.; Zhang, H. Single-Layer MoS_2-Based Nanoprobes for Homogeneous Detection of Biomolecules. *J. Am. Chem. Soc.* **2013**, *135*, 5998−6001.
(385) Huang, J.; Ye, L.; Gao, X.; Li, H.; Xu, J.; Li, Z. Molybdenum Disulfide-Based Amplified Fluorescence DNA Detection Using Hybridization Chain Reactions. *J. Mater. Chem. B* **2015**, *3*, 2395−2401.
(386) Yuan, Y.; Li, R.; Liu, Z. Establishing Water-Soluble Layered WS_2 Nanosheet as a Platform for Biosensing. *Anal. Chem.* **2014**, *86*, 3610−3615.
(387) Zhang, Y.; Zheng, B.; Zhu, C.; Zhang, X.; Tan, C.; Li, H.; Chen, B.; Yang, J.; Chen, J.; Huang, Y.; Wang, L.; Zhang, H. Single-Layer Transition Metal Dichalcogenide Nanosheet-Based Nanosensors for Rapid, Sensitive, and Multiplexed Detection of DNA. *Adv. Mater.* **2015**, *27*, 935−939.
(388) Zhao, M.; Wang, Y.; Ma, Q.; Huang, Y.; Zhang, X.; Ping, J.; Zhang, Z.; Lu, Q.; Yu, Y.; Xu, H.; Zhao, Y.; Zhang, H. Ultrathin 2D Metal−Organic Framework. *Adv. Mater.* **2015**, *27*, 7372−7378.
(389) Han, X.; Zhang, J.; Huang, J.; Wu, X.; Yuan, D.; Liu, Y.; Cui, Y. Chiral Induction in Covalent Organic Frameworks. *Nat. Commun.* **2018**, *9*, 1294.
(390) Wang, H.; Jiao, F.; Gao, F.; Huang, J.; Zhao, Y.; Shen, Y.; Zhang, Y.; Qian, X. Facile Synthesis of Magnetic Covalent Organic Frameworks for the Hydrophilic Enrichment of *N*-Glycopeptides. *J. Mater. Chem. B* **2017**, *5*, 4052−4059.
(391) Royuela, S.; García-Garrido, E.; Martín Arroyo, M.; Mancheño, M. J.; Ramos, M. M.; González-Rodríguez, D.; Somoza, Á.; Zamora, F.; Segura, J. L. Uracil Grafted Imine-Based Covalent Organic Framework for Nucleobase Recognition. *Chem. Commun.* **2018**, *54*, 8729−8732.
(392) Alahakoon, S. B.; Thompson, C. M.; Occhialini, G.; Smaldone, R. A. Design Principles for Covalent Organic Frameworks in Energy Storage Applications. *ChemSusChem* **2017**, *10*, 2116−2129.
(393) Zhang, Y.; Riduan, S. N.; Wang, J. Redox Active Metal− and Covalent Organic Frameworks for Energy Storage: Balancing Porosity and Electrical Conductivity. *Chem. - Eur. J.* **2017**, *23*, 16419−16431.

https://dx.doi.org/10.1021/acs.chemrev.9b00550
Chem. Rev. 2020, 120, 8814−8933

(394) Lin, C.-Y.; Zhang, D.; Zhao, Z.; Xia, Z. Covalent Organic Framework Electrocatalysts for Clean Energy Conversion. *Adv. Mater.* **2018**, *30*, 1703646.
(395) DeBlase, C. R.; Silberstein, K. E.; Truong, T.-T.; Abruña, H. D.; Dichtel, W. R. B-Ketoenamine-Linked Covalent Organic Frameworks Capable of Pseudocapacitive Energy Storage. *J. Am. Chem. Soc.* **2013**, *135*, 16821−16824.
(396) Feng, S.; Xu, H.; Zhang, C.; Chen, Y.; Zeng, J.; Jiang, D.; Jiang, J.-X. Bicarbazole-Based Redox-Active Covalent Organic Frameworks for Ultrahigh-Performance Energy Storage. *Chem. Commun.* **2017**, *53*, 11334−11337.
(397) Khattak, A. M.; Ghazi, Z. A.; Liang, B.; Khan, N. A.; Iqbal, A.; Li, L.; Tang, Z. A Redox-Active 2D Covalent Organic Framework with Pyridine Moieties Capable of Faradaic Energy Storage. *J. Mater. Chem. A* **2016**, *4*, 16312−16317.
(398) Sevilla, M.; Mokaya, R. Energy Storage Applications of Activated Carbons: Supercapacitors and Hydrogen Storage. *Energy Environ. Sci.* **2014**, *7*, 1250−1280.
(399) Gamby, J.; Taberna, P. L.; Simon, P.; Fauvarque, J. F.; Chesneau, M. Studies and Characterisations of Various Activated Carbons Used for Carbon/Carbon Supercapacitors. *J. Power Sources* **2001**, *101*, 109−116.
(400) Mulzer, C. R.; Shen, L.; Bisbey, R. P.; McKone, J. R.; Zhang, N.; Abruña, H. D.; Dichtel, W. R. Superior Charge Storage and Power Density of a Conducting Polymer-Modified Covalent Organic Framework. *ACS Cent. Sci.* **2016**, *2*, 667−673.
(401) Xu, Q.; Dalapati, S.; Jiang, D. Charge up in Wired Covalent Organic Frameworks. *ACS Cent. Sci.* **2016**, *2*, 586−587.
(402) Wu, Y.; Yan, D.; Zhang, Z.; Matsushita, M. M.; Awaga, K. Electron Highways into Nanochannels of Covalent Organic Frameworks for High Electrical Conductivity and Energy Storage. *ACS Appl. Mater. Interfaces* **2019**, *11*, 7661−7665.
(403) Liu, S.; Yao, L.; Lu, Y.; Hua, X.; Liu, J.; Yang, Z.; Wei, H.; Mai, Y. All-Organic Covalent Organic Framework/Polyaniline Composites as Stable Electrode for High-Performance Supercapacitors. *Mater. Lett.* **2019**, *236*, 354−357.
(404) Chandra, S.; Roy Chowdhury, D.; Addicoat, M.; Heine, T.; Paul, A.; Banerjee, R. Molecular Level Control of the Capacitance of Two-Dimensional Covalent Organic Frameworks: Role of Hydrogen Bonding in Energy Storage Materials. *Chem. Mater.* **2017**, *29* (5), 2074−2080.
(405) Halder, A.; Ghosh, M.; Khayum M, A.; Bera, S.; Addicoat, M.; Sasmal, H. S.; Karak, S.; Kurungot, S.; Banerjee, R. Interlayer Hydrogen-Bonded Covalent Organic Frameworks as High-Performance Supercapacitors. *J. Am. Chem. Soc.* **2018**, *140*, 10941−10945.
(406) Khayum M, A.; Vijayakumar, V.; Karak, S.; Kandambeth, S.; Bhadra, M.; Suresh, K.; Acharambath, N.; Kurungot, S.; Banerjee, R. Convergent Covalent Organic Framework Thin Sheets as Flexible Supercapacitor Electrodes. *ACS Appl. Mater. Interfaces* **2018**, *10*, 28139−28146.
(407) Luo, Z.; Liu, L.; Ning, J.; Lei, K.; Lu, Y.; Li, F.; Chen, J. A Microporous Covalent−Organic Framework with Abundant Accessible Carbonyl Groups for Lithium-Ion Batteries. *Angew. Chem., Int. Ed.* **2018**, *57*, 9443−9446.
(408) Díaz, R.; Orcajo, M. G.; Botas, J. A.; Calleja, G.; Palma, J. Co_8-MOF-5 as Electrode for Supercapacitors. *Mater. Lett.* **2012**, *68*, 126−128.
(409) Lee, D. Y.; Yoon, S. J.; Shrestha, N. K.; Lee, S.-H.; Ahn, H.; Han, S.-H. Unusual Energy Storage and Charge Retention in Co-Based Metal−Organic-Frameworks. *Microporous Mesoporous Mater.* **2012**, *153*, 163−165.
(410) Li, S.-L.; Xu, Q. Metal-Organic Frameworks as Platforms for Clean Energy. *Energy Environ. Sci.* **2013**, *6*, 1656−1683.
(411) Gao, Y.; Wu, J.; Zhang, W.; Tan, Y.; Gao, J.; Zhao, J.; Tang, B. Synthesis of Nickel Oxalate/Zeolitic Imidazolate Framework-67 (NiC_2O_4/ZIF-67) as a Supercapacitor Electrode. *New J. Chem.* **2015**, *39*, 94−97.
(412) Hao, L.; Ning, J.; Luo, B.; Wang, B.; Zhang, Y.; Tang, Z.; Yang, J.; Thomas, A.; Zhi, L. Structural Evolution of 2D Microporous Covalent Triazine-Based Framework toward the Study of High-Performance Supercapacitors. *J. Am. Chem. Soc.* **2015**, *137*, 219−225.
(413) Huang, Y.-B.; Pachfule, P.; Sun, J.-K.; Xu, Q. From Covalent-Organic Frameworks to Hierarchically Porous B-Doped Carbons: A Molten-Salt Approach. *J. Mater. Chem. A* **2016**, *4*, 4273−4279.
(414) Han, Y.; Hu, N.; Liu, S.; Hou, Z.; Liu, J.; Hua, X.; Yang, Z.; Wei, L.; Wang, L.; Wei, H. Nanocoating Covalent Organic Frameworks on Nickel Nanowires for Greatly Enhanced-Performance Supercapacitors. *Nanotechnology* **2017**, *28*, 33LT01.
(415) Chen, H.; Armand, M.; Demailly, G.; Dolhem, F.; Poizot, P.; Tarascon, J.-M. From Biomass to a Renewable $Li_xC_6O_6$ Organic Electrode for Sustainable Li-Ion Batteries. *ChemSusChem* **2008**, *1*, 348−355.
(416) Xu, F.; Jin, S.; Zhong, H.; Wu, D.; Yang, X.; Chen, X.; Wei, H.; Fu, R.; Jiang, D. Electrochemically Active, Crystalline, Mesoporous Covalent Organic Frameworks on Carbon Nanotubes for Synergistic Lithium-Ion Battery Energy Storage. *Sci. Rep.* **2015**, *5*, 8225.
(417) Lei, Z.; Yang, Q.; Xu, Y.; Guo, S.; Sun, W.; Liu, H.; Lv, L.-P.; Zhang, Y.; Wang, Y. Boosting Lithium Storage in Covalent Organic Framework Via Activation of 14-Electron Redox Chemistry. *Nat. Commun.* **2018**, *9*, 576.
(418) Yang, D.-H.; Yao, Z.-Q.; Wu, D.; Zhang, Y.-H.; Zhou, Z.; Bu, X.-H. Structure-Modulated Crystalline Covalent Organic Frameworks as High-Rate Cathodes for Li-Ion Batteries. *J. Mater. Chem. A* **2016**, *4*, 18621−18627.
(419) Xu, F.; Chen, X.; Tang, Z.; Wu, D.; Fu, R.; Jiang, D. Redox-Active Conjugated Microporous Polymers: A New Organic Platform for Highly Efficient Energy Storage. *Chem. Commun.* **2014**, *50*, 4788−4790.
(420) Bai, L.; Gao, Q.; Zhao, Y. Two Fully Conjugated Covalent Organic Frameworks as Anode Materials for Lithium Ion Batteries. *J. Mater. Chem. A* **2016**, *4*, 14106−14110.
(421) Haldar, S.; Roy, K.; Nandi, S.; Chakraborty, D.; Puthusseri, D.; Gawli, Y.; Ogale, S.; Vaidhyanathan, R. High and Reversible Lithium Ion Storage in Self-Exfoliated Triazole-Triformyl Phloroglucinol-Based Covalent Organic Nanosheets. *Adv. Energy Mater.* **2018**, *8*, 1702170.
(422) Zhang, Z.; Lai, Y.; Zhang, Z.; Zhang, K.; Li, J. Al_2O_3-Coated Porous Separator for Enhanced Electrochemical Performance of Lithium Sulfur Batteries. *Electrochim. Acta* **2014**, *129*, 55−61.
(423) Li, J.; Huang, Y.; Zhang, S.; Jia, W.; Wang, X.; Guo, Y.; Jia, D.; Wang, L. Decoration of Silica Nanoparticles on Polypropylene Separator for Lithium−Sulfur Batteries. *ACS Appl. Mater. Interfaces* **2017**, *9*, 7499−7504.
(424) Liao, H.; Ding, H.; Li, B.; Ai, X.; Wang, C. Covalent-Organic Frameworks: Potential Host Materials for Sulfur Impregnation in Lithium-Sulfur Batteries. *J. Mater. Chem. A* **2014**, *2*, 8854−8858.
(425) Talapaneni, S. N.; Hwang, T. H.; Je, S. H.; Buyukcakir, O.; Choi, J. W.; Coskun, A. Elemental-Sulfur-Mediated Facile Synthesis of a Covalent Triazine Framework for High-Performance Lithium−Sulfur Batteries. *Angew. Chem., Int. Ed.* **2016**, *55*, 3106−3111.
(426) Zu, C.; Manthiram, A. Hydroxylated Graphene−Sulfur Nanocomposites for High-Rate Lithium−Sulfur Batteries. *Adv. Energy Mater.* **2013**, *3*, 1008−1012.
(427) Yang, X.; Dong, B.; Zhang, H.; Ge, R.; Gao, Y.; Zhang, H. Sulfur Impregnated in a Mesoporous Covalent Organic Framework for High Performance Lithium-Sulfur Batteries. *RSC Adv.* **2015**, *5*, 86137−86143.
(428) Jiang, Q.; Li, Y.; Zhao, X.; Xiong, P.; Yu, X.; Xu, Y.; Chen, L. Inverse-Vulcanization of Vinyl Functionalized Covalent Organic Frameworks as Efficient Cathode Materials for Li−S Batteries. *J. Mater. Chem. A* **2018**, *6*, 17977−17981.
(429) Meng, Y.; Lin, G.; Ding, H.; Liao, H.; Wang, C. Impregnation of Sulfur into a 2d Pyrene-Based Covalent Organic Framework for High-Rate Lithium−Sulfur Batteries. *J. Mater. Chem. A* **2018**, *6*, 17186−17191.
(430) Wang, J.; Si, L.; Wei, Q.; Hong, X.; Lin, L.; Li, X.; Chen, J.; Wen, P.; Cai, Y. An Imine-Linked Covalent Organic Framework as the Host Material for Sulfur Loading in Lithium−Sulfur Batteries. *J. Energy Chem.* **2019**, *28*, 54−60.

https://dx.doi.org/10.1021/acs.chemrev.9b00550
Chem. Rev. 2020, 120, 8814−8933

(431) Ghazi, Z. A.; Zhu, L.; Wang, H.; Naeem, A.; Khattak, A. M.; Liang, B.; Khan, N. A.; Wei, Z.; Li, L.; Tang, Z. Efficient Polysulfide Chemisorption in Covalent Organic Frameworks for High-Performance Lithium-Sulfur Batteries. *Adv. Energy Mater.* **2016**, *6*, 1601250.
(432) Xu, F.; Yang, S.; Jiang, G.; Ye, Q.; Wei, B.; Wang, H. Fluorinated, Sulfur-Rich, Covalent Triazine Frameworks for Enhanced Confinement of Polysulfides in Lithium−Sulfur Batteries. *ACS Appl. Mater. Interfaces* **2017**, *9*, 37731−37738.
(433) Wang, D.-G.; Li, N.; Hu, Y.; Wan, S.; Song, M.; Yu, G.; Jin, Y.; Wei, W.; Han, K.; Kuang, G.-C.; Zhang, W. Highly Fluoro-Substituted Covalent Organic Framework and Its Application in Lithium−Sulfur Batteries. *ACS Appl. Mater. Interfaces* **2018**, *10*, 42233−42240.
(434) Tan, L.; Li, X.; Wang, Z.; Guo, H.; Wang, J. Lightweight Reduced Graphene Oxide@MoS_2 Interlayer as Polysulfide Barrier for High-Performance Lithium−Sulfur Batteries. *ACS Appl. Mater. Interfaces* **2018**, *10*, 3707−3713.
(435) Yoo, J.; Cho, S. J.; Jung, G. Y.; Kim, S. H.; Choi, K. H.; Kim, J. H.; Lee, C. K.; Kwak, S. K.; Lee, S. Y. Cof-Net on Cnt-Net as a Molecularly Designed, Hierarchical Porous Chemical Trap for Polysulfides in Lithium-Sulfur Batteries. *Nano Lett.* **2016**, *16*, 3292−300.
(436) Chen, X.; Zhang, H.; Ci, C.; Sun, W.; Wang, Y. Few-Layered Boronic Ester Based Covalent Organic Frameworks/Carbon Nanotube Composites for High-Performance K-Organic Batteries. *ACS Nano* **2019**, *13*, 3600−3607.
(437) Chen, L.; Furukawa, K.; Gao, J.; Nagai, A.; Nakamura, T.; Dong, Y. P.; Jiang, D. Photoelectric Covalent Organic Frameworks: Converting Open Lattices into Ordered Donor-Acceptor Heterojunctions. *J. Am. Chem. Soc.* **2014**, *136*, 9806−9809.
(438) Vazquez-Molina, D. A.; Mohammad-Pour, G. S.; Lee, C.; Logan, M. W.; Duan, X.; Harper, J. K.; Uribe-Romo, F. J. Mechanically Shaped Two-Dimensional Covalent Organic Frameworks Reveal Crystallographic Alignment and Fast Li-Ion Conductivity. *J. Am. Chem. Soc.* **2016**, *138*, 9767−9770.
(439) Xu, H.; Jiang, D. Covalent Organic Frameworks Crossing the Channel. *Nat. Chem.* **2014**, *6*, 564−566.
(440) Ye, Y. X.; Zhang, L. Q.; Peng, Q. F.; Wang, G. E.; Shen, Y. C.; Li, Z. Y.; Wang, L. H.; Ma, X. L.; Chen, Q. H.; Zhang, Z. J.; Xiang, S. C. High Anhydrous Proton Conductivity of Lmidazole-Loaded Mesoporous Polyimides over a Wide Range from Subzero to Moderate Temperature. *J. Am. Chem. Soc.* **2015**, *137*, 913−918.
(441) Meng, X.; Wang, H.-N.; Song, S.-Y.; Zhang, H.-J. Proton-Conducting Crystalline Porous Materials. *Chem. Soc. Rev.* **2017**, *46*, 464−480.
(442) Chandra, S.; Kundu, T.; Dey, K.; Addicoat, M.; Heine, T.; Banerjee, R. Interplaying Intrinsic and Extrinsic Proton Conductivities in Covalent Organic Frameworks. *Chem. Mater.* **2016**, *28*, 1489−1494.
(443) Schmidt-Rohr, K.; Chen, Q. Parallel Cylindrical Water Nanochannels in Nafion Fuel-Cell Membranes. *Nat. Mater.* **2008**, *7*, 75−83.
(444) Wu, X.; Wang, X.; He, G.; Benziger, J. Differences in Water Sorption and Proton Conductivity between Nafion and Speek. *J. Polym. Sci., Part B: Polym. Phys.* **2011**, *49*, 1437−1445.
(445) Phang, W. J.; Jo, H.; Lee, W. R.; Song, J. H.; Yoo, K.; Kim, B.; Hong, C. S. Superprotonic Conductivity of a UiO-66 Framework Functionalized with Sulfonic Acid Groups by Facile Postsynthetic Oxidation. *Angew. Chem., Int. Ed.* **2015**, *54*, 5142−5146.
(446) Chandra, S.; Kundu, T.; Dey, K.; Addicoat, M.; Heine, T.; Banerjee, R. Interplaying Intrinsic and Extrinsic Proton Conductivities in Covalent Organic Frameworks. *Chem. Mater.* **2016**, *28*, 1489−1494.
(447) Yamada, T.; Sadakiyo, M.; Kitagawa, H. High Proton Conductivity of One-Dimensional Ferrous Oxalate Dihydrate. *J. Am. Chem. Soc.* **2009**, *131*, 3144−3145.
(448) Hurd, J. A.; Vaidhyanathan, R.; Thangadurai, V.; Ratcliffe, C. I.; Moudrakovski, I. L.; Shimizu, G. K. Anhydrous Proton Conduction at 150 C in a Crystalline Metal−Organic Framework. *Nat. Chem.* **2009**, *1*, 705.
(449) Nguyen, N. T.; Furukawa, H.; Gándara, F.; Trickett, C. A.; Jeong, H. M.; Cordova, K. E.; Yaghi, O. M. Three-Dimensional Metal-Catecholate Frameworks and Their Ultrahigh Proton Conductivity. *J. Am. Chem. Soc.* **2015**, *137*, 15394−15397.
(450) Meng, Z.; Aykanat, A.; Mirica, K. A. Proton Conduction in 2D Aza-Fused Covalent Organic Frameworks. *Chem. Mater.* **2019**, *31*, 819−825.
(451) Sasmal, H. S.; Aiyappa, H. B.; Bhange, S. N.; Karak, S.; Halder, A.; Kurungot, S.; Banerjee, R. Superprotonic Conductivity in Flexible Porous Covalent Organic Framework Membranes. *Angew. Chem.* **2018**, *130*, 11060−11064.
(452) Quartarone, E.; Mustarelli, P. Electrolytes for Solid-State Lithium Rechargeable Batteries: Recent Advances and Perspectives. *Chem. Soc. Rev.* **2011**, *40*, 2525−2540.
(453) Montoro, C.; Rodríguez-San-Miguel, D.; Polo, E.; Escudero-Cid, R.; Ruiz-González, M. L.; Navarro, J. A. R.; Ocón, P.; Zamora, F. Ionic Conductivity and Potential Application for Fuel Cell of a Modified Imine-Based Covalent Organic Framework. *J. Am. Chem. Soc.* **2017**, *139*, 10079−10086.
(454) Pili, S.; Argent, S. P.; Morris, C. G.; Rought, P.; García-Sakai, V.; Silverwood, I. P.; Easun, T. L.; Li, M.; Warren, M. R.; Murray, C. A.; et al. Proton Conduction in a Phosphonate-Based Metal−Organic Framework Mediated by Intrinsic "Free Diffusion inside a Sphere. *J. Am. Chem. Soc.* **2016**, *138*, 6352−6355.
(455) Xu, G.; Otsubo, K.; Yamada, T.; Sakaida, S.; Kitagawa, H. Superprotonic Conductivity in a Highly Oriented Crystalline Metal−Organic Framework Nanofilm. *J. Am. Chem. Soc.* **2013**, *135*, 7438−7441.
(456) Panda, T.; Kundu, T.; Banerjee, R. Structural Isomerism Leading to Variable Proton Conductivity in Indium(III) Isophthalic Acid Based Frameworks. *Chem. Commun.* **2013**, *49*, 6197−6199.
(457) Van Humbeck, J. F.; Aubrey, M. L.; Alsbaiee, A.; Ameloot, R.; Coates, G. W.; Dichtel, W. R.; Long, J. R. Tetraarylborate Polymer Networks as Single-Ion Conducting Solid Electrolytes. *Chem. Sci.* **2015**, *6*, 5499−5505.
(458) Kamaya, N.; Homma, K.; Yamakawa, Y.; Hirayama, M.; Kanno, R.; Yonemura, M.; Kamiyama, T.; Kato, Y.; Hama, S.; Kawamoto, K.; et al. A Lithium Superionic Conductor. *Nat. Mater.* **2011**, *10*, 682.
(459) Xu, Q.; Tao, S.; Jiang, Q.; Jiang, D. Ion Conduction in Polyelectrolyte Covalent Organic Frameworks. *J. Am. Chem. Soc.* **2018**, *140*, 7429−7432.
(460) Zhang, G.; Hong, Y.-l.; Nishiyama, Y.; Bai, S.; Kitagawa, S.; Horike, S. Accumulation of Glassy Poly (Ethylene Oxide) Anchored in a Covalent Organic Framework as a Solid-State Li^+ Electrolyte. *J. Am. Chem. Soc.* **2019**, *141*, 1227−1234.
(461) Guo, Z.; Zhang, Y.; Dong, Y.; Li, J.; Li, S.; Shao, P.; Feng, X.; Wang, B. Fast Ion Transport Pathway Provided by Polyethylene Glycol Confined in Covalent Organic Frameworks. *J. Am. Chem. Soc.* **2019**, *141*, 1923−1927.
(462) Jeong, K.; Park, S.; Jung, G. Y.; Kim, S. H.; Lee, Y.-H.; Kwak, S. K.; Lee, S.-Y. Solvent-Free, Single Lithium-Ion Conducting Covalent Organic Frameworks. *J. Am. Chem. Soc.* **2019**, *141*, 5880−5885.
(463) Fischer, S.; Roeser, J.; Lin, T. C.; DeBlock, R. H.; Lau, J.; Dunn, B. S.; Hoffmann, F.; Fröba, M.; Thomas, A.; Tolbert, S. H. Metal-Organic Framework with Tetrahedral Aluminate Sites as a Single-Ion Li^+ Solid Electrolyte. *Angew. Chem.* **2018**, *130*, 16925−16929.
(464) Guo, H.; Wang, J.; Fang, Q.; Zhao, Y.; Gu, S.; Zheng, J.; Yan, Y. A Quaternary-Ammonium-Functionalized Covalent Organic Framework for Anion Conduction. *CrystEngComm* **2017**, *19*, 4905−4910.
(465) Pramudya, Y.; Mendoza-Cortes, J. L. Design Principles for High H_2 Storage Using Chelation of Abundant Transition Metals in Covalent Organic Frameworks for 0−700 bar at 298 K. *J. Am. Chem. Soc.* **2016**, *138*, 15204−15213.
(466) Slater, A. G.; Cooper, A. I. Function-Led Design of New Porous Materials. *Science* **2015**, *348*, aaa8075.
(467) Biswal, B. P.; Chaudhari, H. D.; Banerjee, R.; Kharul, U. K. Chemically Stable Covalent Organic Framework (COF)-Polybenzimidazole Hybrid Membranes: Enhanced Gas Separation through Pore Modulation. *Chem. - Eur. J.* **2016**, *22*, 4695−9.
(468) Thompson, C. M.; Occhialini, G.; McCandless, G. T.; Alahakoon, S. B.; Cameron, V.; Nielsen, S. O.; Smaldone, R. A.

https://dx.doi.org/10.1021/acs.chemrev.9b00550
Chem. Rev. 2020, 120, 8814−8933

Computational and Experimental Studies on the Effects of Monomer Planarity on Covalent Organic Framework Formation. *J. Am. Chem. Soc.* **2017**, *139*, 10506−10513.
(469) Karak, S.; Kandambeth, S.; Biswal, B. P.; Sasmal, H. S.; Kumar, S.; Pachfule, P.; Banerjee, R. Constructing Ultraporous Covalent Organic Frameworks in Seconds Via an Organic Terracotta Process. *J. Am. Chem. Soc.* **2017**, *139*, 1856−1862.
(470) Aiyappa, H. B.; Thote, J.; Shinde, D. B.; Banerjee, R.; Kurungot, S. Cobalt-Modified Covalent Organic Framework as a Robust Water Oxidation Electrocatalyst. *Chem. Mater.* **2016**, *28*, 4375−4379.
(471) Brédas, J.-L.; Norton, J. E.; Cornil, J.; Coropceanu, V. Molecular Understanding of Organic Solar Cells: The Challenges. *Acc. Chem. Res.* **2009**, *42*, 1691−1699.
(472) Gomes, R.; Bhanja, P.; Bhaumik, A. A Triazine-Based Covalent Organic Polymer for Efficient CO_2 Adsorption. *Chem. Commun.* **2015**, *51*, 10050−10053.
(473) Zhao, S.; Dong, B.; Ge, R.; Wang, C.; Song, X.; Ma, W.; Wang, Y.; Hao, C.; Guo, X.; Gao, Y. Channel-Wall Functionalization in Covalent Organic Frameworks for the Enhancement of CO_2 Uptake and CO_2/N_2 Selectivity. *RSC Adv.* **2016**, *6*, 38774−38781.
(474) Xu, Q.; Tang, Y.; Zhang, X.; Oshima, Y.; Chen, Q.; Jiang, D. Template Conversion of Covalent Organic Frameworks into 2D Conducting Nanocarbons for Catalyzing Oxygen Reduction Reaction. *Adv. Mater.* **2018**, *30*, 1706330.
(475) Keller, N.; Bessinger, D.; Reuter, S.; Calik, M.; Ascherl, L.; Hanusch, F. C.; Auras, F.; Bein, T. Oligothiophene-Bridged Conjugated Covalent Organic Frameworks. *J. Am. Chem. Soc.* **2017**, *139*, 8194−8199.
(476) Kang, Z.; Peng, Y.; Qian, Y.; Yuan, D.; Addicoat, M. A.; Heine, T.; Hu, Z.; Tee, L.; Guo, Z.; Zhao, D. Mixed Matrix Membranes (MMMs) Comprising Exfoliated 2D Covalent Organic Frameworks (COFs) for Efficient CO_2 Separation. *Chem. Mater.* **2016**, *28*, 1277−1285.
(477) Rosi, N. L.; Eckert, J.; Eddaoudi, M.; Vodak, D. T.; Kim, J.; Keeffe, M.; Yaghi, O. M. Hydrogen Storage in Microporous Metal-Organic Frameworks. *Science* **2003**, *300*, 1127.
(478) Yuan, D.; Lu, W.; Zhao, D.; Zhou, H. C. Highly Stable Porous Polymer Networks with Exceptionally High Gas-Uptake Capacities. *Adv. Mater.* **2011**, *23*, 3723−3725.
(479) Rose, M.; Böhlmann, W.; Sabo, M.; Kaskel, S. Element−Organic Frameworks with High Permanent Porosity. *Chem. Commun.* **2008**, 2462−2464.
(480) Lee, J.-Y.; Wood, C. D.; Bradshaw, D.; Rosseinsky, M. J.; Cooper, A. I. Hydrogen Adsorption in Microporous Hypercrosslinked Polymers. *Chem. Commun.* **2006**, 2670−2672.
(481) Furukawa, H.; Yaghi, O. M. Storage of Hydrogen, Methane, and Carbon Dioxide in Highly Porous Covalent Organic Frameworks for Clean Energy Applications. *J. Am. Chem. Soc.* **2009**, *131*, 8875−8883.
(482) Ghosh, S.; Singh, J. K. Hydrogen Adsorption in Pyridine Bridged Porphyrin-Covalent Organic Framework. *Int. J. Hydrogen Energy* **2019**, *44*, 1782−1796.
(483) Kahveci, Z.; Islamoglu, T.; Shar, G. A.; Ding, R.; El-Kaderi, H. M. Targeted Synthesis of a Mesoporous Triptycene−Derived Covalent Organic Framework. *CrystEngComm* **2013**, *15*, 1524−1527.
(484) Yuan, D.; Zhao, D.; Sun, D.; Zhou, H.-C. An Isoreticular Series of Metal−Organic Frameworks with Dendritic Hexacarboxylate Ligands and Exceptionally High Gas−Uptake Capacity. *Angew. Chem., Int. Ed.* **2010**, *49*, 5357−5361.
(485) Furukawa, H.; Ko, N.; Go, Y. B.; Aratani, N.; Choi, S. B.; Choi, E.; Yazaydin, A. Ö.; Snurr, R. Q.; O'Keeffe, M.; Kim, J.; Yaghi, O. M. Ultrahigh Porosity in Metal−Organic Frameworks. *Science* **2010**, *329*, 424−428.
(486) Mercado, R.; Fu, R.-S.; Yakutovich, A. V.; Talirz, L.; Haranczyk, M.; Smit, B. In Silico Design of 2D and 3D Covalent Organic Frameworks for Methane Storage Applications. *Chem. Mater.* **2018**, *30*, 5069−5086.
(487) Stephens, F. H.; Pons, V.; Tom Baker, R. Ammonia−Borane: The Hydrogen Source Par Excellence? *Dalton Transactions* **2007**, 2613−2626.
(488) Yang, Y.; Faheem, M.; Wang, L.; Meng, Q.; Sha, H.; Yang, N.; Yuan, Y.; Zhu, G. Surface Pore Engineering of Covalent Organic Frameworks for Ammonia Capture through Synergistic Multivariate and Open Metal Site Approaches. *ACS Cent. Sci.* **2018**, *4*, 748−754.
(489) Cavenati, S.; Grande, C. A.; Rodrigues, A. E. Adsorption Equilibrium of Methane, Carbon Dioxide, and Nitrogen on Zeolite 13X at High Pressures. *J. Chem. Eng. Data* **2004**, *49*, 1095−1101.
(490) Rieth, A. J.; Dincă, M. Controlled Gas Uptake in Metal−Organic Frameworks with Record Ammonia Sorption. *J. Am. Chem. Soc.* **2018**, *140*, 3461−3466.
(491) Rochelle, G. T. Amine Scrubbing for CO_2 Capture. *Science* **2009**, *325* (5948), 1652.
(492) Olah, G. A.; Prakash, G. K.; Goeppert, A. Anthropogenic Chemical Carbon Cycle for a Sustainable Future. *J. Am. Chem. Soc.* **2011**, *133*, 12881−98.
(493) Sumida, K.; Rogow, D. L.; Mason, J. A.; McDonald, T. M.; Bloch, E. D.; Herm, Z. R.; Bae, T. H.; Long, J. R. Carbon Dioxide Capture in Metal-Organic Frameworks. *Chem. Rev.* **2012**, *112*, 724−81.
(494) Aresta, M.; Dibenedetto, A.; Angelini, A. Catalysis for the Valorization of Exhaust Carbon: From CO_2 to Chemicals, Materials, and Fuels. Technological Use of CO_2. *Chem. Rev.* **2014**, *114*, 1709−42.
(495) Zhao, Y.; Yao, K. X.; Teng, B.; Zhang, T.; Han, Y. A Perfluorinated Covalent Triazine-Based Framework for Highly Selective and Water−Tolerant CO_2 Capture. *Energy Environ. Sci.* **2013**, *6*, 3684.
(496) Zeng, Y.; Zou, R.; Zhao, Y. Covalent Organic Frameworks for CO_2 Capture. *Adv. Mater.* **2016**, *28*, 2855−73.
(497) Dawson, R.; Cooper, A. I.; Adams, D. J. Nanoporous Organic Polymer Networks. *Prog. Polym. Sci.* **2012**, *37*, 530−563.
(498) Herm, Z. R.; Swisher, J. A.; Smit, B.; Krishna, R.; Long, J. R. Metal−Organic Frameworks as Adsorbents for Hydrogen Purification and Precombustion Carbon Dioxide Capture. *J. Am. Chem. Soc.* **2011**, *133*, 5664−5667.
(499) Jena, H. S.; Krishnaraj, C.; Wang, G.; Leus, K.; Schmidt, J.; Chaoui, N.; Van Der Voort, P. Acetylacetone Covalent Triazine Framework: An Efficient Carbon Capture and Storage Material and a Highly Stable Heterogeneous Catalyst. *Chem. Mater.* **2018**, *30*, 4102−4111.
(500) Yan, T.; Lan, Y.; Tong, M.; Zhong, C. Screening and Design of Covalent Organic Framework Membranes for CO_2/CH_4 Separation. *ACS Sustainable Chem. Eng.* **2019**, *7*, 1220−1227.
(501) Lan, Y.; Tong, M.; Yang, Q.; Zhong, C. Computational Screening of Covalent Organic Frameworks for the Capture of Radioactive Iodine and Methyl Iodide. *CrystEngComm* **2017**, *19*, 4920−4926.
(502) Yin, Z.-J.; Xu, S.-Q.; Zhan, T.-G.; Qi, Q.-Y.; Wu, Z.-Q.; Zhao, X. Ultrahigh Volatile Iodine Uptake by Hollow Microspheres Formed from a Heteropore Covalent Organic Framework. *Chem. Commun.* **2017**, *53*, 7266−7269.
(503) Wang, C.; Wang, Y.; Ge, R.; Song, X.; Xing, X.; Jiang, Q.; Lu, H.; Hao, C.; Guo, X.; Gao, Y.; Jiang, D. A 3D Covalent Organic Framework with Exceptionally High Iodine Capture Capability. *Chem. - Eur. J.* **2018**, *24*, 585−589.
(504) Yan, Z.; Yuan, Y.; Tian, Y.; Zhang, D.; Zhu, G. Highly Efficient Enrichment of Volatile Iodine by Charged Porous Aromatic Frameworks with Three Sorption Sites. *Angew. Chem., Int. Ed.* **2015**, *54*, 12733−12737.
(505) Hughes, J. T.; Sava, D. F.; Nenoff, T. M.; Navrotsky, A. Thermochemical Evidence for Strong Iodine Chemisorption by ZIF-8. *J. Am. Chem. Soc.* **2013**, *135*, 16256−16259.
(506) Zhu, X.; An, S.; Liu, Y.; Hu, J.; Liu, H.; Tian, C.; Dai, S.; Yang, X.; Wang, H.; Abney, C. W.; Dai, S. Efficient Removal of Organic Dye Pollutants Using Covalent Organic Frameworks. *AIChE J.* **2017**, *63*, 3470−3478.
(507) Xu, L.; Xu, J.; Shan, B.; Wang, X.; Gao, C. Tppa-2-Incorporated Mixed Matrix Membranes for Efficient Water Purification. *J. Membr. Sci.* **2017**, *526*, 355−366.
(508) Kandambeth, S.; Biswal, B. P.; Chaudhari, H. D.; Rout, K. C.; Kunjattu H., S.; Mitra, S.; Karak, S.; Das, A.; Mukherjee, R.; Kharul, U.

https://dx.doi.org/10.1021/acs.chemrev.9b00550
Chem. Rev. 2020, 120, 8814−8933

K.; Banerjee, R. Selective Molecular Sieving in Self-Standing Porous Covalent−Organic−Framework Membranes. *Adv. Mater.* **2017**, *29*, 1603945.
(509) Haque, E.; Jun, J. W.; Jhung, S. H. Adsorptive Removal of Methyl Orange and Methylene Blue from Aqueous Solution with a Metal-Organic Framework Material, Iron Terephthalate (MOF−235). *J. Hazard. Mater.* **2011**, *185*, 507−511.
(510) Zhang, W.; Zhang, L.; Zhao, H.; Li, B.; Ma, H. A Two−Dimensional Cationic Covalent Organic Framework Membrane for Selective Molecular Sieving. *J. Mater. Chem. A* **2018**, *6*, 13331−13339.
(511) Li, Y.; Wee, L. H.; Volodin, A.; Martens, J. A.; Vankelecom, I. F. J. Polymer Supported ZIF-8 Membranes Prepared Via an Interfacial Synthesis Method. *Chem. Commun.* **2015**, *51*, 918−920.
(512) Wang, L.; Fang, M.; Liu, J.; He, J.; Deng, L.; Li, J.; Lei, J. The Influence of Dispersed Phases on Polyamide/ZIF−8 Nanofiltration Membranes for Dye Removal from Water. *RSC Adv.* **2015**, *5*, 50942−50954.
(513) Yang, C.-X.; Zheng, Y.-Z.; Yan, X.-P. γ−Cyclodextrin Metal−Organic Framework for Efficient Separation of Chiral Aromatic Alcohols. *RSC Adv.* **2017**, *7*, 36297−36301.
(514) Zhang, S.; Zheng, Y.; An, H.; Aguila, B.; Yang, C.-X.; Dong, Y.; Xie, W.; Cheng, P.; Zhang, Z.; Chen, Y.; Ma, S. Covalent Organic Frameworks with Chirality Enriched by Biomolecules for Efficient Chiral Separation. *Angew. Chem., Int. Ed.* **2018**, *57*, 16754−16759.
(515) Merí-Bofí, L.; Royuela, S.; Zamora, F.; Ruiz-González, M. L.; Segura, J. L.; Muñoz-Olivas, R.; Mancheño, M. J. Thiol Grafted Imine−Based Covalent Organic Frameworks for Water Remediation through Selective Removal of Hg(II). *J. Mater. Chem. A* **2017**, *5*, 17973−17981.
(516) Li, B.; Zhang, Y.; Ma, D.; Shi, Z.; Ma, S. Mercury Nano-Trap for Effective and Efficient Removal of Mercury(II) from Aqueous Solution. *Nat. Commun.* **2014**, *5*, 5537.
(517) Ai, K.; Ruan, C.; Shen, M.; Lu, L. MoS_2 Nanosheets with Widened Interlayer Spacing for High-Efficiency Removal of Mercury in Aquatic Systems. *Adv. Funct. Mater.* **2016**, *26*, 5542−5549.
(518) Dinari, M.; Hatami, M. Novel *N*-Riched Crystalline Covalent Organic Framework as a Highly Porous Adsorbent for Effective Cadmium Removal. *J. Environ. Chem. Eng.* **2019**, *7*, 102907.
(519) Li, X.; Qi, Y.; Yue, G.; Wu, Q.; Li, Y.; Zhang, M.; Guo, X.; Li, X.; Ma, L.; Li, S. Solvent-and Catalyst-Free Synthesis of an Azine-Linked Covalent Organic Framework and the Induced Tautomerization in the Adsorption of U (VI) and Hg (II). *Green Chem.* **2019**, *21*, 649−657.
(520) Lu, Q.; Ma, Y.; Li, H.; Guan, X.; Yusran, Y.; Xue, M.; Fang, Q.; Yan, Y.; Qiu, S.; Valtchev, V. Postsynthetic Functionalization of Three−Dimensional Covalent Organic Frameworks for Selective Extraction of Lanthanide Ions. *Angew. Chem., Int. Ed.* **2018**, *57* (21), 6042−6048.
(521) Sun, Q.; Aguila, B.; Earl, L. D.; Abney, C. W.; Wojtas, L.; Thallapally, P. K.; Ma, S. Covalent Organic Frameworks as a Decorating Platform for Utilization and Affinity Enhancement of Chelating Sites for Radionuclide Sequestration. *Adv. Mater.* **2018**, *30*, 1705479.
(522) Niu, X.; Ding, S.; Wang, W.; Xu, Y.; Xu, Y.; Chen, H.; Chen, X. Separation of Small Organic Molecules Using Covalent Organic Frameworks−LZU1 as Stationary Phase by Open-Tubular Capillary Electrochromatography. *J. Chromatogr. A* **2016**, *1436*, 109−117.
(523) He, S.; Zeng, T.; Wang, S.; Niu, H.; Cai, Y. Facile Synthesis of Magnetic Covalent Organic Framework with Three−Dimensional Bouquet-Like Structure for Enhanced Extraction of Organic Targets. *ACS Appl. Mater. Interfaces* **2017**, *9*, 2959−2965.
(524) Li, Y.; Yang, C.-X.; Yan, X.-P. Controllable Preparation of Core−Shell Magnetic Covalent-Organic Framework Nanospheres for Efficient Adsorption and Removal of Bisphenols in Aqueous Solution. *Chem. Commun.* **2017**, *53*, 2511−2514.
(525) Liu, Z.; Wang, H.; Ou, J.; Chen, L.; Ye, M. Construction of Hierarchically Porous Monoliths from Covalent Organic Frameworks (COFs) and Their Application for Bisphenol A Removal. *J. Hazard. Mater.* **2018**, *355*, 145−153.
(526) Wang, R.-Q.; Wei, X.-B.; Feng, Y.-Q. β−Cyclodextrin Covalent Organic Framework for Selective Molecular Adsorption. *Chem. - Eur. J.* **2018**, *24*, 10979−10983.
(527) Gao, W.; Tian, Y.; Liu, H.; Cai, Y.; Liu, A.; Yu, Y.-L.; Zhao, Z.; Jiang, G. Ultrasensitive Determination of Tetrabromobisphenol a by Covalent Organic Framework Based Solid Phase Microextraction Coupled with Constant Flow Desorption Ionization Mass Spectrometry. *Anal. Chem.* **2019**, *91*, 772−775.
(528) Lin, G.; Gao, C.; Zheng, Q.; Lei, Z.; Geng, H.; Lin, Z.; Yang, H.; Cai, Z. Room-Temperature Synthesis of Core−Shell Structured Magnetic Covalent Organic Frameworks for Efficient Enrichment of Peptides and Simultaneous Exclusion of Proteins. *Chem. Commun.* **2017**, *53*, 3649−3652.
(529) Wang, H.; Jiao, F.; Gao, F.; Lv, Y.; Wu, Q.; Zhao, Y.; Shen, Y.; Zhang, Y.; Qian, X. Titanium(IV) Ion-Modified Covalent Organic Frameworks for Specific Enrichment of Phosphopeptides. *Talanta* **2017**, *166*, 133−140.
(530) Mellah, A.; Fernandes, S. P. S.; Rodríguez, R.; Otero, J.; Paz, J.; Cruces, J.; Medina, D. D.; Djamila, H.; Espiña, B.; Salonen, L. M. Adsorption of Pharmaceutical Pollutants from Water Using Covalent Organic Frameworks. *Chem. - Eur. J.* **2018**, *24*, 10601−10605.
(531) Liu, C.; Park, E.; Jin, Y.; Liu, J.; Yu, Y.; Zhang, W.; Lei, S.; Hu, W. Separation of Arylenevinylene Macrocycles with a Surface−Confined Two−Dimensional Covalent Organic Framework. *Angew. Chem., Int. Ed.* **2018**, *57*, 8984−8988.
(532) Ji, W.; Xiao, L.; Ling, Y.; Ching, C.; Matsumoto, M.; Bisbey, R. P.; Helbling, D. E.; Dichtel, W. R. Removal of Genx and Perfluorinated Alkyl Substances from Water by Amine-Functionalized Covalent Organic Frameworks. *J. Am. Chem. Soc.* **2018**, *140*, 12677−12681.
(533) Lohse, M. S.; Stassin, T.; Naudin, G.; Wuttke, S.; Ameloot, R.; De Vos, D.; Medina, D. D.; Bein, T. Sequential Pore Wall Modification in a Covalent Organic Framework for Application in Lactic Acid Adsorption. *Chem. Mater.* **2016**, *28*, 626−631.
(534) Ning, G.-H.; Chen, Z.; Gao, Q.; Tang, W.; Chen, Z.; Liu, C.; Tian, B.; Li, X.; Loh, K. P. Salicylideneanilines−Based Covalent Organic Frameworks as Chemoselective Molecular Sieves. *J. Am. Chem. Soc.* **2017**, *139*, 8897−8904.
(535) Rogge, S. M. J.; Bavykina, A.; Hajek, J.; Garcia, H.; Olivos-Suarez, A. I.; Sepúlveda-Escribano, A.; Vimont, A.; Clet, G.; Bazin, P.; Kapteijn, F.; et al. Metal−Organic and Covalent Organic Frameworks as Single−Site Catalysts. *Chem. Soc. Rev.* **2017**, *46* (11), 3134−3184.
(536) Medina, D. D.; Sick, T.; Bein, T. Photoactive and Conducting Covalent Organic Frameworks. *Adv. Energy Mater.* **2017**, *7*, 1700387.
(537) Wei, P.-F.; Qi, M.-Z.; Wang, Z.-P.; Ding, S.-Y.; Yu, W.; Liu, Q.; Wang, L.-K.; Wang, H.-Z.; An, W.-K.; Wang, W. Benzoxazole−Linked Ultrastable Covalent Organic Frameworks for Photocatalysis. *J. Am. Chem. Soc.* **2018**, *140*, 4623−4631.
(538) Banerjee, T.; Gottschling, K.; Savasci, G.; Ochsenfeld, C.; Lotsch, B. V. H_2 Evolution with Covalent Organic Framework Photocatalysts. *ACS Energy Lett.* **2018**, *3*, 400−409.
(539) Yan, Y.; He, T.; Zhao, B.; Qi, K.; Liu, H.; Xia, B. Y. Metal/Covalent−Organic Frameworks−Based Electrocatalysts for Water Splitting. *J. Mater. Chem. A* **2018**, *6*, 15905−15926.
(540) He, T.; Geng, K.; Jiang, D. Engineering Covalent Organic Frameworks for Light-Driven Hydrogen Production from Water. *ACS Materials Lett.* **2019**, *1*, 203−208.
(541) Schwinghammer, K.; Tuffy, B.; Mesch, M. B.; Wirnhier, E.; Martineau, C.; Taulelle, F.; Schnick, W.; Senker, J.; Lotsch, B. V. Triazine−Based Carbon Nitrides for Visible−Light−Driven Hydrogen Evolution. *Angew. Chem., Int. Ed.* **2013**, *52*, 2435−2439.
(542) Zhang, J.; Chen , X.; Takanabe, K.; Maeda, K.; Domen, K.; Epping, J. D.; Fu, X.; Antonietti, M.; Wang , X. Synthesis of a Carbon Nitride Structure for Visible−Light Catalysis by Copolymerization. *Angew. Chem., Int. Ed.* **2010**, *49*, 441−444.
(543) Chen, W.; Yang, Z.; Xie, Z.; Li, Y.; Yu, X.; Lu, F.; Chen, L. Benzothiadiazole Functionalized D−A Type Covalent Organic Frameworks for Effective Photocatalytic Reduction of Aqueous Chromium (VI). *J. Mater. Chem. A* **2019**, *7*, 998−1004.
(544) Banerjee, T.; Haase, F.; Savasci, G.; Gottschling, K.; Ochsenfeld, C.; Lotsch, B. V. Single-Site Photocatalytic H_2 Evolution from Covalent Organic Frameworks with Molecular Cobaloxime Co-Catalysts. *J. Am. Chem. Soc.* **2017**, *139*, 16228−16234.

https://dx.doi.org/10.1021/acs.chemrev.9b00550
Chem. Rev. 2020, 120, 8814−8933

(545) Pachfule, P.; Acharjya, A.; Roeser, J.; Langenhahn, T.; Schwarze, M.; Schomäcker, R.; Thomas, A.; Schmidt, J. Diacetylene Functionalized Covalent Organic Framework (COF) for Photocatalytic Hydrogen Generation. *J. Am. Chem. Soc.* **2018**, *140*, 1423−1427.
(546) Stegbauer, L.; Zech, S.; Savasci, G.; Banerjee, T.; Podjaski, F.; Schwinghammer, K.; Ochsenfeld, C.; Lotsch, B. V. Tailor−Made Photoconductive Pyrene−Based Covalent Organic Frameworks for Visible−Light Driven Hydrogen Generation. *Adv. Energy Mater.* **2018**, *8*, 1703278.
(547) Thote, J.; Aiyappa, H. B.; Deshpande, A.; Diaz Diaz, D.; Kurungot, S.; Banerjee, R. A Covalent Organic Framework-Cadmium Sulfide Hybrid as a Prototype Photocatalyst for Visible-Light-Driven Hydrogen Production. *Chem. - Eur. J.* **2014**, *20*, 15961−5.
(548) Wang, X.; Chen, L.; Chong, S. Y.; Little, M. A.; Wu, Y.; Zhu, W.-H.; Clowes, R.; Yan, Y.; Zwijnenburg, M. A.; Sprick, R. S.; Cooper, A. I. Sulfone-Containing Covalent Organic Frameworks for Photocatalytic Hydrogen Evolution from Water. *Nat. Chem.* **2018**, *10*, 1180−1189.
(549) Jin, E.; Lan, Z.; Jiang, Q.; Geng, K.; Li, G.; Wang, X.; Jiang, D. 2D sp^2 Carbon−Conjugated Covalent Organic Frameworks for Photocatalytic Hydrogen Production from Water. *Chem.* **2019**, *5*, 1632−1647.
(550) Wang, C.; Xie, Z.; deKrafft, K. E.; Lin, W. Doping Metal−Organic Frameworks for Water Oxidation, Carbon Dioxide Reduction, and Organic Photocatalysis. *J. Am. Chem. Soc.* **2011**, *133*, 13445−13454.
(551) Xu, C.; Liu, H.; Li, D.; Su, J.-H.; Jiang, H.-L. Direct Evidence of Charge Separation in a Metal−Organic Framework: Efficient and Selective Photocatalytic Oxidative Coupling of Amines via Charge and Energy Transfer. *Chem.Sci.* **2018**, *9*, 3152−3158.
(552) Yadav, R. K.; Kumar, A.; Park, N.-J.; Kong, K.-J.; Baeg, J.-O. A Highly Efficient Covalent Organic Framework Film Photocatalyst for Selective Solar Fuel Production from CO_2. *J. Mater. Chem. A* **2016**, *4*, 9413−9418.
(553) Ma, W.; Yu, P.; Ohsaka, T.; Mao, L. An Efficient Electrocatalyst for Oxygen Reduction Reaction Derived from a Co-Porphyrin-Based Covalent Organic Framework. *Electrochem. Commun.* **2015**, *52*, 53−57.
(554) Wu, J.; Yang, H. Platinum-Based Oxygen Reduction Electrocatalysts. *Acc. Chem. Res.* **2013**, *46*, 1848−1857.
(555) Lin, C.-Y.; Zhang, L.; Zhao, Z.; Xia, Z. Design Principles for Covalent Organic Frameworks as Efficient Electrocatalysts in Clean Energy Conversion and Green Oxidizer Production. *Adv. Mater.* **2017**, *29*, 1606635.
(556) Wu, D.; Xu, Q.; Qian, J.; Li, X.; Sun, Y. Bimetallic Covalent Organic Frameworks for Constructing Multifunctional Electrocatalyst. *Chem. - Eur. J.* **2019**, *25*, 3105−3111.
(557) Xu, Q.; Tang, Y.; Zhai, L.; Chen, Q.; Jiang, D. Pyrolysis of Covalent Organic Frameworks: A General Strategy for Template Converting Conventional Skeletons into Conducting Microporous Carbons for High-Performance Energy Storage. *Chem. Commun.* **2017**, *53*, 11690−11693.
(558) Xia, B. Y.; Yan, Y.; Li, N.; Wu, H. B.; Lou, X. W.; Wang, X. A Metal−Organic Framework-Derived Bifunctional Oxygen Electrocatalyst. *Nat. Energy* **2016**, *1*, 15006.
(559) Tang, C.; Wang, H.-F.; Chen, X.; Li, B.-Q.; Hou, T.-Z.; Zhang, B.; Zhang, Q.; Titirici, M.-M.; Wei, F. Topological Defects in Metal−Free Nanocarbon for Oxygen Electrocatalysis. *Adv. Mater.* **2016**, *28*, 6845−6851.
(560) Surendranath, Y.; Kanan, M. W.; Nocera, D. G. Mechanistic Studies of the Oxygen Evolution Reaction by a Cobalt−Phosphate Catalyst at Neutral Ph. *J. Am. Chem. Soc.* **2010**, *132*, 16501−16509.
(561) Pintado, S.; Goberna-Ferrón, S.; Escudero-Adán, E. C.; Galán-Mascarós, J. R. Fast and Persistent Electrocatalytic Water Oxidation by Co−Fe Prussian Blue Coordination Polymers. *J. Am. Chem. Soc.* **2013**, *135*, 13270−13273.
(562) Ahn, H. S.; Tilley, T. D. Electrocatalytic Water Oxidation at Neutral Ph by a Nanostructured $Co(PO_3)_2$ Anode. *Adv. Funct. Mater.* **2013**, *23*, 227−233.
(563) Zhu, Y.; Zhou, W.; Chen, Y.; Yu, J.; Liu, M.; Shao, Z. A High-Performance Electrocatalyst for Oxygen Evolution Reaction: $LiCo_{0.8}Fe_{0.2}O_2$. *Adv. Mater.* **2015**, *27*, 7150−7155.
(564) McCrory, C. C. L.; Jung, S.; Peters, J. C.; Jaramillo, T. F. Benchmarking Heterogeneous Electrocatalysts for the Oxygen Evolution Reaction. *J. Am. Chem. Soc.* **2013**, *135*, 16977−16987.
(565) Yang, S.; Hu, W.; Zhang, X.; He, P.; Pattengale, B.; Liu, C.; Cendejas, M.; Hermans, I.; Zhang, X.; Zhang, J.; Huang, J. 2D Covalent Organic Frameworks as Intrinsic Photocatalysts for Visible Light−Driven CO_2 Reduction. *J. Am. Chem. Soc.* **2018**, *140*, 14614−14618.
(566) Wang, Y.; Chen, J.; Wang, G.; Li, Y.; Wen, Z. Perfluorinated Covalent Triazine Framework Derived Hybrids for the Highly Selective Electroconversion of Carbon Dioxide into Methane. *Angew. Chem.* **2018**, *130*, 13304−13308.
(567) Su, P.; Iwase, K.; Harada, T.; Kamiya, K.; Nakanishi, S. Covalent Triazine Framework Modified with Coordinatively−Unsaturated Co or Ni Atoms for CO_2 Electrochemical Reduction. *Chem. Sci.* **2018**, *9*, 3941−3947.
(568) Liu, G.; Sheng, J.; Zhao, Y. Chiral Covalent Organic Frameworks for Asymmetric Catalysis and Chiral Separation. *Sci. China: Chem.* **2017**, *60*, 1015−1022.
(569) Wu, C.-D.; Hu, A.; Zhang, L.; Lin, W. A Homochiral Porous Metal−Organic Framework for Highly Enantioselective Heterogeneous Asymmetric Catalysis. *J. Am. Chem. Soc.* **2005**, *127*, 8940−8941.
(570) Ma, L.; Falkowski, J. M.; Abney, C.; Lin, W. A Series of Isoreticular Chiral Metal−Organic Frameworks as a Tunable Platform for Asymmetric Catalysis. *Nat. Chem.* **2010**, *2*, 838−846.
(571) Zhang, J.; Han, X.; Wu, X.; Liu, Y.; Cui, Y. Multivariate Chiral Covalent Organic Frameworks with Controlled Crystallinity and Stability for Asymmetric Catalysis. *J. Am. Chem. Soc.* **2017**, *139*, 8277−8285.
(572) Lun, D. J.; Waterhouse, G. I. N.; Telfer, S. G. A General Thermolabile Protecting Group Strategy for Organocatalytic Metal−Organic Frameworks. *J. Am. Chem. Soc.* **2011**, *133*, 5806−5809.
(573) Banerjee, M.; Das, S.; Yoon, M.; Choi, H. J.; Hyun, M. H.; Park, S. M.; Seo, G.; Kim, K. Postsynthetic Modification Switches an Achiral Framework to Catalytically Active Homochiral Metal−Organic Porous Materials. *J. Am. Chem. Soc.* **2009**, *131*, 7524−7525.
(574) Dang, D.; Wu, P.; He, C.; Xie, Z.; Duan, C. Homochiral Metal−Organic Frameworks for Heterogeneous Asymmetric Catalysis. *J. Am. Chem. Soc.* **2010**, *132*, 14321−14323.
(575) Kutzscher, C.; Nickerl, G.; Senkovska, I.; Bon, V.; Kaskel, S. Proline Functionalized UiO-67 and UiO-68 Type Metal−Organic Frameworks Showing Reversed Diastereoselectivity in Aldol Addition Reactions. *Chem. Mater.* **2016**, *28*, 2573−2580.
(576) Han, X.; Xia, Q.; Huang, J.; Liu, Y.; Tan, C.; Cui, Y. Chiral Covalent Organic Frameworks with High Chemical Stability for Heterogeneous Asymmetric Catalysis. *J. Am. Chem. Soc.* **2017**, *139*, 8693−8697.
(577) Song, F.; Wang, C.; Falkowski, J. M.; Ma, L.; Lin, W. Isoreticular Chiral Metal−Organic Frameworks for Asymmetric Alkene Epoxidation: Tuning Catalytic Activity by Controlling Framework Catenation and Varying Open Channel Sizes. *J. Am. Chem. Soc.* **2010**, *132*, 15390−15398.
(578) Xia, Q.; Liu, Y.; Li, Z.; Gong, W.; Cui, Y. A Cr(Salen)-Based Metal−Organic Framework as a Versatile Catalyst for Efficient Asymmetric Transformations. *Chem. Commun.* **2016**, *52*, 13167−13170.
(579) Xi, W.; Liu, Y.; Xia, Q.; Li, Z.; Cui, Y. Direct and Post−Synthesis Incorporation of Chiral Metallosalen Catalysts into Metal−Organic Frameworks for Asymmetric Organic Transformations. *Chem. - Eur. J.* **2015**, *21*, 12581−12585.
(580) Wang, C. A.; Zhang, Z. K.; Yue, T.; Sun, Y. L.; Wang, L.; Wang, W. D.; Zhang, Y.; Liu, C.; Wang, W. Bottom-up" Embedding of the Jørgensen−Hayashi Catalyst into a Chiral Porous Polymer for Highly Efficient Heterogeneous Asymmetric Organocatalysis. *Chem. - Eur. J.* **2012**, *18*, 6718−6723.

https://dx.doi.org/10.1021/acs.chemrev.9b00550
Chem. Rev. 2020, 120, 8814−8933

(581) Leng, W.; Ge, R.; Dong, B.; Wang, C.; Gao, Y. Bimetallic Docked Covalent Organic Frameworks with High Catalytic Performance Towards Tandem Reactions. *RSC Adv.* **2016**, *6*, 37403−37406.
(582) Gonçalves, R. S. B.; de Oliveira, A. B. V.; Sindra, H. C.; Archanjo, B. S.; Mendoza, M. E.; Carneiro, L. S. A.; Buarque, C. D.; Esteves, P. M. Heterogeneous Catalysis by Covalent Organic Frameworks (COF): $Pd(OAc)_2$@COF-300 in Cross-Coupling Reactions. *ChemCatChem* **2016**, *8*, 743−750.
(583) Llabrés i Xamena, F. X.; Abad, A.; Corma, A.; Garcia, H. MOFs as Catalysts: Activity, Reusability and Shape-Selectivity of a Pd-Containing MOF. *J. Catal.* **2007**, *250*, 294−298.
(584) Budroni, G.; Corma, A.; García, H.; Primo, A. Pd Nanoparticles Embedded in Sponge-Like Porous Silica as a Suzuki−Miyaura Catalyst: Similarities and Differences with Homogeneous Catalysts. *J. Catal.* **2007**, *251*, 345−353.
(585) Vardhan, H.; Verma, G.; Ramani, S.; Nafady, A.; Al-Enizi, A. M.; Pan, Y.; Yang, Z.; Yang, H.; Ma, S. Covalent Organic Framework Decorated with Vanadium as a New Platform for Prins Reaction and Sulfide Oxidation. *ACS Appl. Mater. Interfaces* **2019**, *11*, 3070−3079.
(586) Opanasenko, M.; Dhakshinamoorthy, A.; Hwang, Y. K.; Chang, J.-S.; Garcia, H.; Čejka, J. Superior Performance of Metal−Organic Frameworks over Zeolites as Solid Acid Catalysts in the Prins Reaction: Green Synthesis of Nopol. *ChemSusChem* **2013**, *6*, 865−871.
(587) Villa de P., A. L.; Alarcón, E.; Montes de Correa, C. Synthesis of Nopol over MCM-41 Catalysts. *Chem. Commun.* **2002**, 2654−2655.
(588) Yu, D.; Gao, W.; Xing, S.; Lian, L.; Zhang, H.; Wang, X.; lou, D. Fe-Doped $H_3PMo_{12}O_{40}$ Immobilized on Covalent Organic Frameworks (Fe/PMA@ COFs): A Heterogeneous Catalyst for the Epoxidation of Cyclooctene with H_2O_2. *RSC Adv.* **2019**, *9*, 4884−4891.
(589) Han, Y.; Zhang, M.; Zhang, Y.-Q.; Zhang, Z.-H. Copper Immobilized at a Covalent Organic Framework: An Efficient and Recyclable Heterogeneous Catalyst for the Chan−Lam Coupling Reaction of Aryl Boronic Acids and Amines. *Green Chem.* **2018**, *20*, 4891−4900.
(590) Pachfule, P.; Panda, M. K.; Kandambeth, S.; Shivaprasad, S. M.; Díaz, D. D.; Banerjee, R. Multifunctional and Robust Covalent Organic Framework−Nanoparticle Hybrids. *J. Mater. Chem. A* **2014**, *2*, 7944−7952.
(591) Bhadra, M.; Sasmal, H. S.; Basu, A.; Midya, S. P.; Kandambeth, S.; Pachfule, P.; Balaraman, E.; Banerjee, R. Predesigned Metal-Anchored Building Block for in Situ Generation of Pd Nanoparticles in Porous Covalent Organic Framework: Application in Heterogeneous Tandem Catalysis. *ACS Appl. Mater. Interfaces* **2017**, *9*, 13785−13792.
(592) Li, J.; Zhang, L.; Liu, X.; Shang, N.; Gao, S.; Feng, C.; Wang, C.; Wang, Z. Pd Nanoparticles Supported on a Covalent Triazine−Based Framework Material: An Efficient and Highly Chemoselective Catalyst for the Reduction of Nitroarenes. *New J. Chem.* **2018**, *42*, 9684−9689.
(593) Jagadeesh, R. V.; Natte, K.; Junge, H.; Beller, M. Nitrogen−Doped Graphene−Activated Iron-Oxide-Based Nanocatalysts for Selective Transfer Hydrogenation of Nitroarenes. *ACS Catal.* **2015**, *5*, 1526−1529.
(594) Datta, K. J.; Rathi, A. K.; Gawande, M. B.; Ranc, V.; Zoppellaro, G.; Varma, R. S.; Zboril, R. Base−Free Transfer Hydrogenation of Nitroarenes Catalyzed by Micro−Mesoporous Iron Oxide. *ChemCatChem* **2016**, *8*, 2351−2355.
(595) Kanagaraj, K.; Suresh, P.; Pitchumani, K. Per-6-Amino-β-Cyclodextrin as a Reusable Promoter and Chiral Host for Enantioselective Henry Reaction. *Org. Lett.* **2010**, *12*, 4070−4073.
(596) Mayani, V. J.; Abdi, S. H. R.; Kureshy, R. I.; Khan, N.-u. H.; Das, A.; Bajaj, H. C. Heterogeneous Chiral Copper Complexes of Amino Alcohol for Asymmetric Nitroaldol Reaction. *J. Org. Chem.* **2010**, *75*, 6191−6195.
(597) Lu, S.; Hu, Y.; Wan, S.; McCaffrey, R.; Jin, Y.; Gu, H.; Zhang, W. Synthesis of Ultrafine and Highly Dispersed Metal Nanoparticles Confined in a Thioether−Containing Covalent Organic Framework and Their Catalytic Applications. *J. Am. Chem. Soc.* **2017**, *139*, 17082−17088.
(598) Yiu, H. H. P.; Wright, P. A.; Botting, N. P. Enzyme Immobilisation Using SBA-15 Mesoporous Molecular Sieves with Functionalised Surfaces. *J. Mol. Catal. B: Enzym.* **2001**, *15*, 81−92.
(599) Johnson, W.; Makame, Y. M.; Mkayula, L. L. Immobilization of Trypsin onto Macroporous Monolithic Poly (Epoxy-Acrylamide) Cryogels. *TaJONAS: Tanz. J. Nat. Appl. Sci.* **2012**, *2*, 382−392.
(600) Sun, Q.; Fu, C.-W.; Aguila, B.; Perman, J.; Wang, S.; Huang, H.-Y.; Xiao, F.-S.; Ma, S. Pore Environment Control and Enhanced Performance of Enzymes Infiltrated in Covalent Organic Frameworks. *J. Am. Chem. Soc.* **2018**, *140*, 984−992.
(601) Liu, J.; Bai, S.; Jin, Q.; Zhong, H.; Li, C.; Yang, Q. Improved Catalytic Performance of Lipase Accommodated in the Mesoporous Silicas with Polymer-Modified Microenvironment. *Langmuir* **2012**, *28*, 9788−9796.
(602) Weiser, D.; Sóti, P. L.; Bánóczi, G.; Bódai, V.; Kiss, B.; Gellért, Á.; Nagy, Z. K.; Koczka, B.; Szilágyi, A.; Marosi, G.; Poppe, L. Bioimprinted Lipases in PVA Nanofibers as Efficient Immobilized Biocatalysts. *Tetrahedron* **2016**, *72*, 7335−7342.
(603) Sun, Q.; Aguila, B.; Perman, J.; Nguyen, N.; Ma, S. Flexibility Matters: Cooperative Active Sites in Covalent Organic Framework and Threaded Ionic Polymer. *J. Am. Chem. Soc.* **2016**, *138*, 15790−15796.
(604) Gole, B.; Bar, A. K.; Mallick, A.; Banerjee, R.; Mukherjee, P. S. An Electron Rich Porous Extended Framework as a Heterogeneous Catalyst for Diels−Alder Reactions. *Chem. Commun.* **2013**, *49*, 7439−7441.
(605) Liu, T.-T.; Xu, R.; Yi, J.-D.; Liang, J.; Wang, X.-S.; Shi, P.-C.; Huang, Y.-B.; Cao, R. Imidazolium-Based Cationic Covalent Triazine Frameworks for Highly Efficient Cycloaddition of Carbon Dioxide. *ChemCatChem* **2018**, *10*, 2036−2040.
(606) Yu, W.; Gu, S.; Fu, Y.; Xiong, S.; Pan, C.; Liu, Y.; Yu, G. Carbazole-Decorated Covalent Triazine Frameworks: Novel Nonmetal Catalysts for Carbon Dioxide Fixation and Oxygen Reduction Reaction. *J. Catal.* **2018**, *362*, 1−9.
(607) Zhi, Y.; Shao, P.; Feng, X.; Xia, H.; Zhang, Y.; Shi, Z.; Mu, Y.; Liu, X. Covalent Organic Frameworks: Efficient, Metal-Free, Heterogeneous Organocatalysts for Chemical Fixation of CO_2 under Mild Conditions. *J. Mater. Chem. A* **2018**, *6*, 374−382.
(608) Mitra, S.; Kandambeth, S.; Biswal, B. P.; Khayum M., A.; Choudhury, C. K.; Mehta, M.; Kaur, G.; Banerjee, S.; Prabhune, A.; Verma, S.; Roy, S.; Kharul, U. K.; Banerjee, R. Self-Exfoliated Guanidinium-Based Ionic Covalent Organic Nanosheets (iCONs). *J. Am. Chem. Soc.* **2016**, *138*, 2823−2828.
(609) Alhmoud, H.; Delalat, B.; Elnathan, R.; Cifuentes-Rius, A.; Chaix, A.; Rogers, M. L.; Durand, J. O.; Voelcker, N. H. Porous Silicon Nanodiscs for Targeted Drug Delivery. *Adv. Funct. Mater.* **2015**, *25*, 1137−1145.
(610) Mitra, S.; Sasmal, H. S.; Kundu, T.; Kandambeth, S.; Illath, K.; Díaz Díaz, D.; Banerjee, R. Targeted Drug Delivery in Covalent Organic Nanosheets (CONs) Via Sequential Postsynthetic Modification. *J. Am. Chem. Soc.* **2017**, *139*, 4513−4520.
(611) Zhang, G.; Li, X.; Liao, Q.; Liu, Y.; Xi, K.; Huang, W.; Jia, X. Water-Dispersible Peg-Curcumin/Amine-Functionalized Covalent Organic Framework Nanocomposites as Smart Carriers for in Vivo Drug Delivery. *Nat. Commun.* **2018**, *9*, 2785.

NOTE ADDED AFTER ASAP PUBLICATION

This paper was posted ASAP on January 22, 2020. An author name was added, and the paper was reposted on March 27, 2020.

https://dx.doi.org/10.1021/acs.chemrev.9b00550
Chem. Rev. 2020, 120, 8814−8933